JOURNAL
OF
APPLIED PHYSICS

ber

32

0

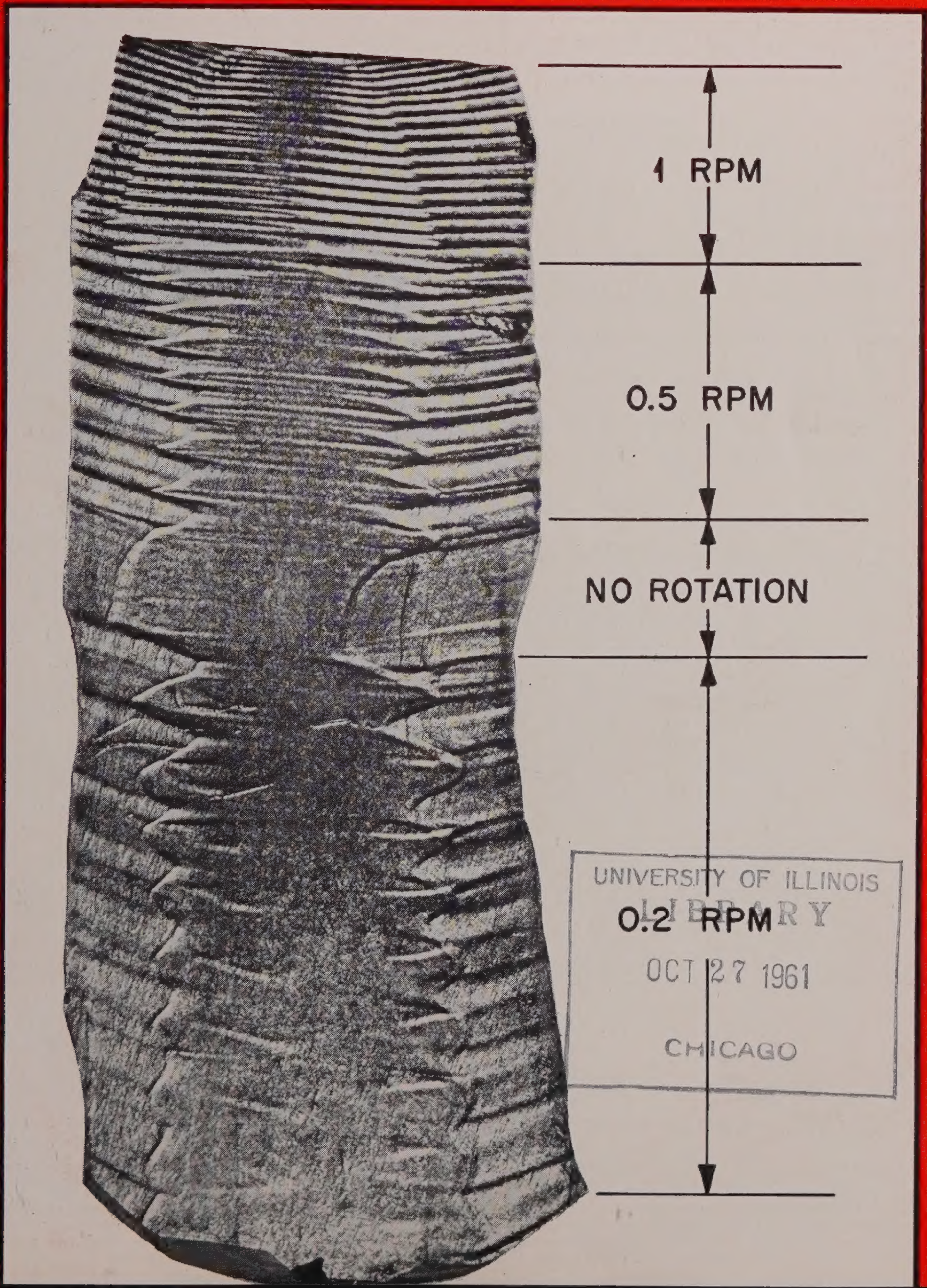

UNIVERSITY OF ILLINOIS
LIBRARY
OCT 27 1961
CHICAGO

Growth
Striations
in InSb wit
and withou
Rotation

See Page 205

TEKTRONIX TRANSISTOR-CURVE TRACER

INVALUABLE TOOL FOR EVALUATING SEMICONDUCTOR DEVICES

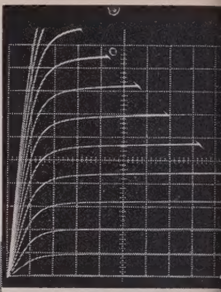

Family of characteristic curves (for NPN transistor).

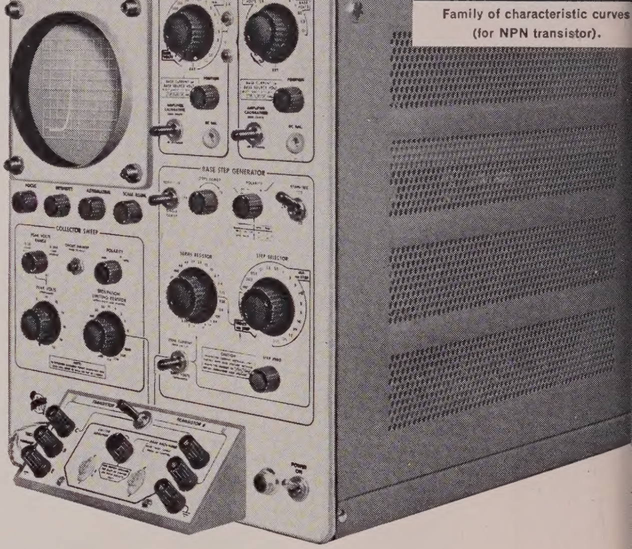

The Type 575 provides 20-ampere collector displays (10-ampere average supply current), two ranges of collector supply (0 to 20 volts, 0 to 200 volts), and 2.4-ampere base supply (positive or negative base stepping).

With a Type 575, you can plot and measure 7 different transistor characteristics. You can display 4 to 12 curves per family—with input current from 1 microampere/step to 200 milliamperes/step or input voltage from 10 millivolts/step to 200 millivolts/step—in repetitive or single-family presentations. You can select either common-emitter or common-base configurations.

Add a Type 175 Adapter and you extend the range of collector displays 10 times and the range of base supply 5 times.

You can also test diodes under a wide variety of conditions and observe waveform characteristics on the 5-inch crt with a high degree of accuracy.

Type 575 Calibrated Displays

Vertical Axis—Collector Current, 16 steps from 0.01 ma/div to 1000 ma/div. Pushbuttons are provided for multiplying each current step by 2 and dividing by 10, increasing the current range to 0.001 ma/div to 2000 ma/div.

Horizontal Axis—Collector Voltage, 11 steps from 0.01 v/div to 20 v/div.

Both Axes—Base Voltage, 6 steps from 0.01 v/div to 0.5 v/div. Base Current, 17 steps from 0.001 ma/div to 200 ma/div. Base Source Voltage, 5 steps from 0.01 v/div to 0.2 v/div.

Type 575 Transistor-Curve Tracer $975

HIGH-CURRENT ADAPTER

For measuring high-powered semiconductor devices which exceed the current capabilities of a Type 575, ask your Tektronix Field Engineer about the Type 175 High-Current Adapter. Not intended for separate use, the Type 175 depends upon the circuitry and crt of a Type 575 to provide *200-ampere collector displays, three ranges of collector supply, and 12-ampere base supply*—for calibrated displays with Collector Current on the Vertical Axis and either Collector Voltage or Base Voltage on the Horizontal Axis.

Type 175 Transistor-Curve Tracer
High-Current Adapter $1425

HIGH-VOLTAGE TYPE 575

Supplied on order from your Tektronix Field Engineer is a special model of the Type 575 Transistor-Curve Tracer. Although similar to the Type 575, the special model provides much higher diode breakdown test voltage (*variable from zero to 1500 volts* at a maximum current of 1 milliampere) and also much higher Collector Supply (*up to 400 volts*, at 0.5 ampere).

For complete specifications of this special model—call your Tektronix Field Engineer.

Type 575 Mod 122C $1175

(prices f.o.b. factory)

. . . for more information about evaluating semiconductor devices with a Type 5 or other Tektronix test equipment, call your Tektronix Field Engineer. He will glad to assist you.

Tektronix, Inc. *P. O. BOX 500 · BEAVERTON, OREGON / MItchell 4-0161 · TWX—BEAV 311 · Cable: TEKTRONIX*

TEKTRONIX FIELD OFFICES: Albuquerque, N. Mex. • Atlanta, Ga. • Baltimore (Towson) Md. • Boston (Lexington) Mass. • Buffalo, N.Y. • Chicago (Park Ridge) Ill. • Cleveland, Ohio • Dallas, Texas • Dayton, Denver, Colo. • Detroit (Lathrup Village) Mich. • Endicott (Endwell) N.Y. • Greensboro, N.C. • Houston, Texas • Indianapolis, Ind. • Kansas City (Mission) Kan. • Los Angeles, Calif. Area (East Los An Encino • West Los Angeles) • Minneapolis, Minn. • Montreal, Quebec, Canada • New York City Area (Albertson, L.I., N.Y. • Stamford, Conn. • Union, N.J.) • Orlando, Fla. • Philadelphia, Pa. • Phoenix (Scottsdale) Portland, Oreg. • Poughkeepsie, N.Y. • San Diego, Calif. • San Francisco, Calif. Area (Lafayette, Palo Alto) • Seattle, Wash. • Syracuse, N.Y. • Toronto (Willowdale) Ont., Canada • Washington, D.C. (Annandale,

ENGINEERING REPRESENTATIVES: Kentron Hawaii Ltd., Honolulu, Hawaii. Tektronix is represented in twenty-five overseas countries by qualified engineering organizations.

European and African countries, the countries of Lebanon and Turkey, please contact TEKTRONIX INTERNATIONAL A.G., Terrassenweg 1A, Zug, Switzerland, for the name of your local engineering represent

JOURNAL OF APPLIED PHYSICS

Vol. 32, No. 10 OCTOBER, 1961

In This Issue

Ferromagnetic Resonance in Thin Magnetic Films at Radio Frequencies . . . Turner E. Hasty and Lee J. Boudreaux 1807
On the Possibility of Detecting Shock-Induced Second-Order Phase Transitions in Solids. The Equation of State of Invar . . . D. R. Curran 1811
Elastic-Plastic Transition in Copper Crystals as Determined by an Etch-Pit Technique . . . F. W. Young, Jr. 1815
Application of the Czochralski Method to Divalent Metal Fluorides . . . K. Nassau 1820
Properties of Heavily Doped n-Type Germanium . . . W. G. Spitzer, F. A. Trumbore, and R. A. Logan 1822
Nonlinear Effects of Z-Directed Spin Waves in Thin Films . . . Jerome I. Kaplan 1831
Growth of ZnSb Single Crystals . . . R. L. Eisner, R. Mazelsky, and W. A. Tiller 1833
Reflection of an Electron Beam from High-Frequency Fields . . . R. B. Hall and Sanborn C. Brown 1835
Effect of Reactor Fast Neutrons on Electron-Hole Recombination in Germanium . . . A. Czachor and J. Piekoszewski 1837
"Anomalous" Electron Double Diffraction . . . O. Haase and R. D. Heidenreich 1840
Observations on the Growth of α-Iron Single Crystals by Halogen Reduction . . . C. M. Wayman 1844
Effect of Torsional Deformation on Self-Diffusion in Silver . . . C. H. Lee and R. Maddin 1846
Curie Temperature of Some Garnets by the Differential Thermal Analysis Technique . . . A. Aharoni, E. H. Frei, Z. Scheidlinger, and M. Schieber 1851
Paramagnetic Resonance of Defects Introduced Near the Surface of Solids by Mechanical Damage . . . G. K. Walters and T. L. Estle 1854
Modification of the Koehler-Granato-Lücke Dislocation Damping Theory . . . J. C. Swartz and J. Weertman 1860
Dislocation Etch Pits on the Basal Plane of Zinc Crystals . . . H. S. Rosenbaum and M. M. Saffren 1866
Energy of a Crossed Grid of Screw Dislocations . . . James C. M. Li 1873
Generation and Distribution of Dislocations by Solute Diffusion . . . S. Prussin 1876
Superconductor-Transition Switching Time Measurements Using a Superconductive Radio-Frequency Mixer . . . Donald L. Feucht and James B. Woodford, Jr. 1882
Experimental Investigation of the Sumoto Effect . . . William F. Pickard 1888
Behavior of Exploding Gold Wires . . . T. J. Tucker 1894
Noise in InSb Photodiodes . . . B. R. Pagel and R. L. Petritz 1901
Microwave Harmonic Generation by Ferrimagnetic Crystals . . . D. D. Douthett, I. Kaufman, and A. S. Risley 1905
Radiation Enhancement of Bulk Diffusion in 10% Zn–90% Cu by 30-kev Ne$^+$ Ion Bombardment . . R. A. Arndt and R. L. Hines 1913
Single and Double Pile-Up of Dislocations in MgO Crystals . . . Y. T. Chou and R. W. Whitmore 1920
Open Circuit Voltages in the Cesium Diode . . . Fred N. Huffman 1927
Mechanism of Chemisorption, Place Exchange, and Oxidation on a (100) Nickel Surface . . . H. E. Farnsworth and Hannibal H. Madden, Jr. 1933
Attainment of Ultrahigh Vacua, Reduction in Surface Desorption, and the Adsorption of Hydrogen by Evaporated Molybdenum . . . Angus L. Hunt, Charles C. Damm, and Earl C. Popp 1937
X-Ray Polarizer . . . H. Cole, F. W. Chambers, and C. G. Wood 1942
Alternating Current Magnetohydrodynamic Generator . . . P. R. Smy 1946
On the Wear of Sapphire . . . R. P. Steijn 1951
Partial Rotation in Permalloy Films . . . S. Methfessel, S. Middelhoek, and H. Thomas 1959
Specific Heat of Superparamagnetic Particles . . . J. D. Livingston and C. P. Bean 1964
Effect of Electron Bombardment on the Near-Infrared Fluorescence of Single-Crystal CdS . . . B. A. Kulp 1966
Influence of the Hall Effect upon the Transverse Magnetoresistance in Indium Antimonide . . . Charles A. Simmons 1970
Use of Idealized Relaxation Spectra in the Interpretation of Experimental Results Concerning Polymer Solutions . . K. Walters 1975
Calculations of the Thermoelectric Parameters and the Maximum Figure of Merit for Acoustical Scattering . . Louis R. Testardi 1978
Experimental Study of the Interrelation between the Theory of Dislocations in Polycrystalline Media and Finite Amplitude Wave Propagation in Solids . . . James F. Bell 1982
Power Output Characteristics of a Ruby Laser . . . Malcolm L. Stitch 1994
Birefringence due to Dislocations in Glide Bands of Rocksalt Single Crystals . . . S. Mendelson 1999
Fast-Risetime Excitation Scheme to Achieve Nonequilibrium and Amplifying Carrier Distributions . . . George C. Dousmanis 2005
Semiconducting Stress Transducers Utilizing the Transverse and Shear Piezoresistance Effects . W. G. Pfann and R. N. Thurston 2008
Majority Carrier Magnetosurface Effect . . . Robert D. Larrabee 2019
Preparation of Monocrystalline Cuprous Oxide . . . Yukiko Ebisuzaki 2027
Conductivity of Seeded Atmospheric Pressure Plasmas . . . L. S. Frost 2029
Effect of Hydrostatic Pressure on the High-Temperature Steady-State Creep of Lead . . . B. M. Butcher and A. L. Ruoff 2036
Emission Fluctuations of Tungsten-Based Barium Dispenser Cathodes . . . I. Brodie 2039

Letters to the Editor:

Electron Emission from Reverse-Biased p-n Junctions in SiC . . . Lyle Patrick 2047
Corbino Disk . . . Milton Green 2047
On the Interpretation of Internal Friction Experiments on Strain Aging of Iron . . . J. C. Swartz 2048
Electron Spin Resonance in Powders . . . Gerald Burns 2048
Stress Dependence of the Piezoresistance Effect . . . Donald Long 2050
Spherical Lenses for Infrared and Microwaves . . . G. Toraldo di Francia 2051
Crystal Structure of Photoelectric Films of Cesium Antimonide . . . W. H. McCarroll 2051
On the Theoretical Limitation of a Radio Telescope in Determining the Sky Temperature Distribution . Y. T. Lo 2052
Probabilities for the Neon Laser Transitions . . . G. F. Koster and H. Statz 2054
Electron Beam Excitation of a Fabry-Perot Interferometer . . . Murray D. Sirkis, Robert J. Strain, and William E. Kunz 2055
Far Infrared and Microwave Detector . . . D. W. Goodwin and R. H. Jones 2056
Impurity Striations in Unrotated Crystals of InSb . H. C. Gatos, A. J. Strauss, M. C. Lavine, and T. C. Harmon 2057
Stress Optical Constants of Germanium . . . K. J. Schmidt-Tiedemann 2058
Effect of Frequency Modulation on Subsidiary Resonance in Ferrites . . . J. F. Ollom and H. L. Goldstein 2059
Thermionic Emission from Spherical Metallic Particles . . . M. S. Sodha 2059
Presence of Carbon in Gallium Phosphide Crystals . . . C. J. Frosch, M. Gershenzon, and L. Derick 2060
Erratum: A Theory for the Cathode Mechanism in Metal Vapor Arcs . . . T. H. Lee and Allan Greenwood 2061

Books Reviewed . . . 2061
Announcements . . . 2062
Index to Advertisers . . . xxx

JOURNAL OF APPLIED PHYSICS

A journal of general physics and its applications to other sciences and to industry

Published by the

American Institute of Physics

GOVERNING BOARD

Members

Ralph A. Sawyer, *Chairman*
James G. Baker
R. H. Bolt
Wallace R. Brode
Harvey Brooks
Dirk Brouwer
J. H. Elliott
Herbert A. Erf
N. S. Gingrich
S. A. Goudsmit
W. W. Havens, Jr.
W. V. Houston
Winston E. Kock
R. Bruce Lindsay
David L. MacAdam
H. Victor Neher
Leonard O. Olsen
C. J. Overbeck
Ray Pepinsky
S. L. Quimby
Ralph A. Sawyer
Francis W. Sears
Frederick Seitz
C. Guy Suits
Mary E. Warga
William R. Willets

ADMINISTRATION

Elmer Hutchisson
Director

Wallace Waterfall
Secretary and Treasurer

Henry A. Barton
Administrative Consultant

W. C. Kelly
Director of Education

Eugene H. Kone
Director of Public Relations

Hugh C. Wolfe
Director of Publications

Kathryn Setze
Assistant Treasurer

James E. Mills
Supervisor, Editorial Department

Sistina Greco
Circulation Manager

Edward Tober
Manager, Production and Distribution

Theodore Vorburger
Advertising Manager

Emily Wolf
Manager, Special Services

Editor
J. H. Crawford, Jr.

Assistant Editor
Ethel McMillan

Editorial Board

J. E. Goldman
J. L. Tuck
C. A. Wert
Herman A. Haus
C. Lester Hogan
R. S. Rivlin
Henry Hurwitz
James A. Krumhansl
C. P. Slichter

THE JOURNAL OF APPLIED PHYSICS is devoted to general physics and its applications to other sciences, to engineering, and to industry. Previous to 1937, this journal was called PHYSICS.

The JOURNAL OF APPLIED PHYSICS welcomes articles of two distinct kinds: (1) Descriptions of new results in experimental or theoretical physics which are of general interest to physicists. The author should explain his contribution in such a way that a physicist or engineer in another field of specialization can appreciate its objectives and essential features. (2) Critical reviews of particular areas of physics or surveys of extensive investigations at a single laboratory. Authors contemplating writing such should correspond with the Editor before they begin writing.

The JOURNAL OF APPLIED PHYSICS welcomes Letters to the Editor which are short [approximately four (4) typewritten pages] communications without abstracts. Timeliness, briefness, and degree of current importance of the subject matter will be of primary concern in the publication of Letters. Letters should not be looked upon as partial publication or announcement of more comprehensive work, but rather self-contained presentations in themselves.

Manuscripts should be submitted to the Editor, J. H. Crawford, Jr., Solid State Division, Oak Ridge National Laboratory, Oak Ridge, Tennessee. Authors should read the "Information for Contributors," facing page 1 of the January issue, before writing articles or letters. The *Style Manual* of the American Institute of Physics is also helpful to writers preparing manuscripts for journals published by the American Institute of Physics. It can be obtained for $1.00 from the American Institute of Physics, 335 East 45 Street, New York 17, New York.

Corrected proofs and all correspondence concerning papers in the process of publication should be addressed to the Supervisor, Editorial Department, American Institute of Physics, 335 East 45 Street, New York 17, New York.

Subscriptions, renewals, and orders for back numbers should be addressed to the American Institute of Physics, 335 East 45 Street, New York 17, New York.

Subscription Price	U.S. and Canada	Elsewhere
To members of member organizations of the American Institute of Physics and Affiliated Societies ..	$12.00	$13.00
To all others	14.00	16.00

Back Number Prices

Yearly back number rate when complete year is available: $17.00.
Single copies: $1.75 each (exception: March, 1958—$3.00 each).

Changes of address should be sent to the American Institute of Physics.

Advertising rates supplied on request. Orders, advertising copy, and cuts should be sent to the American Institute of Physics.

The Journal of Applied Physics is published monthly at Prince and Lemon Streets, Lancaster, Pennsylvania.
Second-class postage paid at Lancaster, Pa.

has contributed notably in developing the art of circuit analysis.

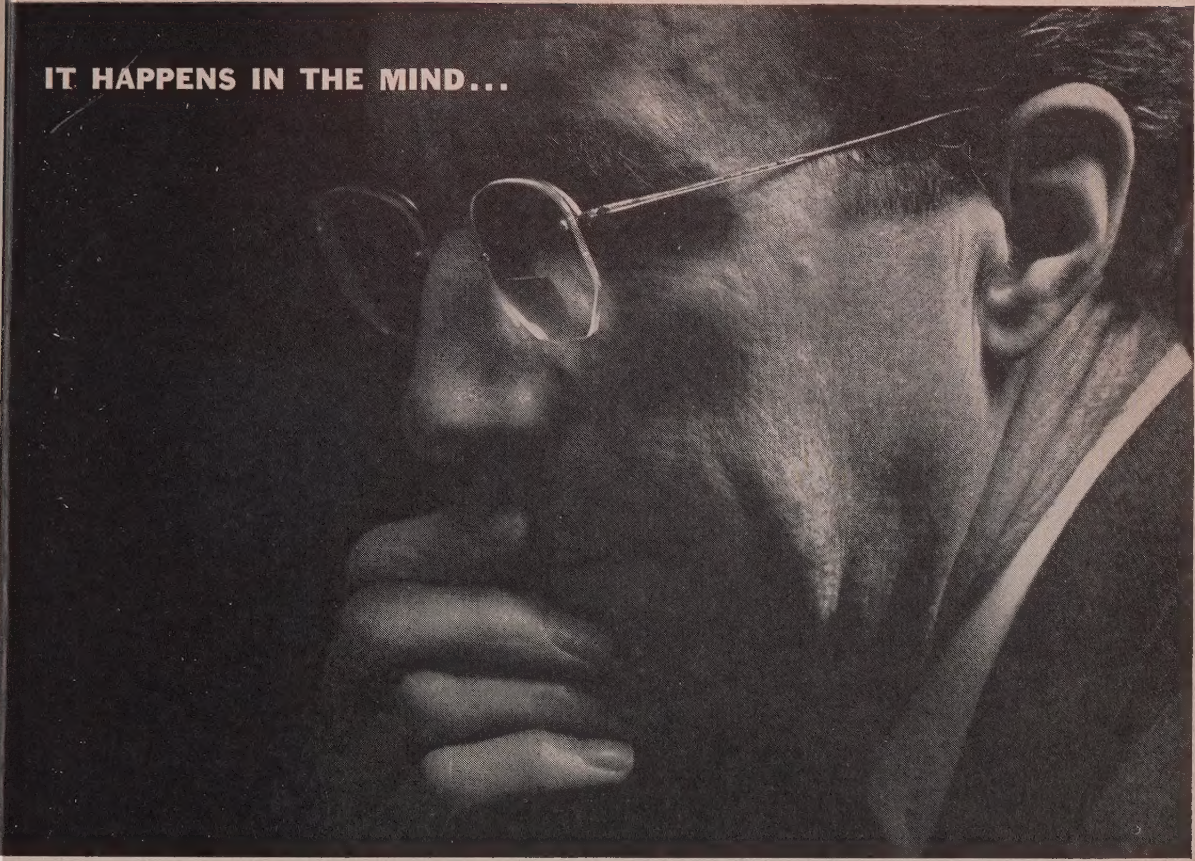
IT HAPPENS IN THE MIND...

. . . It is essentially a thing of the mind for it works through concepts, symbols and relationships . . . it helps man to analyze and synthesize the complex phenomena of the universe and himself . . . it works in many ways to advance electrical communications:

IT IS CALLED MATHEMATICS

At Bell Telephone Laboratories mathematics works powerfully to solve problems involving complex data. For example, engineers must design and synthesize complex systems to process specific signals in precisely controlled ways. At the same time the technology provides a wide choice of circuits and components. Mathematical circuit analysis reveals the circuits which can do the job most efficiently and economically.

Intriguingly, too, the mathematical approach leads to basically new knowledge. For example, it led to the invention of the electric wave filter . . . disclosed a kind of wave transmission which may some day carry huge amounts of information in waveguide systems . . . foretold the feasibility of modern quality control . . . led to a scientific technique for determining how many circuits must be provided for good service without having costly equipment lie idle.

In the continuing creation of new devices, technologies and systems, Bell Laboratories utilizes whatever serves best—mathematical analysis, laboratory experimentation, simulation with electronic computers. Together they assure the economical advancement of all Bell System communications services.

BELL TELEPHONE LABORATORIES

WORLD CENTER OF COMMUNICATIONS RESEARCH AND DEVELOPMENT

depth

The new Sperry Rand Research Center has been established to pursue a specific objective—the advancement of man's knowledge and understanding through basic research in the broad and diversified scientific fields that are of potential long-range interest to the many technical activities of the Sperry Rand Corporation.

To achieve this ambitious goal, many significant investigations must be pursued to great depths. Investigations in depth are vitally important to Sperry Rand in the following areas:

1. **Solid State Physics** including theoretical and experimental studies of magnetic, electrical, optical, chemical, and mechanical properties.
2. **Information Processing** including such areas as communication, information and coding theory; automatic control; modulation, generation and detection techniques; human factors.
3. **Plasma Physics** including electromagnetic wave interactions, reentry problems, propagation studies.
4. **Applied Mathematics** including probability and statistics, discrete mathematics, solid and fluid mechanics.
5. **Earth Sciences** including geophysics, physical oceanography, atmospheric physics, and special topics in Life Sciences.

At the present time professional openings are available to senior scientists with experience in:

- Semiconductor Physics
- Magnetic Resonance Phenomena
- Solid State Theory
- Physical Chemistry
- Communication Theory
- Signal Processing Theory & Application
- Automatic Control Theory
- Plasma Physics
- Wave Propagation
- Reentry Physics
- Stochastic Processes
- Game Theory
- Fluid & Solid Mechanics
- Operations Research
- Geophysics
- Oceanography
- Atmospheric Physics

Inquiries may be directed in complete confidence to:
Mr. Frederick M. Swope, Jr.,
Sperry Rand Research Center,
North Road,
Sudbury, Massachusetts

an important
word
at the new

SPERRY RAND RESEARCH CENTER

SUDBURY, MASSACHUSETTS

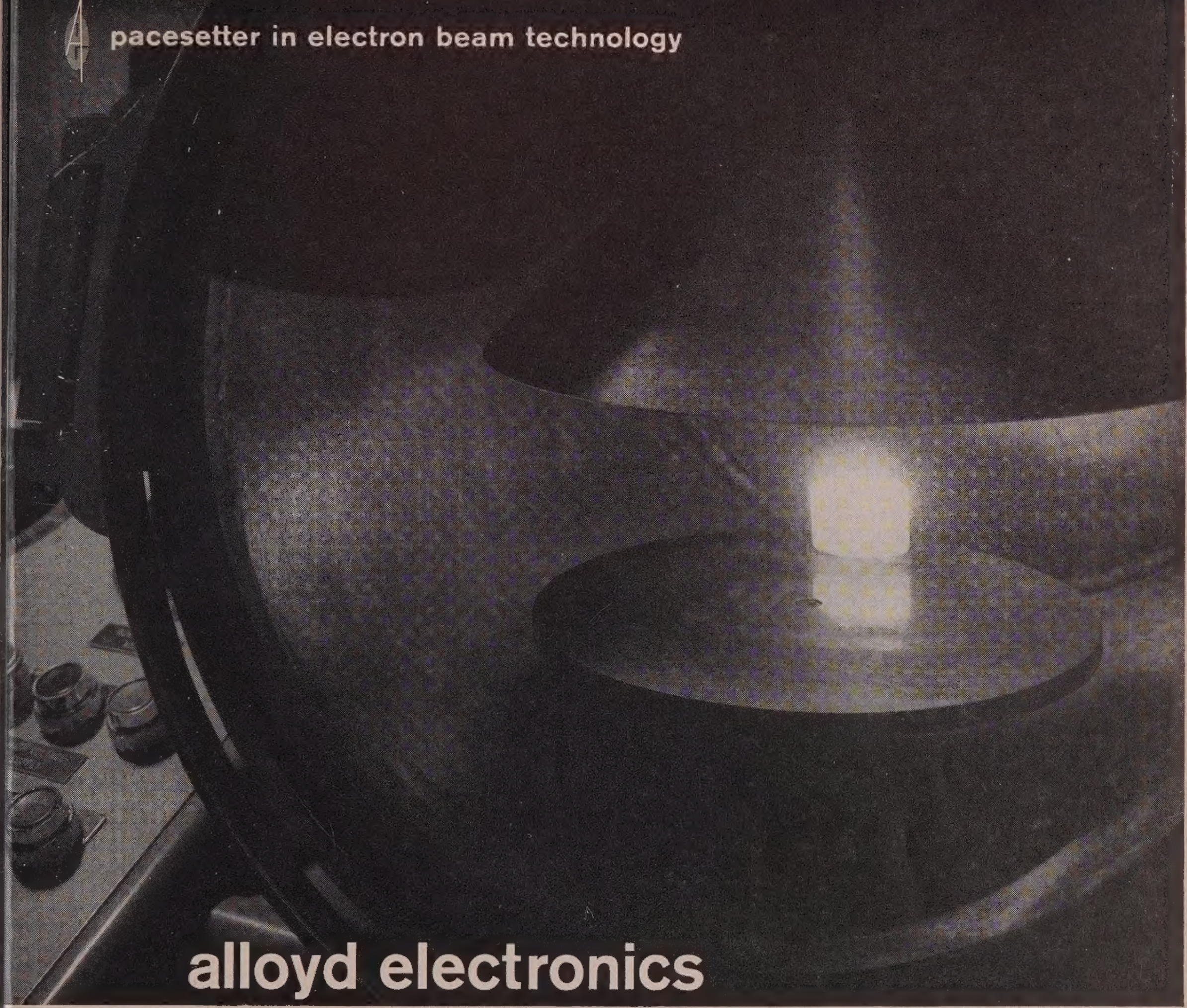

ntroduces the E-beam mark V electron beam evaporator

The Mark V Electron Beam Evaporator is a reasonably priced, highly flexible unit for producing thin metallic and n- metallic films by vapor deposition through electron bombardment heating.

Completely self-contained and free of any radiation hazard, it is an invaluable research and development or limited-oduction tool for thin-film applications, including micro-miniaturized electronic circuitry, optical filters, semicon-ctors, magnetic tapes, and countless other components.

Vacuum system, electron gun, power supply and controls are conveniently arranged for maximum accessibility d simplicity of operation and maintenance.

Only cooling water, electrical power, and low pressure air are needed to make the unit completely operative.

Flexibility is built in: modular design allows for interchangeable chambers, permitting the Mark V to be converted o a welder or a melter by substituting a modified chamber.

For complete information on the Mark V evaporator, the Mark VI welder, and Alloyd's engineering and custom vices in electron beam applications, just write:

alloyd electronics corporation

AN AFFILIATE OF THE ALLOYD CORPORATION,
37 CAMBRIDGE PARKWAY, CAMBRIDGE, MASSACHUSETTS

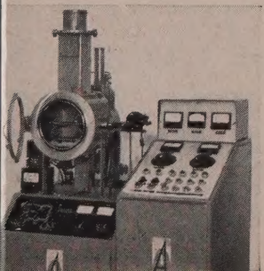

Mark VI Electron Beam Welder — for clean, crack-free welds in even the most refractory and reactive metals by electron bombardment. High vacuum eliminates contamination. Ultra-narrow heating zone permits optimum control and precision in handling very thin pieces or welding thin-to-thick sections.

AMEBA — Alloyd Modular Electron Beam Apparatus is part of an advanced, complete facility for thin film evaporation, welding, brazing, melting, and zone refining maintained by Alloyd to meet custom requirements. We also offer engineering, consulting, and research and development services in system design and development. Ask us for complete information.

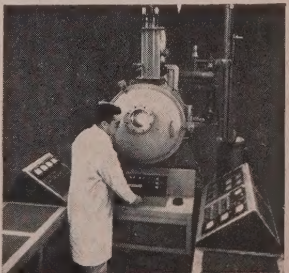

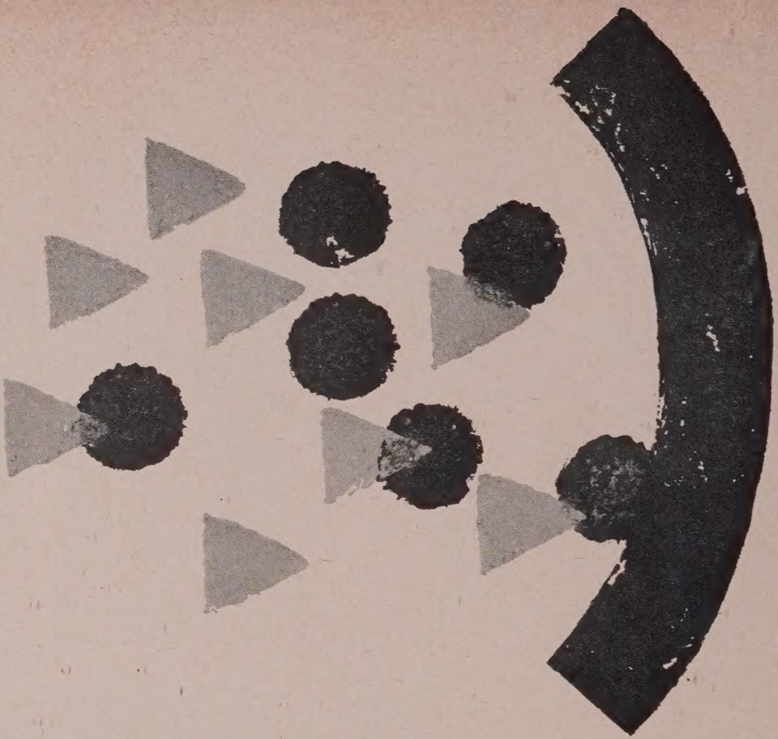

Said Michael Faraday: *"The amounts of different substances deposited or dissolved by t same quantity of electricity, are proportional to their chemical equivalent weights."*

Increasing requirements for pure, very thin films—especially those of ferro-magnetic elements and alloys—have beco critical. To break this bottleneck, one production method under investigation is a chemical process from an aqueous soluti —using metallic salts and a reducing agent.

Scientists at Lockheed Missiles & Space Company have conducted some highly successful experiments, in which extrem pure and thin ferro-magnetic film was deposited on such material as glass and plastics.

Thin film deposition is but one of many phenomena now being investigated at Lockheed Missiles & Space Company Sunnyvale and Palo Alto, California, on the beautiful San Francisco Peninsula. Engineers and scientists of outstanding tal and ability naturally gravitate to Lockheed. For here they can pursue their special fields of interest in an ideal environme

A leader in the aerospace field, Lockheed is Systems Manager for such programs as the DISCOVERER, MIDAS, and ot satellites, and the POLARIS FBM. Why not investigate future possibilities at Lockheed? Write Research and Developm Staff, Dept. M-28B, 962 West El Camino Real, Sunnyvale, California. U.S. citizenship or existing Department of Defe industrial security clearance required. An Equal Opportunity Employer.

LOCKHEED **MISSILES & SPACE COMPAN**

A GROUP DIVISION OF LOCKHEED AIRCRAFT CORPORAT

Systems Manager for the Navy POLARIS FBM and the Air Force AGENA Satellite in the DISCOVERER and MI programs. Other current programs include SAINT, ADVENT and such NASA projects as OGO, OAO, ECHO, and NIME

SUNNYVALE, PALO ALTO, VAN NUYS, SANTA CRUZ, SANTA MARIA, CALIFORNIA • CAPE CANAVERAL, FLORIDA • HAW

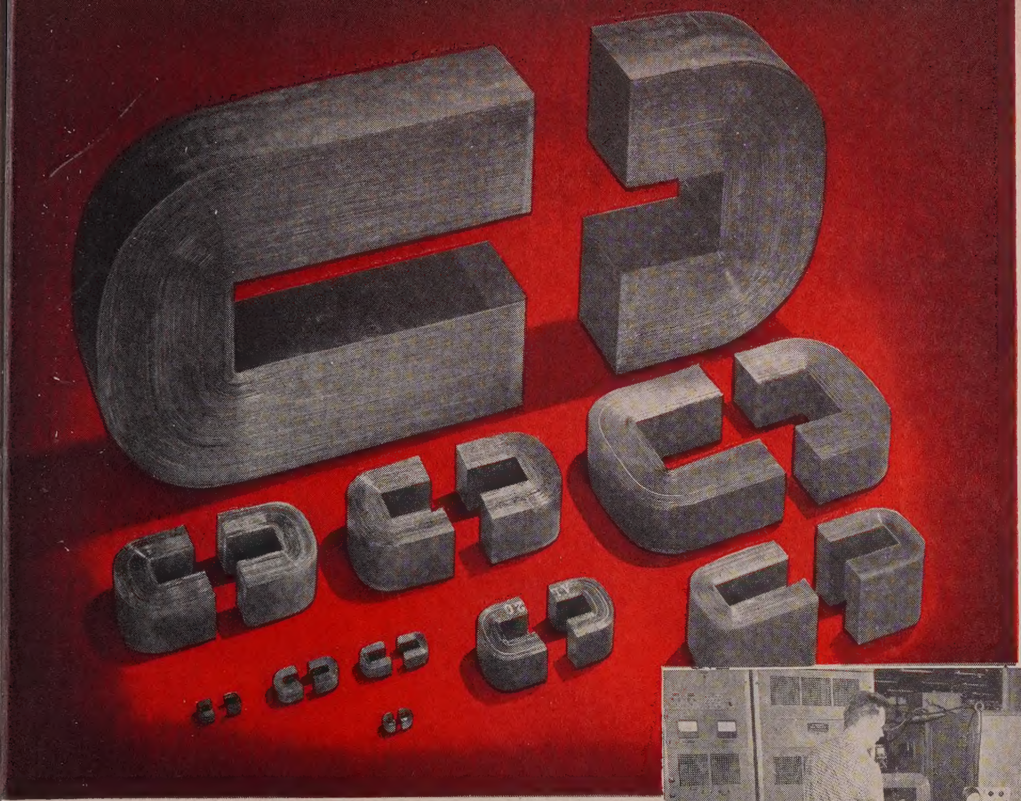

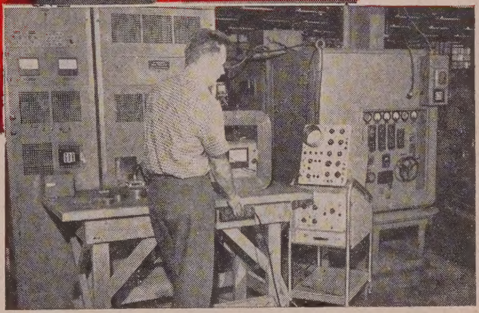

7372D

Arnold Pulse Transformer Cores are individually tested under actual pulse conditions

ere's
echnical data on
RNOLD
ILECTRON
ORES

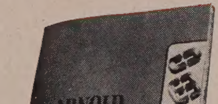

ulletin SC-107 A . . this newly-eprinted 52-page ulletin contains esign information on Arnold Tape Cores wound rom Silectron (grain-oriented silicon steel). It ncludes data on cut C and E cores, and uncut oroids and rectangular shapes. Sizes range from fraction of an ounce to more than a hundred ounds, in standard tape thicknesses of 1, 2, 4 nd 12 mils.

Cores are listed in the order of their power-andling capacity, to permit easier selection to fit our requirements, and curves showing the effect f impregnation on core material properties are ncluded. A valuable addition to your engineering iles—*write for your copy today.*

ADDRESS DEPT. JA-10

The inset photograph above illustrates a special Arnold advantage: a 10-megawatt pulse-testing installation which enables us to test-prove pulse cores to an extent unequalled elsewhere in the industry.

For example, Arnold 1 mil Silectron "C" cores—supplied with a guaranteed minimum pulse permeability of 300—are tested at 0.25 microseconds, 1000 pulses per second, at a peak flux density of 2500 gausses. The 2 mil cores, with a guaranteed minimum pulse permeability of 600, receive standard tests at 2 microseconds, 400 pulses per second, at a peak flux density of 10,000 gausses.

The test equipment has a variable range which may enable us to make special tests duplicating the actual operating conditions of the transformer. The pulser permits tests at .05, .25, 2.0 and 10.0 microsecond pulse duration, at repetition rates varying anywhere from 50 to 1000 pulses per second.

This is just another of Arnold's facilities for better service on magnetic materials of all description. ● Let us supply *your* requirements. *The Arnold Engineering Company, Main Office & Plant, Marengo, Ill.*

AL ARNOLD

ARNOLD

SPECIALISTS in MAGNETIC MATERIALS

BRANCH OFFICES and REPRESENTATIVES in PRINCIPAL CITIES

Find them FAST in the YELLOW PAGES

Sames

ELECTROSTATIC GENERATORS

Utilized Worldwide for Applications in:
Nuclear Physics, Insulation Testing, Electron Microscopy, Mineral Separation, Electrostatic Precipitation

Provide High-Voltage Power Supplies in a Wide Range of Models... Featuring:

- Essentially pure DC output
- Voltages to 600 KV, infinitely variable
- Current to 14 ma
- Medium or High Stability, to 0.1% hr. drift
- Easily adjustable, closely regulated output voltages to .001%
- Simplified maintenance, long life
- Extreme safety: Low output capacitance, Minimal short-circuit & overload currents, Remote adjustment & shut down

Write now for new Catalog 100 covering the complete line of Sames Electrostatic Generators.

SAMES

Sames

Dept. 310, 30 Broad St., New York 4, N.Y.

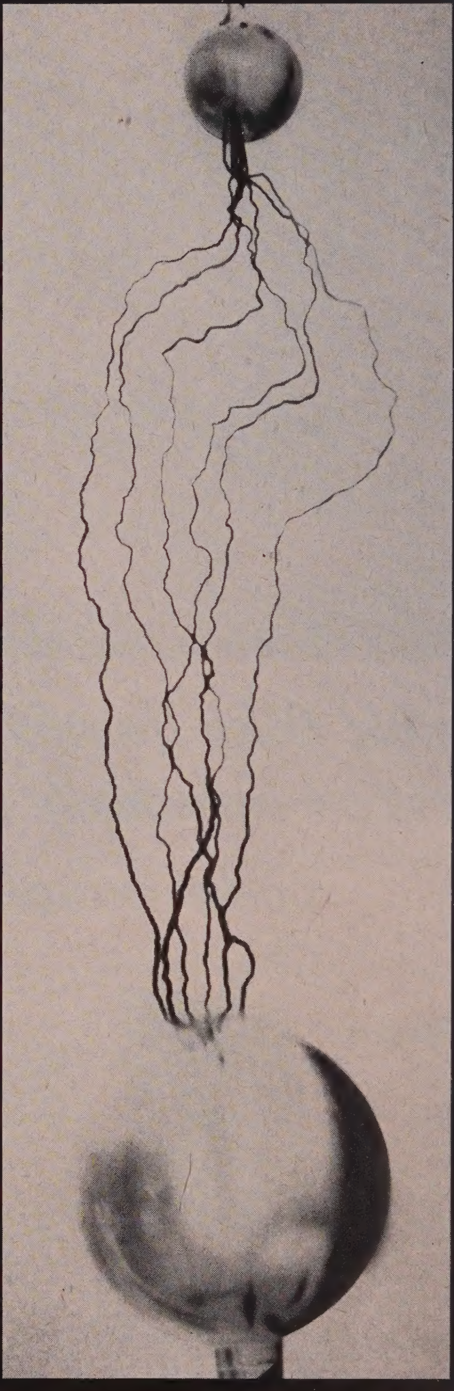

Contemporary education, like contemporary art,
continues to find expression in new areas

Original painting by Louis Ribak, Taos, New Mexico

For employees at Los Alamos, a curriculum in Engineering Science of Materials has been added to these in-residence MS degree programs: Nuclear Engineering, Chemistry, Mathematics, Physics, Mechanical and Electrical Engineering.

Qualified applicants are invited
to send resumes to:
Director of Personnel, Division 61-88

los alamos
scientific laboratory
OF THE UNIVERSITY OF CALIFORNIA
LOS ALAMOS, NEW MEXICO

All qualified applicants will receive consideration for employment without regard to race, creed, color, or national origin. U.S. citizenship required.

THERE IS A BIG DIFFERENCE

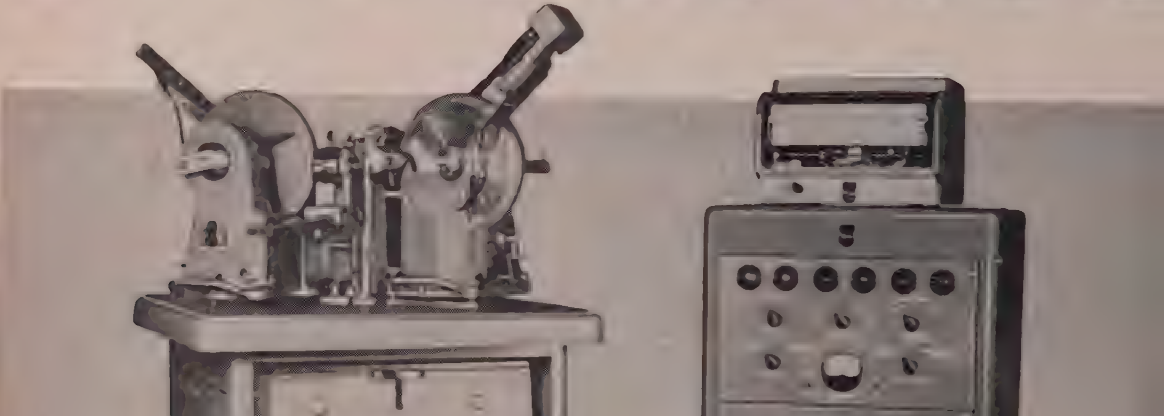

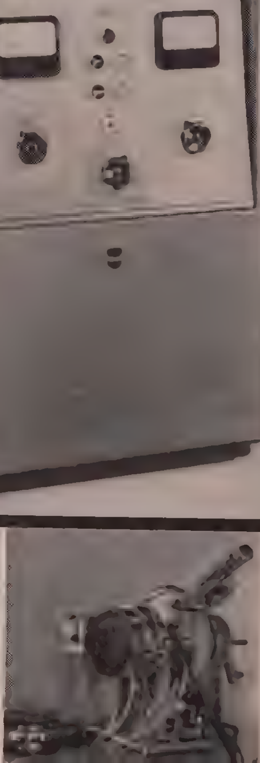

Norelco high temperature, high vacuum diffractometer attachment is available for all diffractometers including competitive makes.

Automatic recording of the diffraction spectr
is achieved by the addition of a wide range g
ometer and new electronic circuit panel to
basic diffraction unit.

..in Norelco®

Analytical Instrumentation*

here have been obvious visual changes in the working tools of X-ray diffractometry and X-ray spectrog-phy – a science which we at Philips Electronic Instruments know best. These Norelco product anges are based on years of experience accumulated in our own research and in the field. As a result, -ray instrumentation for elemental analyses and structure determinations is greatly facilitated by idening investigative areas while producing data faster and easier.

ut what about the physical differences? For one thing, the electronic circuit panel is top-to-bottom ew with a linear/log scaler, double power supply with variable output for detectors operating on fferent voltages up to 3 KV. There is a time and fixed count operations feature also.

ew high-intensity X-ray tubes can now be loaded to double capacity up to 2000 watts. Constant otential high tension transformers now lengthen tube life while providing greater precision in any iven time. Any unit in operation can be updated because the constant potential feature is also ailable in kit form for any existing transformer in the field.

new high-temperature furnace operates at temperatures over 2000° C with tantalum boats and in e cryogenic area – down to minus 185° C. The furnace is adaptable to every Norelco wide-range niometer made.

here you have a quick, boiled-down version of usable news . . . news you can put to work . . . updating ews from Norelco for years of dependable, expandable, top-quality performance.

* Incidentally, there are pronounced differences in all X-ray analytical instrumentation made by Philips. These differences are manifest in "know-how" and quality of apparatus designed from-the-ground-up for specific X-ray analytical work.

If you would like details about this news, ask your Philips Electronics dealer for your copy of the new Norelco X-ray Instrumentation Brochure or write today to:

PHILIPS ELECTRONIC INSTRUMENTS
A Division of Philips Electronics and Pharmaceutical Industries Corp.
750 South Fulton Avenue, Mount Vernon, N. Y.
In Canada: Research & Control Instruments • Philips Electronics Industries Ltd. • 116 Vanderhoof Ave. • Leaside, Toronto 17, Ont.

10th ANNUAL

PHYSICS SHOW

January 24–27, 1962 **Statler Hilton Hotel, N. Y.**

The meeting will bring together five thousand top level physicists—members of the American Physical Society and The American Association of Physics Teachers. Over five hundred technical papers will be presented.

An exhibit of scientific instruments, apparatus, components and technical books. Join the 59 companies who have reserved space, including:

- Academic Press, Inc.—Johnson Reprint Co.
- Addison-Wesley Publishing Co., Inc.
- Allyn and Bacon, Inc.
- Alpha Scientific Labs., Inc.
- American Tradair Corp.
- Baird-Atomic Inc.
- Charles Beseler Company
- Cambridge University Press
- Central Scientific Company
- The Conference Book Service
- Consolidated Vacuum Corp.
- Consultants Bureau
- E-H Research Labs.
- The Ealing Corporation
- Elion Instruments Inc.
- The Gaertner Scientific Co.
- General Radio Company
- Hamner Electronics Co., Inc.
- Harvey-Wells Corp.
- High Voltage
- Holt, Rinehart, and Winston, Inc.
- Ilikon Corp.
- Interscience Publishers, Inc.
- Isomet Corporation
- Keithley Instruments
- Kinney Vacuum Div.—New York Air Brake Co.
- J. Klinger Scientific Apparatus
- Laboratory for Science
- Macalaster Bicknell Corp.
- The Macmillan Company
- Magnion, Inc.
- McGraw-Hill Book Co., Inc.
- Mettler Instruments Corp.
- Modern Learning Aids
- N.R.C. Equipment Corp.
- Nuclear Industries, Inc.
- Oak Ridge Technical Enterprises Corp.
- Ophthos Instrument Co.
- Pacific Electric Motor Co.
- Pergamon Press, Inc.
- Perkin-Elmer Corp.
- Philips Electronic Instruments
- Prentice-Hall, Inc.
- Publishers' Authorized Bindery Service
- Radiation Dynamics Inc.
- Radiation Instrument Development Lab., Inc.
- John F. Rider Publisher, Inc.
- Semi-Elements Inc.
- Solid State Radiations, Inc.
- Space Technology Labs., Inc.
- Spectromagnetic Industries
- Technical Measurement Corp.
- Vacuum-Electronics Corp.
- Vacuum Instrument Corp.
- D. Van Nostrand Company
- Varian Associates
- Victoreen Instrument Co.
- The Welch Scientific Co.
- John Wiley and Sons, Inc.

A limited number of booths are available.

Inquiries should be addressed to:

Mr. T. Vorburger, Exhibit Manager
American Institute of Physics
335 East 45th Street
New York 17, N. Y.

ultra-sensitive Keithley microvoltmeters

When you need to measure dc signals in the microvolt range, you'll find that Keithley Instruments has the ideal instrument to meet your requirements.

Three Keithley microvoltmeters are available. Each offers advanced circuitry, ease of operation, floating or grounded input, bench or rack mounting.

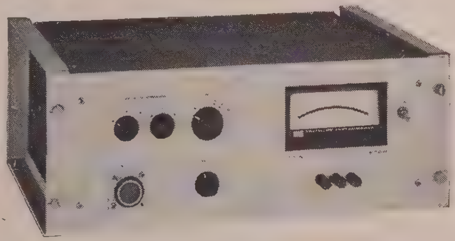

Model 149 can be used to measure outputs from strain gages, bolometers, resistance bridges, barrier layer cells. Other uses are in corrosion work, Hall effect studies.

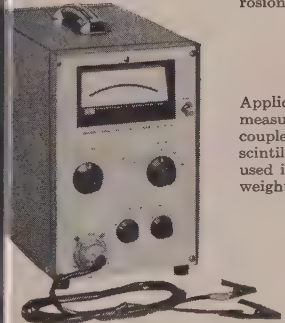

Applications for the 150A include measuring outputs from thermocouples, ion chambers, phototubes, scintillation counters. It can be used in cell studies and molecular weight analysis.

del 151 is useful in applications
ere a suspension galvanometer
be used, or where a galvano-
er is not sufficiently sensitive,
or rugged.

NEW MODEL 149 MILLI-MICROVOLTMETER, measuring 0.1 microvolt full scale, is the most sensitive voltmeter available anywhere today. It is recommended when source resistance is low, as with thermopiles. The 149 features a low-thermal copper circuit, new low-thermal switches, low-level magnetic shielding for the input compartment. Ranges cover 0.1 uv to 100 mv full scale. Maximum gain as a dc amplifier is 100,000,000. Speed of response to 90% of full scale is less than 0.5 second on most ranges. Short term noise is within 3 x 10^{-9} volt peak-to-peak (6 x 10^{-10} volt RMS). The 149 offers zero suppression up to 100 times full scale. $850.00

MODEL 150A MICROVOLT-AMMETER can be used in nearly every branch of research and engineering. As a dc voltmeter, it has ranges from 1uv to 1 volt full scale. Noise is within 0.006 uv RMS. The 150A can also be used as an ammeter, 10^{-10} to 10^{-3} ampere full scale, and as a dc amplifier with gains of 10 to 10,000,000. It may also be used as a micro-microammeter, and (with external voltage supply) as a meg-megohmmeter. The 150A is relatively insensitive to vibration, 60 cycle fields and thermal EMF's. $750.00

MODEL 151 NULL DETECTOR has many applications as a bridge null detector, microvoltmeter and dc amplifier. It has 5 non-linear ranges as well as 11 linear ranges, with a maximum voltage sensitivity of 100 microvolts full scale and a maximum gain as a dc amplifier of 100,000. Currents as low as 2 x 10^{-13} ampere can be detected. Two zero controls are provided for open and short circuit inputs. Other features of the Model 151 are: 500,000:1 in-phase rejection, noise less than 2% of full scale on all its ranges. $420.00

Brief Specifications

MODEL	RANGES	ACCURACY	STABILITY	POWER SENSITIVITY
49	13 overlapping in 1x, 3x steps, 0.1 uv to 100 mv.	2% full scale on all ranges.	After warmup, within 0.01 uv per day.	Greater than 4 x 10^{-18} watt.
50A/150AR* oltmeter	13 overlapping in 1x, 3x steps, 1 uv to 1 v.	2% full scale on all ranges.	After warmup, within 0.1 uv per day.	Greater than 4 x 10^{-18} watt.
mmeter	15 overlapping in 1x, 3x steps, 10^{-10} to 10^{-3} amp.	3% full scale on all ranges.	After warmup, ±2 x 10^{-11} ampere per day.	
51/151R* 51RC†	11 linear, 1x, 3x steps, 0.1 mv to 10 v; 5 non-linear, 0.001 to 10 v; three decades each.	Linear ±3% full scale. Non-linear ±10% of input.	After warmup, below 10 uv per day.	10^{-17} watt.

* Models for rack mounting

† Rack-Contact meter model, same as standard unit except for addition of a contact meter relay.

KEITHLEY INSTRUMENTS, INC.
12415 EUCLID AVENUE
CLEVELAND 6, OHIO

PRECISION HV SUPPLIES

PORTABLE PATTERN

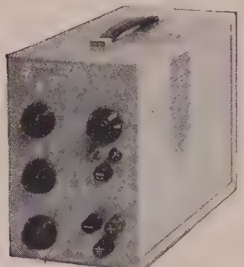

Model	Voltage	Current
RE-1601	0.2-1.6 KV	0-30 Ma
RE-1602	0.3-1.6 KV	0-10 Ma
RE-1903	0.3-1.9 KV	0-30 Ma

RACK PATTERN

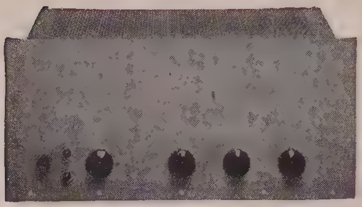

Model	Voltage	Current
RE-1603	0.3-1.6 KV	0-10 Ma
RE-1610	0.3-1.6 KV	0-100 Ma
RE-1611	0.2-1.6 KV	0-100 Ma
RE-1620	0.3-1.6 KV	0-200 Ma
RE-1699	0.3-1.6 KV	0-1 Amp
RE-2003	0.5-2.0 KV	0-30 Ma
RE-2006	0.5-2.0 KV	0-60 Ma
RE-2015	0.5-2.0 KV	0-150 Ma
RE-2060	0.5-2.0 KV	0-600 Ma
RE-3002	0.5-3.0 KV	0-20 Ma
RE-3004	0.5-3.0 KV	0-40 Ma
RE-3006	0.5-3.0 KV	0-60 Ma
RE-3010	0.5-3.0 KV	0-100 Ma
RE-3040	0.5-3.0 KV	0-400 Ma
RE-5001	0.5-5.0 KV	0-10 Ma
RE-5002	0.5-5.0 KV	0-20 Ma
RE-5003	0.5-5.0 KV	0-30 Ma
RE-5005	0.5-5.0 KV	0-50 Ma
RE-5020	0.5-5.0 KV	0-200 Ma
RE-5503	1.0-5.5 KV	0-30 Ma
RE-6003	1.5-6.0 KV	0-30 Ma
RE-6530	0.5-6.5 KV	0-30 Ma
RE-10010	1.0-10 KV	0-10 Ma
RE-10030	1.0-10 KV	0-30 Ma
RE-10100	1.0-10 KV	0-100 Ma

Constant Current Supplies

RI-081	0-81 Ma	0-1000V
RI-234	0-230 Ma	0-350V

A series of high-voltage power supplies providing a stable and ripple-free high-voltage output over a wide range, practically independent of line voltage input or load current variations.

These supplies are completely self-contained and AC operated, and compactly housed in ventilated cabinets designed for either relay-rack mounting or bench use. All operating controls are mounted on front panel; output terminals and input power connection on back.

High-voltage rectifier is a full-wave silicon doubler. Output voltage is continuously variable over entire range in each case, usually variable stepwise in conjunction with a vernier control.

Among special features are molded components — rectifiers, transformers, etc. — cast in epoxy resin, for superior insulation and trouble-free performance.

Any of these supplies can be modified by using meters, polarity switches, co-ax connectors, wire-wound resistors, etc. — or special designs can be built to meet specialized requirements.

The range of any of these supplies can be made to start at zero voltage.

Features

Either positive or negative of any supply may be grounded

Regulation: .01 to .001%

Line Stability: .05 to .005%

Long-term Stability: .01-.05% per hour, about 0.1% per day

Impedance: 1 to 5 Ohms

Ripple: 0.5 to 3 Mv P-P

Standard tubes used

Millimeter Wave Generators

KSG-291	8.3- 8.9 mm
KSG-290	8.9-10. mm
KSG-289	10. -11. mm
KSG-33	12. -13.6 mm

NORTHEAST SCIENTIFIC CORP.

30 WETHERBEE STREET ACTON, MASS.

NRC's Packaged Pumping Systems Produce and Measure "Clean" Vacuum to 10^{-7} Torr

Here's what you get with the NRC Series 3300 line of portable pumping systems:

- **Lightweight, rugged frame design** for "functional" operation, easier maintenance and reliable vacuum performance.
- **Fractionating type diffusion pumps,** for dependable top speed pumping performance, even at lower pressure ranges.
- **High conductance, straight-through pumping** – Gate type main valve has 100% full opening, least restrictive vacuum valve available; no elbow cold traps or angle valves to restrict flow rate; result – more useful pumping speed available.
- **Portable gauge control** – The NRC Model 710 Vacuum Gauge Control assures accuracy and reliability; box mounted, normally rests on shelf in system frame; can be easily moved to any remote location for convenient reading.
- **Wide choice of sizes available;** built around 2", 4", 6" and 10" diffusion pumps; all systems complete and performance tested; wide choice of accessory base plates, bell jars, feed-throughs, power supplies, etc., also available.

Featured in the Series 3300 Systems are NRC's new "HS" fractionating diffusion pumps, producing ultra-high-speed over a wide pressure range. Their extremely low backstreaming rates, in combination with the "optically opaque" baffle cold traps, result in vacuums that can truly be termed "clean".

These complete systems combine such features as fractionating diffusion pumps, conductance slide valves, and full-flow combination baffle cold traps, provide "functional" pumping systems that outperform any other systems available.

The new Series 3300 packaged pumping systems assure you of high vacuum pumping and measurement. All they need for operation are power, water, and a suitable vacuum work or test chamber. Use them whenever you need pressures from 10^{-3} Torr or lower. Can easily be moved from job to job or as a building block for a high performance vacuum installation. Write today for complete data sheet and specifications on the Series 3300 Systems.

NRC
EQUIPMENT
CORPORATION

A Subsidiary of National Research Corporation

160 Charlemont Street, Dept. 45R
Newton 61, Massachusetts

Corporate Associates

American Institute of Physics

The Corporate Associates of the American Institute of Physics are a group of corporations, institutions, and laboratories who believe it is valuable to them and to America to maintain a vigorous advance in the physical sciences. By their membership dues they aid the Institute significantly in carrying out its purpose: the advancement and diffusion of knowledge of the science of physics and its application to human welfare. The Institute is grateful for their assistance.

CORPORATE ASSOCIATES OF THE INSTITUTE

Abbott Laboratories
Academic Press Inc.
Acoustica Associates, Inc.
Aerospace Corporation
Airborne Instruments Laboratory
Air Products, Inc.
Allegheny Ludlum Steel Corporation
Allen-Bradley Company
Allied Research Associates, Inc.
Allis-Chalmers Manufacturing Co.
Aluminum Company of America
American Can Company
American Cyanamid Company
American Machine & Foundry Co.
American Oil Company
American Optical Company
American Radiator & Standard Sanitary Corp.
American Viscose Corporation
Ansco Div. of General Aniline & Film Corp.
Applied Physics Corporation
Armco Steel Corporation
Armour Research Foundation
Armstrong Cork Company
The Atlantic Refining Company
Atomics International Division North American Aviation, Inc.
Automatic Electric Laboratories, Inc.
Avco-Everett Research Laboratory
Avco Research & Advanced Development
Baird-Atomic, Inc.
Ball Brothers Research Corporation
Barnes Engineering Company
Basic Books, Inc.
Battelle Memorial Institute
Bausch & Lomb Incorporated
Beckman Instruments, Inc.
Bell & Howell Research Center
Bell Telephone Laboratories, Inc.
Bendix Corporation
Bethlehem Steel Company, Inc.
Bodine Soundrive Company
Boeing Airplane Company
Bolt Beranek and Newman Inc.
Borg-Warner Corporation
The Budd Company
Bulova Research and Development Laboratories, Inc.
Burroughs Corporation
California Research Corporation
The Carborundum Company
Carrier Corporation
Caterpillar Tractor Company
CBS Laboratories
Celanese Corporation of America
Central Scientific Company
Chance Vought Aircraft, Inc.
Chemstrand Research Center, Inc.
Chrysler Corporation
The Cincinnati Milling Machine Company
Clevite Corporation
Collins Radio Company
Combustion Engineering, Inc.
Continental Can Company, Inc.
Continental Oil Company
Cornell Aeronautical Laboratory, Inc.
Corning Glass Works
Crane Company
The Detroit Edison Company
Douglas Aircraft Co., Inc.
The Dow Chemical Company
E. I. du Pont de Nemours & Co., Inc.
Eastman Kodak Company
Thomas A. Edison Research Laboratory
The Eppley Laboratory, Inc.
Esso Research & Engineering Company
Fairchild Camera & Instrument Corp.
Farrand Optical Co., Inc.
The Firestone Tire & Rubber Co.
Ford Motor Company
The Foxboro Company
General Dynamics Corporation
General Electric Company
General Motors Corporation
General Precision, Inc.
General Radio Company
General Telephone & Electronics Laboratories, Inc.
The Gillette Company
The B. F. Goodrich Company
The Goodyear Tire & Rubber Co.
W. R. Grace & Co.
Grinnell Corporation
Grumman Aircraft Engineering Corp.
Gulf Research & Development Co.
Haller, Raymond and Brown, Inc.
Halliburton Oil Well Cementing Co.
Hercules Powder Company
Hewlett-Packard Company
High Voltage Engineering Corp.
Hughes Aircraft Co.
Humble Oil & Refining Company
International Business Machines Corp.
International Harvester Company
International Minerals & Chemical Corp.
International Nickel Co., Inc.
Itek Corporation
ITT Federal Laboratories
Joslyn Mfg. & Supply Co.
Knowles Electronics, Inc.
Koppers Company, Inc.
Lear, Incorporated
Leeds & Northrup Company
Libbey-Owens-Ford Glass Co.
Arthur D. Little, Inc.
Litton Industries, Inc.
Lockheed Aircraft Corporation
McGraw-Hill Book Company, Inc.
The Magnavox Company
The Martin Company
Massachusetts Institute of Technology
Merck Sharp & Dohme Research Labs.
Minneapolis-Honeywell Regulator Co.
Minnesota Mining & Manufacturing Co.
Monsanto Chemical Company
Motorola Semiconductor Products Division
The National Cash Register Company
National Research Corporation
Northrop Corporation
The Ohio Oil Company
Olin Mathieson Chemical Corp.
Operations Research Incorporated
Outboard Marine Corporation
Owens-Corning Fiberglas Corporation
Owens-Illinois Glass Co.
Pacific Semiconductors, Inc.
Page Communications Engineers, Inc.
Pergamon Press, Inc.
The Perkin-Elmer Corp.
Philco Corporation
Philips Laboratories, Div. of North American Philips Co., Inc.
Phillips Petroleum Company
Pilkington Brothers Limited
Pitney-Bowes, Inc.
Pittsburgh Corning Corp.
Pittsburgh Plate Glass Company Glass Division
Polaroid Corporation
The Procter & Gamble Company
The Pure Oil Company
Radio Corporation of America
Ramo-Wooldridge Division Thompson Ramo Wooldridge Inc.
The Rand Corporation
Raytheon Company
Republic Aviation Corporation
Republic Steel Corporation
Sangamo Electric Company
Schering Corporation
Schlumberger Well Surveying Corp.
Scientific American
Shell Development Company
Shockley Transistor Corporation
Smyth Research Associates
Socony Mobil Oil Company, Inc.
Space Technology Laboratories, Inc.
Sperry Rand Corporation
Sprague Electric Company
A. E. Staley Manufacturing Co.
Sun Oil Company
Technical Operations, Inc.
Texaco, Inc.
Texas Instruments, Inc.
TRG, Incorporated
Tung-Sol Electric Inc.
Union Carbide Corporation
Union Oil Company of California
Union Switch & Signal Div. of Westinghouse Air Brake Co.
United Aircraft Corporation
United Gas Corporation
United Nuclear Corporation Development Division—NDA
United States Rubber Company
United States Steel Corp.
Universal Oil Products Company
The Upjohn Company
Vacuum-Electronics Corp.
Varian Associates
Vitro Laboratories Division of Vitro Corp. of America
Western Union Telegraph Company
Westinghouse Electric Corporation
Whirlpool Corporation
Wyandotte Chemicals Corporation
Xerox Corporation
Zenith Radio Corporation

The American Institute of Physics cordially invites interested corporations and institutions to make application for Corporate Associate membership and will welcome their inquiries addressed to the Secretary.

AMERICAN INSTITUTE OF PHYSICS *335 East 45 Street, New York 17, New York*

Satellites orbiting earth . . . satellites orbiting other planets . . . manned space stations. They represent the today and tomorrow of man's probing of our universe. Consider their value, however, were we not able to communicate with them . . . nor they with us.

At Amherst Laboratories state-of-art advances in microwave and millimeter wave technology are playing an important role in determining the future of aerospace communication and instrumentation systems. Significant advances in this field are being shaped today through individual and team efforts.

PROFESSIONAL STAFF AND MANAGEMENT OPPORTUNITIES are unlimited for Physicists, Mathematicians and Electronic Engineers with advanced degrees and creative desire. All qualified applicants will receive consideration for employment without regard to race, creed, color or national origin. You are invited to direct inquiries in confidence to Mr. C. H. Haushalter, in care of Microwave and Aerospace Systems Department,

AMHERST LABORATORIES • 1183 WEHRLE DRIVE • WILLIAMSVILLE, NEW YORK

SYLVANIA **ELECTRONIC SYSTEMS**
Government Systems Management
for ***GENERAL TELEPHONE & ELECTRONICS***
GENERAL SYSTEM

Soviet Physics — SOLID STATE

A translation, beginning with 1959 issues of "Fizika Tverdogo Tela" of the USSR Academy of Sciences. Offering results of theoretical and experimental investigations in the physics of semiconductors, dielectrics, and on applied physics associated with these problems. Also publishes papers on electronic processes taking place in the interior and on the surface of solids.

Soviet Physics — TECHNICAL PHYSICS

A translation, beginning with 1956 issues of "Zhurnal Tekhnicheskoi Fiziki" of the USSR Academy of Sciences. Contains work on plasma physics and magnetohydrodynamics, aerodynamics, ion and electron optics, and radio physics. Also publishes articles in mathematical physics, the physics of accelerators and molecular physics.

Soviet Physics — CRYSTALLOGRAPHY

A translation, beginning with 1957 issues of the journal "Kristallografiya" of USSR Academy of Sciences. Experimental and theoretical papers on crystal structure, lattice theory, diffraction studies, and other topics of interest to crystallographers, mineralogists, and metallurgists.

Orders and inquiries should be sent to:

American Institute of Physics
335 East 45 Street, New York 17, N.Y.

research in a unique environment

The scientists of Aerospace Corporation's Laboratories are in the forefront of research in the space sciences. With the advantages of stability and permanence in a stimulating environment, Aerospace Corporation scientists are conducting basic and applied research and experimental investigations on a broad spectrum of problems selected by staff members on the basis of their intrinsic scientific interests as well as on problems arising directly from space systems in development. Their singular role within this leadership group installs the scientists of Aerospace Corporation in a position to make real progress toward advancing the space sciences. Now, as new areas of research are being considered, more men with advanced degrees are needed to meet growing responsibilities and are urged to contact Mr. George Herndon, Aerospace Corporation, Room 123, P.O. Box 95081, Los Angeles 45, California.

Organized in the public interest and dedicated to providing objective leadership in the advancement and application of space science and technology for the United States Government.

AEROSPACE CORPORATION

All qualified applicants will receive consideration for employment without regard to race, creed, color or national origin.

Welch

HIGH VACUUM Duo-Seal Mechanical and Diffusion Pump

★ HIGH VACUUM–0.001 Micron GUARANTEED
(0.000 001 mm Hg)

★ CAPACITY AT 0.1 MICRON–600 Liters Per Minute

★ MATCHED PERFORMANCE

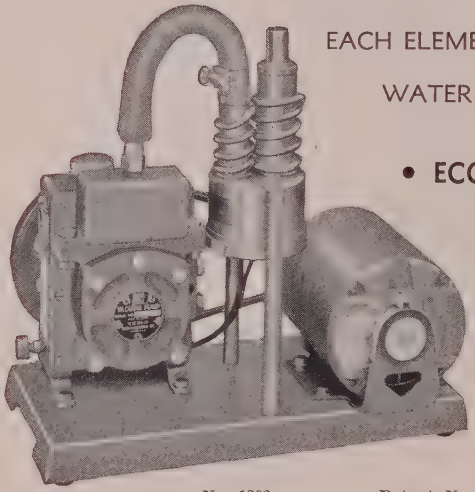

No. 1392 Patent No. 2337849

EACH ELEMENT WITH TWO-STAGE CONSTRUCTION

WATER-COOLED OR AIR-COOLED MODELS

- ECONOMICAL TO RUN AND MAINTAIN
- QUIET OPERATION

$300.00
Complete with Motor

This is an unusually convenient portable diffusion-pump unit, employing a two-stage mechanical pump and an unbreakable, all-metal diffusion pump. The two components are properly matched as to performance and together will produce a vacuum of better than 10^{-6} mm without the use of cold traps. Complete with oil for both pumping elements.

Other combinations are available with speeds up to 16,500 liters per min at 0.1 micron. We will gladly submit full details describing the best combination for your particular application

No.	Item	Price
1392.	**MECHANICAL AND DIFFUSION PUMP, Water-Cooled** For 115 Volts, 60 Cycles, A.C.	Each, $300.00
1392A.	**MECHANICAL AND DIFFUSION PUMP, Air Cooled.** For 115 Volts, 60 Cycles, A.C.	Each, $300.00
	For attached Belt Guard, add $15.00 to above prices.	
1391.	**DIFFUSION PUMP, Only, Water Cooled, With Octoil.**	Each, $160.00
1394.	**DIFFUSION PUMP, Only, Air Cooled, With Octoil.**	Each, $160.00
1393.	**MOUNTING PARTS.** For mounting No. 1391 or No. 1394 Diffusion Pump on base of mechanical pump.	Set, $8.00

THE WELCH SCIENTIFIC COMPANY
ESTABLISHED 1880
1515 SEDGWICK STREET, DEPT. C-1, CHICAGO 10, ILLINOIS, U.S.A.
Manufacturers of Scientific Instruments and Laboratory Apparatus

Journal
of
Applied Physics

Volume 32, Number 10 October, 1961

Ferromagnetic Resonance in Thin Magnetic Films at Radio Frequencies

Turner E. Hasty and Lee J. Boudreaux
Texas Instruments Incorporated, Dallas 22, Texas

(Received April 6, 1961)

Ferromagnetic resonance in thin films has been extended to the radio-frequency region of from 1–20 Mc. Theoretical expressions governing this resonance condition are given along with experimental results. It is found that resonance in this region affords an excellent means of measuring the anisotropy field H_k. Films with compositions near 80% Fe—20% Ni were studied by this technique. The anisotropy field of these films was found to be around 5 oe. The width of the absorption line varied from 0.6 to 2.4 oe, depending on the composition of the film. The minimum linewidth was found to occur for the composition of minimum magnetostriction.

INTRODUCTION

Ferromagnetic resonance in the microwave and uhf region has been used as a tool for investigating the properties of magnetic films for quite some time[1–4]; however, there seems to be no report of resonance conducted in the frequency range of 1–20 Mc. Resonance conducted in the uhf and microwave region affords a means of measuring the g value, saturation magnetization, anisotropy, and damping constant, while resonance in the rf region will only yield information about the anisotropy field and the width of the absorption line. The information obtained at this frequency is somewhat limited, but the ease with which the measurement can be made compensates for this limitation.

One might not expect to observe resonance in this region because of the expectation that the field at which resonance should occur would be so small that the internal fields in the sample would completely obscure the absorption line. This difficulty is removed by using a magnetic film which contains a well-defined uniaxial anisotropy and is reasonably free of strain. In this case the magnetization will be completely aligned in one direction and the sample can be considered saturated.

The basic formula relating precession frequency to magnetocrystalline anisotropy and shape demagnetization was first stated by Kittel.[5] More general relations have been given by Macdonald,[6] Smit and Beljers,[7] Young and Uehling,[8] and Suhl.[9] The formulations of Smit and Beljers have been extended for both single-domain and simple multidomain configurations in thin conducting disks by Artman.[10] A large portion of the theoretical work presented in the next section has been treated by the above authors and is included here for clarity, completeness, and unity of notation.

THEORY

The following analysis pertains only to thin films which have a uniaxial anisotropy in the plane of the film. The film is oriented such that its plane is in the X-Z plane with its easy axis of magnetization directed along the Z axis. The magnetization M forms the angle θ with the Z axis and is inclined out of the plane of the film at the angle ϕ. The applied magnetic field H lies in the plane of the film and is inclined from the Z axis by an angle ψ.

The general equation for resonance has been given by Smit and Beljers[7] as

$$\left(\frac{\omega_0}{\gamma}\right)^2=\frac{1}{M^2\sin^2\theta}(W_{\theta\theta}W_{\phi\phi}-W_{\theta\phi}{}^2). \qquad (1)$$

W is the free energy per unit volume and γ is the gyromagnetic ratio. The second derivatives of Eq. (1)

---

[1] R. L. Conger and F. C. Essig, Phys. Rev. **104**, 915 (1956).

[2] R. H. Kingston and P. E. Tannewald, J. Appl. Phys. **29**, 232 (1958).

[3] D. O. Smith, J. Appl. Phys. **29**, 264 (1958).

[4] P. E. Tannewald and M. H. Seavy, Jr., Phys. Rev. **105**, 377 (1957).

[5] C. Kittel, Phys. Rev. **73**, 155 (1948).

[6] J. R. Macdonald, Proc. Phys. Soc. (London) **A64**, 968 (1951).

[7] J. Smit and H. C. Beljers, Philips Research Repts. **10**, 113 (1955).

[8] J. A. Young, Jr., and E. A. Uehling, Phys. Rev. **94**, 544 (1954).

[9] H. Suhl, Phys. Rev. **97**, 555 (1955).

[10] J. O. Artman, Phys. Rev. **105**, 74 (1957).

Copyright © 1961 by the American Institute of Physics.

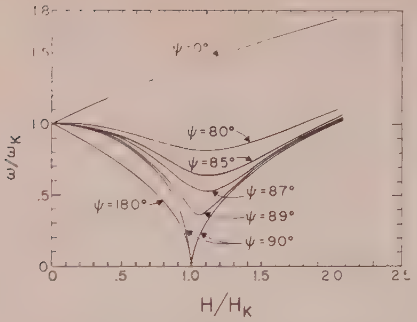

FIG. 1. Resonance relations for thin film with uniaxial anisotropy.

are evaluated at the values of θ and ϕ which are satisfied by the condition $W_\phi = W_\theta = 0$. The demagnetizing factors for thin films are very nearly $n_x = n_z = 0$, and $n_y = 4\pi$.

The free energy per unit volume is

$$W = K\sin^2\theta - MH(\cos\theta\cos\psi + \sin\theta\sin\psi\cos\phi) + \tfrac{1}{2}4\pi M^2\sin^2\theta\sin^2\phi. \quad (2)$$

The first term, in the above equation, represents the energy arising from the uniaxial anisotropy, the second term represents the energy of the sample in an external field, and the third term describes the energy of demagnetization.

The equilibrium conditions are satisfied by $\phi = 0$ and

$$\sin(\psi - \phi) = (H_k/2H)\sin 2\theta, \quad (3)$$

where $H_k = 2K/M$.

Equation (3) can be solved exactly for only two cases, namely $\psi = 0$ and $\psi = \pi/2$. For these two orientations, the equilibrium conditions specified by Eq. (3) reduce to the following special cases:

$$\begin{array}{lll} \theta = 0 & \text{when} & \psi = 0. \\ \theta = \pi/2 & \text{when} & \psi = \pi/2, \text{ and } H \geq H_k. \\ \sin\theta = H/H_k & \text{when} & \psi = \pi/2, \text{ and } H \leq H_k. \end{array}$$

The resonance equations corresponding to the above conditions are

$$\omega_0 = \omega_k(h+1)^{\frac{1}{2}}, \quad \text{when } \psi = 0; \quad (4)$$

$$\omega_0 = \omega_k(h-1)^{\frac{1}{2}}, \quad \text{when } \psi = \pi/2, \text{ and } H \geq H_k; \quad (5)$$

$$\omega_0 = \omega_k(1-h^2)^{\frac{1}{2}}, \quad \text{when } \psi = \pi/2, \text{ and } H \leq H_k, \quad (6)$$

where $h = H/H_k$ and $\omega \sim \gamma\sqrt{4\pi M H_k}$.

For values of ψ other than zero or $\pi/2$, the equation for resonance becomes

$$\omega_0 = \omega_k(\cos 2\theta + h\cos\epsilon)^{\frac{1}{2}}, \quad (7)$$

where $\epsilon = \psi - \theta$.

The values of θ and ϵ in Eq. (7) must be evaluated by Eq. (3). The usual method by which this is done is to assume that ϵ is small enough so that $\sin\epsilon$ can be replaced by ϵ. This assumption leads to the original Kittel formula and is valid for cases where the applied field is much larger than H_k. However, our experiments were performed in fields of the order of H_k; therefore, it was found necessary to use a more exact solution of Eq. (3). This equation has been solved numerically by Stoner and Wohlfarth[11] in connection with their study of magnetization processes in fine particle magnets. With these tables and additional one evaluated by us for values of ψ between 85 and 90°, we were able to determine exactly the low field resonance condition. These are shown in Fig. 1. A typical value for ω_k is 600 Mc; thus, we should expect resonance to occur only for those orientations for which the resonance frequency drops to zero. By Fig. 1, we see that the two orientations which satisfy this condition are $\psi = 90°$ and $\psi = 180°$. For each of these orientations, theory predicts that ω_0 reaches a frequency of a few megacylces when the external field is very nearly H_k. In actual practice, resonance is not possible for the 180° orientation. The reason for this is that a magnetic field which is applied antiparallel to the magnetization vector will cause the magnetization to reverse its direction by domain wall motion for a value of the field less than that required to produce resonance.

EXPERIMENTAL METHOD

The standard method of determining the rf susceptibility of a material is to place the specimen inside of a coil which is part of a resonant circuit. The real part of the susceptibility is then determined by a shift in the resonant frequency and the imaginary part by the change in the Q of the circuit. When the sample is a conductor, the situation is usually complicated by the fact that the electrical losses caused by the finite resistence of the sample cannot be separated from the magnetic losses. However, as in our case, when the skin depth of the radiation is much larger than the thickness of the film, these losses are found to be negligible. This was checked experimentally by placing a copper film with the same dimensions as our magnetic films in the coil and noting the change in its Q. This change was found to be of the order of 1% and was considered negligible when compared with the change of 50% which occurred at resonance. If we represent permeability of the sample by the expression $\mu = \mu_1 - i\mu_2$, then we may state that the frequency shift is proportional to the $\sqrt{\mu_1}$ and the power absorbed by the sample is proportional to $\sqrt{\mu_2}$. The Q with magnetic loss as a function of magnetic field should have the form

$$1/Q_l = A/Q_0, \quad (8)$$

where Q_0 is the unloaded Q. The quantity A is proportional to $\sqrt{\mu_2}$ and has been given by Smith[3] as

$$\frac{4\pi\omega M\gamma^2 H_0}{[(\omega_0^2 - \omega^2)^2 + (4\pi\omega\lambda)^2]^{\frac{1}{2}}}, \quad (9)$$

---

[11] E. C. Stoner and E. P. Wohlfarth, Trans. Roy. Soc. (London) **240**, 599 (1948).

where

$$\lambda=(\gamma^2 M\Delta H)/2\omega. \qquad (10)$$

λ is the Landau-Lifshitz damping constant and ΔH is the width of the absorption line. From Eqs. (5) and (6), we would expect two absorption peaks located at

$$H=H_k+\zeta$$
$$H=H_k(1-\zeta/H_k)^{\frac{1}{2}},$$

where

$$\zeta=\omega^2/4\pi M\gamma^2.$$

For 2.8-Mc resonance, the quantity ζ is of the order of 10^{-4} oe. Thus, we should expect to resolve only a single peak centered at $H=H_k+\zeta/4$. The position of this peak will be virtually insensitive to frequency changes as long as ζ remains much less than one. The shape of the absorption line is determined by Eq. (10) with ω_0 evaluated by Eq. (6) for $H\leq H_k$ and by Eq. (5) for $H\geq H_k$.

A series of thin films were prepared by vacuum evaporation from premelted slugs of alloys with compositions that ranged from 75% Ni—25% Fe, to 85% Ni—15% Fe. The composition of each ingot was determined by a gravimetric analysis. The films were deposited in the presence of a magnetic field onto soft glass substrates. They were approximately 2000 A thick and 1 cm in diameter. Measurements were made by placing a film in an rf coil which formed the tank circuit of a Hartley marginal oscillator. The coil was then placed in two pairs of concentric Helmholtz coils. One pair of the Helmholtz coils was used to supply a variable dc field and the other was used to supply a 30-cycle sinusoidal modulating field. The Helmholtz coils were arranged so that corrections could be made for the horizontal component of the earth's field. The output of the oscillator was detected and fed to the vertical amplifier of an oscilloscope. The horizontal sweep of the oscilloscope was driven by a 30-cycle voltage supplied by a resistor in series with the modulating coils. Several rf coils were prepared so that frequencies between 1 and 20 Mc could be used. Most of the work was carried out at 2.8 Mc. All measurements were made at room temperature.

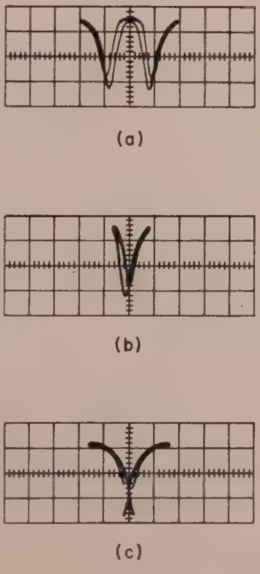

FIG. 2. Photographs of oscilloscope traces of resonance absorption curves. (a) $H_{dc}=0$, $H_{mod}=2H_k$, $H_{mod}\perp$ to Z axis; (b) $H_{dc}=H_k$, $H_{mod}=2\Delta H$, both fields $\perp$ to Z axis; (c) $H_{dc}=0$, $H_{mod}=H_k$, $H_{mod}\parallel$ to Z axis.

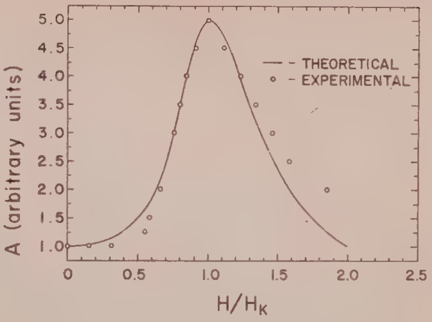

FIG. 3. Variation in Q as a function of applied magnetic field.

A procedure found useful in orienting the film, so that the easy axis of the film is perpendicular to the field, was to set the dc field at zero and use a modulating field large enough to sweep through the line completely. This is shown in Fig. 2(a).

The linewidth and position of the absorption peak were measured by reducing the modulation to one-half linewidth and adjusting the dc field for resonance. Figure 2(b) is a display of the absorption line with the dc field adjusted to H_k and the modulating field sufficient to trace the entire line. The change in the Q of the coil as a function of the magnetic field was measured with a Boonton 260-A Q meter. A plot of this change measured in film No. 2 of Table I, along with that predicted by Eq. (10), is shown in Fig. 3.

In addition to the perpendicular resonance, a signal can be detected when an ac magnetic field is applied parallel to the easy axis of the film. This signal is not a resonance signal as such, but is associated with the fact that the magnetization is switching back and forth between the zero and the 180° direction. The amplitude of this signal is smaller than that of the perpendicular case by a factor of 10. A display of this absorption curve is shown in Fig. 2(c). We can understand the shape of this

TABLE I. Comparison of H_k as measured by resonance and hysteresis-loop techniques with ΔH measured by resonance.

		Substrate temp °C	H_k (resonance) oe	H_k (hysteresis) oe	ΔH oe
1	75% Ni, 25% Fe	220	9.1	9.0	2.2
2	80% Ni, 20% Fe	20	5.6	5.5	2.4
3	80% Ni, 20% Fe	220	5.6	5.4	1.4
4	82% Ni, 18% Fe	220	4.4	4.5	1.2
5	83.5% Ni, 16.5% Fe	220	4.3	4.5	1.6
6	85% Ni, 15% Fe	220	4.5	4.5	0.3

curve by noting the $\psi=180°$ curve of Fig. 1. We see that when a field is placed antiparallel to the magnetization vector ($\psi=180°$), the resonant frequency drops from ω_k to zero as the field is increased from zero to H_k. In actual practice, however, the magnetization will switch, by domain wall motion, at some critical field H_c less than H_k. At this point the magnetization will be parallel to the applied field and the resonant frequency will be given by the $\psi=0$ curve of Fig. 1. Even though switching will occur before the resonant frequency of the film is low enough to cause resonance, the off-resonance permeability will increase until H reaches H_c. At this point it will drop sharply and will continue to drop as the field is further increased.

Although we have discussed only a switching signal for the parallel case, we have observed this signal for all orientations of the film other than $\psi=\pi/2$. This behavior is in accord with that predicted by the solutions of Eq. (7) for values of ψ greater than $\pi/2$. These signals are easily distinguished from the perpendicular case by their decreased magnitude and by the position of their peaks. The peak of these curves occur at the point where the magnetization switches. No critical comparison has yet been made between the positions of these peaks and the critical fields predicted by Stoner and Wohlfarth.

EXPERIMENTAL RESULTS

The values of H_k and ΔH were measured for each of the compositions shown in Table I. The values of H_k were also measured with a 500-cps hysteresis loop tester. The values obtained by the two methods agreed within experimental limits of error. The linewidths measured by the resonance technique ranged from 0.5 to 3 oe, depending on composition and condition of deposition. If we calculate the value of the damping constant λ by Eq. (11), we see that it is of the order of 10^9. This value is abnormally high when compared with the value obtained by microwave measurements, but is in agreement with the increase observed by Kingston and Tannewald[2] and Smith[3] at uhf. We suspect, however, that the major factor contributing to our measured linewidths is the angular dispersion of the anisotropy. Dispersion of this type has been discussed by Alexander,[12] Crowther,[13] Harte,[14] and West.[15] This would cause us to calculate a much higher value of λ than actually exists. This conjecture is supported by the fact that the linewidth decreases for compositions near minimum magnetostriction. If we assume that the total increase in linewidth at low frequencies arises from a dispersion of the anisotropy, we see that the ultimate linewidths that could be obtained at these frequencies are from 0.01 to 0.05 oe. This is probably a poor assumption, but nevertheless it establishes a lower limit on linewidths which can be obtained at these frequencies. Measurements were attempted on films over the entire range of compositions from 50% nickel, 50% iron, to 100% nickel. In most cases, except for the compositions shown in Table I, no absorption could be detected. We suspect that internal strain fields have obscured the resonance signal in these higher magnetostriction compositions. We did observe a very faint absorption in 70% Ni-30% Fe iron films. The peak occurred at a field which was about 1.3 times that measured by the hysteresis-loop method. The signal was approximately 30 db below that observed in the other cases. This anomaly is probably caused by a dispersion of the anisotropy. If the dispersion were such that the major portion of the magnetization lay a degree or so on either side of the mean direction, it would be impossible to align the field perpendicular to a single easy axis. In this case, the curves in Fig. 2 corresponding to $\psi<90°$ would more nearly predict the correct dependence of ω_0 on H than the $\psi=90°$ curve. We can see from these curves that the minimum value of ω_0 occurs at $H/H_k>1$. The maximum value of H/H_k which yields a minimum ω_0 is 1.15 and occurs at $\psi=87°$. While all of these curves predict a minimum ω_0 larger than 2.8 Mc, we would expect the susceptibility to reach a maximum at the point of minimum ω_0. This change can be calculated by use of Eq. (10) and is seen to be considerably smaller than that which occurs when $\psi=90°$. This result is in accord with the smaller signal that is observed. While this simple theory gives a qualitatively correct amount of this anomalous behavior, it is probably not the entire answer. Further annealing experiments on films of this composition may shed more light on this phenomenon.

ACKNOWLEDGMENTS

The authors wish to express their appreciation to J. Ross Macdonald and F. G. West for their many helpful suggestions during the course of this work.

---

[12] R. G. Alexander, Fourth Conference, Magnetism and Magnetic Materials, Philadelphia, Pennsylvania, November 17–20, 1958.

[13] T. S. Crowther, Lincoln Laboratory Group Rept. No. 51–2 (1959).

[14] K. J. Harte, J. Appl. Phys. **31**, 2835 (1960).

[15] F. G. West, Sixth Conference, Magnetism and Magnetic Materials, New York, November 14–17, 1960.

On the Possibility of Detecting Shock-Induced Second-Order Phase Transitions in Solids. The Equation of State of Invar

D. R. Curran
Poulter Laboratories, Stanford Research Institute, Menlo Park, California

(Received May 1, 1961)

First-order phase changes in shock-loaded solids have been previously detected from the formation of multiple-wave structures in the solids. It is shown theoretically that a multiple-shock structure under shock loading also may be produced by a second-order phase transition. Accordingly, the possibility of detecting shock-induced demagnetization of ferromagnetic metals and alloys is discussed and an experimental attempt to detect such a demagnetization in shock-loaded Invar (64 Fe, 36 Ni) is reported. Extrapolation of data by Patrick suggests a Curie point transition in Invar in the neighborhood of 50 kbar. The Hugoniot equation of state of Invar has been obtained over a pressure range of 35 to 160 kbar. No double-shock structure was observed, but a decrease in compressibility observed in the neighborhood of 60 kbar is thought to be evidence of demagnetization.

INTRODUCTION

When a high explosive is placed in contact with a solid the interaction of the detonation wave with the explosive-solid interface produces a shock wave in the solid. First-order phase transitions involving a decrease in volume have the effect of making a single shock wave within a certain pressure range unstable and two shock waves are formed. Known first-order phase changes have been detected by the observation of double-shock structures in bismuth and antimony.[1,2] However, the existence of a double-shock structure does not necessarily mean that a first-order phase change is present. It will be shown that a double-shock structure may also result from second-order phase changes.

CONDITIONS FOR DOUBLE-SHOCK FORMATION

Bethe[3] has shown that, if the Hugoniot equation of state is nearly adiabatic, a single shock wave becomes thermodynamically unstable in a region where

$$(\partial^2 P/\partial V^2)_s < 0. \qquad (1)$$

Drummond[4] has shown, again in the adiabatic approximation, that a discontinuity in $(\partial P/\partial V)_s$ which satisfies this inequality gives rise to a double shock. It therefore appears that relation (1) may be considered the necessary and sufficient condition for double shock formation in the adiabatic approximation. Let us therefore examine the adiabatic slope, $(\partial P/\partial V)_s$. The thermodynamic identity

$$(\partial P/\partial V)_s = (\partial P/\partial V)_T + (\partial P/\partial T)_V (\partial T/\partial V)_s \qquad (2)$$

can be converted by means of Maxwell's equations to

$$V\left(\frac{\partial P}{\partial V}\right)_s = -\frac{1}{k} - \frac{\beta^2 TV}{k^2 C_V} = -\frac{1}{k}\left[\frac{1}{1-TV\beta^2/kC_p}\right], \qquad (3)$$

where $k=-(1/V)(\partial V/\partial P)_T$ is the isothermal compressibility and $\beta=(1/V)(\partial V/\partial T)_P$ the coefficient of of thermal expansion.

A second-order phase change is defined as one in which there are no discontinuities in volume or entropy but in which there do exist discontinuities in k, β, and C_p. Therefore, in a second-order transition there will be a discontinuity in $(\partial P/\partial V)_s$ unless the discontinuities in k, β, and C_p happen to cancel. If the discontinuity in $(\partial P/\partial V)_s$ satisfies relation (1), a single shock is unstable and a double shock may form. Therefore, it is possible for a double-shock structure to result from a second-order phase transition as well as from a first-order transition.

The Ehrenfest equations for a second-order phase transition may be written as

$$dP/dT = \Delta C_p / TV\Delta\beta \qquad (4)$$

and

$$dP/dT = \Delta\beta/\Delta k.$$

These relations may be used to predict whether a given second-order transition will produce a double shock. For example, if dP/dT, $\Delta\beta$, and ΔC_p are known experimentally, we may calculate Δk from Eq. (4) and the change in adiabatic slope $(\partial P/\partial V)_s$ from Eq. (3). If the calculated change in adiabatic slope is large enough to be observable and is correct in sign, then double-shock formation would be predicted.

SECOND-ORDER TRANSITIONS

A double-wave structure probably caused by a second-order transition is often observed in metals in which an elastic wave propagates ahead of the shock wave. This phenomenon results from the discontinuity in the slope of the idealized stress-strain curve which occurs upon plastic yielding. Because of work hardening there is no discontinuity in strain or entropy but there may be discontinuities in their derivatives.

Perhaps more interesting is the possibility of detecting Curie point transitions in ferromagnetic metals and alloys. If a Curie point transition resulted in double-shock formation, then by performing dynamic experi-

---

[1] R. E. Duff and F. S. Minshall, Phys. Rev. **108**, 1207 (1957).

[2] S. Katz, D. G. Doran, and D. R. Curran, J. Appl. Phys. **30**, 568 (1959).

[3] H. A. Bethe, Office of Scientific Research and Development Rept. No. 545, Serial No. 237 (1942).

[4] W. E. Drummond, J. Appl. Phys. **28**, 998 (1957).

ments at different initial temperatures, it would be possible to obtain the high-pressure phase diagram of the magnetic transition. The volume dependence of the Curie point would be of particular theoretical interest.

In order to test the plausibility of detecting a demagnetization transition by means of a dynamic experiment, let us estimate the amount of magnetic energy involved in demagnetizing iron at its Curie point. Weiss and Tauer[5] have shown that the limiting value of the magnetic component H_{mag}, of the enthalpy of α iron is of the order RT_c, where T_c is the Curie temperature. In addition, they find that about 60–75% of the available magnetic enthalpy is liberated when the temperature is raised to the Curie point. The total change in H_{mag} up to the Curie point is thus of the order

$$\Delta H_{\text{mag}} \cong 0.60RT_c = 1250 \text{ cal/mole}. \tag{5}$$

It can be seen, therefore, that the magnetic energy change involved in demagnetization is of the order of the thermal energy and is large enough to cause observable effects. This fact may be of interest with respect to the double-shock transition in iron and iron-nickel-chromium alloys observed by Bancroft *et al.*,[6] and Fowler *et al.*[7] This transition was originally attributed to the high-pressure low-temperature form of the α-γ transition (bcc-fcc). However, thermodynamic calculations by Jamieson[8] and others[9,10] and recent experimental data obtained by Strong[11] and Claussen[12] have shown that this identification is probably incorrect.[13] Jamieson[14] has suggested that different magnetic forms of α and γ iron may have to be considered.

However, for the sake of argument, let us assume here that the observed double shock in iron at 130 kbar is due to demagnetization alone. If we approximate the demagnetization by a first-order transition we may write the Clapeyron equation as

$$dP/dT = \Delta H_{\text{mag}}/T_c\Delta V, \tag{6}$$

where T_c is the Curie temperature and dP/dT is a measure of the pressure dependence of the Curie point. Kornetski,[15] using magnetostriction data, has calculated dP/dT to be of the order of -0.1 to -0.2 kbar/deg C. This is the right order of magnitude for 130 kbar to lower the Curie point from its ambient value of about 770 deg C to the neighborhood of 100 deg C, which is roughly the temperature expected behind a 130-kbar shock front. However, Patrick[16] has measured the pressure dependence of the Curie point experimentally for several ferromagnetic metals and alloys and finds that the Curie point of iron is unaffected by pressure up to 9 kbar. If, nevertheless, we assume that the Curie point is decreased by pressure between 9 and 130 kbar in such a way as to meet the shock conditions, then Kornetski's value for dP/dT may be put into Eq. (6) along with the value of ΔH_{mag} in Eq. (5), and ΔV of the transition may be calculated. This calculation is an estimate of the cumulative volume change to be expected during demagnetization and yields a value of $\Delta V \cong -0.3$ cm³/mole. This is of the order of magnitude actually observed in the 130-kbar transition in iron. In view of Patrick's data for iron, however, it is felt that demagnetization alone is an unlikely cause of the observed 130-kbar effect in iron. On the other hand, these considerations show that magnetic effects may be appreciable.

It may be noted that if $\Delta H_{\text{mag}} \cong RT_c$, T_c cancels out in the Clapeyron equation,

$$\frac{dP}{dT} = \frac{\Delta H_{\text{mag}}}{T_c\Delta V} \cong \frac{R}{\Delta V}. \tag{7}$$

Thus, the effective ΔV of the transition depends only on the value of dP/dT and is large when the Curie point is strongly pressure dependent.

EQUATION OF STATE OF INVAR

Although Patrick's measurements showed no variation of Curie point with pressure for iron, in the case of Invar alloy (64% Fe 36% Ni) he found, up to 9 kbar, a constant $dT/dP = -3.6 \pm 0.1$ deg/kbar. Extrapolation

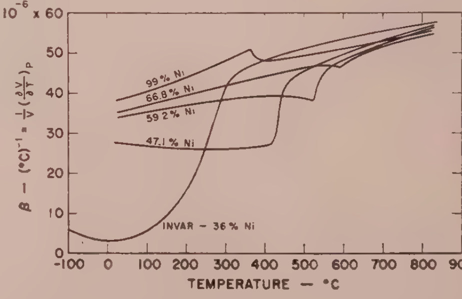

FIG. 1. Thermal expansion coefficient β of Invar as a function of temperature [from R. M. Bozorth, *Ferromagnetism* (D. Van Nostrand Company, Inc., Princeton, New Jersey, 1951), pp. 106 and 447].

---

[5] R. J. Weiss and K. J. Tauer, Phys. Rev. **102**, 1490 (1956).

[6] D. Bancroft, E. L. Peterson, and S. Minshall, J. Appl. Phys. **27**, 291 (1956).

[7] C. M. Fowler, F. S. Minshall, and E. G. Zukas, Proceedings of the Conference on Response of Materials to High Velocity Deformation, Physical Metallurgy Committee of the AIME, Estes Park, Colorado, July, 1960.

[8] J. C. Jamieson, Second Annual Report to ONR, High Pressure Research, Ser. II.

[9] L. Kaufman, discussion for the Conference on Response of Materials to High Velocity Deformation, Physical Metallurgy Committee of the AIME, Estes Park, Colorado, July, 1960.

[10] D. R. Curran and P. S. DeCarli, Stanford Research Institute, Poulter Laboratories Lab. Tech. Rept. 014–58 (1958).

[11] H. M. Strong, J. Geophys. Research **64**, 653 (1959).

[12] W. F. Claussen, GE Research Laboratory Rept. No. 60-RL-2441M (1960).

[13] *Note added in proof.* P. Johnson, B. Stein, and R. S. Davis (personal communication) have recently obtained additional evidence that the dynamic transition is not the α-γ, observing a triple point in the vicinity of 115 kbar and 775°K.

[14] J. C. Jamieson (personal communication).

[15] M. Kornetski, Zt. Physik **98**, 289 (1935).

[16] L. Patrick, Phys. Rev. **93**, 384–392 (1954).

of these data suggests that the Curie temperature would be lowered from its ambient pressure value (about 250 deg C) to near room temperature by a pressure in the neighborhood of 50 kbar. Since this alloy is stable in the fcc phase there is little likelihood of a first-order phase change under compression.

For these reasons an experimental program was undertaken to obtain the Hugoniot equation of state of Invar in the pressure range in the vicinity of 50 kbar. It was hoped that if the material were driven through the Curie point by the shock compression the demagnetization would be observed, either through double shock formation or by an abrupt change of slope of the Hugoniot curve.

If we again take $\Delta H_{\text{mag}} \cong RT_c$ and Patrick's value of dT/dP, Clapeyron's equation yields an estimate of the cumulative volume change expected during demagnetization:

$$\Delta V \cong R(dT/dP) = -0.299 \text{ cm}^3/\text{mole}. \tag{8}$$

If we assume by analogy to the case of iron that about 60–75% of ΔH_{mag} has been yielded at the Curie point, then

$$\begin{aligned} \Delta V &\cong 0.6R(dT/dP) \cong -0.169 \text{ cm}^3/\text{mole} \\ &\cong -0.003 \text{ cm}^3/\text{gm}. \end{aligned} \tag{9}$$

Another way of estimating the expected ΔV is by estimating the amount of thermal expansion which would have taken place from room temperature to the Curie point if magnetic contraction were not present. That is, in Invar the magnetic contraction opposes the normal thermal expansion so that the net expansion is almost zero below the Curie point (see Fig. 1). The normal thermal expansion coefficient β of iron-nickel alloys is in the neighborhood of 40×10^{-6}/deg. Therefore, an estimate of the magnetic contraction can be obtained by equating it to the normal thermal expansion which would have been observed if the magnetic contraction were not present.

$$\begin{aligned} \left|\frac{\Delta V}{V}\right|_{\text{transition}} &\cong \beta(T_c - T_0) \cong (40\times10^{-6}/\text{deg})(250 \text{ deg}) \\ &= 0.010 \\ \Delta V &\cong -0.0012 \text{ cm}^3/\text{g} \cong -0.08 \text{ cm}^3/\text{mole}. \end{aligned} \tag{10}$$

These results show that the expected volume change is appreciable and of the order of -0.08 to -0.17 cm^3/mole.

Since data are available concerning the thermal expansion coefficient of Invar as a function of temperature we may also use the Ehrenfest relations [Eq. (4)] in conjunction with Eq. (3) to estimate the change in $(\partial P/\partial V)_s$ during demagnetization. From an examination of these equations it is apparent that if dP/dT is negative the sign of $\Delta(\partial P/\partial V)_s$ will be opposite that of $\Delta\beta$. Thus a decrease in β corresponds to a "softening" of the material and an increase in β corresponds to a "hardening" of the material. This means that a double shock is expected if β first decreases and then increases in the vicinity of the Curie point. $\beta(T)$ curves for Invar and several other Fe—Ni alloys are plotted in Fig. 1. It can be seen that for percentages of Ni below 70%, $\beta(T)$ does decrease and then increase at the Curie point. However, Invar at room temperature is already losing its magnetic enthalpy and $\beta(T)$ is beginning to increase. This makes double shock formation in Invar look unlikely. Of course, β is actually $\beta(T,P)$ and increasing P tends to decrease β so that at high pressures it is conceivable that β decreases before increasing to its nonmagnetic value. However, $\beta(T,P)$ is initially much more temperature than pressure dependent so it seems more likely that $\Delta\beta(T_c,P)$ at 50 kbar will be similar to $\Delta\beta(T_c,0)$. If we assume that this is the case then $\Delta\beta \cong (40)(10^{-6})$ deg^{-1}. Using Patrick's value $dT/dP = -(3.6)$ deg/kbar, Eq. (4) yields

$$\Delta k = (\Delta\beta)(dT/dP) \cong -(1.4)(10^{-4}) \text{ kbar}^{-1}. \tag{11}$$

Combining this with Eq. (3), we arrive at an estimate of

$$\Delta[(1/V)(\partial V/\partial P)_s] \cong (1.6)(10^{-4}) \text{ kbar}^{-1}. \tag{12}$$

Since the Hugoniot equation of state is nearly adiabatic at 50 kbar this would predict that at the Curie point the P-V curve would suddenly steepen by the amount given in Eq. (12).

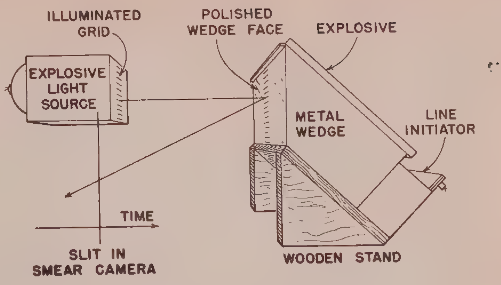

FIG. 2. Experimental arrangement for equation of state shots.

EXPERIMENTAL ARRANGEMENT

The experimental method used to obtain the Hugoniot equation of state of Invar was developed by G. R. Fowles and is described in detail elsewhere.[17] The arrangement is shown in Fig. 2. An oblique shock produced by a running detonation on the back of an Invar wedge is incident at a small angle on the polished wedge face. The resultant slight turning of the wedge face is detected by the displacement of reflected images from a grid illuminated by an explosive light source. The reflected images are observed through a slit in the focal plane of a smear camera. The measured displacement of a given image can be related to the free surface velocity of the area on the wedge face which reflects the image into the camera aperture. Due to attenuation of the oblique shock, a wide pressure range may be ob-

---

[17] G. R. Fowles, J. Appl. Phys. (to be published).

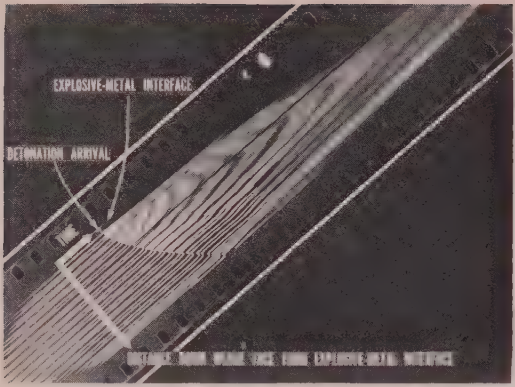

FIG. 3. Streak-camera record of shot No, 7221.

served in a single experiment. The estimated experimental error is 4% in pressure at a given density.

In the smear camera record shown in Fig. 3 we observe the arrival of the elastic wave and the following shock wave. There is no evidence of a double-shock structure. The complicated structure observed behind the shock wave is thought to be due to reverberations in the spall, but has not been quantitatively analyzed.

The resulting pressure-density data cover a pressure range of from 35 to 160 kbar and are plotted in Fig. 4. Supporting data are given in Table I. For comparison we have also plotted in Fig. 4 the Hugoniot curves of other iron-nickel alloys obtained by Fowler, Minshall, and Zukas.[7] The cusps in their curves represent the transitions (130 kbar in Fe) discussed earlier.

It can be seen that the Invar is elastic up to a stress of 12.5 kbar, after which it yields and is initially relatively compressible, but at about 60 kbar it becomes less compressible and parallels the curves of the other iron-nickel alloys. If it is assumed that the initial "softness" of the Invar is due to demagnetization and that the steepening of the curve at 60 kbar indicates the material is going through the Curie point, we may measure approximate values of $\Delta[(1/V)(\partial V/\partial P)_s]$ and the effective value of ΔV. These may be compared with the predicted values calculated earlier. The results are:

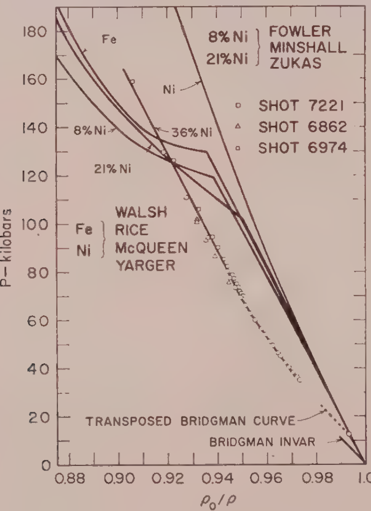

FIG. 4. Hugoniot equations of state of iron-nickel alloys.

TABLE I. Properties of Invar used in experiments.

Supplier: Carpenter Steel Company
Composition: 62.62% Fe, 35.89% Ni, 0.19% Se, 0.07% C, 0.86% Mn, 0.35% Si, 0.010% P, 0.008% S.
Heat Treatment: Specimens were annealed by the following heat treatment: 1450°F for $1\frac{1}{2}$ hours, cooled in furnace to 800°F. Air-cooled to room temperature.
Crystal Structure: This alloy is stable in the γ(fcc) phase. X-ray examination of the annealed specimens showed no evidence of α(bcc) phase. Experimental accuracy of the measurement places the amount of α phase at below 5%.
Compressional Elastic Wave Velocity:
Ultrasonic measurement at 9.0 Mc yields $C_0 = 4.73$ mm/μsec
Dynamic measurements: Shot 7221–4.90 mm/μsec
Shot 6862–4.84 mm/μsec
Initial Density: $\rho_0 = 8.08 \pm 0.01$ g/cm^3

$$\Delta\left[\frac{1}{V}\left(\frac{\partial V}{\partial P}\right)_s\right]\Bigg|_{\substack{\text{measured from}\\ \text{experimental curve}}} \cong (2.5)(10^{-4})\ \text{kbar}^{-1}$$

$$\Delta\left[\frac{1}{V}\left(\frac{\partial V}{\partial P}\right)_s\right]\Bigg|_{\text{predicted}} \cong (1.6)(10^{-4})\ \text{kbar}^{-1}$$

$$[\Delta V]^{\text{effective}}_{\substack{\text{measured from}\\ \text{experimental curve}}} \cong -0.11\ \text{cm}^3/\text{mole}$$

$$[\Delta V]^{\text{effective}}_{\text{predicted}} \cong -0.08 \text{ to } -0.17\ \text{cm}^3/\text{mole}.$$

We conclude that it is likely that the initial large compressibility is due to demagnetization, but that quantitative verification will require further analysis and experimentation.

CONCLUSIONS

We have seen that second-order phase changes in a shock-loaded solid may result in double-shock formation or in a decrease in compressibility; therefore, demagnetization of ferromagnetic metals and alloys should be dynamically observable in some cases. In Invar, a decrease in compressibility observed in the neighborhood of 60 kbar is thought to be evidence of demagnetization.

ACKNOWLEDGMENTS

Part of this work was performed at Washington State University under the supervision of Dr. William Band, and was supported by the NSF. The experimental work was done for the Air Force Office of Scientific Research, ARDC. In addition, the author has benefited from many discussions with P. S. DeCarli, G. R. Fowles, and Dr. George E. Duvall.

JOURNAL OF APPLIED PHYSICS VOLUME 32, NUMBER 10 OCTOBER, 1961

Elastic-Plastic Transition in Copper Crystals as Determined by an Etch-Pit Technique

F. W. Young, Jr.
Solid State Division, Oak Ridge National Laboratory, Oak Ridge, Tennessee*

(Received April 3, 1961)

Copper (99.999%) crystals with a dislocation density of 50/mm² have been prepared. These crystals were stressed by applying a pure bending moment, and they were etched with a dislocation etch either before and after or while the stress was applied. The motion of dislocations was determined by observing the size and nature of the dislocation etch pits. The resolved stress necessary to move grown-in dislocations was about 4 g/mm². Examples of dislocation motion under stress, then return motion when the stress was removed, and of multiple motion under stress were observed. Multiplication of dislocations occurred at a resolved stress of about 18 g/mm². The observed phenomena are discussed in terms of simple dislocation theory.

INTRODUCTION

It has recently become possible to prepare copper crystals with a dislocation density as low as 50/mm². These crystals were stressed by applying a pure bending moment, and they were etched with a dislocation etch either before and after or while the stress was applied. The motion of the dislocations was determined by observing the size and nature of the dislocation etch pits which were formed. This paper is a description of the motion of dislocations in copper caused by stresses in the vicinity of the elastic limit.

EXPERIMENTAL

Parallelepipeds, about 5×6×25 mm with the 6×25-mm face (111), were sawed with an acid saw from a 1-in. diameter copper crystal (99.999% Cu grown by a Bridgman technique), acid polished,[1] and annealed four days at 1050°C in vacuum. These crystals were stressed using a four-point bending jig which was arranged so the crystal could be etched while the stress was applied. The dislocation etch used was 1*M* $FeCl_3 \cdot 6H_2O$, 12*M* HCl, 0.25*M* HBr.[2] The crystal was electropolished prior to each experiment, and special care in handling was necessary to avoid the unwanted introduction and/or movement of dislocations.

This dislocation etch forms tetrahedral-shaped pits at both old (dirty) and new (clean) dislocations on the (111) face of 99.999% copper. The bottom of a pit is sharp so long as the dislocation remains in this position and has a component normal to the surface. When the dislocation moves away, the pit becomes flat bottomed. This behavior appears to be analogous to that observed on LiF by Gilman and Johnston.[3] The edges of the pits lie along [110] directions. For etching times of a few seconds, the etch pits are easily observable with an optical microscope.

The stress applied with the four-point bending jig can be calculated from classical mechanics using the formula

$$\sigma_{\max}(\mathrm{g/mm^2}) = 3Wd/a^2b,$$

where W = weight in grams, and a, b, and d are defined in Fig. 1. The resolved stress can then be computed using the formula

$$\sigma_R = (\mathbf{n}\cdot\mathbf{v})(\mathbf{s}\cdot\mathbf{v})(\sigma_{\max}),$$

where $\mathbf{n}$ = slip plane, $\mathbf{s}$ = slip direction, and $\mathbf{v}$ = orientation of crystal ($[\bar{1}21]$ in Fig. 1).

RESULTS

A crystal of the orientation shown in Fig. 1 was electropolished, placed in the bending jig, and etchant added. After etching for 7 sec, a stress $\sigma_{\max} = 9$ g/mm² was applied for five additional seconds as the etching continued. The stress was removed and the etching stopped (by flooding with water) simultaneously. No

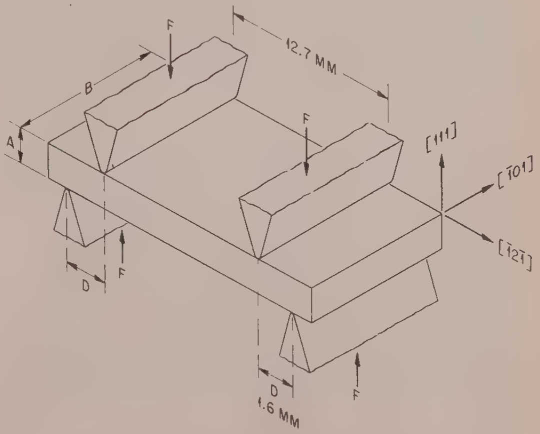

Fig. 1. Orientation of crystal and schematic representation of the arrangement in the bending jig.

---

* Oak Ridge National Laboratory is operated by Union Carbide Corporation for the U. S. Atomic Energy Commission.

[1] F. W. Young, Jr. and T. R. Wilson, Rev. Sci. Instr. **32**, 559 (1961).

[2] F. W. Young, Jr., J. Appl. Phys. **32**, 192 (1961).

[3] J. J. Gilman and W. G. Johnston, *Dislocations and Mechanical Properties of Crystals*, edited by J. C. Fisher, W. G. Johnston, R. Thomson, and T. Vreeland, Jr. (John Wiley & Sons, Inc., New York, 1957), p. 116.

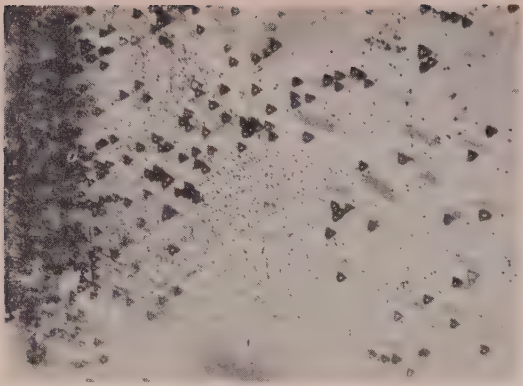

FIG. 2. Etch pits at new dislocations formed where bending jig made contact. 50×.

dislocations were moved in the central part of the crystal by this stress. Of course, some new dislocations were formed where the bending jig made contact (Fig. 2). The density of dislocations N in this crystal was 50/mm², with approximately random distribution and with no sub-boundaries.

The experiment was repeated with an applied stress of $\sigma_{\max}=12.8$ g/mm². About 1% of the dislocations in the central part were moved by this stress. In the photomicrographs of Fig. 3, flat-bottomed pits, each with a corresponding small sharp-bottomed pit nearby, can be seen. The small pits would fit exactly on the flat-bottomed pits, and an imaginary line connecting the two lies along a slip direction. The resolved stresses for the principal slip systems for this orientation are as follows (slip planes in parentheses, slip directions in brackets):

$$\sigma_R(\bar{1}11)\longrightarrow[0\bar{1}1]=0.408\,\sigma_{\max}=\sigma_R(11\bar{1})\longrightarrow[1\bar{1}0]$$

$$\sigma_R(1\bar{1}1)\longrightarrow[011]\quad\text{or}\quad[110]=0.272\,\sigma_{\max}.$$

Movement in all three planes was observed. Thus, movement occurred at resolved stresses of 3.5 and 5.2 g/mm². Most of the movement was in a direction corresponding to the higher stress, and the distance of motion was greater in that direction.

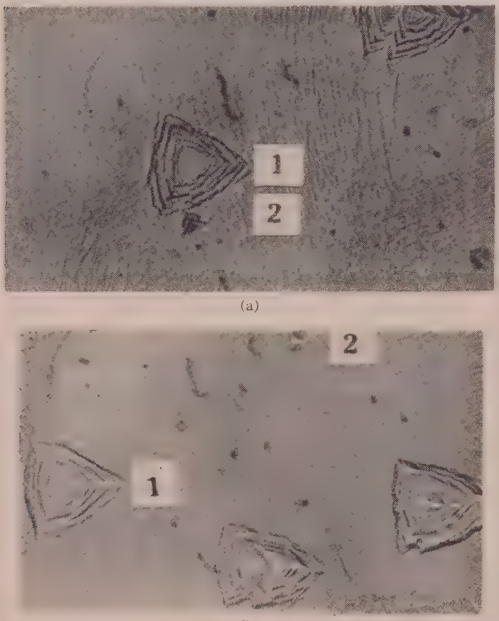

FIG. 3. Dislocation motion at stress of (a) 3.5 g/mm², 500×. (b) 5 g/mm, 500×. Initial positions of dislocations designated 1; final position, 2.

The dislocations which moved as described above were old (dirty) dislocations. There was also motion of nearly all of the new (clean) dislocations which were formed where the jig made contact in the previous experiment (Fig. 4). Apparently, the stress necessary for motion, $\sigma_{(\text{motion})}$, is less for clean dislocations than for dirty ones. The conclusion is that there is a pinning of the dislocations by the impurities in 99.999% copper.

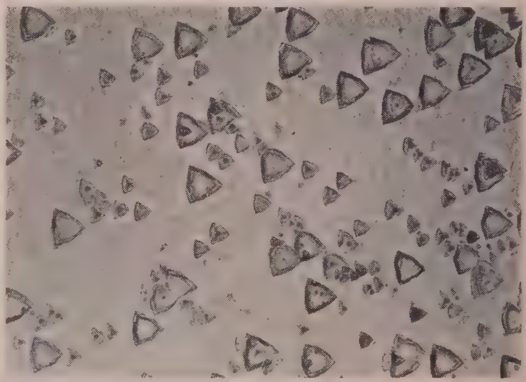

FIG. 4. Motion of clean dislocations at same stress as for Fig. 3. 200×.

It was determined that the dislocations did not move back when the stress was removed by repeating the experiment with the same stress, but this time allowing the etching to continue after the stress was removed. The experiment was also repeated with $\sigma_{\max}$ of 14 and 17 g/mm² with essentially the same results stated above. The number of dislocations which moved increased with the stress.

In an experiment in which the crystal was etched continuously for 21 sec, with a stress $\sigma_{\max}=22.4$ g/mm² applied during the middle 7 sec, it was observed that about 10% of the dislocations had moved. A few which had moved under the stress had moved back when the stress was relieved. In the example shown in Fig. 5, the dislocation moved about 23 μ, then moved back to within about 1 μ of its original position. It should be noted that the three pits, two flat-bottomed and one sharp-bottomed, would fit almost exactly on each other in the proper sequence. For the ones which moved back, $\sigma_R = 10$ g/mm^2.

For a stress $\sigma_R = 18$ g/mm^2, multiplication of dislocations was observed. The crystal was electropolished and etched for 8 sec, the stress applied for an additional 8 sec as the etching continued, and the stress and etchant were removed simultaneously. It was concluded that multiplication had occurred because groups of new dislocations (small pits) along the glide directions were observed (Fig. 6). Also, the over-all density of dislocations was now about 10^4/cm^2.

The experiment was repeated at the same stress except that this time it was etched, stressed, then re-etched. After the first etching, a group (pile-up?) of dislocations was observed. After stressing and re-etching, all but one of this group had moved (Fig. 7). This observation demonstrates: (1) that multiplication had occurred in the previous experiment, and (2) that the clean dislocations move more easily than dirty ones, since only a few other dislocations in this vicinity had moved. The resolved stress σ_R for this multiplication in this crystal was 18 g/mm^2. It is possible that multiplication would occur at a slightly lower stress; it did not occur at $\sigma_R = 10$ g/mm^2.

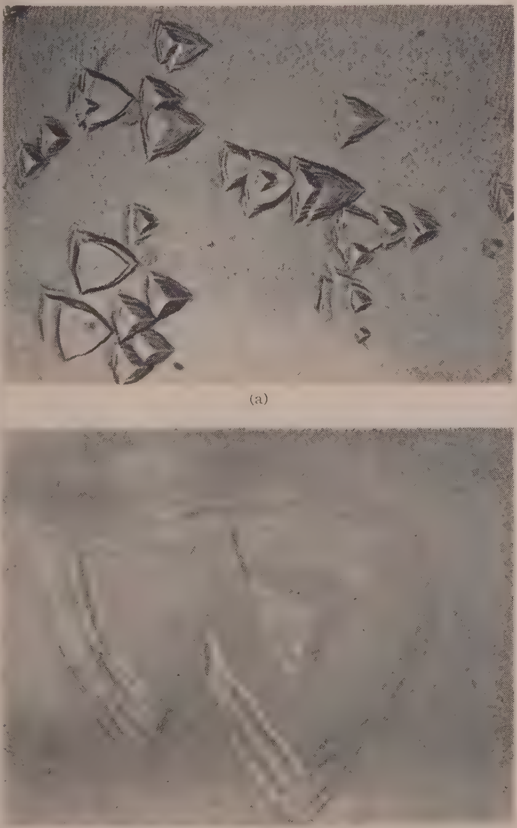
(a)

(b)

Fig. 5. Showing back motion when stress is relieved $\sigma_R = 10$ g/mm^2. (a) 200×. (b) 1000×.

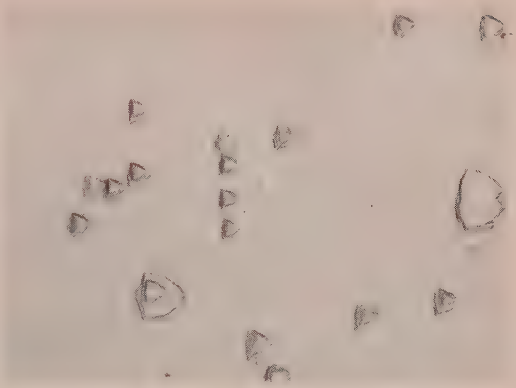
Fig. 6. Pits at new dislocations after multiplication. 200×.

An example of glide polygonization[4] was observed for the stress of 18 g/mm^2 (Fig. 8). Here three new dislocations are nearly aligned in a direction perpendicular to a slip direction.

Some interesing examples of multiple dislocation motion while under stress have been obtained in these experiments. Another crystal ($N \cong 50$/mm^2) was etched 4 sec and a stress $\sigma_R = 20$ g/mm^2 applied as the etching was continued for an additional 4 sec, the stress and etchant being removed simultaneously. An example of multiple motion is shown in Fig. 9. Here the dislocation moved three times, then apparently started to multiply. The distance of each movement was approximately the same, $\sim 10\ \mu$. Multiple motion was also observed for $\sigma_R = 10$ g/mm^2.

The results presented here for this crystal have been confirmed by experiments on other crystals, which were cut from the same rod and from another rod. For all crystals tested $\sigma_{(\text{motion})}$ was about 4 g/mm^2. The initial density of dislocations varied from 50–500/mm^2. The

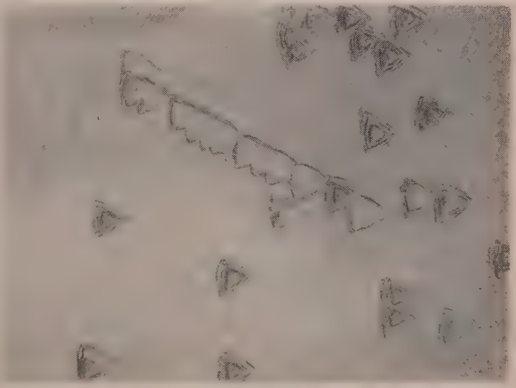
Fig. 7. Showing motion of new dislocations in a pile up under a second stress. 200×.

---

[4] J. D. Livingston, J. Appl. Phys. 31, 1071 (1960).

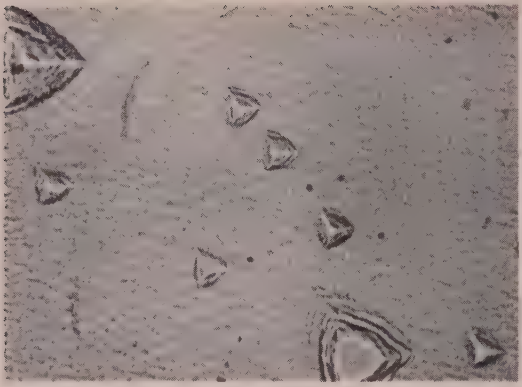

FIG. 8. Showing glide polygonization.

motion back when the stress was removed was observed only for stresses greater than 4 g/mm². On a crystal ($N=500/\text{mm}^2$, $\sigma_R=10$ g/mm²), two examples were observed in which a dislocation moved a distance A under stress, then moved back a distance B, with $B<A$, (Fig. 10). The values for A and B were 35 and 29 μ for dislocation I, and 24 and 21 μ for dislocation II, respectively.

There was no observable bending of the crystals in any of these experiments. The strain at a stress of 4 g/mm² was 10^{-6}; at 18 g/mm² the strain was probably $\sim 10^{-5}$.

DISCUSSION

While it is not intended here to give a comprehensive treatment of the relation of these experiments to the theory of the elastic-plastic transition of crystals, it is of interest to apply some of the theory which has been proposed to the experimental results presented in this paper.

For a stress of approximately 4 g/mm², motion of dirty dislocations was observed. This value did not vary appreciably with initial dislocation density. Clean dislocations move at a stress less than 4 g/mm². These facts suggest impurity pinning of the dislocations.

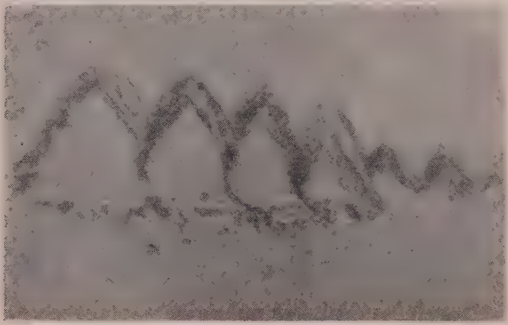

FIG. 9. Showing multiple motion under stress.

Cottrell[5] gives an expression for the energy of attraction of an impurity atom to a dislocation. If the impurity atom is considered fixed and if it holds the dislocation with the corresponding amount of force, then the number of impurity atoms necessary to pin the dislocations can be estimated. According to Cottrell, $U_i=4\mu b\epsilon r_0^3 \times(\sin\alpha/R)$, where ϵ is the misfit of the impurity atom $(r-r_0/r_0)$, r is the radius of the impurity atom, and α and R are polar coordinates of the impurity atom with respect to the dislocation. The force then is $F=-\partial U/\partial R$, and if this force is maximized,

$$F_i=(4\mu b\epsilon r_0^3/R^2).$$

For $\epsilon=10\%$, and $R=2\times10^{-7}$ mm, $F=2\times10^{-8}$ g/atom. This force would be temperature dependent and this computation is for absolute zero. A reasonable estimate might be that the force would be ½ as large at room temperature. Thus, the pinning force $F_i\sim10^{-8}$ g/atom.

For the measured stress for motion, $\sigma=4$ g/mm², the corresponding force on the dislocation line $F=\sigma_b=10^{-6}$ g/mm. Thus, about 100 impurity atoms per millimeter would be required to account for the force necessary to move the dislocations. This corresponds to only about a factor of two in the concentration of impurity atoms at the dislocations over the concentration in the lattice. It follows from this argument that, for reasonably low dislocation densities, $\sigma_{(\text{motion})}$ is dependent on the purity of the crystal and not on the dislocation density.

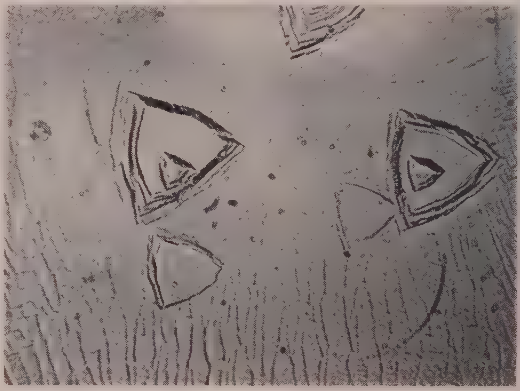

FIG. 10. Showing back motion when stress is relieved. 500×.

The dislocations which move under a stress of about 4 g/mm² do not return to their original positions when the stress is relieved. Thus, they must be bound by something in the lattice. It is reasonable to assume that this binding force, which the moving dislocation meets in the lattice, must be smaller than the original pinning force. From these assumptions an estimate can be made of the length of the dislocations which moved.

The stress σ_0 necessary to maintain a dislocation of Burgers vector b and line tension T with a radius r is

---

[5] A. H. Cottrell, *Dislocations and Plastic Flow in Crystal* (Oxford University Press, New York, 1953), p. 56.

$\sigma_0=T/br$.[6] The line tension can be expressed as $T=\alpha\mu b^2$. It has generally been considered that $\alpha\cong\frac{1}{2}$,[6] but recent calculations by Paré,[7] based on the work of DeWit and Koehler,[8] give $\alpha\cong1$ for edge dislocations in copper. Therefore, both values for α will be considered. A dislocation of length l, ending at the surface, is moved a distance S under an applied stress [see Fig. 11(a)].[9] For this condition $r=[(l)^2+S^2/2S]$. Then $\sigma=\alpha\mu b/r=[2\alpha S\mu b/(l)^2+S^2]$; $\alpha=1$ or $\alpha=\frac{1}{2}$. Since for copper $\mu=4\times10^6$ g/mm², $b=2.5\times10^{-7}$ mm, $\sigma=[2\alpha S/(l)^2+S^2]$. Then if we assume that the dislocations are held in their new position with a force sufficient to overcome a stress $\sigma=2$ g/mm² (i.e., one-half the stress necessary to break away from the impurity pinning force), the length l of the dislocation can be computed, and they are given in Table I. The values for S varied between 10 and 75 μ for a stress of about 4 g/mm², so calculations are shown for 10, 50, and 75 μ. The values for l should be compared with $l_N=(N)^{-\frac{1}{2}}$; $l_N=0.14$ mm for this crystal.

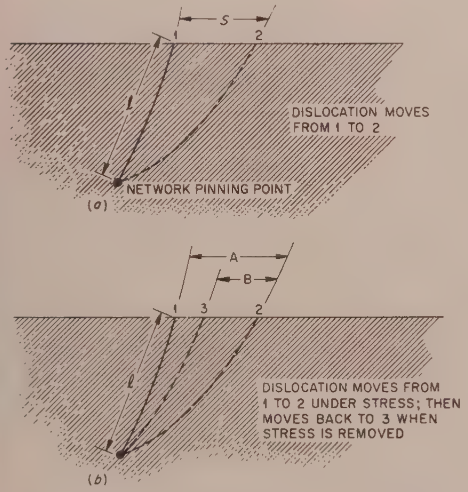
S
1
2
l
DISLOCATION MOVES FROM 1 TO 2
NETWORK PINNING POINT
(a)
A
B
1
3
2
l
DISLOCATION MOVES FROM 1 TO 2 UNDER STRESS; THEN MOVES BACK TO 3 WHEN STRESS IS REMOVED
(b)

FIG. 11. Schematic representation of (a) simple dislocation motion; (b) return motion when stress is relieved.

TABLE I. Computed length of dislocations for simple motion.

S(mm)	l(mm) $\alpha=\frac{1}{2}$	$\alpha=1$
1×10^{-2}	0.07	0.1
5×10^{-2}	0.15	0.21
7.5×10^{-2}	0.18	0.26

For stresses in the vicinity of 10 g/mm² some of the dislocations moved under the stress, then moved back, or part of the way back, when the stress was removed. It is assumed that when they moved only part of the way back they were held in this position in an analogous way to that postulated above for the lower stresses. Here we assume that a dislocation of length l, ending at the surface, is moved by the stress a distance A, which corresponds to the maximum radius this stress can bow the dislocation. When the stress is relieved, the dislocation returns a distance $B\leqq A$. If $B<A$ the stress tending to return the dislocation from $(A-B)$ to its original position should be less than the original pinning force of 4 g/mm² [see Fig. 11(b)].

TABLE II. Computed length of dislocations which moved under stress and moved back when stress was relieved.

Example	l(mm) $\alpha=\frac{1}{2}$	$\alpha=1$
I	0.048	0.076
II	0.042	0.065

The dislocation length l was computed for the two examples shown in Fig. 10, and they are listed in Table II. The values of l should be compared with $l_N=(N)^{-\frac{1}{2}}=0.045$ mm for this crystal. It may also be noted that the stress tending to return the dislocation from its final position to its original position is about 2 g/mm² for both I and II.

For the crystal with $N=50/\text{mm}^2$, $\sigma_{(\text{multiplication})}$ was approximately 18 g/mm². Also multiplication was apparently occurring for the sample shown in Fig. 9; $N\cong50/\text{mm}^2$, $\sigma=20$ g/mm². Multiplication occurs when the radius of a bowed-out dislocation becomes equal to one-half its length. Then, $\sigma_{(\text{multiplication})}=[\alpha\mu b^2/b(l/2)]=2\alpha/l$ for copper. Consider a dislocation of length l', which ends at the surface, and a dislocation of length l'' with both ends fixed inside the crystal. Then, for l', $\sigma_{(\text{multiplication})}=\alpha/l'$; for l'', $\sigma_{(\text{multiplication})}=2\alpha/l''$. The computed values for l' and l'' are shown in Table III for $\sigma_{(\text{multiplication})}=18$ g/mm². These values for l' and l'' should be compared with $l_N=0.14$ mm.

It appears that agreement between theory and experiment is best for $\alpha=\frac{1}{2}$ for stresses less than the multiplication stress. For multiplication there is reasonable agreement only for $\alpha=1$ and for dislocation with both ends fixed inside the crystal. The value of $\alpha=1$ was obtained by Paré[7] for the situation in which the dislocation was bowed out to its maximum radius before multiplication. Therefore, it should apply more accurately for this case.

TABLE III. Computed length of dislocations which multiplied.

	$\alpha=\frac{1}{2}$	$\alpha=1$
l'	0.028	0.056
l''(mm)	0.056	0.111

---

[6] See reference 5, p. 53.

[7] V. K. Paré (private communication).

[8] G. DeWit and J. S. Koehler, Phys. Rev. **116**, 1113 (1959).

[9] A dislocation ending at a surface should act under stress as if it were twice as long as it is.

It is not clear why the dislocations which end at the surface do not multiply at a stress at least a factor of two lower than 18 g/mm². Since it appears that new dislocations may be piling up, even at this low stress, one may postulate some interaction with the old dislocations, or possibly with some small precipitate particles in the lattice. Additional information on the multiplication and motion of dislocations at higher stresses will be presented in another paper.

ACKNOWLEDGMENTS

It is a pleasure to acknowledge many helpful discussions with T. H. Blewitt, D. K. Holmes, and V. K. Paré of this Division.

JOURNAL OF APPLIED PHYSICS VOLUME 32, NUMBER 10 OCTOBER, 1961

Application of the Czochralski Method to Divalent Metal Fluorides

K. Nassau
Bell Telephone Laboratories, Inc., Murray Hill, New Jersey

(Received April 12, 1961)

The Czochralski method of pulling from the melt has been applied to the growth of single crystals of divalent fluorides of Ca, Sr, Ba, Co, and Mn, and the compound $KMnF_3$. The trivalent rare earth ions Ce, Nd, Sm, Eu, Gd, Tb, and Yb were introduced into CaF_2 and the distribution coefficient was determined to be close to unity in all cases.

THE preparation of single crystals of fluorides, both pure and "doped" with rare-earth or other inorganic ions, is of considerable interest in view of their amenability to study by means of a variety of powerful techniques such as fluorescence, nuclear magnetic resonance, semiconductivity, and acoustic absorption. Of the various methods available for the production of single crystals, growth from the melt is a preferred method if the properties of the material are suitable.[1] The customary method is the Bridgman-Stockbarger technique,[2] using a graphite crucible. In a number of instances, difficulties are encountered chiefly as the result of cracking of the boules and occasional reaction with the graphite.

The Czochralski method of continuous pulling from the melt has been applied to the fluorides of Ca, Ba, and Sr, both pure and doped, to the transition metal fluorides CoF_2, MnF_2, and to the mixed fluoride $KMnF_3$.[3] The same technique is expected to be applicable to other fluorides, being limited, however, by the higher volatility of some of the transition compounds. In such cases, the use of a sealed crucible in the Bridgman-Stockbarger technique as described by Guggenheim[4] would be preferred.

The fluorides of Ca, Sr, and Ba were obtained from the Harshaw Chemical Company. Other fluorides were prepared by the reaction of carbonates or oxides with aqueous HF, drying, and sintering at about 700°C in dry HF gas.

The apparatus used is shown in Fig. 1. The water-cooled brass end plates were held together by aluminum tie rods not shown. The crucibles were $1\frac{1}{2}$ in. o.d., $1\frac{1}{4}$ in. high and $\frac{1}{16}$ in. thick and made of Rh, Pt—20% Rh or Ir. Radio-frequency power at 450 kc was coupled directly into the wall of the crucible and controlled by a Leeds & Northrup type H controller activated by a Pt/Pt-10% Rh thermocouple in a grounded platinum shielding tube located as shown. The seed crystal was rotated at 25 rpm and the pulling rate used was generally $\frac{1}{2}$ to $1\frac{1}{2}$ in. per hour. The seed did not have to be a single crystal, since the technique of necking down and broadening out by careful temperature control as shown in Fig. 1 can be used to select one of the crystallites in a polycrystalline seed. The apparatus was evacuated and filled with Ar to slightly above atmospheric pressure.

The maximum diameter obtainable was approximately $\frac{1}{2}$ in., being limited by the radial temperature gradient which is, among other factors, a function of the size of the crucible. The length was limited by the apparatus; in the case of CaF_2, an additional problem is the pronounced {111} cleavage, which made it difficult to pull faster than $\frac{1}{2}$ in. per hour and produced cracking if crystals more than about 1 in. in length were pulled. Reheating the pulled crystal in a furnace in an inert atmosphere to about 1000°C for several hours and cooling slowly appeared to help in preventing further cracking on handling the crystals.

The appreciable vapor pressure of CoF_2 at its melting point resulted in a deposit on the quartz tube after about $\frac{1}{2}$ hr and necessitated lowering of the temperature at the control point, as radiant energy was being reflected by this coating. A shield movable from the outside by a magnet (not shown in Fig. 1) permitted continued observation and control of growth.

---

[1] M. Tanenbaum in *Methods of Experimental Physics*, edited by K. Lark-Horowitz and V. A. Johnson (Academic Press, Inc., New York, 1959), Vol. 6A, p. 86 ff.

[2] D. C. Stockbarger, J. Am. Opt. Soc. **39**, 731 (1949).

[3] $KMnF_3$ and other mixed fluorides have also been pulled by P. E. Freeland and D. W. Mitchell of these Laboratories.

[4] H. Guggenheim, J. Phys. Chem. **64**, 938 (1960).

A number of distribution coefficients were determined for rare-earth fluorides added to CaF_2 at about the 1 at.% level. Fluorescent spectroscopic analyses of the crystal and melt phases gave values as follows:

Ce	0.88	Gd	1.07
Nd	1.06	Tb	1.10
Sm	0.98	Yb	0.88.
Eu	0.81		

The accuracy of these values is estimated to be better than ±3% since only the ratio of two analyses, which were done at the same time and were close together in magnitude, was involved. Since the crystal structure is cubic, a large change in distribution coefficient with crystallographic direction is not expected. In view of the fairly low viscosity of CaF_2, the reasonable rotation rates and the rather slow pulling rates used, the distribution coefficients listed can be taken as close approximations to the equilibrium (thermodynamic) distribution coefficients.

The fact that the distribution coefficients are close to unity indicates that any of the melt methods would produce crystals with fairly uniform dopant concentrations. Even better uniformity was obtained in the case of pulling since less than 20% of the crucible content was pulled at one time. The same improvement can be achieved by the technique of zone leveling[5] as has been done by Guggenheim.[6]

Fluorescent and absorption spectroscopy indicated that under the conditions used, all the rare earths went into the trivalent state, with only a trace of the divalent state in the case of Sm. Since a monovalent ion was not added and only a trace of oxygen could have entered via the gas stream, the environment is expected to be cubic or axial, with ordered or random arrangement of the charge-compensating interstitial fluoride ions, depending on the exact nature of the annealing process used.[7]

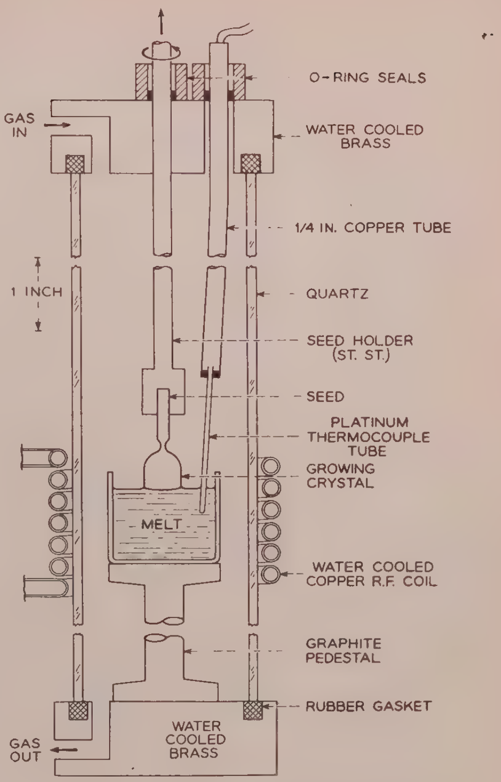

FIG. 1. Apparatus used for the Czochralski pulling in a protective atmosphere.

An alternative charge-compensation technique is the addition, for example, of one mole of LiF per mole TbF_3. In this case, one Li^+ plus one Tb^{3+} replace two Ca^{2+} ions in the CaF_2 lattice. The distribution coefficient of Tb was determined in the example cited and found to be 1.08. It is interesting that this is not significantly different from the value of 1.10 when no LiF is added, indicating that the free energy involved is not appreciably different with this type of charge compensation. No vapors due to the possible volatility of LiF were observed and it is assumed that the Li accompanied the Tb, as is in fact indicated by the presence of changes in the spectrum.

Two other doping experiments were performed. The addition of 1 at.% CoF_2 to CaF_2 gave a distribution coefficient of 0.56, indicating an energetically less favorable arrangement than in the case of the rare-earth ions, despite the now identical charges. Co^{2+} has an ionic radius of 0.72 A compared with 0.99 for Ca^{2+} and 0.86 to 1.07 for the rare-earth ions. Accordingly, it is probably the geometrical disposition of the partly occupied *3d* orbitals that produces this lowering of stability. The attempt to dope CoF_2 with LiF without trying to influence charge compensation gave a distribution coefficient of 0.03.

ACKNOWLEDGMENTS

The author wishes to thank A. M. Broyer for assistance with the experiments, Miss S. Vincent for performing the fluorescent spectroscopic analyses, D. L. Wood for the emission and absorption spectroscopic examinations, and H. Guggenheim for suggesting part of this work and assistance in the preparation of the starting materials.

---

[5] W. G. Pfann, *Zone Melting* (John Wiley & Sons, Inc., New York, 1958), p. 153.

[6] H. Guggenheim (to be published).

[7] E. Friedman and W. Low, J. Chem. Phys. **33**, 1275 (1960).

JOURNAL OF APPLIED PHYSICS VOLUME 32, NUMBER 10 OCTOBER, 1961

Properties of Heavily Doped *n*-Type Germanium

W. G. Spitzer, F. A. Trumbore, and R. A. Logan
Bell Telephone Laboratories, Inc., Murray Hill, New Jersey

(Received April 27, 1961)

The electrical and optical properties of *n*-type germanium have been studied for doping levels greater than 5×10^{18} cm^{-3}. Hall coefficient and resistivity measurements show that the electron mobility μ depends upon the specific group V donor used as a dopant and, at a given carrier concentration, increases in the order $\mu_{\text{As}}<\mu_{\text{P}}<\mu_{\text{Sb}}$. In material doped very heavily with arsenic, a large fraction of the arsenic was found to be electrically inactive. Rapid quenching of this material resulted in larger carrier concentrations and a better correlation with crystal growth parameters. Distribution coefficients were calculated from the electrical measurements on antimony-doped crystals grown by a solvent evaporation technique. No significant "facet effect" was observed for these crystals. Reflectivity measurements between 2 and 24 μ were used to deduce the electron effective mass as a function of carrier concentration. In the carrier concentration range studied (up to 8×10^{19} cm^{-3}), the effective mass increases only slightly and is independent of the specific dopant. The free carrier absorption is dependent on dopant. The absorption and electrical data are correlated by using elementary conduction theory.

I. INTRODUCTION

RECENTLY, considerable interest has been aroused in the properties of heavily doped semiconductors because of their use in Esaki diodes. The present work is an investigation of the electrical and optical properties of heavily doped *n*-type germanium and their dependence upon the group V impurity used to dope the material. In the course of this study, data were also obtained on the distribution coefficient of antimony in germanium and on the partial pressure of arsenic over certain germanium-arsenic alloys. Some unusual features involved in the preparation of these materials are also discussed.

Evidence has been presented in the literature that some of the electrical properties of *n*-type germanium are influenced by whether arsenic, antimony, or phosphorus is used as the dopant. It is well known that arsenic-doped germanium yields Esaki diodes with significantly higher peak-to-valley current ratios than does phosphorus-doped germanium. Furukawa[1] has also reported that the current densities in Esaki diodes made with arsenic are greater than in those doped with antimony to the same concentration. Furthermore, phonon assisted tunnelling is more pronounced in diodes made with antimony than in those doped with phosphorus or arsenic.[2] In addition, Furukawa[1] and Moody and Strauss[3] have reported that at sufficiently high carrier concentrations the electron mobility in antimony-doped germanium becomes appreciably larger than in arsenic-doped material. A similar effect has been observed by Logan *et al.*[4] for arsenic, antimony, and phosphorus in silicon.

In addition to the work on electrical properties, studies have been reported on the optical properties of highly doped *n*-type germanium. From a study of the infrared reflectivity, Cardona *et al.*[5] have reported a nearly twofold increase in effective mass m^* in the range of carrier concentration N from 2×10^{18} to 5×10^{19} cm^{-3}. However, the magnetic susceptibility measurements of Bowers[6] showed no change in m^* up to values of $N\sim3\times10^{19}$ cm^{-3}. Pankove[7] has reported observing structure in the free carrier absorption at a wavelength λ of 2.5 μ which was interpreted as the threshold for indirect transitions in the heavily doped material. However, Keyes[8] was unable to find this structure in similar material. Pankove[7] also reports the free carrier absorption coefficient α to be proportional to λ^2 for $N\sim2\text{–}3\times10^{19}$ cm^{-3}. Keyes finds that α does not have a simple power law dependence on λ.

In the present work, resistivity and Hall effect data show that at sufficiently high carrier concentrations the electron mobility μ decreases in the order $\mu_{\text{Sb}}>\mu_{\text{P}}>\mu_{\text{As}}$, which is the same order observed in silicon.[4] Infrared reflectivity and transmission data show that the free carrier absorption is a function of doping element but that there is no effect of specific donor upon the value of m^*. The optical data also indicate only a very slight increase in m^* with carrier concentration up to values of $N=8\times10^{19}$ cm^{-3}. While, in regions of optical dispersion caused by free carriers, the free carrier absorption does not obey a λ^2 law, the high frequency conductivity σ_{ac} is proportional to λ^2. The optical and electrical data are quantitatively correlated by using elementary conduction theory.

In the preparation of these heavily doped samples, one also encounters certain differences in behavior. While the preparation of antimony-doped germanium crystals involves no unusual or unexpected difficulties, the situation with arsenic is quite different. As indicated briefly elsewhere,[9] and in greater detail here, the electrically active arsenic in our heavily doped crystals is seldom present in the amounts expected from availible solid solubility data. Minden[10] has found, from vacuum fusion analysis, that in some cases the electrically active arsenic is a relatively small fraction of the total arsenic present. A similar effect has been reported by Tannenbaum[11] in studies of the diffusion of phosphorus in silicon. The situation for germanium is complicated by the presence of p-type germanium arsenide occlusions. In the present work quenching experiments are reported along with attempts to correlate the results with growth conditions and crystalline perfection.

---

[1] Y. Furukawa, J. Phys. Soc. Japan **15**, 730 (1960).

[2] N. Holonyak *et al.*, Phys. Rev. Letters **3**, 167 (1959).

[3] P. L. Moody and J. A. Strauss, Electrochem. Soc. Meeting, Chicago, May 1–5, 1960.

[4] R. A. Logan, J. F. Gilbert, and F. A. Trumbore, J. Appl. Phys. **32**, 131 (1961).

[5] M. Cardona, W. Paul, and H. Brooks, Helv. Phys. Acta **33**, 329 (1960).

[6] R. Bowers, Phys. Rev. **108**, 683 (1957).

[7] J. I. Pankove, Phys. Rev. Letters **4**, 454 (1960).

[8] R. J. Keyes, Quarterly Progress Report, Solid State Research, Lincoln Laboratory, MIT, April 15, 1960.

[9] F. A. Trumbore, *Proceedings of a Technical Conference on Metallurgy of Elemental and Compound Semiconductors, Boston, Massachusetts, August 29, 1960* (to be published).

II. CRYSTAL GROWTH EXPERIMENTS

A. Antimony-Doped Germanium

1. Preparation of Materials

A solvent preparation technique[9,12] was used to grow all but one of the antimony-doped samples. Weighed amounts of antimony (Ohio Semiconductor, 99.999% pure) and germanium (Eagle Picher, "intrinsic" grade) were melted under a helium atmosphere in an inductively heated graphite crucible contained in a conventional crystal pulling apparatus. Ideally, with the solvent evaporation technique, crystal growth occurs on a rotating seed crystal due solely to the evaporation of antimony from the melt saturated with germanium. However, weight loss measurements in two runs showed a higher percentage of antimony in the melt at the end of the run than was present initially. This result indicates that part of the crystal growth was due to cooling of the melt and not to vaporization of antimony. The presence of cooling is probably caused by a change in thermal environment due to the growing crystal and is consistent with the growth technique since the temperature was monitored and controlled in the crucible instead of directly in the melt. Calculations based on the Sb-Ge phase diagram indicate that only $\sim$25–35% of the crystal growth in these two runs was due to evaporation. A photograph of one of these crystals grown from a melt containing 25–27 atom percent antimony is shown in Fig. 1(a).

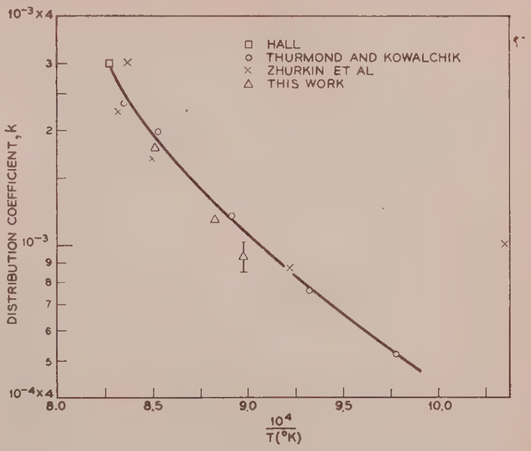

FIG. 2. Plot of the distribution coefficient of antimony in germanium as a function of the reciprocal of the absolute temperature. The point with the limits of error corresponds to crystal 4A (see Table I) which was nonuniform; reflectivity measurements on this sample support the upper limit in good agreement with the curve drawn to correspond to the diffusion measurements of Thurmond and Kowalchik.

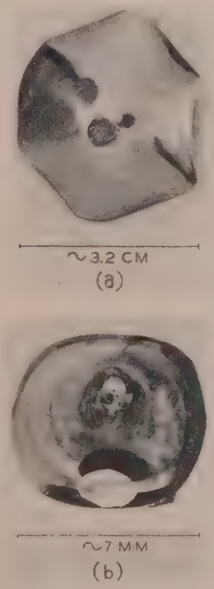

FIG. 1. (a) Antimony-doped germanium crystal grown by solvent evaporation and cooling in a ⟨211⟩ direction. The melt composition varied from 25–27 atom percent antimony during growth. (b) Antimony-doped germanium crystal grown by solvent evaporation in a ⟨311⟩ direction from a melt containing 20 atom percent antimony. Note the {111} facets in both crystals.

Two experiments were carried out with a resistance heated pot furnace where the temperature was more uniform than in the inductivity heated apparatus. The rates of crystal growth were appreciably smaller than in the preceding experiments as would be expected if cooling no longer played as significant a role. A photograph of a crystal grown in the resistance furnace is shown in Fig. 1(b). Note the {111} facets formed on both crystals shown in Fig. 1.

2. Solid Solubility of Antimony in Germanium

The distribution coefficient k of antimony in germanium was calculated as a function of temperature from the melt compositions and the Hall effect data, to be discussed later (see Table I), for the three crystals Sb2, Sb3, and Sb4. In these calculations it was assumed that the carrier concentrations and the antimony concentrations were equal. The data are presented in Fig. 2 which is a plot of $\log k$ as a function of $1/T$ where T is the absolute temperature. The temperatures were determined from the melt compositions and the liquidus

---

[10] H. Minden, *Proceedings of a Technical Conference on Metallurgy of Elemental and Compound Semiconductors, Boston, Massachusetts, August 29, 1960* (to be published).

[11] E. Tannenbaum, Solid State Electronics 2, 123 (1961).

[12] F. A. Trumbore and E. M. Porbansky, J. Appl. Phys. 31, 2068 (1960).

TABLE I. Electrical data and growth parameters.

Sample No.[a]	ρ(ohm cm)$\times10^3$	N(cm^{-3})$\times10^{-18}$	x^L	Remarks
		(a) Sb-doped Ge		
Sb1*A*	1.84	5.84	...	Pulled; polycrystalline
	1.84	5.96		
Sb2*A*	1.56	7.65	0.095	Solvent evap.; polycrystalline
	1.72	7.46		
Sb1*B*	1.46	8.50	...	Pulled; polycrystalline
	1.46	8.47		
Sb3*A*	1.12	10.8	0.21	Solvent evap. + cooling; single crystal
	1.13	10.5		
Sb3*B*	1.08	11.2	0.21	Solvent evap. + cooling; single crystal
	1.12	10.7		
Sb4*A*	1.03 ± 0.09	10.0+1.0	0.25–0.27	Solvent evap. + cooling; single crystal but very nonuniform; range of ρ and N values found in a number of measurements are given at left.
		(b) As-doped Ge		
As1*A*	2.20	6.65	...	Pulled
As2*A*	1.78	9.68	...	Pulled
As2*B*	1.12	21.0	...	Pulled
As3*A*	0.950	24.3	...	Zone leveled from Semimetals Co.
As4*A*	0.710	39.2	0.09–0.1	Solvent evap.; single crystal
As4*B*	0.700	40.7	0.09–0.1	Solvent evap.; single crystal
As4*C*	0.680	41.4	0.09–0.1	Solvent evap.; single crystal
As4*A**	0.675	44.9	0.09–0.1	Quenched (see Table II)
As4*B**	0.684	44.8	0.09–0.1	Quenched (see Table II)
As5*A*	0.665	49.8	0.25–0.40	Thermal gradient; polycrystalline; contained numerous arsenide occlusions
As5*B*	0.664	49.2	0.25–0.40	Thermal gradient; polycrystalline; contained numerous arsenide occlusions
As5*C*	0.650	51.0	0.25–0.40	Thermal gradient; polycrystalline; contained numerous arsenide occlusions
As5*D*	0.625	53.9	0.25–0.40	Thermal gradient; polycrystalline; contained numerous arsenide occlusions
As5*B**	0.509	75.9	0.25–0.40	Quenched (see Table II)
As5*A**	0.508	80.9	0.25–0.40	Quenched (see Table II)
		(c) P-doped Ge		
P1*A*	1.79	8.39		All samples single crystal; grown from calcium orthophosphate-doped melts
	1.79	7.95		
P2*A*	1.11	15.0		
	1.18	14.9		
P1*B*	0.795	25.3		
	0.820	23.4		
P3*A*	0.536	47.0		
	0.525	41.0		

[a] Note that the sample number designates dopant, crystal number, and slice, respectively.

curve of Thurmond and Kowalchik.[13] Also plotted in Fig. 2 are values of k obtained from the work of Hall[14] and of Zhurkin *et al.*[15] from crystal pulling experiments and of Thurmond *et al.*[16] from diffusion measurements.

As was also observed for the case of antimony in silicon,[4] the solvent evaporation data are in good agreement with diffusion data. This agreement may be taken as evidence that near-equilibrium solid solubilities have been obtained in the solvent evaporation work. A comparison of the shape of the log$k$ vs $1/T$ plot for the Sb-Ge system with a similar plot for the Sb-Si system[1 reveals that the departure from linearity is much greater in the latter case. This behavior, similar to that discussed previously for the Sn-Ge and Sn-Si systems,[18] may be attributed primarily to the significantly larger departures from ideal liquid solution behavior in the Sb-Si system.[13]

---

[13] C. D. Thurmond and M. Kowalchik, Bell System Tech. J. **39**, 169 (1960).

[14] R. N. Hall, General Electric Research Lab. Report No. 58-RL-1874.

[15] B. G. Zhurkin, V. S. Zemskov, D. A. Petrov, and A. D. Suchkova, Izvest. Akad. Nauk S.S.S.R., Otdel. Tekh. Nauk, MIT, **5**, 86 (1959).

[16] C. D. Thurmond, F. A. Trumbore, and M. Kowalchik, J. Chem. Phys. **25**, 799 (1956); see also reference 21.

[17] F. A. Trumbore, P. E. Freeland, and R. A. Logan, J. Electrochem. Soc. **108**, 458 (1961).

In order to determine whether or not a "facet" effect[19] was present, optical reflectivity measurements were made both on and off the {111} facets in crystals Sb3 and Sb4. These measurements indicate that within ±10% there was no significant difference in the amount of antimony incorporated into the crystals on or off the facets. This result compares with a 45% effect found by Dikhoff[20] for crystals pulled from melts containing much smaller concentrations of antimony. An even larger facet effect would be required to explain the disagreement with the data of Zhurkin *et al.* It is not clear from the data presently available whether or not the lack of a significant facet effect is inherent in the solvent evaporation method or whether melt concentration or other crystal growth parameters are involved. Along these lines, Dikhoff has reported some evidence that, in the crystal pulling experiments, the facet effect becomes smaller with lower pull rates.

B. Arsenic-Doped Germanium

The arsenic-doped germanium samples were prepared by crystal pulling, solvent evaporation, and thermal gradient techniques with the exception of one zone leveled sample obtained commercially. The arsenic, obtained from the American Smelting and Refining Company, was of 99.999% purity. In the pulling experiments, the germanium was doped by using either germanium arsenide (~40 atom percent arsenic) or by adding arsenic through a pill tube. The relativity high volatility of arsenic presents an obvious problem in the preparation of arsenic-doped germanium. Moody and Strauss[3] and Minden[10] have used syringe-type and magnetic crystal pullers, respectively, to overcome this difficulty. However, the problem is not as severe as might be expected as shown by the data in Fig. 3 which is a plot of the approximate partial pressure of arsenic as a function of temperature along the germanium-rich liquidus (solidus) curve.[21] These data were obtained as described in the Appendix.

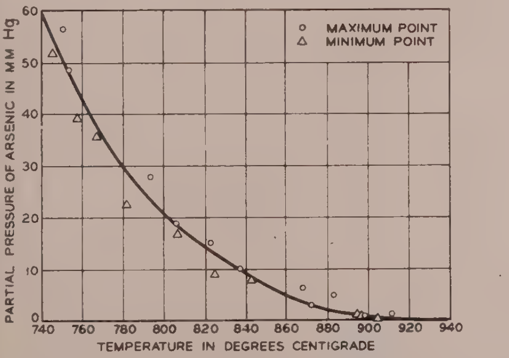

FIG. 3. Approximate partial pressure of arsenic over the germanium-arsenic alloys of compositions lying along the germanium-rich liquidus or solidus curves as a function of temperature.

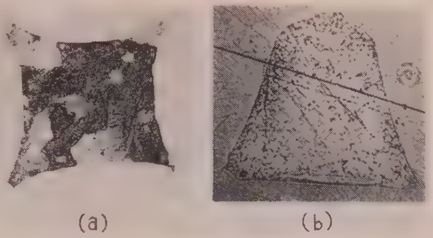

FIG. 4. (a) A *p*-type germanium arsenide occlusion (0.3-mm wide) found on a {100} plane of an arsenic-doped crystal pulled in a ⟨100⟩ direction. (b) Antimony occlusion (~0.01-mm wide) found in the crystal shown in Fig. 1(b).

However, a much more serious problem soon became evident. It was found that although carrier concentrations of $\sim 3\text{–}4\times10^{19}$ cm^{-3} could be obtained with relative ease, addition of more arsenic to the melts, even as much as 15–20 atom percent, resulted in the same carrier concentrations or in some cases even less. In only two experiments were carrier concentrations as high as 5×10^{19} cm^{-3} obtained even though concentrations in excess of 1×10^{20} cm^{-3} were expected from the solidus curve.[22] In many of the crystals of anomalously low carrier concentration, occlusions of germanium arsenide were detected. In measurements on some of the germanium arsenide used for doping purposes, Wolfe[23] found that the material was *p*-type with a resistivity of ~0.01 ohm-cm and a hole concentration on the order of 10^{20} cm^{-3}. The arsenide is a soft material resembling germanium in physical appearance. However occlusions in the germanium were readily observed by lapping the samples. Some rather striking occlusions were observed on a {100} surface of a crystal grown in a ⟨100⟩ direction as shown in Fig. 4(a). There were a large number of these occlusions all oriented in the same direction, showing the ⟨100⟩ fourfold symmetry.

The solvent evaporation technique has been used to grow heavily doped material with melt concentrations ranging as high as ~13 atom percent arsenic. Whether or not cooling was present here could not be determined from the weight loss measurements since arsenic is much more volatile than antimony. Although single crystal material was achieved much more readily with this technique than with the pulling technique and although the material appeared to contain fewer occlusions, the

---

[18] F. A. Trumbore, C. R. Isenberg, and E. M. Porbansky, J. Phys. Chem. Solids **9**, 60 (1959).

[19] K. F. Hulme and J. B. Mullin, Phil. Mag. 4, 1286 (1959).

[20] J. A. M. Dikhoff, Solid State Electronics **1**, 202 (1960).

[21] The partial pressures over the solidus and liquidus alloys are equal at a given temperature since they are in equilibrium.

[22] F. A. Trumbore, Bell System Tech. J. **39**, 205 (1960).

[23] R. Wolfe (private communication).

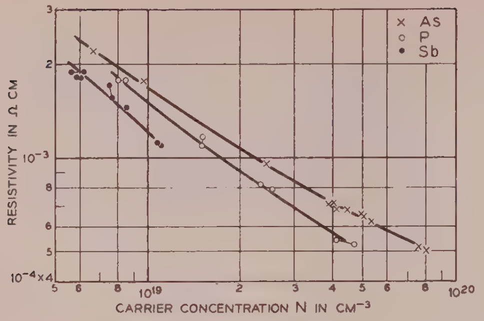

FIG. 5. Plot of resistivity as a function of carrier concentration for antimony-, arsenic-, and phosphorus-doped germanium.

highest carrier concentration obtained was still only $\sim 4\times 10^{19}$ cm^{-3}.

The most interesting arsenic-doped sample was obtained by using a thermal gradient technique similar to that used previously to grow gallium-doped germaniun.[24] Germanium arsenide and excess germanium were sealed in an evacuated 3-cm diam vitreous silica tube which was heated for 26 days in a furnace where the temperature ranged from ~750° to ~800°C with an average thermal gradient of ~10°/cm. The resulting material was polycrystalline, contained numerous occlusions of germanium arsenide, and yet most of the sample was remarkably uniform in resistivity in the range 0.00065–0.00070 ohm cm. However, a resistivity profile on one section of this material indicated that ~1 mm³ of the material had a resistivity of 0.0003–0.0004 ohm cm corresponding to the $1\text{–}2\times 10^{20}$ cm^{-3} doping level expected from the solidus curve. This was the only case where such agreement was obtained.

C. Phosphorus-Doped Material

All of the phosphorus-doped samples, obtained from D. Lassota, were pulled single crystals with calcium orthophosphate as the dopant.

III. ELECTRICAL PROPERTIES

Hall effect and resistivity measurements were made by using standard techniques. The results of these measurements are summarized in Table I along with the atom fraction of dopant in the melt x^L together with other pertinent information on crystal growth. A plot of the resistivity ρ as a function of the carrier concentration N is given in Fig. 5. The conventional Hall bridge yields two Hall voltages and two resistivity values. In cases where a sample was sufficiently nonuniform so as to yield significantly different values for N and ρ, two points connected by a tie line have been plotted in Fig. 5.[25] It may be noted that this nonuniformity is not present in the arsenic-doped samples. The resistivity and Hall measurements are believed to be accurate to within ±5%. Carrier concentrations were calculated from the Hall coefficient R_H by using the degenerate formula $R_H=1/Ne$, where e is the electron charge.

The data in Fig. 5 are seen to confirm the previously reported differences in the electron mobility in arsenic- as compared to antimony-doped samples. As in the case of silicon,[4] the mobilities in the phosphorus-doped samples lie between the mobility values for germanium doped with arsenic and antimony.

It will be noted in Fig. 5 that points are plotted for carrier concentrations of $\sim 8\times 10^{19}$ cm^{-3} even though, as mentioned previously, the maximum carrier concentration in the as-grown samples was $\sim 5\times 10^{19}$ cm^{-3}. The larger carrier concentrations were obtained in quenching experiments performed in an attempt to resolve the anomalous N vs doping results. In these experiments, the samples were heated and then quenched to room temperature in either ethylene glycol or a jet of nitrogen gas. The quenching apparatus and procedure have been described previously.[26] Upon quenching in ethylene glycol, it is estimated that the samples cool to near room temperature in about 0.1 sec, whereas the nitrogen jet quenched the samples in about 5 sec. Both methods of quenching produced the same changes in the electrical properties of the samples.

The effect of variations in the heating cycle was investigated with crystal As5. The largest decrease in resistivity was obtained by heating at 870°C rather than 805°C or 905°C and a further small decrease was observed when heating for 30 min rather than 15 min prior to quenching.

The values of ρ measured before and after quenching for various heavily doped Ge samples are summarized in Table II and the results of Hall effect measurements on four quenched samples are included in Table I. Although significant increases in carrier concentration were achieved in arsenic-doped germanium by quenching, the resulting ρ and N values were quite consistent with those of Fig. 5 which were obtained on as-grown crystals. The effect of this treatment was therefore to increase the concentration of dissolved arsenic in th

TABLE II. Results of quenching experiments.

Sample No.	ρ(ohm cm) $\times 10^4$ Initial	ρ(ohm cm) $\times 10^4$ Final	Heat Cycle Temp. °C	Heat Cycle Time (min
As4*A*	7.06	6.75	870	15
As4*B*	7.03	6.84	870	15
As5*A*	6.65	5.08	870	15
As5*B*	6.64	5.09	870	15
As5*E*	6.64	4.88	870	30
As5*F*	6.64	5.35	905	15
As5*G*	6.64	5.68	805	15
As6*A*	6.82	5.96	870	30
As6*B*	6.82	5.95	870	20
Sb3*C*	11.4	11.6	870	15
P3*B*	6.60	6.62	870	30

---

[24] F. A. Trumbore, C. R. Isenberg, and A. A. Tartaglia, J. Phys. Chem. Solids **11**, 239 (1959).

[25] Some of the nonuniformity in the Sb-doped samples may be related to the presence of occluded antimony. A particularly interesting antimony occlusion, found in the crystal of Fig. 1(b), is shown in Fig. 4(b).

[26] R. A. Logan, Phys. Rev. **101**, 1455 (1956).

crystal rather than to produce any anomalous effect on the carrier mobility.

While the quenching experiments furnish some clues as to the source of the anomalously high resistivities in the as-grown arsenic-doped crystals, a complete explanation is still lacking. In the samples used here, estimates of the volume occupied by *p*-type arsenide occlusions indicate that there should be no significant volume effect on ρ as discussed by Herring.[27] Even where visible occlusions were found, the electrical and optical data are consistent with the data obtained on more perfect samples. Furthermore, the reasonably good agreement between our measurements and those of others[1,3,10,15,28,29] on samples prepared by using different techniques also argues against any important bulk effect due to occlusions.

From the decrease in ρ observed in the quenching experiments, it seems most likely that the electrically inactive arsenic is simply precipitated on cooling the crystal after growth. One observation that must be explained is the fact that different resistivities are obtained in samples grown under essentially the same conditions. This is strikingly illustrated in the case of sample As5 where the very small region of $\sim 3\times10^{-4}$ ohm cm material was found in what was predominantly 5.5×10^{-4} ohm cm material. Since the 3×10^{-4} ohm cm figure is the value expected from the solidus curve, it does not appear that any fundamental interactions involving interstitial arsenic or vacancies are limiting the solubility as have been suggested.[10] The most likely explanation of the anomalous behavior is that the precipitation of arsenic depends on the presence of nucleation centers such as small germanium arsenide occlusions, dislocations,[30] or perhaps other imperfections. It should also be noted that in diffusion studies, Tannenbaum[11] has observed what appears to be precipitation of phosphorus in silicon where dislocations, but not occlusions, could serve as nucleation sites.

It is worthwhile pointing out that the carrier concentrations in the quenched arsenic-doped crystals increase in the order As4<As6<As5 which, unlike in the as-grown crystals, is the order expected from the melt compositions. The results on the quenched crystals are also in much better agreement with the available solidus curve data[22] although, except for the 3×10^{-4} ohm cm material found in As5, a discrepancy of about a factor of two still exists.

Whether or not the absence of quenching effects with antimony- and phosphorus-doped germanium can be explained in terms of the presence or nature of nucleation sites is uncertain, especially since the concentration of antimony was appreciably less than that of arsenic in the crystals used in these experiments. It is perhaps worth noting, however, that there are no Sb-Ge compounds and one might speculate that the nucleation of a germanium arsenide phase would occur more readily than the aggregation of individual antimony atoms. In the case of phosphorus, the phase diagram is unknown although compound formation has been reported.[31] A possible explanation for the lack of a quenching effect in this case is that, due to the larger solubility of phosphorus,[32] precipitation at a given concentration of phosphorus would take place at a lower temperature (where diffusion is less rapid) than for the same concentration of arsenic.

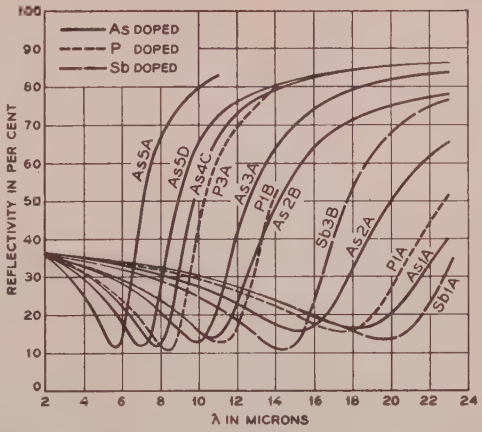

FIG. 6. Room temperature reflectivity as a function of wavelength for samples doped with arsenic, phosphorus, or antimony.

IV. OPTICAL PROPERTIES

A. Measurements and Results

Room temperature reflectivity and transmission measurements have been made between 2 and 24 μ for samples doped to different carrier concentrations with arsenic, phosphorus, or antimony. The specimens were among those used to obtain the electrical data of Fig. 5. The reflectivity was measured on polished surfaces with respect to a front surface aluminum mirror and corrected for the reflectivity of aluminum, while the transmission was measured by using the conventional sample in-sample out technique. The reflectivity R of a number of samples is shown in Fig. 6. To verify that the optical measurements were not influenced by the surface preparation, from two to four mils were etched off two samples and the reflectivity measurements repeated without any change being observed. The

---

[27] C. Herring, J. Appl. Phys. **31**, 1939 (1960).

[28] W. W. Tyler and T. J. Soltys, General Electric Research Lab. Memo Report No. P-193.

[29] J. O. McCaldin (private communication).

[30] G. Schwuttke has recently examined some 7×10^{-4} ohm cm material (grown by Moody and Strauss) by using x-ray diffraction microscopy and has found evidence indicating arsenic precipitation on dislocations (private communication).

[31] See M. Hansen, *Constitution of Binary Alloys* (McGraw-Hill Book Company, Inc., New York, 1958), 2nd ed., p. 771.

[32] One may reasonably assume that, at a given temperature, the solid solubility of phosphorus is larger than arsenic since the distribution coefficient of phosphorus at the melting point of germanium is larger than that of arsenic.

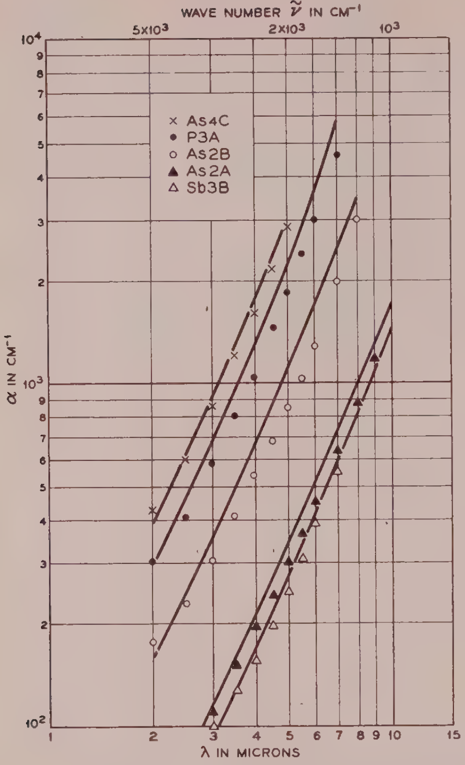

FIG. 7. Absorption coefficient vs wavelength for samples of different carrier concentrations and different impurity types. The curves are calculated from the dc electrical measurements with $m^*=0.18\ m$.

absorption coefficients for some of these same samples, given in Fig. 7, were calculated from the measured transmission and reflectivity.

A method of determining the carrier effective mass[5,33,34] from reflectivity data such as shown in Fig. 6 has been successfully applied to a variety of semiconducting materials. The free carriers contribute an electric susceptibility χ_c to the semiconductor

$$\chi_c=-\frac{Ne^2\tau^2}{m^*(1+\omega^2\tau^2)},$$

where m^* is the susceptibility effective mass, ω the angular frequency of measurement related to λ by $\lambda\omega=2\pi c$, and τ the carrier relaxation time. The significance of m^* will depend upon the energy band structure near the band edge and has been discussed in considerable detail elsewhere.[33] The dielectric constant ϵ is given by

$$\epsilon=\epsilon_0+4\pi\chi_c=n^2-\kappa^2,$$

where ϵ_0 is the dielectric constant in the absence of free carriers, n the refractive index, and κ the extinctio coefficient related to the absorption coefficient α b $\lambda\alpha=4\pi\kappa$. The reflectivity of the material at norma incidence is determined by the optical constants n an κ and is given by

$$R=\frac{(n-1)^2+\kappa^2}{(n+1)^2+\kappa^2}.$$

Measurements of reflectivity and transmission on a impure and a pure sample determine n, κ, and ϵ_0. Th measurements indicate that for all samples investigated $\chi_c\propto\omega^2$ and hence $\omega^2\tau^2\gg1$. It has been previously pointe out[5,33] that the value of κ is small compared to $n-$ throughout most of the wavelength range on the short wavelength side of the reflectivity minimum. In thi region, χ_c can be determined from R alone. If κ, whic increases with increasing λ (see Fig. 7), remains sma up to the reflectivity minimum, then $R_{\min}\approx0$ since thi will be the λ at which $n=1$. If the value of $R_{\min}\neq0$, th value of κ cannot be insignificant at this wavelength. I is apparent that the latter is the case in Fig. 6. In ord to obtain a quantitative value for m^*, it is necessary t know N. For our samples, the values of $N=1/(R_He)$ a given in Table I. For reasons which will becom apparent later, the value of R_H was checked on eac optical sample several times, and in some cases eve by using two different sets of Hall apparatus. An sample which showed appreciable inhomogeneity eith electrically or optically was not used.

The effective mass m^* was deduced for all of th samples in Fig. 6 according to the procedure describe above and the results are shown in Fig. 8. The point $N=3.9\times10^{18}$ cm^{-3} was taken from the literature.[33]

From Fig. 8 it is apparent that the values of m^*, terms of the free electron mass m_0, increase only slight with increasing N in the range studied. Since th experimental error is $\pm0.015\ m_0$, the small increase $0.03\ m_0$ should be viewed with some caution. Within th stated accuracy, there is no observable differen between the m^* values for n-type germanium dope with the three donor impurities. Therefore, the o served differences in the mobility must be the result a relaxation time effect. The nearly constant value m^* with increasing N is in agreement with the magnet

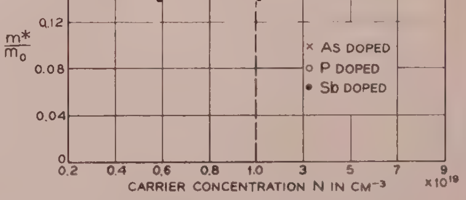

FIG. 8. Electron effective mass as a function of carrier concentration.

---

[33] W. G. Spitzer and H. Y. Fan, Phys. Rev. **106**, 882 (1957).
[34] W. G. Spitzer and J. M. Whelan, Phys. Rev. **114**, 59 (1959).

susceptibility studies of Bowers[6] where no change in m^* was observed up to $N\sim 3\times 10^{19}$ cm^{-3}. However, the m^* values presented here and by Bowers are in quantitative disagreement with the results of Cardona *et al.*[5] This disagreement is particularly disturbing since they used the same experimental procedure and analysis as were used here. Cardona *et al.* found m^* to be 0.14 m_0 at $N=2.0$ and 3.7×10^{18} cm^{-3} in good agreement with our values at the lower end of the carrier concentration range. However, for three samples between $N=1.1$ and 5.2×10^{19} cm^{-3}, m^* increased from 0.21 m_0 to 0.26 m_0 which is considerably larger than our values for similar carrier concentrations. It was because of this discrepancy that the extreme caution, described previously, was used in determining the carrier concentration. It has been suggested[35] that the high values of m^* obtained by Cardona *et al.* might be due to the presence of large concentrations of the impurity in a precipitated or electrically inactive form in their samples. Our $\sim 20\%$ increase in m^* at $N\simeq 5\times 10^{19}$ cm^{-3} as compared to much lower carrier concentrations is not an unreasonable result according to an estimate based on the nonparabolic behavior of the conduction band minima.[5] Therefore, the results indicate that, for our present material, it is not necessary to invoke any explicit effect of the high impurity concentration on the shape of the energy minima.

If the relation[5] between N and R_H is assumed to be

$$N=\frac{3}{R_He}\,\frac{K_H(K_H+2)}{(1+2K_H)^2},$$

where $K_H=m_{\|}\tau_{\perp}/m_{\perp}\tau_{\|}$ and where $m_{\|}$, $m_{\perp}$, $\tau_{\|}$, and $\tau_{\perp}$ are the longitudinal and transverse effective masses and components of the scattering time tensor, then the values of m^* in Fig. 8 would range from 0.11 m_0–0.13 m_0. These values of m^* assume that $\tau_{\perp}=\tau_{\|}$ and that $m_{\|}$ and $m_{\perp}$ are given by the cyclotron resonance values (i.e., $3K_H(K_H+2)/(1+2K_H)^2=0.79$).

B. Correlation of the Carrier Absorption and the Electrical Measurements

While the effective mass is the same for the three impurities, it may be seen from Fig. 6 that there is a difference in the reflectivity curves. Specifically, at a given carrier concentration the value of R at the minimum is largest for arsenic-doped, lower for phosphorus-doped, and lowest for antimony-doped material. Therefore, one would expect, for constant N and λ, $\kappa_{\text{As}}>\kappa_{\text{P}}>\kappa_{\text{Sb}}$. This observation is verified by the absorption data of Fig. 7. Samples As4C and P3A have identical carrier concentrations but the absorption of the arsenic-doped sample is higher than that of the phosphorus-doped sample. Also, Sb3B has a higher carrier concentration that As2A but a lower absorption. It is apparent therefore that, for $N\gtrsim 1\times 10^{19}$ cm^{-3}, the free carrier absorption is dependent on the specific group V impurity used to dope the material.

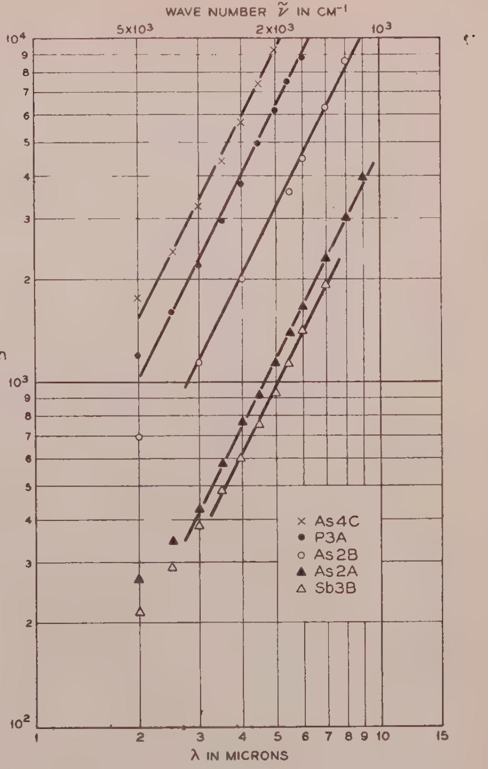

FIG. 9. Absorption coefficient times refractive index vs wavelength for the samples of Fig. 7. The straight lines indicated a λ^2 dependence.

While detailed theories have been derived[36–38] for the effect of impurity scattering on free carrier absorption, none of these theories accounts for the difference between the three group V donors. It is of interest to note that the observed dependence can be predicted semiquantitatively from the dc measurements of N and ρ by assuming elementary conduction theory, if the dispersion due to the free carriers is taken into account. The dc resistivity is given by $\rho_{\text{dc}}=m^*/Ne^2\tau_{\text{dc}}$. At a constant N, Fig. 5 shows $(\tau_{\text{dc}})_{\text{As}}<(\tau_{\text{dc}})_{\text{P}}<(\tau_{\text{dc}})_{\text{Sb}}$. The ac conductivity is given[33] by $\sigma_{\text{ac}}=Ne^2\tau_{\text{ac}}/[m^*(1+\omega^2\tau_{\text{ac}}^2)]$. Since we have previously noted that $\omega^2\tau_{\text{ac}}^2\gg 1$, we have $\sigma_{\text{ac}}=Ne^2/(m^*\omega^2\tau_{\text{ac}})$. If the τ_{ac} values are ordered in the same way as those of τ_{dc} then, for $Ne^2/(m^*\omega^2)=$ constant, we have $(\sigma_{\text{ac}})_{\text{As}}>(\sigma_{\text{ac}})_{\text{P}}>(\sigma_{\text{ac}})_{\text{Sb}}$. Since $\alpha=4\pi\sigma/(nc)$, it follows that $\alpha_{\text{As}}>\alpha_{\text{P}}>\alpha_{\text{Sb}}$.

If τ_{ac} is independent of wavelength, then $\alpha n\propto\lambda^2$. Figure 9 shows a plot of $\log\alpha n$ vs $\log\lambda$ for the same five samples given in Fig. 7, where n as a function of λ is determined for each sample from its reflectivity curve in Fig. 6. For $\lambda > 2\mu$, the data for each sample lie close to a λ^2 dependence (solid lines). If the wavelength independence of τ extends to dc then $\tau_{dc} = \tau_{ac}$, in which case $\alpha = 4.05 \times 10^2\ \rho_{dc}\lambda^2/[nR_H(m^*)^2]$, where m^* is in units of m_0, ρ_{dc} in ohm cm, λ in microns, and R_H in cm^3/coul. The curves of Fig. 7 were calculated from this expression with $m^* = 0.18$. The curves are in reasonable quantitative agreement with the data throughout most of the measured spectral range. The value of m^* is larger but close to the values obtained from the reflectivity data.[39]

---

[35] M. Cardona (private communication).

[36] H. Y. Fan, W. G. Spitzer, and R. J. Collins, Phys. Rev. **101**, 566 (1960).

[37] R. Rosenberg and M. Lax, Phys. Rev. **112**, 843 (1958).

[38] H. J. Meyer, Phys. Rev. **112**, 298 (1958).

Pankove[7] recently reported some transmission studies on heavily doped n-type germanium. He obtained three principle results which are as follows: (1) upon increasing N, there is a shift of the direct transition portion of the absorption edge to longer wavelengths, (2) the free carrier absorption follows a λ^2 dependence from $\lambda = 2\mu$ to 4μ, and (3) there is structure in the free carrier absorption near $2.5\,\mu$ which is interpreted as the threshold for indirect transitions across the energy gap for material with $N = 2\text{–}3 \times 10^{19}$ cm^{-3}.[40] We also made measurements on the direct transition portion of the absorption edge in some of our more heavily doped samples and observed the shift to lower energy reported by Pankove. However, we were unable to observe any clear difference in the shift between the three different donor types. While we do not observe a λ^2 or, in fact, any power dependence of α on λ, the departure from the λ^2 dependence is caused by the change in n with λ so that $\sigma_{ac} \propto \lambda^2$. For the carrier concentrations and wavelengths used by Pankove, the dispersion effect of the free carriers would be small.

ACKNOWLEDGMENTS

The authors are indebted to L. E. Howarth and J. F. Gilbert for the optical and electrical measurements; to E. Porbansky, P. E. Freeland, M. Kowalchik, and A. A. Tartaglia for the preparation and characterization of the crystals; and to R. Wolfe for the use of his Hall apparatus. Discussions with C. D. Thurmond and D. Kleinman have also been helpful in this work.

APPENDIX. PARTIAL PRESSURE OF ARSENIC

The partial pressure data shown in Fig. 3 were obtained from "inverted" dew-point experiments. In a conventional dew-point experiment,[41] the arsenic pressure would be determined by measuring the condensation temperature of the arsenic vapor in equilibrium with the liquidus (solidus) alloy. Attempts to perform such experiments were unsuccessful due to supercooling of the arsenic vapor.[42] To overcome this difficulty, the dew-point technique was modified in two ways. First, a germanium sample was sealed in an evacuated vitreous silica tube together with an amount of arsenic sufficient to exceed the liquidus composition at all temperatures studied. Second, after adjusting the temperatures of the arsenic and germanium to the desired values and waiting for equilibrium to be attained, the tube was removed from the furnace and examined for the presence or absence of melting of the germanium. From the known vapor pressure of pure arsenic as a function of temperature, maximum and minimum values of the equilibrium pressure over the liquidus or solidus alloys were calculated, thus permitting the bracketing of the true vapor pressure curve. The furnace used in these experiments was relatively short and, because of the large thermal gradients, did not permit an accurate determination of the arsenic temperature, thus accounting for the semiquantitative nature of the data. It is apparent from Fig. 3 that the pressure is only on the order of millimeters or less for melt compositions up to about 10 atom percent arsenic (30–40°C below the melting point of germanium) but increases relatively rapidly at lower temperatures and higher arsenic liquidus compositions.

---

[39] T. Seidel [*Proceedings of a Technical Conference on Metallurgy of Elemental and Compound Semiconductors, Boston, Massachusetts, August 29, 1960* (to be published)] has treated the absorption of two As-doped samples by using Drude theory and purports to find an ~10% increase in m^* between $N = 8.7 \times 10^{18}\text{–}1.8 \times 10^{19}$ cm^{-3}.

[40] Pankove now ascribes this latter result to an experimental error (private communication).

[41] See, for example, O. Kubaschewski and E. L. Evans, *Metallurgical Thermochemistry* (Pergamon Press, New York, 1958), 3rd ed., p. 144.

[42] L. Brewer and J. S. Kane, J. Phys. Chem. **59**, 105 (1955).

JOURNAL OF APPLIED PHYSICS VOLUME 32, NUMBER 10 OCTOBER, 1961

Nonlinear Effects of *Z*-Directed Spin Waves in Thin Films

Jerome I. Kaplan*
Lockheed Research Laboratory, Palo Alto, California

(Received March 15, 1961)

A calculation is made for the high-power instability of the *Z*-directed spin waves in a thin insulating ferromagnetic film. For complete pinning, the critical field is found to be

$$(\gamma h)^2=\Delta_n{}^3 n^2\pi^2[9\sqrt{3}(\omega_M+\tfrac{1}{3}\omega_{\text{ex}}a^2k_n{}^2)]^{-1}.$$

The calculation is also made for the critical field, assuming a mixed boundary condition.

1. INTRODUCTION

THE nonlinear effects of finite spin-wave amplitudes in insulating ferromagnetic materials has been the subject of a large number of papers.[1] In this paper we consider such effects in thin films where the applied magnetic field H_0 is perpendicular to the film. Physically, the effect is similar to the nonlinear instability in a thin disk, as first suggested by Suhl.[2] Each of the thin-film low-power resonant peaks will have its own instability field, which is related to its own linewidth and pinning condition. In the first part of this paper, the nonlinear effect is calculated, assuming complete pinning, and, in the second part, the calculation is repeated, assuming a mixed boundary condition.

2. COMPLETE PINNING

The usual dynamic equation

$$\dot{\mathbf{M}}=\gamma(\mathbf{M}\times\mathbf{H}_{\text{eff}})+\text{damping} \tag{1}$$

is assumed, where H_{eff} is the sum of the effective fields H_{applied}, $H_{\text{demagnetizing}}$, and H_{exchange}, defined as

$$\begin{aligned}\mathbf{H}_{\text{applied}}&=\mathbf{i}H_1\cos\omega t+\mathbf{j}H_1\sin\omega t+\mathbf{k}H_0\\ \mathbf{H}_{\text{demagnetizing}}&=-4\pi\mathbf{M}_z\\ \mathbf{H}_{\text{exchange}}&=a^2H_{\text{ex}}\nabla^2\mathbf{M}/M_0.\end{aligned} \tag{2}$$

The only spin waves we will consider will be *Z*-directed spin waves; thus, using complex notation

$$M^+=M_x+iM_y,$$

we have as the form of our solution

$$\alpha=\alpha_k\sin kz=M^+/M_0, \tag{3}$$

where M_0 is the saturation magnetization and k is determined by the equation $\sin kL=0$, or $k_n=n\pi/L$. Note there is absorption only for n odd.[3] Thus we have

$$\begin{aligned}H^+&=h\exp(-i\omega t)-H_{\text{ex}}a^2k^2\alpha_k\sin kz\\ H_z&=H_0-4\pi M_z+H_{\text{ex}}a^2\nabla^2(M_z/M_0),\end{aligned} \tag{4}$$

where

$$\frac{M_z}{M_0}=a_z=\left(\frac{1-M_x{}^2-M_y{}^2}{M_0{}^2}\right)^{\frac{1}{2}}$$

$$\begin{aligned}a_z&\simeq 1-\tfrac{1}{2}\alpha\alpha^*\\ &\simeq 1-\tfrac{1}{2}\alpha_k\alpha_k{}^*\sin^2kz=1-\varphi_k(1-\cos 2kz),\end{aligned} \tag{5}$$

and $\varphi_k=\frac{1}{4}\alpha_k\alpha_k{}^*$. Substituting Eqs. (4), (5) into Eq. (1) we obtain

$$\begin{aligned}-i\omega\alpha_k\sin kz=&\,i(\omega_1e^{-i\omega t}-\omega_{\text{ex}}a^2k^2\alpha_k\sin kz)\\ &\times(1-\varphi_k+\varphi_k\cos 2kz)-i\alpha_k\sin kz\\ &\times(\omega_0+\omega_M\varphi_k-\omega_M\varphi_k\cos 2kz\\ &\quad-4\omega_{\text{ex}}a^2k^2\varphi_k\cos 2kz),\end{aligned} \tag{6}$$

where

$$\omega_1=\gamma h_1,\ \omega_{\text{ex}}=\gamma H_{\text{ex}},\ \omega_M=\gamma 4\pi M_0,$$

and

$$\omega_0=\gamma(H_0-4\pi M_0).$$

One solves for α_k by multiplying through by $\sin kz$ and integrating from $0-L$. The result is

$$\alpha_k=\frac{-\omega_1e^{-i\omega t}[(1-\varphi_k)C_k+\varphi_kD_k]}{[\omega-\omega_0-\omega_M\varphi_k-\omega_{\text{ex}}a^2k^2(1-\varphi_k)]A_k+[\omega_M\varphi_k+3\omega_{\text{ex}}a^2k^2\varphi_k]B_k+i\Delta_kA_k}. \tag{7}$$

Note that a phenomenological linewidth Δ_k has been introduced. The symbols A_k, etc., are given as

$$\begin{aligned}A_k&=\int_0^L\sin^2kz\,dz=\tfrac{1}{2}L & C_k&=\int_0^L\sin kz\,dz=2L/n\pi\\ B_k&=\int_0^L\sin^2kz\cos 2kz\,dz=-\tfrac{1}{4}L & D_k&=\int_0^L\sin kz\cos 2kz\,dz=-2L/3n\pi.\end{aligned} \tag{8}$$

---

* Permanent address: Brandeis University, Waltham, Massachusetts.

[1] E. Schlömann, Raytheon Research Laboratory Tech. Rept., No. R-48. This review gives a large number of references.

[2] P. W. Anderson and H. Suhl, Phys. Rev. **100**, 1788 (1955).

[3] P. Pincus, Phys. Rev. **118**, 658 (1960).

In terms of φ_k, Eq. (7) becomes

$$\varphi k_n = \frac{\frac{1}{4}(4/n\pi)^2\omega_1{}^2(1-\frac{4}{3}\varphi k_n)^2}{[\omega-\omega_0-\omega_{\mathrm{ex}}a^2k_n{}^2-\frac{3}{2}\varphi k_n(\omega_M+\frac{1}{3}\omega_{\mathrm{ex}}a^2k_n{}^2)]^2+\Delta k_n{}^2}. \tag{9}$$

Heretofore the subscript n has been omitted for brevity, but now in the final result it is included for emphasis.

Equation (9) is a cubic equation with either one or three real roots. With $\omega_1{}^2$ very small there will be only one real root—for a certain critical value of $\omega_1{}^2$ there will be three roots; this effect is often referred to as the fold over of the resonance line. One obtains the critical field at which one changes from one to three roots to be

$$(\gamma h_n)_{\mathrm{crit}}{}^2 = \frac{\Delta_n{}^3n^2\pi^2}{9\sqrt{3}(\omega_M+\frac{1}{3}\omega_{\mathrm{ex}}a^2k_n{}^2)}. \tag{10}$$

The determination of the critical field thus gives an independent method of obtaining the linewidth Δ_n.

The out-of-phase susceptibility χ'' is given as the imaginary part of $\alpha_k/e^{-i\omega t}$. It is, of course, a function of φ_k which is obtained from Eq. (9). The particular solution one takes depends on the direction one approaches the resonance, and, thus, the line shape above the critical field will have a discontinuity. The first appearance of the discontinuity experimentally defines h_{crit}.

3. MIXED BOUNDARY CONDITION

The calculation for the mixed boundary in form is the same as in Sec. 2 and only differences will be brought out in this section. For the mixed boundary condition neither the magnetization nor its first derivative will be zero at the surface, so the general form of the solution will be[3]

$$\alpha = \alpha_k(\sin kz + g\cos kz), \tag{11}$$

with

$$a_z \simeq 1-\varphi_k[(1+g^2)+(g^2-1)\cos 2kz+2g\sin 2kz], \tag{12}$$

and $\varphi_k=\frac{1}{4}\alpha_k\alpha_k{}^*$ as before. The allowed k values are determined by the condition

$$\sin kL + g\cos kL = g \tag{13}$$

or equivalently

$$\sin kL = 2g/(g^2+1). \tag{14}$$

Using Eq. (2), the effective fields are

$$\begin{aligned} H^+ &= he^{-i\omega t}-\omega_{\mathrm{ex}}a^2k^2\alpha_k(\sin kz+g\cos kz)\\ H_z &= H_0-4\pi M_0\{1-\varphi_k(1+g^2)-\varphi_k\\ &\qquad\times[(g^2-1)\cos 2kz+2g\sin 2kz]\}\\ &\qquad\qquad+4\omega_{\mathrm{ex}}a^2k^2\varphi_k[(g^2-1)\cos 2kz+2g\sin 2kz]. \end{aligned} \tag{15}$$

Substitution of the effective fields into Eq. (1) then gives an equation for α_k. The quantity α_k is found by multiplying this equation by $\sin kz+g\cos kz$ and integrating from $0-L$. The result is that

$$\alpha_k = \frac{-he^{-i\omega t}[\{1-\varphi_k(1+g^2)\}C_k{}'+\varphi_k(g^2-1)D_k{}'+2g\varphi_kE_k{}']}{\{[\omega-\omega_0-\omega_M\varphi_k(1+g^2)-\omega_{\mathrm{ex}}a^2k^2+\omega_{\mathrm{ex}}a^2k^2(1+g^2)\varphi_k]A_k{}' -\varphi_k[\omega_M+3\omega_{\mathrm{ex}}a^2k^2][(g^2-1)B_k{}'+g(g^2-1)F_k+2gG_k+2g^2H_k]+i\Delta_kA_k\}}, \tag{16}$$

where

$$\begin{aligned} A_k{}' &= \int_0^L (\sin kz+g\cos kz)^2dz = \frac{L}{2}(g^2+1)+\frac{g}{k}\\ B_k{}' &= \int_0^L (\sin kz+g\cos kz)\sin kz\cos 2kz\,dz\\ &= -\frac{L}{4}+\frac{g}{2k(g^2+1)^4}(5g^6+g^4-5g^2-1)\\ C_k{}' &= \int_0^L (\sin kz+g\cos kz)dz = \frac{2}{k}\\ D_k{}' &= \int_0^L (\sin kz+g\cos kz)\cos 2kz\,dz\\ E_k{}' &= \int_0^L (\sin kz+g\cos kz)\sin 2kz\,dz\\ F_k &= \int_0^L (\sin kz+g\cos kz)\cos kz\cos 2kz\,dz\\ &= \frac{gL}{4}+\frac{g}{2k(g^2+1)^4}(3g^6-g^4-3g^2+1)\\ G_k &= \int_0^L (\sin kz+g\cos kz)\sin kz\sin 2kz\,dz\\ &= \frac{gL}{4}+\frac{g^2}{2k(g^2+1)^4}(-g^6+7g^4+9g^2+1)\\ H_k &= \int_0^L (\sin kz+g\cos kz)\cos kz\sin 2kz\,dz\\ &= \frac{L}{4}+\frac{g}{2k(g^2+1)^4}(7g^6+7g^4+g^2+1). \end{aligned} \tag{17}$$

As before, one obtains a cubic equation for φ_k by multiplying Eq. (1) by its complex conjugate. The critical field is then obtained in a way exactly equivalent with Sec. 1; the result is that

$$\gamma^2 h_{\mathrm{crit}}^2 C_k'^2 \frac{3\sqrt{3}}{8\Delta_k^3}\{\omega_M[(1+g^2)A_k'+\beta_k] + \omega_{\mathrm{ex}} a^2 k^2[-(1+g^2)A_k'+\beta_k]\}=1, \quad (18)$$

where

$$\beta_k=(g^2-1)B'_k+g(g^2-1)F_k+2gG_k+2g^2H_k, \quad (19)$$

or after substituting from Eq. (17)

$$\beta_k=\frac{L}{4}(g^2+1)^2+\frac{g}{2k(g^2+1)^4} \times(3g^{10}+13g^8+22g^6+18g^4+7g^2+1).$$

Also, as before, the out-of-phase susceptibility is given as the imaginary part of $\alpha_k/e^{-i\omega t}$.

JOURNAL OF APPLIED PHYSICS VOLUME 32, NUMBER 10 OCTOBER, 1961

Growth of ZnSb Single Crystals

R. L. Eisner, R. Mazelsky, and W. A. Tiller
Westinghouse Research Laboratories, Beulah Road, Churchill Boro, Pittsburgh 35, Pennsylvania

A zone technique which should be applicable to many peritectic type compounds has been used to grow good-quality single crystals of ZnSb. It consists here of moving a molten antimony-rich zone along a charge of stoichiometric composition headed by some crystalline ZnSb.

THE compound ZnSb forms from a zinc-antimony melt by a peritectic reaction,[1] and it is therefore difficult, if not impossible, to prepare a single crystal from a stoichiometric melt by standard techniques. It is obvious from the phase diagram[1] that single crystals should be grown from a nonstoichiometric melt having its liquidus temperature between the peritectic temperature, 546°C, and the eutectic temperature 505°C, by either the "normal-freeze" or "zone-melting" technique.[2] Stevenson[3] has utilized the former technique using the conventional pulling arrangement with success, while Mason and Cook[4] have applied the latter to the peritectic compound $CdIn_2Te_4$. We have used both techniques successfully and intend to point out the relative merits of the second technique in this note. Some preliminary measurements on the single crystals are included as an indication of their quality.

NORMAL-FREEZE

A starting charge of 40 atomic percent zinc and 60 percent antimony was prepared by melting in an evacuated and sealed Vycor capsule. The resulting ingot was placed in the $\frac{1}{4}$-×4-×$\frac{1}{4}$-in. cavity of a graphite boat, the cavity being pointed at one end. The charged boat was next placed in a Vycor container which was then evacuated and sealed. The container was placed in a horizontal split-tube furnace powered from a constant voltage source. The sample was melted and solidified from the tapered end under a temperature gradient of about 10°C/in. by automatically reducing the furnace power so that the temperature of the sample at midpoint decreased at the rate of 1°C/hr. (Thus, the freezing velocity must have been about 1 μ per sec.)

The tapered end of the resultant ingot was covered with a forest of faceted needles about 500 μ in length by 20 μ in diameter. Some of the needles were examined by oscillation and Weissenberg photographs[5] and identified as ZnSb. Some back reflection photographs indicated that the first centimeter of the ingot was also single-crystal ZnSb.

The "normal-freeze" technique has two drawbacks when one is interested in the material property measurements. First, the crystals are limited in length because of the appearance of a second phase when the liquid reaches the eutectic composition. In fact, even if complete mixing conditions exist in the liquid, the maximum length of single crystal of compound $X_{\max}$, compared to the total ingot length L, is given by

$$X_{\max}/L=(C_0-C_E)/(C_c-C_E), \quad (1)$$

where C_E, C_0, and C_c are the average concentrations of the eutectic, starting liquid, and compound respectively. In our case, $X_{\max}=0.44\ L$, whereas, experimentally we found $X_{\exp}\approx 0.1\ L$. This indicates that only partial mixing existed during the crystal growth process and that an Sb build-up occurred at the solid-liquid interface. Second, since the compound has a certain solid-solubility range, the solidus line on the phase diagram is not vertical and the crystal will therefore exhibit a slightly different composition at different distances from the end first to freeze. This can produce a large spatial variation in the electrical properties of the crystal making it difficult to accurately evaluate these properties.

---

[1] M. Hansen, *Constitution of Binary Alloys* (McGraw-Hill Book Publishing Company, Inc., New York, 1958), p. 1184.

[2] W. G. Pfann, *Zone Melting* (John Wiley & Sons, New York, 1959).

[3] M. J. Stevenson (private communication).

[4] D. R. Mason and J. S. Cook, J. Appl. Phys. **32**, 475 (1960).

[5] F. Carter and R. Mazelsky (to be published).

ZONE-MELTING

We next tried the "zone-leveling" technique.[2] A ZnSb seed[6] was placed in a horizontal Lavite boat which was about 12 in. in length and which had been coated with Aquadag and baked in vacuum. Next to the seed a 1-in. length of charge, consisting of 40 atomic percent zinc and 60 atomic percent antimony, was placed. The remainder of the boat was charged with stoichiometric ZnSb. The various charges were prepared in such a manner that only short range chemical segregation along the charge length was expected. The charged boat was fixed in a Vycor tube which was then evacuated to less than $5\cdot10^{-4}$ mm Hg at 250°C and sealed off. The container was placed in a horizontal transparent tube furnace wound with an ambient heater to provide a uniform temperature over the entire sample length ($T_A\approx475°$C). A 1-in. long annular zone heater which could be rotated slightly about a vertical axis was used to provide the molten zone.

The entire antimony-rich segment was melted with the zone heater and the molten zone moved slowly back over part of the seed ($T_{\max}\approx560°$C–575°C). When a portion of the seed had been melted, the zone heater was rotated so that the solid-liquid interface at the seed end was no longer normal to the specimen axis. The zone was then moved away from the seed at about 0.3 μ/sec. Since the seed used in the initial attempt was polycrystalline and since grain boundaries tend to align themselves in a normal direction to the solid-liquid interface, the use of the rotated interface caused all but one grain to be quickly grown out of the sample. In this manner, single crystals of about 4-in. length, which were of almost constant carrier concentration, could be grown.

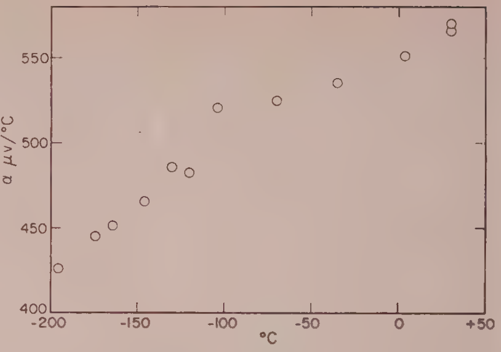

FIG. 2. Thermoelectric power of ZnSb single crystal in a direction nearly perpendicular to ⟨100⟩, at 23° to ⟨010⟩, and 67° to ⟨001⟩. α along the ⟨100⟩ direction is similar, but falls a bit lower at low temperatures.

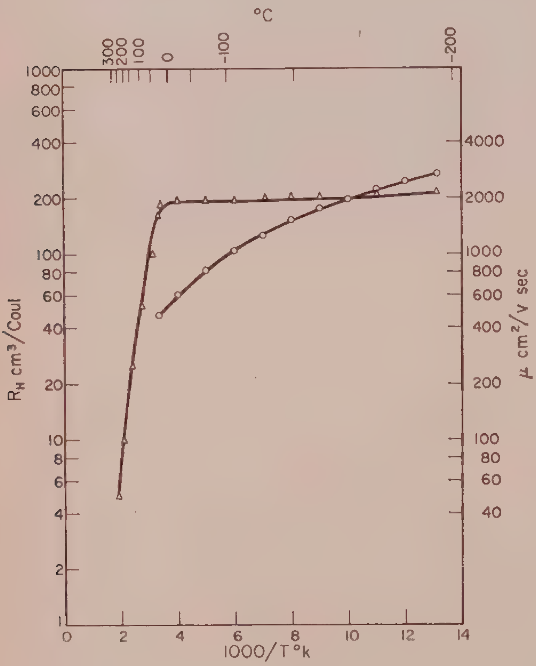

FIG. 1. Hall constant $R_H(\Delta)$ and mobility $\mu(o)$ for ZnSb single crystal. Current nearly parallel to ⟨100⟩. Hall voltages were measured in a direction about 23° from ⟨010⟩, 67° from ⟨001⟩.

The crystals were quite brittle, cleaving readily on the (100) plane, occasionally on the (010) plane, and more rarely on the (001) plane. As an indication of the quality (higher mobility than any ZnSb yet reported in the literature) obtained, some preliminary measurements on the first crystal grown by this zone technique are presented in Figs. 1 and 2. The Hall measurements indicate a carrier concentration of close to $10^{16}/\text{cm}^3$. Intrinsic conduction becomes dominant at ~10°C. From the slope of a plot of $\ln(R_HT^{3/2})$ vs $1/T$ in the intrinsic range, the effective gap was calculated to be 0.49 ev. The (100) axis of this crystal made an angle of 7° with respect to the specimen axis, the side faces of the specimen being about 23° away from the other principal crystallographic axes. The preliminary measurements presented here were made on a 1-in. length of the as-grown crystal (oriented parallel to the walls of the boat). Cutting to crystallographic parallelepiped orientation was postponed (because of the extreme brittleness) in favor of these preliminary measurements on a sound specimen.

ACKNOWLEDGMENT

The authors wish to express their thanks to Brenda Kagle for performing the x-ray back-reflection work to determine the orientation of the single crystals.

---

[6] The first seed was prepared by powder metallurgy techniques. The elements were reacted in a sealed evacuated tube. The quenched ingot was ground to 200-mesh powder, compacted at 50 tsi and annealed for 18 hr at 500°C. The resultant thermoelectric power was close to 500 μv/°C.

JOURNAL OF APPLIED PHYSICS VOLUME 32, NUMBER 10 OCTOBER, 1961

Reflection of an Electron Beam from High-Frequency Fields*

R. B. Hall† and Sanborn C. Brown
Department of Physics, Department of Electrical Engineering, and Research Laboratory of Electronics, Massachuettts Institute of Technology, Cambridge, Massachusetts

(Received April 20, 1961)

Experimental verification of time-average forces due to an rf field acting on charged particles is obtained by measuring the transmission of an electron beam through the high-frequency fields of a cavity. By adjusting the external dc magnetic field so that cyclotron resonance is approached, it is possible to reflect high-energy beams; that is, 66 w of microwave power completely reflected a 24-v beam. Agreement between experiment and theory was close.

THERE have been several experiments reported which have shown the existence in high-frequency fields of time-average forces on charged particles. In one of the earliest experiments, described by Wuerker,[1] several charged dust particles were held in suspension in a highly nonuniform quadrupole electric field. The suspension, observed by reflected light, could be contained indefinitely. There have also been several experiments reported in Russian publications. Vedenov and his co-workers[2] demonstrated the existence of time-average plasma forces caused by electromagnetic fields of large amplitude. The experimental arrangement was to produce the plasma in a cavity with a high-power signal, and observe the detuning of the cavity as the time-average forces pushed this plasma to the low-field-strength regions outside of the cavity. Although this experiment gave qualitative verification to the time-average theory developed by Boot,[3] no results of a quantitative nature were presented. The basic trouble in demonstrating time-average plasma forces is that the large-amplitude electric fields required can also cause breakdown of the background gas. Thus, it is difficult to determine whether a plasma is confined by the use of time-average forces or whether plasma is being produced.

In order to verify the time-average theory of forces caused by nonuniform electromagnetic fields, Miller[4] demonstrated the reflection of an electron beam from the fields of a microwave cavity. He gave the result that electrons with an energy linearly related to the microwave power input to the cavity can be reflected. The linear dependence of beam voltage and microwave power does agree with the time-average theory. The experiment reported here is an attempt at a quantitative verification of the time-averaged theory in the presence of a static magnetic field.

Our experimental arrangement is shown in Fig. 1. An electron beam is focused by the external magnetic field B_0. Situated between the anode and cathode of the electron-beam tube is a TE_{111}-mode cylindrical S-band cavity through which the beam passes. The experimental procedure consists in applying a voltage V_1 to the electron beam and then measuring the dependence of the electron-beam current on the microwave power input to the cavity and different magnetic fields.

The experiment was carried out under conditions of constant microwave power input to the cavity, and we measured the transmitted beam current as the external magnetic field was varied. Typical results of the experiment are shown in Fig. 2. In particular, the asymmetry of the tube current around the cyclotron frequency should be noticed. The presence of electrons striking the tube wall can also be measured from the lower part of Fig. 2. This wall current was collected on a very thin coating of metal evaporated on the inside surface of the tube, and then led to the external circuit by means of a press in the tube envelope. This wall current exists only in a region around cyclotron resonance where the electron orbit size should be large. A calculation of the electron orbit size, with the beam diameter and a possible radial displacement of the beam taken into account, yields the theoretical regions of wall current shown for comparison in Fig. 2.

According to the time-average theory,[3] electrons with an energy

$$U \leq 0.25(e/m)(E_{\max}{}^2/\omega^2)\text{ volts,} \tag{1}$$

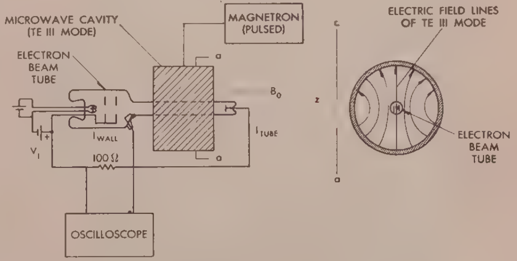

Fig. 1. Schematic diagram of electron-beam reflection experiment.

---

* This research was supported in part by the U. S. Army Signal Corps, the Air Force Office of Scientific Research, and the Office of Naval Research; and in part by the Atomic Energy Commission.

† Now at Boeing Scientific Research Laboratories, Seattle, Washington.

[1] R. F. Wuerker, H. Shelton, and R. V. Langmuir, J. Appl. Phys. 30, 342 (1959).

[2] A. A. Vedenov, T. F. Volkov, L. I. Rudakov, R. Z. Sagdeev, V. M. Glasgolev, G. A. Yeliseyev, and V. V. Khilil, *Proceedings of the Second United Nations International Conference on the Peaceful Uses of Atomic Energy* (United Nations, Geneva, 1958), Vol. 32, p. 239.

[3] H. A. H. Boot, S. A. Self, and R. B. R. Shersby-Harvie, J. Electronics and Control 4, 434 (1958).

[4] M. A. Miller, Soviet Phys.—JETP 8, 206 (1959).

where (e/m) is the ratio of charge to mass, ω is the radian applied frequency, and $E_{\max}$ is the maximum electric field along electron trajectory, should be reflected from the high-frequency fields of the cavity. The modification of Eq. (1) introduced due to the presence of a dc magnetic field is not difficult to derive.[5] One solves for the ac velocity of a charged particle in the magnetic field and as expected a cyclotron resonance exists. The resultant equation reads

$$U \leq 0.25(e/m)[E_{\max}{}^2/(\omega^2-\omega_b{}^2)] \text{ volts}, \tag{2}$$

where ω_b is the cyclotron frequency. It should be noted from Eq. (2) that when $\omega_b/\omega > 1$ no reflection of charged particles is possible. Since the maximum electric field is related to the power input to the cavity when the cavity Q is known, it is possible to rewrite Eq. (1) in terms of the actual geometry of the cavity,

$$U \leq 0.036P/(1-\omega_b{}^2/\omega^2), \tag{3}$$

where P is the microwave power in watts. The cavity used in the experiment had a resonant frequency of of 3000 Mc, had a Q of 4400, and was excited in the TE_{111} mode.

If the electron beam were monoenergetic, the tube current I_T would either be fully cut off or fully transmitted; both conditions depend on the magnetic field and the microwave power. In the electron-beam tube that was used, the distribution of beam energy was far from monoenergetic. The electron beam of 1-mm diameter in an 8-mm diameter tube was obtained from a simple tungsten filament heated with a dc current and immersed in the external magnetic field. A current of 12 μa was used. The energy characteristic of the beam for a particular beam voltage is shown in Fig. 3 for different magnetic fields. These curves were obtained by placing a variable voltage source in the external circuit of the beam current and measuring the volt-ampere characteristics.

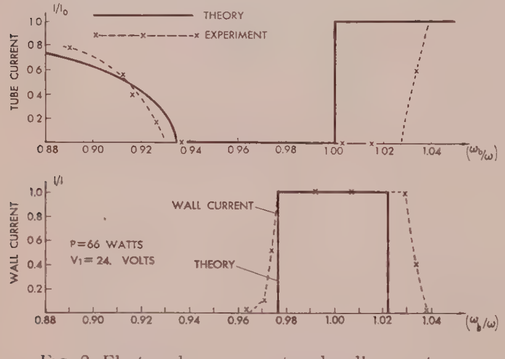

FIG. 2. Electron-beam current and wall current as a function of magnetic field.

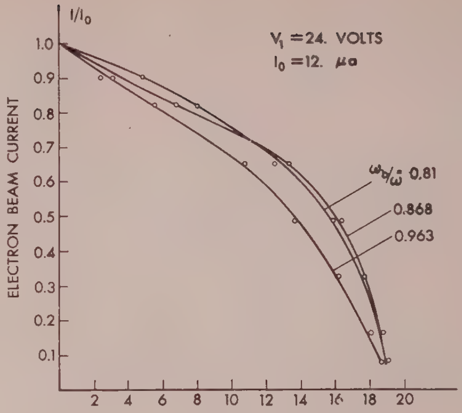

FIG. 3. Energy characteristics of the electron beam.

With the experimentally determined electron-beam characteristics given in Fig. 3, it is possible to calculate the electron-beam current as a function of the magnetic field and thus make a comparison between theory and experiment. To do this, it is only necessary to calculate the electromagnetic potential given by Eq. (2) from the experimentally measured microwave power of 66 w and the actual magnetic field. Since the electromagnetic potential U given by Eq. (2) is directly related to an accelerating potential, it is possible to find the tube current from Fig. 3. This theoretical calculation of the transmitted electron current makes use of the single particle analysis of Eq. (2) in determining that all particles in the beam which do not satisfy Eq. (2) will be transmitted through the high-intensity fields of the cavity. This expected electron-beam current is also shown in Fig. 2 in which it can be seen that theory and experiment agree very closely for $\omega_b/\omega < 1$. It can be observed that there is an appreciable range of magnetic field in which the electron beam is reflected without striking the tube walls. The asymmetry of the electron-beam current around the cyclotron frequency shows that the beam is reflected from the cavity only when $\omega_b/\omega < 1$. The presence of wall currents explains the difference between experiment and theory for $\omega_b/\omega > 1$. The experiment shows a double verification of the presence of time-averaged forces—the close agreement between Eq. (2) and the theory for $\omega_b/\omega < 0.94$ and the cyclotron effect indicated by a change in the direction of force for $\omega_b/\omega > 1$.

Results of experiments at different electron-beam voltages and for different microwave powers lead to the same conclusions as those stated above.

---

[5] R. B. Hall, "Large Signal Behavior of Plasmas," thesis in Department of Electrical Engineering, Massachusetts Institute of Technology, September, 1960.

JOURNAL OF APPLIED PHYSICS VOLUME 32, NUMBER 10 OCTOBER, 1961

Effect of Reactor Fast Neutrons on Electron-Hole Recombination in Germanium

A. Czachor and J. Piekoszewski
Polish Academy of Sciences, Institute of Nuclear Research, Warsaw, Poland

(Received March 22, 1961)

The properties of recombination centers introduced by reactor fast neutrons in n-type germanium were investigated. From carrier lifetime temperature measurements, using Shockley-Read statistics, recombination-level position has been calculated and found to be dependent on resistivity of germanium. It has been observed for the first time that in the region of low temperature, lifetime increases with decreasing temperature.

INTRODUCTION

IRRADIATION of high-energy particles introduces a damage into the structure of solids. These particles, by collision with single atoms, give them part of their kinetic energy. The struck atom, if its kinetic energy is sufficiently large, goes into an interstitial position in the crystal lattice. The resulting vacancy-interstitial pairs are called Frenkel defects, and their appearance in groups or as single pairs is the most probable kind of defect in crystal. Their properties have been investigated by many authors.

The presence of lattice defects changes physical parameters of a crystal. Especially the electrical parameters of semiconductors are known to be sensitive to the presence of such defects. Because of its physical nature, minority carrier lifetime is more sensitive than other parameters of semiconductors.

Let the irradiating particles be the fast neutrons from a nuclear reactor and let the irradiated crystal be a germanium crystal. The defects are introduced into the crystal and localized levels appear in a forbidden zone of the band model of germanium. Four levels have been considered for Frenkel defects. However, it is not well known which one depends on the interstitial or on the vacancy. This problem has been dealt with by James and Lark-Horovitz,[1] and in a different way by Blount.[2] Because some of the defects play a role in the recombination processes, they could be investigated by measuring the lifetime of minority carriers.

The recombination of electrons and holes in germanium is discussed on the basis of the theory of localized levels in a forbidden zone. There are many papers which deal with the problem of recombination in semiconductors. Recombination occurring through a single level has been treated by Shockley and Read[3] and Hall[4] for stationary cases, and by Sandiford[5] for transit cases. Recombination statistics for multilevel cases have been considered by Wertheim,[6] Okada,[7] and Kalashnikov.[8] Several publications have recently appeared which treat the recombination through flaws with many charge conditions.[9,10]

Practically, only the Shockley-Read single-level statistics were in use to explain results of measurement on irradiated germanium. In this way, the position of the recombination level, which has been identified with the highest Lark-Horovitz level, has been determined as being 0.20 ev below the bottom of the conductivity zone.[11–14]

In this work, experiments similar to those described in papers mentioned above were carried out. However, the results are different and would indicate that recombination level lies nearer the middle of the forbidden zone. Besides, in the region of low temperatures, lifetime increases with decreasing temperature. Both effects have not been observed so far.[15]

EXPERIMENTAL PROCEDURE

Carrier lifetimes in germanium samples were measured by the steady photoconductivity method and the Many bridge method.[16] The first method is based on measurement of changes in photoconductivity when the surface of the sample is illuminated. When this time of illumination is long enough, the excess concentration of the hole-electron pairs, liberated by light, will obtain the steady value $\Delta n = \Delta p = g\tau$, where g is the rate of

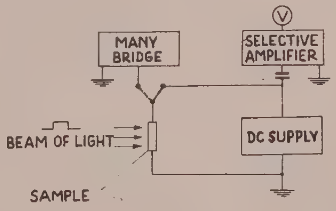

FIG. 1. Electrical arrangement used for lifetime measurements.

---

[1] H. James and K. Lark-Horovitz, Z. Physik. Chem. **198**, 107 (1952).
[2] E. I. Blount, Phys. Rev. **113**, 995 (1959).
[3] W. Shockley and W. T. Read, Phys. Rev. **87**, 835 (1952).
[4] R. N. Hall, Phys. Rev. **87**, 387 (1952).
[5] D. J. Sandiford, Phys. Rev. **105**, 524 (1957).
[6] G. K. Wertheim, Phys. Rev. **109**, 1086 (1958).
[7] J. Okada, J. Phys. Soc. Japan **12**, 1338 (1957).
[8] S. G. Kalashnikov, Zhur. Tekh. Fiz. **26**, 241 (1956).
[9] W. Shockley and J. T. Last, Phys. Rev. **107**, 392 (1957).
[10] C. T. Sah and W. Shockley, Phys. Rev. **109**, 1103 (1958).
[11] O. L. Curtis, J. W. Cleland, J. H. Crawford, and J. C. Pigg, J. Appl. Phys. **28**, 1161 (1957).
[12] G. C. Messenger and J. P. Spratt, Proc. Inst. Radio Engrs. **46**, 1038 (1958).
[13] O. L. Curtis, J. W. Cleland, and J. H. Crawford, J. Appl. Phys. **29**, 1722 (1958).
[14] O. L. Curtis, J. Appl. Phys. **30**, 1174 (1959).
[15] A. Czachor and J. Piekoszewski, Inst. Nuclear Research Rept. No. 201/*I-B*, Warsaw, December (1960).
[16] A. Many, Proc. Phys. Soc. (London) **B67**, 9 (1954).

generation and τ is the lifetime of current carriers. Thus, if g is known, the absolute value of lifetime can be measured, or in the case of g being constant, the relative changes of lifetime can be determined.

Figure 1 shows the electrical circuit which was used in our measurements. The germanium sample was included into a dc circuit, and one of its surfaces was illuminated by white light. The light beam was chopped at a low audio-frequency rate by an electromagnetic chopper. The ΔV, ac voltage across the sample, was amplified by means of a selective amplifier and measured with a voltmeter.

In this case lifetime is determined by the following relation: $\Delta V = A(\mu_n + \mu_p)\rho^2\tau$, where ρ is the resistivity, μ_n, μ_p are electron and hole mobilities, respectively, and A is a constant. The light pulse width t is chosen to be $t \gg \tau$.

Before every experiment we checked whether the photovoltaic parasitic effect on contacts was negligible.

As can be seen in Fig. 1, the lifetime may also be measured with the aid of the Many bridge. We have used the same contacts in both methods since ohmic contacts to some extent become rectifying when current through the sample is large enough.

As the photoconductivity method gives only relative dependence, we used the Many bridge method primarily in order to normalize results obtained by the first method.

Injection level (coefficient) in the measurement with both methods was so low that we could assume $\tau_{\text{photo}} = \tau_{\text{Many bridge}}$. Temperature measurements have been made by means of a vacuum cryostat (Fig. 2). The temperature and temperature gradients across the sample were controlled by placing two thermocouples on the sample. The temperature varied in the range from $-60°$ to $+100°\text{C}$ and the temperature gradient was not greater than $\pm 1°\text{C cm}^{-1}$.

Measurements of the lifetime as a function of the integrated fast neutron flux were made during irradiation. The samples were placed in the beam of fast neutrons from a horizontal channel of the EWA reactor.

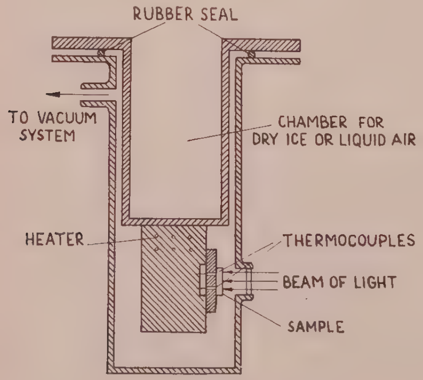

FIG. 2. Vacuum cryostat used for temperature measurements.

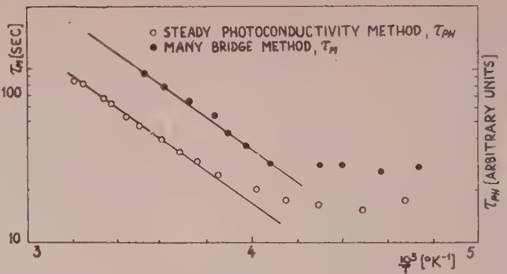

FIG. 3. A plot of minority carrier lifetime measured by Many bridge and photoconductivity method vs reciprocal temperature $1/T$ for n-type unirradiated sample of germanium.

The specimens used in the experiments were in the form of rods of about $1.5 \times 0.3 \times 0.2\ \text{cm}^3$ cut from n-type germanium single crystal (doped antimonium). Each sample was well cleaned with organic solution, etched with $H_2O_2 + KOH$, and again washed with distilled water.

In order to examine whether the influence of surface recombination of the measured lifetime is negligible, the influence of air pressure on τ was examined before each experiment. If the measured lifetime showed pressure dependence, it meant that the surface preparation had to be repeated.

Measurements $\tau(T)$ and $\tau(\phi t)$ were carried out on several germanium samples with various resistivities ranging from 2 to 10 ohm cm. Some experimental results and their analysis are presented below.

RESULTS

In Table I, resistivities and initial lifetimes of some samples at 292°K are shown. Figure 3 shows the experimental curves of the dependence of lifetime on temperature, as found in our measurements. In this experiment the carrier lifetime has been measured by two different methods.

Lifetime during irradiation was measured only by the method of steady conductivity. Generally, the samples were irradiated till the carrier lifetime decreased about ten times (Table I). After irradiation the lifetime temperature dependence was measured in the same way as before. Because of the decrease of the lifetime, the Many bridge measurement became difficult and errors grew greater. For this reason, only the results obtained

TABLE I. Values of recombination-level position for the n-type germanium irradiated with fast neutrons, given by other authors.

Author(s)	$E_c - E_r$ ev	Reference
Curtis, Cleland, Crawford, and Pigg	0.23	11
Messenger and Spratt	0.23	12
Curtis, Cleland, and Crawford	0.20	13
Curtis	0.20	14

TABLE II. List of data of our experiments.

Number of sample	τ_0 before irradiation [μsec]	ρ ohm-cm	E_c-E_r before irradiation (ev)	τ after irradiation [μsec]	Values of $10^2/T$ for bending of $\log\tau(1/T)$ after irradiation	E_c-E_r after irradiation (ev)
34*N*	75	2.0	0.18	9	3.6	0.24
29*N*	75	5.0	0.18	6.5	3.7	0.30
27*N*	200	10.4	0.18	20.5	3.8	0.34

by the photoconductivity method are shown in Figs. 4 and 5.

DISCUSSION

The dependence of $\log\tau(1/T)$ for the *n*-type germanium samples irradiated by fast neutrons presented in other papers[13,14] shows leveling off in the low-temperature range and a linear increase in the high-temperature range. This kind of dependence could be explained on the basis of simple Shockley-Read recombination theory.[3] In the steady case for the strongly *n*-type germanium, with the recombination level above the center of the forbidden zone ($n_1 \gg p_1$), τ is determined by the following expression:

$$\tau=\frac{1}{C_pN_t}\left(1+\frac{n_1}{n_0}\right). \tag{1}$$

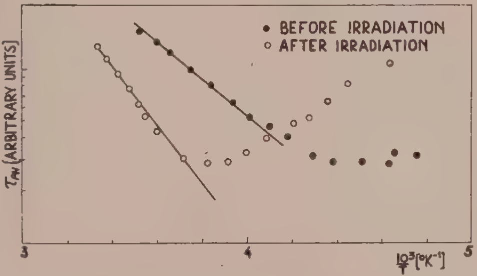

FIG. 4. A plot of minority carrier lifetime vs $1/T$ for the same sample 27*N* unirradiated and irradiated.

In the high-temperature region, relation (1) becomes

$$\tau=\text{const}\,T^{\frac{3}{2}}\exp[-(E_c-E_r/kT)], \tag{2}$$

where E_c-E_r represents the distance of the recombination level from the bottom of the conduction zone. On using these equations, the values of E_c-E_r were found from $\tau(1/T)$ and $\tau(\phi t)$ curves. These data are shown in Table I. From all temperature dependencies found in our measurements, only these, which were obtained before irradiation of samples (Fig. 3), could be interpreted on the basis of simple S-R statistics. The level position calculated by means of S-R statistics is very similar for all samples and is located about 0.18 ev below the bottom of the conduction band. Values similar to those mentioned above are often found in investigations of pure *n*-type germanium samples.

In Figs. 4 and 5 are shown the temperature behaviors of lifetime after the irradiation had been stopped. In the low-temperature part of the curves, the lifetime increases with the decreasing of the temperature. This behavior has not been observed by other authors. At a high temperature, the slopes of the linear parts of the curves become greater with the increase of the resistivity of the samples. Values of E_c-E_r, calculated on the basis of the S-R statistics, are different for each sample, and they are also different from the results obtained by other authors (Tables I and II). Measurements of de-

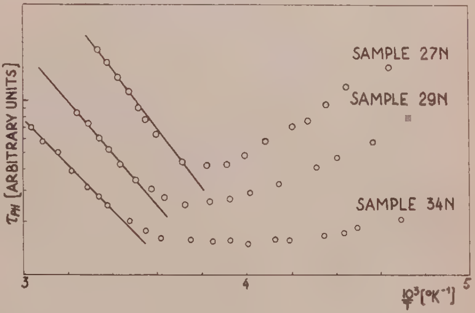

FIG. 5. A plot of minority lifetime vs $1/T$ for three *n*-type fast neutron irradiated samples of germanium: 27*N*, 29*N*, 34*N*.

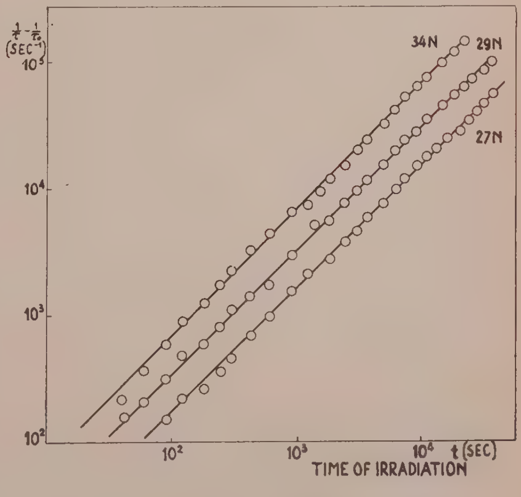

FIG. 6. A plot of $(1/\tau)-(1/\tau_0)$ vs time of the fast neutron irradiation for three *n*-type samples 34*N*, 29*N*, 27*N*.

pendence of lifetime on irradiation time (Fig. 6) give $E_c - E_r = 0.25$ ev, assuming the above-mentioned statistics.

The differences between the values of $E_c - E_r$, especially between those calculated from temperature curves, as well as the low-temperature increase of the lifetime, completely disagree with S-R statistics for recombination through one level in the forbidden zone. It is, therefore, necessary to consider the case when recombination occurs through more than one level. Especially, the presence of low-temperature increase of lifetime suggests that recombination occurs through levels due to flaws with many charge conditions.[10,17] This problem is now being investigated in our laborartoy.

ACKNOWLEDGMENTS

The authors are grateful to Dr. H. Rzewuski for his interest in this work and for helpful discussion. They also wish to thank E. Szyszko from TEWA for the germanium single crystals which he kindly provided.

---

[17] A. A. Grinberg, Fiz. Tverdogo Tela **1**, 192 (1959).

JOURNAL OF APPLIED PHYSICS VOLUME 32, NUMBER 10 OCTOBER, 1961

"Anomalous" Electron Double Diffraction

O. Haase and R. D. Heidenreich
Bell Telephone Laboratories, Incorporated, Murray Hill, New Jersey

(Received April 26, 1961)

Double diffraction of electrons by tandem foils of polycrystalline MgO and single crystal silicon is demonstrated. The patterns are very similar irrespective of which foil the electrons pass through first. The effect is explained by elastic bending of the thin, silicon crystal. The relationship between the double diffraction features, Kikuchi lines, and angular distortion of the crystal is discussed.

IT is the purpose of this paper to call attention to a diffraction effect in thin foils which at first glance appears anomalous. The phenomenon must be very commonplace in crystalline foils used for transmission electron microscopy and diffraction. Apparently, its existence has not been appreciated although it operates extensively in composite thin films such as oxide-on-metal, bimetallic films for moire patterns, precipitation in alloy films, etc.

The common form of double diffraction involving two thin foils in tandem is exemplified by a single crystal foil producing a cross-grating pattern and a polycrystalline foil producing a ring pattern. If the foils are so arranged that the electron beam passes first through the single-crystal foil and then through the polycrystalline foil, it is found that the Laue beams from the single crystal behave as incident beams in the polycrystalline foil.[1,2] The result, called case I here, is a spot array for the single crystal, a set of concentric polycrystalline rings about the transmitted beam and secondary rings centered on one or more of the Laue spots. That is, the Laue spots from the single crystal behave as origins for the polycrystalline rings. Figure 1(a) illustrates case I for a single-crystal silicon foil followed by a mesh containing MgO smoke.

Figure 1(a) was taken in an electron diffraction camera operating at 60 kv with a beam diameter of about 0.1 mm, a divergence of about 1.5×10^{-3} rad and a specimen-to-plate distance of 600 mm. The foils were separated by 1 mm with the beam passing first through the silicon. Figure 1(b) shows schematically how the pattern is generated from reciprocal lattice $\mathbf{g}_1$ and $\mathbf{g}_2$ of the single crystal with origin O and the reciprocal lattice vectors of the polycrystalline foil with origins O_1, O_2, O_3, etc.

If the tandem films of case I are interchanged so that the MgO foil is now struck first, the pattern shown in Fig. 2(a) is obtained. The similarity between Fig. 2(a), called case II, and Fig. 1(a) is at first sight rather surprising. Except where Kikuchi lines are involved, they are indistinguishable. Case II double diffraction patterns were first observed with a polycrystalline film evaporated directly onto one surface of the single crystal.

At this time, speculation arose as to whether the uncertainty principle was not being demonstrated in that an electron could not be located sufficiently well to determine which film it was in. However, when the effect was observed just as well with the films separated by relatively large distances (1 mm), the geometric construction of Fig. 2(b) was arrived at. Although it appears in Fig. 2(a) that the Laue spots are origins for the concentric polycrystalline rings, it is concluded that this cannot be so. It must be that the diffracted

---

[1] F. Kirchner, Z. Physik **76**, 576 (1932).

[2] H. R. Thirsk and E. T. Whitman, Trans. Faraday Soc. **36**, 565 (1940). It can be essential that double diffraction is recognized in the interpretation of patterns: see also, R. D. Burbank and R. D. Heidenreich, Phil. Mag. **5**, 373 (1960).

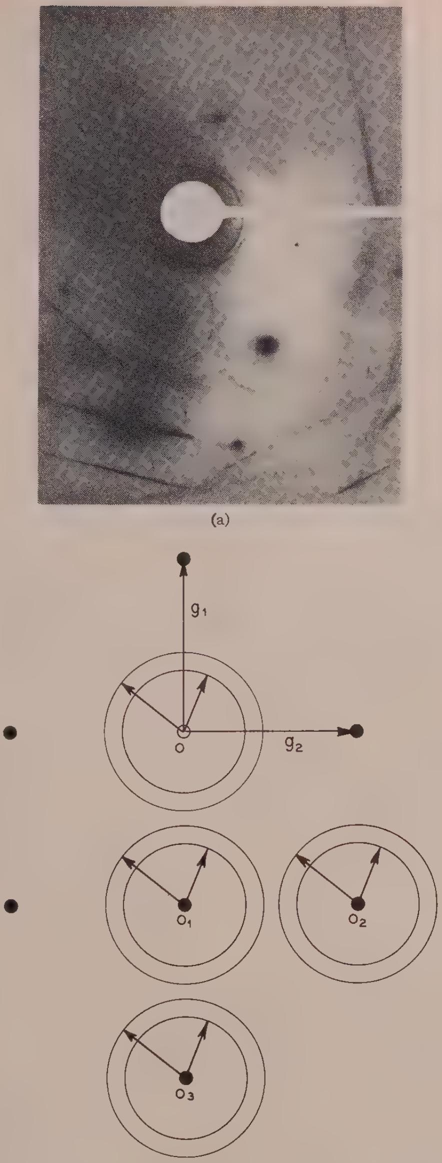

(a)

(b)

Fig. 1. (a) Normal double diffraction pattern produced by a silicon single crystal followed by MgO smoke on a grid. The grip wires tend to shadow portions of the pattern. This is case I double diffraction. 60-kv electrons. (b) Schematic representation of (a) showing the reciprocal lattice vectors. The central spot O and the Laue spots O_1, O_2, O_3 serve as origins for the ring patterns.

cones from the polycrystalline foil are incident beams to the single crystal and are diffracted as Laue beams by the single crystal.

The observations of case II are still anomalous unless another condition is introduced since Fig. 2 cannot be valid for a perfect, single crystal. It is necessary that the "angular relaxation" of the Laue conditions in the single crystal β be

$$\beta \geq 2\theta_1 = \lambda/d_1, \tag{1}$$

where θ_1 is the Bragg angle for the ring undergoing diffraction, λ is the electron wave length, and d_1 the interplanar spacing corresponding to θ_1. Observed values of β are as high as 0.04 rad or more than 2°. A relaxation of the Laue conditions of this magnitude can only be accomplished by bending of the crystal or by

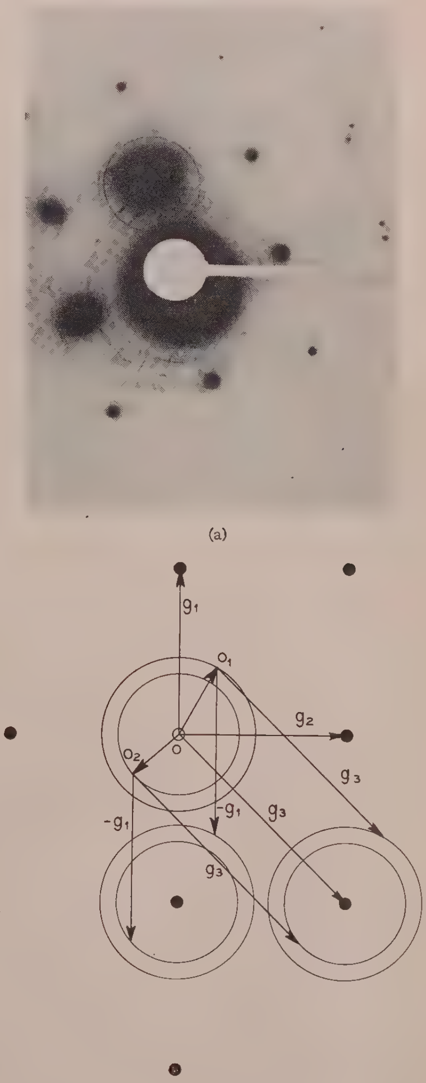

(a)

(b)

Fig. 2. (a) "Anomalous" double diffraction pattern produced by MgO on a grid followed by a silicon single crystal with a separation of 1 mm. This is case II double diffraction. 60-kv electrons. (b) Schematic representation of (a) showing how the secondary rings are generated by the reciprocal lattice vectors of the single crystal. The MgO reciprocal vectors generate *only* the primary ring about the center spot O. The Laue spots are *not* the origins for the rings centered upon them.

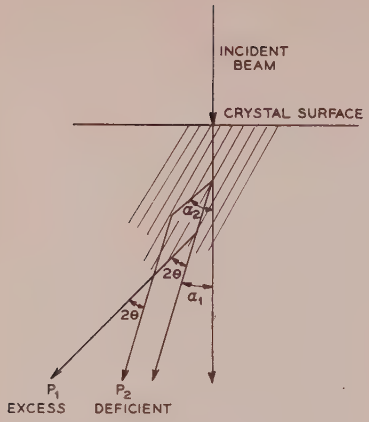

FIG. 3. Cross section through a crystal showing a set of net planes and the usual geometry of the formation of Kikuchi lines. Here $\alpha_2 > \alpha_1 (\alpha_2 = \alpha_1 + 2\theta)$ so that there is an excess of electrons at P_1 removed from P_2. Inelastically scattered electrons occur for all angles, including α_1 and α_2, and produce the background.

extreme thinness. The thickness of the crystal regions giving rise to the diffraction pattern is of the order of 500 A, or more, which allows an intensity spike normal to the crystal surface of about 3×10^{-3} A^{-1} in the reciprocal lattice. The associated angular relaxation of the Laue condition is then about 8×10^{-3} rad, which is only one-fifth of that required. Thus, elastic bending in the single-crystal film must be the chief factor in the relaxation of the Laue condition. The presence of sharp Kikuchi lines in the pattern indicates a high degree of angular perfection in the original silicon crystal. The absence of case II double diffraction in reflection experiments using massive crystals again is evidence that bending is essential.

If the foils are separated by a distance s, the radius of the diffracted cone entering the single crystal is $r = \lambda s / d_1$, where d_1 is the interplanar spacing in the polycrystalline foil associated with $2\theta_1$. It follows that in the area struck by this cone there must be regions of bending where $\beta = 2\theta_1$. The distribution of intensity in the secondary ring is thus a map of constant bending $= 2\theta_1$ in the area. Pure cylindrical bending, for example, would allow only short arcs of the secondary rings. Uniform rings require that $\beta = 2\theta_1$ occurs in all directions in the surface of the crystal. A single-crystal foil that is randomly rumpled or crinkled will produce uniform secondary rings centered on a Laue spot provided the diameter of the electron beam is sufficient to sample regions bent in all orientations. If the size of the incident beam is made small, such as in selected area diffraction, not all bending orientations in a rumpled film are sampled by the beam and only segments of secondary rings will occur.

An interesting situation arises when the single crystal foil produces Kikuchi lines. Examination of a number of case II double diffraction patterns exhibiting Kikuchi lines indicates a close relation between the double diffraction features and the lines. As is well known, if the single crystal is sufficiently thick to produce a divergent beam of inelastically scattered electrons, those portions of the beam making the Bragg angle with a set of net planes give rise to Kikuchi lines. The well known geometric representation is shown in Fig. 3. Electrons from the incident beam are scattered inelastically through a range of angles.[3] Those scattered through an angle α_1 make the Bragg angle with a set of planes and are diffracted to P_1. Electrons scattered through α_2 are diffracted by the same set of planes to

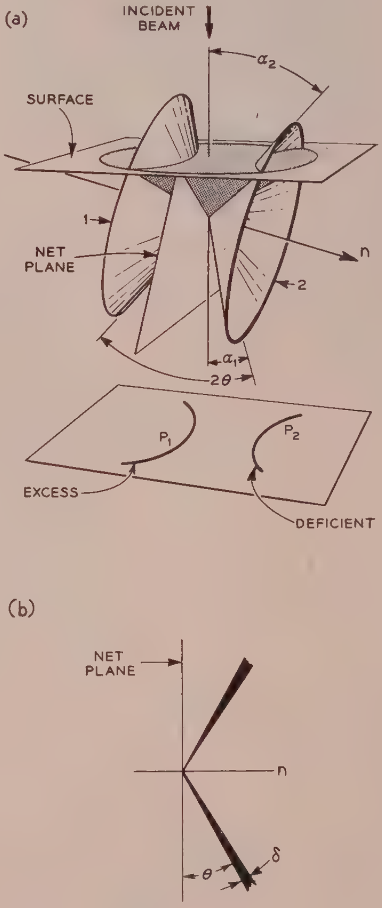

FIG. 4. (a) Three dimensional representations for generation of Kikuchi lines by the mechanism of Fig. 3 using diffraction cones on the normal **n** to a set of Bragg planes. The intersections of the inelastically scattered, divergent beam of electrons with the diffraction cones define the Kikuchi lines. (b) Cross section of a diffraction cone in (a) showing the angular width δ determined by the angular perfection of the crystal. If the crystal is bent, the width δ increases in the direction of bending.

---

[3] Recent measurements of energy losses in Kikuchi lines from silicon show that the electrons appearing in Kikuchi lines have lost about 10 v. W. Hartl and H. Raether, Z. Physik **161**, 238 (1961).

P_2. Since $\alpha_2-\alpha_1=2\theta$, electrons that would have reached P_2 if there were no diffraction are actually diffracted to P_1. Since $\alpha_2>\alpha_1$, the intensity diffracted to P_1 is greater than that to P_2 as the inelastic scattering is mainly forward. It is seen that P_2 will have less than background intensity and P_1 will exceed background so that P_2 is the deficiency line and P_1 is the excess line. In three dimensions, the situation can be represented as in Fig. 4(a). Two cones, apex-to-apex, with their common axis normal to a set of planes are drawn with a half-angle $(90-\theta)$ to represent the Bragg conditions of the net plane. Incoming beams are the primary beam and the inelastically scattered electrons over all angles. These are represented by the entire solid cone. The intersection of cone (1) with the photographic plate produces the excess line and cone (2) the deficiency line.

The linewidth δ in Fig. 4(b) is determined by the angular perfection of the crystal. It is apparent from Fig. 4(b) that a crystal producing sharp Kikuchi lines (angular width δ) can produce case II double diffraction only where the polycrystalline or Debye-Scherrer cone intersects the diffraction cone—that is, only where the Debye-Scherrer ring coincides with an excess Kikuchi line. As the angular thickness of the diffraction cone δ increases due to angular distortion of the crystal, the Kikuchi line broadens and the case II Debye-Scherrer arcs increase in length. Figure 5(a) is a case II pattern with the Debye-Scherrer rings visible only where they are coincident with a Kikuchi line. Figure 5(b) is the geometric explanation. If the crystal is tilted slightly so that the Kikuchi line moves across the pattern, those portions of the ring coinciding with the line become visible.

As the diffraction cone thickness δ increases, the intensity of the Kikuchi line diminishes and the visible arc length of the Debye-Scherrer ring increases. Finally, when $\delta=\beta=2\theta_1$, the full Debye-Scherrer ring is visible but the Kikuchi line intensity has decreased until it is not discernible above the background. The angular distortion of the crystal in the area struck by the incident beam is first apparent in the Kikuchi linewidth. As the distortion increases, the Kikuchi lines become less distinct and the distortion is more easily seen in the lengths of the Debye-Scherrer arcs. Thus, angular distortion can be measured by Kikuchi line breadth from about 10^{-3} rad to about 6×10^{-3} rad. For greater breadth (or angular distortions) the arcs of the secondary rings must be used.

If a polycrystalline foil with a large d value is used in case II double diffraction, it is possible to map the intensity region about a reciprocal lattice point. With a d value of 10–15 A, crystal imperfections such as stacking faults should show double diffraction arcs where the rings intersect the spikes in reciprocal space. Likewise, double diffraction arcs would be visible where the rings intersect the intensity regions produced by thermal motion. The effect thus offers possibilities for mapping reciprocal space by electron diffraction using discrete angular displacements.

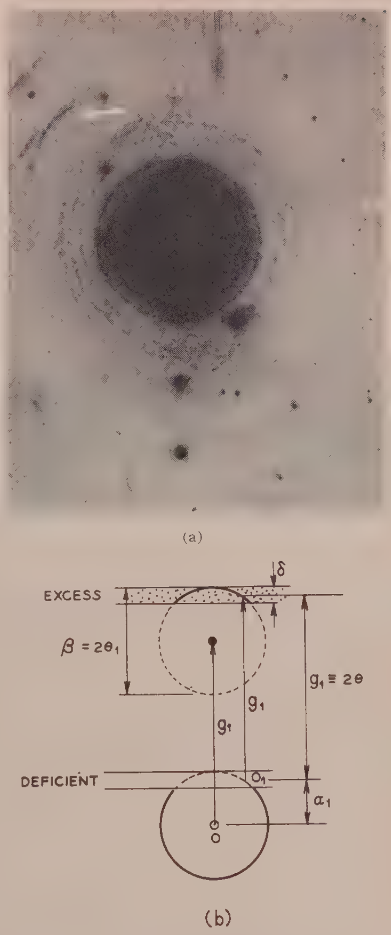
(a)

(b)

FIG. 5. (a) Selected area diffraction pattern taken at 100 kv. Evaporated germanium on a silicon single crystal. Case II double diffraction showing the relation with Kikuchi lines (see arrow). (b) Schematic diagram for (a). Portions of the primary ring centered at O are diffracted through 2θ as are the Kikuchi lines. However, electrons producing the arcs need not have suffered any energy loss as have those in the Kikuchi lines.

ACKNOWLEDGMENTS

The authors are grateful to Messrs. C. Herring and W. Boyle for helpful discussions.

JOURNAL OF APPLIED PHYSICS VOLUME 32, NUMBER 10 OCTOBER, 1961

Observations on the Growth of α-Iron Single Crystals by Halogen Reduction

C. M. WAYMAN
Department of Metallurgy, University of Illinois, Urbana, Illinois

(Received April 18, 1961; in final form, June 5, 1961)

By large scale modification of established whisker growing techniques, it was possible to produce single crystals of alpha iron between 1 and 2 mm in diameter and up to 80 mm in length. These crystals grew along a ⟨100⟩ axis and had {100} faces. The final size of the crystals appeared to depend upon the quantity of $FeCl_2$ vapor available for reduction. Some growth features are reported.

IRON whiskers have been grown successfully by the hydrogen reduction of $FeCl_2$ and $FeBr_2$ with {100} and {110} faces and ⟨100⟩, ⟨110⟩, and ⟨111⟩ growth directions.[1] By field ion emission microscopy, Muller[2] has obtained evidence to indicate that a screw dislocation growth mechanism may be likely for iron whiskers. Coleman[3] has grown iron whiskers of sizeable diameter and of lengths up to 50 mm by the hydrogen reduction of $FeCl_2$ in soft steel boats. While it is generally thought[4] that only the very small iron whiskers ($<10\,\mu$) are mechanically perfect (i.e., can withstand elastic strains in excess of one percent), Coleman[3] could not produce etch pits in whiskers up to 500 μ in diameter with optically good surfaces (no growth steps) unless they were first deformed, polygonized, etc.

By increasing the scale of the conventional technique for growing iron whiskers, it was possible to produce single crystals of alpha iron 1–2 mm in diameter and up to 80 mm in length. Nearly all these crystals grew with {100} faces and exhibited a ⟨100⟩ growth axis. Reduction of $FeCl_2$ by hydrogen at 731°C was employed, using a 125-mm diam, hinged-type tube furnace with a 24-in. hot zone. Approximately 0.6 kg $FeCl_2\cdot 4H_2O$ (Baker's analyzed grade) was placed in a semicylindrical boat of commercial ingot iron, 8 cm in diameter and 30 cm long. This boat was then placed in a 90-mm diam Vycor tube, and purged with He at room temperature. The reaction tube was subsequently placed into the furnace which was preheated to 731°C. The salt was dehydrated and melted at this temperature under a He flow rate of 0.3 liters/sec (STP). After the salt was molten, hydrogen was introduced into the system, and a flow rate of 1.1 liters/sec (STP) was maintained until the end of the run. To ensure that all chloride was reduced and that all HCl vapor was removed from the system, a reaction time of 12 hr was permitted.

Most crystals grown according to this technique were considerably longer and thicker than those obtained by the use of a smaller amount of salt (30 g in a boat $10\times3\times2$ cm) at the same reducing temperature and gas flow rate. X-ray diffraction confirmed that these crystals were in fact single crystals. Evidently the final size of the crystals depends upon the amount of salt available for reduction for a given reducing temperature and gas flow rate. It is felt that even larger crystals can be obtained by the use of more $FeCl_2$ in the chamber. It has been suggested[5] that the final length of a whisker or crystal should be governed by the time of retention of a dislocation which perpetuates the growth steps at the tip. It is difficult to see how the presence of a greater amount of chloride would favor the dislocation remaining in the crystal for longer times. The same boats which contained the large diameter crystals also contained whiskers less than 25 μ in diameter, but of considerable length (greater than 50 mm). This would suggest that the whiskers first grow to some extensive length, and then thicken into crystals by two-dimensional nucleation and monolayer addition.

A typical boat grown under the conditions described above is shown in Fig. 1. The hydrogen flowed in the direction of decreasing scale marks. The size of the crystals is apparent. Seven different runs were made, and large crystals were always obtained.

In Fig. 2 it can be seen that the crystals have a tendency to grow in clumps. Many different crystals appear to radiate from a common nucleus, the result resembling in some respects a pincushion. This effect

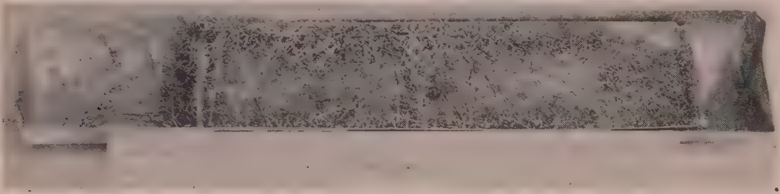

FIG. 1. Boat of iron crystals grown by the reduction of $FeCl_2$ at 731°C. The smaller whiskers (near the 12-in. mark) formed at the gas entry end of the reaction tube.

---

[1] R. V. Coleman, in *Growth and Perfection of Crystals* (John Wiley & Sons, Inc., New York, 1958), p. 239.
[2] E. W. Muller, J. Appl. Phys. **30**, 1843 (1959).
[3] R. V. Coleman, *Internal Stresses and Fatigue in Metals* (Elsevier Publishing Company, Inc., New York, 1959), p. 163.
[4] S. S. Brenner, in *Growth and Perfection of Crystals* (John Wiley & Sons, Inc., New York, 1958), p. 157.
[5] W. J. Allan and W. W. Webb, Acta. Met. **7**, 646 (1959).

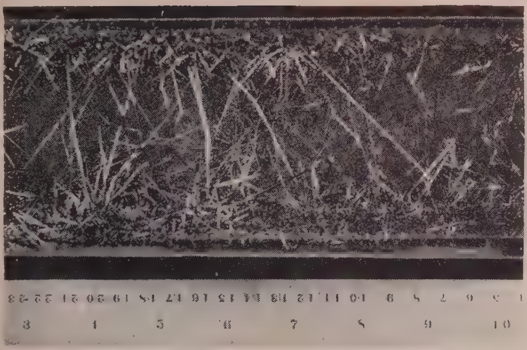

FIG. 2. Close-up view of iron crystals shown in Fig. 1. The three clusters of crystals (above the numeral 6 on the inch scale) are likely to be noted.

is also observed when whiskers are grown in small boats, but on a much finer scale.

In one instance during the reduction process, the system was accidentally opened to the atmosphere for approximately one minute. Many of the crystals were later observed to take on a dendritic appearance, indicating that nucleation had occurred at places on crystals which were substantially well developed at the time the system was opened to the atmosphere. It may be that oxide nuclei were responsible for this secondary growth. This growth habit is distinct from the usual formation of growth bends in crystals. Figure 3 shows such a dendritic crystal. As further evidence for the nucleation of crystals on already well-developed crystals, some very small whiskers were observed to be growing from the tips of the larger crystals in this same boat.

If the furnace is turned off and permitted to cool before all the molten chloride is reacted, crystals of $FeCl_2$ form at various places when the temperature reaches the vicinity of the melting point of the salt. Oftentimes these crystals form at the tip of whiskers. In one case such an $FeCl_2$ crystal formed at the tip of a grown iron crystal. However, there was still substantial vapor pressure of $FeCl_2$ and apparently a very small iron whisker continued to grow at a growth step on the halide crystal. This is shown in Fig. 4.

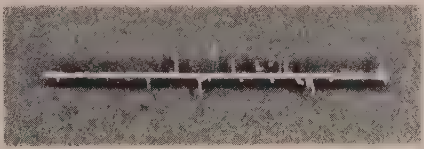

FIG. 3. Dendritic-like crystal (actual size) showing growth of smaller crystals from main crystal.

No attempt has been made to determine the effect of salt purity on growth conditions since the reagent used always gave reproducible results and large crystals. At present time, information on the mechanical perfection of these large crystals is not available although it is likely that growth accidents render these crystals relatively imperfect. Studies on the perfection and properties are now under way. Nonetheless, it is felt that such crystals represent a reproducible source of high purity, i.e., single crystals of alpha iron which are of reasonable size for experimentation and which are conveniently "preoriented" by growth. Such sizeable crystals should facilitate future work on the nature and properties of alpha iron, and clearly have advantages over conventionally produced strain-anneal crystals of pure iron.

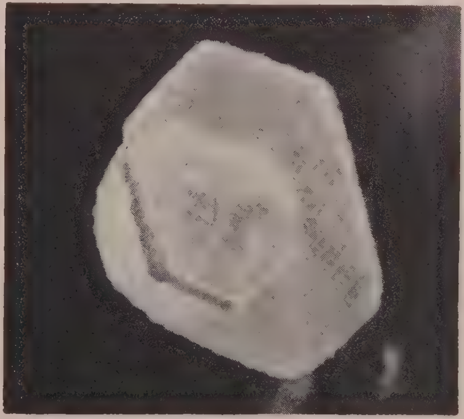

FIG. 4. $FeCl_2$ crystal grown at tip of iron crystal. A small iron whisker can be seen growing from what appears to be a growth step on the $FeCl_2$ crystal. The porous appearance of the $FeCl_2$ is due to moisture absorption from the atmosphere. Photograph at 17 diameters.

The helpful discussion with Professor R. V. Coleman is appreciated, and the assistance of J. F. Breedis and M. A. Gedwill on the growth of the crystals has been valuable. This work was supported by the Air Force Office of Scientific Research.

JOURNAL OF APPLIED PHYSICS VOLUME 32, NUMBER 10 OCTOBER, 1961

Effect of Torsional Deformation on Self-Diffusion in Silver*

C. H. LEE†
Bell Telephone Laboratories, Murray Hill, New Jersey

AND

R. MADDIN
School of Metallurgy, University of Pennsylvania, Philadelphia 4, Pennsylvania

(Received March 22, 1961)

Data are presented to show that plastic deformation by torsion occuring at temperatures between 700° and 800°C enhance self-diffusion in silver single crystals. The enhancement varies linearly with surface strain rate, is larger the lower the temperature and is independent of surface strain. The results of experiments at constant stress are discussed in relation to ideas developed by Weertmann. The lifetime of point defects (assumed to be vacancies) at 800°C has been measured as about 100 sec. This permitted the calculation of the concentration of vacancies produced per unit strain.

THE effect of plastic deformation on self-diffusion in metals has been investigated very extensively in the last few years. In addition to the early work of Buffington and Cohen[1] on self-diffusion in alpha-iron under compression, we have reported previously on the effect or torsional strains on self-diffusion in silver single crystals.[2] Both groups[3] found that the enhancement of diffusivity by plastic deformation is a linear function of strain rate and that the enhancement was an inverse function of temperature. Similar results of the enhancement of diffusivity in silver by compressive strains have been reported by Forestieri and Girilfaco.[4] The recent work of Hirano and Cohen[5] on the effect of compression on self-diffusion in nickel show a similar enhancement.

On the other hand, Darby, Tomizuka, and Balluffi[6] have investigated the effect of tension and compression, on self-diffusion in silver single crystals and the effect of torsion on silver polycrystalline specimens.[7] They, however, found little or no effect under approximately the same experimental conditions as those reported in references 1, 2.

In view of the lack of agreement among the various investigators, we have extended our measurements under a variety of conditions. For example, we have twisted single crystalline specimens to various ranges of surface strain at constant strain rate and increased the number of strain rates. The results, shown in Fig. 1 and Table I, confirm the earlier findings that the enhancement is linear in strain rate and offer the additional conclusion that the enhancement is independent of strain. Secondly, measurements at constant stress were made according to a suggestion by Weertman[8] that the magnitude of the stress might be the deciding factor in observing an enhanced diffusion. Thirdly, in

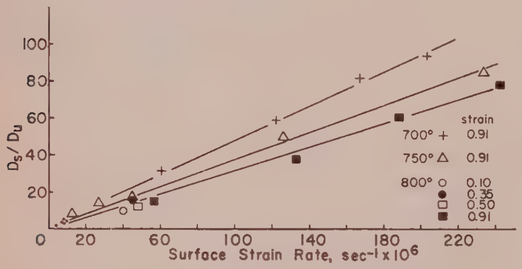

FIG. 1. D_s/D_u versus surface strain rate.

TABLE I. Constant strain rate data.

Diff. temp. °C	Surface strain %	Surface strain rate $\sec^{-1}\times10^5$	Diffusivity $\text{cm}^2/\sec\times10^{10}$	D_s/D_u
800	0	0	3.4	1
800	10	0.4	8.7	2.5
800	10	0.8	11.8	3.6
800	10	4.0	35.8	10.5
800	35	0.4	6.8	2.0
800	35	0.9	15.5	4.6
800	35	4.5	56.8	16.7
800	50	0.8	19.7	5.7
800	50	4.8	43.4	12.7
800	91	5.7	51.4	15.1
800	91	13.3	131.0	38.5
800	91	18.8	207.8	61.1
800	91	24.2	266.4	78.4
750	0	0	1.2	1
750	91	0.7	4.2	3.5
750	91	1.3	10.8	9.0
750	91	2.7	18.0	15.0
750	91	4.5	20.8	17.3
750	91	12.6	61.9	51.5
750	91	23.3	103.0	85.8
700	0	0	0.7	1
700	91	6.1	20.8	32.0
700	91	12.2	38.4	59.0
700	91	16.7	53.3	82.1
700	91	20.3	61.2	94.1

---

* Sponsored by the Atomic Energy Commission.

† Part of a thesis submitted by C. H. Lee to the faculty of the Graduate School of Arts and Sciences, University of Pennsylvania in partial fulfillment of the requirements for the Ph.D. degree.

[1] F. S. Buffington and M. Cohen, Trans. AIME **194**, 859 (1952).

[2] C. H. Lee and R. Maddin, Trans. AIME **215**, 397 (1959).

[3] N. Ujiiye, M. Cohen, and D. L. Averbach (private communication).

[4] A. F. Forestieri and L. A. Girifalco, J. Phys. Chem. Solids **19**, 99 (1959).

[5] K. Hirano and M. Cohen (private communication).

[6] J. N. Darby, Jr., C. T. Tomizuka, and R. W. Balluffi, J. Appl. Phys. **30**, 104 (1959).

[7] J. N. Darby, Jr., C. T. Tomizuka, and R. W. Balluffi, AIME Fall Meeting, Philadelphia, Pennsylvania, October, 1960.

[8] J. Weertman (private communication).

Table II. Constant stress data.

Diff. temp. °C	Stress psi	Diffusivity cm^2/sec$\times 10^{10}$	D_s/D_u
800	0	3.4	1
800	358	4.9	1.5
800	768	7.1	2.1
800	876	13.9	4.1
800	884	13.8	4.1
800	1010	15.5	4.6
800	1088	27.5	8.1
800	1130	45.9	13.5
700	0	0.7	1
700	550	1.4	2.2
700	699	2.0	3.1
700	885	3.5	5.3
700	946	3.7	5.7
700	1016	5.4	8.3
700	1048	9.1	13.9
700	1125	9.9	15.3

order to obtain a better understanding of the enhancement of diffusivity, the lifetime of the enhancement has been measured by means of a twist-rest experiment. Finally, measurements at constant strain rate were made on polycrystalline specimens to compare with the recent data of Darby, Tomizuka, and Balluffi.[7]

I. CONSTANT STRESS MEASUREMENTS

Experimental Procedure

The experimental procedure described in the earlier paper[2] has been used in the present work with the following slight modification. The torque was applied to the specimen at constant load through a pulley. The surface stress was calculated from the torque as

$$T=\int_0^r \sigma_{z\theta}2\pi r^2 dr, \qquad (1)$$

where T is the applied torque, $\sigma_{z\theta}$ the stress, and r the radius of the specimen. The stress $\sigma_{z\theta}$ may be considered as a constant stress, for the most part distributed uniformly in the specimen except for the small portion around the central axis. Equation (1) may be integrated as

$$T=\tfrac{2}{3}\pi r^3\sigma_{z\theta}$$

or

$$\sigma_{z\theta}=\tfrac{3}{2}T/\pi r^3. \qquad (2)$$

In practice, the torque or stress is kept constant for each experiment but varies from experiment to experiment to an upper limit of about 1200 psi.

Experimental Results and Discussion

The constant stress results were obtained at 800° and 700°C. Six to seven stress levels between 500 and 1200 psi were used to establish the results on the enhancement of diffusion at each temperature. The diffusion coefficients were calculated following the same procedure as for the constant strain rate experiment.[2] These data are shown in Table II. The relation between stress and enhancement is shown in Fig. 2 where D_s/D_u is the ratio of the enhanced diffusivity D_s to the unstressed diffusivity D_u.

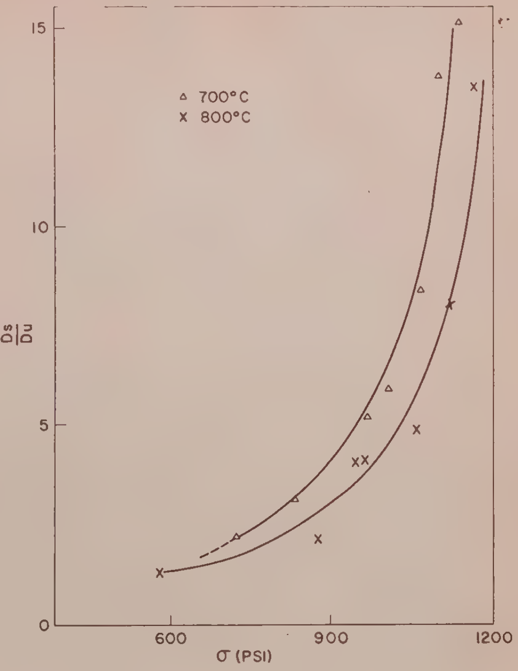

Fig. 2. D_s/D_u versus stress (σ).

Along with Nabarro,[9] Weertmann[8] suggests that, when dislocations climb during high-temperature creep, they do so either by generating lattice vacancies or by absorbing them. The thermodynamic analysis of Bardeen and Herring[10] states that the concentration of vacancies in equilibrium with dislocation line will be either

$$N_0 \exp[Fb/kT]$$

or

$$N_0 \exp[-Fb/kT],$$

where N_0 is the equilibrium concentration of vacancies in an unstrained lattice, F is the force per atomic length of dislocation line exerted normal to slip plane, b is the length of the Burger's vector, k is the Boltzmann constant, and T is the absolute temperature. What occurs depends on whether the force F tends to push the dislocation line in the direction which creates vacancies or in that which absorbs them. In any crystal strained at a high temperature, half the dislocations climb by giving off vacancies and half by absorbing them. Assuming that dislocations are the major vacancy sources and sinks, the average vacancy concentration throughout such a crystal is proportional to a term of the type

---

[9] F. R. N. Nabarro, Proc. Phys. Soc. (London) 47, (1947).

[10] J. Bardeen and C. Herring, Trans. Am. Soc. Metals **49**, 87 (1957).

$$N_\sigma=\tfrac{1}{2}N_0[\exp(Fb/kT)+\exp(-Fb/kT)], \tag{3}$$

where F is now some suitable average force exerted normal to a dislocation line and is adjusted to take account of the fact that the dislocation line may not be purely edge in character. For small deforming stresses, the number of vacancies is equal to that characteristically present at thermal equilibrium. Only when large stresses are employed does the equation give an over-all excess vacancy concentration which hence is available to enhance the rate of diffusion.

The plot of N_σ/N_0 versus Fb/kT resulting from the above equation is shown in Fig. 3. This curve exhibits the same shape as the experimental curve of D_s/D_u versus σ in Fig. 2; however, for a given value of N_σ/N_0, the stress calculated from the present experimental conditions is on the order of 10^{+3} less than the force F calculated from the equation. This disagreement may be qualitatively explained as follows: Weertman's calculation is based on thermodynamic equilibrium. When a stress is applied to the specimen, it affects the total number of vacancies. In this case, the total number of vacancies N_v may be expressed as

$$N_v=N_0+N(\sigma)+N(\epsilon), \tag{4}$$

where N_0 is thermal equilibrium number of vacancies, $N(\epsilon)$ the number of vacancies produced by the strain, and $N(\sigma)$ is the contribution suggested by the Weertman analysis. Calculation shows that, in this investigation, the effect of $N(\sigma)$ is minor. (Say $\sigma=1000$ psi$\times 7\times 10^{7}$ d/cm^2, $b=3\times 10^{-8}$ cm, $F=\sigma b^2=7\times 10^{-8}$ d, $k=1.4\times 10^{-16}$ ergs/deg, and $Fb/kT\approx 10^{-2}$ so that $N_\sigma/N_0=\frac{1}{2}[\exp(Fb/kT)+\exp(-Fb/kT)]\approx 1$.

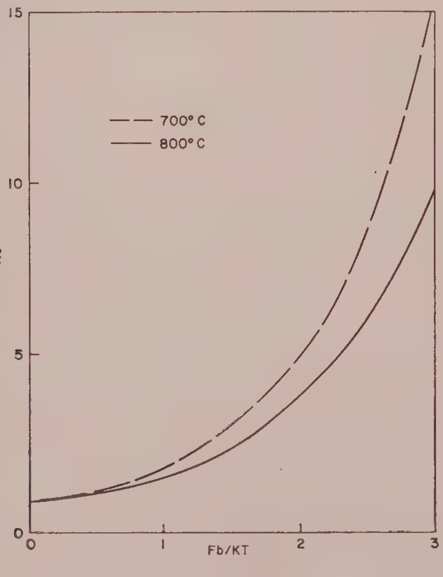

FIG. 3. N_σ/N_0 versus Fb/kT.

One may see from Eq. (3) that when the stress is not large enough to produce a considerable strain both $N(\epsilon)$ and $N(\sigma)$ are small; therefore the diffusion is the normal D_u. If the stress is large enough to deform the specimen, however, $N(\epsilon)$ will be greatly increased, but $N(\sigma)$ will not change significantly. In the latter case enhanced diffusion can be achieved since the total number of vacancies is increased.

It may then be concluded that the enhanced diffusion by plastic deformation is mainly due to the rate of straining, and appears not to be a function of stress or total strain. According to the thermodynamic calculation described above, the part of the enhanced diffusion due to stress is almost certainly too small to be detected by the present techniques.

II. REST-TIME EXPERIMENTS

Theoretical Analysis

Since diffusivity is directly proportional to the number of defects in the metal, the enhancement of diffusion during the plastic deformation is related to the nonequilibrium number of defects thus produced. It is also generally understood that the nonequilibrium number of defects decays when their production rate is small in comparison with their rate of decay. Therefore, enhanced diffusivity starts to decrease when plastic deformation stops. The enhancement of the diffusion coefficient decreases gradually at a rate which is proportional to the annihilation rate of the nonequilibrium defects. Based on these physical arguments, theoretical and experimental treatments have been established to determine the decay factor, or the lifetime of the new equilibrium number of defects induced by plastic deformation based upon enhanced diffusivity, nonenhanced diffusivity, and "partially" enhanced diffusivity.

Consider the schematic diagram shown in Fig. 4. If a specimen is twisted at a high temperature for a length of time t_s after which it is permitted to rest at this temperature for a length of time t_r, the diffusion coefficient measured will be D_s if the lifetime of defect generated by the deformation is infinite. If, however, the lifetime of the defect is zero, the diffusion coefficient will be D_u. On the other hand, for a finite lifetime of the defect a decay rate will result in a measured diffusion coefficient D_i. Assuming a simple rate of decay, the diffusion coefficient after a certain rest time t_r following a twist for time t_s will be given by

$$D_i=(D_s-D_u)\exp(-t_r/\tau)+D_u, \tag{5}$$

where τ is the average lifetime of the defects.

We treat the problem as if D_i remained constant at D_s and find the time factor t_e which would yield the same diffusion as the actual rest time t_r does on D_i. Thus t_e is defined as the effective rest time. Since the product of the diffusion coefficient and time may be used as a quantity to measure the amount of diffusion, the diffusion quantity in the transient period of time t_r may be expressed as

$$\int_0^{t_r} D_i dt_r.$$

By definition of t_e, we then may write

$$\int_0^{t_e} D_s dt_r = \int_0^{t_r} D_i dl_r. \qquad (6)$$

Equation (6) may be integrated if the value of D_i in Eq. (5) is substituted into the equation

$$D_s t_e = \int_0^{t_r} (D_s - D_u)\exp(-t_r/\tau)dt_r + \int_0^{t_r} D_u dt_r$$

and

$$t_e = \frac{D_s - D_u}{D_s}\tau[1-\exp(-t_r/\tau)] + \frac{D_u}{D_s}t_r. \qquad (7)$$

Although "partially" enhanced diffusion takes place with coefficients D_s, D_i, and/or D_u according to the applied conditions, these coefficients are not separable in one experiment. In order to calculate τ from Eq. (7), D_s and D_u must be determined from individual experiments. The average diffusion coefficient D from the "partially" enhanced diffusion experiment is used in determining t_e. In establishing D, the experiment must be performed using the same straining conditions as were used for D_s in the first period of diffusion (t_s), and with a period of rest time (t_r), at the same diffusion temperature. With a total diffusion time equal to the sum of t_s and t_r, the diffusion quantity of the experiment will be $D(t_s+t_r)$. This quantity may also be expressed in terms of D_s, giving $D_s(t_s+t_e)$, where D_s may be obtained from another experiment. From the equality of these two expressions of one quantity, t_e may therefore be obtained, that is

$$t_e = (D/D_s)(t_s+t_r) - t_s. \qquad (8)$$

Examining Eq. (7), we find that D_s, D_u, t_r, and t_e are all experimentally determinable quantities. The average lifetime of defects τ thus can be calculated from that equation.

For the "rest-time" experiment, the specimens were prepared by using the same procedure as mentioned previously. The diffusion anneal, with simultaneous deformation at a strain rate of 4.2×10^{-5}/sec to a total surface strain of 0.1, was performed in exactly the same manner as previously described in determining D_s until "rest" began. Thereafter the specimens were held at the same temperature for various periods of time, 300, 600, and 1200 sec, designated as "rest time" t_r. Three experiments were performed for each t_r. Diffusion annealing was completed at the end of the "rest period." The specimens were then taken out of the furnace and air cooled. Sectioning of the specimens, counting radioactivity, and calculating D values followed the standard procedure as described in the early paper.[2] Three D values were obtained for each "rest time." Using all the $D(t_s+t_r)$ quantities and the strained diffusion coefficient D_s, the values of the corresponding effective rest times t_e were calculated according to Eq. (8). The τ values were obtained from Eq. (7), since all the necessary information was available. The results of τ, t_e, and the corresponding t_r are listed in Table III.

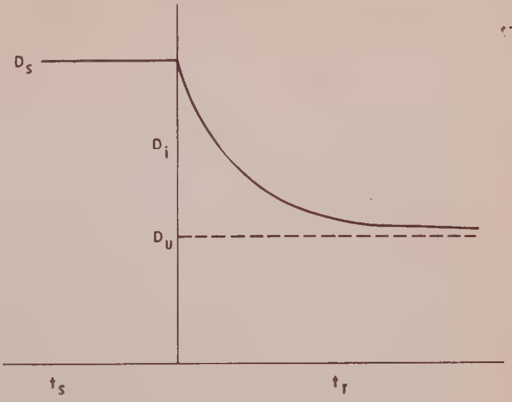

FIG. 4. "Rest time" experiments.

As shown in Table III, a rest time of 300 sec gave an average lifetime of defects as 58 sec. For a rest time of 600 sec an average τ value of 193 sec was obtained. When the rest time was raised to 1200 sec, τ increased to 202 sec. Although the error in determining τ was great, there is a tendency for τ to increase very rapidly in the first 600 sec and very slowly thereafter approaching as asymtotic value of about 200 sec.

Assuming that the predominate defect sink is a dislocation line, Dienes[11] as well as Girifalco and Grimes[12] have given an expression for the decay factor

TABLE III. Values of rest time, effective rest time, and average lifetime of point defects.

Rest time t_r (sec)	Eff. rest time t_e (sec)	Lifetime (sec)
300	35	40
300	23	43
300	113	92
600	329	299
600	204	160
600	171	120
1200	217	108
1200	460	377
1200	229	121

---

[11] G. J. Dienes, *Proceedings of the Second United Nations International Conference on the Peaceful Uses of Atomic Energy* (United Nations, Geneva, 1958).

[12] L. A. Girifalco and H. H. Grimes, NASA TN 4408.

of defects (in their case, vacancies) as

$$1/\tau=2\pi D_v N_d/\ln(r_i/r_0),$$

where τ is the average lifetime of vacancies, D_v is the diffusion coefficient for vacancies in the metal, N_d the number of dislocation lines per square centimeter, and r the effective radius of a cylindrical line of dislocations. According to Girifalco and Grimes' approximation $1/\tau$ should be in the range of 1 to 10^{-2}. Consequently, vacancies must have an average lifetime from 1 to 100 sec. This is in agreement with the present experimental results for the lifetime of defects generated by plastic deformation.

At present, there is no literature available for comparison with these experimental data and the theoretical analysis. Thus, we may tentatively conclude that the lifetime of the defects (which we assume to be vacancies) at the present experimental condition is of the order of 100 sec, a value which varies slightly with the decay of dislocations. It has however been pointed out by D. Wilsdorf[13] that the annihilation of dislocations during the rest time t_r may contribute vacancies in the same manner produced by the movement of dislocations during creep. Consequently, there is both a decay and a build up of vacancies occurring simultaneously. This idea lends itself to possible experimental confirmation.

It should be pointed out that the derivation of the theory assumes a first-order decay of the vacancy concentration. A second or higher order decay rate of vacancies may not be detectable by the diffusion experiments.

The analysis of Cohen[14] suggests that the total concentration of vacancies (those in thermal equilibrium and those produced by deformation) at steady state is equal to the concentration of vacancies produced and those annihilated at sinks, i.e.,

$$dN_\sigma=\eta\dot{\epsilon}dt-(N_\sigma/\tau)dt, \tag{9}$$

where η is the concentration of vacancies produced per unit strain, $\dot{\epsilon}$ is the strain rate, and τ is the time. At steady state this should equal

$$N_\sigma=\eta\dot{\epsilon}\tau. \tag{10}$$

N_σ may be determined from the slope D_s/D_u versus $\dot{\epsilon}$, $\dot{\epsilon}$ is known, and using 200 sec for τ, η turns out as about 10^{-3}. A value of $\eta=10^{-3}$ per unit strain is not unreasonable in view of the theoretical estimates of $\eta=10^{-4}\epsilon-10^{-5}\,\epsilon$.[13]

The number of jumps made by a vacancy during a lifetime of 200 sec is calculated as 10^{12}–10^{13}. The average path traveled would then be $S=b/n$ and taking b as 2.5 A, S is about $\frac{1}{2}$ mm. We can suggest no reason at the present time to explain this unusually high number of jumps or large mean distance traveled except to say that the normal traps for vacancies may not be too effective at the high temperatures.[15]

TABLE IV. Measurements of enhanced diffusivity in polycrystalline specimens.[a]

Diff. temp. °C	Surf. strain %	Strain rate $\text{sec}^{-1}\times10^5$	Diffusivity $\text{cm}^2/\text{sec}\times10^{10}$	D_s/D_u
700	91	9.5	6.9	10.6
700	91	10.0	8.5	13.1
700	91	9.8	5.4	8.3
800	91	9.5	...	6.5[b]
800	91	10.0	...	8.2[b]
800	91	9.8	...	5.4[b]

[a] Grain size, $\frac{1}{10}$ to $\frac{1}{2}$ mm in diameter.
[b] Extrapolated values.

Consideration of the Darby, Tomizuka, and Balluffi Experiment

In view of the lack of agreement of our results and others with those of Darby, Tomizuka, and Balluffi[7] and considering that their results in torsion were obtained on polycrystalline samples, three polycrystalline specimens were prepared from cold-worked silver rods having the same purity as that of the single crystalline specimens. The silver rods were first recrystallized at 400°, 600°, and 800°C for about an hour; the resulting grain size varied from $\frac{1}{10}$ to $\frac{1}{2}$ mm in diameter. The preparation of these specimens followed the exact procedure as described in the early paper. In order to maintain the above grain sizes, stress relief annealing treatments of the specimens, after machining, were conducted at a temperature somewhat less than 400°C. The diffusion annealing of specimens having the three grain sizes was performed at 700°C. They were simultaneously annealed and deformed at a constant strain rate of about 10×10^{-5}/sec to a total surface strain of 91%. Specimens were then analyzed in the usual manner, and diffusion coefficients were calculated. The results of these three tests and three extrapolated values from the 800°C curve of Fig. 4 in the early paper are tabulated in Table IV. This extrapolation was made by taking the same ratio from the 800°C curve as that of the determined value to the value from 700°C curve in the same figure. One can see from Table IV that the enhancement of diffusion in polycrystals under these conditions is about 4 or 5 times smaller than that for single crystals.

This may be qualitatively explained by assuming that the grain boundaries are effective traps for vacancies. The excess number of vacancies produced in polycrystals may be less than that in single crystals, and hence, less enhanced diffusion results. In addition, the deformation of polycrystals takes place mostly by gliding along grain boundaries. Grains themselves may thus be insufficiently deformed resulting in a smaller number of excess vacancies. This may be another reason why the diffusivities in polycrystalline specimens are less enhanced by plastic deformation than in single crystals.

---

[13] D. Wilsdorf (private communication).
[14] M. Cohen (private communication).
[15] D. Wilsdorf, R. Maddin, and H. Wilsdorf, Trans. Am. Soc. Metals 53, (1961).

Note added in proof. Since submitting the above manuscript, L. M. Shestopalov and Yu. P. Romashkin [Soviet Physics—Solid State **2** (12), 2664 (1961)] have reported the enhancement of diffusion of silver in plastically deformed copper. The deformation used by them was compression under constant stress (creep) where the creep velocity operated from zero to 2000%/hr at 600°C and a constant deformation at 50%. They report an enhancement linear with strain rate up to a D_s/D_u of 24 in polycrystalline copper.

ACKNOWLEDGMENTS

The authors are grateful to Professor J. N. Hobstetter for his help and suggestion in the development of the "rest-time" experiment. They also wish to thank Professor D. Kuhlmann-Wilsdorf for many helpful discussions.

JOURNAL OF APPLIED PHYSICS VOLUME 32, NUMBER 10 OCTOBER, 1961

Curie Temperature of Some Garnets by the Differential Thermal Analysis Technique*

A. Aharoni, E. H. Frei, Z. Scheidlinger, and M. Schieber
Department of Electronics, The Weizmann Institute of Science, Rehovoth, Israel

(Received April 3, 1961)

The differential thermal analysis (DTA) technique is used to measure the Curie temperature of yttrium iron garnets, and of the garnets obtained by partially substituting Sm, Nd, Pr, or La for the Y. The accuracy of the method is within about 1°C. It is found that in all the above substitutions the Curie point is increased more or less linearily in the rare-earth contents, with the largest slope for Pr, somewhat less for Nd and Sm. For La, only the compound $Y_{2.5}La_{0.5}Fe_5O_{12}$ could be prepared and it did not show any measurable change from the Curie point of pure yttrium iron garnet. Two possible explanation are suggested to the increase in Curie point by Sm substitution, which does not change the magnetization of the garnet.

I. INTRODUCTION

THE magnetic moments of yttrium iron garnets (YIG) substituted by Sm, Nd, Pr, and La were recently studied.[1–3] It was found[3] that the magnetic moment of YIG is increased by substitutions of Nd and Pr and it remains practically unchanged in the case of substitutions by Sm or La. The Curie points of these garnets showed some small and irregular increase with the substitutions of Y by the magnetic ions of Sm, Nd, or Pr but the poor accuracy of the method of measurements did not suffice for conclusive determination of the difference in Curie points.

As an alternative method, the differential thermal analysis (DTA) was undertaken. Fairly good results were reported by this method,[4] which utilizes the change in the specific heat at the Curie temperature[5] as a second-order transition point. This is done by plotting the difference of temperature increases between a magnetic and inert (nonmagnetic) material, as a function of the temperature, when both materials are heated in the same oven, under similar conditions.

In Sec. II the DTA technique is described and its application to the measuring of Curie points of the several substituted YIG is described. In Sec. III the results of the measurements are given and discussed.

II. EXPERIMENTAL SETUP

The DTA experimental setup is shown in Fig. 1. It consists of an oven (O), a ceramic muffle (M), two ceramics rods (R) with several openings and slits in the axial direction, and two stainless steel holders (H) containing the magnetic and inert powdered materials.

The (Δt) thermocouples were platinum-platinum 13% rhodium wires, which ensured high chemical stability, thus avoiding any spurious voltages. They are connected in antiseries so as to measure the difference in temperature between inert and magnetic powders. The (t) thermocouple is of the iron Constantan type which has a better temperature resolution. It measures the temperature of the sample.

The output of the (t) thermocouple is connected directly to the X input of the X-Y recorder (Autograph model 3) in series with a fixed voltage, which serves as a zero shift and enables the recording of the 12 to 17-mv voltage range (which is the range of the measured Curie points) on the most sensitive scale of the recorder (5-mv full scale).

---

* Part of a Ph.D. thesis by M. Schieber, to be submitted to the Hebrew University, Jerusalem.

[1] G. Goldring, M. Schieber, and Z. Vager, J. Appl. Phys. **31**, 2057 (1960).

[2] M. Schieber, Bull. Research Council Israel **9A**, 37 (1960).

[3] A. Aharoni and M. Schieber, J. Phys. Chem. Solids **19**, 304 (1961).

[4] S. L. Blum, A. E. Palladiono, and L. G. Rubin, Bull. Am. Ceram. Soc. **36**, 175 (1957).

[5] R. M. Bozorth, *Ferromagnetism* (D. Van Nostrand Company, Inc., Princeton, New Jersey, 1951), p. 735.

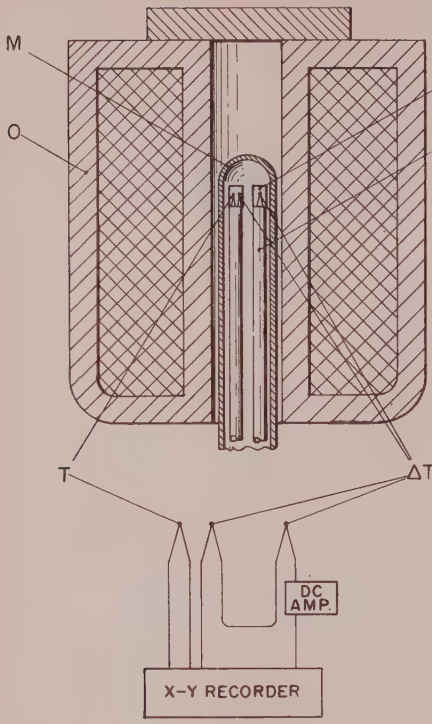

FIG. 1. Schematic view of DTA apparatus. (See text for description).

The output of the differential thermocouple (Δt) is connected to a sensitive dc amplifier.

The diagram of this amplifier is shown in Fig. 2. In the input circuit a dc shift network is included to compensate the emf caused by different thermal conductivity between the investigated and inert material. This network also compensates the inaccuracies in positioning of the holders in the oven. The input voltage is fed to the contacts 1, 2, and 3 of a chopper (Stevens Arnold 60-cps chopper with doubling). The chopper coil frequency is different from the 50-cps mains frequency and calls for a special source (60 cps, 6.3 v, 180 ma). This frequency was chosen in order to reduce the mains pickup.

The input transformer of the toroidal kind also enhances freedom from mains pickup. It is triply screened with a double mumetal shield which offers some 20 db advantage over an ordinary shell-type transformer.

The first stage is an EF91 because of its low microphonic effect. The second stage (the EF-86) provides most of the amplification. In the anode circuit of this tube, besides the 100-kΩ resistor, there is a highly selective twin-T network which cuts off the 120 cps. All other frequencies are amplified by one-half of the 6AX7 triode and fed the cathode and suppressor grid of the input tube. They provide a negative feedback voltage and assure sinusoidal output from the anode of the first tube. The second EF-86 tube is the output stage. The output of the amplifier is shunted by a condenser to further reduce noise.

The maximum sensitivity of this amplifier, working in series with an Autograph model 3 X-Y recorder, is 1μv/in., with a signal to noise ratio of 20 db in the frequency range from zero to 5 cps.

The detecting contacts of the chopper (5, 6, and 7) are connected in such a way that the output voltage is to a great extent independent of the swell time of the chopper.[6]

The oven was heated by direct current, to reduce direct pickup, at a rate of about 10°C/min in the vicinity of the expected Curie temperature.

The diameter of the cylindrical sample holder H (Fig. 1) was 5 mm and its height 10 mm. About 200 mg of the material under study were used in it, and about the same amount if inert material was used in each of the two similar holders. The "inert" material was in most cases YIG and in this way the difference in the transition points could be more accurately measured.

When the temperature reached about 150°C, the input circuit balanced by means of resistor R_7 (Fig. 2) and the recording was started. Preliminary runs determined the right setting of the sensitivity of the X-Y recorder. A run takes about 20 min. The discontinuity points were measured after the run by disconnecting the thermocouple and bringing the pointer back to the marked point by means of a voltage from a precision potentiometer. In a way of calibration, Curie temperature was read as the difference from that of yttrium iron garnet taken as[7] 272.5°C. The reproducibility in different runs was within $\pm\frac{1}{2}$°C.

The garnets used in these experiments were prepared by the method described before.[1–3] Prior to DTA measurements they were checked by x ray for purity of phase and by the pondermotive method for their magnetic moments, then ground and sieved.

III. RESULTS AND DISCUSSION

Figure 3 summarizes the results for the Curie points of $Y_{3(1-x)}M_{3x}Fe_5O_{12}$ with M standing for Sm, Pr, Nd, and La. It is seen that the Curie point increases rather linearily with x. This increase from 272.5°C for pure YIG reaches 289°C in SmIG, 284°C in $YNd_2Fe_5O_{12}$, and 280°C for $Y_2PrFe_5O_{12}$. The Curie point of $Y_{2.5}La_{0.5}Fe_5O_{12}$ is about 273°C.

The difference in the Curie points between SmIG and YIG, as determined in this work, was found to be $289-272.5=16.5$°C. This difference agrees with that of the respective Curie points reported by Pauthenet,[8] i.e., $305-287=18$°C.

The increase of the Curie temperature by successive additions of the magnetic ions to the rare-earth side of YIG can be explained by an increased magnetic interaction in these materials. However, it is of interest to note that there is a change in the Curie temperature of Sm as a function of concentration although there is hardly any change in the magnetization at room temperature. A possible explanation of this[9] is as follows. It has been pointed out[10] that the increase in magnetization of neodymium follows from the electronic configuration of the neodymium ion. In the first half of the f shell L and S are antiparallel, and J, as well as the magnetic moment, antiparallel to S, and therefore parallel to the iron magnetization. Using this criterion it is obvious that Sm^{3+} is an exception in that the ground state $^6H_{\frac{5}{2}}$ implies that the magnetic moment $M=-gJ\beta J$ is nearly four times smaller than that found for Nd^{3+} or Pr^{3+}. This occurs because of the virtual cancellation of the orbital and spin contribution to the resultant magnetic moment. Nevertheless, a change in the Curie temperature as a function of the concentration is to be expected. At 500°K the next $J=\frac{7}{2}$ at about 1000 cm^{-1} is already fairly populated and may contribute somewhat to the net magnetic moment. Indeed it is well known from paramagnetic resonance data that there is a considerable admixture of $J=\frac{7}{2}$ state by the crystal field to the ground state because of the proximity of the $j=\frac{7}{2}$ level.[11] This is similar to the explanation[12] given to the unusual temperature behavior[13] of Sm^{3+} in paramagnetic compounds.

---

[6] F. Offner, Electronics **33**, No. 7, 55 (1960).

[7] S. S. Geller and M. A. Gilleo, Acta Cryst. **10**, 239 (1957).

[8] R. Pauthenet, thesis, Université de Grenoble, Grenoble, France, 1957.

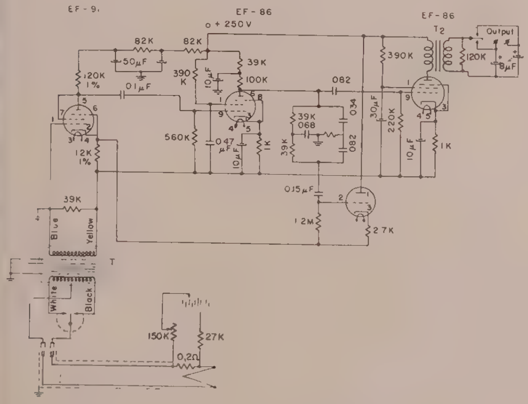

FIG. 2. The dc amplifier.

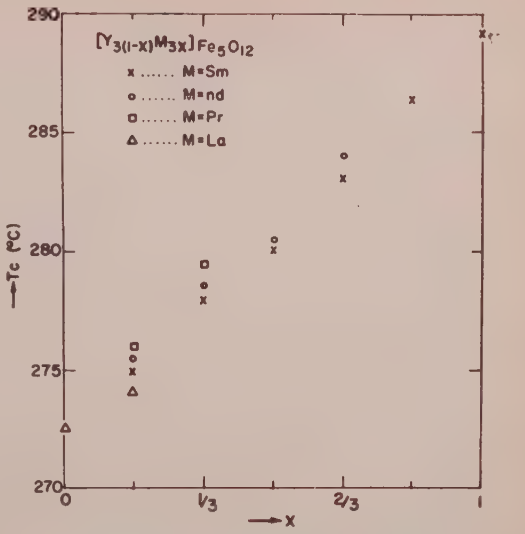

FIG. 3. The Curie points of YIG plotted against the amount of rare-earth substitution for yttrium.

Professor C. Kittel has pointed out[14] that the change in Curie points from that of YIG might be due to the change in unit cell dimensions,[15] which modifies the very short range exchange interaction between the irons. This can be seen from the change of Curie point[16] with hydrostatic pressure. However, this cannot fully explain our data, since in Fig. 3 there is a considerable difference between $x=\frac{1}{6}$ for La and $x=\frac{1}{3}$ for Sm, whereas the lattice constant for these two components[15] is practically the same. The difference might be due to somewhat different structures, since it is known that angles can change with substituent,[17] and that the angles between iron ions, through the oxygen, are important in determining the strength of exchange interaction.[18]

ACKNOWLEDGMENTS

We are very grateful to Professor W. Low and Professor C. Kittel for helpful discussions on the theoretical aspects. We wish also to thank J. Shopen and Y. Cohen for their help in executing this work.

---

[9] W. Low (private communication).

[10] R. L. White, J. Appl. Phys. **32**, 1178 (1961); S. S. Geller, H. J. Williams, and R. C. Sherwood, Bull. Am. Phys. Soc. **6**, 230 (1961); P. W. Wolf, J. Appl. Phys. **32**, 742 (1961).

[11] W. Low, *Paramagnetic Resonance in Solids* (Academic Press, Inc., New York, 1960).

[12] J. H. Van Vleck, *Electric and Magnetic Susceptibilities* (Oxford University Press, New York, 1932), p. 253.

[13] P. W. Selwood, *Magnetochemistry* (Interscience Publishers, Inc., New York, 1956), 2nd ed., pp. 140–157.

[14] C. Kittel (private communication).

[15] M. Schieber and Z. H. Kalman, Acta Cryst. (to be published); J. R. Cunningham, Jr., and E. E. Anderson, J. Appl. Phys. **31**, 45S (1960).

[16] K. Werner, Ann. Phys. (Liepzig) Folge 7, **2**, 403 (1959).

[17] S. C. Abrahams and S. Geller, Acta Cryst. **11**, 437 (1958).

[18] For a review see S. Geller, J. Appl. Phys. **31**, 30S (1960).

JOURNAL OF APPLIED PHYSICS VOLUME 32, NUMBER 10 OCTOBER, 1961

Paramagnetic Resonance of Defects Introduced Near the Surface of Solids by Mechanical Damage

G. K. WALTERS AND T. L. ESTLE
Central Research Laboratories, Texas Instruments Incorporated, Dallas, Texas

(Received April 13, 1961)

Electron spin resonance characteristics of a number of materials subjected to violent mechanical treatment are reported. A line with $g=2.0055$ observed in silicon is attributed to defects introduced near the surface by mechanical damage. The resonance properties are uninfluenced by interactions of the silicon surface with atmospheric gases. Similar lines appear in germanium, silicon carbide, and diamond. The dominant line produced by mechanical damage to MgO is attributed to F centers. Similar lines are observed in other II-VI compounds. Results are also reported for a number of other materials. Similarity between defects produced mechanically and by fast neutrons is noted.

I. INTRODUCTION

THE physical nature of a solid surface is determined to a great extent by mechanical processes involved in surface preparation. If a surface is mechanically damaged as by cutting, abrading, sandblasting, or pulverizing, there may result a surface layer of considerable depth (typically several microns) which has physical and chemical properties quite different from those of the bulk material.[1] In particular, such damage to a semiconductor often causes drastic changes in the electrical behavior of the surface region. Measurements of such properties as surface electrical conductivity, field effect mobility, and surface recombination velocity as a function of surface mechanical treatment have been reported for a number of semiconductors.[1] However, very little is known about the effect of mechanical damage on the magnetic properties of the surface region.

In the course of early experiments on n-type silicon, Fletcher *et al.*[2] observed an electron spin resonance line which they attributed to the sample surface. Feher[3] has reported some of the properties of this resonance line. He found that the line appears when the sample surface is mechanically damaged, and it disappears upon removal of about 10^{-4} cm of the silicon by etching. Chemical treatments which act only to remove, produce, or otherwise alter the surface film have no effect on the resonance characteristics. For silicon wafers sandblasted with 600-mesh SiC, Feher found that the line at 1.25°K and 9 Gc/sec is homogeneously broadened, has a g value of 2.0061 ± 0.0002, a spin-lattice relaxation time of 10^{-5} sec, and a linewidth of 6 oe. He reports the surface density of paramagnetic centers as 3×10^{14} per cm^2. The same resonance line is observed in both n- and p-type silicon.

Further study of this resonance line was undertaken by the authors in the hope that electron paramagnetic resonance might prove to be a useful technique in the study of solid surfaces, in particular, semiconductor surfaces.[4] Our objectives were to determine the nature of the paramagnetic centers introduced by mechanical damage, and to determine the effects of ambient atmospheres on the resonance characteristics of the centers. Besides silicon, resonance studies were made on a number of other group IV semiconductors, on II-VI compounds, and on some other materials.

Perhaps the most striking aspect of our results is the fact that in a large fraction of the materials investigated, mechanical damage produced new paramagnetic centers. In some cases, the paramagnetism results from the production of defects during the damage process, and in others it is possibly due to damage-induced charge transfer among impurities and defects. These findings indicate that paramagnetic centers resulting from mechanical damage are of common occurrence in insulators and semiconductors. The density of such centers can be very high.

II. EXPERIMENTAL APPARATUS AND TECHNIQUES

A. Magnetic Resonance

Most of the electron paramagnetic resonance measurements were performed at a frequency of about 9300 Mc/sec. The spectrometer employed balanced-mixer barretter detection. The magnetic field was modulated at 165 cps, and signal detection was phase sensitive. Spin-lattice relaxation times T_1 were measured by the cw saturation technique.[5] Experiments were conducted over a temperature range from 1.3°K to room temperature. For measurements at low temperatures, the microwave cavity was suspended in a Dewar system. Samples could be introduced into the cavity through the top of the cryostat; an air lock[6] facilitated changing of samples when the cryostat was operating under reduced pressure. This arrangement allowed us to make measurements on several samples at temperatures as low as 1.3°K with a single transfer of liquid helium to the cryostat.

---

[1] T. M. Buck in *The Surface Chemistry of Metals and Semiconductors*, edited by H. C. Gatos (John Wiley & Sons, Inc., New York, 1960), p. 107.

[2] R. C. Fletcher, W. A. Yager, G. L. Pearson, A. N. Holden, W. T. Read, and F. R. Merritt, Phys. Rev. **94**, 1392 (1954).

[3] G. Feher, Phys. Rev. **114**, 1219 (1959).

[4] G. K. Walters, J. Phys. Chem. Solids **14**, 43 (1960).

[5] For a comprehensive discussion of magnetic resonance see D. J. E. Ingram, *Spectroscopy at Radio and Microwave Frequencies* (Butterworths Scientific Publications, Ltd., London, 1955).

[6] T. L. Estle and G. K. Walters (to be published).

The concentrations of paramagnetic centers were estimated by comparison of the resonance signal strength from the samples with that from a known quantity of $CuSO_4 \cdot 5H_2O$. The temperature dependence of sample susceptibility was determined by comparing signal strengths of the sample and copper sulfate as a function of temperature, assuming the susceptibility of copper sulfate to be proportional to $1/T$. Since there was some doubt as to the validity of this assumption at the lowest temperatures, it was checked by making an absolute comparison of signal intensities over the liquid helium temperature range. Within the accuracy of measurement ($\approx 10\%$), the assumption was justified.

The g values were measured by three different techniques. For room temperature determinations, a proton resonance probe mounted on the side of the microwave cavity was used to measure the magnetic field strength. At low temperatures, the magnetic field was determined from the nuclear resonance frequency of a small quantity of liquid He^3 in which the sample was immersed. The use of this technique required that the rf coil used for excitation of the He^3 nuclei be situated inside the microwave cavity. For this purpose, a special cylindrical cavity was constructed with a small coil mounted on the cavity axis. The cavity was excited in the TM_{110} mode. This technique for g-value determination at low temperatures proved to be exceptionally accurate since sample and He^3 are intimately mixed with one another and therefore see exactly the same magnetic field. In the techniques described above, microwave and radio frequencies were measured with a Hewlett-Packard type 524 frequency counter and type 540A transfer oscillator. In a third method for measuring g values, the two hyperfine lines from phosphorus-doped silicon served as magnetic field markers, allowing an accurate estimate to be made of the resonance magnetic field strength.

B. Sample Preparation

The majority of the samples investigated were single crystals which were reduced to powders by violent agitation in room air at 20 cps in a Spex Industries model 8000 Mixer-Mill. Thirty minutes of agitation was sufficient to reduce silicon to an average particle size of about 1 μ, as determined by examination with an optical microscope. The paramagnetic resonance properties of materials used in sample preparation were carefully studied in both bulk and pulverized forms. By suitable choice of the containers and grinding balls used in sample powdering, it was found possible in most cases to eliminate interference of spurious resonances arising from the small chips of container and ball which always contaminated the samples. Brass sample containers and "Arlcite" ceramic[7] or steel grinding balls proved to be the most satisfactory combination, but Pyrex, quartz, and plastic balls and containers were employed on occasion.

Samples which were powdered in vacuum or in specific ambient atmospheres were sealed with polystyrene balls in small Pyrex containers. Powdering was accomplished with a Spex Industries model 3140 amalgamator. The powder could be tapped into a side tube small enough to insert into the microwave cavity. In this manner, samples could first be studied in vacuum or while exposed to specific ambients, then again later after exposure to room air (accomplished by breaking the side tube).

Silicon platelets were studied in some of the experiments. They were prepared by first etching in CP-4, then lapping with 600-mesh SiC.

III. EXPERIMENTAL RESULTS

A. Silicon

When the silicon surface is disturbed mechanically, as by lapping or pulverizing, there results a single electron spin resonance line with a g value of approximately 2. No other resonance lines could be detected at a frequency of 9.3 Gc/sec for fields below 9.5 koe. Sensitivity was sufficient to establish that there is no resolved, or partially resolved, hyperfine structure due to the 4.7% abundant Si^{29} isotope. The resonance properties are stable in time for periods of the order of a year, the approximate duration of these experiments.

We can distinguish no significant differences between the resonance behavior of lapped single crystals and that of powders obtained by pulverizing. The resonance at 9.3 Gc/sec is typically 7- to 8-oe wide, and it is intermediate between Gaussian and Lorentzian in shape. Powdered silicon studied at 18.5 Gc/sec exhibits a Gaussian-shaped line with a width of 13 oe. Thus, it would appear that the line is predominately inhomogeneously broadened[8] at 18.5 Gc/sec, while at 9.3 Gc/sec there are both homogeneous and inhomogeneous contributions to the linewidth.

Most of our measurements were made on powdered silicon prepared in room air as described in Sec. II. The density of centers in silicon powdered to about 1-μ average particle size varied between 1×10^{18} and 5×10^{18} per gram, depending on the purity of the starting material and the exact conditions under which it was powdered. For all samples, the spin susceptibility was found to be inversely proportional to temperature between 1.3° and 300°K.

The g value for the silicon damage line is 2.0055 ± 0.0002. We feel that the quoted uncertainty in g value represents a real variation from sample to sample in position of the center of the resonance line. The line is easily saturated with low microwave power levels at 1.3°K. Assuming the spin-spin relaxation time T_2 is approximately equal to $(\gamma \Delta H)^{-1}$ at 9.3 Gc/sec, the values of the spin-lattice relaxation time T_1 lie in the range 3×10^{-2} to 3×10^{-4} sec. There appears to be some systematic variation in T_1 with exact sample treatment, but the study of such effects was not attempted because of large variations observed in T_1 for samples receiving nominally the same treatment.

---

[7] Manufactured by the Patterson Foundary and Machine Company, Houston, Texas.

[8] A. M. Portis, Phys. Rev. **91**, 1071 (1953).

One of the primary objectives of this work was to determine what role, if any, is played by ambient atmospheres in the formation of the damage centers in silicon. In view of the high affinity which the clean silicon surface has for certain atmospheric gases, we thought it possible that the paramagnetic centers were complexes formed by chemical interaction between the silicon and an atmospheric gas. To investigate this possibility, silicon samples were pulverized in vacuum and in the presence of various specific ambients.

It was found that the resonance characteristics of damaged silicon are in no way influenced by interactions with ambient atmospheres. Silicon powdered in vacuum shows exactly the same resonance behavior before and after exposure to room air, and that behavior is the same as for silicon powdered in oxygen or in air. A search for O^{17} hyperfine structure from a sample powdered in oxygen enriched to 4% O^{17} yielded a negative result.[9]

On several occasions, the pulverizing process was carried out in the microwave cavity at a temperature of 1.3°K; the sample resonance spectrum was studied *in situ* without allowing any sample warming to occur. In each case, the resonance line arising from mechanical damage appeared instantly upon pulverizing; the density, linewidth, and g value of damage-induced paramagnetic centers did not change appreciably upon warming the sample to room temperature and exposing it to air.[10]

The invariance of the resonance properties with different ambients, together with the fact that a layer of silicon about 10^{-4} cm thick must be removed to render the resonance line unobservable, indicates that the paramagnetic centers introduced in silicon by mechanical damage are not at the silicon surface, but rather are distributed through a 10^{-4} cm thick region of the bulk beneath the surface, i.e., in the space-charge region.[11] The various ambient conditions lead to different surface potentials and thus to different space-charge densities. Since the resonance properties are independent of thes variations in space-charge density, electron spin resonance of mechanically damaged surfaces cannot b used to study surface-state distributions. Therefore the technique will not be of much utility for silicon surface studies, except as a specific test for the presenc of damage.

Further experiments were conducted toward the goa of determining the nature of the paramagnetic center resulting from mechanical damage. The possibility tha impurities, especially dissolved oxygen, were require for formation of the centers was eliminated by studyin high-purity float-zoned silicon with low oxygen content When such material was pulverized in vacuum, th resonance intensity and characteristics observed wer the same as for powders prepared from silicon with hig oxygen content.

It was noted that when n-type silicon was pulverized the resonance lines associated with shallow donors wer greatly decreased in intensity or disappeared. Damagin had no effect, however, on the donor line shape o width.[2,12]

In a series of samples studied, the density of observable damage centers produced by pulverizin heavily n-doped silicon decreased as the donor concentration increased. Typical values were 3×10^{18} damag centers per gram for 8×10^{17} arsenic atoms per gram and 8×10^{17} damage centers per gram for 3×10^{19} arseni atoms per gram. These data suggest that the paramagnetic centers, and perhaps other centers also, tha are produced by the damage process trap electrons from the shallow donors and hence lower the Fermi level. A quantitative study of this effect was precluded by th uncertainty in distribution of the damage center through a given powder particle and the resulting uncertainty in the role played by space charge in preventing electrons from migrating to the damage centers

Heating silicon powder in vacuum at 650°C for 6 h has no effect on the density of paramagnetic damag centers or on other properties of the resonance line However, heating in air for 10 min at 400°C results i the destruction of 80 to 90% of the centers; the fina 10 to 20% of the centers required a temperature o 800°C for their removal. This result suggests that a least two different types of paramagnetic centers contribute to the resonance line observed. One type o center either is destroyed by oxygen (or some othe atmospheric gas) diffusing into the silicon during hea treatment in air, or else is so close to the silicon surfac that it is destroyed by thermal oxidation at the surface

On the basis of the experiments described above, w conclude that the process of mechanical damage of th silicon surface introduces a high density of paramagnetic lattice imperfections in the silicon bulk to a dept of the order of 1 μ. This is not a surprising result inas uch as it has been known for some time that the depth f surface damage in semiconductors produced by brasion is of that order of magnitude.[1] The damage rocess is of sufficient energy to disrupt severely the rystalline lattice near the surface, probably creating acancies, interstitials, dislocations, and more complex ttice defects. Feher[13] has found that silicon samples ith high dislocation densities in the bulk do not exhibit ny paramagnetic resonance lines. Hence, we attribute e resonance line observed to more localized lattice efects. Vacancies in silicon are mobile at room temerature[14] and they probably recombine with intertitials, combine with impurities, migrate to the surface, r become parts of aggregates of defects. Since intertitial silicon produced by electron or neutron irradiaion apparently does not give rise to an observable esonance spectrum,[14,15] neither is it likely that such terstitials, if present, are responsible for the resonance ne reported here. Therefore, the centers observed in echanically damaged silicon probably involve clusters f defects associated with a number of lattice sites.

---

[9] The enriched oxygen was obtained from the Weizmann Institute of Science, Rehovot, Israel.

[10] Silicon powdered and studied at 1.3°K does show some differences in resonance behavior from silicon powdered at room temperature. The spin-lattice relaxation time in the former case is about three orders of magnitude shorter than in the latter; the line shape in the former case is approximately Lorentzian and is somewhat asymmetric. After warming to room temperature and recooling, the resonance properties at 1.3°K are the same as for silicon powdered at room temperature. It is likely that some defects introduced by mechanical damage at 1.3°K are altered or removed as a result of annealing at higher temperatures. This could account for the change in resonance characteristics observed on warming the sample.

[11] G. C. Dousmanis and R. C. Duncan, Jr., J. Appl. Phys. **29**, 1627 (1958).

[12] R. C. Fletcher, W. A. Yager, G. L. Pearson, and F. R. Merritt Phys. Rev. **95**, 844 (1954).

One might well expect the paramagnetic defect nters described above to be very similar to those prouced by neutron irradiation of silicon. Each incident eutron will produce catastrophic damage over a fairly calized region of the silicon lattice. Nisenoff and Fan[15] ropose that clustering of these defects will occur, and hey interpret their paramagnetic resonance results on eutron-irradiated silicon as arising from such aggreates. From annealing studies they have determined hat at least four different kinds of defect centers are roduced by neutron irradiation.

In order to investigate the possibility that neutron rradiation and mechanical damage produce similar efect centers, the electron spin resonance spectrum of sample of neutron-irradiated silicon[16] was studied in owder pattern. It is suggestive that a single resonance ne is observed with the same g value as pulverized ilicon. However, the resonance linewidth was about 16 20 oe for neutron-irradiated silicon, in contrast to 8 e for pulverized silicon. Also, the density of observable aramagnetic centers was much lower in the neutronrradiated sample, which probably accounts for their pin-lattice relaxation time being much longer. As ated earlier, several different types of centers are roduced in each of the damage processes. The relative bundance of each type depends on the conditions under hich damage takes place, postdamage treatment, and perhaps degree of damage. The difference in linewidth noted above between pulverized and neutron-irradiated silicon may result from such variables. Similarities in paramagnetic resonance behavior between neutron and mechanically damaged samples of other materials will be discussed below.

It is of interest also that silicon powder precipitated as a result of cracking trichlorosilane at high temperatures exhibits a resonance line similar in all respects to that observed in mechanically damaged silicon. This result is not surprising in view of the extreme rapidity with which the precipitated silicon particles are formed. One would expect a high density of defects.

Finally, we should like to comment on the resonance line observed by Borel[17] in silicon monoxide. This line is similar to the line seen in mechanically damaged and in precipitated silicon. In view of the uncertain composition of silicon monoxide powders, and of the fact that small particles of silicon are usually unavoidably mixed in with the silicon monoxide, we think it possible that the line Borel has observed is due to defects in the silicon contaminant.

B. Group IV Materials Other Than Silicon

Although the majority of our studies were conducted on silicon, other Group IV semiconductors were also subjected to limited examination. Strong single resonance lines with $g \approx 2$ appeared in each case when bulk germanium, silicon carbide, and diamond were pulverized in air at room temperature. The resonance properties remained stable in air over the course of these investigations, a period of about one year. No attempts were made to pulverize the materials reported on in this section in vacuum or in controlled ambients.

The resonance behavior associated with mechanical damage of the materials reported here are markedly similar to those of damaged silicon. We believe the nature of the paramagnetic centers introduced in these materials to be generally of the same type as described above for silicon.

Powdered germanium exhibits a single, slightly asymmetric, paramagnetic resonance line with g value of 2.023 ± 0.003, appreciably greater than that of silicon. The resonance linewidth is about 50 oe. The spin-lattice relaxation time was found to be much shorter than for the centers in silicon. The density of paramagnetic centers introduced in germanium is approximately ten times smaller than for silicon receiving nominally the same mechanical treatment. The paramagnetic susceptibility is inversely proporational to temperature from 1.3° to 300°K.

Colorless diamond and hexagonal silicon carbide exhibit almost identical resonance lines upon pulverizing. In each case, the g value is 2.0027 ± 0.0002, and the linewidth is 5.5 oe.

---

[13] G. Feher, private communication referred to by T. M. Buck *The Surface Chemistry of Metals and Semiconductors*, edited by . C. Gatos (John Wiley & Sons, Inc., New York, 1960), p. 128.

[14] G. D. Watkins, J. W. Corbett, and R. M. Walker, J. Appl. hys. **30**, 1198 (1959); G. Bemski, *ibid.* **30**, 1195 (1959); H. H. oodbury and G. W. Ludwig, Phys. Rev. Letters **5**, 96 (1960).

[15] M. Nisenoff, Ph.D. thesis, Purdue University, 1960 unpublished).

[16] The sample used was irradiated in the Materials Testing eactor, Idaho Falls, Idaho, to an integrated dosage of 10^{18} nvt. he resulting density of paramagnetic centers was about 10^{17} m^{-3}.

[17] J. Borel, Helv. Phys. Acta **32**, 448 (1959).

TABLE I. Properties of resonance lines resulting from mechanical damage.

Material	g value	Linewidth in oersteds
Ge	2.023 ±0.003	50
Si	2.0055±0.0002	7–8
SiC (hexagonal)	2.0027±0.0002	5.5
C (diamond)	2.0027±0.0002	5.5
MgO	2.0021±0.0001	1.2
CaO	1.9992±0.0002	2
	2.0044±0.0003	8.5
CaS	2.0028±0.0002	2
ZnO	2.0050±0.0006	8
ZnS	2.0031±0.0003	4
	2.0099±0.0003	10
SrO	1.9844±0.0002	2
	2.0044±0.0003	10

We find that powdered graphite shows a weak resonance line of width approximately 25 oe; its properties are quite different from the lines of any of the other materials studied. This is reasonable since graphite is unlike the group IV semiconductors in structure and in nearly all physical properties. Mrozowski and Andrew[18] have reported some of the properties of the resonance line observed in powdered graphite. They attribute the resonance to broken σ bonds of carbon. It is interesting that, in contrast to our results on silicon, they find the resonance line to be partially destroyed upon exposure of the powder to air or oxygen.

Table I summarizes the g value and linewidth data on the group IV semiconductors. It is seen that the shift in g value from that of the free electron (2.0023) becomes larger as the atomic weight increases. This is to be expected in view of the corresponding increase in spin-orbit coupling for the heavier atoms.

C. II–VI Compounds

Most of our work on the II-VI compounds was confined to pulverized single crystals of MgO. This was the only material studied in which a positive identification of the damage center could be made.

Upon pulverizing, MgO exhibits an easily saturable, strong resonance line of width 1.2 oe, and g value equal to 2.0021±0.0001. A weak hyperfine structure can be resolved which is similar to that reported by Wertz *et al.*[19] for F centers in MgO.[20] The hyperfine structure arises from those F centers having one Mg^{25} neighbor. We could not detect hyperfine patterns corresponding to two or more Mg^{25} neighbors. Mg^{25} has a nuclear spin of $\frac{5}{2}$ and a relative abundance of 10%; the other common isotopes, Mg^{24} and Mg^{26}, have zero spin and hence are nonmagnetic. Relative to the intense central line, the hyperfine lines are considerably weaker and somewhat broader than those observable from F centers in MgO single crystals. This result partially arises from the anisotropic part of the hyperfine structure splitting, which tends to broaden the hyperfine lines when observed in a powder. Variable local distortions would also tend to broaden these lines and therefore reduce their intensity.

The results on MgO add strong support to our contention that the defects introduced in solids by mechanical damage are often similar to those produced by neutron irradiation. In this case we find that F centers can be produced in MgO either by mechanical damage or by neutron irradiation. The mechanical-damage process must create the negative ion vacancies required for F-center formation. In addition to the F-center line, two weak asymmetric lines of unknown origin appear in MgO as a result of powdering. These lines lie to the low-field side of the F-center resonance.

The six-component spectrum characteristic of the $M_S=\frac{1}{2}$ to $M_S=-\frac{1}{2}$ transitions of the Mn^{++} impurity present in all our MgO samples was observable in powder pattern.[21] (The $\frac{1}{2}$ to $-\frac{1}{2}$ transitions are almost isotropic; transitions between other M sublevels are anisotropic, and were unobservable in powder pattern.) It was noted that the intensity of this spectrum decreased as the pulverization process proceeded. The linewidths, however, were unaffected. Although this effect may result, in part, from lattice distortions introduced by the damage process, it probably is the result of charge transfer[22] from the Mn^{++} sites to newly created negative ion vacancies (F-center formation), or to other defects or impurities. This would leave the manganese in a charge state in which a resonance is unobservable. A similar reduction was noted, as pulverization proceeded, in the resonance intensity of the Cr^{3+} impurity present in some samples.[23] MgO crystals with large impurity contents (up to 1% Cr, or 1% Mn) showed resonance lines upon pulverizing which were quite different from those seen in purer MgO.

Except for MgO, no II-VI materials were studied other than as pure or reagent-grade powders. CaO, CaS, SrO, and ZnS powders, as obtained, were found to exhibit no resonance line other than the six-component spectrum characteristic of the Mn^{++} impurity. After subjecting these powders to the same mixer-mill mechanical treatment as was used for crystalline materials, new electron spin resonance lines could be observed. All materials showed a narrow resonance line at about $g=2$ (see Table I for exact positions). SrO, CaO, and ZnS all showed, in addition, a broad line to the high-field side of the narrow line.

---

[18] S. Mrozowski and J. F. Andrew, in *Proceedings of the Fourth Conference on Carbon* (Pergamon Press, New York, 1960), p. 207.

[19] J. E. Wertz, P. Auzins, R. A. Weeks, and R. H. Silsbee, Phys. Rev. **107**, 1535 (1957).

[20] After completion of these studies, we learned that J. E. Wertz also has produced F centers in MgO by powdering. A summary of his results appears in ASTIA Rept. AD 237004 (1960).

[21] W. Low, Phys. Rev. **105**, 793 (1957).

[22] J. E. Wertz, P. Auzins, J. H. E. Griffiths, and J. W. Orton, Discussions Faraday Soc. **26**, 66 (1958).

[23] W. Low, Phys. Rev. **105**, 801 (1957).

Although there appear to be at least eight satellite lines symmetrically disposed about the narrow line in SrO, we are unable to make an identification of the center. The pattern is not what one would expect for F centers in SrO since the integrated intensities of the satellites are unequal. Nevertheless, it is suggestive that all these materials exhibit narrow lines at $g\approx 2$. One cannot rule out the possibility that in some of these materials the line results from F centers.

It was observed that, as was the case with crystalline MgO, subjection of these powders to the mechanical treatment described above resulted in a great reduction in the intensity of the Mn^{++} electron spin resonance, presumably due to charge transfer to other impurities or to newly created lattice defects. If the defect were a negative ion vacancy, this process would lead to F-center formation. It is possible that impurities such as chromium or iron, which are initially in charge states not showing a resonance, may become observable as a result of the charge transfer, in this way accounting for the appearance of some of the new resonance lines observed after mechanical damage.

Broad resonance lines appeared also in BeO and ZnO powders after subjecting them to mechanical treatment in the mixer mill. However, no resonance signal could be detected from CdO, CdS, BaS, or HgO after mechanical treatment.

D. Miscellaneous Materials

A cursory resonance examination was made of a variety of other materials after subjection to the mixer-mill treatment.

Two IV-VI crystals, SiO_2 and TiO_2, were studied. After pulverizing, both exhibited very asymmetric resonance lines which looked somewhat similar to one another. In each case, the g value is approximately 2. The breadth of the resonance line is about 100 oe in SiO_2, and about 400 oe in TiO_2 (rutile). Fused quartz showed a resonance line 35 oe in breadth, but otherwise similar in shape to that of crystalline SiO_2. Again, there is a similarity between resonance lines produced in quartz by powdering and that produced by neutron irradiation.[24]

Other materials in which broad resonance lines appeared as a result of mechanical damage were Al_2O_3, Te, and $MgO\cdot Al_2O_3$ (spinel). No resonance signal could be detected in pulverized samples of $CaCO_3$, CaF_2, GaAs, Se, KCl, LiF, Bi_2Te_3, and PbTe.

IV. CONCLUSIONS

Mechanical damage results in the creation of paramagnetic centers in the region of the surface in a wide variety of solids. In many cases, electron paramagnetic resonance techniques can be used to study the properties of such damaged surfaces.

An electron paramagnetic resonance investigation of mechanically damaged silicon was undertaken for the pusposes of evaluating the potential utility of the technique as a tool for the study of semiconductor surfaces, and in order to further elucidate the nature of the paramagnetic centers introduced. It was found that the resonance properties were in no way influenced by the presence of ambient gases, either during or after the damage process. Thus, paramagnetic resonance shows little promise in this connection as a tool for semiconductor surface study, except as a method for determining the degree of surface mechanical damage.

In silicon, and in most of the other materials studied, it was found that the paramagnetic centers introduced by the damage process do not involve impurities present in the starting material. Instead, it is apparent that these centers are lattice defects, or clusters of defects, resulting from catastrophic damage to the crystalline lattice during mechanical treatment. In this respect, the paramagnetic centers might be expected to be similar to those produced in the same materials by neutron irradiation. This view is substantiated in the case of magnesium oxide, where the primary result of both neutron and mechanical damage is shown to be the production of F centers. Silicon also represents a suggestive case, since the resonance g values are identical for the single lines observed from pulverized silicon and from the powder pattern of neutron-irradiated silicon.

Finally, in view of the variety of materials in which paramagnetic centers have been demonstrated to result from mechanical damage, it must be realized that powders prepared from diamagnetic starting materials might turn out to be strongly paramagnetic.

ACKNOWLEDGMENTS

The authors would like to express their gratitude for the helpful discussions and assistance rendered by their colleagues. In particular, we wish to acknowledge the efforts of Dr. W. R. Savage, Dr. R. Stratton, Dr. C. G. McCormick, and Professor C. P. Slichter. Dr. N. G. Einspruch made helpful comments on the manuscript. Dr. G. R. Finlay of the Norton Company kindly furnished the MgO crystals used in this study.

---

[24] R. A. Weeks, J. Appl. Phys. **27**, 1376 (1956).

JOURNAL OF APPLIED PHYSICS VOLUME 32, NUMBER 10 OCTOBER, 196

Modification of the Koehler-Granato-Lücke Dislocation Damping Theory

J. C. Swartz
Edgar C. Bain Laboratory for Fundamental Research, United States Steel Corporation, Research Center, Monroeville, Pennsylvania

AND

J. Weertman
Materials Science Department, The Technological Institute, Northwestern University, Evanston, Illinois

(Received April 26, 1961)

The dislocation damping theory of Koehler, Granato, and Lücke is modified for metals with high stacking fault energy. It is assumed that the most abundant impurity atom species interacts only with the edge component of each dislocation. For this model the hysteretic, or frequency independent damping initially increases linearly with stress amplitude and approaches the Granato-Lücke amplitude dependence at higher stresses. The influence of a second, less abundant impurity atom species which can interact with *both* screw and edge components also is considered. When the glide distance of a dislocation after breakaway becomes comparable with the mean spacing of the second type of impurity, the hysteretic damping becomes amplitude independent. This modification is best suited for application to the damping of bcc metals containing a higher concentration of substitutional impurities than interstitial impurities.

INTRODUCTION

THE most successful theory developed to date to account for the internal friction arising from dislocation motion is the theory originally proposed by Koehler[1] and further developed by Granato and Lücke.[2-4] Niblett and Wilks[5] recently have reviewed the Koehler-Granato-Lücke theory (called KGL theory hereafter) and the experimental data pertinent to it.

The KGL theory assumes the dislocations move both viscously and hysteretically. The theory predicts that (1) the damping component resulting from the viscous motion is dependent on the frequency and independent of the amplitude of the stress oscillations; and (2) the damping component resulting from the hysteretic motion is frequency independent and increases from the origin exponentially with increasing stress amplitude.

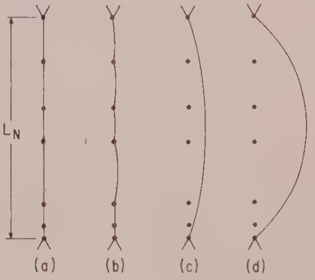

Fig. 1. The Granato-Lücke model. In (a) the applied stress is zero and the dislocation is straight between nodal points of the dislocation network. As the applied stress is increased from zero, (b) shows the bowing of segments between the impurity atoms, and (c) and (d) show the positions of the line after catastrophic breakaway at a low and a high stress, respectively.

Measurements of the frequency dependence in the ultrasonic frequency range support the KGL theory for the viscous component.[6-8] If then the theory is used to extrapolate from the ultrasonic data to lower frequencies, the viscous damping becomes negligibly small in the audio-frequency range. Direct measurement of the frequency dependence in this range is difficult, but there are several indications that below frequencies of order 10^4 cps the damping is independent of or only weakly dependent on the frequency.[9-11] For instance, damping values at 1 cps are generally the same order of magnitude as those at 10^4 cps.[4]

Wilks[12] has suggested that the viscous damping of the KGL theory could be relatively frequency independent if the average length of the oscillating dislocation segments varies with temperature and frequency as a result of thermal activation processes during each stress cycle. However, this suggestion implies the damping would be strongly temperature dependent, contrary to most damping data at and below room temperature.

The amplitude-independent (viscous) damping of the KGL theory depends inversely on the fourth power of the impurity concentration. Only in the Thompson-Holmes[13] experiments on irradiated high-purity copper vibrating at about 10^4 cps has direct evidence of the fourth-power dependence been found. Generally, the amplitude-independent damping has a weaker impurity dependence. (For example, see reference 10.) Indeed, if the fourth-power law were always obeyed, the damping would be immeasurably small in dilute alloys in which easurable damping is observed. The Thompson-olmes data do not necessarily contradict the data n less pure metals because, when the impurity content very low, the viscous damping of the KGL theory an be significant even at 10^4 cps.

---

[1] J. S. Koehler, *Imperfections in Nearly Perfect Crystals* (John Wiley & Sons, Inc., New York, 1952), Ch. 7, p. 197.

[2] A. Granato and K. Lücke, J. Appl. Phys. **27**, 583 (1956).

[3] A. Granato and K. Lücke, J. Appl. Phys. **27**, 789 (1956).

[4] K. Lücke and A. Granato, *Dislocations and Mechanical Properties of Crystals* (John Wiley & Sons, Inc., New York, 1957), p. 425.

[5] D. H. Niblett and J. Wilks, Advances in Phys. **9**, 1 (1960).

[6] A. Hikata and R. Truell, J. Appl. Phys. **28**, 522 (1957).

[7] G. A. Alers and D. O. Thompson, J. Appl. Phys. **32**, 283 (1961).

[8] A. Granato (private communication).

[9] A. S. Nowick, Phys. Rev. **80**, 249 (1950).

[10] S. Takahashi, J. Phys. Soc. Japan **11**, 1253 (1956).

[11] W. P. Mason and H. Bömmel, J. Acoust. Soc. Am. **29**, 1261(A), (1957).

[12] J. Wilks, Phil. Mag. **4**, 1379 (1959).

[13] D. O. Thompson and D. K. Holmes, J. Appl. Phys. **27**, 191, 713 (1956).

To summarize, it appears that an amplitude-ndependent damping exists which is independent of requency and which varies with the impurity content nversely to a power less than four. The frequency ndependence suggests that this damping arises from ysteretic rather than viscous motion of the dislocations. he KGL theory provides no explanation for amplitude-ndependent hysteresis.

The KGL theory of the hysteretic motion also fails o account for some of the observed amplitude-dependent amping. The shape of the amplitude dependence is pparently sensitive to small differences in impurity ontent or dislocation arrangement, since in copper inear,[10] quadratic,[9] and exponential[14] amplitude depend-nces have been reported. Often data which approach he theoretical amplitude dependence at high ampli-udes vary with amplitude slower than the theory at ow amplitude.[15]

Apparently the KGL theory for the frequency-ndependent damping must be modified or replaced by nother to account for these observations at low mplitude and frequency. The present contribution onsiders two changes in the KGL model for the islocation hysteresis. These changes modify the redicted amplitude dependence in the desired direction. However, the necessary assumptions limit the appli-ation of the theory to certain metal-impurity systems. Therefore, this modification is not a general solution o the low-frequency difficulty of the KGL theory.

THEORY

In the model of the KGL theory, shown in Fig. 1, dislocation line is pinned along its length by impurity toms. At low stresses the dislocation segments between inning points bow out as shown in Fig. 1(b). It is ssumed that a viscous retarding force is exerted on this islocation motion which leads to a frequency-dependent nd strain-amplitude-independent damping. At higher stresses the segments can break away from the impurity toms, the breakaway always occurring first at the longest segment, making it even longer, and leading to he subsequent escape of the whole dislocation line as shown in Fig. 1(c). This dislocation motion is hysteretic nd introduces a damping which is frequency in-dependent and strain-amplitude dependent.

We shall use the model of Fig. 1 with two modifications. The first is that the pinning force F of the impurity atom which arises from elastic interactions depends on the orientation of the dislocation line. For an edge dislocation, F is given approximately by[16]

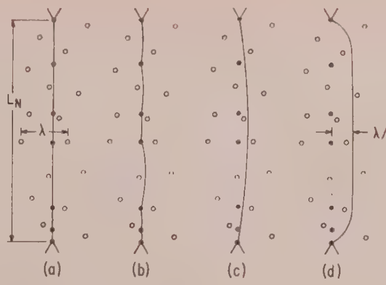

Fig. 2. The Granato-Lücke model modified by restraining effect of impurities near the dislocation. The impurities are assumed to be randomly distributed (not necessarily in glide plane) with a mean spacing λ throughout the material. As the stress is increased from zero, steps (a) and (b) are the same as for Fig. 1. When breakaway occurs at a low stress, the dislocation bows out to the limit of its line tension as shown in part (c). When the breakaway occurs at a higher stress, the dislocation motion after the breakaway is limited approximately to λ/2 as shown in part (d).

$$F\approx 4\mu b\epsilon r^3\partial(\sin\theta/R)\partial x=4\mu b\epsilon r^3\sin 2\theta/R^2, \tag{1}$$

evaluated at $\theta=5\pi/4$ and $R\approx\sqrt{2}a$, the polar coordinates assumed for the position of maximum pinning force. In these equations μ is the shear modulus, b the length of the Burgers vector, ϵ the fractional difference in radius between the impurity and the host atom, r the radius of the host atom, (R,θ) are the polar coordinates of the impurity atom relative to the dislocation line and the slip plane, and $x=R\cos\theta$. Evaluating the above equation yields $F\approx\mu\epsilon b^2/4$ for a pure edge dislocation. Assuming the impurities interact only with the edge component of any dislocation, the general expression for F is

$$F=F_0\sin\alpha, \tag{2}$$

where $F_0\approx\mu\epsilon b^2/4$, and α is the angle between the Burgers vector and the tangent to the dislocation line. ($\sin\alpha$ is zero for a screw dislocation and one for an edge dislocation.)

The second modification of the model of Fig. 1 is shown in Fig. 2. We assume that, once a dislocation has broken away from its pinning points, its motion is not necessarily limited by its line tension, as is the case in Fig. 1(c). The distance it moves may be determined by the stress field of neighboring impurity atoms as given by the Mott-Nabarro theory.[17] Let λ be the average distance between these impurity atoms. The average distance $\bar{x}$ a dislocation will move during breakaway will be one of the two following values.

(1) Line-tension controlled[1] [Fig. 2(c)]:

$$\bar{x}\approx\tfrac{1}{6}(\sigma L_N^2/\mu b), \tag{3a}$$

where σ is the applied stress and L_N is the distance between nodal pinning points of the dislocation network.

---

[14] D. N. Beshers, J. Appl. Phys. **30**, 252 (1959).

[15] For example, H. L. Caswell, J. Appl. Phys. **29**, 1210 (1958).

[16] A. H. Cottrell, *Dislocations and Plastic Flow in Crystals* (Clarendon Press, Oxford, England, 1953), p. 57.

[17] N. F. Mott, reference 1, p. 173.

(2) Impurity-spacing controlled[17] [Fig. 2(d)]:

$$\bar{x}\approx\lambda/2=b/2c^{\frac{1}{3}}, \qquad (3b)$$

where c is the atom fraction of impurity. If Eq. (3a) gives a smaller value than (3b), obviously it will determine the value of $\bar{x}$. Equation (3b) will determine $\bar{x}$ whenever it yields the smaller value and the stress is not sufficient to cause escape from the Mott-Nabarro potential well. The latter requirement will be considered in more detail later.

Figure 3(a) illustrates the hysteresis in the dislocation strain resulting from breakaway of a dislocation according to the model of Fig. 1 or Fig. 2(c). As the stress increases from zero, the segments between impurity atom pinning points bow slightly thereby contributing a small elastic strain. When breakaway from these pinning points occurs, a large dislocation strain results essentially instantaneously. Further stress changes merely move the network length elastically until it becomes pinned again at zero stress. Similar hysteresis is assumed to occur during the other half of the stress cycle.

It is clear from the construction of Fig. 3(a) that the dislocation strain resulting from breakaway increases linearly with the breakaway stress as Eq. (3a) specifies. When the dislocation motion after breakaway is limited by the neighboring impurities such that Eq. (3b) applies, the hysteresis diagram can be represented by Fig. 3(b). Obviously, the assumption of Eq. (3b) implies that the stress field resulting from the neighboring impurities varies much more rapidly than linearly with the dislocation strain.

The total area of a hysteresis loop represents the energy lost during the stress cycle. The area of the loop in Fig. 3(a) is half the product of the stress σ at the moment of breakaway and the dislocation strain resulting from breakaway. The area of the loop in Fig. 3(b) is greater than that of Fig. 3(a) by a factor between 1 and 2. Consequently, we may write

$$\text{Energy density lost/cycle}=\beta\sigma bL_N\bar{x}, \qquad (4)$$

where β is a parameter equal to one for tension-limited motion and between one and two for impurity-limited motion. To compute the decrement resulting from dislocation hysteresis, the energy loss of Eq. (4) first must be summed over all the dislocations which break away. The logarithmic decrement is the total energy loss per cycle divided by twice the vibrational energy in a unit volume.

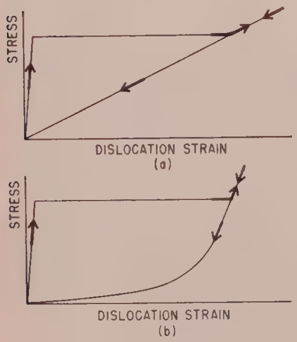

FIG. 3. Hysteresis in the stress-dislocation strain diagram for (a) tension-limited motion, and (b) impurity-limited motion.

The stress at which breakaway will occur depends on the probability of finding a long dislocation segment in a dislocation line of length L_N. The probability of finding a dislocation segment of length between l and $l+dl$ in a dislocation line of total length L_N has been calculated by Koehler[1] to be

$$(L_N/L^2)\exp(-l/L)dl, \qquad (5)$$

where L is the average distance between impurity atoms on a dislocation line, namely b/c. The stress required to break away a long loop, and hence the whole dislocation line, from its pinning points is given approximately by the equation

$$\sigma bl=2F, \qquad (6)$$

when $l>L$, the region in which we are interested. By using this last equation, one finds that the probability $P(\sigma,\alpha)d\sigma$ that a dislocation line of length L_N will break away from its pinning points in the stress interval from σ to $\sigma+d\sigma$ is

$$P(\sigma,\alpha)d\sigma=(2FL_N/\sigma^2bL^2)\exp(-2F/\sigma bL)d\sigma, \qquad (7)$$

where $F=F_0\sin\alpha$.[18] In a unit volume of material containing a total length of dislocation line N, there will be N/L_N segments of length L_N which are pinned at nodal points in a three-dimensional network ($L_N\approx\{3/N\}^{\frac{1}{2}}$). Assuming all the dislocations are in glide planes, the number of segments which break away between σ and $\sigma+d\sigma$ is $(N/L_N)P(\sigma,\alpha)d\sigma$. Using Eq. (4) for the energy loss incurred in each breakaway and assuming the segments of the network are randomly oriented, the decrement Δ due to the hysteretic dislocation motion can be written as

$$\Delta=(\mu/\sigma_0^2)(2/\pi)\int_0^{\pi/2}\int_0^{\sigma_0}(N/L_N)P(\sigma,\alpha)\beta\sigma bL_N\bar{x}d\sigma d\alpha, \qquad (8)$$

where σ_0 is the amplitude of the stress oscillation (σ_0^2/μ is twice the vibrational energy per unit volume). If the distance $\bar{x}$ dislocations move after breakaway is line-tension controlled and therefore is given by Eq.

---

[18] Actually, one must consider the length of the dislocation segments on either side of a pinning impurity when calculating the probability for obtaining breakaway at any stress level. Equation (7) is a good approximation to the more exact but more cumbersome expression.

(3a), Eq. (8) becomes

$$\Delta=\frac{2}{3}\frac{NL_N{}^3F_0}{\pi b\sigma_0{}^2L^2}\int_0^{\pi/2}\int_0^{\sigma_0}\sin\alpha \times\exp\left(-\frac{2F_0\sin\alpha}{\sigma bL}\right)d\sigma d\alpha. \quad (9a)$$

At low stresses where we may use $\sin\alpha\approx\alpha$, Eq. (9a) approximates

$$\Delta\approx\frac{NL_N{}^3b}{9\pi F_0}\sigma_0 \quad (10a)$$

(for $\sigma_0bL\ll 2F_0$). If the breakaway distance is impurity controlled and thus is given by Eq. (3b), one obtains the following equation for the decrement:

$$\Delta=\frac{2\beta\mu NbL_NF_0}{\pi\sigma_0{}^2c^{\frac{1}{3}}L^2}\int_0^{\pi/2}\int_0^{\sigma_0}\frac{\sin\alpha}{\sigma} \times\exp\left(-\frac{2F_0\sin\alpha}{\sigma bL}\right)d\sigma d\alpha, \quad (9b)$$

which at low stresses approximates the following expression

$$\Delta\approx\frac{\beta\mu Nb^3L_N}{4\pi c^{\frac{1}{3}}F_0}=\frac{\beta NbL_N}{\pi c^{\frac{1}{3}}\epsilon} \quad (10b)$$

(for $\sigma_0bL\ll 2F_0$).

The criterion as to which of the two equations, (10a) or (10b), should be used in any particular situation is quite simple. The equation that predicts the smaller damping is the one to use since the equation with the smaller damping involves the smaller breakaway distance. Therefore, at very low stresses the breakaway distance is line-tension controlled and the decrement resulting from hysteretic motion is initially proportional to stress. At somewhat higher stresses, the breakaway distance may be limited by the stress field of impurity atoms in the neighborhood of the dislocation line, in which case the decrement becomes independent of stress. At stresses sufficiently high to break away the edge dislocations, Eqs. (9a) and (9b) predict decrements varying exponentially with reciprocal stress such as predicted by Granato and Lücke.[2] Figure 4 illustrates the stress dependence of the decrement for dislocation hysteresis according to the modified KGL model. Since this damping is the result of hysteretic motion, it is independent of the frequency of vibration.

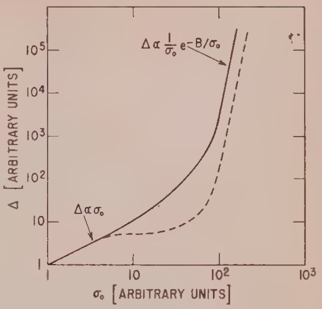

FIG. 4. The dependence of the damping Δ on the stress amplitude σ_0 for this modification of the KGL theory. The solid line represents the solution of Eq. (9a), which was derived for tension-limited motion. The dashed line demonstrates the effect of impurity-limited motion on the amplitude dependence.

Impurity-Limited Dislocation Motion

A necessary condition for impurity-limited motion is that the stress at breakaway be smaller than that necessary to escape from the Mott-Nabarro potential trough. Equation (6) gives the breakaway stress for a line the longest unpinned segment of which is l. Since $l>L\approx b/c$, the stress at breakaway from Eqs. (2) and (6) is less than but generally the order of $\mu\epsilon c\sin\alpha/2$. The stress to escape from the Mott-Nabarro potential trough associated with these impurities is the same order of magnitude.[17] Consequently, the type of impurity that is originally pinning the dislocation may not in general limit the dislocation motion after breakaway.

In order to get impurity-limited motion over a wide range of stress amplitude, as Eq. (10b) requires, it is necessary to have two types of impurity atoms, one type which interacts strongly with both screw and edge dislocations and another type which cannot interact with screw dislocations. The body-centered cubic metals with high stacking fault energy offer a good possibility of providing these two types of impurities. Interstitial impurity atoms in this lattice interact strongly with both screw and edge dislocations. The high stacking fault energy prevents the dislocations from splitting into partials, so substitutional impurity atoms should not interact with pure screw dislocations. If the concentration of interstitial impurity atoms is smaller than that of substitutional atoms, one has an ideal situation for the application of Eq. (10b). The interstitial atoms themselves can limit the motion of dislocation segments which have broken away from substitutional impurity atoms. The interstitial atoms also would pin the dislocation lines, but if their concentration is much smaller than that of the substitutional impurities, these interstitial pinning points merely determine the average length L_N to be used in the equations we have derived rather than the distance between nodal points. Hence if c^* is the atom fraction of interstitial impurities, so that $\lambda=b/c^{*\frac{1}{3}}$ and $L_N=b/c^*$, Eq. (10b) becomes

$$\Delta=\frac{\beta Nb^2}{\pi\epsilon c^{*\frac{1}{3}}}. \quad (10c)$$

The concentration of substitutional atoms does not enter into this equation even though it is these atoms which give rise to the hysteretic motion producing the damping.

Even if the type of impurity atom which can pin both screw and edge dislocations is not present, it still may be possible to have Eq. (10b) valid. Suppose only impurities with spherically symmetrical strain fields are present in a metal lattice in which the dislocations, or at least a fraction of the dislocations, are not split up into partial dislocations. Even these impurities could pin a screw dislocation if they come together to form pairs (di-impurities), since the stress field of a di-impurity is not spherically symmetrical. If there is no interaction between impurity atoms, the concentration of di-impurities in a lattice where every site has 12 nearest neighbors is $12c^2$ when c is small. If there is an interaction force between the impurity atoms, the equilibrium concentration will be this value multiplied by a term like $\exp(Q/kT)$, where Q is the energy of interaction and kT is the usual thermal energy. If the concentration of di-impurities is substituted into Eq. (10b) in the same way as was c^*, the concentration of interstitials, one obtains the equation

$$\Delta=\frac{Nb^2}{12^{4/3}\pi\epsilon c^{8/3}}e^{-4Q/3kT}, \tag{10d}$$

where T is either the acual temperature of measurement or, for measurements made at low temperatures, the lowest temperature at which appreciable diffusion takes place. This last equation would be applicable only when the concentration of impurities is large enough to produce a reasonable number of di-impurities; that is, when the average separation of di-impurities along a dislocation line is smaller than the separation of nodal points.

Modulus Defect

If μ is the true modulus of the material and μ^* the experimentally determined modulus, the modulus defect is defined by the expression

$$\text{modulus defect}=(\mu-\mu^*)/\mu. \tag{11}$$

In our model, at any particular stress level the dislocation segments L_N close to the edge orientation are well pinned and do not contribute hysteresis, and others close to the screw orientation are not pinned except at their ends because the thermal and applied stresses are more than sufficient to break the weak pinning points. Both the pinned and the unpinned dislocation segments contribute to the strain by dislocation motion and hence to the modulus defect. At low stresses and temperatures, most of the dislocations are pinned by impurities giving an average segment length L. The modulus defect resulting from motion of these pinned dislocations is given by the following equation,

$$(\mu-\mu^*)/\mu=NL^2, \tag{12}$$

which results from Koehler's equation[1] upon substitution of $\mu b^2/2$ for the dislocation line tension.

The dislocations which are moving by hysteretic motion also make a contribution to the modulus defect. This contribution is approximately equal to the decrement resulting from hysteretic motion.

DISCUSSION

The foregoing modification of the KGL theory will not apply to metals in which the dislocations are extended. The reason is that one of the two partials of an extended dislocation always will have an appreciable edge component regardless of the orientation of the dislocation. The results for tension-limited motion might be applicable to high-purity copper, a metal which has been employed in a great many internal friction experiments, since recent evidence[19,20] indicates that the stacking fault energy of copper may be high.

Since this modification to the KGL theory concerns the damping resulting from dislocation hysteresis, the Granato-Lücke amplitude dependence[2] is altered. In particular, at low amplitudes the damping should increase much more gradually with amplitude than the exponential increase of the original theory. At high stress amplitudes, the damping of the modified theory approaches the Granato-Lücke dependence on stress amplitude because pinned edge-like dislocations begin to contribute to the hysteretic damping.

When the hysteretic dislocation motion is limited by neighboring impurities, the damping can be amplitude independent. The concentration dependence of this amplitude-independent damping is much milder than the fourth-power dependence predicted by the KGL theory of amplitude-independent damping. These are the characteristics of the hysteretic damping which are required to resolve the frequency and concentration difficulties of the original theory. However, the assumptions we have employed to obtain this amplitude-independent hysteresis seriously restrict its application.

It remains to compare the predicted damping for impurity-limited motion with experimental data from systems for which the theory is applicable. The damping predicted by Eq. (10c) can be relatively large. For instance, with $b=3\times10^{-8}$ cm, $\beta=1.5$, $\epsilon=0.05$, and $c^*=10^{-4}$, decrements of 2×10^{-3} and 2×10^{-2} are predicted for $N=10^6/\text{cm}^2$ and $10^7/\text{cm}^2$, respectively.[21] Lower values of the decrement would be predicted if allowance were made for the difference between the applied stress and the resolved shear stress on the various slip planes. The above estimates of the decrement for bcc metals might be compared with experi-

---

[19] A. Seeger, R. Berner, and H. Wolf, Z. Physik **155**, 180 (1959).

[20] P. B. Hirsch, J. Inst. Metals **87**, 406 (1958–59).

[21] The density of glissile dislocations N in a well-annealed metal is expected to be less than the total dislocation density.

mental values, which are generally of the order of 10^{-4}.[22–24]

No extensive study of the amplitude dependence of the damping in bcc metals appears to have been published. A recent study[25] by one of us (JCS) of the dislocation damping in iron at low frequency shows that the damping approaches amplitude independence both at low and at high amplitude and increases linearly with amplitude in the intermediate region. Our modification of the KGL theory might be used to account for the linear region and for the region of amplitude independence at high amplitude. It appears that the amplitude-independent damping at low amplitude still lacks theoretical interpretation.

SUMMARY

The Koehler-Granato-Lücke theory has been modified by taking into account the fact that some impurities may not interact with screw dislocations although they can pin dislocations with an edge component. Thus, at low stress levels hysteretic motion of dislocation lines occurs contributing a damping which initially increases linearly with stress. This may account for departure of metals with high stacking fault energy from the Granato-Lücke amplitude dependence. When the hysteretic motion is limited by neighboring impurity atoms in the vicinity of the dislocation lines, damping results which is both frequency independent and strain-amplitude independent. For this situation to occur, a second type of impurity must be present which interacts strongly with both screw and edge dislocations. The body-centered cubic metals with high stacking fault energy offer an ideal example of materials containing both these types of impurities. Interstitial impurities interact with both the screw and edge dislocations, while substitutional impurities do not interact elastically with screw dislocations which are not extended. If the only type of impurity present is that which cannot pin screw dislocations, the hysteretic motion still may be limited if an appreciable number of pairs are present.

---

[22] T. S. Ke, Trans. Am. Inst. Mining, Met., Petrol., Engrs. **176**, 448 (1948).

[23] L. J. Bruner, Phys. Rev. **118**, 339 (1960).

[24] R. H. Chambers and J. Schultz, Acta Met. **8**, 585 (1960).

[25] J. C. Swartz, (to be published).

JOURNAL OF APPLIED PHYSICS VOLUME 32, NUMBER 10 OCTOBER, 1961

Dislocation Etch Pits on the Basal Plane of Zinc Crystals

H. S. Rosenbaum and M. M. Saffren
General Electric Research Laboratory, Schenectady, New York

(Received March 24, 1961)

An etch pit technique has been developed that reveals the sites of dislocations which intersect the basal plane surface of zinc crystals. Pits can be formed by either Cl_2, HCl, Br_2, HBr, or HI dissolved in an appropriate organic solvent. Etchants made with Cl_2 or HCl produce hexagonal pyramidal pits whose edges are parallel to $\langle 10\bar{1}0\rangle$ directions; but Br_2, HBr, or HI etchants produce hexagonal pits whose edges are parallel to $\langle 11\bar{2}0\rangle$ directions. The technique is useful for observing glide which occurs on nonbasal planes. The dislocation etch pits are seen to form a "polygonization" pattern in a crystal that was annealed after deformation. A discussion is presented on the mechanism of etch pit formation and the factors which might determine the shape of the pits.

INTRODUCTION

THE possibility of revealing the positions of dislocations by means of a suitable etchant was demonstrated by Vogel and co-workers[1,2] and is now widely known. These workers showed the correspondence of etch pits to edge dislocations in a low-angle tilt boundary in germanium. Soon etchants were found that could reveal dislocations in metal crystals when an "atmosphere" of solute atoms had segregated to the dislocations. Thus Gilman revealed dislocations in zinc, using cadmium as a decorating solute[3]; and Suits and Low[4] revealed the dislocations in a Fe($3\frac{1}{4}$ wt% Si) alloy, using carbon to decorate the dislocations. While these "decoration" techniques have the great experimental advantage of revealing the dislocations that intersect any convenient surface, they have the disadvantage of failing to reveal those dislocations which do not have an atmosphere of solute atoms.

More recently, etchants have been found that reveal dislocations in some relatively pure metal crystals without requiring that solute atoms be segregated at the dislocation. These techniques usually suffer the disadvantage that the etchant works only on those surfaces nearly parallel to certain crystallographic planes of high atomic density. For example, Lovell and Wernick[5] were able to reveal undecorated dislocations on $\{111\}$ faces in copper. At present, there are etchants which are reported to reliably reveal undecorated dislocations in several metals and on several of the low index crystallographic surfaces: copper on $\{111\}$,[6,7] $\{110\}$,[7] and $\{100\}$[7]; iron on $\{100\}$ and $\{110\}$[8]; cadmium on $\{10\bar{1}0\}$[9]; and tungsten on $\{100\}$ and $\{112\}$.[10]

With respect to zinc, Sinha[11] very recently reported that he is able to etch the $\{10\bar{1}0\}$ prism planes to reveal undecorated dislocations. There were earlier attempts to etch dislocations in zinc, but in each case there is insufficient evidence to determine whether individual dislocations are revealed or whether decoration is required.[12–15]

In the present work, a technique was found to produce etch pits on the basal plane of zinc crystals; the pits correspond to dislocations which intersect the basal plane. The evidence indicates that for screw dislocations a solute decoration is not required; whether decoration is needed for edge dislocations could not be determined. For many deformation studies this technique has only limited usefulness because the dislocations which lie in the basal plane cannot be revealed; these contribute most to the deformation and are by far the most numerous. However, the technique does enable us to examine nonbasal slip.

EXPERIMENTAL PROCEDURE

Throughout this work, monocrystals grown from the melt were used. The material was nominally 99.999% Zn obtained from the New Jersey Zinc Company. Some of the crystals used in this work were kindly supplied to the authors by J. J. Gilman.

In preparation for the metallography, the crystals were cleaved in liquid N_2 using a razor blade and a light hammer. Prior to etching, the crystals usually were chemically polished in a solution containing equal volumes of HNO_3 (70%), H_2O_2 (30%), and ethanol (200 proof) as suggested by Gilman and DeCarlo.[16] On those occasions where the freshly cleaved surface was to be etched, the cleaved crystal was quickly transferred from the liquid N_2 into ethanol at room temperature. The ethanol was then warmed to about 35°C before removing the crystal and drying it in a stream of air. This was done to avoid condensation of atmospheric water vapor on the surface.

---

[1] F. L. Vogel, Jr., W. G. Pfann, H. E. Corey, and E. E. Thomas, Phys. Rev. **90**, 489 (1953).

[2] F. L. Vogel, Jr., Acta Met. **3**, 245 (1955).

[3] J. J. Gilman, Trans. AIME **206**, 998 (1956).

[4] J. C. Suits and J. R. Low, Jr., Acta Met. **5**, 285 (1957).

[5] L. C. Lovell and J. H. Wernick, J. Appl. Phys. **30**, 590 (1959).

[6] J. D. Livingston, J. Appl. Phys. **31**, 1071 (1960).

[7] F. W. Young, Jr., J. Appl. Phys. **32**, 192 (1961).

[8] P. D. Gorsuch (to be published).

[9] J. H. Wernick and E. E. Thomas, Trans. AIME **218**, 763 (1960).

[10] H. W. Schadler in *Direct Observations of Imperfections in Crystals* (American Institute of Mining Engineers, New York), to be published.

[11] P. Sinha (private communication).

[12] A. H. A. Meleka, Phil. Mag. **1**, 803 (1956).

[13] S. S. Servi, Phil. Mag. **3**, 63 (1958).

[14] G. Bassi and J. P. Hugo, J. Inst. Metals **87**, 376 (1958–1959).

[15] J. George, Phil. Mag. **4**, 1142 (1959).

[16] J. J. Gilman and V. J. DeCarlo, Trans. AIME **206**, 511 (1956).

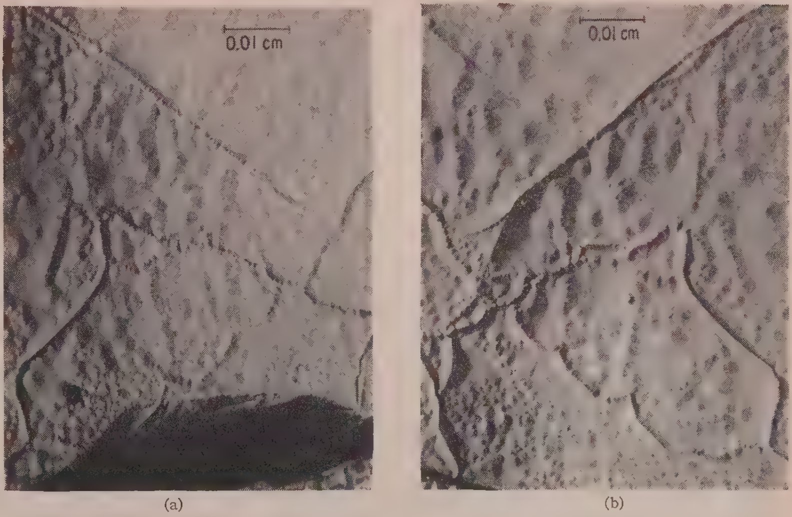

(a) (b)

FIG. 1. Corresponding areas on the halves of a cleaved crystal. Etchant: 1 part by volume liquid Br:5 parts ethanol. Except for the region near the bottom of the photographs where the cleavage caused obvious damage, the pits in the networks match each other almost exactly; and of those not in the networks about 80% can be matched.

In preparing the etchants either halide acids or halogens were dissolved in an appropriate solvent. The halide acids: HCl, HBr, or HI were used in their aqueous reagent form. The halogens were added to their solvents directly: Cl_2 gas was bubbled through the solvent until the solution had a distinctly greenish color; liquid Br_2 and crystalline I_2 were added to their respective solvents in the indicated amounts.

The usual etching procedure was to dip the crystal into the solution with the surface to be observed facing upward. The specimen was then washed in ethanol and dried in a stream of air.

Mechanical deformation experiments were performed on some of the crystals. These crystals were of square cross section of dimensions 0.6×0.6×4.6 cm oriented so that one pair of the lateral faces corresponded to the basal plane. They were deformed in a four-point bending jig with the axis of bending along the [0001] direction. The bending jig was loaded by squeezing it in a vise at room temperature.

For annealing, the crystals were placed in a graphite boat inside a Vycor tube furnace with an atmosphere of continuously flowing hydrogen. The crystals were cooled to nearly room temperature while in the reducing atmosphere by moving the boat to a cold section of the Vycor tube.

RESULTS

Etching

An etchant consisting of 1 part by volume liquid bromine in 5 parts ethanol[17] produced pits in the form of hexagonal pyramids with the sides of the hexagon parallel to the $\langle 11\bar{2}0\rangle$ close-packed directions. These pits were shallow and could be seen in an optical microscope only with oblique illumination.

To ascertain that pits correspond to crystal defects, the crystals were cleaved and the etch pit patterns on the two halves of each crystal compared. An example of this is shown in Fig. 1. This crystal had been previously deformed in tension at 300°C parallel to the

TABLE I. Etchants of Br_2 in various diluents.

Diluent	Conc. of Br_2 (parts by vol. liq. Br_2: parts diluent)	Results with Br_2	Results with other oxidizer
Methanol	1:5	Good	Good with 0.5*M* HBr and 0.5*M* HCl. HBr produces pits with sides parallel to $\langle 11\bar{2}0\rangle$. HCl produces pits with sides parallel to $\langle 10\bar{1}0\rangle$.
Ethanol	1:10	Good	See Table II
	1:5	Good	Good with HBr, HI, HCl, Cl_2
	2:5	Good	
Di-ethyl ether	1:25	Good	
Glycerol	1:25	Good	Good with HBr
Toluene	1:25	No pitting	
	1:5	Stain	
Benzene	1:5	No pitting Stain	Anhydrous HBr bubbled through; no pitting
Acetic acid	1:5	General attack	
Water		When mixed with ethanol in ratios 1:1 or less; good results with HBr and with Br_2	Unsuccessful with HBr, HCl, HI, $HC_2H_3O_2$, HNO_3, H_2SO_4, H_3PO_4

---

[17] Care must be exercised in mixing bromine in alcohol because the heat liberated can cause the mixture to boil violently.

basal plane. Gilman has shown that such deformation causes prismatic glide of the type $\{10\bar{1}0\}\ \langle\bar{1}2\bar{1}0\rangle$.[18]

Another test that was applied to determine whether the pits correspond to dislocations was to etch, strain the specimen slightly, and then re-etch. Such tests showed that the strain caused the appearance of many new pits; moreover, many of the original pits that had been present prior to straining now had flat bottoms. This is illustrated in Fig. 2 for a modification of this etchant.

Various diluents for the bromine were tried. They are listed in Table I. Of the organic solvents, only benzene and toluene failed to produce acceptable results. (Acetic acid will not be considered here as a solvent.) It is difficult to dissolve bromine in water directly. However, if one first dissolves the bromine in ethanol and then mixes with water, good results are obtained when the water:ethanol proportion is 1:1 by volume or less.

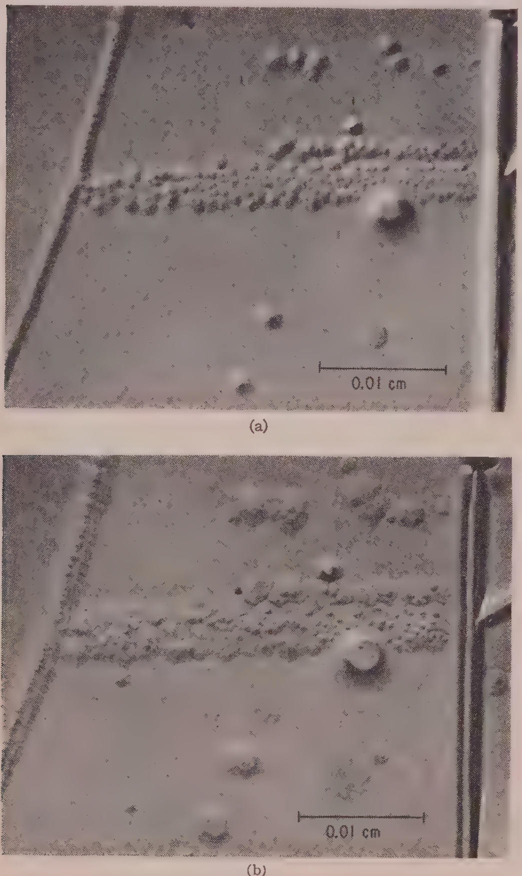

FIG. 2. Results of an etch : strain : re-etch sequence showing dislocation redistribution after a very slight strain. (a) The crystal was chemically polished and then etched in 0.5M HBr in ethanol. (b) The specimen was re-etched after the application of a stress. We see the same field of view as in (a).

TABLE II. Etchants of various oxidizing agents in ethanol.

Oxidants in ethanol	Conc.	Results
Cl_2(g)	Bubbled through	Conical[a] and pyramidal pits. Edges of pit parallel to $\langle 10\bar{1}0\rangle$
Br_2(l)	1:10	Pits with edges parallel to $\langle 11\bar{2}0\rangle$
	1:5	
	2:5	
I_2(s)	0.1% by wt. 1%	No pits after several minutes
HCl(aq)	0.2–0.6M	Conical[a] and pyramidal pits with edges parallel to $\langle 10\bar{1}0\rangle$
HBr(aq)	0.2–0.6M	Pyramidal pits with edges parallel to $\langle 11\bar{2}0\rangle$
HI(aq)	0.2–0.6M	Pyramidal pits with edges parallel to $\langle 11\bar{2}0\rangle$
HNO_3	0.2–0.6M	No pitting
H_2SO_4	0.2–0.6M	No pitting
H_3PO_4	0.2–0.6M	No pitting
Formic acid	0.2–0.6M	No pitting
Acetic acid	0.2–0.6M	No pitting
Propionic acid	0.2–0.6M	No pitting
HF	0.2–0.6M	No pitting

[a] The pits produced by Cl_2 or HCl in ethanol tend to be conical when anhydrous alcohol is used, and are more sharply pyramidal with 180 proof ethanol.

Other oxidizing agents in ethanol (See Table II) were tried, and good results were obtained with Cl_2, HCl, HBr, and HI. It is significant that the pits produced with either Cl_2 or HCl etchants are of different orientation than those produced with Br_2, HBr, or HI. This i illustrated in Fig. 3. Gilman and Johnston[19] found a similar phenomenon when comparing two etchants for lithium fluoride. It is interesting to note that if a crystal is dipped into concentrated, reagent grade halide acid, a rapid pitting attack occurs. This produces terraces whose orientation is characteristic of etchants made with that particular acid. That is, the action of concentrated HI or HBr results in terraces parallel to $\langle 11\bar{2}0\rangle$ directions, while concentrated HCl causes terraces parallel to $\langle 10\bar{1}0\rangle$ directions.

When etching with either the halide acid etchants or the halogen etchants, a slow gas evolution occurs at the zinc surface. This gas was identified as H_2 by means of mass spectrometry[20] for a Br_2:ethanol etchant.

---

[18] J. J. Gilman, Trans. AIME **206**, 1326 (1956).

[19] J. J. Gilman and W. G. Johnston in *Dislocations and Mechanical Properties of Crystals* (John Wiley & Sons, Inc., New York, 1957), pp. 116–161.

[20] The analysis was carried out by F. J. Norton. The vapors over the etchant were analyzed both before and after a zinc specimen was dropped into the solution. It was determined that the hydrogen was caused by the action of the Br_2: ethanol mixture on the zinc.

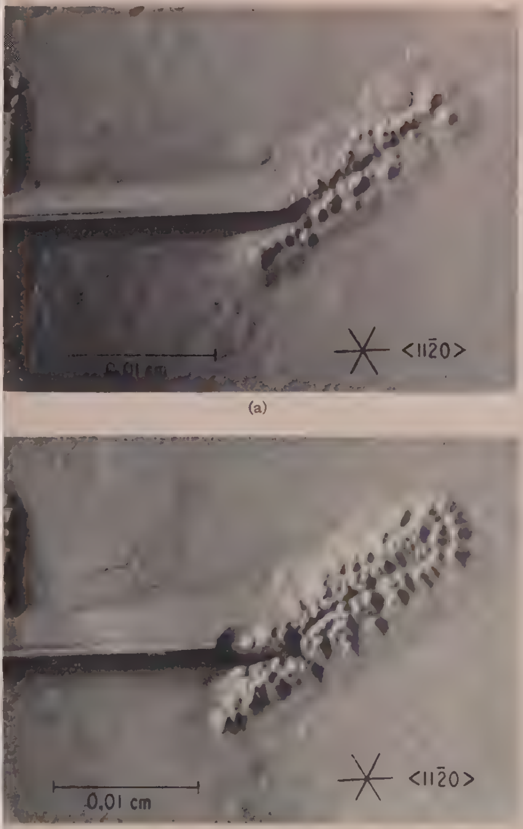

(a)

(b)

Fig. 3. Etch pits produced by HBr and by HCl etchants. The pits present a cluster of dislocations at the tip of a twin. (a) Crystal tched in 0.5M HCl in ethanol. The pits are oriented with their ges parallel to $\langle 10\bar{1}0\rangle$, i.e., at 30° and 90° to the $\langle 11\bar{2}0\rangle$. (b) The me area as in (a). The surface was chemically repolished and en re-etched in 0.5M HBr in ethanol. The new pits have edges irallel to $\langle 11\bar{2}0\rangle$.

Nonbasal Slip and Polygonization

Figure 4(a) shows the etch pits near the neutral axis f a bent crystal. The pits are aligned in bands along $1\bar{1}00\rangle$ directions. These glide bands are consistent with lip on second-order pyramidal $\{11\bar{2}2\}$ planes as found y Bell and Cahn.[21] After annealing [Fig. 4(b)], the its are redistributed with some realignment to form ows roughly parallel to the neutral axis. This realignient or "polygonization" is most prevalent near the eutral axis.

Slip on planes of type $\{11\bar{2}2\}$ was confirmed by means f a stereographic projection analysis of slip markings nd will be reported elsewhere.[22] If it is assumed that the ending occurred by slip on $\{11\bar{2}2\}$ planes and in the $\bar{1}\bar{1}23\rangle$ directions as described by Bell and Cahn,[21] then the pits in Figs. 4(a) and (b) should correspond to screw dislocations. The slip system $\{11\bar{2}2\}$ $\langle\bar{1}\bar{1}23\rangle$ for tensile stresses parallel to the basal plane was recently confirmed by Price[23] by means of electron transmission microscopy. The defects caused by such deformation can be etched without any apparent need for decoration with solute atoms. Even deformations carried out in liquid N_2 produce the expected etch pit glide bands (consistent with slip in $\{11\bar{2}2\}$ planes) when etched immediately after warming the specimen to room temperature.

Although annealing after deformation causes a re-

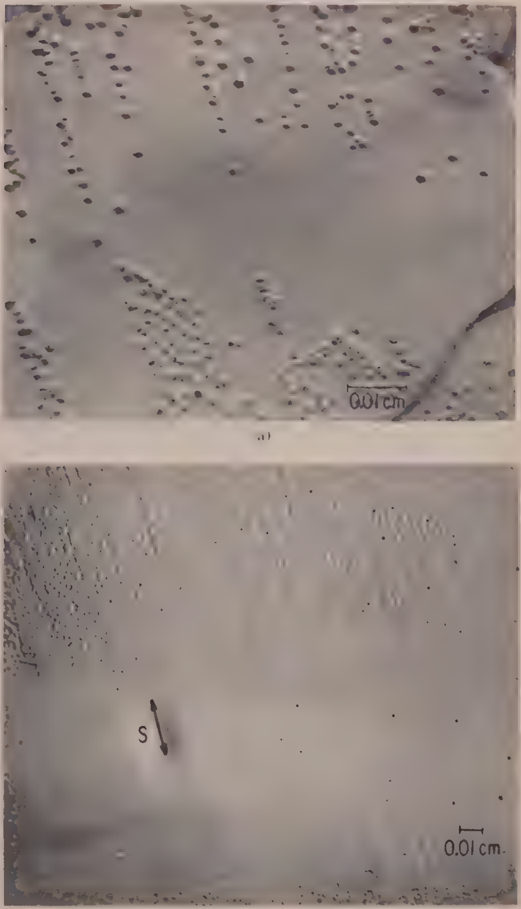

a)

(b)

Fig. 4. A crystal deformed in four point bending at room temperature about an axis perpendicular to the basal plane. The plane of view in the photographs is the basal plane. After bending, the crystal was chemically polished and etched in a solution of 0.5M HBr in ethanol. (a) The dislocations near the neutral axis are seen. (b) After anneal in a H_2 atmosphere for 20 min at 250°C. Then it was chemically repolished and re-etched. We see polygonization of the dislocations near the neutral axis of the specimen. The orientation of the original glide bands is indicated at S.

---

[21] R. L. Bell and R. W. Cahn, Proc. Roy. Soc. (London) **A239**, 94 (1957).

[22] H. S. Rosenbaum, Acta Met. (to be published).

[23] P. B. Price, Phil. Mag. **5**, 873 (1960).

distribution of the etch pit patterns, the shape and depth of the etch pits are not affected by annealing. Gilman, Johnston, and Sears[24] found a difference in etch pit depth between "aged" and "fresh" dislocations in lithium fluoride, but no difference was observed in the present work.

Ocassionally, etch pits are observed which are much deeper than those caused by the room temperature deformations. [Some can be seen in Fig. 4(a).] The shape of these pits was also unaffected by heat treatments. The imperfections which cause these pits can be matched on the mating faces of a cleaved crystal, but they are relatively immobile during deformations at room temperature.

DISCUSSION

Correspondence of Pits to Dislocations

The following evidence implies that the pits correspond to the sites of emerging dislocations:

(1) The pits on two halves of a cleaved crystal can be matched, showing that the pits correspond to defects of the crystal.

(2) Flat-bottomed pits are produced when the crystal is re-etched after a slight strain. From this we see: (a) The pits cease to deepen when the defect is no longer at the pit site. (b) At sharp-bottomed pits the defects have length at least as great as the pit depth. The fact that pits remain sharp and continue to deepen after long etching times shows that the defects are linear. (c) These linear defects can be moved by the application of a stress.

(3) After bending a crystal about the [0001] axis the pits are aligned in glide bands, and a pit-free region is observed in the vicinity of the neutral axis.

(4) The pits are redistributed by annealing. A kind of "polygonization" pattern results.

Thus it has been shown that most of the pits are caused by dislocations. Whether *all* of the pits correspond to dislocations or whether *all* of the emerging dislocations cause pits is not known.

The dislocations produced by deformations at room temperature were observed to occur on $\{11\bar{2}2\}$ planes.[22] By analogy with the works of Bell and Cahn[21] and of Price[23] the slip direction can be assumed to be $\langle\bar{1}\bar{1}23\rangle$ and the dislocations as seen on the basal plane are of screw character. Such dislocations require no special decoration treatment. If a solute atmosphere exists at these dislocations, it must form at room temperature in about 15 sec.

Deformation by tension parallel to the basal plane at 300°C has been reported to cause slip on $\{10\bar{1}0\}$ $\langle\bar{1}2\bar{1}0\rangle$ systems.[18] Such deformation should produce edge dislocations which intersect the basal plane. Figure 1 shows that the etch pattern which results consists of a network of pits. That the pits in the networks repr sent edge dislocations is supported by two pieces evidence: (1) This type of pattern is peculiar to th high temperature nonbasal glide, and (2) no cleavag steps were produced as is the case when a cleavag crack intersects a large number of screw dislocations. Although the dislocations have had an opportunity climb and to interact with each other at the hig temperature, they are still mainly of edge characte However, since such dislocations cannot be produce by deformation at low temperatures, it is not know whether edge dislocations can be etched without solu decoration.

Etching

In discussing the significance of these observatio it must be said at the outset that the mechanism etch pit formation in this case is not known. Furthe more, the chemical reactions which might occur at metal surface in these solutions are also not know Therefore, the discussion which follows is speculative

It has been suggested[24,26] that etch pits form atomically close-packed surfaces at undecorated di locations by the nucleation of atomic steps at the co of the dislocation; the steps then migrate along th surface as atoms are removed at each step. Gilma Johnston, and Sears[24] have shown that etch pit form tion is enhanced in lithium fluoride by the addition small amounts of metallic ions (e.g., Fe^{3+}) to th etchant. They interpreted this in terms of the Fe^{3+} i "poisoning" the dissolution process by retarding th motion of the steps. Assuming that the nucleation new steps is unaffected by the poison, the poison caus pits to become deep enough to be seen in an optic microscope. In agreement with this interpretati Young[7] found that in etching copper on {111} fac the addition of Br^- ion was necessary, and he co vincingly showed that the role of Br^- ion was *reduce* the dissolution rate. The results in the prese work can be interpreted according to this model.

The similarity in pit orientation produced by halogen and by the corresponding halide acid sugges that in both cases the chemical reactions might be th same. One possibility is that the acid (i.e., hydrog ion) is the oxidizing agent and that the halogen ato or ion acts as a poison to inhibit the motion of atom steps across the metal surface. The chemical reacti suggested, then, is one involving the reduction H^+, i.e.,

$$2H^+ + Zn \rightarrow H_2 + Zn^{++}.$$

Indeed, H^+ is the only obvious oxidizing agent prese in acid:ethanol etchants. As for solutions of halogen an organic solvent, it is known that Cl_2 or Br_2 can rea with these organic solvents to form HCl or HBr. Therefore the reaction suggested above might occur either when a halogen or when a halide acid is used. In agreement with a mechanism involving such a reaction is the fact that a gas is evolved. This gas has been identified as H_2 for the case of a Br_2:ethanol etchant, and it can be assumed to be H_2 for the halide acid etchants. The H_2 evolved by the action of a Br_2:ethanol solution on zinc must certainly come from the alcohol. Thus it appears that the oxidation of zinc, which occurs as it dissolves, is accompanied by the reduction of hydrogen. Whether the reaction occurs simply, as written above, or whether there is a more complicated sequence of reactions is not known. Nor is it known whether this reaction is precisely the one which creates pits at the dislocations.

---

[24] J. J. Gilman, W. G. Johnston, and G. W. Sears, J. Appl. Phys. **29**, 747 (1958).

[25] J. J. Gilman, Trans. AIME **212**, 310 (1958).

[26] W. G. Johnston in *Progress in Ceramic Science, Vol. 2* (P gamon Press, New York), to be published.

The function of the solvent in these reactions is not understood. It was suggested that the halogen could react with its organic solvent to produce some halide acid, but why a mixture of halide acid in water was not able to produce satisfactory pits is not known.

Etch Pit Shape

Regardless of the exact chemical reactions, these experiments clearly show that the halogen or the halide ion plays an important role in determining the shape of the etch pit. The difference in the orientation of pits caused by Cl_2 or HCl etchants as opposed to the Br_2, HBr, or HI etchants can only be explained by the effect of the specific halogen or halide ion. According to the model involving the motion of close-packed atomic steps across the surface, one could say that chlorine, in either its ionic, atomic, or molecular forms, most effectively retards the motion of steps which are parallel to $\langle 10\bar{1}0\rangle$ directions, while bromine and iodine retard $\langle 11\bar{2}0\rangle$ steps most effectively. This is because a pit composed of atomic steps must be bounded by steps normal to the direction of slowest motion; those parts of the steps which move faster tend to disappear.

We shall now consider a different approach to the problem of understanding etch pit shape. Batterman[27] analyzed etch figures in germanium on the basis of his measurements of the orientation dependence of dissolution rate. His work was recently extended by Irving[28] and by Riessler.[29] The latter author devised a geometric construction which predicts the shape of dislocation etch pits. This predicts that pits will be bounded by such crystallographic planes for which $w(\alpha)/\cos\alpha$ is smallest but greater than $w(0)$. Here $w(0)$ is the dissolution rate normal to the plane being etched (called the ground plane) and not influenced by a dislocation. $w(\alpha)$ is the dissolution rate normal to a plane making the angle α with the ground plane. α was implicitly assumed to be the over-all slope of the pit facets.

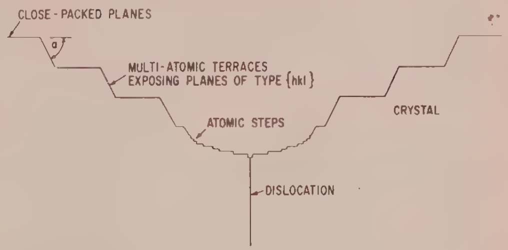

FIG. 5. Schematic diagram showing the cross section of an etch pit that is made by the agglomeration of moving atomic (or molecular) steps to form multiatomic (or multimolecular) terraces bounded by certain crystallographic planes. The angle α is assumed to be $<90°$.

In the present work the information concerning the orientation dependence of the dissolution rate of zinc in these etchants is not yet available, so this analysis cannot be applied quantitatively. However, it is interesting to compare this kind of analysis to the model involving the motion of separate atomic steps.

In both the present work on zinc and that by Livingston on copper,[30] pits are observed with different depths and similar widths. This indicates that the widening of a pit does not depend on the dissolution rate along the dislocation, as is implied by Riessler's analysis[29]; but this is consistent with the step motion model. However, the results for copper clearly show that the shape of etch pits is not determined by the motion of separate atomic steps. Young[7] and Livingston[6,30] find that on the close-packed {111} faces of copper the etch pits are triangular. If pits formed by the motion of separate atomic steps, there is no reason why hexagonal pits should not be formed just as they are in zinc. Since there is six-fold symmetry (three close-packed directions) of the atom positions on the {111} faces, a pit could be made up of concentric hexagonal atomic steps. It is only if the pits were constrained to be bounded by certain crystallographic planes {*hkl*} that triangular pits must be formed. Furthermore, one needs the assumption that the angle α between the ground plane and that exposed by the etchant is acute. The facts that the pits have different depths and are all very shallow[30] require that these facets or bounding planes form terraces. The model for etch pit formation which evolves from such an argument involves the agglomeration of the atomic steps to form multiatomic terraces bounded by certain crystallographic surfaces.[31] Such a pit is schematically shown in Fig. 5. The conditions for which one might expect atomic steps to agglomerate were discussed by Cabrera and Vermilyea[32] and by Frank[33] in terms of a kinematic theory of step motion.

---

[27] B. W. Batterman, J. Appl. Phys. **28**, 1236 (1957).

[28] B. A. Irving, J. Appl. Phys. **31**, 109 (1960).

[29] W. Riessler Z. angew. Phys. **12**, 433 (1960).

[30] J. D. Livingston in *Direct Observations of Imperfections in Crystals* (American Institute of Mining Engineers, New York), to be published.

[31] Similar reasoning can be used to show that the triangular pits that are produced on the {111} cleavage surfaces of fluorite[26] cannot be the result of the motion of separate atomic or molecular steps. It must be assumed that the pit is constrained by the necessity to be bounded by certain crystallographic surfaces.

If we interpret the etch pits on the basal plane of zinc in this way, we conclude that chlorine causes a face of the type $\{11\bar{2}l\}$ to form while bromine and iodine cause some face of type $\{10\bar{1}l\}$ to form. Whether these individual terraces form according to the $w(\alpha)/\cos\alpha$ criterion is not yet known. We emphasize, however, that hexagonal pits on the basal plane of zinc can be explained by the motion of either *atomic* steps or *multiatomic* terraces. It is the results in other materials which point to a model involving multiatomic terraces.

Polygonization

The observations of polygonization were included in this report mainly to help verify that the pits correspond to dislocations, but we feel that this polygonization is unusual and deserves comment. The polygonization that was observed in this situation [see Fig. 4(b)] appears to consist of the rearrangement of screw dislocations from their glide bands into rows that are roughly parallel to the neutral axis. The nature of the dislocations after polygonization is not known, but if we assume them to be of screw character, then they represent twist boundaries. We suggest that the reason that such boundaries form can be associated with the different lattice rotations experienced by the crystal in the tension and compression regions of the bent specimen. In the tension region the slip directions tend to rotate *towards* the stress axis, while in the compression regions they tend to rotate *away* from the stress axis. Thus by considering the bent crystal to have been half in tension and half in compression we expect that these halves should have suffered a net rotation with respect to each other.

SUMMARY

(1) A system of dislocation etchants based on solutions of halide acids or halogens in some organic solvents has been developed. These etchants can reveal the sites of emerging dislocations on the basal plane of zinc.

(2) Screw dislocations can be etched without deliberate solute decoration; and although edge dislocations can be etched, it is not known whether the technique requires decoration on edge dislocations.

(3) The etchant reveals evidence of glide that occurs on nonbasal planes.

(4) The glide dislocations become redistributed during an anneal, forming a "polygonization" pattern.

ACKNOWLEDGMENTS

It is a pleasure to acknowledge the help given to us by many of our colleagues. J. J. Gilman supplied some of the crystals. Some of the other crystals used here were produced for us by V. J. DeCarlo. F. J. Norton performed the mass spectrometer gas analysis. W. G. Johnston, J. D. Livingston, H. W. Schadler, and D. A. Vermilyea critically reviewed the manuscript and offered many helpful suggestions.

---

[32] N. Cabrera and D. A. Vermilyea in *Growth and Perfection of Crystals* (John Wiley & Sons, Inc., New York, 1958), pp. 393–408.

[33] F. C. Frank in *Growth and Perfection of Crystals* (John Wiley & Sons, Inc., New York, 1958), pp. 411–418.

JOURNAL OF APPLIED PHYSICS VOLUME 32, NUMBER 10 OCTOBER, 1961

Energy of a Crossed Grid of Screw Dislocations*

JAMES C. M. LI
Edgar C. Bain Laboratory for Fundamental Research, United States Steel Corporation, Monroeville, Pennsylvania

(Received March 23, 1961)

The strain energy of a crossed grid of screw dislocations is calculated using isotropic elasticity theory. It is found that a distortion from the stable structure requires a large amount of strain energy. It is indicated that long-range stresses can exist in metastable dislocation networks without a long pile-up of like dislocations. Possible rearrangements of dislocation networks in both fcc and bcc metals are shown.

BAILEY and Hirsch[1] found that considerable energy release (about one-half of the total stored energy) during the recovery stage of deformed polycrystalline silver produces no observable change in dislocation distribution. We would like to show that this is possible by examining the simple case of a low-angle twist boundary formed by a crossed grid of screw dislocations. The purpose is to demonstrate that a large energy difference can be associated with a rearrangement. Using isotropic elasticity theory, the energy of such a crossed grid of screw dislocations, all of the same sign, can be calculated from the stress field and energy of a wall of parallel screw dislocations[2,3] and the interaction of such a wall with nonparallel screw dislocations[3] oriented at an arbitrary angle ϕ. The result is (when $R>h>r_0$):

$$\gamma=(\mu b/2\pi)\theta[(\pi R/h)(1+\cos 2\phi)+A-\ln\theta] \quad \text{per unit area,} \qquad (1)$$

where R is the size of the subgrain, h is the spacing between the parallel screw dislocations, r_0 is the radius of the core of the dislocation, γ is the strain energy of the boundary per unit area, μ is the shear modulus, b is the Burgers vector, θ is the angle of twist, ϕ is the angle between the two sets of parallel screw dislocations, and A is $\ln(b/2\pi r_0)$ plus the core energy per unit length in units of $\mu b^2/4\pi$. The strain energy of a stable twist boundary (corresponding to $\phi=\pi/2$) is

$$\gamma_0=(\mu b/2\pi)\theta(A-\ln\theta) \text{ per unit area.} \qquad (2)$$

This is a small fraction of γ since A is of the order[4] of 0.5 and $\pi R/h$ can be as much as 1000. The quantity $2(\gamma-\gamma_0)/\mu R\theta^2$ is plotted in Fig. 1. The strain energy of two sets of parallel screw dislocations isolated with respect to each other is also plotted in the same figure. It is seen that a rearrangement from $\phi=60°$ to a stable twist boundary releases almost the same amount of strain energy as the loss of one whole wall of parallel screw dislocations. It is thus confirmed that a rearrangement in the dislocation network could indeed release a considerable amount of energy as a result of the long-range stresses.

The formation of such a crossed grid of screw dislocations during deformation is partially controlled by the free energy of formation (as indicated in Fig. 1) when one slip band of screw dislocations is running into another helped by cross slip. If the two sets of parallel screw dislocations are forced together by external stresses so that the free energy of formation is positive, the system is unstable and considerable rearrangement might happen during recovery or even immediately after the external stresses are released. Another situation occurs when the two sets of screw dislocations are of different sign so that they attract each other for $0\leq\phi<\pi/4$ or $3\pi/4<\phi\leq\pi$ and repel each other for $\pi/4<\phi<3\pi/4$. In the case of attraction, the metastable structure formed cannot become stable by a slight rearrangement. Considerable cancellation of dislocations would have to be necessary in order to lower its energy. Therefore, the only interesting case is the first case where all screw dislocations are of the same sign. We shall discuss in the following some possible rearrangements from the metastable structure ($\pi/4<\phi<3\pi/4$) formed during deformation to the stable structure after recovery.

One of the possible rearrangements in an fcc metal is as follows. Screw dislocations of Burgers vectors $(a/2)$ $[\bar{1}10]$ and $(a/2)$ $[01\bar{1}]$ can form a metastable network in the plane (111) as shown in Fig. 2(a). The structure is such that $\phi=2\pi/3$. It can be formed either by two sets of parallel screw dislocations in the slip plane (111), by one set in (111) and another in $(\bar{1}11)$, by one set in $(11\bar{1})$ and another in (111), or by one set in $(11\bar{1})$ and

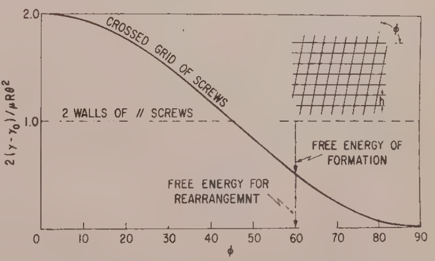

FIG. 1. The strain energy of a crossed grid of screw dislocations with respect to that of a stable twist subboundary of the same angle of misfit.

---

* Presented in part at the Annual AIME Meeting, Feb. 27–March 2, 1961, St. Louis, Missouri; J. Metals **13**, 70 (1961).

[1] J. E. Bailey and P. B. Hirsch, Phil. Mag. **5**, 485 (1960).

[2] S. Amelinckx and W. Dekeyser, Solid State Physics **8**, 409 (1959).

[3] J. C. M. Li and C. D. Needham, J. Appl. Phys. **31**, 1318 (1960).

[4] D. McLean, *Grain Boundaries in Metals* (Oxford University Press, New York, 1957), p. 33.

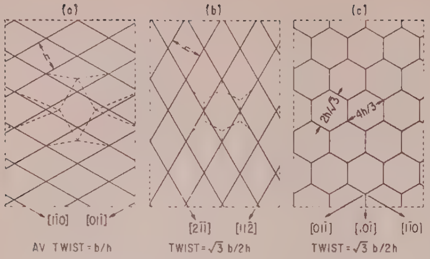

FIG. 2. Rearrangement of dislocation networks in (111) plane of fcc metal. $b=(a/2)\langle 110\rangle$.

another in ($\bar{1}$11), altogether four possibilities involving three slip planes. No cross slip is necessary in the first case. Cross slip of one set of parallel screw dislocations is necessary in the second and third cases. Cross slip of both sets of dislocations is necessary in the last case. That the formation of such a metastable net is possible is seen from the free energy of formation in Fig. 1 for $\phi=\pi/3$. Although such a net is stable with respect to separation of the two sets of parallel screw dislocations, it is metastable since it still has long-range stresses. Such long-range stresses can be easily seen from the interaction of such a net with another screw dislocation of the same sign parallel to the plane of the net. Let the angle between the foreign dislocation and one set of parallel screw dislocations in the net be ψ and that between the same dislocation and another set in the net be $\psi-\pi/3$. The repulsive force exerted by the net on the foreign dislocation is simply (isotropic elasticity)

$$(\mu b^2/2h)\cos[(\pi/3)-2\psi] \text{ per unit length} \qquad (3)$$

and is not a function of the distance between the foreign dislocation and the net. The angle ψ at which the net shows the strongest repulsion is $\pi/6$ and that at which it shows the strongest attraction is $2\pi/3$. Such long-range stresses indicate that the net can undergo a rearrangement. For the two sets of dislocations with the same set of Burgers vectors, Frank's formula[5] indicates a net with dislocation lines parallel to [2$\bar{1}\bar{1}$] and [11$\bar{2}$] as shown in Fig. 2(b). Since now the dislocations are all of mixed character, this net cannot easily be formed during deformation. However, this net can be formed by a rearrangement from the previous net [Fig. 2(a)] either by a nucleation and growth procedure, as indicated in dotted lines in Fig. 2(a), or by stretching the net in the direction [10$\bar{1}$] into high-angle boundaries or free surfaces and contracting the net in the direction [1$\bar{2}$1] where the high-angle boundaries or free surfaces will have to supply some dislocations to preserve the continuity of the net. Exactly in what manner the rearrangement takes place is immaterial so far as the release of the strain energy is concerned. However, it seems likely that some thermal activation is necessary and that therefore it takes place during recovery. The net of Fig. 2(b) is now stable and has no long-range stresses. This can be seen from the following: (i) it obeys Frank's formula, (ii) the energy of the net, calculated (isotropic elasticity) by separating the two sets of dislocations into two infinite walls of mixed parallel dislocations, taking into account the interactions between the various screw and edge components, and by relaxing the stresses of the two infinite walls and eliminating them from the crystal, is given by Eq. (2), and (iii) there is no interaction between such a net and another screw dislocation parallel to the net oriented in any direction. It is thus seen that all the long-range stresses of the net of Fig. 2(a) are relaxed, and hence the stored energy released, by rearranging into the net of Fig. 2(b), and yet there is no difference in external appearance of the two nets except their orientation. The net of Fig. 2(b) will be rearranged further into a hexagonal network of Fig. 2(c) by releasing further some (about 15%) of the core energy, which is a small fraction of the energy released in the first rearrangement. As indicated earlier, the energy released in the first rearrangement is about equal to the strain energy of one set of parallel, like, screw dislocations. The relative twist between the two subgrains will be slightly different if the spacings between the dislocations remain the same in Figs. 2(a) and (b). However, if the relative twist remains unchanged, the spacings would have to be slightly different in Fig. 2(b) after the rearrangement.

A similar rearrangement can take place in the case of a bcc metal. Screw dislocations of Burgers vectors $(a/2)$ [$\bar{1}$1$\bar{1}$] and $(a/2)$ [1$\bar{1}\bar{1}$] can form a metastable network in the plane (110) as shown in Fig. 3(a). Since [$\bar{1}$1$\bar{1}$] can be in (110), (011), or ($\bar{1}$01), and [1$\bar{1}\bar{1}$] can be in (110), (101), or (0$\bar{1}$1), there are altogether nine possibilities involving five slip planes to form such a net, in which one of them requires no cross slip, four of them require cross slip of one set of parallel screw dislocations, and the remaining four of them require cross slip of both sets. This metastable net has a strain energy corresponding to $\phi=70.5°$ and thus will have about one-half of the strain energy of one set of parallel, like, screw dislocations available for rearrangement into a stable network. In this case, Frank's

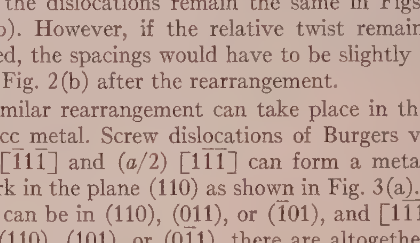

FIG. 3. Rearrangement of dislocation networks in (110) plane of bcc metal. $b=(a/2)\langle 111\rangle$.

---

[5] F. C. Frank, Report Symposium on Plastic Deformation of Crystalline Solids, Carnegie Institute of Technology, Pittsburgh, Pennsylvania, (1950), p. 150.

formula[5] (1950) gives a net of Fig. 3(b) which has no long-range stresses. The rearrangement can take place by a mechanism similar to that in the fcc metal just discussed. Such a net will rearrange further into a net of Fig. 3(c) by releasing about 6% of its core energy of dislocations. The second rearrangement, although the driving force is small, ought to be relatively easy since it involves only gliding of small segments of dislocations in their slip planes. The exact shape of the net of Fig. 3(c) can not be determined from elastic theory alone. Any shape derived from Fig. 3(b) by using different lengths of [00$\bar{1}$] dislocation segments can be shown to have no long-range stresses. The line tension arguments put forward by Carrington *et al.*[6] have thus the uncertainty in the contribution of core energies of the dislocations. By superimposing two (110) planes of a bcc lattice rotating an angle with respect to each other, it is shown in Fig. 4 that a pattern develops which gives exactly the net of Fig. 3(c). However, this argument which involves minimum misfit in terms of nearest-neighbor interactions, does not constitute a proof that the most stable net is of the shape of Fig. 3(c). It merely indicates that if the core energy is the important part of line tension, the shape of the net is likely that of Fig. 3(c). Exact experimental determination would be necessary to settle this question.

In summary, two sets of parallel screw dislocations of the same sign can form a metastable network when $\pi/4<\phi<3\pi/4$ with an average twist of b/h. Such a net has long-range stresses, as can be seen from its repulsion of an approaching, like, screw dislocation oriented with an angle ψ with one set and $\psi-\phi$ with the other. The repulsion is $(\mu b^2/h)\cos\phi\cos(2\psi-\phi)$ per unit length and does not depend on the distance between the net and the approaching dislocation. The strain energy associated with these long-range stresses can be relaxed by rearranging the metastable net to a position in which each set of the dislocations is perpendicular to the Burgers vector of the other set. This net, which obeys Frank's formula, no longer has any long-range stress. But since such rearrangement does not change the external appearance of the net, one sees that some stored energy can be released during recovery without discernible changes in dislocation substructure. One sees also that the measurement of dislocation density by stored energy is questionable. A mechanism of work hardening utilizing the long-range stresses of the dislocation tangles will be proposed elsewhere.

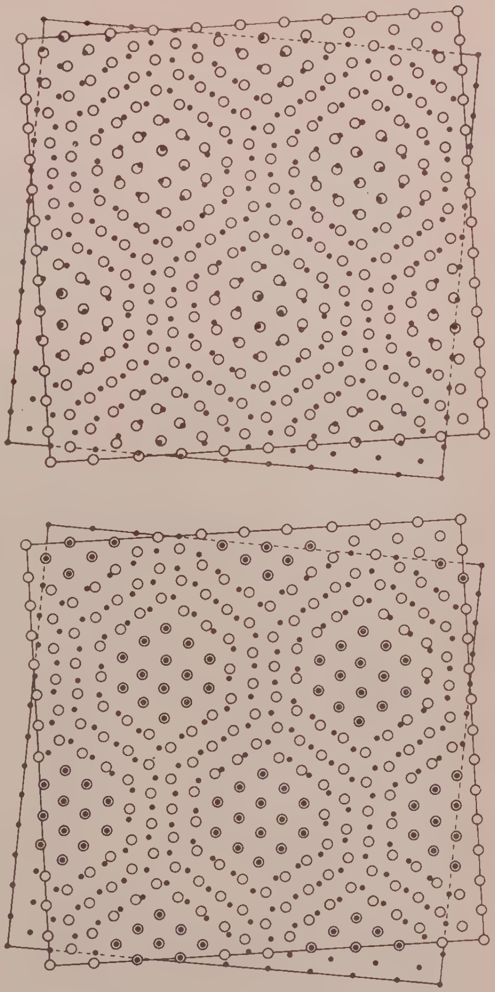

FIG. 4. Two superimposed (110) planes of a bcc lattice showing the formation of the network of Fig. 3(c).

The author wishes to thank Dr. R. L. Segall of the Cavendish Laboratory, Cambridge, England, for pointing out a possible evidence of the large strain energy associated with the dislocation tangles by showing that such tangles are capable of bending a high-angle boundary.[7] He also wishes to thank Dr. H. Wilsdorf of the Franklin Institute for pointing out that long-range stresses could indeed be associated with the dislocation tangles from the observation that isolated dislocations are attracted to the tangles and that the cell dimension remains essentially constant. If the stress field of the tangles were not as long as that of the single dislocations, dislocations would rather tangle within the cells and thus the cell dimension should decrease continuously with deformation.

---

[6] W. Carrington, K. F. Hale, and D. McLean, Proc. Roy. Soc. (London) **A259**, 203 (1960).

[7] R. L. Segall and P. G. Partridge, Phil. Mag. **4**, 912 (1959), Fig. 9.

JOURNAL OF APPLIED PHYSICS VOLUME 32, NUMBER 10 OCTOBER, 1961

Generation and Distribution of Dislocations by Solute Diffusion

S. Prussin*
Pacific Semiconductors Inc., Culver City, California

(Received March 13, 1961)

The stress introduced by solute lattice contraction of boron and phosphorus in silicon is shown to be sufficient to generate dislocations in silicon wafers. Such dislocations were observed. Expressions for the density distribution and for the total number of dislocations generated are derived and a mechanism of dislocation generation and distribution during the diffusion process is postulated. The dislocation distribution is shown to be highly dependent upon the nature of the diffusion process, expressions being derived for the conditions of (1) constant surface concentration of solute and (2) diffusion from a finite source. An expression for and means to determine the residual stresses in diffused silicon wafers are given.

I. INTRODUCTION

STUDIES of diffusion in semiconductor materials over the past decade have been stimulated by the development of solid-state devices. The influence of dislocations on the properties of such devices has recently been reviewed in the literature.[1] The possible introduction of dislocations into crystals by solute concentration gradients set up during solidification has been described.[2,3] The introduction by diffusion processes of stresses sufficient to generate dislocations in silicon could have been calculated then, but observation of this phenomenon required the development of dislocation-free silicon[4] as well as of new techniques.

In its simplest form, the diffusion process utilized in silicon device fabrication consists in subjecting a wafer of single-crystal silicon, 0.5 to 1.0 mm thick, to a gaseous, liquid, or solid source of diffusant at elevated temperatures. Under the proper conditions, we can maintain a constant solute concentration at the surface. In such a situation, the solute concentration profile can be described by a complementary error-function distribution, i.e.,

$$C=C_s\,\mathrm{erfc}[(a-y)^2/4Dt]^{\frac{1}{2}}, \tag{1}$$

where C is the solute concentration at y and t, C_s is the surface concentration, a and y are shown in Fig. 1, D is the diffusion coefficient, and t is time after initiation of diffusion.

We could also use a two-step diffusion process as follows. In the short first step, the prediffusion, the desired amount of solute is absorbed at the wafer surface. In the second step, the redistribution, no additional diffusant is introduced, but the solute near the surface diffuses in to the desired depth. The resulting solute concentration can be described by a Gaussian distribution, i.e.,

$$C=C_s\cdot\exp-[(a-y)^2/4Dt]. \tag{2}$$

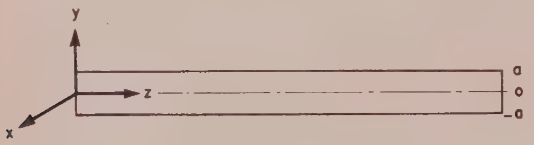

FIG. 1. Schematic diagram of the cross section of a wafer whose surfaces are $y=a$ and $y=-a$.

II. STRESSES GENERATED BY DIFFUSION IN A WAFER

The stresses caused by concentration gradients are similar to those caused by temperature gradients in an otherwise unstressed body. Both are based on linear strain coefficients. For concentration gradients we have the relation

$$e_x=-\beta C, \tag{3}$$

where e_x is a component of strain and β is the solute lattice contraction coefficient.

Timoshenko[5] has derived an expression for the stresses in a thin plate bounded by the planes $y=\text{constant}$ when the temperature distribution is independent of the x and z coordinates. By analogy we find the stresses developed in a wafer by diffusion in from the surfaces to be

$$\sigma_x=\sigma_z=\frac{\beta CE}{1-\nu}-\frac{\beta E}{2a(1-\nu)}\int_{-a}^{+a}Cdy-\frac{3\beta Ey}{2a^3(1-\nu)}\int_{-a}^{+a}Cydy, \tag{4}$$

where E is Young's modulus, and ν is Poisson's ratio.

The last term in the expression gives the stress relief by buckling when the stresses developed are nonsymmetrical about the central plane, $y=0$. For a symmetrically diffused wafer we can drop this term and obtain the following:

$$\sigma_x=\frac{\beta E}{1-\nu}\left[C-\frac{1}{2a}\int_{-a}^{a}Cdy\right]. \tag{5}$$

For the erfc concentration distribution given by

---

* Present address: MonoSilicon, Inc., Gardena, California.

[1] W. Bardsley, *Progress in Semiconductors*, edited by A. F. Gibson (John Wiley & Sons, Inc., New York, 1960), Vol. 4, p. 155.

[2] F. C. Frank, Advances in Phys. **1**, 91 (1952).

[3] A. J. Goss, K. E. Benson, and W. G. Pfann, Acta Met. 4, 332 (1956).

[4] W. C. Dash, J. Appl. Phys. **30**, 459 (1959).

[5] S. Timoshenko, *Theory of Elasticity* (McGraw-Hill Book Company, Inc., New York, 1934), 1st. ed., p. 203.

Eq. (1), Eq. (5) becomes

$$\sigma_x=\frac{\beta C_s E}{1-\nu}\left[\operatorname{erfc}\frac{a-y}{(4Dt)^{\frac{1}{2}}}-\frac{2(\pi Dt)^{\frac{1}{2}}}{a\pi}\right]. \qquad (6)$$

For the Gaussian concentration distribution given by Eq. (2), Eq. (5) becomes

$$\sigma_x=\frac{\beta C_s E}{1-\nu}\left[\frac{2}{\pi}\exp-\left[\frac{(a-y)^2}{4Dt}\right]-\frac{2(\pi Dt)^{\frac{1}{2}}}{a\pi}\right]. \qquad (7)$$

For both concentration distributions, we note that the same maximum stress develops at the beginning of the diffusion process, $t=0$. For both,

$$(\sigma_x)_{\max}=(\beta C_s E/1-\nu). \qquad (8)$$

The earliest values of β were obtained by Pearson and Bardeen[6] in 1949 for boron and phosphorus in polycrystalline silicon. Later evaluations for boron by Horn[7] and Epel'baum *et al.*,[8] gave consistently higher values. This was attributed to boron precipitation in the grain boundaries of the polycrystalline samples. All investigators determined β by means of room temperature lattice constant measurements.

Saturation of the wafer surfaces by the diffusant is not an uncommon occurrence at the beginning of the diffusion process. Trumbore[9] found solubility values at 1225°C of 1.5×10^{21} atoms/cm^3 for phosphorus and 5×10^{20} atoms/cm^3 for boron. Recent data for boron in single-crystalline silicon yielded a value for β of 5.6×10^{-24} cm^3/atom at room temperature. The assumption that this value will hold for elevated temperatures is not unreasonable. The elastic constants of silicon and their temperature coefficients given by McSkimin *et al.*,[10] yield a value of 21.56×10^{11} d/cm^2 for $(c_{11}+c_{12})$ at 1225°C. For diffusion into a $\{100\}$ surface, $(c_{11}+c_{12})$ equals $E/1-\nu$. On substituting these values into Eq. (8), we obtain a value of 6.0×10^9 d/cm^2 for the maximum possible stress developed at the silicon surface as a result of the lattice contraction caused by substitutional boron atoms. Taking into account that the only available β value for phosphorus is probably too low by a factor of two to three as a result of grain boundary precipitation, the stress possible with phosphorus as the solute is even greater than with boron.

Pearson *et al.*,[11] give 5.5×10^9 d/cm^2 as the stress necessary to cause yield in silicon whiskers at 800°C. Extrapolating their data to 1225°C reduces the necessary stress by an order of magnitude. It would thus appear that, even without considering surface stress raisers, the stresses developed by solute lattice contraction are sufficient to cause plastic deformation and thus generate dislocations in dislocation-free silicon. For less than perfect material, stresses of a lower order of magnitude would be required.

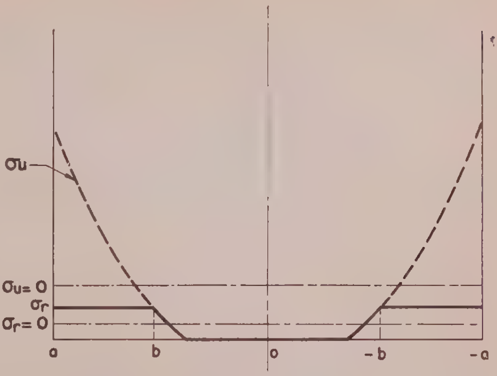

FIG. 2. Distribution of stresses over the cross section of a diffused wafer when the stress is relieved by the generation of dislocations, solid curve marked σ_r, and when the stress is unrelieved, curve σ_u, as given by Eq. (5). Each curve has its own datum given by $\sigma_r=0$ and $\sigma_u=0$.

III. EXPERIMENTAL OBSERVATION OF DISLOCATIONS

The detection of dislocations in diffused layers proved impossible by decoration techniques. The solute atoms made the silicon opaque to the wavelengths of infrared radiation observable with an image converter tube. The following etch-pit evaluation technique was used instead. The diffused wafer was coated with Apiezon wax and cleaved. It was then placed in an agitated Dash etch solution[12] for a period ranging from 15 sec to several minutes. The attack was sufficient to bring out the dislocation etch pits in the diffused layer. Figures 5 and 6 illustrate the results obtained. The dislocation arrays were typical of a polygonized structure, which would be expected, considering that the material was subjected for relatively long times to a temperature of 1225°C.

The interior of the wafer was much less rapidly attacked than the diffusion layers. Thus, if the cleavage plane was etched sufficiently long to bring out dislocation etch pits in the interior, the diffused layers were heavily eroded, making it very difficult to discern the dislocation etch pits there.

IV. RELIEF OF STRESS BY THE GENERATION OF DISLOCATIONS

Equation (5) gives the stress in a wafer as equal to a constant multiplied by the difference between the concentration and an integral term. Thus, with appropriate ordinates, the stress distribution can be identical to the concentration profile from which it was derived, but

---

[6] G. L. Pearson and J. Bardeen, Phys. Rev. **75**, 865 (1949).

[7] F. Hubbard Horn, Phys. Rev. **97**, 1521 (1955).

[8] V. A. Epel'baum, M. A. Gurevich, and M. S. Starostina, Russian J. of Inorg. Chem. **4**, 851 (1959), in translation.

[9] F. A. Trumbore, Bell System Tech. J. **39**, 205 (1960).

[10] H. J. McSkimin, W. L. Bond, E. Buehler, and G. K. Teal, Phys. Rev. **83**, 1080 (1951).

[11] G. L. Pearson, W. T. Read, Jr., and W. L. Feldmann, Acta Met. **5**, 181 (1957).

[12] 1 part hydrofluoric, 3 parts nitric, and 10 parts acetic acid.

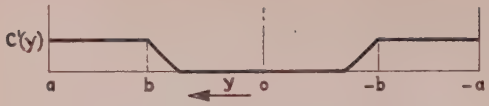

FIG. 3. Equivalent solute profile corresponding to the relieved stress distribution shown in Fig. 2.

will have a different datum, introduced by the integral term. This term, $(1/2a)\int_{-a}^{a} C dy$, is the average concentration across the wafer, the concentration at which the stress is zero. It satisfies the condition that the sum of the tensile forces is equal to the sum of the compressive forces. Where the datum concentration intersects the concentration profile, it defines the neutral x-z planes which separate the outside layers in the wafer which are in tension from the interior in compression.

In Fig. 2, the distribution of stresses across a diffused wafer induced by an arbitrary solute distribution is shown with the stress datum $\sigma_u=0$. Curves above the datum represent tensile stresses, those below, compressive stresses.

The presence of dislocations in the diffused layers of originally dislocation-free silicon[4] indicates that the dislocations were generated by the solute lattice contraction stresses and in turn partially relieved these stresses. Solid lines in Fig. 2 give the expected stress distribution if all tensile stresses above σ_r were reduced to this value. The new datum, $\sigma_r=0$, is determined by the requirement that the sum of the compressive forces equals the sum of the tensile forces. As a result of stress relief, the neutral planes are moved farther in from the surfaces of the diffused wafer. The greater the stress relief, the closer do the neutral planes approach the depth of solute penetration. Since the datum must be positive when the applied stresses are in tension, it is impossible for a neutral plane to penetrate farther than the depth of solute penetration.

From the stress distribution resulting from partial stress relief, we can define an equivalent solute profile $C'(y)$. This hypothetical solute distribution is that which will produce the specific stress distribution on the basis of solute lattice contraction alone. Figure 3 illustrates the equivalent concentration profile corresponding to the relieved stress distribution shown in Fig. 2 by solid lines. We can describe the equivalent concentration distribution as follows:

$$\begin{aligned} C'(y)&=C(y) \quad 0<|y|<b \\ C'(y)&=C(b) \quad b<|y|<a. \end{aligned} \tag{9}$$

We can now concentrate on the volume of the diffused layer lying between the planes $y=a$ and $y=b$, Fig. 2, in which the stress has been partially relieved. Let us examine an element of volume in the form of a thin plate parallel to the wafer surface. It is 1 cm in the x and z directions and dy cm thick. In Fig. 4 let C be the solute concentration at the bottom surface y of the element. The concentration at the upper surface $y+dy$ then becomes $C+(\partial C/\partial y)\cdot dy$.

Let the dislocation density (total length of dislocations per unit volume) be ρ. We note that each positive edge dislocation contributes one extra plane of atoms that exists at $y+dy$ that did not exist at y. The increase Δz in the z dimension of the element is equal to the total number of dislocations in the element ρdy multiplied by the contribution of each dislocation α, i.e.,

$$\Delta z=\rho\alpha dy.$$

In general, α is the component in the z direction of the edge component of the Burgers vector of the dislocation. It is a function of the slip system of the material and the crystallographic orientation of the diffused wafer. In the Appendix the value of α is calculated for silicon wafers with {111} diffusion surfaces.

The solute lattice contraction between y and $y+dy$, $\Delta'z$, is equal to the product of the lattice strain coefficient β and the difference in concentration, i.e.,

$$\Delta'z=\beta\cdot(\partial C/\partial y)\cdot dy.$$

If dislocations relieve the solute lattice contraction strain within the element, we have an expression for the dislocation density in terms of the solute concentration gradient:

$$\rho=(\beta/\alpha)\cdot(\partial C/\partial y).$$

This expression gives the dislocation density between $y=b$ and $y=a$. The solute strain has been relieved here but the residual stress distribution given in Fig. 2 remains. The level of residual stress is directly dependent upon the depth in the diffused layer to which the dislocations penetrate. This determines b and thereby $C'(y)$.

We can now give the equivalent concentration at any point in the diffused layer as a function of the solute concentration and dislocation density distribution in the diffused layer:

$$C'(y)=\int_0^y\left(\frac{\partial C}{\partial y}-\frac{\alpha}{\beta}\cdot\rho\right)dy. \tag{10}$$

V. TOTAL NUMBER OF DISLOCATIONS

The dislocation density distribution in a diffused wafer may be described as follows:

$$\begin{aligned} \rho&=(\beta/\alpha)\cdot(\partial C/\partial y) \quad b<|y|<a \\ \rho&=0 \quad 0<|y|<b. \end{aligned} \tag{11}$$

The total number of dislocations N per unit length of diffused layer, the z dimension in Fig. 4, can be determined as follows:

$$\begin{aligned} N&=\int_b^a \rho dy=(\beta/\alpha)\int_b^a (\partial C/\partial y)\cdot dy \\ N&=(\beta/\alpha)[C_s-C(b)]. \end{aligned} \tag{12}$$

hen $C_s \gg C(b)$ as often happens, N will be directly oportional to the surface concentration.

VI. MECHANISM OF DISLOCATION GENERATION

As has been described, the highest stress that de-lops is found at the surface at the very beginning of e diffusion process. As diffusion proceeds, this surface ress decreases as a result of increase of the datum, crease of the surface concentration, or both. The itial stress, including the effect of surface stress raisers, ay exceed the stress σ_g necessary to generate disloca-ons. When this happens, the stress can be developed ly to this level. The total number of dislocations nerated, in number per unit length of cross section, N, where

$$N=(\beta/\alpha)(C_s-C_g) \tag{13}$$

d where C_g is determined by σ_g according to Eq. (8). The dislocations generated must lie in the surface d their Burgers vectors must have a positive edge mponent in the surface. Otherwise, they could not ieve the solute lattice contraction strain in the surface. With increasing diffusion, the stress imposed by tice contraction decreases at the surface. The trans-rt of solute into the interior of the silicon wafer in-eases the stress there. These stresses are equalized by e movement of dislocations into the interior. The stribution of dislocations is given by Eq. (11).

After equalization, the residual stress is less than σ_g. his removes the possibility of generating additional slocations at the surface.

A. Constant Surface Solute Concentration Diffusion

When diffusion proceeds under conditions of constant rface concentration, the total number of dislocations mains fixed at $N=(\beta/\alpha)(C_s-C_g)$. The dislocations e dispersed over a greater depth as b increases with ffusion. The form of the dislocation distribution can obtained by substituting the concentration erfc dis-ibution, Eq. (1), into Eq. 11. This gives us for $<|y|<a$

$$\rho=\frac{\beta}{\alpha}\cdot\frac{C_s}{(\pi Dt)^{\frac{1}{2}}}\cdot\exp-\left[\frac{(a-y)^2}{4Dt}\right]. \tag{14}$$

hus, for an erfc solute profile we have a Gaussian dislocation distribution from the surface in to point b, where the dislocation density drops to zero.

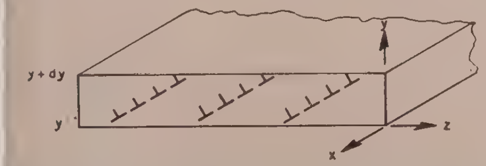

FIG. 4. Element of a diffused layer of a wafer whose solute strain s been partially relieved by the generation and distribution of olcations.

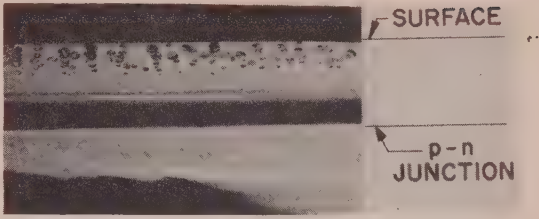

FIG. 5. Etched cleavage plane showing a diffused layer produced by the closed-tube diffusion of boron into n-type silicon. The source of diffusant, KBH_4, was sealed in a quartz tube with the silicon wafers and the tube was then held at 1225°C for 75 hr. The junction depth as shown is 79 μ. The wafer surface was prepared by chemical polishing.

Figure 5 is a photomicrograph of a diffused layer produced by the closed-tube diffusion of boron into n-type silicon. This technique was chosen as it approximates constant surface concentration conditions. A significant feature of the etch-pit distribution is the fact that it penetrates only about halfway into the diffused layer.

B. Finite Surface Solute Source Diffusion

In the two-step diffusion process previously described, the prediffusion step can be considered as occurring under conditions of constant surface concentration. The redistribution step produces a Gaussian distribution of the solute, the surface concentration C_s decreasing as diffusion proceeds. From Eq. (12) we might expect that as C_s drops off there would be an excess of dislocations and $C(b)$ would drop off to zero, signifying complete relief of residual stress. However, in order to relieve the residual stresses, dislocations must move into the area of solute penetration. The stress necessary to move the dislocations through the crystal against resistances such as Peierls force and impurity locking is the new residual stress σ_0. Since the temperature at which the dislocations move is high, the rate low, and the mechanism partly by climb, σ_0 will be relatively low.

For the residual stress to remain constant during the diffusion, excess dislocations must escape at the surface. Equation (11) would then describe the dislocation density distribution and Eq. (12) would give the total number of dislocations at any one time. On combining a Gaussian solute concentration with Eq. (11) we have for $b<|y|<a$

$$\rho(y)=(\beta/\alpha)\cdot[(a-y)/4Dt]\cdot C(y). \tag{15}$$

The maximum dislocation density occurs at a depth of $(2Dt)^{\frac{1}{2}}$ from the surface and is equal to $0.428(\beta/\alpha)\cdot[C_s/(Dt)^{\frac{1}{2}}]$ or approximately $0.428N/(Dt)^{\frac{1}{2}}$ when $C_s \gg C(b)$.

Figure 6 is a photomicrograph of a diffused layer produced by a two-stage open-tube diffusion of phosphorus into p-type silicon. One significant feature is

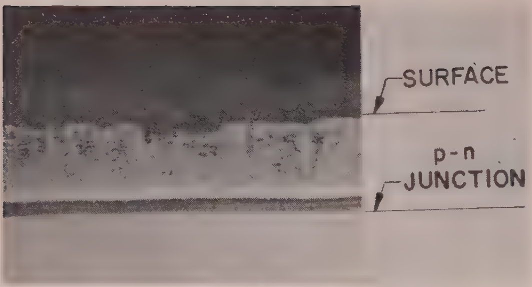

FIG. 6. Etched cleavage plane showing the diffusion layer produced by a two-stage open-tube diffusion of phosphorus into p-type silicon. The source of the diffusant, P_2O_5, was passed over the heated wafers for a few hours to form a phosphorus—containing glass on the silicon surface. Phosphorus was absorbed by the wafers by heating them for 18 hr at 1225°C. Following this, the glass was stripped from the wafers with hydrofluoric acid and the wafers were returned to the furnace for an additional 125 hr at 1225°C. The junction depth as shown is 93 μ. The wafer surface was prepared by mechanical lapping.

that, unlike Fig. 5, the etch pits here penetrate almost up to the p-n junction. Another is that the etch-pit density reaches a maximum part way between the surface and the junction, as predicted for a Gaussian concentration distribution.

Studies of actual concentration distributions by measurements of sheet resistivities indicate that they are in the main neither exactly Gaussian or erfc.[13] Determination of the dislocation distribution in the diffused layer would indicate what the actual concentration distribution is.

VII. RESIDUAL STRESS IN DIFFUSED WAFERS

The level of residual stress in a diffused wafer is of practical interest as it is certain to affect the wafer in further operations such as lapping and additional heat treatments. It is also of academic interest, being related to the stresses required to generate dislocations and to move them.

We can calculate this stress by introducing the equivalent concentration of Eq. (9) into Eq. (5). The calculation requires the same basic assumption as was made for the determination of the maximum unrelieved stress, namely, that the coefficient of thermal expansion is unaffected by the small concentrations involved. The desired relation is Eq. (16).

$$\sigma_r = \frac{\beta E}{1-\nu} C(b) \cdot \frac{b}{a} + \frac{2\beta E C_s (\pi D t)^{\frac{1}{2}}}{a(1-\nu)\pi} \times [1 + b\pi^{\frac{1}{2}} \operatorname{erfc} b - \exp(-b^2)]. \quad (16)$$

To apply this equation we need values for C_s, b, and $C(b)$. The first can be obtained by applying the method of Backenstoss,[14] and the second by noting the depth of penetration of the dislocation etch pits into the diffused layer. Finally, $C(b)$ can be obtained by substituting C_s and b into Eq. (1) or (2), whichever i applicable.

TABLE I. Surface dislocations and their slip systems.

Slip system	Slip plane	Burgers vector[a]	Dislocation direction
1	$(11\bar{1})$	$a[011]/2$	$[110]$
2	$(11\bar{1})$	$a[101]/2$	$[\bar{1}10]$
3	$(1\bar{1}1)$	$a[110]/2$	$[\bar{1}01]$
4	$(1\bar{1}1)$	$a[011]/2$	$[\bar{1}01]$
5	$(\bar{1}11)$	$a[110]/2$	$[0\bar{1}1]$
6	$(\bar{1}11)$	$a[101]/2$	$[0\bar{1}1]$

[a] a = lattice constant.

APPENDIX

In the derivation of Eq. (9), α was defined as th component in the z direction of the edge component c the Burgers vector of the dislocation. We can illustrat the calculation of this value easily for silicon, whos slip planes are **{111}** and whose slip directions are ⟨110

In Fig. 7, the base of the **{111}** tetrahedron, the (111 plane, represents the wafer surface. Since the dislocations must lie in the surface plane, only the six sli systems listed in Table I can be activated. The Burger vector in slip system 1 can be resolved into screw ar edge components. The edge component can be furth resolved into a component lying in the surface plan and one normal to it.

$$\frac{a}{2}[011] = \frac{a}{4}[110] + \frac{a}{4}[112]$$

$$\frac{a}{4}[112] = \frac{a}{3}[111] + \frac{a}{12}[\overline{11}2].$$

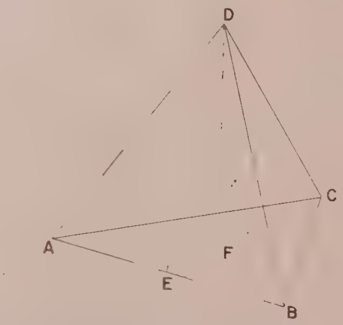

FIG. 7. The **{111}** tetrahedron showing the orientation of t various slip planes, dislocations, and Burgers vectors. These a as follow:

$ABC = (111)$ $DE = [112]$ $AB = [\bar{1}10]$ $DA = [011]$
$ABD = (11\bar{1})$ $DF = [111]$ $BC = [0\bar{1}1]$ $DB = [101]$
$BCD = (\bar{1}11)$ $EF = [\overline{11}2]$ $CA = [\bar{1}01]$ $DC = [110]$
$ACD = (1\bar{1}1)$.

---

[13] T. J. LaChapelle (personal communication).
[14] G. Backenstoss, Bell System Tech. J. **37**, 699 (1958).

gure 8 illustrates the surface plane components of the ge components of the Burgers vectors of the six p systems.

If our cross-sectional plane is the $(11\bar{1})$ cleavage ne, our z direction becomes $[1\bar{1}0]$. The only contribuon to strain in the z direction comes from the dislocaons lying in the $[\bar{1}01]$ and $[0\bar{1}1]$ directions. Their rface edge components can be resolved further as lows;

$$\frac{a}{12}[\bar{1}2\bar{1}]=\frac{a}{24}[11\bar{2}]+\frac{a}{8}[\bar{1}10]$$

$$\alpha=\frac{a}{8}[110]=\frac{a(2)^{\frac{1}{2}}}{8}.$$

milar calculations for a $\{100\}$ surface plane yield a ue for α that is twice as large.

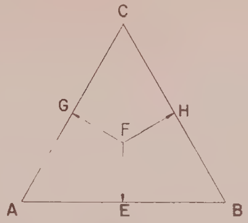

FIG. 8. The components of the edge components of the Burgers vectors lying in the (111) surface plane for the six possible slip systems.

$FE=a[\bar{1}\bar{1}2]/12$, $FG=a[\bar{1}2\bar{1}]/12$, $FH=a[2\bar{1}\bar{1}]/12$.

ACKNOWLEDGMENTS

The author wishes to thank his colleagues W. R. Wilcox, F. T. C. Bartels, T. J. LaChapelle, P. Friebertshauser, N. Sandler, and A. Stevenson for helpful discussions of various aspects of diffusion and dislocation theory.

Superconductor-Transition Switching Time Measurements Using a Superconductive Radio-Frequency Mixer*

DONALD L. FEUCHT
Department of Electrical Engineering, Carnegie Institute of Technology, Pittsburgh 13, Pennsylvania

AND

JAMES B. WOODFORD, JR.
Aerospace Corporation, Los Angeles 45, California

(Received April 14, 1961)

The transition properties of thin superconducting tin films are determined through measurements on a new device, the superconductive radio-frequency mixer. An equivalent circuit for this device is presented which permits the prediction of mixer performance using static transmission curves for the particular films employed. Experimental transmission curves and their characteristics are discussed. The measured mixer performance is compared with theoretical performance for operation in the frequency range of 240 to 840 Mc. It is shown that the transition speed of the superconducting thin films can be determined and that film-switching times are at least as short as 0.625 nsec.

INTRODUCTION

SINCE the liquefaction of helium and the subsequent discovery of superconductivity by Kammerlingh Onnes,[1] a great deal of effort has been applied in searches for new superconducting materials, and in broadening the understanding of the phenomenon of superconductivity. Recently it has been found possible to advantageously employ the properties of superconductors in circuit elements for use in computers and related devices.

Buck[2] has reported on the cryotron, a superconducting computer-memory element. In his original wor with bulk superconductors, he found that the "*L/* time constant of a cryotron" imposes a limit to th speed with which the memory device may be switche from one state to the other. To reduce this switchin time cryotrons have been developed that use evaporate thin films. Newhouse and Bremer[3] have reported on thin film cryotron with a switching time of less tha one microsecond.

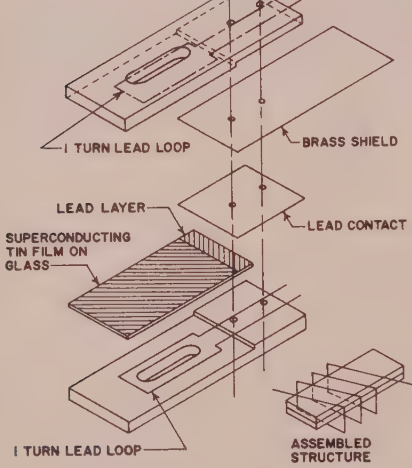

FIG. 1. Experimental shielded loop configuration of a superconductive radio-frequency mixer.

Crowe[4] has developed a high-speed, high-capacit thin film memory device based on the principle trapped flux. With this device switching speeds of th order of 10 nsec have been obtained. Work with bot cryotrons and trapped-flux units have suggested tha switching speeds obtained to date have been limited b circuit considerations rather than the superconductin transition phenomenon in the film itself. Douglass an Maxwell[5] have recently reported on preliminary obse vations which indicate the phase transition may occur 0.25×10^{-10} sec. A major purpose of this investigation the switching properties of thin superconducting films to avoid some of the circuit limitations in determinin the switching speed of superconducting thin films of t in a transition between the normal-conducting ar superconducting state.

The problem of determining the switching properti of thin superconducting films was approached throug measurements on a new device, the superconducti radio-frequency mixer. This device uses a thin film high-purity tin, evaporated on a suitable substrat which serves as a flux shield in the coupling pa between an input and an output loop. The couplir loops are embedded in small pieces of polystyrene whi are clamped to a piece of 0.010-in. brass. The film whi is held between these loops has a heavy layer of le deposited on one end which serves to electrically ground the film to the brass through a piece of 0.005-in. lead foil. The assembled configuration is shown in Fig. 1. A radio-frequency local oscillator signal is fed to a field coil surrounding the film-loop assembly, and serves to switch the shielding material in and out of the superconducting state at a rate equal to twice the oscillator frequency. A signal fed to the input loop is thus mixed with a signal of twice the local oscillator frequency and a signal of the difference frequency is retrieved in the output loop. Measurements are made of the quantities involved on a steady-state basis so that circuit time constants in the configuration do not impose a direct limit on observations of the switching speed of the film. From observations of the operating frequency and performance of the mixer the switching speed and characteristics of the film transition can be deduced.

---

* Support for this work was provided in part by the International Business Machines Corporation, the Office of Naval Research and the U. S. Army. This is a portion of the work submitted by D. L. Feucht as partial fulfillment of the requirements for the Ph.D. degree at Carnegie Institute of Technology.

[1] H. K. Onnes, Commun. Kammerlingh Onnes Lab. Univ. Leiden, Suppl. **34b**, 55 (1913).

[2] D. A. Buck, Proc. Inst. Radio Engrs. **44**, 482 (1956).

[3] V. L. Newhouse, J. W. Bremer, and H. H. Edwards, Pr Inst. Radio Engrs. **48**, 1395 (1960).

[4] J. W. Crowe, IBM J. Research Develop. **1**, 294 (1957).

[5] D. Douglass and E. Maxwell, Proceeding of the Symposiu on Superconductive Techniques for Computing Systems, Ma 1960, p. 238.

SUPERCONDUCTOR SWITCH MIXER

Basic Concept

An ideal switch, opened and closed at regular intervals, placed in the output of a signal source of frequency f_1 would produce at its terminals an interrupted signal, as shown in Fig. 2. This discontinuous output contains frequency components corresponding to the input signal frequency f_1, the interruption rate of the switch f_0, and combinations of these frequencies $f_1 \pm n f_0$. By an appropriate filter, a specific component such as the difference frequency $f_1 - f_0$ could be selected at the output and the device would then serve as a mixer.

A superconductor may act as a switch in either of two related ways. Its magnetic property of flux exclusion in the superconducting state may be utilized by employing the superconductor as a flux shield between an input and an output loop. Alternatively, the rapid change of electrical conductivity from a finite value in the normal-conducting state to infinity in the superconducting state may be used as a switch by short-circuiting the signal through a strip of a superconducting material. In either method a signal appears at the output only when the superconducting material is in the normal-conducting state. The superconductor in either instance may be driven from the superconducting state to the normal-conducting state by means of a magnetic field. This magnetic field may result either from a current flowing in the superconductor itself, or from an external source, such as a coil wrapped around the superconductor. If the magnetic field has no dc component but is alternating at some frequency $\frac{1}{2} f_0$ the transition from a superconducting to normal-conducting state will occur twice within a period $2/f_0$, since the transition depends on the magnitude rather than the sign of the magnetic field. Consequently, the superconducting-to-normal-conducting transition will take place at a rate equal to f_0, twice the frequency of the applied field. The effective switching frequency of the local oscillator is thus defined as f_0.

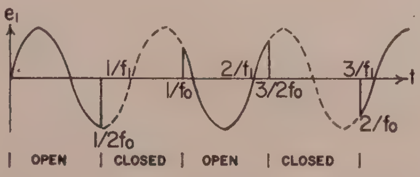

FIG. 2. Interrupted output signal of an ideal switch.

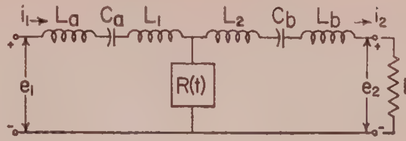

FIG. 3. Equivalent circuit of a superconductor mixer.

Four-Terminal Equivalent Circuit

If it is assumed that no signal is received in the output when the film is in the superconducting state and that the total input signal strength appears at the output when the film is in the normal-conducting state, then either method of mixing may be represented by the equivalent circuit of Fig. 3.

In the equivalent circuit L_a and C_a are reactive elements that are inserted in series with the leads to the input of the device in order to cancel by resonance the lead inductance L_1 at the input signal frequency f_1. Similarly C_b and L_b are reactive elements that are inserted in the output circuit to be resonant with the output lead inductance L_2 at the desired intermediate frequency $f_1 - f_0$. In this manner the output network serves to select the desired intermediate frequency.

In the equivalent circuit the transition of the superconducting film from one state to the other is represented by a resistance $R(t)$ which varies with time. $R(t)$ is a periodic function whose particular form is dependent upon the shape of the transition curve of the film in the device. $R(t)$ has a maximum value of R_0 when the film is in the normal-conducting state and a value of zero when the film is in the superconducting state. Since $R(t)$ is finite and periodic it may be represented by a Fourier series. It then becomes possible to calculate the performance of the mixing device and to determine input and output impedances.

If it is assumed that the transition from the normal to the superconducting state is identical with the inverse transition, $R(t)$ will possess symmetry about the half-cycle point. Time may be picked so that $R(t)$ is an even function reducing the expression of $R(t)$ to a Fourier series of cosine terms. If f_0 represents the frequency of superconducting to normal-conducting transitions, twice the frequency of the applied alternating magnetic field, the Fourier series expression for $R(t)$ is

$$R(t) = R_0(a + b \cos\omega_0 t + c \cos 2\omega_0 t + d \cos 3\omega_0 t + \cdots), \quad (1)$$

where $\omega_0=2\pi f_0$ and a, b, c, d, etc., are arbitrary constants whose value is determined by the manner in which the film switches from one state to the other. Let the input signal frequency f_1 be greater than the effective local oscillator switching frequency f_0 and the intermediate frequency component f_2 be selected such that $f_2=f_1-f_0$. As a result of the series resonant circuits in the leads to the mixer, the only component of the current in the input is at a frequency f_1 and the only component of the current in the output is at a frequency f_2. Let $i_1=I_1\cos(\omega_1 t+\theta_1)$ be the current flowing into the device and $e_2=E_2\cos[(\omega_1-\omega_0)t+\theta_2]$ be the voltage appearing across the load resistance R, where $\omega_1=2\pi f_1, (\omega_1-\omega_0)=2\pi(f_1-f_0)$ and where θ_1 and θ_2 are constants. Using the Fourier series representation for $R(t)$ as given by (1) and the expression for i_1 and e_2, the voltage across $R(t)$ is

$$\begin{aligned} e=aR_0I_1\cos(\omega_1 t+\theta_1) & \\ -(R_0/R)aE_2\cos[(\omega_1-\omega_0)t+\theta_2] & \\ +\tfrac{1}{2}bR_0I_1\cos[(\omega_1-\omega_0)t+\theta_1] & \\ -\tfrac{1}{2}(R_0/R)bE_2\cos(\omega_1 t+\theta_2), & \quad (2) \end{aligned}$$

plus additional terms involving neither ω_1 nor $\omega_1-\omega_0$. Selecting only those components of the voltage across $R(t)$ at a frequency f_1 gives the input signal voltage e_1.

$$e_1=aR_0I_1\cos(\omega_1 t+\theta_1)-\tfrac{1}{2}(R_0/R)bE_2\cos(\omega_1 t+\theta_2). \quad (3)$$

Collecting the terms of (2) which have a frequency of f_1-f_0 gives

$$\begin{aligned} E_2\cos(\omega_2 t+\theta_2) & \\ =\tfrac{1}{2}bR_0I_1\cos(\omega_2 t+\theta_1)-aE_2(R_0/R)\cos(\omega_2 t+\theta_2), & \quad (4) \end{aligned}$$

where $\omega_2\equiv\omega_1-\omega_0=2\pi(f_1-f_0)$. Equation (4) will be satisfied for $\theta_1=\theta_2$ or $\theta_1+\pi=\theta_2$. For these two cases

$$E_2=\pm\tfrac{1}{2}bR_0RI_1/(R+aR_0), \quad (5)$$

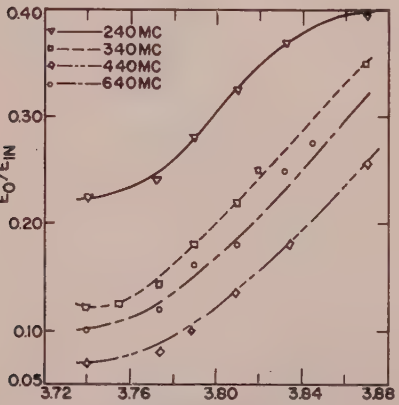

FIG. 4. Transmission E_0/E_{in} as a function of temperature with no applied H at several input signal frequencies for thin superconducting film #145.

where the positive sign indicates $\theta_1=\theta_2$ and the negative sign indicates $\theta_1+\pi=\theta_2$. Inserting this value for E_2 into (4) gives

$$e_1=R_0I_1[a-\tfrac{1}{4}b^2R_0(R+aR_0)^{-1}]\cos(\omega_1 t+\theta_1) \quad (6)$$

for either set of values for θ_1 and θ_2. The input impedance for the device is

$$R_{\text{in}}=E_1/I_1=R_0[a-\tfrac{1}{4}b^2R_0(R+aR_0)^{-1}]. \quad (7)$$

The output power which is delivered to the load resistance R is

$$P_{\text{out}}=\tfrac{1}{2}E_2^2/R=\tfrac{1}{8}R[bR_0I_1/(R+aR_0)]^2. \quad (8)$$

Power and Efficiency

In order to find the maximum output power which may be obtained from the mixer in terms of the available input power, let the input be supplied from a generator with an output voltage $E\cos\omega_1 t$ and an internal impedance R_1+j0. This may be transformed by an ideal transformer of turns ratio α to maximize the power transferred by matching the effective source impedance α^2R_1 to the input impedance of the mixer.

The available power from this source is

$$P_{\text{av}}=\tfrac{1}{2}[(\tfrac{1}{2}\alpha E)^2/\alpha^2R_1]=\tfrac{1}{8}(E^2/R_1). \quad (9)$$

The maximum output power may then be calculated in terms of this available power. If the phase angle $\theta_1=0$ the output power may be expressed as

$$P_{\text{out}}=\frac{\tfrac{1}{2}b^2R_0^2E^2\beta R}{[2R(aR_0+\beta R_1)+2a\beta R_0R_1+(2a^2-b^2/2)R_0^2]^2} \quad (10)$$

for $\beta=\alpha^2$. Maximizing this expression for the power out with respect to R yields

$$P_{\text{out}}=\frac{\tfrac{1}{16}b^2R_0^2E^2\beta}{[2a\beta R_0R_1+(2a^2-b^2/2)R_0^2](aR_0+\beta R_1)}. \quad (11)$$

Maximizing this expression with respect to β, and hence the input source impedance, gives for the maximum output power attainable from the mixer with either configuration

$$P_{\text{out}}=\frac{b^2E^2}{32R_1[a+(a^2-b^2/4)^{\frac{1}{2}}]^2}. \quad (12)$$

The ratio of this power to the available power of the source is a measure of the efficiency of the device and is given by

$$P_{\text{out}}/P_{\text{av}}=\tfrac{1}{4}b^2[a+(a^2-b^2/4)^{\frac{1}{2}}]^{-2}. \quad (13)$$

The value of the load impedance R for this condition of maximum output power is

$$R=R_0(a^2-b^2/4)^{\frac{1}{2}}, \quad (14)$$

which is identical to the desired value of input impedance R_{in}.

The efficiency of the device as well as the image mpedances depend upon the manner in which the film witches from one state to the other. If the film switches nstantaneously from one state to the other as soon as he applied field passes through the critical value, the esistance $R(t)$ varies according to

$$R(t)=\tfrac{1}{2}R_0+(2R_0/\pi)(\cos\omega_0 t-\tfrac{1}{3}\cos 3\omega_0 t+\tfrac{1}{5}\cos 5\omega_0 t+\cdots),\quad(15)$$

where $\omega_0=2\pi f_0$ and f_0 is the effective switching frequency of the local oscillator. For this mode of operation the ratio of the maximum power output to the available input power is $P_{\text{out}}/P_{\text{av}}=1/7.74$ which corresponds to an 8.9-db loss inherent in the device when the film is switching in this idealized mode. The input and output mpedances have a value $R_{\text{in}}=R=0.386R_0$, where R_0 is the normal-conducting resistance of the material at its operating temperature.

If the film does not have an abrupt transition from one state to the other, but changes linearly with the absolute magnitude of the applied magnetic field, then ts resistance would vary from $R=0$ to $R=R_0$ like a rectified sine wave. It could then be expressed by a Fourier series as

$$R(t)=(2R_0/\pi)[1+(2/3)\cos\omega_0 t-(2/15)\cos 2\omega_0 t+(2/35)\cos 3\omega_0 t+\cdots],\quad(16)$$

where $\omega_0=2\pi f_0$ and f_0 is the effective local oscillator switching frequency. For this mode of operation the ratio of the maximum power output to the available nput power is $P_{\text{out}}/P_{\text{av}}=1/33.97$ which corresponds to 15.3-db loss inherent in the device when the film is switching in this mode. The input and output impedances have a value $R_{\text{in}}=R=0.6R_0$ where R_0 is the normal-conducting resistance of the material at its operating temperature.

The mixer will also function if, instead of using a local oscillator signal at one-half the desired switching frequency, a local oscillator signal of the desired switching frequency is superimposed upon a dc biasing field. If the film switches abruptly the result should be the same as that calculated for the ideal case for a local oscillator field of one-half the desired frequency and no bias field. If the film changes linearly from one state to the other with the absolute magnitude of the applied magnetic field, a different $R(t)$ is obtained as expressed by

$$R(t)=\tfrac{1}{2}R_0(1+\cos\omega_0 t),\quad(17)$$

where $\omega_0=2\pi f_0$ and f_0 is the effective local oscillator switching frequency. For this type of operation the ratio $P_{\text{out}}/P_{\text{av}}=1/13.93$ which corresponds to an inherent device loss of 11.44 db. The impedances R_{in} and R are then equal to 0.433 R_0.

The efficiency of the mixer may be calculated for other switching modes by selecting the appropriate unction for $R(t)$ and expressing it in a Fourier series.

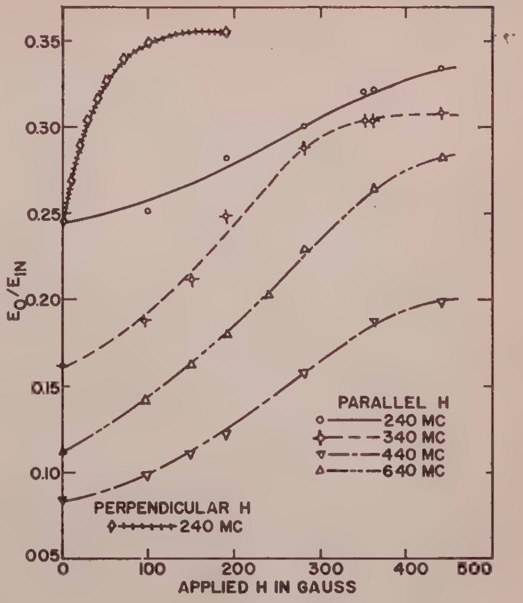

FIG. 5. Transmission E_0/E_{in} as a function of applied H at several input signal frequencies and at a bath temperature of 3.77°K for thin superconducting film #145.

EXPERIMENTAL RESULTS

Transmission characteristics of thin films of tin (approximately 1000 A thick) used in this work were obtained by supplying a radio-frequency signal to the input loop and retrieving this signal from the output loop. The ratio of the magnitude of the output signal E_0 to the magnitude of the input signal E_{in} is plotted as a function of temperature for a representative film in Fig. 4. The curve for 440 Mc appears below that for 640 MC as a result of a resonance in the measuring configuration near 440 Mc. All the films used exhibited a broad transition from the normal to the superconducting state, as the temperature was reduced, indicating impurities and strains in the film. Figure 5, depicting the ratio of the output signal E_0 to the input signal E_{in} as a function of the strength of the dc applied magnetic field, is more directly applicable to the operation of the configuration as a mixer. In addition to a broad transition, the slope of each curve is not constant. As a result, if the film is not being switched completely from one state to the other, the over-all efficiency of the mixer will depend upon its operating point on the transmission curve. Figure 5 also shows that if the magnetic field is applied perpendicularly to the plane of the film, the transition is accomplished with a much smaller value of applied H than if the field is applied parallel. This effect has been observed by other investigators[6] and indicates that portions of the film are being switched into the intermediate state with less field than is required to switch the film uniformly into the normal-conducting state.

---

[6] V. L. Newhouse and J. W. Bremer, J. Appl. Phys. 30, 1458 (1959).

From the static transmission curves of a film and from the calculations based on the four-terminal equivalent circuit, the efficiency of the mixer configuration with a given film can be predicted. Since the thin superconducting films tested exhibited a broad transition, the calculations based on the film switching linearly with the absolute magnitude of the applied magnetic field are best suited to describe the switching action of these films. The assumptions at the beginning of the calculations concerning the amount of input signal which is retrieved in the output loop for each film state are not valid for the films tested. From the transmission curves, Figs. 4 and 5, it is seen that the film still allows some input signal to be transferred to the output loop when the film is in the superconducting state. Similarly, when the film is in the normal-conducting state, not all the input signal appears at the output, but the film attenuates a portion of it. Thus, in addition to the inherent loss in the mixer due to the switching process, an additional film loss must be derived from the static transmission curves for each film in order to predict the total loss of the mixer. Let the ratio of the magnitude of the output signal E_0 to the magnitude of the input signal E_{in} when the film is in the superconducting state be designated as A, and the same ratio when the film is in the normal-conducting state be B. The difference in transmission between the two states is then given as $B-A$. With the input and output impedances matched to the same impedance level the theoretical power loss of the film in decibels is

$$F_L = -20 \log_{10}(B-A). \tag{18}$$

The total theoretical mixer loss is then the sum of the film loss, F_L and the loss inherent to the mixer because of the switching process, S_L.

Experimentally the impedances of the input loop and the output loop of the mixer are matched to the same impedance level. The over-all efficiency of the device is then dependent upon the relative values of the input signal, and the difference frequency output signal, E_2. Throughout the experiments the input signal and switching frequencies were chosen to give 40 megacycles as the difference frequency output. The actual power loss of the mixer in decibels is given by $20 \log_{10}(E_{\text{in}}/E_2)$. A graph of the theoretical and actual mixer loss as a function of frequency for two of the thin superconducting films tested is shown in Fig. 6. The scatter in the data in Fig. 6 is characteristic of all of the films tested and presumably is a result of thermal cycling of the film causing additional strains and finally cracks or islands in the film.

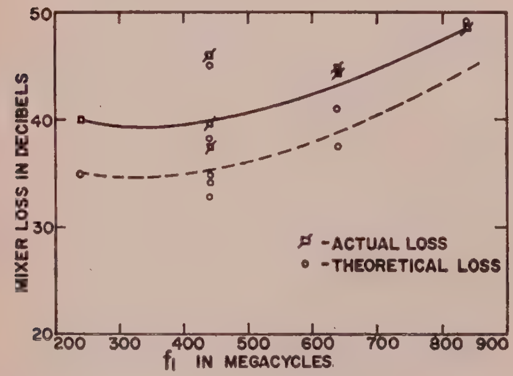

FIG. 6. Theoretical and actual mixer loss as a function of input signal frequency f_1 for thin superconducting film #145.

The theoretical and actual loss curves for each film have very similar shapes and lie close together, differing approximately by a constant factor. This indicates that the mixer loss may be fairly successfully predicted from the static transmission curves.

There is a maximum disagreement between theoretical and actual mixer loss of approximately 5 db. This corresponds to a voltage ratio of approximately 1.8 to 1. This discrepancy may have resulted from errors in experimental measurements or errors dependent on the fundamental properties of the thin film used. The film may be heated, thereby changing its operating temperature so that a different static transmission curve applies; or it is possible that different points of the film are not being switched simultaneously from one state to the other.

DISCUSSION

The most important result of this superconducting radio-frequency mixer investigation is the information it provides concerning the speed of transition of the thin superconducting film from one state to the other. In order for the device to function properly as a mixer, the film must be undergoing a transition under the influence of an applied radio-frequency magnetic field. The maximum frequency at which the mixer will operate should be a measure of the inherent switching speed of the thin film. It is expected that the mixer efficiency will drop as the switching frequency is increased to the point where the film can no longer switch as fast as is required by the applied magnetic field, but that an output signal at the intermediate frequency will still be detected. The mixer efficiency would be expected to decrease with increasing frequency from this point onward until no intermediate frequency component could be detected. Mere detection of an intermediate frequency component, therefore, is not enough to determine whether the film is switching completely. A measure of the efficiency of film switching can be derived from a comparison of the theoretical and actual efficiency of the mixer when it is operating at various frequencies. Figure 7 shows the ratio of the theoretical loss of the mixer in decibels to the actual experimental loss of the mixer in ecibels as a function of the input signal frequency for veral films. This ratio appears virtually constant for ach film investigated in the input signal frequency range f 240 to 840 Mc. This indicates that the film switches as mpletely at the highest input signal frequency of 40 Mc as it does at the lowest frequency of 240 Mc. he ratio of the theoretical mixer loss to the actual ixer loss lies close to unity indicating that the film is witching completely from one state to the other at all he frequencies considered.

The time required for the film to switch from one tate to the other and then back to the original state is qual to the reciprocal of the effective local oscillator requency. For the measurements made at the highest cal oscillator of 400 Mc, corresponding to an effective witching frequency of 800 Mc, the time required for he film to complete the transition from one state to the ther and then back again is 1.25 nsec. Assuming that he normal-conducting to superconducting transition equires the same time as the superconducting to ormal-conducting transition, the time required for the lm to change states is 0.625 nsec. There is no reason to believe that faster transition speeds are not possible. No higher frequency switching was investigated since the experimental configuration employed imposed a frequency limit of approximately 900 Mc.

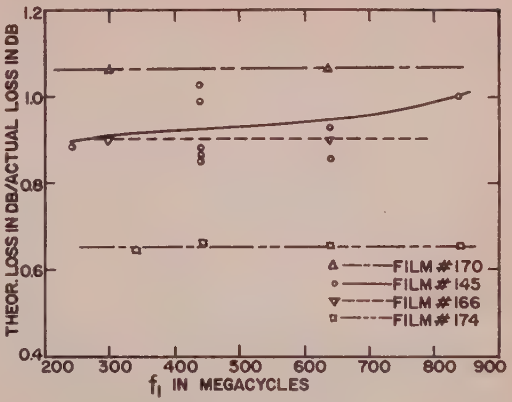

FIG. 7. Ratio of theoretical to actual mixer loss as a function of input signal frequency f_1 for several thin superconducting films.

JOURNAL OF APPLIED PHYSICS VOLUME 32, NUMBER 10 OCTOBER, 1961

Experimental Investigation of the Sumoto Effect*

William F. Pickard
Cruft Laboratory, Harvard University, Cambridge, Massachusetts

(Received March 23, 1961)

The rising of a dielectric liquid along high-voltage electrodes that are dipped into it is investigated. Qualitative results are given for a number of different combinations of electrode material and liquid. The effects observed for molybdenum-acetone systems, excited by low-frequency applied voltage are discussed in detail.

1. INTRODUCTION

IN 1956 Sumoto[1] reported the rising of liquid dielectrics along electrodes which were immersed in them and maintained at a high dc potential difference. The electrodes he used were copper or nickel, and the test liquids were chloroform, xylol, or benzol.

In this paper will be discussed: (i) A number of simple experiments to determine the effects of different combinations of liquid and electrode metal, first at dc and later at 60-cps ac; these studies lead to the conclusion that acetone-molybdenum systems are best suited to detailed investigation. (ii) Studies of the temporal variation of the effects, the influence of liquid temperature, and the influence of liquid purity. (iii) Experiments over the previously uninvestigated range of $\frac{1}{2}$ to 2500 cps. The rising of the liquid at ac is most peculiar in that for electrode wires of small diameter and frequencies of above 2–3 cps it occurs not as a sheath about one electrode, as in the dc case, but as a small bead of liquid around each electrode; these beads rise and fall with a definite period. It is believed that this effect has not been reported previously.

Although Sumoto investigated only the dc phenomenon, the rising of liquids will, in this paper, be referred to as Sumoto effects regardless of the frequency of the applied voltage.

2. EFFECT OF VARIOUS LIQUID-METAL COMBINATIONS

The apparatus used for this portion of the work was the cell shown in Fig. 1. The system was illuminated by a spotlight which was placed beneath the glass bead at the bottom of the stem.[2] The electrodes used were wires of various metals and diameters, cleaned by polishing with crocus cloth and washing in acetone; they were straightened as much as possible by placing them under tension. The liquids used were, insofar as was readily possible, of reagent grade.

In the first tests, the height of rise of acetone along the electrodes was observed for dc voltages. The metals used were molybdenum, tungsten, tantalum, columbium, nickel, silver (fine), copper (OFHC), aluminum, gold (18K), magnesium, titanium, lead, cadmium, indium, platinum-clad molybdenum, and stainless steel. The observed effects increased with the applied voltage and decreased with increasing electrode diameter and spacing.[3] The heights of rise were somewhat different on the anode and the cathode; in general, the greater the rise on one electrode the less on the other. The metals of group VIB of the periodic table gave the largest rise; and of these, molybdenum was generally used since it could most easily be drawn and machined. When some of the metals were retested at ac (60 cps), it was observed that the height to which acetone would rise was not significantly inferior to that obtained using molybdenum electrodes. That is, with acetone the superiority of group VIB metals is most clearly seen only at dc.

When 60-cps ac and acetone were used, the pronounced polarity dependence disappeared. The rising of the liquid with dc tended to be along one electrode in the form of a sheath. The rising at ac was in the form of a small bead of liquid on each electrode; these beads rose and fell periodically. With either ac or dc there tended to be a transfer of liquid (as spray) between electrodes when the applied voltage reached sufficiently

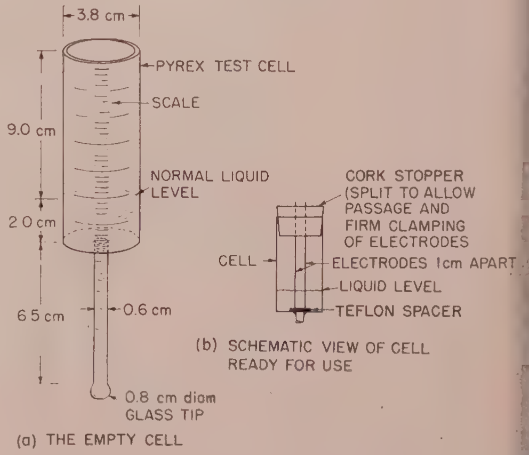

Fig. 1. Test cell for Sumoto effects.

---

* The research reported herein was supported by National Science Foundation grants.

[1] I. Sumoto, Ôyô Butsuri **25**, 264 (1956).

[2] A somewhat more detailed account of the experiments described in this paper is given in W. F. Pickard, Cruft Lab. Tech. Rept. No. 337 (1961).

[3] The studies of the effect of spacing were made using a cell somewhat different from that shown in Fig. 1.

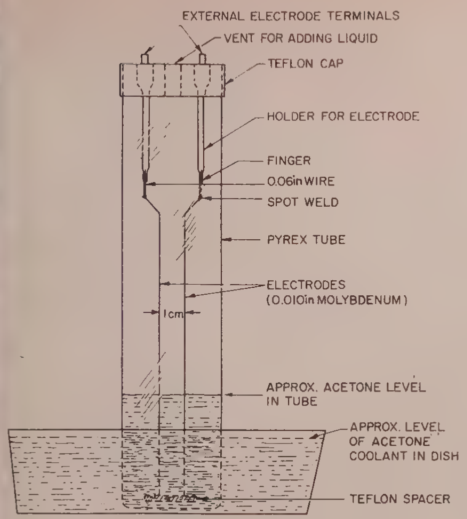
EXTERNAL ELECTRODE TERMINALS
VENT FOR ADDING LIQUID
TEFLON CAP
HOLDER FOR ELECTRODE
FINGER
0.06in WIRE
SPOT WELD
PYREX TUBE
ELECTRODES (0.010in MOLYBDENUM)
1cm
APPROX. ACETONE LEVEL IN TUBE
APPROX. LEVEL OF ACETONE COOLANT IN DISH
TEFLON SPACER

G. 2. Device for studying temporal variation of Sumoto effects.

gh levels. In general, the effects at ac were more able and easier to observe than those at dc.

A number of runs were made using 0.010-in. molyb- num electrodes, 60-cps voltages, and various liquids; eshly prepared electrodes were used to test each uid. Among the liquids tested were *n*-octane, nitro- nzene, chlorobenzene, benzene, carbon tetrachloride, ichloroethylene, ethyl ether, iso-amyl acetate, methyl hyl ketone, toluene, methyl alcohol, ethylene glycol, hyl formate, pentane, *n*-propyl alcohol, and methyl etate. Acetone and methyl ethyl ketone gave by a rge factor the greatest rises with acetone giving larger sults than methyl ethyl ketone. A repeat of these runs ing 0.010-in. tantalum electrodes gave similar results.

Since acetone and methyl ethyl ketone, both ketones, ere characterized by large Sumoto effects, some studies ere made to examine the effect of chemical structure behavior. Using molybdenum electrodes and both ternating (60 cps) and direct applied voltages, the llowing ketones were studied: methyl methyl cetone), methyl ethyl, methyl iso-propyl, ethyl hyl, methyl *n*-propyl, methyl iso-butyl, butyl ethyl, ethyl amyl, and methyl hexyl. The effects tended to e more pronounced at ac and to decrease very rapidly one ascended the series. Acetone was found to give e largest effects by far. The effects of chemical struc- re were also studied by comparing acetone with its omer ally alcohol and by comparing with one another e four butyl alcohols. Allyl alcohol gave a negligible se along the electrodes at voltages at which acetone ould rise several centimeters. The butyl alcohols all ave much smaller effect than acetone although they ehaved differently from one another, *n*-butyl and iso- utyl giving the largest effects at ac and *n*-butyl and rt-butyl giving the largest effects at dc.

In summation, the following comments can be made: (i) The rising of dielectric liquids along high-voltage leads dipped into them varies strongly from electrode metal to electrode metal and from liquid to liquid. (ii) The effect is also strongly conditioned by the nature of the applied voltage. (iii) The exact structure of the liquid molecules appears to be important since the isomers of a given compound tend to behave differently. (iv) Of the numerous liquids and electrode metals tested, the combination showing the largest Sumoto effects at both ac and dc is the acetone-molybdenum one.

3. VARIATION WITH TIME, TEMPERATURE, AND PURITY

For the experiments to be described in this section, the liquid was normally reagent-grade acetone and the electrodes were normally 0.010-in. molybdenum wires. The apparatus was different for the several experiments.

The setup to study temporal effects, less a thermometer and a scale for determining the height of rise, is shown schematically in Fig. 2. The coolant was evaporated by air from a small blower and provided a rough means of inhibiting the temperature rise of the liquid in the cell. In a typical run, acetone at ambient temperature is poured into the tube and the vent loosely corked; the applied voltage is then set to 4 kv (dc or 60-cps ac) and the temperature and height of rise monitored over a period of a few hours. Typical curves from such runs are shown in Fig. 3. With respect to temperature, it can be seen that the general tendency is monotonic increasing,[4] although the increase is much less rapid than would be the case in the absence of an external coolant; this upward tendency is about what one would expect from ohmic heating since the electric current (not shown in Fig. 3) exhibits roughly the same temporal variation. The rise shows no strong relationship to the temperature over the small range studied here, although

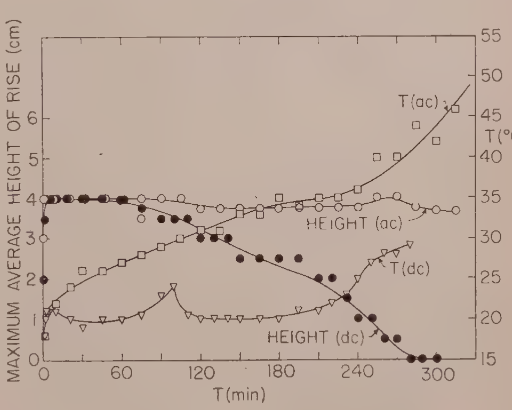

FIG. 3. Temporal variation of Sumoto effect.

---

[4] The local maximum near the 90-min point on the dc temperature curve was caused by the failure to control adequantly the coolant level and graphically illustrates the effect of the coolant.

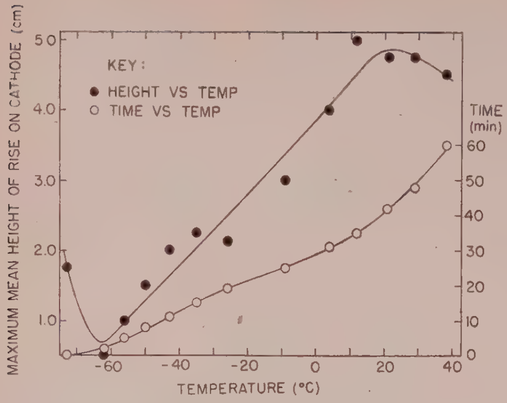

FIG. 4. The variation of dc Sumoto effect with temperature; 0.010-in. molybdenum electrodes spaced approximately 1 cm apart and held at 4-kv dc potential difference.

such a relationship does exist. The general conclusion is that ac effects are more stable than dc; this is not surprising since electrochemical processes tend to be more stable at ac because alterations in the properties of the fluid and the electrodes are slower. Whether the variation in current (temperature) with time is occasioned by alterations in the properties of the liquid or in the properties of the electrode surfaces is not made clear by this type of experiment.

The effects of temperature variation were measured by using an unsilvered Dewar flask as test cell. To make a run, reagent-grade acetone, chilled to near its freezing point, is poured into the Dewar and the rise and the temperature measured as functions of the time. A typical result is shown in Fig. 4. Clearly, the rise depends upon the temperature. The curve also illustrates the rolloff in the height which (cf. Fig. 3) occurs after about an hour in the dc effect. No explanation is known for the odd inflections in the height versus temperature curve although it can be stated that, due to the strong short-term instability in the height of rise which is characteristic of the dc Sumoto effect and due to the parallax error introduced by the necessity of placing the height-measuring scale several centimeters from the electrodes, it is difficult to measure the mean height of rise to better than about ±0.2 cm in a rise of 1.5 cm or larger.

Microanalytic techniques[5] were employed to study the mechanisms causing the observed effects. A cell of the type shown in Fig. 1 was used with reagent-grade acetone and one molybdenum electrode and one copper electrode and dc voltages. Spot tests indicated that for either polarity of the electrodes there was a transfer of molybdenum to the copper electrode and no transfer of copper. This would suggest, in accord with the theory of Stuetzer[6] that motion effects in dielectric liquids a the result of ion emission from the electrodes. Th distinct electrode processes of some sort are taking pla can also be inferred from the observation that in mo Sumoto experiments one or both of the electrodes w show the effects of corrosion over those portions whi were beneath the liquid surface.

Finally, a very important influence on the Sumo effect is the purity of the test liquid. As an examp consider the case of 0.010-in. OFHC copper electrod used in the apparatus of Fig. 1 and cleaned by polishin with crocus cloth and washing in acetone. If ordina reagent-grade acetone is used, no significant dc Sumo effect can be observed. If reagent acetone, dried passing it over anhydrous $MgSO_4$ is used, a catho rise of about 2 cm can be observed for 4-kv dc appli potential. As a general rule, the conductivity and t rise depend to a considerable extent upon the purity the liquid. In acetone the purity effects seem to be lea important at ac and in systems using molybdenu electrodes; this is fortunate since acetone is extreme difficult to purify and to keep pure.[7]

To conclude this section, the following summati can be made: (i) The ac Sumoto effect displays co siderably more temporal stability than the dc effec (ii) The effects are temperature dependent and can much reduced by lowering the temperature to near t freezing point of the liquid. (iii) The Sumoto effe appears to involve chemical action at the electrod and ion transfer. (iv) The state of purity of the te liquid is important.

4. ac SUMOTO EFFECT

As was mentioned earlier, when a balanced ac volta is applied between the electrodes of a test cell (Fig. 1 the tendency of the liquid is to rise along the electrod

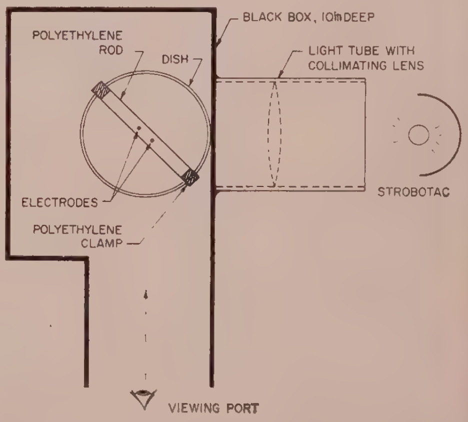

FIG. 5. Top view of apparatus for studying ac Sumoto effect.

---

[5] F. Feigl, *Spot Tests in Inorganic Analysis*, translated from the Spanish by Ralph E. Oesper (D. Van Nostrand Company, Inc., Princeton, New Jersey, 1958), 5th ed.

[6] O. M. Stuetzer, J. Appl. Phys. **31**, 131 (1960).

[7] A. Weissberger, E. S. Proskauer, J. A. Riddick, and E. Troops, *Techniques of Organic Chemistry, Volume VII: Organ Solvents* (Interscience Publishers, Inc., New York, 1955).

s a small bead on each electrode; these beads rise and ll periodically. If the ac voltage has a dc component that one electrode is always negative with respect to e other, a bead will appear on the negative electrode ly; that is, the forces producing the effect are polarity pendent. On the basis of these observations, it is ssible to make a few simple predictions[8]: (i) The ean maximum height of rise h will vary inversely as e applied frequency f. A certain amount of time will required for a bead to form and begin to rise up the ectrode; and the motion of this bead along the electode will be slowed by viscous drag. Thus, the height rve will lag the voltage curve, especially if the latter es quickly. Hence, as f rises the bead will be able to ach only successively smaller heights before the ltage curve peaks and the force raising the bead minishes. Therefore, for fixed voltages, h should crease as f increases. (ii) For fixed frequencies, h will ry directly as V, the rms value of the applied voltage. he greater the applied voltage, the greater should be e accelerating force on the bead and the height to hich it rises. (iii) There exists an rms voltage V_T, e threshold voltage, below which no bead will form. certain amount of force is necessary to overcome the rce of gravity. (iv) V_T will vary directly with f. The ne t necessary to form a bead and begin to raise it ill diminish as the applied voltage increases. Since t ould be less than $1/f$ if a bead is to be simply formed, must decrease with increasing f and, hence, V_T must crease. (v) The frequency of bounce ν_0 should equal for suitable f and V. (vi) But, if $\nu_0 \neq f$, then it should a subharmonic of f. This is not really obvious from *priori* consideration. However, subharmonic oscillan is not at all unusual in nonlinear systems, and in is case can be given a sort of heuristic justification f. reference 2).

The apparatus used consists of a Pyrex dish conining about 5 cm of acetone. As shown in Fig. 5, the sh is in a black box with three openings: one to admit the beam of a strobotac by means of which ν_0 was determined, one to permit visual observation, and one to pass the electrodes. The dish has along its bottom a polyethylene rod with holes drilled through it every 1 cm. The electrodes are fastened to the rod by passing them through holes the desired distance apart; they are then passed through a slot in the top of the box, pulled taut, and clamped into position. A centimeter scale fastened to the back of the box enables one to measure h.

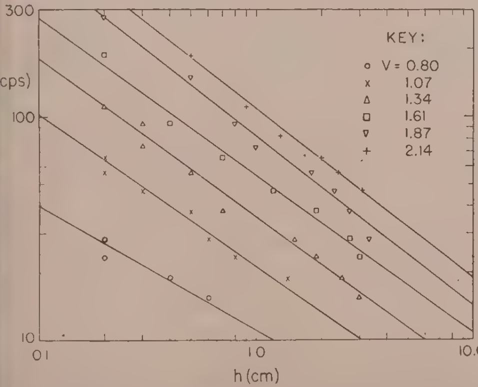

G. 6. f vs h for fixed voltages (in kv); 2-cm electrode spacing.

TABLE I. Computation of the parameters A and α for values of V.

V(kv)	A	α
0.80	77	1.8
1.07	98	1.5
1.34	150	1.4
1.61	270	1.4
1.87	320	1.3
2.14	440	1.3

The liquid used was reagent-grade acetone purified by drying over anhydrous magnesium or calcium sulphate and by subsequent filtering and distillation; for the data reported in Figs. 6–9, the acetone was dried over the calcium sulphate which is somewhat more effective[7] than the magnesium. The drying and distillation effected a marked decrease in the conductivity of the liquid. The electrodes used were 0.010-in. molybdenum wires cleaned by immersion in a hot 20% solution of potassium hydroxide.

Figure 6 shows the variation of h with f for various fixed sinusoidal voltages. As a result of experimental difficulties, h is known to only about ±0.1 cm below $h=1.5$ cm and ±0.2 cm above this point. f was determined to within about 2% using a good oscilloscope. V was measured to within about 4% with a voltmeter and a frequency-compensated voltage divider. The electrode spacing 2 cm was picked because it seemed to give a somewhat cleaner cut effect than the 1-cm spacing and a somewhat larger effect than greater spacings. The data plotted in Fig. 6 indicated that, very roughly, $h(f)$ is of the form

$$h = Af^{-\alpha}. \tag{1}$$

This agrees with prediction (i). Although there is a tendency for nonoscillatory data in general to lie in the neighborhood of straight lines on loglog paper, it is instructive to compute the parameters A and α for the several values of V; this has been done and the results are shown in Table I. A slight but definite falloff in α can be noticed as V increases. The steady increase in A is in accord with prediction (ii).

Figure 7 illustrates a typical run with f fixed and h and V variable. The data in this case roughly fit curves of the form

$$h = BV_K{}^{\beta}, \tag{2}$$

where V_K is the rms voltage in kilovolts. Actually, the curves for $f > 50$ cps show a distinct concavity to the

---

[8] These are discussed in considerably expanded detail in rence 2.

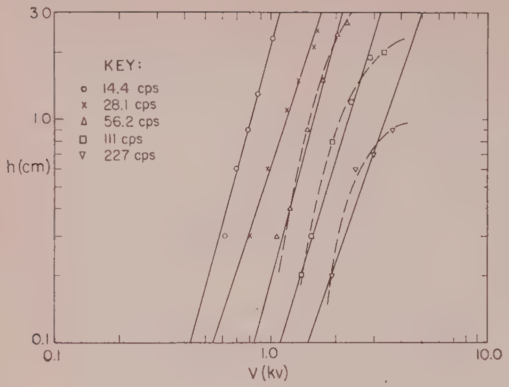

FIG. 7. h vs V for fixed frequency.

right; this agrees with the general observation that for large f the height tends to go up more slowly with increasing V, the added force going into increasing the size of the bead rather than its height of rise. Table II lists the calculated values of B and β for the several values of f. These data show, in accord with prediction (ii), that h increases with V for fixed f, and confirm, in accord with prediction (i), that h increases for decreasing f and fixed V.

Figure 8 illustrates the behavior of V_T with[9] f; predictions (iii) and (iv) are fully borne out. At higher frequencies (>300), one notices at V_T, in addition to the bead, a general rise of the liquid about each electrode; this is thought to be an example of polarity-independent dielectrophoretic forces.[10] Below 10 cps the curve will show a slight upward concavity continuing, it is thought, down to about 2 or 3 cps where the ac effect begins to shade into the dc and the rising of the liqui ceases to be in the form of beads.

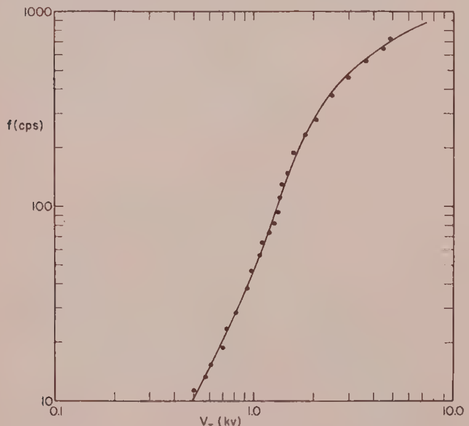

FIG. 8. Applied frequency vs threshold voltage.

Along with the data displayed in Figs. 6 and 7 wer collected data on the oscillation frequency of the beads a ν_0 being obtained for each h measured. Figure 9 illus trates the relationship of ν_0 and h; the units of ν_0 ar oscillations per minute but are commonly referred to a rpm. The points in Fig. 9 cluster along the line

$$\nu_0=425h^{-0.40}. \qquad (3$$

This relationship is one of the most reproducible en countered in the research performed. It has been con firmed using numerous different pairs of 0.010-in molybdenum electrodes and acetone dried with eithe $MgSO_4$ or $CaSO_4$; it appears to be independent of th electrode spacing. The mean of the data collected i nine separate experiments (two with 3-cm electrod spacing, three with 2-cm electrode spacing, four wit 1-cm electrode spacing) is

$$\nu_0=(424\pm11)h^{-(0.39\pm0.03)}. \qquad (4$$

Equation (4) gives partial confirmation to predictio (vi). To supplement Eq. (4), the following rule can b stated:

> A bead rising to a maximum height h will oscillate o the frequency $\nu_0=f/p$ lying nearest to the curv specified by (4).

Given this empirical rule, one can predict that th scatter of points about the line should be greatest fo low h and f since the subharmonics of f will be furthe apart (p small) in this region; Figure 9 confirms th prediction.

For the exact confirmation of predictions (v) and (v and of the rule relating ν_0 and h, one must study f, and ν_0 simultaneously. This has been done and, with th exception of very low frequencies and relatively hig voltages, the rules are confirmed to within the limits experimental accuracy. At subaudio frequencies an high voltages (h large) there is a marked tendency fo the beads to add mass rather than height with increasin voltage and to oscillate on a higher subharmon (p larger) than the one predicted. The factors in accu racy are the measurements of ν_0 and f. Where wel defined beads exist (f>3 cps) the uncertainty in measurement is, except in a region of transition betwee subharmonics, about 2% in both f and ν_0. In transitio

TABLE II. Calculated values of B and β for values of f.

f(cps)	B	β[a]
14.4	2.2	3.6
28.1	0.61	3.0
56.2	0.19	3.6
111	0.074	3.2
227	0.036	3.8

[a] Mean $\beta=3.3\pm0.4$.

---

[9] V_T is defined to be that voltage at which one can clearly observe a bead in oscillation; it corresponds to a height of rise of 0.1 or 0.2 cm.

[10] H. A. Pohl, J. Appl. Phys. **29**, 1182 (1958).

gions one will sometimes find two fundamental ν_0 ommon at low f) or encounter up to 5% uncertainty ν_0 (common at high f). The result of these limitations that it is impossible to check accurately the prediction i) for $f>60$ cps and $p>7$ or 8 since the possible error sufficient to shift the answer over the range $p-1$ to +1.

On the basis of the knowledge that h rises faster than nearly with V, one can predict that of two voltage aves of equal fundamental frequency and rms value he one having the greater peak voltage will produce e larger h. This prediction has been borne out by periment as is illustrated in Fig. 10. The tendency of e curves to converge for higher voltages is explained the fact that at these voltages the beads tend to ecome larger rather than to bounce higher (cf. Fig. 7) nd that, for a given frequency, this behavior depends ore upon height than upon waveform. For waves of ual peak-to-peak voltage one would expect the one ith the greater rms value to produce the greater h; is expectation, too, has been borne out experimentally.

As was mentioned previously, the frequency range elow 2 or 3 cps is characterized by a transition from ead formation to sheath formation. The rising induced $\frac{1}{2}$ cps square pulses illustrates the transition nicely. pon the application if the leading edge of a pulse the etone rises along the cathode to some height $h_{\max}$ nd then quickly falls back to a height h_{equil} which it aintains for the duration of the pulse; the ratio $_{\max}/h_{\text{equil}}$ is of the order of two. If f were increased mewhat, one would observe only a rise of the liquid ward $h_{\max}$ and its falling back at the end of the pulse. ith increasing f the liquid would have less time to e toward $h_{\max}$ and would, therefore, exhibit a smaller in accord with prediction (i) (cf. Fig. 6). If f were creased from $\frac{1}{2}$ cps, one would observe a relatively ratic "steady state" about $h=h_{\text{equil}}$, this equilibrium, course, having been preceded by a transient rise to $_{\max}$; this is commonly observed at dc when the voltage switched on suddenly.

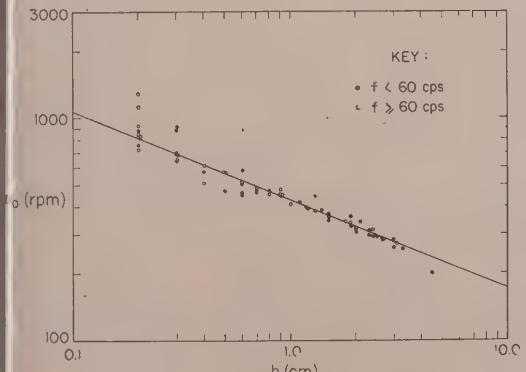

FIG. 9. ν_0 vs h.

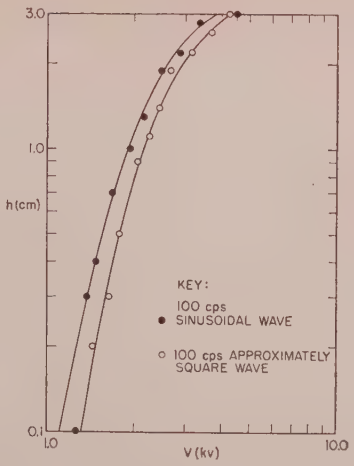

FIG. 10. h vs V.

In summation, the height of rise of a bead is, over a wide range of f and V, given by an equation of the form

$$h=G_\phi(V,f), \tag{5}$$

where ϕ denotes the waveform, V its rms value, and f its fundamental frequency; and

$$\partial^2 h/\partial V^2>0 \tag{5a}$$

$$\partial h/\partial f<0. \tag{5b}$$

Further, over the frequency range at which bead formation occurs, an equation of the form (4) and the rule associated with it are excellent guides for predicting the frequency of oscillation of the beads. Finally, there is a smooth transition between the ac and dc effects.

CONCLUSIONS

The rising of a liquid dielectric along high-voltage electrodes dipped into it (Sumoto effect) has been discussed from a phenomenological point of view. This rising has been shown to be influenced by the choice of liquid, by the purity of the liquid, by the choice of the electrode metal, by the temperature, and by the frequency, rms value, and waveform of the applied voltage. Qualitative rules have been given to predict the nature of the rising for alternating voltages.

Of the many unsolved questions connected with Sumoto phenomena, the most interesting is that of the origin and nature of the forces which produce them. These problems are worthy of considerable further attention.

ACKNOWLEDGMENT

The author wishes to express his thanks to Professor Ronold W. P. King for his encouragement and advice during the course of this research.

JOURNAL OF APPLIED PHYSICS VOLUME 32, NUMBER 10 OCTOBER, 196

Behavior of Exploding Gold Wires*

T. J. Tucker
Sandia Corporation, Albuquerque, New Mexico

(Received April 14, 1961)

A square-wave generator current source was used to study the behavior of gold wires exploded by current densities in the range of 0.25×10^8 to 3.26×10^8 amp/cm². Measurements of wire resistance vs cumulative energy and action at various current densities are compared with a simple theoretical exploding wire model and the results of Kerr cell photographic studies. Experimentally, the total energy input to the time of maximum wire resistance increases with current density and may exceed by threefold the normal vaporization energy. Also, the instantaneous wire resistance at any point is smaller with a larger current density. The resistance depression is first apparent in the region following vaporization. At higher current densities, the effect is observed to occur at progressively earlier phases up to and including the point at which melting occurs.

INTRODUCTION

It has previously been reported that at current densities greater than 5×10^6 amp/cm² the resistance of exploding wires and their energy input before peak resistance depend on current density.[1–3] At such extreme current densities, the wire resistance is not a unique function of energy input and, at least in late stages of the heating cycle, appears to be reduced. Similarly, total energy input increases with current density and may exceed the energy required to vaporize the wire as determined from handbook values. Theoretical explanations of these effects have been hindered by a lack of quantitative data. At current densities of interest, metals undergo heating and phase transformations in sub-μsec times; thus accurate measurement is difficult. This problem has been simplified by utilization of a square-wave generator current source with which a time resolution of a few nanoseconds is easily attained.

This paper presents the results of an experimental study of the electrical behavior of gold in the current density range of 0.25×10^8 to 3.26×10^8 amp/cm². Also presented are Kerr cell photographs of exploding wires and the derivation of a simple mathematical exploding wire model.

EXPERIMENTAL PROCEDURE

The experimental equipment has been previously described and will not be discussed in detail here.[4] Basically, the square output current pulse from a discharging coaxial line is used as a current source. The system produces a current pulse of 3-μsec duration, 6-nsec risetime, whose amplitude is variable up to a maximum of 2000 amp. A schematic diagram of the experimental system is shown in Fig. 1. Minor modification from that described in reference 4 includes a redesigned shaping gap to minimize the spacing between the voltage monitor point and wire termination, and improved Kerr cel camera optics.

The electrical results were obtained with 0.1-in lengths of Sigmund Cohn 1-mil-diam, 99.99% pure gol wire. Photographic results were obtained using 2-mil diam, ¼-in. samples of the same purity gold. All wire were soldered at the terminals with a low-temperatur solder "Ceroloy 147." Samples were fabricated under stereomicroscope and the initial resistance measured Samples which deviated from the calculated resistanc by more than 5% were discarded.

All electrical values were calculated from the exploding wire voltage waveforms using the calibrating resistor technique discussed in reference 4. Approximatel 100 displacement values per waveform were measure with a comparator. Numerical reduction was performe by an IBM 704 computer.

THEORETICAL

To provide a guide for the determination of dynami effects in the behavior of exploding wires, a simpl theoretical model is set forth.

Let metallic phase be denoted by superscripts: solid; *sl*, solid+liquid; *l*, liquid; *lv*, liquid+vapor; an *v*, vapor. Temperature considered will be denoted b subscripts: *t*, temperature at arbitrary time *t*; 0, 0°C; *m*

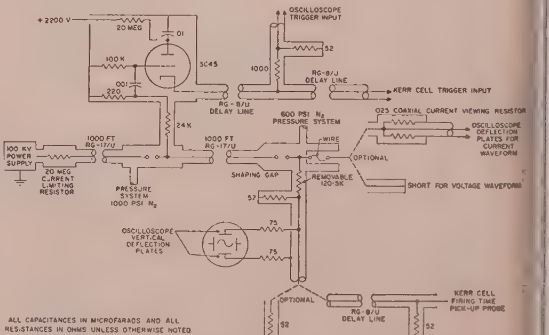
+2200 V
20 MEG
.01
100 K
3C45
.001
220
24 K
RG-8/U DELAY LINE
OSCILLOSCOPE TRIGGER INPUT
52
1000
RG-8/U DELAY LINE
KERR CELL TRIGGER INPUT
600 PSI N₂ PRESSURE SYSTEM
.023 COAXIAL CURRENT VIEWING RESISTOR
OSCILLOSCOPE DEFLECTION PLATES FOR CURRENT WAVEFORM
100 KV POWER SUPPLY
20 MEG CURRENT LIMITING RESISTOR
1000 FT RG-17/U
PRESSURE SYSTEM 1000 PSI N₂
1000 FT RG-17/U
WIRE
OPTIONAL
SHAPING GAP
REMOVABLE 120·5K
SHORT FOR VOLTAGE WAVEFORM
52
OSCILLOSCOPE VERTICAL DEFLECTION PLATES
75
75
OPTIONAL
52
RG-8/U DELAY LINE
52
KERR CELL FIRING TIME PICK-UP PROBE
ALL CAPACITANCES IN MICROFARADS AND ALL RESISTANCES IN OHMS UNLESS OTHERWISE NOTED

Fig. 1. Schematic diagram of experimental system.

---

[*] This work was done under the auspices of the U. S. Atomic Energy Commission.

[1] T. J. Tucker and F. W. Neilson, *Exploding Wires*, edited by W. G. Chace and H. K. Moore (Plenum Press, Inc., New York, 1959), p. 73.

[2] F. H. Webb, Jr., H. H. Bingham, and A. V. Tollestrup, Phys. Fluids **3**, 318 (1960).

[3] M. Keilhacker, Z. angew. Physik **12**, 49 (1960).

[4] T. J. Tucker, Rev. Sci. Instr. **31**, 165 (1960).

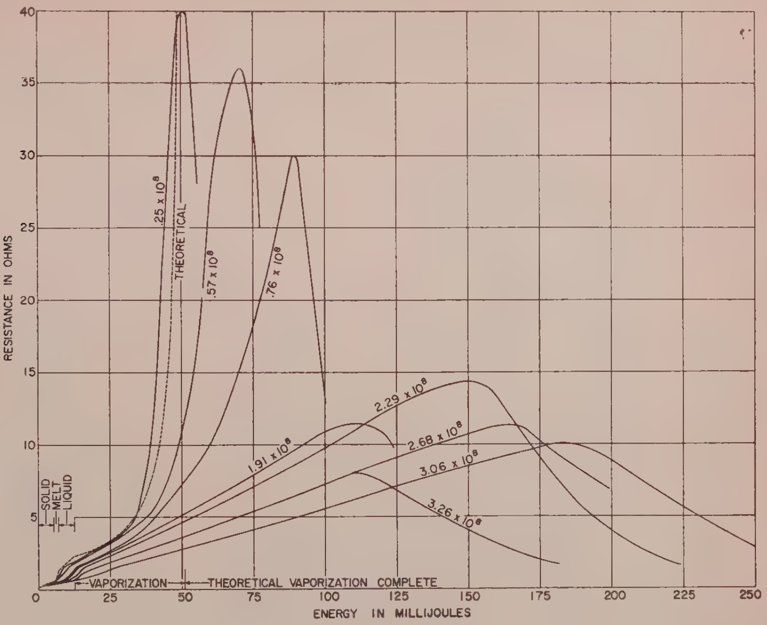

FIG. 2. Wire resistance versus energy input.

melting temperature; and v, vaporization temperature.

During heating of the solid metal, conservation of energy yields

$$dE_t^s = MC_t^s dT, \tag{1}$$

where E = input electrical energy in calories, C_t^s = specific heat at constant pressure, M = mass, and T = temperature.

Assume

$$R_t^s = R_0^s(1+\beta_0^s T), \tag{2}$$

$$C_t^s = C_0^s(1+\alpha_0^s T). \tag{3}$$

Then it can be shown that the instantaneous wire resistance (R_t^s) during heating of the solid is given by,

$$\frac{R_t^s}{R_0^s} = 1 + \frac{\beta_0^s}{\alpha_0^s}\left[\left(1+\frac{2E_t^s\alpha_0^s}{C_0^s M}\right)^{\frac{1}{2}} - 1\right]. \tag{4}$$

Melting is assumed to occur isothermally; thus from energy conservation

$$dE_t^s = -H_m dM_t^s, \tag{5}$$

where H_m = latent heat of fusion.

Assume that melting proceeds such that

$$dM_t^s = Lb_m^s dA_t^s, \tag{6}$$

where L is the wire length, and b_m^s and A_t^s are the density and cross-sectional area, respectively. If ρ = resistivity, then

$$R_t^s = (\rho_m^s \rho_m^l L)/(\rho_m^s A_t^l + \rho_m^l A_t^s). \tag{7}$$

If it is assumed that the volume change upon fusion is negligible, it can be shown that,

$$\frac{R_t^{sl}}{R_m^s} = \left[1 - \left(\frac{\rho_m^l - \rho_m^s}{\rho_m^l}\right)\left(\frac{E_t^s - E_m^s}{H_m M}\right)\right]^{-1}. \tag{8}$$

Heating of the liquid is of the same form as heating of the solid; however, it will be assumed that the specific heat (C_m^l) is constant. With this modification the equation becomes

$$\frac{R_t^l}{R_m^l} = 1 + \beta_m^l\left(\frac{E_t^l - E_m^l}{MC_m^l}\right). \tag{9}$$

Vaporization follows the fusion derivation except that it will be assumed that the vapor is non-conducting. The result is

$$\frac{R_t^{lv}}{R_v^l} = \left[1 - \frac{E_t^{lv} - E_v^l}{H_v M}\right]^{-1}. \tag{10}$$

Because of its subsequent use, we also present here the results of a calculation of resistance as a function of another independent variable which we have called action.

$$(G) = \int_0^t i^2 dt.$$

The use of action in exploding wire studies has been previously reported[5] and will only be discussed briefly here. From Eqs. (4), (8), (9), and (10) and from Eqs.

---

[5] G. W. Anderson and F. W. Neilson, *Exploding Wires*, edited by W. G. Chace and H. K. Moore (Plenum Press, Inc., New York, 1959), p. 97.

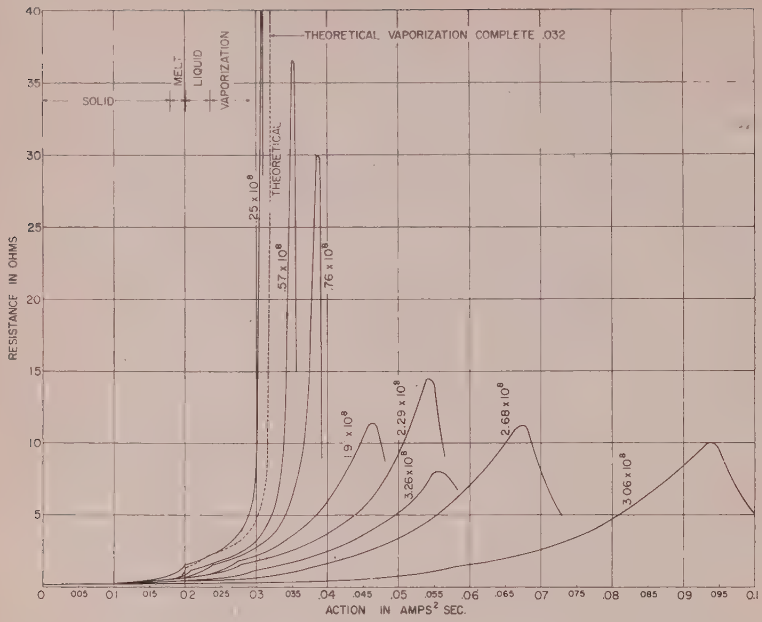

FIG. 3. Wire resistance versus action input.

(11), (12), (13), and (14) to follow, it can be seen that resistance can be expressed as a unique function of either energy or action. Energy, although perhaps physically more meaningful, contains resistance implicitly; on the other hand, action involves only current and time and is independent of quantities associated with the exploding wire material. Moreover, to anticipate the experimental data, the action required to reach a particular metallic phase, although not a true constant as was previously thought,[5] appears to be much more independent of current density effects than is energy. In these results, all assumptions used in the energy derivation apply, and in all cases the solutions were obtained by transfer of the resistance term in the conservation of energy equation from the left to the right-hand side prior to integration. The results of this calculation for the four regions of interest were as follows:

(1) Heating of the solid

$$G_t^s=\frac{C_0^sM}{\beta_0^sR_0^s}\left[(\beta_0^s-\alpha_0^s)\ln\left(\frac{R_t^s}{R_0^s}\right)+\alpha_0^s\left(\frac{R_t^s}{R_0^s}-1\right)\right]. \qquad (11)$$

(2) Melting

$$\frac{R_t^{sl}}{R_m^s}=\left[1-\frac{2R_m^s}{H_mM}\left(\frac{\rho_m^l-\rho_m^s}{\rho_m^l}\right)(G_t^{sl}-G_m^s)\right]^{-\frac{1}{2}}. \qquad (12)$$

(3) Heating of the liquid

$$G_t^l-G_m^s=\frac{MC_m^l}{R_m^l\beta_m^l}\left[\ln\left(\frac{R_t^l}{R_m^l}\right)\right]. \qquad (13)$$

(4) Vaporization

$$\frac{R_t^{lv}}{R_v^l}=\left[1-\frac{2R_v^l}{H_vM}(G_t^{lv}-G_v^l)\right]^{-\frac{1}{2}}. \qquad (14)$$

The equations derived are useful for prediction of general behavior; however, it must be admitted that the assumptions used to derive them are questionable in several particulars.

First, it was assumed that during melting, the energy input to both solid and liquid portions of the wire is utilized only for transformation of phase, and also that the process occurs isothermally. These two assumptions are contradictory since there would exist no temperature gradient to provide a mechanism for the transport of heat from interior regions to the melting interface. Indeed, it is probable that portions of the solid material exist at elevated temperatures and pressures. In addition, at all times the total electrical energy input was assumed to be utilized only for heating and phase transformation; no attempt was made to evaluate the energy utilized for mechanical expansion.

Second, numerical reduction of the equations approximates the temperature coefficient of resistance by the coefficient of resistivity. Determination of the latter coefficient is based upon a density change which keeps sample dimensions constant, a condition not realized in exploding wires, since thermal expansion is appreciable for the extended temperature range of interest. The approximation is particularly doubtful following melting since subsequent expansion probably occurs only radially.

Finally, electrical effects such as magnetic pressure

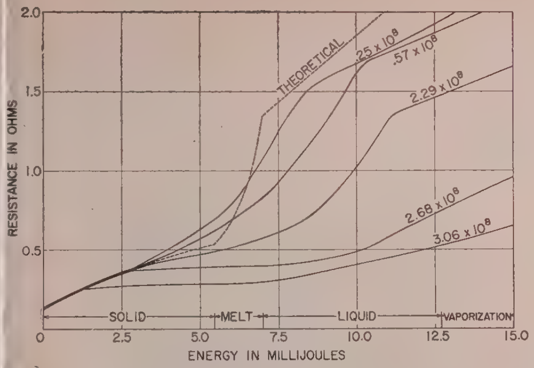

FIG. 4. Wire resistance versus energy input at early times.

and skin effect have been neglected. The maximum magnetic pressure at current densities which produce resistance depression is less than 100 bars and thus should be negligible. The penetration time associated with skin effect appears to be too short to produce significant effects. Even if the wire conductivity were to remain constant, the current density at the wire center would achieve one-half its ultimate value in approximately 1 nsec.

EXPERIMENTAL RESULTS

Experimental resistance versus energy and action curves in the current density range of 0.25×10^8 to 3.26×10^8 amp/cm^2 are presented in Figs. 2 and 3. Also shown are the theoretical curves and phase regions calculated from the equations of the preceding section. A correction to 20°C ambient temperature is straightforward and was utilized in the reduction. Theoretically, both energy and action exhibit a limit at which the resistance becomes infinite. Experimentally, this does not happen since, as will be shown in the Kerr cell photographs to follow, arc breakdown terminates the resistance rise.

From the figures, it can be seen that the experimentally determined peak resistance occurs at energies and actions considerably exceeding the theoretical maximums. Associated with increased current density, there is a decrease in the instantaneous wire resistance and an increase in the energy and action at which the resistance maximum occurred. The decrease of wire resistance is most pronounced and occurs at the lowest current densities in the region following the theoretical beginning of vaporization. With increasing current densities, the decrease in wire resistance progressively extends into earlier metallic phases and at 2.29×10^8 amp/cm^2 is observed at the beginning of melting. The effects occurring during the early phase are shown in greater detail in Figs. 4 and 5. In these figures, it can be seen that the points of change of slope which appear to correspond with the beginning and end of melting occur at lower resistances and at higher energies and actions as the current density is increased. With the present equipment, the voltage waveform is not well defined during the first 5 nsec. Thus, in Figs. 4 and 5, the initial portion of the solid region is doubtful. To provide a point of reference, in Fig. 5 the action input at the end of 5 nsec for a current density of 2.29×10^8 amp/cm^2 was 0.0065 amp^2 sec. Action at the 5-nsec time for any other current density is given by

$$G=(0.0065)(\text{current density})^2/(2.29\times10^8)^2.$$

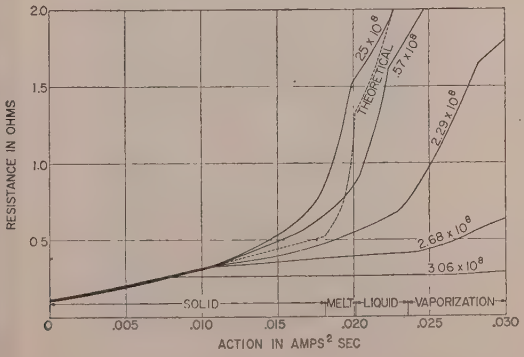

FIG. 5. Wire resistance versus action input at early times.

FIG. 6. Total energy input to resistance maximum versus current density.

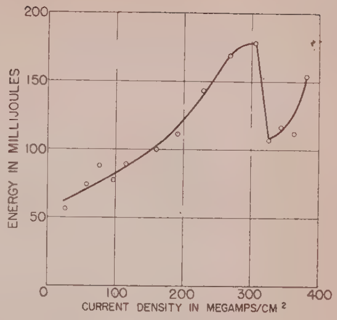

The total energy and action input experimentally required to achieve peak resistance are shown in Figs. 6 and 7. As previously noted, the resistance maximum occurs as a result of arc breakdown termination of the normal resistance rise. Thus, for the short times

FIG. 7. Total action input to resistance maximum versus current density.

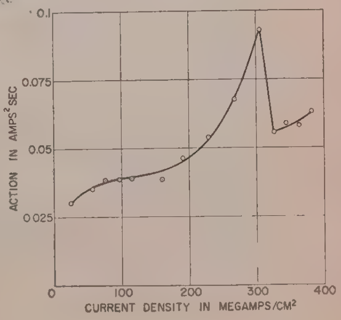

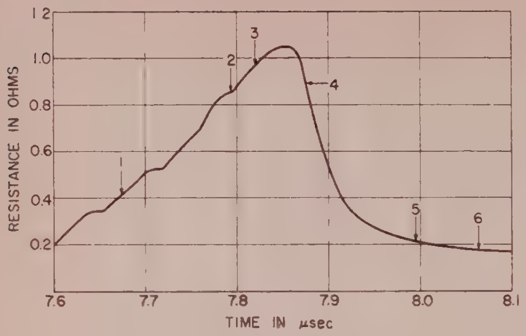

FIG. 8. Wire resistance versus time at a current density of 0.13×10^8 amp/cm^2.

herein considered, statistical variations normally found in the time of initiation of arc breakdown would be expected to produce some deviation in quantities based upon the resistance maximum. The total energy measurements are much more sensitive to variations of peak resistance than is action, since, as can be seen in Figs. 2 and 3, a major fraction of the total energy input occurs during the high resistance vaporization phase while the largest fraction of action input occurs during the solid and liquid phases. The insensitivity of the action variable to variations of resistance during the vaporization phase also explains the relative constancy of action at current densities below 0.20×10^8 amp/cm^2.

The sudden decrease of both total energy and action above 3×10^8 amp/cm^2 is not as yet understood. Further study of this region is planned but will be delayed until a faster oscilloscope can be acquired.

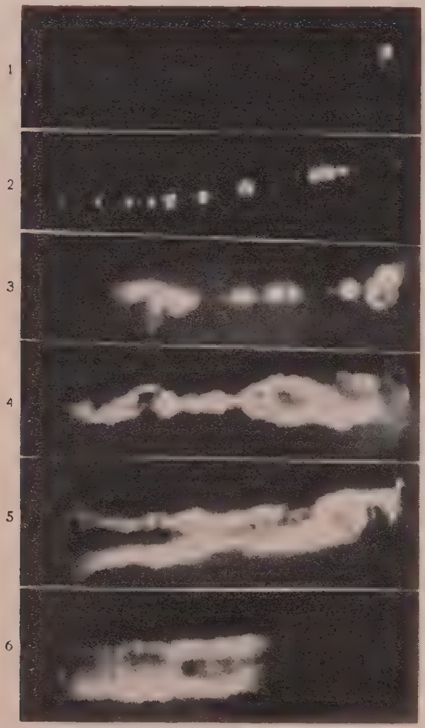

FIG. 9. Kerr cell photographs of wires exploded by a current density of 0.13×10^8 amp/cm^2.

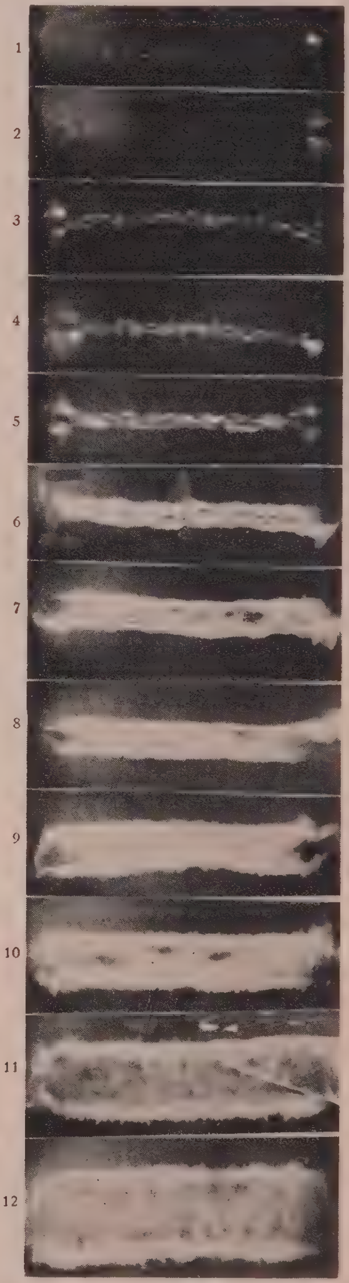

FIG. 10. Kerr cell photographs of wires exploded by a current density of 0.24×10^8 amp/cm^2.

Attempts were made to extend the current density range down to 0.13×10^8 amp/cm². The waveform, although it followed the 0.25×10^8 amp/cm² waveform through the liquid phase, assumed a random step structure during vaporization. An example of the waveform is shown in Fig. 8. It should also be noted that the peak resistance achieved was relatively low. It was assumed that the effects observed were due to the formation of high resistance sections along the wire which were subsequently bypassed by arcing. This assumption was verified by the Kerr cell photographs shown in Fig. 9. The photograph numbers correspond to those in Fig. 8, and are indicative of the resistance region in which exposure occurred. The formation of small arcs along the wire axis prior to the time of peak resistance is clearly shown.

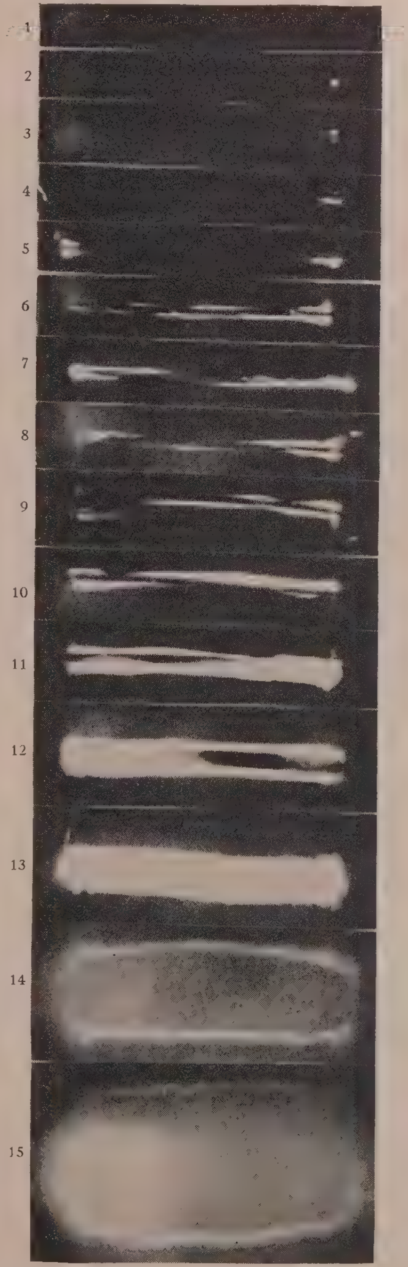

Fig. 11. Kerr cell photographs of wires exploded by a current density of 1×10^8 amp/cm².

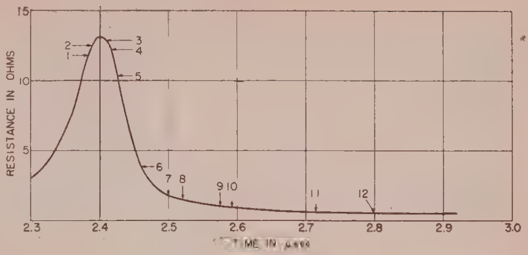

Fig. 12. Wire resistance versus time at a current density of 0.24×10^8 amp/cm².

It was previously reported that exploding wires exhibit two arc breakdown modes.[6] The low current density mode was interpreted as breakdown in metallic vapor, the high current density mode as breakdown in the air environment. It was proposed that the energy and resistance anomalies observed at high current densities were a result of small air arcs which were formed prior to the time of peak resistance. Extension of these studies utilizing the improved instrumentation now available indicates that arcing does not occur prior to the resistance peak. Kerr cell photographs of wires carrying current densities of 0.24×10^8 and 1×10^8 amp/cm² are shown in Figs. 10 and 11, respectively. A typical sample mounting is shown at the top of Fig. 14. Each picture is of a separate wire explosion, but exposure occurred at successively later times as shown by corresponding numbers in Figs. 12 and 13.

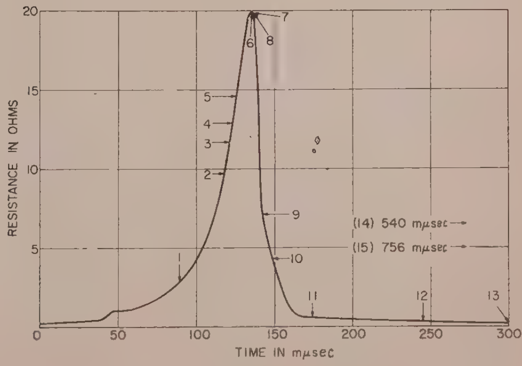

Fig. 13. Wire resistance versus time at a current density of 1×10^8 amp/cm².

---

[6] T. J. Tucker, J. Appl. Phys. **30**, 1841 (1959).

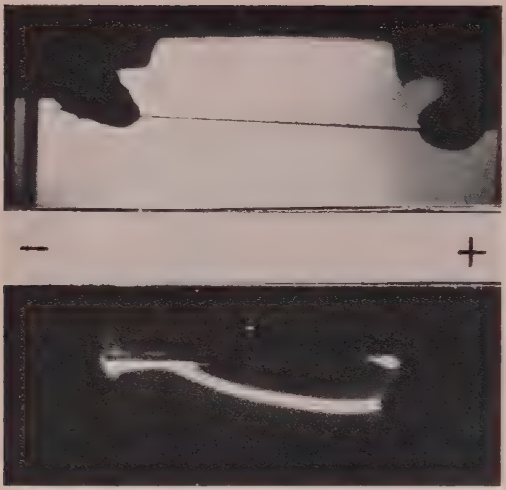

Fig. 14. Top—typical sample mounting. Bottom—arc leaving wire vicinity at a current density of 1×10^8 amp/cm^2.

In contrast to the pictures obtained at the current density of 0.13×10^8 amp/cm^2, the two higher current sequences show no sign of extensive arc formation prior to the time of peak resistance. The arc breakdown at current densities on the order of 1×10^8 amp/cm^2 is characterized by the formation of small arcs apparently external to the wire material and by a well-defined interface between the wire material and the arcs. Additional evidence that breakdown occurs in the air environment at this current density is shown at the bottom of Fig. 14 by an arc which jumped from the wire to a solder projection at the anode terminal. Arc breakdown at current densities on the order of 0.3×10^8 amp/cm^2 were again observed to be irregular and somewhat striated in appearance. It was reported in reference 6 that an interface between wire material and arc was not observed. The improved resolution of the optical system used for this work shows that such an interface does exist. This interface is considerably more irregular and less well defined than that observed at the higher current density. No examples of arcs which left the wire were observed at this current density.

A possible explanation of the finite resistivity observed in exploding wires at energy inputs exceeding the vaporization energy is indicated in photograph 6 of Fig. 11. If, as was assumed, the arc breakdown occurred in the environment and that no extensive vaporization had occurred, then from the observed diameter, the density of the metallic vapor is approximately 1 gm/cm^3. The electrical properties of metallic gases at such densities are not well known. David,[7] from theoretical considerations, has predicted that copper vapor at this density should be conductive. A similar behavior would be expected in gold. Interestingly, it is possible that the dense metallic vapor by remaining conductive continues to accept energy and thus may achieve a temperature in excess of the critical temperature.

SUMMARY

It has been shown in gold wires exploded by current densities in the range of 0.25×10^8 to 3.26×10^8 amp/cm^2 that electrical resistance and total energy input of exploding gold wires are functions of current density. Total energy to peak resistance increases with increasing current density to values exceeding the theoretical vaporization energy by factors as large as three. The additional energy input primarily occurs during a period immediately following the calculated vaporization energy where, if the assumption of the nonconductivity of the vapor were valid, the circuit should be open. Kerr cell camera photographs, although indicating environmental breakdown at current densities of 10^8 amp/cm^2 show no sign of extensive arc formation prior to the time of peak resistance. At the time of arcing the photographs indicate that although the energy input greatly exceeds vaporization energy, the vapor density is about 1 gm/cm^3 and thus may itself be a conductor.

The electrical resistance, besides being finite at energies exceeding vaporization energy, was decreased with increased current densities. This decrease is first evident during the vaporization phase. With increasing current density, the resistance depression is observed to extend progressively into earlier phases, and at a current density of 2.29×10^8 amp/cm^2 is observed at the beginning of melting. Comparison of the experimental data with a theoretically determined curve indicates that with increasing current densities, the slope discontinuities corresponding to beginning and end of melt occur at greater energies and actions and at reduced resistances. The theoretical treatment presented in this paper is based upon static constants and thus, although predicting general features relatively well, it is not adequate to explain the observed resistance and energy dependency upon current density.

No attempt has as yet been made to formulate a more complete theoretical model including dynamic effects; however, it is hoped that the experimental results presented in this paper will provide a guide to such a formulation.

ACKNOWLEDGMENTS

The author is indebted to Mr. H. P. Kelsey for technical assistance and particularly to Mrs. D. M. Martin for her help in data reduction and preparation of illustrations. He also wishes to thank Dr. M. L. Merritt and Mr. E. C. Cnare for many helpful discussions.

---

[7] E. David, Z. Physik **150**, 162 (1958).

Noise in InSb Photodiodes

B. R. Pagel and R. L. Petritz
Texas Instruments Incorporated, Dallas, Texas

(Received December 9, 1960; in final form, May 16, 1961)

Experimental investigation of noise generation in InSb infrared photodiodes is reported. Minimum noise occurs when the diode is biased to zero potential. Noise spectra taken on seven photodiodes determined the white noise level above 1 kc. The experimental value of white noise is compared with the noise induced by random fluctuations in background radiation. The photonoise is calculated from

$$\langle i^2\rangle/\Delta f=2qI_{\mathrm{PH}}$$

for an equivalent noise generator. The photoinduced current I_{PH} is measurable directly for zero bias potential. The total measured white noise is of the order of one decibel above the calculated photoinduced noise. Thus the photoinduced noise is the primary source observed, and InSb photodiodes closely approach the ideal case of being background-limited infrared detectors.

INTRODUCTION

THIS paper reports experimental studies of noise characteristics of indium antimonide photodiodes. The detector is a solid-state diode generating a voltaic signal in response to infrared radiation. The long-wave cutoff corresponding to a gap width of 0.23 ev is 5.4 μ. As with all electronic devices, ability to detect low intensities of radiation is limited by several noise causing phenomena. It has been shown that the fundamental limit to the detecting ability of infrared devices is associated with the random incidence and absorption of photons by the device.[1,2] Detectors receive infrared radiation from the viewing background as well as from the signal source of interest. The signal must be identified from the fluctuations generated by the background radiation. However, background radiation is not the only important source of detector noise. Detectivity, therefore, is not limited by the background radiation noise, but rather by the total noise. This work compares the total measured white noise of the detector with the predicted background radiation noise.

Measurements of the total noise generated in photodiodes as a function of bias showed that the noise is minimal with the detector biased at zero voltage. The noise character of the detector with zero voltage was studied in detail by measuring the spectra of seven photodiodes. Results show that indium antimonide photodiodes approach the ideal case of being limited in sensitivity only by the radiation noise.

Previous studies of shot noise in *p-n* junctions have been made by Slocum and Shive,[3] and by Spescha and Strutt.[4] In both studies, an external source of radiation was used to increase the total shot noise level so noise resulting from radiation was observable. Our experiments differ from these earlier shot noise studies since only background radiation at room temperature falls on the detector; no additional illumination source is used.

DESCRIPTION OF InSb DETECTOR

Photodiodes were prepared by diffusing a *p*-type surface onto an *n*-type indium antimonide base and then sectioning into circular disks 0.6 mm thick and from 0.04–0.2 cm² in area. The small energy gap of indium antimonide leads to a large intrinsic carrier density at room temperature which masks minority carrier effects. The junction characteristic is established only at reduced temperatures, so the wafers were mounted in small dewar flasks to allow cooling with liquid nitrogen. The *n*-type portion served as the base and the thin *p*-type surface, the radiation receiving area. Electrical contact was made to both sides of the junction by soldering.

NOISE CHARACTERISTICS

Photodiode noise was measured and compared with background radiation noise calculated from the expression[1,5]:

$$\langle i^2\rangle/\Delta f=2qI_{\mathrm{PH}}, \tag{1}$$

where $\langle i^2\rangle/\Delta f$ is the mean square noise current per cycle of an equivalent generator, q the electronic charge, and I_{PH} the average current generated by background radiation. The photoinduced current is measured directly, and is equal to the diode current with the bias voltage zero, as can be seen from the equation describing the diode characteristics. These characteristics of indium antimonide photodiodes are well described, for low-bias conditions, by[2,6,7]:

$$I=-I_{\mathrm{PH}}+I_{\mathrm{S}}[\exp(qV/\beta kT)-1]+G_{\mathrm{S}}V. \tag{2}$$

The total current I through the detector contains three components. I_{PH} is induced by the detector-collected infrared radiation and is equal to $q\eta JA$, where η = quantum efficiency, J = incident photon flux with energy

---

[1] R. Clark Jones, *Advances in Electronics*, edited by L. Marton (Academic Press, Inc., New York, 1953), Vol. 5, pp. 1–96.

[2] G. Pruett and R. L. Petritz, Proc. Inst. Radio Engrs. **47**, 1524 (1959).

[3] A. Slocum and J. N. Shive, J. Appl. Phys. **25**, 406 (1954).

[4] G. A. Spescha and M. J. O. Strutt, Helv. Phys. Acta **33**, 69 (1960); Scientia Electrica **5**, 121 (1959).

[5] R. L. Petritz, *Photoconductivity Conference*, edited by R. G. Breckenridge, B. R. Russel, and E. E. Hahn (John Wiley & Sons, Inc., New York, 1956), pp. 49–77.

[6] W. Craven and R. Genoud, "InSb Photodiode Characteristics," paper presented at the meeting of the Optical Society of America, April, 1959.

[7] J. L. Moll, Proc. Inst. Radio Engrs. **46**, 1076 (1958).

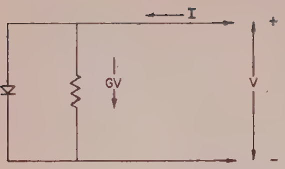

Fig. 1. Electrical model of the InSb photodiode showing the surface leakage as a shunt conductance across the diode junction.

greater than the band gap of indium antimonide, and A = photodiode area.[2] The bracketed term describes the characteristic diode current where I_S is the saturation current, V the junction voltage, k Boltzmann's constant, and T degrees Kelvin. The empirical factor β was introduced to fit the data for forward bias. This parameter reflects phenomena possibly present as generation and recombination in the transition region,[7] and contact resistance.

Figure 1 shows the equivalent electrical circuit for the photodiode and gives the sign convention. The third component of the diode current arises from the shunt conductance G_S which represents a current leakage path across the junction on the semiconductor surface. For zero bias volts, all terms but I_{PH} in (2) vanish, and the current is equal to the photoinduced current: $I_{SC} = -I_{PH}$ at $V = 0$, i.e., for a dc short circuit. If the background infrared source is at 77°K, the same temperature as the detector, then the detector and its surroundings are in radiative equilibrium, and the bias current and voltage are concurrently zero: I_{SC} represents the current generated by the background infrared radiation.

Figure 2 shows a typical curve of the diode characteristics for photodiode I-186. The slope of the curve is the differential conductance of the detector, $G = \partial I/\partial V$. The shunt conductance $G_S = 53.5$ μmhos, $I_{SC} = 41.5$ μa, and $\beta = 4.11$. The solid curve was the fit obtained to the data points. Table I gives parameter values for representative diodes tested.

EXPERIMENTAL METHODS

Measurements were made with the diode viewing a blackbody cavity at room temperature; there was no other radiation source. The detector views radiatio over a hemisphere. Noise spectra were taken with zer bias potential, the point at which noise is near minimum. This was determined experimentally. Figure gives a typical noise response as a function of bias.

Table I. InSb photodiodes. Characteristic parameters of measured indium antimonide photodiodes. A = active area, Z_{SC} = th detector differential impedance at zero bias potential, I_{SC} = short-circuit current, G_S = shunt conductance, β = empirical paramete I_S = saturation current, and F_d = noise figure of the white nois level referred to the radiation noise.

	A cm²	Z_{SC} $K\Omega$	I_{SC} μa	G_S μmhos	β	I_S μa	F_d db
MH-195	0.0706	0.660	39.7	1070	2.58	2.83	1.0
I-120	0.0416	0.470	38.0	1850	2.86	3.10	2.2
I-180	0.0416	7.83	30.0	34.0	3.55	6.25	−0.9
I-184	0.0416	18.5	58.4	53.0	4.04	6.2	0.8
I-186	0.0416	5.92	41.5	53.5	4.11	4.75	0.0
I-211	0.0416	11.4	41.5	16.5	3.91	3.6	0
N-109	0.126	1.0	110	159	7.78	34.0	2–3

Figure 4 demonstrates the experimental arrangement. The photodiode was biased with a battery E and a large wire-wound resistor R_B. After the bia current and diode potential were measured, the diod was connected directly across the input of the preamplifier for noise measurements. R_B was much large than the differential cell impedance so that the nois signal was not shunted.

Noise fluctuations in the cell were first amplified i a low-noise transistor preamplifier, schematically show in Fig. 5. The input stage transistor operating with hig gain and low collector current was selected for its low noise figure. Wire-wound resistors and batteries in th power supply were used to minimize amplifier noise The preamplifier was shielded with mumetal to minimize noise pickup. Its characteristics are shown i Fig. 6. The secondary amplifier was a Tektronix typ 122.[8] The amplified signal was read with a Genera Radio 736A wave analyzer modified to increase it response time and smooth out noise fluctuations. Th

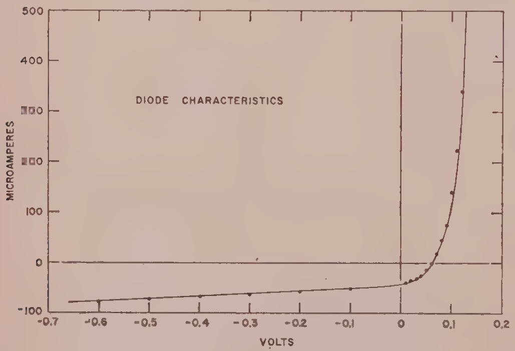

Fig. 2. Current-potential characteristics of the InSb photodiode TI I-186. Ambient temperature of the background infrared radiation, 25°C. Points are experimental values; solid line is the fitted curve.

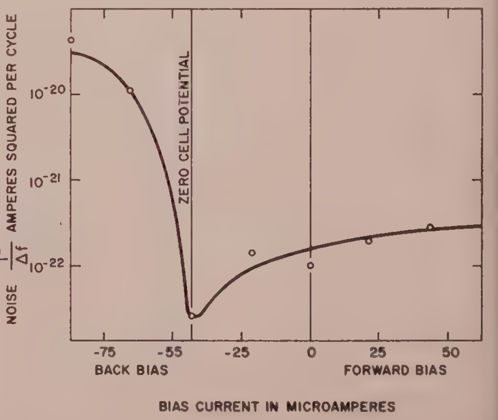

Fig. 3. Typical noise response as a function of bias at 100 cps.

---

[8] J. J. Brophy, Rev. Sci. Instr. 26, 1076 (1955).

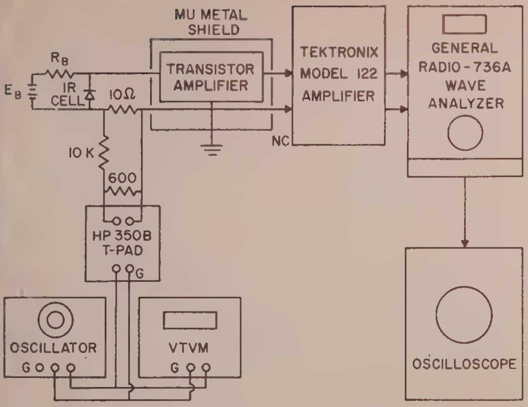

FIG. 4. Experimental arrangement for measuring noise generated in InSb photodiodes and accessory equipment to measure the gain G' of the amplifier system.

fluctuations were further averaged by recording the output of the analyzer for about 10 min and estimating the mean value.

Noise generated by the photodiode was amplified, frequency analyzed, and recorded. The average of the recording was estimated. This reading contains noise power contributions from the photodiode and the amplification system

$$\langle e^2\rangle=\langle e^2_{\text{diode}}\rangle+\langle e^2_{\text{amp}}\rangle, \tag{3}$$

where $\langle e^2\rangle$ is the measured value of the noise level. To obtain an absolute value of the photodiode noise level, the amplifier noise power must be measured and subtracted. To measure the noise figure of the amplifier, a wire-wound resistor with resistance R equal to the photodiode impedance was used as a known noise source across the amplifier input replacing the cell. This reading contains the noise power component from the amplifier and the thermal noise of the wire-wound resistor:

$$\langle e^2_{\text{R+amp}}\rangle=\langle e^2_{\text{R}}\rangle+\langle e^2_{\text{amp}}\rangle, \tag{4}$$

where

$$\langle e^2_{\text{R}}\rangle=4kT_{\text{A}}R\Delta f(G')^2. \tag{5}$$

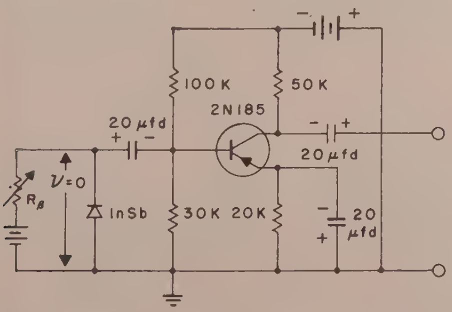

FIG. 5. Circuit of special low-noise transistor preamplifier used in noise measurements of InSb photodiodes.

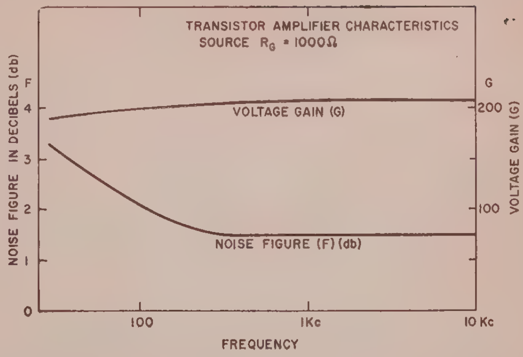

FIG. 6. Noise figure spectrum and voltage gain of special transistor preamplifier. Source resistance was 1000-Ω wire-wound resistor.

G' is the voltage gain of the system, and T_{A} the ambient temperature of the wire-wound resistor in degrees Kelvin. The amplifier noise power $\langle e^2_{\text{amp}}\rangle$ was subtracted from the photodiode noise reading to give an absolute value of the noise level. The noise level reflects back to the generator in series with the diode impedance by dividing by G':

$$\frac{\langle e^2_{\text{d}}\rangle}{\Delta f}=\frac{\langle e^2_{\text{d+amp}}\rangle}{(G')^2\Delta f}-\left[\frac{\langle e^2_{\text{R+amp}}\rangle}{(G')^2\Delta f}-4kT_{\text{A}}R\right]. \tag{6}$$

$\langle e^2_{\text{d}}\rangle$ is the absolute noise level of the photodiode. Figure 7 shows a plot of the two terms in this equation. The upper curve, a plot of the first term versus frequency, represents measured noise level. The lower curve corresponding to the last term represents the amplifier noise. The amplifier noise is a decade below the total observed noise. The absolute noise level of the diode is the difference between these two.

Note: to use Eq. (6), the product $(G')^2\Delta f$ must be evaluated. One way to do this involves using a noise diode in shunt with the photodiode. This technique was not selected because the product $(G')^2\Delta f$ must be measured at each frequency and is very time consuming for narrow-band studies. Though the emphasis in this

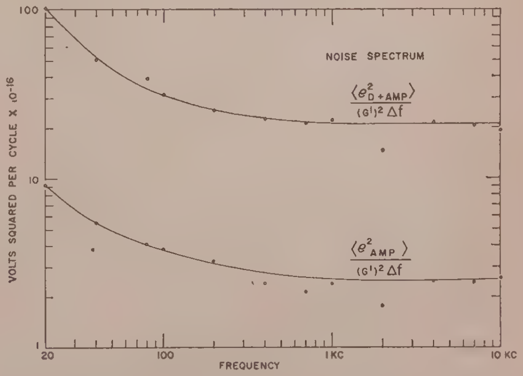

FIG. 7. Noise power spectrum of the measured noise level of TI-211 including amplifier noise. Also a spectrum of the amplifier noise alone.

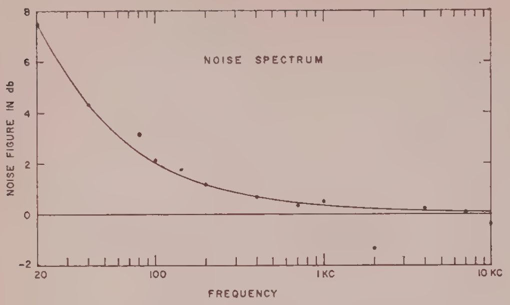

FIG. 8. Noise spectrum of InSb photodiode TI I-211 taken with zero bias potential in terms of 10 $\log_{10}F_d$(noise).

paper is on the white noise region above 1 kc, the study included the $1/f$ noise at low frequencies. We were not confident that a noise diode would be white at these low frequencies.

The method chosen required the effective bandwidth Δf of the system be determined only once using wire-wound resistors and the Nyquist expression for noise. The gain as a function of frequency was measured as shown in Fig. 4. The technique includes the effects of the injection loss into the amplifier and proved very satisfactory.

RESULTS

Seven photodiodes were investigated for noise characteristics. Data on a representative cell, TI I-211, are given in Fig. 8. The spectrum shows the characteristic fall of the excess noise and levels off to a white noise above 1 kc. Data are in terms of a noise figure for the photodiode. Noise figure applied to a system like an amplifier is a ratio of the actual noise power generated to the performance of an ideal system. An ideal photodiode would have only radiation noise. A noise factor[2] for the photodiode is defined with the radiation noise power as the reference

$$F_d(\text{noise})=\frac{\langle e^2{}_d\rangle}{2qI_{SC}R^2\Delta f}.$$

The noise figure in decibels is obtained by taking 10 $\log_{10}F_d$(noise). The curve of Fig. 8 is a plot of the data used in Fig. 7 in terms of the photoinduced noise, F_d. The white level approaches zero decibels and $F_d\rightarrow 1$ so the primary contribution to the total is the photoinduced noise.

Table I lists the measured white noise levels and characteristic diode parameters for all the photodiodes. The noise figures approach zero decibels very closely, indicating that the photodiodes approach the ideal of being limited in detectivity by the background photon noise. Variation from zero is generally within the accuracy of measurements.

To the authors' knowledge, this is the first infrared detector to have ambient background radiation-induced noise as the predominant portion of its noise output.[9] Using the photodiode model in Fig. 1 and described by (2) for the voltage-current characteristics, expressions for the noise generators can be given. The white noise components that may be expected are[10]:

$$\langle i^2\rangle/\Delta f=2qI_{PH}+2qI_S/\beta[e^{qV/\beta kT}+1]+4kTG_S.$$

The first term is the photoinduced shot noise; the second term is the shot noise from the ideal diode currents which are uncorrelated and add; and the final term is the Nyquist noise generated in the shunt conductance G_S. Noise is expressed in terms of equivalent current generators.

Note that under the bias condition of $V=0$, the above equation can be expressed in terms of a parameter $M=qI_{SC}/2kTG$, where

$$G=(qI_S/\beta kT)+G_S,$$

so that

$$\langle i^2\rangle/\Delta f=(1+1/M)2qI_{SC}.$$

In the absence of excess noise, the radiation-referenced noise factor becomes $[F_d(\text{noise})]_{V=0}=1+1/M$. This equation sets the lower limit of white noise for a detector at $V=0$, neglecting the presence of excess noise.

Quantum loss factor, similar to the noise factor discussed above, has been derived for the detector signal, and is defined as $F_d(\text{signal})=1/\eta$. η is the quantum efficiency of the detector, representing the fraction of the incoming photon flux which is converted into charge carriers participating in the current I_{PH}.

A value of M for an InSb photovoltaic detector is typically the order of 20 (I-186). Thus, F_d(noise) has a value of only 1.05, and introduces little degradation from ideal performance. This is to be compared with the value of the quantum loss factor, which is 3.5 for unit I-186 ($\eta=0.28$). Though smaller values of the quantum loss factor have been observed, a maximum value of $\eta=0.65$ is determined from surface reflection. This indicates a value of 1.55 for the quantum loss factor, still considerably greater than the noise loss $[F_d(\text{noise})]$. Further improvement of InSb photodiode detector performance will be in increasing the value of the quantum efficiency. Optical coating to reduce surface reflection is one possibility. Note, however, that the over-all noise factor F_d of the unit described (I-186) was found to be 3.7, indicating that the detector has its detectivity less than a factor of two removed from the ideal.

CONCLUSIONS

In the bias region of zero cell potential, the indium antimonide photodiode approaches the ideal detector. Noise generated in the detector is predominantly that induced by the background radiation.

---

[9] B. R. Pagel, Bull. Am. Phys. Soc. **5**, 186 (1960).

[10] K. M. Van Vliet, Proc. Inst. Radio Engrs. **46**, 1044 (1958).

JOURNAL OF APPLIED PHYSICS VOLUME 32, NUMBER 10 OCTOBER, 1961

Microwave Harmonic Generation by Ferrimagnetic Crystals

D. D. Douthett, I. Kaufman, and A. S. Risley
Space Technology Laboratories, Canoga Park, California

(Received March 13, 1961)

The experimental behavior of isotropic ferrimagnetic insulators in second harmonic generation at microwave frequencies has been investigated and compared with the behavior predicted by the equations of motion with Landau-Lifshitz and with Bloch-Bloembergen damping. In general, a close agreement between experiment and theory was found. The experiments were carried out with small samples of single-crystal manganese ferrite, YIG, and other ferrimagnetic materials. Since harmonic generation results from asymmetries in the precessional orbit, measurements were made with disk-shaped specimens in which the demagnetizing fields create the asymmetry. The technique employed a cavity simultaneously resonant to 8.5 and 17 kMc. Absolute values of field intensities and magnetizations were computed from absolute power measurements. A figure of merit F for a ferrimagnet is defined. In a practical 2ω generator the output power $P_{2\omega}$ is expected to vary as the product $F^2P_i^2$, where P_i is the input ω power. In comparing materials at ferrimagnetic resonance (FMR), F should vary as χ_0''. This was verified experimentally, even at high drive levels. At constant frequency and drive level F should be nearly independent of H_{dc}. Only slight deviations from this were found at low drive levels.

I. INTRODUCTION

MOST applications of ferrimagnetic materials to microwaves utilize the linear anisotropic behavior resulting from their gyromagnetic properties. The subject of this paper is second harmonic generation, which is a direct consequence of one of the nonlinear effects present in ferrimagnetic materials under particular experimental conditions.

Frequency doubling in ferrites has been demonstrated experimentally and analyzed by a number of investigators.[1–6] In previous experimental work, the major aim was to achieve as much harmonic power as possible. Ferrites of various compositions, shapes, and sizes were placed into waveguides and excited with high-intensity microwave power. By this technique as high as 8 kw of second harmonic power was obtained from 32 kw of 9-kMc input.[2] This result represents a significant achievement.

While these earlier experiments demonstrated that ferrites are capable of efficient harmonic generation, they did not lend themselves to quantitative comparison with results expected from theory. Qualitatively, there was no consistent correlation between the relative amounts of 2ω power with the output predicted by a theoretical figure of merit $M_s/\Delta H$.

This paper compares the experimental behavior of ferrimagnets with the predictions of a phenomenological theory. In particular, we studied the influence of material linewidth, magnetization, dc magnetic field, and drive level, on second harmonic magnetization. (The effect of magnetocrystalline anisotropy on the results reported here is small and will be neglected.) It was felt that experiments with small samples could provide the maximum amount of basic information, unobscured by propagation and variable coupling effects. We used small, disk-shaped samples, located in a cavity simultaneously resonant to 8.5 and 17 kMc. The experimental arrangement allowed absolute measurements of exciting field, absorption, and second harmonic magnetization. Throughout this text, we have used mks units, with $\mathbf{B}=\mu_0\mathbf{H}+\mathbf{M}$, where $\mu_0=4\pi\times10^{-7}$ h/m.

A portion of this work was reported earlier in an oral paper.[7]

II. THEORY

It can be shown from a geometrical argument[4] that if the magnetization precesses asymmetrically, it will contain harmonics of the fundamental frequency. In discussions of second harmonic generation, a linearly polarized, rather than a circularly polarized, driving field often has been stressed as the means for inducing a noncircular precession.

In the following we show, from an analysis of the *freely* precessing magnetization, that the internal fields resulting from shape anisotropy alone may be very effective in producing a noncircular precession.

In addition, we consider a uniformly excited disk-shaped specimen with magnetic losses, and calculate the fundamental absorption and second harmonic magnetization for this case.

Finally, a detailed discussion is given in which a figure of merit for 2ω generation by a lossy nonlinear material is derived.

The process of generation of rf fundamental and harmonic frequency components of the magnetization in a ferrimagnet can be described by an analysis of the equation of motion of the magnetization. Including an appropriate damping term, this equation is

$$d\mathbf{M}/dt=\gamma(\mathbf{M}\times\mathbf{H})+(\gamma\alpha/M_s)[\mathbf{M}\times(\mathbf{M}\times\mathbf{H})]. \quad (1)$$

$\mathbf{M}$ is the instantaneous magnetization, $\mathbf{H}$ is the total internal magnetic field, γ is the gyromagnetic ratio for an electron, $\alpha(\approx\Delta H/H_0)$ is the Landau-Lifshitz damping parameter, and M_s is the saturation magnetization.

---

[1] W. P. Ayres, P. H. Vartanian, and J. L. Melchor, Phys. Rev. **100**, 1791 (1955).

[2] J. H. Melchor, W. P. Ayres, and P. H. Vartanian, Proc. Inst. Radio Engrs. **45**, 644 (1957).

[3] E. Stern and P. S. Pershan, presented at Symposium on the Role of Solid State Phenomena in Electric Circuits, Polytechnic Institute of Brooklyn, Brooklyn, N. Y., April 23, 1957.

[4] J. E. Pippin, Proc. I. R. E. **44**, 1054 (1956).

[5] R. L. Jepsen, Gordon McKay Laboratory, Air Force Cambridge Research Center, 1958.

[6] W. P. Ayres, IRE Trans. Microwave Theory Tech. **MTT-7**, 62 (1959).

[7] I. Kaufman, A. S. Risley, and D. D. Douthett, Bull. Am. Phys. Soc. **5**, 297 (1960).

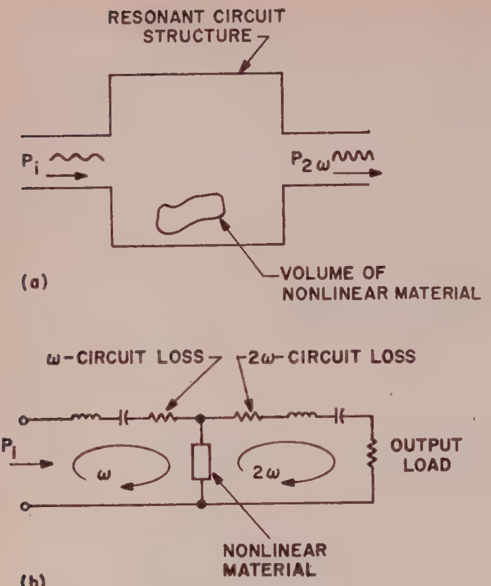

FIG. 1. Frequency doubling by nonlinear material. (a) Suggested physical embodiment. (b) Equivalent circuit.

Free Precession

Let us consider the motion of the freely precessing magnetization in an ellipsoidal specimen for which the concept of demagnetizing factors (N_x,N_y,N_z) is valid. The static field H_0 is applied in the y direction. The total magnetization and internal field of (1) are given by

$$\mathbf{M}=m_x\hat{\imath}+(M_s+m_y)\hat{\jmath}+m_z\hat{k}, \tag{2}$$

and

$$\mathbf{H}=-\frac{N_x}{\mu_0}m_x\hat{\imath}+\left[H_0-\frac{N_y}{\mu_0}(M_s+m_y)\right]\hat{\jmath}-\frac{N_z}{\mu_0}m_z\hat{k}. \tag{3}$$

Retaining second-order terms, we express (1) in component form without the loss term as

$$\dot{m}_x=-\gamma[H_0+(N_z-N_y)(M_s/\mu_0)]m_z; \tag{4}$$

$$\dot{m}_y=\gamma[(N_z-N_x)/\mu_0]m_xm_z; \tag{5}$$

$$\dot{m}_z=\gamma[H_0+(N_x-N_y)(M_s/\mu_0)]m_x. \tag{6}$$

The coupled equations, (4) and (6), for the transverse components of the rf magnetization, can be easily uncoupled, with the result that m_x, or m_z, satisfies the harmonic oscillator equation $\ddot{m}_{x,z}+\omega_0^2m_{x,z}=0$. The angular frequency ω_0 is

$$\omega_0=|\gamma|\left\{\left[H_0+(N_x-N_y)\frac{M_s}{\mu_0}\right]\times\left[H_0+(N_z-N_y)\frac{M_s}{\mu_0}\right]\right\}^{\frac{1}{2}}. \tag{7}$$

Equation (5) reveals that the product of the two transverse components of $\mathbf{m}$ gives rise to a double frequency magnetization m_y along the dc field direction, since both m_x and m_z vary as $e^{j\omega t}$. This nutational component will exist whenever the transverse demagnetizing factors are unequal.

Uniform Precession with Applied rf *h* Field

We note that m_y is maximum for a disk with $N_x=N_y=0$, $N_z=1$. Let us, therefore, consider the motion of the magnetization in a disk-shaped ferrimagnet with losses included. The static field is again along y, and now an rf driving field, $h_x=h_\omega \sin\omega t$, is applied in the x direction. As shown in Appendix, (a), the first-order solution of (1) yields the susceptibility tensor χ, relating the fundamental rf magnetization to the driving field. The particular quantity of interest is χ'', the imaginary part of m_x/μ_0h_ω, given by (A4). Its value at FMR is

$$\chi_0''=\frac{M_s[1+M_s/\mu_0H_0]^{\frac{1}{2}}}{\mu_0\alpha H_0[2+M_s/\mu_0H_0]}, \tag{8}$$

or, expressed in terms of the quantities ω and H_0 measured experimentally,

$$\chi_0''=\omega(\omega^2-\gamma^2H_0^2)/\gamma\alpha H_0(\omega^2+\gamma^2H_0^2). \tag{8'}$$

For future reference, we note that the specific power loss, i.e., the power absorbed per unit volume at the fundamental frequency, is computed from the relation

$$p_\omega=\tfrac{1}{2}\mu_0\omega\chi''h_\omega^2. \tag{9}$$

A second-order calculation, while it leaves the fundamental magnetization unchanged, includes second-order terms which describe a second harmonic magnetization in the dc field direction. The amplitude of this 2ω magnetization is given in Appendix A(b). At FMR, $(m_{2\omega})_0$ may be expressed as

$$(m_{2\omega})_0=\mu_0h_\omega^2M_s^2/4\alpha^2H_0(2\mu_0H_0+M_s)^2, \tag{10}$$

or

$$(m_{2\omega})_0=\mu_0h_\omega^2(\omega^2-\gamma^2H_0^2)^2/4\alpha^2H_0(\omega^2+\gamma^2H_0^2)^2. \tag{10'}$$

Figure of Merit

According to (10), $m_{2\omega}$ is proportional to α^{-2}, so that the power output could be expected to vary as α^{-4}. However, a comparison of materials on this basis is somewhat unsatisfactory, for it assumes a constant intensity of exciting field h_ω. A more realistic approach determines a figure of merit of a material from the initial assumption of constant input power P_i, which is dissipated in the material and input circuit in the process of harmonic generation. Such an approach involves a consideration of (9) as well as (10).

To arrive at this figure of merit, let us consider frequency doubling by a volume of nonlinear reactive material with ω loss, but with negligible 2ω loss. This description fits our ferrimagnets in the range where small-signal theory applies.

We define the following two material parameters:

$$r \equiv 2p_\omega / h_\omega^2, \tag{11}$$

and

$$k_2 \equiv 2\omega m_{2\omega} / h_\omega^2. \tag{12}$$

The factor 2ω appears in (12) to be consistent with the more general case presented elsewhere.[8]

We assume a doubly resonant circuit configuration, as shown in Fig. 1. This diagram suggests a metallic circuit structure, although such is not necessary. It is also possible to allow the nonlinear material to act as a self-resonant circuit.

We further postulate that there is no "loading" of the input, or ω circuit, by the 2ω-output power. This approximation is valid for conversion efficiencies up to about 10%. For simplicity, we also assume that the material is uniformly excited, and couples out energy uniformly. To relate directly to ferrimagnets, the following discussion is in terms of magnetic fields and magnetizations.

The ω power P_i, dividing into circuit and material losses, is given by

$$P_i = \tfrac{1}{2} L h_\omega^2 + p_\omega V = \tfrac{1}{2}(L + rV) h_\omega^2, \tag{13}$$

where L is related to the total ω-circuit structure loss.

Acting as a source, $m_{2\omega}$ gives rise to an $h_{2\omega}$ field in circuit and material. For maximum power output, both ω and 2ω circuits are tuned to resonance. Then $m_{2\omega}$ and the generated $h_{2\omega}$ will be in phase. The average power developed by the material is then

$$P_{2\omega} = \omega m_{2\omega} h_{2\omega} V. \tag{14}$$

We assume that the 2ω structure is not loaded by an output circuit. $P_{2\omega}$ will then be dissipated in the 2ω-resonant structure. Thus,

$$P_{2\omega} = \tfrac{1}{2} h_{2\omega}^2 R_{2\omega}, \tag{15}$$

where $R_{2\omega}$ is a coupling "impedance" that relates cavity field $h_{2\omega}$ (at the material) to $P_{2\omega}$.

Combining (11)–(15), we find that

$$P_{2\omega} = \frac{2}{R_{2\omega}} P_i^2 k_2^2 \left(\frac{V}{rV + L} \right)^2. \tag{16}$$

If $rV \gg L$, then (16) approaches the value

$$P_{2\omega} \approx (2/R_{2\omega}) P_i^2 (k_2/r)^2. \tag{17}$$

[If the cavity is properly loaded by an output circuit, the output power is one-fourth of (17).] The ratio k_2/r is determined entirely by material properties. We therefore define $F = k_2/r =$ *figure of merit for 2ω generation.*

In particular, for the ferrimagnetic disk, oriented and driven as described above, the theoretical value of F at FMR is

$$F_0 = \frac{\omega (m_{2\omega})_0}{(p_\omega)_0} = \frac{|\gamma| M_s}{2\omega\mu_0\alpha[(M_s/\mu_0)^2 + 4(\omega/\gamma)^2]^{\frac{1}{2}}}. \tag{18}$$

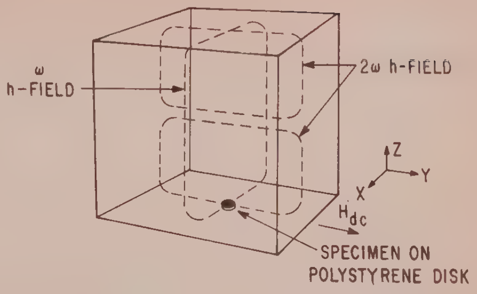

FIG. 2. Ferrimagnetic specimen in doubly resonant cavity.

For most ferrimagnets, if $\omega/2\pi > 8 \times 10^9$, then

$$4(\omega/\gamma)^2 \gg (M_s/\mu_0)^2,$$

and

$$F_0 \approx \gamma^2 M_s / 4\omega^2 \mu_0 \alpha. \tag{19}$$

Therefore, from (17) we see that $P_{2\omega}$ is proportional to α^{-2}.

From (16) and (17) we note the following with regard to practical 2ω generators:

(a) If losses in the material greatly exceed the ω-circuit loss (i.e., $rV \gg L$), a high Q ω-circuit structure is not necessary. This applies to narrow linewidth materials at FMR.

(b) If U is the energy stored in the 2ω circuit, then $R_{2\omega} = 4\omega U / (Q_{2\omega} h_{2\omega}^2)$, where $Q_{2\omega}$ is the Q of the 2ω-circuit. Thus, to maximize $P_{2\omega}$, a high $Q_{2\omega}$ and a small ratio $U/h_{2\omega}^2$ are required.

(c) If $R_{2\omega}$ is independent of V, as in the case for a ferrimagnet in a given metallic cavity, $P_{2\omega}$ is nearly independent of V. Thus, the largest practical value of V will minimize saturation effects without decreasing $P_{2\omega}$. It has been shown that this does not apply to the generation of higher harmonics.[8]

Next, we examine the dependence of F on H at a fixed frequency. Since $r = \mu_0 \omega \chi''$, the expression for F as a function of H is given by the product of (18) with the ratio of the normalized values of $m_{2\omega}$ and χ''. Thus,

$$F = F_0 \frac{m_{2\omega}/(m_{2\omega})_0}{\chi''/\chi''_0}. \tag{20}$$

Representative values of these normalized quantities, computed on the basis of (1), are given by the curves (L−L) of Figs. 4–7. For a narrow linewidth material, $m_{2\omega}/(m_{2\omega})_0$ and χ''/χ_0'' are nearly identical functions over a wide range of magnetic field; hence, F is independent of dc field. For broad linewidth materials, F is slightly field dependent.

This result does not imply that, in general, $P_{2\omega}$ is independent of H. Sufficiently far from resonance, $rV < L$, and $P_{2\omega}$ is given by (16). Near resonance, $P_{2\omega}$ is given by (17). Since the magnitude of (17) exceeds that of (16), operation near FMR is preferable.

Finally, we examine the frequency dependence of $P_{2\omega}$. From (19) we see that it is necessary here to know the frequency dependence of α. Measurements per-

---

[8] I. Kaufman, presented at Conference on Electron Tube Research, Seattle, July 1, 1960 (to be published).

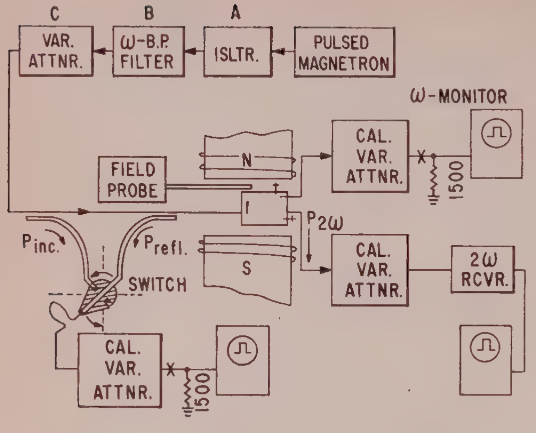

FIG. 3. Block diagram of experimental arrangement.

formed in this laboratory on highly polished single-crystal YIG have indicated that, over a broad range, α is nearly frequency independent.[9] Hence, for ferrimagnets with this behavior, $F_0\propto 1/\omega^2$. The frequency dependence of $R_{2\omega}$ follows no general law, but depends on the type of structure. For the particular case of hollow metal resonators, whose three dimensions vary linearly with wavelength,[10] $U_{2\omega}\propto 1/\omega^3$, and $Q_{2\omega}\propto\omega^{-\frac{1}{2}}$. Then $R_{2\omega}\propto\omega^{-\frac{3}{2}}$; and, therefore, $P_{2\omega}\propto\omega^{-\frac{5}{2}}$.

III. EXPERIMENTAL TECHNIQUE

The specimens used in these experiments were disks (approximately 0.040 in. diameter, and 0.004 in. thick), fabricated from various ferrimagnetic materials. The dimensions were necessarily small to ensure uniform internal driving fields. A specimen, mounted in a rectangular cavity as shown in Fig. 2, is in a region of uniform h field of nearly maximum intensity. To prevent image effects, the specimen is spaced from the wall by a polystyrene disk, 0.045 in. thick. Two tuning screws adjust the resonant frequencies of the cavity to 8.5 kMc in the TE_{101} mode, and to 17.0 kMc in the TE_{012} mode. The fundamental fields are supplied by an X-band magnetron, operating with 3-μsec pulses, with a duty cycle of 10^{-4}. The rf and dc magnetic fields lie in the plane of the disk with the ω field orthogonal to the 2ω and dc fields, the latter two being parallel to one another. A weakly coupled capacitive probe monitors the fundamental field intensity within the cavity.

The microwave circuit is shown in Fig. 3. With this scheme, simultaneous measurements were made of the fundamental absorption and second harmonic generation at discrete values of static magnetic field.

Element A isolates the magnetron; element B essentially eliminates the 2ω magnetron power. The h field within the cavity is maintained at a constant level by attenuator C.

The wall loss P_c, corresponding to a particular value of cavity field intensity, is determined from a measurement on the empty cavity of the coupling coefficient β_e and the incident power P_{i0}.[11] From a measurement of $Q_{0\omega}$, the unloaded Q at ω, the stored energy in the cavity is given by $U=P_cQ_{0\omega}/\omega$. Then, h_ω is found from U and the cavity dimensions.[10] Since the energy stored in the specimen is always negligibly small compared to U, the latter is constant as long as h_ω remains unchanged. It can be shown[12] that the power P_s absorbed by the specimen in the cavity is then given by

$$P_s=\left[\left(\frac{P_i}{P_{i0}}\right)^{\frac{1}{2}}-1\right]\frac{4P_{i0}\beta_e}{1+\beta_e},\tag{21}$$

where P_i is the power incident on the cavity. To obtain a fundamental absorption curve, P_i was measured as a function of dc field while h_ω was kept constant. Then

$$\chi''=2P_s/\mu_0\omega V_sh_\omega^2,\tag{22}$$

where V_s is the volume of the specimen.

To find $m_{2\omega}$, the 2ω output power $\mathcal{P}_{\text{out}}$ is measured by the microwave receiver. The 2ω power $\mathcal{P}_{2\omega}$ generated by the specimen is then

$$\mathcal{P}_{2\omega}=\mathcal{P}_{\text{out}}[(1+\beta_2)/\beta_2],\tag{23}$$

where β_2 is the coupling coefficient of the 2ω cavity.

The stored 2ω energy in the cavity is given by $U_{2\omega}=\mathcal{P}_{2\omega}Q_{L2\omega}/2\omega$, where $Q_{L2\omega}$ is the measured loaded Q at 2ω.[11] From this $U_{2\omega}$ and the cavity dimensions, $h_{2\omega}$ is found.[10]

Finally,

$$m_{2\omega}=\mathcal{P}_{2\omega}/\omega h_{2\omega}V_s.\tag{24}$$

It was observed that the 2ω cavity parameters were unaffected by the presence of the specimen. In all cases, the pulsed microwave power was determined by a measurement of output voltages from crystal detectors. These had been calibrated by a substitution technique, using cw power.

IV. RESULTS

Table I summarizes representative results of measurements on several ferrimagnetic crystals at FMR. Because of the common usage of cgs units, we have listed h_ω both in oersteds and amperes/meter. The values of α were computed from measurements of linewidth and resonant field [see Appendix (c)].

For an infinite disk, the saturation magnetization M_s is related to ω and H_0 by the resonance equation,

$$M_s=\mu_0/H_0[(\omega^2/\gamma^2)-H_0^2].\tag{25}$$

---

[9] D. D. Douthett and I. Kaufman, IRE Trans. Microwave Theory Tech. **MTT-9**, 261 (1961).

[10] S. Ramo and J. R. Whinnery, *Fields and Waves in Modern Radio* (John Wiley & Sons, Inc., New York, 1948), Chap. 10, pp. 383–395

[11] R. A. Lebowitz, IRE Trans. Microwave Theory Tech. **MTT-4**, 51 (1956).

[12] E. G. Spencer, R. C. LeCraw, and F. Reggia, Proc. Inst. Radio Engrs. **44**, 790 (1955).

TABLE I. Summary of results at FMR.

	h_ω		ΔH_{meas}	$M_s\times10^4$		$(p_\omega)_0\times10^{-10}$		$(m_{2\omega})_0\times10^4$		$F_0\times10^5$	
	oe	amp/m	oe	webers/m^2	$\alpha\times10^3$	Meas w/m^3	Calc w/m^3	Meas webers/m^2	Calc webers/m^2	Meas m/amp	Calc m/amp
MnFe$_2$O$_4$ (A) (single xtal)	0.35	28	14	2400	4.4	0.93	0.30	0.18	0.080	10	14
MnFe$_2$O$_4$ (A)	2.4	190	20	2400	6.6	23	9.7	3.5	1.7	8.1	9.4
MnFe$_2$O$_4$ (B) (single xtal)	0.76	60	17	2700	5.0	1.4	1.1	0.27	0.20	10	9.7
MnFe$_2$O$_4$ (B)	2.4	190	17	2700	5.0	7.6	11	1.2	2.0	8.4	9.7
MnFe$_2$O$_4$ (C) (single xtal)	2.4	190	24	2690	5.0	15	15	2.3	3.8	8.2	13
YIG (single xtal)	1.4	110	16	1660	5.8	1.9	2.4	0.25	0.36	7.0	8.0
YIG	14	1100	59	1530	18	46	72	1.8	3.2	2.1	2.4
R−1 (poly xtal)	2.9	230	180	2460	69	1.1	1.0	0.032	0.013	1.6	0.69
R−1	9.0	720	190	2440	76	9.9	9.5	0.19	0.12	1.0	0.67
R151 (poly xtal)	78	6200	330	1800	130	3.1×10^2	3.0×10^2	1.1	1.8	0.19	0.32

When (25) is applied to a finite disk, a correction factor is necessary. Since the diameters of our specimens were approximately 10 times their height, they closely approximate ellipsoids of revolution. It can be shown that the actual M_s is then found by dividing M_s of (25) by $(1-3N_x)$, where N_x is the demagnetizing factor in the plane of the disk. The same correction must be applied to (8′) and (10′). The numerical value of N_x can be obtained from the paper by Osborn.[13]

Table I lists the values of M_s thus obtained. The measured amounts of the specific power loss p_ω were found from (21) and $p_\omega=P_s/V_s$. The calculated values of p_ω were computed from (8′), properly corrected, and (9). The measured values of $m_{2\omega}$ were found from (24); the corresponding calculated values from (10′), again corrected. The values of F were found from $\omega m_{2\omega}/p_\omega$, using measured and calculated values, respectively.

The measured and calculated values of p_ω and $m_{2\omega}$ are in fairly good agreement in most cases. We estimate the accuracy of absolute power measurements to be about 2 db. Good agreement is found between measured and calculated values of F.

Representative curves showing the field dependence of fundamental absorption and second harmonic magnetization are given in Figs. 4–8 and are discussed below. In each case the ordinate has been normalized to its value at FMR. The abscissa $b\alpha$ is the fractional deviation of the magnetic field from its FMR value, i.e., $b\alpha=(H-H_0)/H_0$.

Results for a particular specimen of single-crystal manganese ferrite, for two different drive levels, are shown in Figs. 4 and 5. Experimental plots are compared with theoretical curves, derived from the equations of motion with Landau-Lifshitz (L-L) or Bloch-Bloembergen (B-B) damping (see Appendix A). There are only small differences between L-L and B-B, and very good agreement between theory and experiment is found at both drive levels.

Similar results for single-crystal YIG at a very high drive level are plotted in Fig. 6. While a good fit exists for absorption, some discrepancy appears in the $m_{2\omega}$ data. Principally, in this curve, as in others for this specimen at lower drives, the peak in experimental $m_{2\omega}$ occurs on the low-field side of resonance. This discrepancy could be due to a magnetostatic mode, since at a much lower drive level a subsidiary peak could be distinguished in both $m_{2\omega}$ and χ''.

The curves of Fig. 7, for polycrystalline R-1, again show a slight shift of the $m_{2\omega}$ peak toward lower fields.

Although the absorption curves for all specimens of single-crystal manganese ferrite were consistent with the theory, one specimen displayed an unusual behavior in $m_{2\omega}$. This is shown in Fig. 8, for three different drive levels. The corresponding absorption curves are not included here, since their agreement with theory was very close. The change in linewidth did not exceed

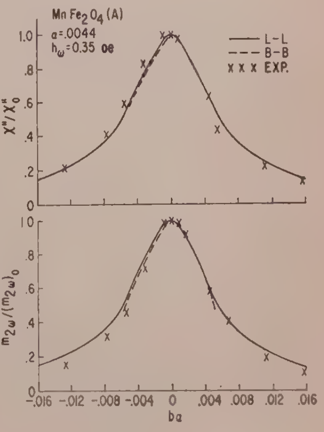

FIG. 4. Absorption and second harmonic magnetization in manganese ferrite. $b\alpha=(H-H_0)/H_0$.

---

[13] J. A. Osborn, Phys. Rev. **67**, 351 (1945).

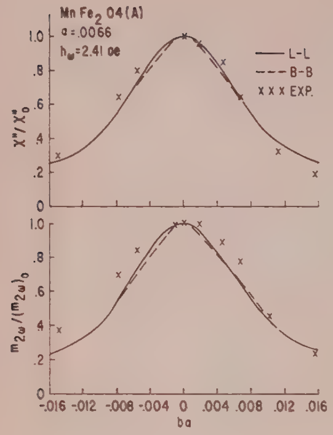

FIG. 5. Absorption and second harmonic magnetization in manganese ferrite. $b\alpha=(H-H_0)/H_0$.

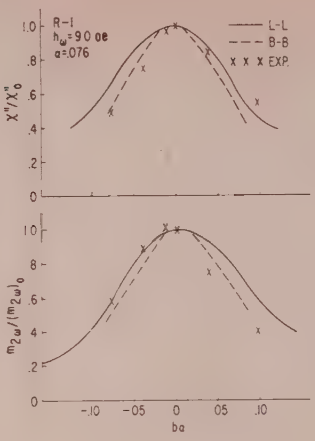

FIG. 7. Absorption and second harmonic magnetization in R-1. $b\alpha=(H-H_0)/H_0$.

10% over these drive levels. The anomaly in $m_{2\omega}$ is not yet understood. It is possibly due to crystalline anisotropy.

As stated in Sec. II, the value of F for narrow linewidth materials is expected to remain constant over a wide range of magnetic field about FMR. Figure 9 shows experimental results of normalized F for various specimens. The range of interest here is within one linewidth of FMR. Although there are deviations from the theoretical curve, it is seen that, in general, F does not differ very much from its resonance value.

Results of the influence of drive level on χ'', $m_{2\omega}$, and F for a specimen of single crystal manganese ferrite are shown in Fig. 10. Values are plotted as a function of h_ω^2, since $m_{2\omega}$ is expected to vary linearly with h_ω^2. The ordinate variables are quantities normalized with respect to their values at the lowest drive level (l.d.), $h_\omega=27.7$ amp/m. The dashed line illustrates the manner in which $m_{2\omega}$ would be expected to increase in the absence of saturation.

From the geometrical derivation[4] for $m_{2\omega}$, we expect F to change at the same rate as χ''. This, indeed, is verified by Fig. 10.

For the specimen of Fig. 10, $m_{2\omega}$ increases roughly as h_ω, instead of h_ω^2, thus indicating saturation and departure from the present theory. It was found for this as for all others tested, that as the exciting field was raised to progressively higher levels, $m_{2\omega}$ always continued to increase. There was no upper maximum.

An exception was a specimen of single-crystal manganese ferrite, with ΔH of 17 oe. Any attempt to drive this sample with $h_\omega>3.5$ oe at FMR resulted in a catastrophic switching away from FMR, with resulting decrease in $m_{2\omega}$. Similar high power instabilities have been reported by Weiss.[14]

In a further observation of high-power effects, we found that in several cases the linewidth ΔH, or α, changed very little as h_ω was increased. χ'' computed on the basis of (8) would therefore have only the same small changes. However, χ'' calculated from the measurement of p_ω at FMR, as for Fig. 10, decreased considerably, with an accompanying decrease in observed value of F.

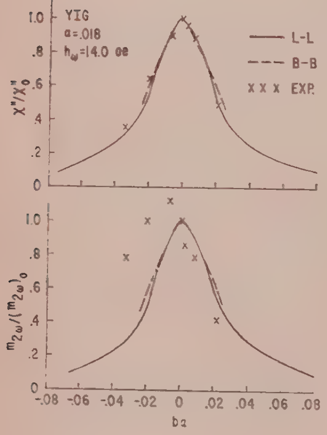

FIG. 6. Absorption and second harmonic magnetization in YIG. $b\alpha=(H-H_0)/H_0$.

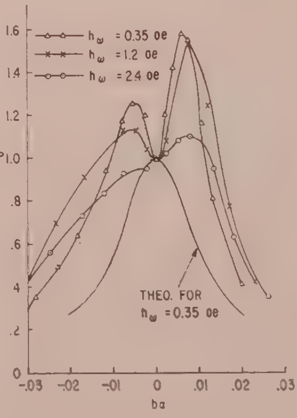

FIG. 8. Anomalous behavior in $m_{2\omega}$ of a specimen of manganese ferrite. $b\alpha=(H-H_0)/H_0$.

---

[14] M. T. Weiss, J. Appl. Phys. 31, 103S (1960).

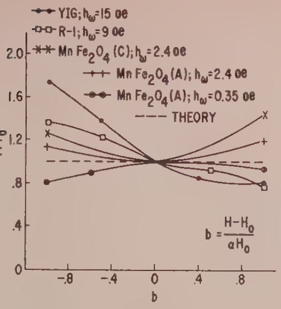

Fig. 9. Normalized F curves for several ferrimagnets within approximately one linewidth of resonance.

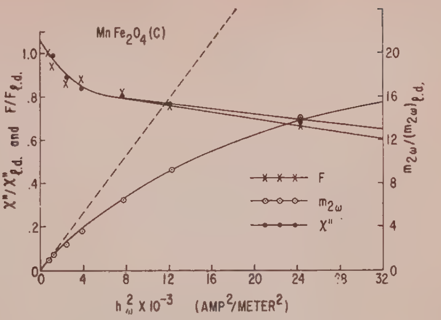

Fig. 10. Experimental curves of χ'', $m_{2\omega}$, and F vs h_ω^2 for manganese ferrite.

V. CONCLUSIONS

(1) Isotropic ferrimagnets generate energy at the second harmonic of a driving frequency because of an asymmetry in the precession of the magnetization. In small ellipsoids the asymmetry may be produced by proper use of demagnetizing factors.

(2) At conversion efficiencies below 10%, the output power is determined by input power, input circuit loss, material volume, the material parameters k_2 and r, and a coupling impedance to the 2ω circuit. In some cases, the output power becomes independent of input circuit loss and material volume. In principle, this should permit the use of large material volumes, in order to avoid saturation caused by excessive driving fields.

(3) A figure of merit F for ω to 2ω conversion is defined for a lossy, nonlinear material. For a ferrimagnet, F is proportional to the ratio of $m_{2\omega}$ to specific power loss. On the basis of the material alone, at constant input power, $P_{2\omega}$ varies as F^2.

(4) $P_{2\omega}$ is also dependent on a 2ω coupling "impedance," $R_{2\omega}$. A favorable value of $R_{2\omega}$ is achieved if the 2ω circuit has high Q and a small ratio of stored energy to $h_{2\omega}^2$.

(5) For a disk operated at FMR, as described in this paper, F is expected to vary as $1/\alpha$ in the absence of high-power effects. Our experiments have substantiated this dependence. Moreover, the equations relating p_ω and $m_{2\omega}$ to ω, M_s, h_ω, and α have also been verified.

(6) The behavior of p_ω, or χ'', and $m_{2\omega}$ vs H_{dc} were computed for both L-L and B-B damping. For relatively narrow linewidths, only slight differences exist in the B-B and L-L results.

(7) A number of experimental plots of χ'', or p_ω, $m_{2\omega}$ vs H_{dc} were compared with these theoretical curves. In all cases good agreement between the χ'' curves exists. In most cases, the $m_{2\omega}$ curves matched equally well. However, anomalies were found here in a few instances. These were double peaks in $m_{2\omega}$, or a slight shift to fields lower than that for FMR of the peak in $m_{2\omega}$.

(8) According to theory, for a material of relatively narrow linewidth, F is almost independent of H_{dc} over a broad range about FMR. However, from a consideration of the interaction of the material with the input circuit structure, operation at FMR or in its immediate vicinity is actually preferred. An experimental evaluation showed that, although there is some field dependence of F, it does not deviate much from its FMR value.

(9) As a material is driven with very high field intensities, it "saturates." A computation of χ_0'' from (8), where α is calculated from the measured linewidth, is now invalid. The actual value of χ_0'' may be obtained from measurements of p_ω and h_ω. It was observed that the relation of measured F vs h_ω is essentially the same as that of this χ_0'' vs h_ω.

(10) As h_ω is increased to very high drive levels, $m_{2\omega}$ continues to increase, although at much lower rates than at low levels. In general, $m_{2\omega}$ will increase until complete saturation in m_ω is reached.

ACKNOWLEDGMENTS

The authors gratefully acknowledge the assistance in the experimental work of R. P. Kemp, and the discussions with Dr. H. C. Corben and Dr. E. T. Kornhauser.

APPENDIX

(a) Calculation of Susceptibility for a Disk with $N_x=N_y=0$, $N_z=1$

We assume that the static and rf magnetic fields are applied parallel to the plane of the disk, and are mutually perpendicular. The magnetization and internal field are given by

$$\mathbf{M}=m_x\hat{\imath}+M_s\hat{\jmath}+m_z\hat{k}, \tag{A1}$$

$$\mathbf{H}=h_x\hat{\imath}+H\hat{\jmath}-(m_z/\mu_0)\hat{k}, \tag{A2}$$

where $h_x=h_\omega \sin\omega t$, and m_x and m_z have the form

$$m_x=\mu_0 h_\omega(\chi' \sin\omega t+\chi'' \cos\omega t),$$

$$m_z=\mu_0 h_\omega(K'' \sin\omega t-K' \cos\omega t).$$

To first order, the y component of $M\approx M_s$. $\omega/2\pi$ is the fixed driving frequency.

Substituting (A1) and (A2) into (1), and solving for the components of the susceptibility, we get

$$\chi'=(\gamma^2M_s/\mu_0^2D)[B(\gamma^2BH/\mu_0-\omega^2)+\omega^2\alpha^2(B+\mu_0H)], \quad \text{(A3)}$$

$$\chi''=(\omega\gamma\alpha M_s/\mu_0D)[\omega^2+(\gamma^2B^2/\mu_0^2)], \quad \text{(A4)}$$

$$K'=(\omega\gamma M_s/\mu_0D)[(\gamma^2BH/\mu_0)-\omega^2], \quad \text{(A5)}$$

$$K''=(\omega^2\gamma^2\alpha M_s/\mu_0^2D)(B+\mu_0H), \quad \text{(A6)}$$

where

$$D=\left[\frac{\gamma^2BH}{\mu_0}-\omega^2\right]^2+\left[\frac{\omega\gamma\alpha}{\mu_0}(B+\mu_0H)\right]^2,$$

and $B=\mu_0H+M_s$. At FMR the angular frequency is $\omega=(\gamma^2B_0H_0/\mu_0)^{\frac{1}{2}}$. The field dependence of χ'' for several values of α is shown by the curves labeled L-L in Figs. 4–7. In each case χ'' is normalized to its resonance value (8′).

(b) Calculation of 2ω Magnetization

In the second-order calculation for $m_{2\omega}$, it can be shown that there are no double frequency components in the x or z directions. Therefore, the expressions for **M** and **H** given by (A1), (A2) may be rewritten as

$$\mathbf{M}=(\chi'\sin\omega t+\chi''\cos\omega t)\mu_0h_\omega\hat{\imath}+(M_s+m_1\sin2\omega t+m_2\cos2\omega t)\hat{\jmath}+(K''\sin\omega t-K'\cos\omega t)\mu_0h_\omega\hat{k}, \quad \text{(A7)}$$

$$\mathbf{H}=h_\omega\sin\omega t\hat{\imath}+H\hat{\jmath}-h_\omega(K''\sin\omega t-K'\cos\omega t)\hat{k}. \quad \text{(A8)}$$

Substituting (A7) and (A8) into (1), and neglecting terms of order h_ω^3, the solution for the amplitude of the second harmonic magnetization $m_{2\omega}$ is

$$m_{2\omega}=(m_1^2+m_2^2)^{\frac{1}{2}}, \quad \text{(A9)}$$

where

$$m_1=\frac{-\mu_0^{\frac{3}{2}}h_\omega^2}{4(BH)^{\frac{1}{2}}}\left[K''+\chi'K''+\chi''K'+\frac{\alpha}{M_s}\{M_s\chi'+B(K'^2-K''^2)+\mu_0H(\chi''^2-\chi'^2)\}\right], \quad \text{(A10)}$$

and

$$m_2=\frac{\mu_0^{\frac{3}{2}}h_\omega^2}{4(BH)^{\frac{1}{2}}}\left[K'+\chi'K'-\chi''K''+\frac{\alpha}{M_s}\{-M_s\chi''-2BK'K''+2\mu_0H\chi'\chi''\}\right]. \quad \text{(A11)}$$

To compare with experiment, $m_{2\omega}$ is normalized to its value at FMR given by (10′). The curves labeled L-L in Figs. 4–7 show the variation of $m_{2\omega}/(m_{2\omega})_0$ in the vicinity of resonance.

(c) Determination of Loss Parameter α

To find the value of α from experimental data, w compared the χ''/χ_0'' curve with a series of theoretica curves, computed from (A4). We observed fron the latter that for the disk, α is not merely th ratio $\Delta H/H_0$, where ΔH is the measured half-linewidth Instead, a corrected value δH must be used. The rati $\delta H/\Delta H$ is a function of M_s, or the ratio $\omega/\gamma H_0$.

From the series of theoretical χ'' curves,

$$\alpha=\frac{\delta H}{H_0}=\frac{1}{H_0}\left[\frac{(\Delta H)^+}{0.39(\omega/\gamma H_0)^2+0.57}\right], \quad \text{(A12}$$

where $(\Delta H)^+=H^+-H_0$; and H^+ is the high-field valu of H at which $\chi''/\chi_0''=\frac{1}{2}$.

The values of α used in plotting the theoretica curves labeled L-L of Figs. 4–7 were found from th corresponding experimental curves by this method.

For cases in which an experimental curve is asym metric, the agreement between theory and experimen in χ''/χ_0'' is better on the high-field side of FMR thar on the low-field side. This is not surprising since α wa derived from H^+.

(d) Bloch-Bloembergen Damping for a Disk with $N_x=N_y=0$, $N_z=1$

The equation of motion for **M** with Bloch-Bloem bergen damping is

$$\dot{M}_{x,z}=\gamma(\mathbf{M}\times\mathbf{H})_{x,z}-(M_{x,z}/T_2), \quad \text{(A13}$$

$$\dot{M}_y=\gamma(\mathbf{M}\times\mathbf{H})_y-[(M_y-M_s)/T_1], \quad \text{(A14}$$

where T_1, T_2 are the longitudinal and transverse relaxa tion times, respectively. At low-signal levels, whe $\gamma^2h_\omega^2T_1T_2\ll1$, the half-linewidth within a few percen is given by $\Delta H_{\text{meas}}=1/(|\gamma|T_2)$. This is in contrast t the case of L-L damping, where α can differ by as muc as 30% from the measured $\Delta H/H_0$. In general, sinc $\alpha H_0\neq1/(|\gamma|T_2)$, it was of interest to compare th measured values of χ'' and $m_{2\omega}$ with the theoretica curves computed with B-B damping.

Equations (A13) and (A14) are solved as before fo χ'' and $m_{2\omega}$, using the expressions for **M** and **H** give by (A1) and (A2). At FMR, $\chi_{\text{B-B}}''$ is

$$(\chi_{\text{B-B}}'')_0\approx\frac{|\gamma|M_sT_2(1+M_s/\mu_0H_0)^{\frac{1}{2}}}{2\mu_0}. \quad \text{(A1}$$

The second harmonic magnetization at FMR is foun to be

$$(m_{2\omega\text{B-B}})_0\approx\gamma^2M_s^2T_2^2h_\omega^2/16\mu_0H_0. \quad \text{(A16}$$

Though not given here, the off-resonance expressior for χ'' and $m_{2\omega}$ were calculated. These were the normalized by (A15) and (A16), respectively. Th resulting curves labeled B-B are shown in Figs. 4–7. I computing each curve, the appropriate value of T derived from ΔH_{meas}, was used.

Radiation Enhancement of Bulk Diffusion in 10% Zn–90% Cu by 30-kev Ne$^+$ Ion Bombardment*

R. A. Arndt† and R. L. Hines
Northwestern University, Evanston, Illinois

(Received May 29, 1961)

Diffusion coefficients for the diffusion of zinc in 10% Zn−90% Cu single crystals are determined for both irradiated samples and unirradiated samples. This is accomplished by measuring the zinc lost from the samples when they are heated in a vacuum of 3×10^{-5} mm Hg at temperatures from 207°C to 316°C. The zinc loss is measured by observing the change in optical reflection coefficient at a wavelength of 550 mμ. The diffusion length $(Dt)^{\frac{1}{2}}$ is then found using the known optical constants of ZnCu alloys and the expected concentration distribution. The diffusion lengths thus obtained range from 20 to 1000 A. Bombardment by a 30-kev Ne$^+$ ion beam of 2.9 μa/cm^2 produces defects at a calculated rate of 4.5×10^{-2} atomic fractions/sec over the depth of 300 A penetrated by the beam. For well-annealed samples the bombardment enhances the diffusion. The radiation-enhanced diffusion coefficient depends on the square root of the bombarding flux density and has an activation energy of 9300±1700 cal/g mole. The results agree with theoretical predictions for enhanced bulk diffusion for the case of defects annealing by direct recombination plus linear anneal to fixed sinks.

INTRODUCTION

THE study of radiation effects in solids has been limited for the most part to the investigation of hanges in physical properties such as electrical resisivity, density, thermal conductivity, stored energy, tc., due to the imperfections produced by the radiation. he effect of radiation on diffusion and other rate procsses is usually small because of the low rate of defect roduction by most radiation sources. Since bombardnent with heavy ions (mass number 20 to 200) at nergies of 5 to 50 kev gives very high defect production ates, it is possible to measure the effect of ion bombardnent on diffusion. The defect production rate employed ı this experiment is 4.5×10^{-2} atomic fractions/sec as ontrasted with a typical neutron reactor exposure hich gives 10^{-10} atomic fractions/sec.[1] The interpretaion of the experiment should fall within the general heory of radiation effects since the end result of any ype of radiation (1-Mev neutrons, 30-kev Ne$^+$ ions, tc.) is the production of defects in the bombarded solid.

To date, the only successful measurements of the fect of irradiation upon diffusion have been from inirect observations such as the ordering rates in alloys. he primary difficulty encountered is the rapid anneal f the defects produced by the irradiation since any etectable diffusion requires either very high tempertures or very long times. Experiments that have ielded enhanced diffusion under neutron irradiation re those of Adam and Dugdale[2] and Blewitt and Coltnan.[3] Increased ordering has also been found with rradiation by electrons[4] and gamma rays.[5] More recently, Dienes and Damask[1] have found enhanced diffusion in α brass under neutron bombardment and have formulated a theory for radiation enhanced diffusion. Johnson and Martin[6] have looked for enhanced macroscopic self-diffusion in silver but found no effect because the defect production rate was too low.

This paper is concerned with the effect of 30-kev neon ion bombardment on the diffusion of zinc in a 10% Zn−90% Cu alloy. The diffusion coefficient is determined from the change in optical reflection coefficient of the alloy as it is heated in a vacuum and loses its zinc by evaporation. The diffusion lengths are determined from the optical reflection coefficients and range from 20 to 1000 A.

THEORY

Since the ion beam dimensions and crystal dimensions are large compared to the distances involved in the coordinate x perpendicular to the target surface, the problem reduces to diffusion in one dimension. The basic relationship used to define the diffusion coefficient D is then[7]

$$J(t,x)=-D[\partial c(t,x)/\partial x], \tag{1}$$

where $J(t,x)$ is the flux density of the diffusing material in g/cm^2 sec, c is the concentration of the diffusing material in g/cm^3, x is in cm, t is the time, and D is in cm^2/sec. Actually, the removal of zinc atoms from the sample involves both the diffusion of zinc in the interior of the sample and its evaporation from the surface. The evaporation at the surface depends on the zinc concentration and the zinc partial pressure at the surface. Since the flux of evaporating atoms is the product of the probability of a zinc atom evaporating from a surface site times the concentration at the surface, it appears justifiable to regard the evaporating flux as proportional

---

* Supported by the U. S. Atomic Energy Commission.

† This work is based on a thesis submitted to the Department physics, Northwestern University, in partial fulfillment of he requirements for the degree of Doctor of Philosophy.

[1] G. J. Dienes and A. C. Damask, J. Appl. Phys. **29**, 1713 1958).

[2] J. Adam and R. A. Dugdale, Nature **168**, 581 (1951).

[3] T. H. Blewitt and R. R. Coltman, Acta Met. **2**, 549 (1954).

[4] J. Adam, A. Green, and R. A. Dugdale, Phil. Mag. **43**, 1216 1952).

[5] R. A. Dugdale, Phil. Mag. **1**, 537 (1956).

[6] R. D. Johnson and A. B. Martin, J. Appl. Phys. **23**, 1245 (1952).

[7] J. Crank, *Mathematics of Diffusion* (Oxford University Press, New York, 1955), Chap. 2.

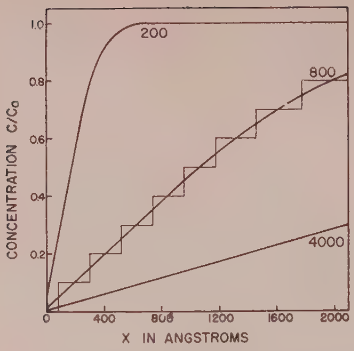

FIG. 1. Concentration distributions for evaporation of zinc. The numbers on the curves are values of $(Dt)^{\frac{1}{2}}$ in angstroms and all three are calculated for $h=5\times10^6$ cm^{-1}. The light line on the $(Dt)^{\frac{1}{2}}=800$ A curve is the approximation used to compute the optical reflection coefficient.

to the zinc concentration at the surface. Equating the diffusion flux to the evaporation flux, we find the boundary condition at $x=0$ to be

$$J(t,0)=-p(M/2\pi RT)^{\frac{1}{2}}c(t,0)/c(0,0), \qquad (2)$$

where p is the partial pressure at the absolute temperature T of the sample, M is the molecular weight, and R is the gas constant. The walls of the vacuum system are at room temperature and completely trap the evaporated zinc atoms. The flux of zinc atoms re-evaporated from the walls can be neglected because the vapor pressure of zinc at room temperature is a factor of 10^9 less than that at the sample surface.[8]

The time-dependent equation for diffusion,

$$(\partial c/\partial t)=D(\partial^2 c/\partial x^2), \qquad (3)$$

subject to the boundary condition (2) and the condition $c(0,x)=c_0$ for $x\geqslant 0$, where c_0 is the initial concentration, yields the solution

$$c/c_0=\operatorname{erf}[\tfrac{1}{2}x(Dt)^{-\frac{1}{2}}] + \exp(hx+h^2Dt)\operatorname{erfc}[\tfrac{1}{2}x(Dt)^{-\frac{1}{2}}+h(Dt)^{\frac{1}{2}}], \qquad (4)$$

where $h=p(M/2\pi RT)^{\frac{1}{2}}/Dc_0$.[7] The parameter can be estimated from the known vapor pressure of zinc when alloyed with copper,[8,9] and the values of D obtained below. The value of h varies from 4.1×10^6 cm^{-1} at 316°C to 7.6×10^6 cm^{-1} at 243°C. The exact value of h has only a minor effect and is taken to be 5×10^6 cm^{-1}. The profiles of c/c_0 for several values of $(Dt)^{\frac{1}{2}}$ for $h=5\times10^6$ cm^{-1} are shown by the solid curves in Fig. 1. The concentration profile is not too different from that obtained when the vapor pressure is large enough to ensure a vanishing zinc concentration at the surface.

Although the diffusion lengths $(Dt)^{\frac{1}{2}}$, where t is the time in seconds, involved in this experiment are very small, the diffusion does produce marked changes in the reflection coefficient for visible light. The quantitativ relationship between the reflection coefficient and th diffusion length can be calculated from the concentration distribution given by (4) and the known optica constants for α brass as a function of zinc concentration. The problem is easily handled using the method Rouard where the actual problem of a thin film continuously varying optical properties is replaced b a series of films, each of which has uniform properties. The calculation of the reflection coefficient R of such series of uniform films is then a straightforward, although tedious, procedure. A typical approximate concentration distribution is shown in Fig. 1 as the ligh line superimposed on the $(Dt)^{\frac{1}{2}}=800$ A curve. Th calculated values of R/R_0 are shown in Fig. 2 as a function of diffusion length where R_0 is the reflection coefficient in the absence of diffusion. Subdividing the concentration distribution still further produces less tha 1% change in R/R_0. With the aid of Fig. 2, the diffusio coefficient can be directly determined from measurements of the reflection coefficient and the length of tim of the diffusion experiment.

An idea of the depth of a zinc-depleted layer require to produce a significant change in reflection coefficien is useful in interpreting the experimental results. It ca be obtained by calculating the reflection coefficient a layer of pure copper of depth d on a substrate 10% Zn–90% Cu. The calculation is straightforwar using the known optical constants and the metho given by Heavens.[11] The calculated values are shown Fig. 3 and it is seen that, roughly speaking, the reflection coefficient is determined by the first 300 A material.

The production rate of defects in the solid is discusse

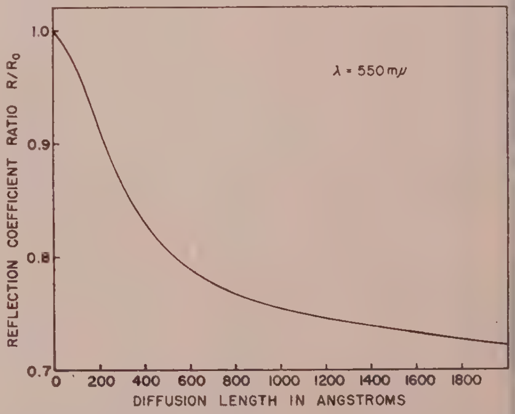

FIG. 2. Reflection coefficient ratio R/R_0, for $\lambda=550$ mμ, as function of diffusion length, $(Dt)^{\frac{1}{2}}$. The value for $h=5\times10^6$ cm This curve is obtained by computing R/R_0 by the method Rouard for approximate distributions as shown in Fig. 1.

---

[8] E. W. Washburn, *International Critical Tables* (McGraw-Hill Book Company, Inc., New York, 1928), Vol. 3.

[9] R. Hargreaves, J. Inst. Metals **64**, 115 (1939).

[10] H. Lowery, H. Wilkinson, and D. L. Smare, Proc. Phys. Sc (London) **49**, 345 (1937).

[11] O. S. Heavens, *Optical Properties of Thin Solid Film* (Academic Press, Inc., New York, 1955), p. 63.

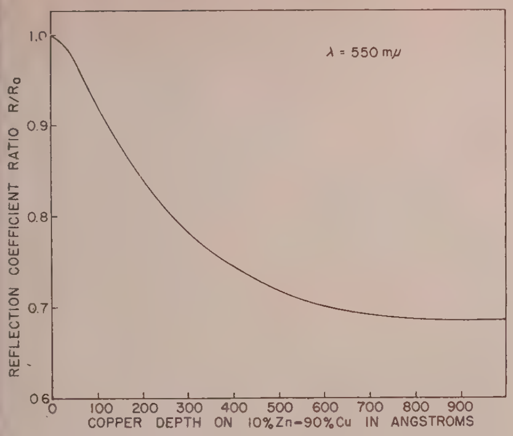

FIG. 3. Reflection coefficient ratio R/R_0, for $\lambda = 550$ mμ as a unction of the depth of a copper layer. The substrate is taken as 0% Zn–90% Cu.

by Dienes and Vineyard[12] who show that N, the number of defects produced per incident particle, is given by

$$N = E_i/2E_d, \tag{5}$$

where E_i is the energy of the incident particles that is effective in producing displacements and E_d is the energy required to displace an atom from its lattice position ($E_d \approx 25$ ev). The magnitude of E_i is obtained rom the relation

$$E_i = ME_f/16m, \tag{6}$$

where M is the mass of the incident particle, m is the electronic mass, and E_f is the Fermi energy of the target metal. Since the Fermi energy depends on the two-hirds power of the number of electrons per atom, the Fermi energy of 10% Zn–90% Cu is 7.5 ev by applying his relationship to the known Fermi energies of copper and zinc.[13] For 30-kev neon ions incident on 10% Zn–90% Cu, $E_i = 17$ kev. Actually, E_i is the threshold for he onset of energy loss by ionization and energy loss by onization will dominate only if $E \gg E_i$, where E is the particle energy.[12] For this reason it appears desirable to eplace E_i by E in (5). As is discussed below, the energy oss due to displacements is independent of energy, so hat for depths less than the range $\mathcal{R}$ of the ions, the defect production rate K per unit volume is given by

$$K = EF/2E_d\mathfrak{N}\mathcal{R}, \tag{7}$$

where F is the incident flux density and $\mathfrak{N}$ is the number f atoms/cm³ in the alloy.

The effect of the ion bombardment on the diffusion determined by the production rate of defects in the nterior of the solid. Ideally, the bombardment should reate defects at a rate independent of the distance from the surface so that the diffusion conditions are uniform. The range and energy loss characteristics of heavy particles has been discussed by Bohr[14] and Nielsen.[15] For the 30-kev Ne$^+$ ions employed here, the energy loss per unit distance is independent of energy, and the range $\mathcal{R}$ of the particles is calculated from Eq. (11) of Nielsen to be $\mathcal{R} = 400$ A. However, the low energy of the neon ions and the relative masses of the beam particles and the target atoms are such that the penetration depth is governed by diffusion effects. Nielsen[15] has shown that neutron scattering theory can be adapted to yield penetration depths for charged particles assuming enough collisions so that the particle motion is random. Equation (21) of Nielsen[15] gives $\mathcal{R} = 235$ A for 30-kev neon ions in copper. Actually, the number of collisions is not large enough to ensure pure diffusion motion nor can scattering effects be neglected. A compromise to use a range value between the two extremes so the value $\mathcal{R} = 300$ A is used for 30-kev Ne$^+$ ions in all calculations below.

The theory of radiation-enhanced diffusion as given by Dienes and Damask[1] is presented below. They consider three different cases for annealing the defects introduced by radiation: (a) linear anneal of defects to dislocations and surfaces, (b) direct recombination of interstitials and vacancies, and (c) linear anneal to dislocation and surfaces plus direct recombination. The three different cases give different activation energies and flux dependence as shown in Table I from Dienes and Damask.[1] Here E_m^v is the energy of motion of a vacancy and E_m^i is the energy of motion of an interstitial.

The diffusion coefficient D_v for diffusion of a vacancy is expressed as

$$D_v = v\nu_v\lambda^2, \tag{8}$$

where λ = jump distance, ν_v = jump frequency, and v = atomic fraction of vacancies. The jump frequency, as a function of temperature, is given by

$$\nu_v = A_2^v \exp(-E_m^v/kt). \tag{9}$$

TABLE I. Activation energy and flux dependence of radiation-enhanced diffusion as determined by the annealing mechanism of radiation-produced defects.

Annealing mechanism	Activation energy for enhanced diffusion	Dependence of enhanced diffusion on flux
Linear	0	Linear
recombination	Vacancies $E_m^v - \frac{1}{2}E_m^i$ Interstitials $\frac{1}{2}E_m^i$	Square root
Recombination plus linear anneal	$\frac{1}{2}E_m^v$	Square root

---

[12] G. J. Dienes and G. H. Vineyard, *Radiation Effects in Solids* Interscience Publishers, Inc., New York, 1959).

[13] A. H. Wilson, *The Theory of Metals* (Cambridge University ress, New York, 1953), 2nd ed.

[14] N. Bohr, Kgl. Danske Videnskab. Selskab. Biol. Medd. **18**, No. 8 (1948).

[15] K. O. Nielsen, *Electromagnetically Enriched Isotopes and Mass Spectroscopy*, edited by M. L. Smith (Academic Press, Inc., New York, 1956), p. 68.

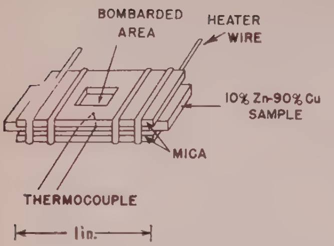

FIG. 4. Diagram of heating unit. The sample is placed between the slices of mica. The thermocouple rests on the sample surface and is shielded from the ion beam.

The steady-state vacancy concentration at a defect production rate K for the general case of (c) above is

$$v=-\tfrac{1}{2}(\alpha\lambda^2+v_0)+\tfrac{1}{2}[(\alpha\lambda^2+v_0)^2+4K/\nu_v]^{\frac{1}{2}}, \qquad (10)$$

where α is a proportionality constant for linear anneal of defects. In Eq. (10), v_0 is the thermal equilibrium concentration of vacancies and is given by

$$v_0=A_1^v \exp(-E_f^v/kt), \qquad (11)$$

where E_f^v is the energy of formation of a vacancy, and k is Boltzmann's constant. At large defect production rates, the last term in (10) predominates and gives a square-root dependence of diffusion coefficient on flux and an activation energy for enhanced diffusion of $\frac{1}{2}E_m^v$. The values of the various parameters for copper, as given by Dienes and Damask,[1] are $\lambda^2=10^{-15}$ cm^2, $A_1^v=1.0$, $A_2^v=10^{15}$ sec^{-1}, $E_f^v=1.2$ ev$=27\,600$ cal/g mole, and $E_m^v=0.8$ ev$=18\,400$ cal/g mole. The magnitude of the constant α enters through the assumption that the defects anneal out at dislocations present in the sample. With ion bombardment, the region of interest is close to the surface and the defects may anneal to the surface. In this case, by comparing the discussions of annihilation of defects at surfaces and at dislocations given by Dienes and Vineyard[12] [Eqs. (5–14) and (5–18)] it is seen that $\alpha=1/\mathcal{R}^2$.

Although (10) applies only in steady-state conditions, the buildup times are usually short compared to the experimental times involved. An approximate solution for the buildup time τ is

$$\tau=(K\nu_v)^{-\frac{1}{2}}. \qquad (12)$$

APPARATUS AND EXPERIMENTAL PROCEDURE

The bombarding apparatus for this experiment is the same as that used in the study of radiation effects of positive ion bombardment of quartz.[16] The ion beam is about 2×2 mm in cross section and has a uniform current density of 2.9 μa/cm^2. The sample to be bombarded is held in a heater unit which consists of two thin slices of mica wound with tungsten wire (see Fig. 4). The sample is sandwiched between the strips of mica and one mica strip has a hole in it so that the ion beam strikes the sample directly. A Chromel P Alumel thermocouple rests on the surface of the sample and is shielded from the beam. Temperatures at the sample can be measured and controlled to ±1°C. A Faraday cup that can be swung in and out of the beam path is calibrated to read the beam current at the target. The beam area is determined by measuring the bombarded area by observation with a microscope having a calibrated mechanical stage. All experimental runs are performed in a vacuum of 1 to 3×10^{-5} mm Hg. The sample temperature during bombardment is high enough to prevent hydrocarbon film formation on the samples.[17]

The samples of 10%Zn–90%Cu alloy are $\frac{1}{4}\times\frac{3}{4}\times0.020$ in. and are cut from large sheets of 0.020-in. thickness. Spectroscopic examination shows no impurities greater than 0.03%. To anneal the samples without dezincification or oxidation, they are sealed in an evacuated Vycor tube along with chips of the same alloy. Four different prediffusion anneals are employed: 2 hr at 750°C, 48 hr at 750°C, 165 hr at 750°C, and 2 hr at 850°C. After annealing, the strips are electrolytically polished and etched in a solution of two parts orthophosphoric acid to one part water. The average grain size is about 0.5 mm.

The reflection coefficients are measured using the optical system of a vertical illumination microscope (0.40-N.A., 20-× objective) with the eyepiece replaced by a barrier layer photocell. The spot size of the ligh beam is 0.2 mm in diameter which is considerably smaller than the crystal diameter so that all measurements are done on single crystals. The crystal orientation is determined from etch-pit examination, and all measurements are for crystals with the {110} plane parallel to th sample surface.[18] After selecting a particular grain o a sample and measuring its reflection coefficient R relative to a partially silvered mirror, the sample i subjected to the experimental diffusion conditions. Then the reflection coefficient R of the same grain is again measured relative to the partially silvered mirror and the experimental quantity R/R_0 is obtained. The experimental values of R/R_0 for a given set of conditions are reproducible within 1%.

The wavelength of the light used in measuring R/R is 550 mμ and is obtained by using an interference filter of 18 mμ half-width. This wavelength is used because it gives a maximum change in R/R_0 when the zinc content of the alloy changes from 10% to zero.[10] The reflection is nominally measured at normal incidence, but, since 0.40-N.A. objective was used, the measurement is actually an average over angles ±24° from normal incidence.

RESULTS

Typical results for reflection coefficient for a 10%Zn–90%Cu sample heated in a vacuum for various temperatures and various times are shown in Fig. 5. The samples used to obtain the data shown in Fig. 5 have been annealed 48 hr at 750°C. The different prediffusion anneals all give approximately the same results. It is necessary to correct the time of the diffusion anneals because of the thermal lag of the samples. With the experimentally known temperature versus time dependence and the known activation energy for diffusion, an effective time, at the desired temperature, for the heating and cooling periods can be calculated. This effective time is added to the experimentally measured time of the diffusion anneals and is always less than 7.5 sec.

---

[16] R. L. Hines and R. Arndt, Phys. Rev. **119**, 623 (1960).

[17] A. E. Ennos, Brit. J. Appl. Phys. **4**, 101 (1953).

[18] See, for example, C. S. Barrett, *Structure of Metals* (McGraw-Hill Publishing Company, Inc., New York, 1943), 1st ed., p. 17

Figure 6 shows values of R/R_0 for samples with a prediffusion anneal of 48 hr at 750°C that are bombarded with 30-kev Ne^+ ions at a current density of 2.9 $\mu a/cm^2$ while held at the temperatures shown. Thus, the change in reflection coefficient is due both to thermal diffusion and the effect of the bombardment on the diffusion.

Before diffusion coefficients can be calculated, the sputtering effect of the ion beam on the target has to be considered. Sputtering modifies the theoretical concept of the surface conditions in two ways. First, sputtering can roughen the surface and destroy specular reflection. Second, sputtering removes a thin surface layer so that the reflection coefficient measures the optical properties of the sample with a thin surface layer removed. If the thickness removed by sputtering is larger than the diffusion length, the effect of diffusion will be completely obscured. The first effect of sputtering is checked by bombarding an annealed sample of pure copper. No change of R/R_0 is found, within experimental error, for a bombardment of 12 min at 2.9 $\mu a/cm^2$. This also shows that the bombardment has negligible effect on the reflection coefficient in the absence of diffusion. Samples bombarded longer than 20 min do have roughened surfaces so that this limits the length of bombardment time that can be employed.

The second effect of sputtering can be corrected for by assuming that the surface layer can be approximated by a layer of pure copper on a 10% Zn–90% Cu substrate. Figure 3 gives the reflection coefficient ratio R/R_0 as a function of copper depth. The amount of copper sputtered away during the bombardment is easily computed from the data of Yonts, Normand, and Harrison.[19] For 30-kev neon ions at a current density of 2.9 $\mu a/cm^2$, copper is removed at a rate of 5 A/min. The value of R/R_0, corrected for sputtering, can be found from Fig. 3 in the following manner. First, the observed R/R_0 is used to find an effective copper depth. Second, the thickness of copper sputtered away is added to the effective copper depth. Last, this total copper depth is used in conjunction with Fig. 3 to obtain a value of R/R_0 corrected for sputtering. The largest correction for sputtering is only 6% for a 16-min bombardment. This method of correction is checked by first heating a sample for a short period of time and then bombarding at a greatly reduced temperature so that no additional diffusion takes place during the bombardment. The observed R/R_0 is exactly as expected from applying the above correction. The values given in Fig. 6 are corrected for sputtering.

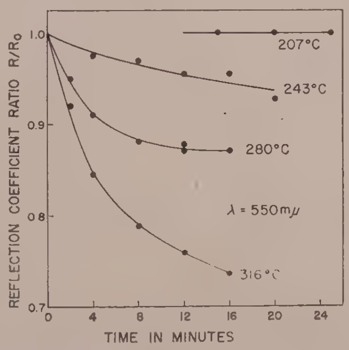

Fig. 5. Reflection coefficient ratio R/R_0 as a function of diffusion time. The samples are not bombarded and have had a prediffusion anneal of 48 hr at 750°C.

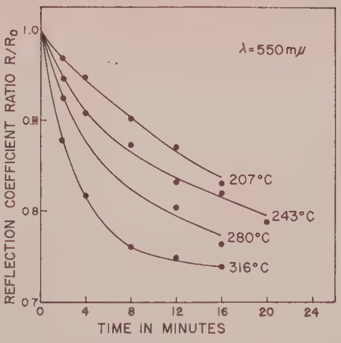

Fig. 6. Reflection coefficient ratio R/R_0 for samples that are bombarded with 30-kev Ne^+ ions at a current density of 2.9 $\mu a/cm^2$ while held at the temperatures shown. The points shown include a correction for the sputtering effect of the ion beam.

The data given in Figs. 5 and 6 are used in conjunction with Fig. 2 to calculate the actual diffusion coefficients. Each value of R/R_0 determines a value of $(Dt)^{\frac{1}{2}}$ and since t is known, D is directly determined. At each diffusion anneal temperature, several values of R/R_0 at different t are obtained and hence several different determinations of D. These values are averaged and the deviations are used to find the probable error of the average. Values of the diffusion coefficient obtained in this manner are shown in Table II. Figure 7 shows log D as a function of I/T for both bombarded and unbombarded samples. Also in Fig. 7, log D for high-temperature diffusion data extropolated to the temperatures of this experiment.[20] The slopes of these curves yield the activation energy for diffusion which are 30 000±3000 cal/g mole for the unbombarded samples and 9300 ±1700 cal/g mole for bombarded samples. The depend-

---

[19] O. C. Yonts, C. E. Normand, and D. E. Harrison, Jr., J. Appl. Phys. **31**, 447 (1960).

[20] R. M. Barrer, *Diffusion In and Through Solids* (Cambridge University Press, New York, 1941).

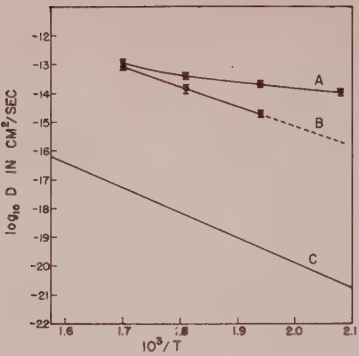

FIG. 7. Log D as a function of reciprocal absolute temperature. Curve A is for bombarded samples and curve B is for unbombarded samples. Curve C is extrapolated from high-temperature data of diffusion zinc in 10% Zn−90% Cu.

ence of diffusion coefficient on flux is shown in Fig. 8.

Two possible side effects of the neon bombardment which could influence the diffusion are the presence of neon ions as impurities and the finite range of the neon ions. First, if all of the neon incident on the target remained uniformly distributed over the bombarded depth of 300 A, there would be about 0.9% neon concentration after 2 min of bombardment and about 7½% after 16 min. If the presence of neon affected the diffusion, one would expect to see a steady increase or decrease in D as the bombardment time increased. No such trend is observed and the deviations in D are random. The effect of impurities on the diffusion of zinc in brass has been studied as a function of the valence of the impurity.[21] It was found that the greater the valence of the impurity the greater was its effect on the diffusion of zinc in brass. Aluminum was found to have no effect when present in quantities as great as 2 at.%. Consequently, neon as an impurity should have no effect at these concentrations.

The second aspect of the finite range of the neon ions is that the reflection coefficient method measures the zinc loss from a region having two different diffusion coefficients. The bombarded layer will have one diffusion coefficient and the region beyond the neon range of 300 A will have a different diffusion coefficient. The light used in measuring the reflection coefficient, however, is sensitive only to depths less than 300 A. Thus, if the concentration distribution is assumed to have a discontinuity at 300 A, such that c/c_0 rises to unity, the resulting R/R_0 does not deviate from the R/R_0 for the continuous distribution by more than $\frac{1}{2}\%$ at $(Dt)^{\frac{1}{2}} = 3\times10^{-6}$ cm and 7% at $(Dt)^{\frac{1}{2}} = 1\times10^{-5}$ cm.

TABLE II. Experimental diffusion coefficients of zinc in 10% Zn−90% Cu for pure thermal diffusion and for thermal diffusion in the presence of 30-kev Ne$^+$ ion bombardment at a current density of 2.9 μa/cm^2.

	Diffusion coefficients in cm^2/sec	
Temp °C	D (unbombarded)	D (bombarded)
207	less than 10^{-16}	$1.1\pm0.1\times10^{-14}$
243	$2.2\pm0.2\times10^{-15}$	$2.1\pm0.2\times10^{-14}$
280	$1.4\pm0.2\times10^{-14}$	$3.8\pm0.6\times10^{-14}$
316	$8.6\pm1.8\times10^{-14}$	$1.2\pm0.2\times10^{-13}$

DISCUSSION

It is seen from Fig. 7 that the diffusion coefficient obtained by reflection coefficient measurements is much higher than the expected value of the bulk diffusion coefficients extrapolated from high temperatures. Furthermore, the activation energy of 30 000±3000 cal/g mole is lower than the observed value of 42 000 cal/g mole at higher temperatures. It is well known, however, that at low temperatures, dislocations can provide "short-circuit" paths for diffusion and give much higher diffusion constants than predicted by bulk diffusion.[22] From Figs. 2 and 5, it is seen that the diffusion lengths investigated in this experiment range from 20 to 1000 A. For diffusion over such distances, dislocations could be very effective in providing short-circuit paths. These diffusion lengths are to be contrasted with those employed by Dienes and Damask.[8] They observed enhanced diffusion coefficients of $D\sim10^{-20}$ cm^2/sec with diffusion times of 10^4 sec so that $(Dt)^{\frac{1}{2}}\sim1$A. For such short diffusion lengths, dislocation diffusion can be ignored. A second reason for believing dislocation diffusion to be important in this experiment is that the diffusion coefficient of unbombarded samples depended on the previous history of the samples. Samples which were annealed and then mechanically polished and chemically etched showed diffusion coefficients a factor of 5 to 10 larger than the electropolished samples. The high diffusion coefficients of the mechanically polished samples is thus believed due to the dislocations introduced by the cold work of mechanica polishing. Also, unannealed samples with very smal grain size showed diffusion coefficients higher than those

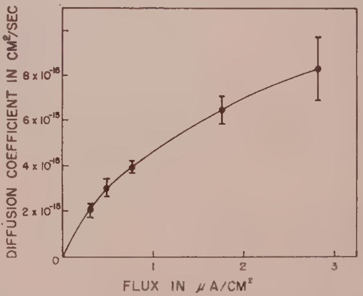

FIG. 8. Diffusion coefficient, at 207°C as a function of bombarding flux of 30-kev Ne$^+$ ions. This data can be fitted with a straight line on a D vs square root of flux plot.

---

[21] A. Accary, *Colloque sur la diffusion a l'état solide, Saclay, 1958* (North-Holland Publishing Company, Amsterdam, 1959), p. 45.

[22] D. Turnbull, *Defects in Crystalline Solids* (The Physical Society, London, 1955), p. 203.

given in Table II. Attempts to measure dislocation densities by etch-pit counting were not successful. Jacquet's method[23] of developing dislocation etch pits on cadmium-doped α brass did not work on the undoped 10% Zn-90% Cu used in this experiment. It is known, however, that even well-annealed metal crystals contain 10^5 to 10^9 dislocations/cm^2.[24] All of this information suggests that the diffusion in the annealed, electropolished samples is primarily along dislocations in the absence of bombardment.

When the well-annealed samples are bombarded, it is seen that diffusion coefficients are increased and that the activation energy for low temperatures is only 9300±1700 cal/g mole. Moreover, when samples with different histories are bombarded, the diffusion coefficient under bombardment is virtually independent of the previous history of the sample. Thus, for samples with large amounts of cold work, and consequent high diffusion coefficients for pure thermal diffusion, the bombardment actually lowers the diffusion coefficient.[25] These facts suggest that the diffusion coefficient under bombardment does not depend on dislocation density and that only bulk diffusion is important during bombardment. The reason probably lies in the high production rate K of defects. Substituting the conditions $F=2.9\ \mu\text{a/cm}^2$ and $\mathcal{R}=300$ A into (7), the defect production rate is found to be $K=4.5\times10^{-2}$ atomic fractions/sec. On the average, any given atom is displaced every 22 sec. Furthermore, the steady-state concentration of vacancies is calculated from (10) to be 2.1×10^{-5} at 243°C. Since a dislocation consists of an array of several hundred or more atoms with a special type of order, the high defect concentrations formed in this experiment may well disturb the dislocations enough to remove their effectiveness as "short-circuit" diffusion paths. Since bombardment inhibits dislocation diffusion and yet enhanced diffusion is observed in well-annealed samples, it is believed that the predominant diffusion mechanism in well-annealed samples under bombardment is radiation-enhanced bulk diffusion.

From Table I it is seen that the different cases of radiation-enhanced bulk diffusion are characterized by the activation energy of the enhanced diffusion and the flux dependence of the diffusion. From Fig. 8 it is seen that the enhanced diffusion observed here is proportional to the square root of the flux. The activation energy for enhanced diffusion at the lower temperatures is seen from Fig. 7 to be 9300±1700 cal/g mole. This is equal, within experimental error, to half the activation energy for vacancy motion in copper, $\frac{1}{2}E_m{}^v=9200$ cal/g mole as given by Dienes and Damask.[1] Thus, we are dealing with case (c) presented by Dienes and Damask where the enhanced diffusion is due to a vacancy mechanism with the steady-state concentration of vacancies limited by linear anneal to surfaces and dislocations plus direct recombination of vacancies and interstitials. From (12) it is seen that the buildup time is 0.001 sec at 243°C so that the steady-state approximation is justified in this experiment.

At 243°C, the $4\text{K}/\nu_v$ term of Eq. (10) has a value of 1×10^{-8}. The term $(\alpha\lambda^2+v_0)^2$ is very nearly 1×10^{-8} since, at this temperature, v_0 is very much smaller than $\alpha\lambda^2$, which has a value of 1×10^{-4} for $\mathcal{R}=300$ A. The square-root dependence of diffusion on flux with an activation energy of $\frac{1}{2}E_m{}^v$ is expected only if $(\alpha\lambda^2+v_0)^2\ll4\text{k}/\nu_v$. This suggests that either the $(\alpha\lambda^2+v_0)$ term is too large or the $4K/\nu_v$ term is too small since the experimental results show the predicted behavior for case (c). At present it is not possible to determine which of these two theoretically determined quantities is off in magnitude from the true physical phenomena.

From Eq. (8), the ratio of the enhanced diffusion coefficient to the thermal diffusion coefficient should equal the ratio of the steady-state concentration of vacancies under bombardment to the thermal equilibrium concentration of vacancies. At 243°C, the ratio of the vacancy concentrations is $v/v_0=8.5\times10^6$. The ratio of the measured diffusion coefficient under bombardment to the pure thermal diffusion coefficient extrapolated from high data is 5×10^5. The disagreement between these two numbers is not too serious in view of the approximations used in Eq. (10) to arrive at a value for v, the steady-state vacancy concentration.

CONCLUSIONS

The diffusion of zinc in 10%Zn–90%Cu is found to be enhanced by the radiation effect of 30-kev positive ion bombardment. The enhancement is in agreement with theoretical predictions based on a vacancy mechanism for zinc diffusion. The activation energy for enhanced diffusion and the flux dependence of the enhanced diffusion suggest that the steady-state vacancy concentration under bombardment is limited by linear anneal of defects to surfaces and dislocations and direct recombination of interstitials and vacancies.

ACKNOWLEDGMENT

We wish to thank G. J. Dienes for his interest in this work and for several stimulating and helpful discussions.

---

[23] P. A. Jacquet, Acta Met. 2, 752 (1954).

[24] C. Kittel, *Introduction to Solid State Physics* (John Wiley & Sons, Inc., New York, 1956), 2nd ed., p. 554.

[25] R. Arndt and R. L. Hines, Bull. Am. Phys. Soc. II-5, 147 (1960).

JOURNAL OF APPLIED PHYSICS VOLUME 32, NUMBER 10 OCTOBER, 1961

Single and Double Pile-Up of Dislocations in MgO Crystals

Y. T. Chou and R. W. Whitmore
Edgar C. Bain Laboratory for Fundamental Research, United States Steel Corporation, Research Center, Monroeville, Pennsylvania

(Received February 17, 1961)

A quantitative analysis has been made of elastic interactions in three types of pile-up groups of dislocations in MgO crystals; (i) single pile-up, (ii) double pile-up on two orthogonal slip planes, and (iii) double pile-up on two slip planes intersecting at 120°. The equilibrium positions of dislocations in these groups are given. It is found that the stress concentration factor is highest in type (iii) and lowest in type (i). The number of dislocations in the pile-up groups sufficient to raise the tip stress to $1000\sigma_0$ is 1000 in type (i), about 120, determined by extrapolation, in type (ii), and 62 in type (iii).

INTRODUCTION

Recent observations on deformed MgO crystals have shown three types of pile-up groups of dislocations which are believed to be responsible for crack formation.[1-3] These types are: (i) a single pile-up arrested by a slip band and initiating {110}-type cracks; (ii) a double pile-up on two orthogonal {110} slip planes, forming {100}-type cleavage cracks, and (iii) a double pile-up on two {110} slip planes intersecting at 120°, forming {110}-type cracks. A simplified schematic representation of these groups is shown in Fig. 1. Because of the importance of these pile-up groups in the fracture process in MgO, a quantitative study is made to determine the distribution of glide dislocations along their slip plane and the strength of these simplified groups. For simplicity it is assumed in each case for the double pile-up groups that the number of dislocations in each of the two slip planes is the same.

The analytic solutions for a single dislocation pile-up are well known and are summarized here for convenience of reference and comparison. Presently, no analytical solutions are available for types (ii) and (iii). The calculations presented here for these cases are thus numerical in form and were performed on a digital computer. The stress analysis is based on the elastic interaction between dislocations using the following set of elastic constants for MgO taken from Dourand's measurements[4,5] at 300°K:

$$C_{11}^0=28.93\times10^{11}\ \mathrm{d/cm^2}$$

$$C_{12}^0=8.77\times10^{11}\ \mathrm{d/cm^2}$$

$$C_{44}^0=15.477\times10^{11}\ \mathrm{d/cm^2}.$$

The elastic anisotropy of MgO crystals is taken into account by employing the theory developed by Eshelby, Read, and Shockley.[6]

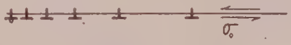

(a) SINGLE PILE-UP

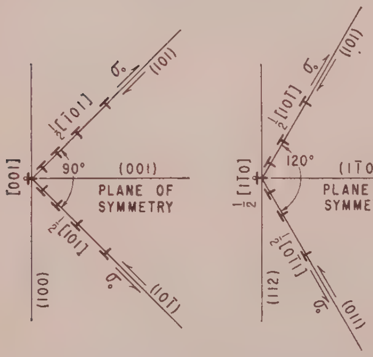

(b) 90° DOUBLE PILE-UP (c) 120° DOUBLE PILE-UP

Fig. 1. Schematic representation of various dislocation pile-up groups in MgO crystals.

SINGLE PILE-UP ON {110} PLANES

This type of pile-up is formed when n edge dislocations, gliding in a single slip plane under the action of a stress σ_0, are arrested in front of a sufficiently stable barrier. In the simplest case when an analytic solution is obtainable, the leading dislocation is assumed to be locked at some point x_0 in a stress field which is in proportion to $\delta'(x-x_0)$, where δ' is the derivative of Dirac's δ function. This case has been studied in great detail by Eshelby, Frank, and Nabarro.[7] They found that the equilibrium positions x_i of the individual gliding dislocations in a group of size n can be represented by the zeros of the first derivative of the Laguerre polynomial of nth order, $L_n'(x)$. Numerical values for small values of n have been determined by Chou, Garofalo, and Whitmore.[8] Fortunately, for large values of n, x_i can be closely approximated by the zeros of the first-order Bessel function J_1. Thus, Eshelby, Frank, and Nabarro concluded:

(1) The distance x_1 between the first gliding and the

---

[1] R. J. Stokes, T. L. Johnston, and C. H. Li, Phil. Mag. **3**, 718 (1958); **4**, 920 (1959).

[2] J. Washburn, A. E. Gorum, and E. R. Parker, Trans. Am. Inst. Mining, Met., Petrol., Engrs. **215**, 230 (1959).

[3] A. S. Keh, J. C. M. Li, and Y. T. Chou, Acta Met. **7**, 694 (1959).

[4] M. A. Durand, Phys. Rev. **50**, 449 (1936).

[5] C_{ij}^0 refers to the standard coordinate system where x, y, and z axes coincide with three cubic edges.

[6] J. D. Eshelby, W. T. Read, and W. Shockley, Acta Met. **1**, 251 (1953).

[7] J. D. Eshelby, F. C. Frank, and F. R. N. Nabarro, Phil. Mag. **42**, 351 (1951).

[8] Y. T. Chou, F. Garofalo, and R. W. Whitmore, Acta Met. **8**, 480 (1960).

TABLE I. Equilibrium positions x_i of glide dislocations in the pile-up groups in MgO crystals (unit length $A/2\sigma_0$).

Group n	Single	90° double	120° double
2	2.000	2.000	1.236
3	1.268	1.078	0.5413
	4.732	4.922	3.824
4	0.9358	0.7070	0.3107
	3.305	3.193	2.134
	7.759	8.100	6.935
5	0.7432	0.5125	0.2043
	2.571	2.306	1.393
	5.731	5.737	4.361
	10.95	11.44	10.32
6	0.6170	0.3950	0.1458
	2.113	1.775	0.9920
	4.611	4.393	3.070
	8.399	8.537	6.976
	14.26	14.90	13.88
7	0.5275	0.3174	0.1100
	1.796	1.425	0.7475
	3.876	3.519	2.302
	6.918	6.790	5.160
	11.23	11.51	9.854
	17.65	18.44	17.57
8	0.4610	0.2628	0.08636
	1.564	1.179	0.5864
	3.352	2.909	1.802
	5.916	5.597	4.013
	9.421	9.404	7.549
	14.19	14.61	12.92
	21.09	22.04	21.34
9	0.4094	0.2226	0.06983
	1.385	0.9984	0.4740
	2.956	2.461	1.455
	5.182	4.729	3.230
	8.162	7.916	6.032
	12.07	12.18	10.16
	17.25	17.81	16.14
	24.59	25.68	25.18
10	0.3680	0.1919	0.05780
10	1.243	0.8607	0.3923
	2.645	2.121	1.203
	4.616	4.072	2.666
	7.220	6.803	4.960
	10.57	10.42	8.292
	14.83	15.07	12.96
	20.38	21.09	19.47
	28.12	29.37	29.08
15	0.2445	0.1088	0.02810
	0.8228	0.4877	0.1907
	1.740	1.201	0.5841
	⋮	⋮	⋮
	46.18	48.22	49.15
20	0.1837	0.07285	0.01692
	0.6168	0.3266	0.1148
	1.301	0.8038	0.3517
	⋮	⋮	⋮
	64.65	67.49	69.81
25	0.1469	0.05341	0.01144
	0.4932	0.2394	0.07763
	1.039	0.5893	0.2378
	⋮	⋮	⋮
	83.37	87.02	90.80
30	0.1224	0.04146	0.008319
	0.4106	0.1859	0.05644
	0.8646	0.4574	0.1728
	⋮	⋮	⋮
	102.2	106.7	112.0
40	0.09178	0.02782	0.005038
	0.3078	0.1247	0.03418
	0.6477	0.3069	0.1047
	⋮	⋮	⋮
	140.4	146.5	154.9
60		0.01587	0.002490
		0.07112	0.01689
		0.1750	0.05174
		⋮	⋮
		226.8	241.9

locked dislocation is

$$x_1=1.84A/n\sigma_0, \qquad (1)$$

where A is a function of the elastic constants C_{ij}^0 dependent on the orientation and is equal to $Gb/2\pi(1-\nu)$ for isotropic solids, where G is the shear modulus, and ν is Poisson's ratio.

(2) The distance L between the locked and the last glide dislocation or the range of the pile-up is

$$L=2nA/\sigma_0. \qquad (2)$$

(3) The shear stress along the slip plane at a distance x ahead of the locked dislocation is

$$\sigma_{xy}=\sigma_0\{1+(L/x)^{\frac{1}{2}}\}, \quad (1.15)x_1\ll x\ll L. \qquad (3)$$

(4) At the tip of the pile-up the shear stress is exactly[9]

$$(\sigma_{xy})_0=n\sigma_0. \qquad (4)$$

The normal stresses around the tip were first estimated for large values of n by Koehler.[11] However, a more elaborate expression was later derived by Stroh[12] and is given by

$$\sigma_n=3(n/r)^{\frac{1}{2}}\sigma_0 \sin\theta \cos(\theta/2), \quad (1/n)\ll r\ll 4n, \qquad (5)$$

where σ_n is the normal stress at a distance r from the tip and acting on a plane which makes an angle θ with the slip plane, and r is dimensionless with a unit of $A/2\sigma_0$. For purposes of comparison in a later section, the numerical values of x_i are listed in Table I.

DOUBLE PILE-UP ON TWO ORTHOGONAL {110} PLANES

The formation of this group is geometrically similar to the double pile-up described by Cottrell[13] for bcc metals.[8,14] When two identical dislocation rows, one gliding on (101) with Burgers vector $\frac{1}{2}[\bar{1}01]$, and the other on $(10\bar{1})$ with Burgers vector $\frac{1}{2}[101]$, meet under the action of a shear stress σ_0, the two leading dislocations may coalesce to form a new edge dislocation of the [001]/(100) type,[15] i.e.,

---

[9] The same expression was given earlier by Cottrell (see reference 10) employing the virtual work principle.

[10] A. H. Cottrell, Progr. in Metal Phys. **1**, 77 (1949).

[11] J. S. Koehler, Phys. Rev. **85**, 480 (1952).

[12] A. N. Stroh, Proc. Roy. Soc. (London) **A223**, 404 (1954); **A232**, 548 (1955).

$$\tfrac{1}{2}[\bar{1}01]+\tfrac{1}{2}[101]\rightarrow[001]. \qquad (6)$$

Since reaction (6) does not involve a lowering of elastic energy (isotropic or anisotropic), the stability of the new edge seems questionable. However, the stability of the newly formed dislocation can not be fully determined until more knowledge is available on core energies. Let us assume therefore that the [001]/(100) edge is stable and a symmetrical double pile-up group does exist.

The stress field of a straight edge dislocation along a cubic axis with Burgers vector on {100} or {110} is given by[6,8]:

$$\sigma_{xx}=-A\frac{y[(C+3)x^2+y^2]}{(x^2+y^2)^2+Cx^2y^2}$$

$$\sigma_{yy}=A\frac{y(x^2-y^2)}{(x^2+y^2)^2+Cx^2y^2}$$

$$\sigma_{xy}=A\frac{x(x^2-y^2)}{(x^2+y^2)^2+Cx^2y^2},^{16} \qquad (7)$$

where

$$A=\frac{b_e^0}{2\pi}(C_{11}^0+C_{12}^0)\left[\frac{C_{44}^0(C_{11}^0-C_{12}^0)}{C_{11}^0(C_{11}^0+C_{12}^0+2C_{44}^0)}\right]^{\frac{1}{2}}=A^0$$

for [100]/(100) type with $b_e^0=a$,

$$C=(C_{11}^0+C_{12}^0)(C_{11}^0-C_{12}^0-2C_{44}^0)/(C_{11}^0C_{44}^0)=C^0,$$

and

$$A=\frac{b_e}{2\pi}(C_{11}^0+C_{12}^0)\left[\frac{C_{44}^0(C_{11}^0-C_{12}^0)}{C_{11}^0(C_{11}^0+C_{12}^0+2C_{44}^0)}\right]^{\frac{1}{2}}$$

for [011]/(110) type with $b_e=\sqrt{2}/2a$

$$C=\frac{4(C_{11}^0+C_{12}^0)(-C_{11}^0+C_{12}^0+2C_{44}^0)}{(C_{11}^0-C_{12}^0)(C_{11}^0+C_{12}^0+2C_{44}^0)}.$$

The z axis coincides with the dislocation line and the y axis is normal to the slip plane. The jth glide dislocation is then subjected to a total shear force which is the sum of the following:

(1) Force due to the [001]/(100) edge

$$F_{j1}=b_e(\sqrt{2}/2)A^0(1/x_j)=b_eA(1/x_j), \qquad (8)$$

(2) Force due to all other gliding dislocations on the same slip plane

$$F_{j2}=Ab_e\sum_{\substack{i=1\\i\neq j}}^{n-1}\frac{1}{x_j-x_i}, \qquad (9)$$

(3) Force due to all gliding dislocations on the conjugate slip plane

$$F_{j3}=Ab_e\sum_{i=1}^{n-1}\frac{x_i(x_j^2-x_i^2)}{(x_i^2+x_j^2)^2+Cx_i^2x_j^2}, \qquad (10)$$

and

(4) Force due to the applied shear stress σ_0

$$F_{j4}=-b_e\sigma_0. \qquad (11)$$

In equilibrium the shear force on each gliding dislocation is equal to zero, leading to

$$\frac{1}{x_j}+\sum_{\substack{i=1\\i\neq j}}^{n-1}\frac{1}{x_j-x_i}+\sum_{i=1}^{n-1}\frac{x_i(x_j^2-x_i^2)}{(x_i^2+x_j^2)^2+Cx_i^2x_j^2}-\tfrac{1}{2}=0$$

$$j=1,2,3,\cdots(n-1), \qquad (12)$$

where x_i has a unit of $A/2\sigma_0$.

The numerical solution of Eq. (12) was obtained by using a modified Newton-Raphson iteration method[17] on a Burrough's 205 computer and an IBM 704 digital computer. The computed values of x_i's for $n=2-10$, 15, 20, 25, 30, 40, 60 are also given in Table I. For large values of n only the first three (x_1,x_2,x_3) and the last (x_{n-1} or L) dislocation positions are listed.

The results can also be empirically formulated by the following expressions:

$$\begin{aligned}x_1&=(4.69)(1/n)^{1.39},\\x_2&=(21.1)(1/n)^{1.39}, \quad 10\leq n\leq 60\\x_3&=(51.8)(1/n)^{1.39},\end{aligned} \qquad (13)$$

with an error of ±1%, and

$$L=(3.96)n-(10.7), \quad 10\leq n\leq 60 \qquad (14)$$

with an error of ±2%.

The stress values which have been computed include:

(a) the normal stress along the plane of symmetry (001), $(\sigma_n)_{ps}$;

(b) the shear stress along the plane of symmetry (001), $(\sigma_{xy})_{ps}$; and

(c) the shear stress at the tip on the slip plane $(\sigma_{xy})_0$

---

[13] For the double pile-up in MgO, only pure edge dislocations are involved. In bcc metals, dislocations of the mixed type are encountered.

[14] A. H. Cottrell, Trans. Am. Inst. Mining, Met., Petrol., Engrs. **212**, 192 (1958).

[15] [*uvw*] refers to Burgers vector with a unit *a*, and (*hkl*) refers to the slip plane.

[16] The identity $B\equiv C+3$ is not shown in reference 8.

[17] F. B. Hildebrand, *Introduction to Numerical Analysis* (McGraw-Hill Book Company, Inc., New York, 1956), p. 447.

The corresponding expressions for these are, respectively,

$$(\sigma_n)_{ps}=-2\sigma_0\sum_{i=1}^{n-1}\frac{x[(C+2)(x-x_i)^2+2x^2]+2(x-x_i)[(x-x_i)^2-x^2]}{[(x-x_i)^2+x^2]^2+Cx^2(x-x_i)^2},^{18} \tag{15}$$

$$(\sigma_{xy})_{ps}=2\sigma_0\sum_{i=1}^{n-1}\frac{(C+4)x(x-x_i)^2}{[(x-x_i)^2+x^2]^2+Cx^2(x-x_i)^2}, \tag{16}$$

nd

$$(\sigma_{xy})_0=\sigma_0\left\{1+4\sum_{i=1}^{n-1}\frac{1}{x_i}\right\}. \tag{17}$$

n Eqs. (15), (16), and (17), the contribution of the [100]/(010) edge is excluded. The applied shear tress σ_0 is included in $(\sigma_{xy})_0$, but not in $(\sigma_n)_{ps}$ and $\sigma_{xy})_{ps}$.

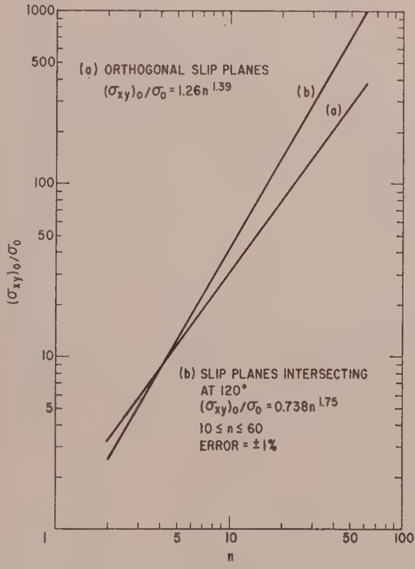

FIG. 2. Relationship between tip stress $(\sigma_{xy})_0$ on the slip planes nd the number of dislocations n for a double pile-up on two slip lanes in MgO.

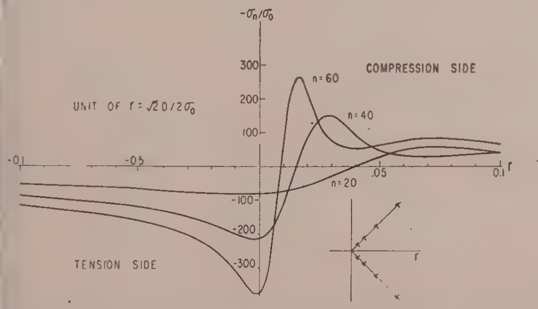

FIG. 3. Distribution of normal stress σ_n along the (001) plane f symmetry for a double dislocation pile-up on two orthogonal lip planes.

Some computed results are shown in Figs. 2–4. Table II also lists the $(\sigma_{xy})_0$, $(\sigma_n)_{ps0}$, and $(\sigma_{xy})_{ps0}$ values[19] for various n's. The linear part of the curve in Figure 2 may be expressed by

$$(\sigma_{xy})_0=(1.26)n^{1.39},\quad 10\leq n\leq 60 \tag{18}$$

with an error of ±1%.

DOUBLE PILE-UP ON TWO {110} PLANES INTERSECTING AT AN ANGLE OF 120°

This type of pile-up group was first suggested by Keh, Li, and Chou[3] to explain the observation of

TABLE II. Tip stresses of the pile-up groups in MgO crystals

		$(\sigma_{xy})_0/\sigma_0$		$(\sigma_n)_{ps0}/\sigma_0$		$(\sigma_{xy})_{ps0}/\sigma_0$	
n	Single	90° double	120° double	90° double	120° double	90° double	120° double
2	2	3.00	2.52	2.00	1.76	0	1.02
3	3	5.52	4.97	4.52	4.59	0	2.65
4	4	8.40	8.22	7.40	8.34	0	4.81
5	5	11.6	12.2	10.6	12.9	0	7.46
6	6	15.0	16.8	14.0	18.3	0	10.6
7	7	18.7	22.1	17.7	24.4	0	14.1
8	8	22.6	28.0	21.6	31.2	0	18.0
9	9	26.7	34.5	25.7	38.7	0	22.3
10	10	30.9	41.6	29.9	46.9	0	27.1
15	15	54.5	84.9	53.5	96.9	0	55.9
20	20	81.5	141	80.5	161	0	93.1
25	25	111	208	110	239	0	138
30	30	143	285	142	328	0	190
40	40	213	471	212	543	0	313
60	60	374	952	373	1098	0	634

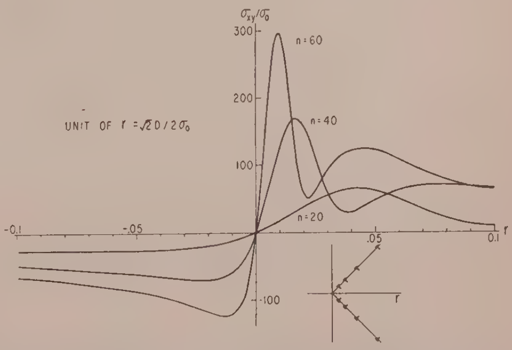

FIG. 4. Distribution of shear stress σ_{xy} along the (001) plane of symmetry for a double dislocation pile-up on two orthogonal slip planes.

---

[18] In Eqs. (15) and (16), x is the distance measured on the slip lane 0x, the corresponding value on the symmetry plane, or, will e $\sqrt{2}x$.

[19] $(\sigma_n)_{ps0}$ and $(\sigma_{xy})_{ps0}$ are, respectively, the values of $(\sigma_n)_{ps}$ and $(\sigma_{xy})_{ps}$ at the tip.

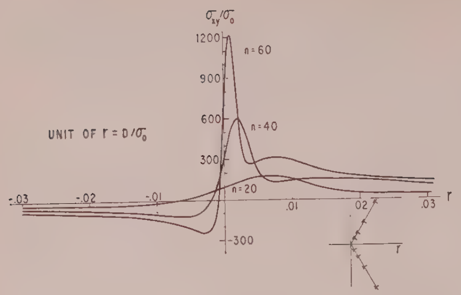

FIG. 5. Distribution of normal stress σ_n along the $(1\bar{1}0)$ plane of symmetry for a double dislocation pile-up on two {110} slip planes intersecting at an angle of 120°.

{110}-type cracks in indented MgO crystals. The formation of this group is very similar to that of the 90° double pile-up, except that in this case the two slip planes, say (011) and (101), intersect at an angle of 120° and the glide dislocations are of the mixed type. The coalescence reaction is

$$\tfrac{1}{2}[0\bar{1}1]+\tfrac{1}{2}[10\bar{1}]\rightarrow\tfrac{1}{2}[1\bar{1}0]. \tag{19}$$

In so combining the two leading dislocations, $\frac{1}{2}[0\bar{1}1]/(011)$ and $\frac{1}{2}[10\bar{1}]/(101)$, 38% of the elastic energy is released (see Appendix). The new edge $\frac{1}{2}[1\bar{1}0]/(112)$ should be therefore relatively stable.

A particular feature of this type of pile-up is that the dislocation lines are oriented in the $[\bar{1}\bar{1}1]$ direction, which makes the anisotropic analysis much more laborious. The detailed data of the stress field for both the glide dislocations and the $\frac{1}{2}[1\bar{1}0]/(112)$ edge are given in the Appendix.

It is possible now to examine the shear forces acting on the jth glide dislocation. The factors contributing to these forces and their magnitude are:

(1) The newly formed edge, $\frac{1}{2}[1\bar{1}0]/(112)$

$$F_{j1}=(2\sigma_0)(\alpha/x_j),^{20} \tag{20}$$

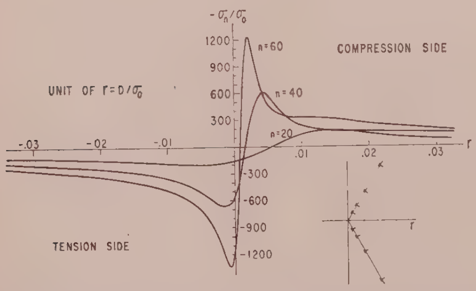

FIG. 6. Distribution of shear stress σ_{xy} along the $(1\bar{1}0)$ plane of symmetry for a double dislocation pile-up on two {110} slip planes intersecting at an angle of 120°.

(2) All glide dislocations on the same slip plane

$$F_{j2}=(2\sigma_0)\sum_{\substack{i=1\\i\neq j}}^{n-1}\frac{\beta}{x_j-x_i}, \tag{21}$$

(3) All glide dislocations on conjugate slip planes

$$F_{j3}=-(2\sigma_0)\sum_{i=1}^{n-1}\sum_{l=1}^{3}\frac{a_{(l)}x_i+b_{(l)}x_j}{x_i^2+c_{(l)}x_ix_j+d_{(l)}x_j^2}, \tag{22}$$

and

(4) The applied shear stress σ_0

$$F_{j4}=-\sigma_0 b_e, \tag{23}$$

where α, β, $a_{(l)}$, $b_{(l)}$, $c_{(l)}$, and $d_{(l)}$ are numerical constants and are found to be

α	β	l	$a_{(l)}$	$b_{(l)}$	$c_{(l)}$	$d_{(l)}$
		1	1.0361	0.2583	1	1.8247
0.9420	1.5203	2	0.2143	0.2952	1.4520	1
		3	−0.4902	0.07757	0.5480	1

The force equilibrium equations then become

$$\frac{\alpha}{x_j}+\sum_{\substack{i=1\\i\neq j}}^{n-1}\frac{\beta}{x_j-x_i}-\sum_{i=1}^{n-1}\sum_{l=1}^{3}\frac{a_{(l)}x_i+b_{(l)}x_j}{x_i^2+c_{(l)}x_ix_j+d_{(l)}x_j^2}-\tfrac{1}{2}=0,$$
$$j=1,2,3,\ldots,(n-1) \tag{24}$$

when x_i has the same unit of $A/2\sigma_0$ as in case (i) and case (ii). The equilibrium deposition of $2(n-1)$ glide dislocations is thus determined by Eqs. (24). The results are listed in Table I.

The empirical expressions for x_1, x_2, x_3, and L are

$$\begin{aligned}x_1&=(3.22)(1/n)^{1.75},\\x_2&=(21.9)(1/n)^{1.75},\quad 10\leq n\leq 60\\x_3&=(67.0)(1/n)^{1.75},\end{aligned} \tag{25}$$

with an error of ±1%, and

$$L=(4.25)n-(13.9),\quad 10\leq n\leq 60 \tag{26}$$

with an error of ±2%.

The three stress functions $(\sigma_n)_{ps}$, $(\sigma_{xy})_{ps}$, and (σ_{xy}) for this case are

$$(\sigma_n)_{ps}=4\sigma_0\sum_{i=1}^{n-1}\sum_{l=1}^{3}\frac{e_{(l)}x_i+f_{(l)}x}{x_i^2+g_{(l)}x_ix+h_{(l)}x^2},^{21} \tag{27}$$

$$(\sigma_{xy})_{ps}=4\sigma_0\sum_{i=1}^{n-1}\sum_{l=1}^{3}\frac{p_{(l)}x_i+q_{(l)}x}{x_i^2+g_{(l)}x_ix+h_{(l)}x^2}, \tag{28}$$

and

$$(\sigma_{xy})_0=\sigma_0\left\{1+1.8841\sum_{i=1}^{n-1}\frac{1}{x_i}\right\}, \tag{29}$$

---

[20] No contribution from the screw part is indicated.

[21] In Eqs. (27) and (28), x is the distance measured on the slip plane $0x$; $0r$ the corresponding value on the symmetry plane is $2x$.

where $e_{(l)}$, $f_{(l)}$, $g_{(l)}$, $h_{(l)}$, $p_{(l)}$, and $q_{(l)}$ are constants. Their values are listed below:

l	$e_{(l)}$	$f_{(l)}$	$g_{(l)}$	$h_{(l)}$	$p_{(l)}$	$q_{(l)}$
1	1.1146	−4.0678	−2.0000	7.2988	0.6435	2.3485
2	−0.4387	0.4820	−2.9039	4.0000	−0.02502	−0.4832
3	−0.1321	0.3614	−1.0961	2.1921	−0.3045	−0.09636

The calculated results for $(\sigma_n)_{ps}$, $(\sigma_{xy})_{ps}$, and $(\sigma_{xy})_0$ are shown in Figs. 5, 6, and 2, respectively. Numerical values for $(\sigma_{xy})_0$, $(\sigma_n)_{ps0}$, and $(\sigma_{xy})_{ps0}$ are listed in Table II. Values of $(\sigma_{xy})_0$ satisfy the empirical expression

$$(\sigma_{xy})_0=(0.738)n^{1.75}\sigma_0,\quad 10\leq n\leq 60 \qquad (30)$$

with an error of $\pm 1\%$.

DISCUSSION

When two parallel dislocation lines lie on two separate slip planes, the screw parts are always totally attractive or repulsive according to their signs but not to their relative position. This, however, is not true for the edge parts in which case the interaction energy changes sign with the relative distance. Therefore, we expect that in a double pile-up of dislocation lines the screw part may have a greater influence on the equilibrium positions, and consequently the stress concentration, than the edge component. This is shown to be the case in the calculations presented here. In case (ii) mentioned in the introduction, where the glide dislocations are of pure edge type, the stress concentration factor increases slowly with increasing n. On the other hand, in case (iii) where the glide dislocations are of the mixed type and the screw parts are attractive, the stress concentration factor increases rapidly with n in spite of the larger intersecting angle. However, because of the sign change in the interaction energy between edges and the larger intersecting angle, a longer range for the 120° pile-up is covered. To some extent this is also true of the 90° pile-up.

If it is assumed for purposes of comparison that an MgO crystal ruptures when the tip stress on {110} planes reaches $1000\sigma_0$, it follows from the above data that the number of dislocations in the pile-up groups sufficient to raise its tip stress to such a magnitude will be 1000 for type (i), 120 (by extrapolation) for type (ii), and 62 for type (iii). Under these conditions[22] the distance between the locked and the first glide dislocation (x_1) becomes less than one lattice spacing in all three cases, indicating the onset of microcrack formation.[12,23]

Although the foregoing calculations give certain quantitative information on the stress concentrations due to pile-up of dislocations in MgO crystals, little can be said as yet about the nature of the barrier. It is not known how a conjugate slip plane can serve as an effective barrier, nor whether the [001]/(100) edge in type (ii) group can be stable. It would be of particular interest to determine if a type (iii) crack could be formed upon testing, under simple tension or compression, a crystal properly oriented for slip on {110} slip planes intersecting at 120°. Further theoretical and experimental work is needed to obtain answers to these questions.

ACKNOWLEDGMENTS

The authors wish to thank Dr. F. Garofalo and Dr. L. S. Darken for their constant guidance and support, and Dr. J. C. M. Li and Dr. A. S. Keh for many useful discussions.

APPENDIX

The numerical data for three types of dislocation lines parallel to $[\bar{1}\bar{1}1]$ direction in MgO crystals are given below.

(a) For the $\frac{1}{2}[0\bar{1}1]/(011)$ dislocations, the coordinate system chosen is

$$x\colon[2\bar{1}1]$$
$$y\colon[011]$$
$$z\colon[\bar{1}\bar{1}1],$$

and the corresponding elastic constants are

$$\begin{bmatrix}
\frac{1}{2}(C_{11}^0+C_{12}^0+2C_{44}^0) & \frac{1}{6}(C_{11}^0+5C_{12}^0-2C_{44}^0) & \frac{1}{3}(C_{11}^0+2C_{12}^0-2C_{44}^0) & 0 & -(\sqrt{2}/6)(C_{11}^0-C_{12}^0-2C_{44}^0) & 0 \\
\frac{1}{6}(C_{11}^0+5C_{12}^0-2C_{44}^0) & \frac{1}{2}(C_{11}^0+C_{12}^0+2C_{44}^0) & \frac{1}{3}(C_{11}^0+2C_{12}^0-2C_{44}^0) & 0 & (\sqrt{2}/6)(C_{11}^0-C_{12}^0-2C_{44}^0) & 0 \\
\frac{1}{3}(C_{11}^0+2C_{12}^0-2C_{44}^0) & \frac{1}{3}(C_{11}^0+2C_{12}^0-2C_{44}^0) & \frac{1}{3}(C_{11}^0+2C_{12}^0+4C_{44}^0) & 0 & 0 & 0 \\
0 & 0 & 0 & \frac{1}{3}(C_{11}^0-C_{12}^0+C_{44}^0) & 0 & (\sqrt{2}/6)(C_{11}^0-C_{12}^0-2C_{44}^0) \\
-(\sqrt{2}/6)(C_{11}^0-C_{12}^0-2C_{44}^0) & (\sqrt{2}/6)(C_{11}^0-C_{12}^0-2C_{44}^0) & 0 & 0 & \frac{1}{3}(C_{11}^0-C_{12}^0+C_{44}^0) & 0 \\
0 & 0 & 0 & (\sqrt{2}/6)(C_{11}^0-C_{12}^0-2C_{44}^0) & 0 & \frac{1}{6}(C_{11}^0-C_{12}^0+4C_{44}^0)
\end{bmatrix}.$$

---

[22] An applied stress σ_0 of 10^4 psi was employed for this calculation. This value was obtained from the results of Stokes *et al.*[1] as the fracture stress of MgO.

[23] F. Garofalo, Y. T. Chou, and V. Ambegaokar, Acta Met. 8, 504 (1960).

The stress field around the $\frac{1}{2}[0\bar{1}1]/(011)$ dislocations is described by

$$\sigma_{xx}=10^{11}\times a\left\{\frac{-4.5443y}{x^2+2.0996y^2}+\frac{0.3935x+0.3872y}{(x+0.2609y)^2+0.6306y^2}+\frac{-0.3935x+0.3872y}{(x-0.2609y)^2+0.6306y^2}\right\}$$

$$\sigma_{yy}=10^{11}\times a\left\{\frac{2.1644y}{x^2+2.0996y^2}+\frac{-0.1492x-0.6320y}{(x+0.2609y)^2+0.6306y^2}+\frac{0.1492x-0.6320y}{(x-0.2609y)^2+0.6306y^2}\right\}$$

$$\sigma_{xy}=10^{11}\times a\left\{\frac{2.1644x}{x^2+2.0996y^2}+\frac{-0.5541x+0.1043y}{(x+0.2609y)^2+0.6306y^2}+\frac{-0.5541x-0.1043y}{(x-0.2609y)^2+0.6306y^2}\right\}\qquad\text{(A1}$$

$$\sigma_{xz}=10^{11}\times a\left\{\frac{-1.9600y}{x^2+2.0996y^2}+\frac{-0.2918x-0.04455y}{(x+0.2609y)^2+0.6306y^2}+\frac{0.2918x-0.04455y}{(x-0.2609y)^2+0.6306y^2}\right\}$$

$$\sigma_{yz}=10^{11}\times a\left\{\frac{0.9335x}{x^2+2.0996y^2}+\frac{0.06376x-0.2586y}{(x+0.2609y)^2+0.6306y^2}+\frac{0.06376x+0.2586y}{(x-0.2609y)^2+0.6306y^2}\right\}.^{24}$$

(b) For the $\frac{1}{2}[10\bar{1}]/(101)$ dislocation, the coordinate system is

$$x:[1\bar{2}\bar{1}]$$
$$y:[101]$$
$$z:[\bar{1}\bar{1}1].$$

The C_{ij} and σ_{ij} are identical with those in case (a) except that the following terms are opposite in sign:

$$C_{15}=-C_{25}=-C_{46},\ \sigma_{xz},\ \text{and}\ \sigma_{yz}.$$

(c) For the $\frac{1}{2}[1\bar{1}0]/(112)$ edge dislocation, the coordinate system is

$$x:[1\bar{1}0]$$
$$y:[112]$$
$$z:[\bar{1}\bar{1}1].$$

The C_{ij}'s are the same as those in case (a) except her

$$C_{15}=C_{25}=C_{46}=0$$

and

$$C_{14}=-C_{24}=C_{56}=-(\sqrt{2}/6)(C_{11}{}^0-C_{12}{}^0-2C_{44}{}^0).$$

The σ_{ij}'s are

$$\sigma_{xx}=10^{11}\times a\left\{\frac{0.5282y}{x^2+0.4763y^2}+\frac{1.0330x-2.1027y}{(x+0.3735y)^2+1.2918y^2}+\frac{-1.0330x-2.1027y}{(x-0.3735y)^2+1.2918y^2}\right\}$$

$$\sigma_{yy}=10^{11}\times a\left\{\frac{-1.1090y}{x^2+0.4763y^2}+\frac{-1.4885x+0.3573y}{(x+0.3735y)^2+1.2918y^2}+\frac{1.4885x+0.3573y}{(x-0.3735y)^2+1.2918y^2}\right\}$$

$$\sigma_{xy}=10^{11}\times a\left\{\frac{-1.1090x}{x^2+0.4763y^2}+\frac{1.4691x+2.1304y}{(x+0.3735y)^2+1.2918y^2}+\frac{1.4691x-2.1304y}{(x-0.3735y)^2+1.2918y^2}\right\}\qquad\text{(A2}$$

$$\sigma_{xz}=10^{11}\times a\left\{\frac{0.4783x}{x^2+0.4763y^2}+\frac{-0.06904x+1.2448y}{(x+0.3735y)^2+1.2918y^2}+\frac{-0.06904x-1.2448y}{(x-0.3735y)^2+1.2918y^2}\right\}$$

$$\sigma_{yz}=10^{11}\times a\left\{\frac{0.4783y}{x^2+0.4763y^2}+\frac{-0.8698x-0.7187y}{(x+0.3735y)^2+1.2918y^2}+\frac{0.8698x-0.7187y}{(x-0.3735y)^2+1.2918y^2}\right\}.$$

It is seen that for the anisotropic case a pure edge may involve all six components of stress. The same is true for a pure screw. This means that a pure screw dislocation in an anisotropic crystal should be defined by both the Burgers vector and the reference plane as is the case for a pure edge dislocation.

(d) The elastic energy per unit length of a $\frac{1}{2}[0\bar{1}1]/(011)$ or $\frac{1}{2}[10\bar{1}]/(101)$ dislocation E_1 can be determined from

$$E_1=\tfrac{1}{2}\int_{r_0}^{R}[(\sigma_{xy})_{y=0}b_e+(\sigma_{yz})_{y=0}b_s]dx$$

$$=0.5219\times10^{11}\times a^2\times\ln(R/r_0)\ \text{ergs/cm.}\qquad\text{(A3)}$$

The elastic energy of the $\frac{1}{2}[1\bar{1}0]/(112)$ edge E_2 is

$$E_2=\tfrac{1}{2}\int_{r_0}^{R}(\sigma_{xy})_{y=0}b_e dx$$

$$=0.6467\times10^{11}\times a^2\times\ln(R/r_0)\ \text{ergs/cm.}\qquad\text{(A4}$$

The elastic energy decrease in combining two leadin dislocations indicated by the reaction in Eq. (19) i therefore

$$\Delta E=(2E_1-E_2/2E_1)\times100=38\%.\qquad\text{(A5}$$

---

[24] The component σ_{zz} is not involved in the calculation.

JOURNAL OF APPLIED PHYSICS VOLUME 32, NUMBER 10 OCTOBER, 1961

Open Circuit Voltages in the Cesium Diode*

FRED N. HUFFMAN†
The Martin Company, Nuclear Division, Baltimore, Maryland

(Received March 20, 1961; in final form, April 24, 1961)

A plasma model and a close-spaced model are used to analyze the detailed variation of the open circuit voltage of the cesium diode. The plasma model open circuit voltage expression is compared to one derived by Lewis and Reitz in which the ion contribution to the net electron current is neglected. For either model the main features of the open circuit voltage at emitter temperatures less than 1800°K arise from the complex ion and electron emission properties as a function of emitter temperature and cesium pressure. Although at higher emitter temperatures the plasma model open circuit voltage becomes independent of the detailed surface characteristics of the emitter, the two models continue to give similar numerical results. Calculations based on these models and incorporating the data of Langmuir agree qualitatively with the sinusoidal and discontinuous open circuit voltage variations observed by Pidd *et al.*, as well as the anomalous load characteristic observed by Wilson.

I. INTRODUCTION

THIS paper discusses the detailed variations in the open circuit voltage of the cesium diode as a function of emitter temperature and cesium pressure. A proper interpretation of these variations is a necessary first step in the analysis of the more involved current-voltage characteristics. Since the open circuit voltage is usually independent of the space charge and plasma resistance which complicate the current-voltage problem, the open circuit voltage variations are particularly valuable in the diagnosis of the mechanisms in the cesium diode.

The analysis described here rests heavily on the experimental data of Taylor and Langmuir, the philosophy being that advanced by Nottingham, ". . . that estimates based on an extrapolation from existing data are better than pure guesses without a systematic relation to established facts."[1]

II. TAYLOR-LANGMUIR DATA

It is not generally appreciated that the thorough study of cesium films on tungsten by Taylor and Langmuir[2] is one of the most valuable bodies of information available on the interpretation of cesium diodes. Later studies by Müller[3] and Becker[4] with field emission microscopy have shed additional insight into the detailed surface phenomena, but the thermodynamic analysis that Langmuir applied to his data retains its validity. Langmuir reduced the experimental data in such a fashion that the zero field evaporation rates (ν_i) of ions, electrons, and atoms from a cesiated tungsten emitter at temperature T(°K) can be readily calculated by the formula $\log_{10}\nu_i = A_i - B_i/T$. Electrons, positive ions, and atoms are represented by e, p, and a subscripts, respectively. Functions A_i and B_i depend upon the fractional coverage θ of the cesium layer and are given in Table I (taken from reference 2). Figure 1 is a typical plot of evaporation rates constructed from this table. The particle impingement rate μ may be related to the cesium vapor pressure p by the usual gas kinetic expression. At steady state the impingement rate equals the sum of the ion and atom evaporation rates. Specification of the cesium pressure (and, hence, impingement rate) will establish the fractional coverage of cesium on tungsten and the associated electron, ion, and atom evaporation rates. Further, the fractional coverage can be related to the contact potential v of the absorbed cesium layer relative to tungsten (Table I) to give the zero field emitter work function,

$$\phi_E = 4.62 - v[\theta(p,T)]. \tag{1}$$

In the following analysis the zero field emitter work function will be assumed to be independent of any internal fields in the cesium diode. "Patch effects" are incorporated in the experimental data.

A close examination of Fig. 1 reveals an apparent ambiguity. For small coverages, a region in which a single impingement rate corresponds to three different fractional coverages seems to exist. Langmuir's explanation is that at a given cesium pressure two values of θ may exist, corresponding to a dilute and a concentrated phase. The intermediate θ is unstable. The exploded view of this region in Fig. 1 is plotted on a linear scale. The dotted line and the impingement curve enclose the areas X_1 and X_2. The condition for a stable boundary between the dilute and concentrated phases is that X_1 equal X_2. If the impingement rate is raised slightly above the value at the dotted line, the concentrated phase will appear; if the impingement rate is dropped below that of the dotted line, the dilute phase will appear. In Sec. VI, this discontinuous surface phase change in ion and electron evaporation rates will be shown to correspond to discontinuities in the open circuit voltage.

---

* Supported in part by the U. S. Atomic Energy Commission.

† Presently U. S. Atomic Energy Commission Advanced Health Physics Fellow, Department of Physics, Johns Hopkins University, Baltimore, Maryland.

[1] W. B. Nottingham, *Direct Conversion of Heat to Electricity* (Addison-Wesley Publishing Company, Inc., Reading, Massachusetts, 1960).

[2] J. B. Taylor and I. Langmuir, Phys. Rev. **44**, 412 (1933).

[3] R. H. Good and E. W. Müller, *Handbuch Der Physik*, edited by S. Flügge (Springer-Verlag, Berlin, 1956), Vol. XXI, pp. 176–231.

[4] J. A. Becker, *Solid State Physics* (Academic Press, Inc., New York, 1958), Vol. 7, pp. 379–424.

TABLE I. Langmuir data for calculation of evaporation rates.

	Atoms (ν_a)		Ions (ν_p)		Electrons (ν_e) $A_e = 27.55$	
θ	A_a	B_a	A_p	B_p	B_e	v
0		14 061.2		10 293.6	23 990	0.000
0.002	24.2328	14 043.2	23.9318	10 409	23 853	0.0268
0.005	24.6401	14 013.3	24.3391	10 515.6	23 716	0.0540
0.01	24.9558	13 963.8	24.6549	10 730.1	23 452	0.1064
0.02	25.2859	13 866	24.9849	11 141.8	22 941	0.2079
0.03	25.4913	13 769	25.1904	11 530	22 457	0.3038
0.04	25.6459	13 673	25.3450	11 898	21 992	0.3960
0.05	25.7719	13 579	25.4709	12 248	21 549	0.4840
0.06	25.8804	13 486	25.5795	12 582	21 122	0.5686
0.07	25.9764	13 394	25.6755	12 894	20 719	0.6487
0.08	26.0633	13 304	25.7623	13 196	20 325	0.7267
0.10	26.2179	13 127	25.9169	13 761	19 584	0.8738
0.12	26.3556	12 954	26.0546	14 284	18 888	1.012
0.15	26.5388	12 703	26.2379	15 029	17 893	1.2094
0.20	26.8081	12 306	26.507	16 095	16 429	1.500
0.25	27.050	11 934	26.749	17 061	15 089	1.7658
0.30	27.276	11 583	26.975	17 907	13 891	2.0034
0.40	27.707	10 939	27.406	19 365	11 792	2.420
0.50	28.142	10 364	27.841	20 350	10 230	2.73
0.55	28.375	10 098	28.069	20 588	9726	2.83
0.60	28.629	9849	28.328	20 638	9424	2.89
0.65	28.916	9623	28.612	20 563	9272	2.92
0.70	29.256	9425	28.955	20 368	9272	2.92
0.75	29.683	9256	29.377	20 103	9373	2.90
0.80	30.266	9110	29.965	19 800	9524	2.87
0.85	31.159	8985				
0.90	32.821	8881				
0.95	37.495	8798				
1.00		8733				

Unfortunately, most of the experimental data used in constructing the evaporation rate parameters comes from lower temperatures than those of primary interest in thermionic conversion. Hence, use of these data does involve an extrapolation in the high-temperature regions.

III. DERIVATION OF PLASMA MODEL OPEN CIRCUIT VOLTAGE EXPRESSION

In their original paper Lewis and Reitz[5] analyzed the case of a high-density cesium vapor in thermal equilibrium with both the emitter and the collector. In this case, the emitter and collector work functions drop out of the open circuit expression.[6] It is of interest to investigate the case of the high-density cesium diode under the assumption that the cesium vapor is in thermal equilibrium with the emitter but not with the collector. This assumption probably corresponds more closely to experiment. This case has also been treated by Lewis and Reitz.[6] A comparison will be made with their results.

If the random electron current density due to thermal ionization exceeds that due to thermionic emission, sheaths will be formed at both electrodes. Lewis and Reitz have pointed out that in the measurement of the open circuit voltage a very small current density is drawn through the diode by the voltmeter. If the plasma IR drop is neglected, the open circuit voltage V for this trickle current density is (see Fig. 2)

$$V(j) = \phi_E(p,T) - B_E(j_E) + B_c(j_c) - \phi_c, \tag{2}$$

where ϕ_E is the emitter work function given by (1), B_E is the emitter sheath, B_c is the collector sheath, and ϕ_c is the collector work function. The net emitter and collector electron current densities are, respectively, j_E and j_c, corresponding to the net electron density j flowing through the voltmeter. The net electron current density through the emitter is given by

$$j_E = AT^2 \exp\left(-\frac{e\phi_E}{kT}\right) - \nu_p e \exp\left(-\frac{eB_E}{kT}\right) - J_e \exp\left(-\frac{eB_E}{kT}\right) + J_p, \tag{3}$$

where A is Richardson's constant, T is the emitter temperature, e is the electronic charge, k is Boltzmann's constant, and ν_p is the emitter ion evaporation rate (ions/cm^2-sec). The factors J_e and J_p represent the random current densities of electrons and ions, respectively, impinging on both the emitter and collector sheaths from the plasma. For thermal equilibrium $J_e/J_p = (m_p/m_e)^{\frac{1}{2}}$, where m_p and m_e are the ion and electron masses, respectively. For cesium

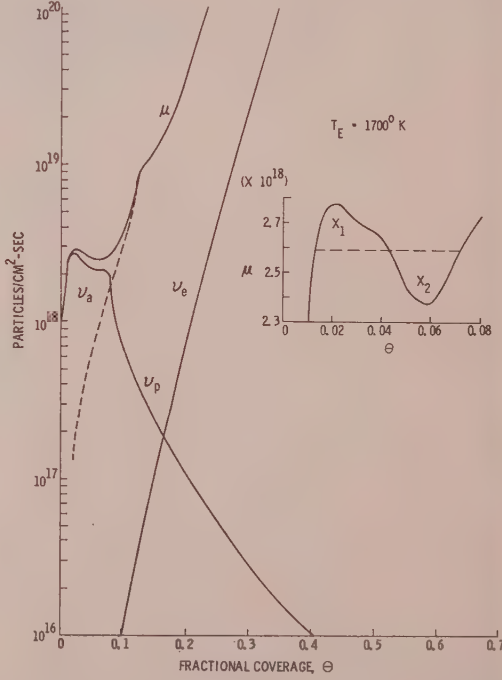

FIG. 1. Atom (ν_a), ion (ν_p) and electron (ν_e) evaporation rates for zero field. The impingement rate is given by $\mu = \nu_a + \nu_p$. The insert is a linear plot for lower values of θ.

---

[5] H. W. Lewis and J. R. Reitz, J. Appl. Phys. **30**, 1439 (1959).

[6] H. W. Lewis and J. R. Reitz, J. Appl. Phys. **30**, 1839 (1959).

$(m_p/m_e)^{\frac{1}{2}}\approx 500$. Then

$$B_E(j_E)=-\frac{kT}{e}\ln\left[\frac{AT^2\exp\left(-\frac{e\phi_E}{kT}\right)+J_p-j_E}{\nu_p e+(m_p/m_e)^{\frac{1}{2}}J_p}\right]. \qquad (4)$$

To simplify the analysis, the following assumptions will be made: (1) the collector is cool enough so that the ion and electron currents from the collector are negligible; and (2) the photoelectron current from the collector due to blackbody radiation from the emitter will be neglected although this contribution becomes significant at high temperature and low cesium pressures. Under these assumptions the collector net current density is given by

$$j_c=J_e\exp\left(-\frac{eB_c}{kT}\right)-J_p \qquad (5)$$

so that

$$B_c(j_c)=\frac{kT}{e}\ln\left[\left(\frac{J_p}{J_p+j_c}\right)\left(\frac{m_p}{m_e}\right)^{\frac{1}{2}}\right]. \qquad (6)$$

When (4) and (6) are substituted in (2), the result is

$$V(j)=\phi_E(p,T)+\frac{kT}{e}\ln\left\{\left[\frac{AT^2\exp\left(-\frac{e\phi_E}{kT}\right)+J_p-j_E}{\nu_p e+(m_p/m_e)^{\frac{1}{2}}J_p}\right]\times\left(\frac{J_p}{J_p+j_c}\right)\left(\frac{m_p}{m_e}\right)^{\frac{1}{2}}\right\}-\phi_c. \qquad (7)$$

IV. COMPARISON TO LEWIS AND REITZ RESULT

In Sec. II it was shown that the emitter work function and ion evaporation rate are sensitive functions of emitter temperature and cesium pressure. These relations cannot be calculated but must be supplied by experiment. Since the only available data are those of Langmuir on the cesium-tungsten system, it is interesting to investigate the conditions under which the work function and ion evaporation rate need not be specified. Langmuir's data and the Saha equation may be used in conjunction with (7) to establish these conditions. To simplify the problem, the case of plane electrodes, in which $j=j_E=j_c$, may be used. Detailed calculations show that for emitter temperatures in excess of 1800°K and cesium pressures greater than 10^{-1} mm Hg, the following inequalities apply:

$$(J_p-j)/AT^2\exp(-e\phi_E/kT)\ll 1 \quad\text{and}\quad \nu_p e/J_e\ll 1. \qquad (8)$$

For good experimental technique,

$$j/J_p\ll 1 \qquad (9)$$

and (7) becomes

$$V(j/J_p\ll 1)=\frac{kT}{e}\ln\left[\frac{AT^2}{J_p}\right]-\phi_c. \qquad (10)$$

The random ion current density is given by

$$J_p=\left(\frac{m_e}{m_p}\right)^{\frac{1}{2}}J_e=\left(\frac{m_e}{m_p}\right)^{\frac{1}{2}}\frac{p_e e}{(2\pi m_e kT)^{\frac{1}{2}}}, \qquad (11)$$

where p_e is the electron pressure calculated from Saha's equation. To obtain the result of Lewis and Reitz from (7), the assumptions of (8) must be made as before. However, in contradiction to (9), it must be assumed that $j/J_p\gg 1$, corresponding to neglecting the ion contribution to the net collector electron current. When this assumption, along with the assumptions of (8), are made in (7), the following expression results:

$$V(j/J_p\gg 1)=\frac{kT}{e}\ln\left[\frac{AT^2}{j}\right]-\phi_c. \qquad (12)$$

This equation is identical to (10) of reference 6. The only difference between (10) and (12) is in the assumption regarding the magnitude of j/J_p. However, this difference represents a factor of infinity as the experimental measurement becomes ideal. Equation (12) is valid for appreciable load currents if the *IR* drop is neglected, but for genuine open circuit conditions the current balance at the collector is critical and the ion contribution should not be neglected. For cesium diode electrode areas of 1 square centimeter, a 20 000-ohm voltmeter measuring an open circuit voltage of two volts would require a current density $j=10^{-4}$ amp/cm². A vacuum tube voltmeter or an oscilloscope would require an even smaller current density. The Saha equation shows that for emitter temperatures greater than 1800°K and cesium pressures in excess of 10^{-1} mm Hg, $J_p\gg 10^{-4}$ amp/cm². The expression $j/J_p\ll 1$, in agreement with (9) and (10), becomes the preferred open circuit voltage expression.

For emitter temperatures above 1800°K and cesium pressures greater than 10^{-1} mm Hg, the ion density n_p is governed by the Saha equation. For emitter temperatures in excess of 1800°K and cesium pressures less than 10^{-1} mm Hg, the inequalities in (8) are not always valid and it would be preferable to use the general open circuit voltage expression (7). However, in this pressure-

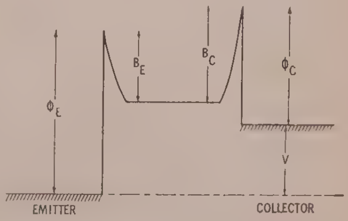

FIG. 2. Open circuit potential diagram for plasma model of cesium diode.

temperature region, (11) is not sufficient to establish J_p because the contribution of ν_p to the ion density becomes comparable to that due to thermal ionization in the plasma.

For temperatures less than 1800°K, the contribution of thermal ionization to the ion density becomes small and n_p will be determined by the competition between ν_p, volume recombination, and loss at the collector. For this case n_p, and hence J_p, is proportional to ν_p. That is, $J_p=K\nu_p e$, where K is an undetermined proportionality factor. With this substitution, (7) may be rewritten as

$$V=\frac{kT}{e}\ln\left[\frac{AT^2}{\nu_p e}\left(\frac{1+K(\nu_p/\nu_e)}{1+K(m_p/m_e)^{\frac{1}{2}}}\right)\left(\frac{m_p}{m_e}\right)^{\frac{1}{2}}\right]-\phi_c. \quad (13)$$

If K is of the order of one and $(\nu_p/\nu_e)\ll 1$, (13) reduces to the same form as (10). At high temperatures J_p is governed by slowly varying thermal ionization given by (11), whereas at lower temperatures the open circuit voltage equation (13) varies as ν_p, which depends on rapidly changing emitter properties.

V. DERIVATION OF CLOSE-SPACED MODEL OPEN CIRCUIT VOLTAGE EXPRESSION

It is instructive to compare the plasma model derivations to those for the most simple analytic model, the close-spaced model, in which the Langmuir data can be incorporated. The plasma model derivation assumed that the interelectrode space is many electron mean free paths in length and filled with cesium vapor at the emitter temperature. In this section, two apparently contradictory assumptions will be made. These are: (1) the electron and ion mean free paths are greater than the interelectrode spacing; and (2) the interelectrode cesium vapor is at the bath temperature. The two previous assumptions, in regard to collector emission, given in Sec. III, will be retained. The physical model corresponding to these assumptions is a close-spaced diode. That is, the cesium diode is considered to be close-spaced in the sense that the electrode spacing is less than the electron mean free path and also in the sense that double electrode sheaths are not formed. If the emitter temperature and cesium pressure are such that $(\nu_e/\nu_p)\gtrsim 500$, the electron space charge will not be eliminated and potential sheaths will not be formed. The electron mean free path is roughly 2 and 0.02 cm at cesium pressures of 10^{-3} and 10^{-1} mm Hg, respectively. In this sense, the open diode configurations described by Hernqvist[7] and Pidd *et al.*,[8] are often operated at cesium pressures at which they may be considered close-spaced. If $(\nu_e/\nu_p)\lesssim 500$, potential sheaths would normally be expected. In this case, the close-spaced model must correspond to spacings of the order of the Debye shielding length in order that sheaths not be formed. In both cases the vapor particles that impinge on the emitter do so with kinetic energies and rates corresponding to the cesium bath temperature rather than the emitter temperature.

The assumption that the interelectrode cesium vapor is at the bath temperature poses a problem. Langmuir analyzed his data on the basis that the evaporation rates be so related to one another that the concentrations of atoms, ions, and electrons in the vapor space near the emitter agree with thermodynamic equilibrium as determined by the Saha equation. However, in this analysis, as with the experiments of Taylor and Langmuir, the assumption is that the particles immediately outside the emitter are far from being in thermodynamic equilibrium with the emitter. Therefore, the paradox of applying equilibrium theory to nonequilibrium experiments in which essentially all impinging particles are atoms must be resolved. Nevertheless, all the evaporation rates from the emitter will be in thermodynamic equilibrium with the emitter, provided there is no direct reflection of either particle and that the impinging particles have an appreciable absorption life on the emitter.[9] In this case the condition in which a particle evaporates can hardly be affected by either the velocity or charge with which it hits the emitter. Datz and Taylor[10] report that the ionization of all alkali metals on a tungsten surface follows the Saha-Langmuir equation with no reflection. Studies by Langmuir[11] indicate that for atoms of metal vapor the relaxation time is short compared to the natural period of oscillation of tungsten atoms. Consequently, the evaporating ions, electrons, and atoms are nearly in perfect thermal equilibrium with the emitter although the impinging atoms are not. The paradox is resolved. It is seen that an analysis that assumes the cesium to be in equlilbrium with the emitter may agree with cesium diode experiments in which the cesium is far from equilibrium with the emitter, provided there is little scattering.

A cesium diode operating at a given emitter temperature and cesium pressure will correspond to one of two cases: case I—the evaporation rate of electrons is greater than the evaporation rate of ions from the emitter; case II—the evaporation rate of electrons is less than the evaporation rate of ions from the emitter. Figures 3 and 4 give the open circuit potential diagrams for these two cases. In general, the potential distribution will not be linear as shown but will be distorted by space-charge effects. However, the equations which follow will apply to any distribution, provided the potential exhibits no maximum or minimum. The open circuit voltage is simply the potential shift between the collector and emitter Fermi levels so that the net electron current density is zero. For case I (Fig. 3) the open circuit voltage is given by $V=\phi_E+\Delta\phi-\phi_c$, where $\Delta\phi$ is the incremental potential. The net electron current density is given by

---

[7] K. G. Hernqvist, M. Kanefsky, and F. H. Norman, RCA Rev. **19**, 244 (1958).

[8] R. W. Pidd, G. M. Grover, E. W. Salmi, D. J. Roehling, and G. F. Erickson, J. Appl. Phys. **30**, 1861 (1959).

[9] A. L. Reimann, *Thermionic Emission* (John Wiley & Sons, Inc., New York, 1934), p. 299.

[10] S. Datz and E. H. Taylor, J. Chem. Phys. **25**, 389 (1956).

[11] I. Langmuir, *Phenomena, Atoms and Molecules* (Philosophical Library, New York, 1950), p. 317.

$$j=AT^2\exp\left(-\frac{e\phi_E}{kT}\right)\exp\left(-\frac{e\Delta\phi}{kT}\right)-e\nu_p(p,T). \quad (14)$$

When the net electron density goes to zero, the expression becomes

$$V=\frac{kT}{e}\ln\left[\frac{AT^2}{e\nu_p(p,T)}\right]-\phi_c. \quad (15)$$

For case II (Fig. 4) the open circuit voltage is $V=\phi_E-\Delta\phi-\phi_c$, and the net electron current density is given by

$$j=AT^2\exp\left(-\frac{e\phi_E}{kT}\right)-e\nu_p(p,T)\exp\left(-\frac{e\Delta\phi}{kT}\right). \quad (16)$$

When j approaches zero, (15) results. That is, (15) is the correct open circuit voltage expression for both case I and case II. Although (15) has the deceptive appearance of being independent of the emitter work function, the emitter work function appears implicitly in the ion evaporation rate.

It is apparent that for small $K(\nu_p/\nu_e)$, (15) differs from (13) only through constant factors inside the logarithm. This agreement in open circuit voltage expressions at low temperature may appear surprising considering the disparity between the plasma and close-spaced models until it is realized that both models have an essential feature in common. That is, the temperature distribution of the charge carriers at the collector is in equilibrium with the emitter in both models. Although at high emitter temperatures the plasma model open circuit voltage becomes independent of surface contact ionization, Eqs. (10) and (15) give similar numerical results for reasons to be discussed in Sec. VII.

VI. OPEN CIRCUIT VOLTAGE DISCONTINUITIES

Open circuit voltage discontinuities occur naturally in this analysis as a result of the discontinuous phase change of the adsorbed cesium layer on the emitter, as discussed in Sec. II. Such discontinuities were observed by Pidd.[12] Theory, in agreement with experiment, predicts that there will be only one discontinuity with increasing emitter temperature for a given pressure and that the discontinuities will disappear above 1900°K. In this dual phase region, Hatsopoulos[13] has pointed out, metastable coverages corresponding to impingement rates between the value at the dashed line (Fig. 1) and both the maximum and minimum impingement rates are possible, providing the correct path is taken. Thus, the size of the discontinuity depends somewhat on the path by which it is approached. For a given emitter temperature the open circuit voltage discontinuity at the critical pressure for that temperature is the difference between the open circuit voltages, as given by (13) or (15), for the ion evaporation rates at the first and third intersections of the dashed line and impingement curve (shown in the insert of Fig. 1).

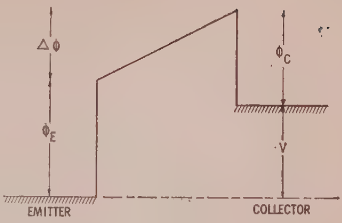

Fig. 3. Case I potential diagram for close-spaced model of cesium diode. (Electron evaporation rate greater than ion evaporation rate.)

The phase discontinuities always occur for values of $(\nu_p/\nu_e)\gg 1$ so that (13) takes the same form as (15) with the exception that ν_p is replaced by ν_e. This exception is significant because ν_p and ν_e break in opposite directions at the phase discontinuity. Hence, for a given cesium pressure, the plasma model predicts that the open circuit voltage will break to a higher voltage with increasing emitter temperature whereas the close-spaced model predicts an opposite effect. There is little doubt that the plasma model best approximates experimental converters operating in the pressure-temperature region in which the discontinuities occur.

VII. PARAMETRIC STUDY

The ion evaporation rate in (13) or (15) may be supplied by the Langmuir data as discussed in Sec. II. These data permit the calculation of the close-spaced open circuit voltage for a tungsten emitter in a cesium atmosphere for any combination of cesium pressure, emitter temperature, and collector work function. Such a study of the open circuit voltage as a function of emitter temperature, parametric in cesium pressure for a collector work function of 1.81 v, is given in Fig. 5. A comparison of the calculated tungsten data (Fig. 5) with the experimental tantalum data of Pidd *et al.* (see Fig. 3 of reference 8) gives qualitative agreement. Although (15) was used in this study, it is clear that (13) would give qualitatively the same behavior at low temperatures if the proportionality factor were specified.

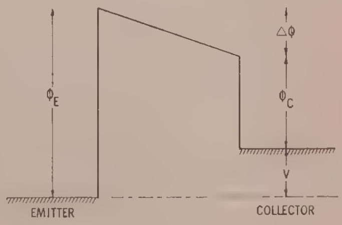

Fig. 4. Case II potential diagram for close-spaced model of cesium diode. (Electron evaporation rate less than ion evaporation rate.)

---

[12] R. W. Pidd (private communication).

[13] G. N. Hatsopoulos (private communication).

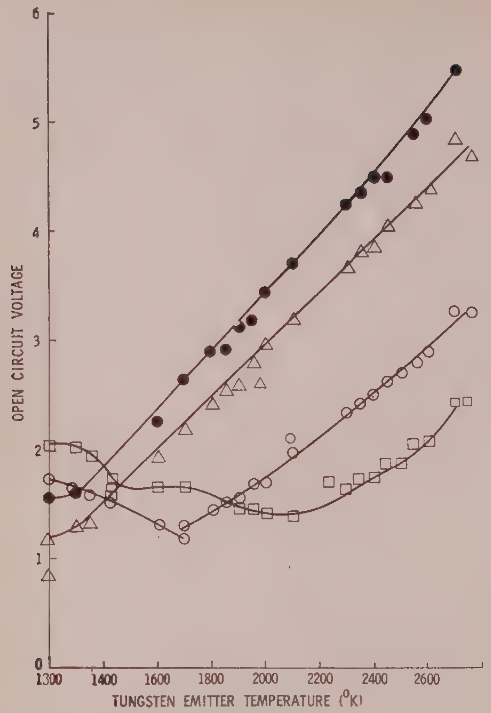

FIG. 5. Calculated open circuit voltage versus tungsten emitter temperature. Curve a (●): cesium at a pressure of 10^{-6} mm Hg. Curve b (Δ): cesium at a pressure of 10^{-5} mm Hg. Curve c (○): cesium at a pressure of 10^{-2} mm Hg. Curve d (□): cesium at a pressure of 4×10^{-1} mm Hg.

Parametric studies of (10) and (15) give agreement above 2000°K. This agreement may seem surprising since J_p as computed from (11) is independent of surface contact ionization. Above 2000°K, $e\nu_p$ becomes a smooth function. Although $e\nu_p$ is typically one or two orders of magnitude larger than J_p, the logarithmic argument in either (10) or (15) is so large that a factor of one magnitude results in only a 10 or 20% difference in open circuit voltage.

VIII. ANOMALOUS LOAD CHARACTERISTIC

Langmuir's data also provides a possible explanation for the anomalous load characteristic of Wilson (see Fig. 5, reference 14) in which the current-voltage curve exhibits a sharp break. Wilson has suggested that the behavior is due to two types of emitter surface, one with a higher work function than the other. However, emitter temperatures and cesium pressure combinations may be found from Langmuir's data, in which the load characteristic as calculated from (14) and (16) exhibits the anomalous break. In this analysis, the break occurs as a result of the exponential competition between the ion and electron components of the net current as the output voltage is reduced below the open circuit value.

If plasma resistance is neglected, the load characteristic for a given emitter temperature, cesium pressure, and collector work function may be calculated by the following procedure. First, the open circuit voltage is determined from (15). Next, an output voltage V less than the open circuit value is assumed. If $V+\phi_c>\phi_E$, the incremental potential is given by $\Delta\phi=V-\phi_E+\phi_c$, and (14) may be used to calculate the net electron current density corresponding to the assumed output voltage. If the assumed output voltage is such that $V+\phi_c<\phi_E$, the incremental potential is given by $\Delta\phi=\phi_E-V-\phi_c$ and (16) must be used.

IX. SUMMARY

The open circuit voltage of the cesium diode has been analyzed in accordance with two models. The plasma model analysis is similar to a previous study by Lewi and Reitz, but the present analysis takes into account the ion contribution to the net electron current flowing through the diode. The close-spaced model treatment is analogous to that of the vacuum diode. Both models give similar analytic and numerical results. Calculation based on these models and incorporating the data o Langmuir give qualitative agreement with three features of the experimental data of Pidd *et al.*, and Wilson. These features are: (1) the sinusoidal open circuit voltage variations, (2) the discontinuous open circuit voltage behavior and (3) the anomalous load characteristic. Although both models are crude representations of actual experiments, the results of this analysis indicate that at low emitter temperatures th main features of the open circuit voltage variation arise from the complexion and electron emitter emission properties as a function of emitter temperature and cesium pressure.

ACKNOWLEDGMENT

The author gratefully acknowledges the many stimulating discussions of the cesium diode problem with Dr. George Hatsopoulos of the Massachusetts Institute of Technology and the Thermo Electron Engineering Corporation, without whose encouragement and critica review this analysis would not have been possible.

---

[14] V. C. Wilson, J. Appl. Phys. **30**, 475 (1959).

Mechanism of Chemisorption, Place Exchange, and Oxidation on a (100) Nickel Surface*

H. E. Farnsworth and Hannibal H. Madden, Jr.†
Barus Physics Laboratory, Brown University, Providence, Rhode Island

(Received March 27, 1961)

Results obtained by low-energy electron-diffraction and photoelectric work-function measurements indicate that the following features result from exposure to oxygen at room temperature. Initial adsorption occurs in an amorphous molecular form. Some of the adsorbed molecules diffuse over the surface to lattice-defect sites where they dissociate. The resulting atoms form in a lattice structure surrounding the defect site. With continued exposure to oxygen, a place exchange between some oxygen and nickel atoms occurs to form a single-spaced simple-square structure with a slight increase in the lattice constant. This place exchange immediately precedes, in exposure, the formation of the oxide structure of the rock-salt type. The work function of clean (100) nickel depends on the type of anneal. $\varphi=5.08$ ev after argon ion bombardment, $\varphi=5.12$ ev after a small anneal, $\varphi=5.22$ ev after a more complete anneal.

INTRODUCTION

PREVIOUS results obtained in this laboratory[1,2] have been interpreted as evidence that oxygen adsorbs on a (100) nickel surface in two structures which depend on the pressure and time of exposure, namely, a double-paced face-centered and a single-spaced simple-square tructure. The amount of oxygen adsorbed in these tructures at a given exposure is strongly dependent on he state of anneal following ion-bombardment clean-ng,[2] in addition to the temperature during exposure. Certain observations showed that the extinction of the iffraction pattern from nickel[2] does not appear to epend on the percent coverage by the chemisorbed rystalline layer (dependent on the state of anneal ollowing ion-bombardment cleaning) but rather on the xposure, thus indicating that the oriented gas lattice epresents only part of the adsorption process.

More comprehensive and detailed observations have ow been made which yield further information on the mechanism of the adsorption process as well as the ransition from adsorption to oxidation, and show that hese mechanisms are more complicated than the ormer interpretation indicated.

Although the low-energy electron-diffraction method eveals lattice structures, it does not readily identify he type of atom on the surface. For this reason, a method of measuring the photoelectric work function as been incorporated in the diffraction tube to aid in dentifying the surface atoms.

APPARATUS AND EXPERIMENTAL PROCEDURES

The conventional low-energy electron-diffraction pparatus has been modified so that the photoelectric ield and work-function determinations can be made nder the same conditions as those for the diffraction measurements.[3] A diagram of the arrangement is shown in Fig. 1. The diffraction unit is similar in principle to that described previously.[4] However, because of the shape of the tube envelope, the gun structure was assembled on one framework and the remaining parts on another framework. These two frames were inserted in opposite ends of the envelope and were aligned and maintained in position by rods and springs not shown. Checks on the alignment were made by an optical method.

The ultraviolet light from a quartz mercury arc passed through a quartz monochromator, lens, and window, and was focused onto the crystal at an angle of incidence of about 45°. The saturated photocurrent was collected by the drum and shield of the Faraday collector to determine the work function by the Fowler method.[5] A vacuum thermopile measured the light intensity. Photoelectric and diffraction currents were measured by a vibrating reed electrometer. The vacuum techniques and methods of cleaning the crystal by argon ion bombardment and annealing have been described elsewhere.[4] The "small" anneal consisted of heating the crystal to a temperature of 350°C (thermocouple temperature) in 3 or 4 min, followed by cooling to room temperature by radiation and conduction. For a "more complete" anneal, the crystal was heated at a temperature of 750°C for at least 30 min after which the heating power to the crystal was gradually reduced to zero during a period of one hour. The crystal was held by tungsten springs against the end of a molybdenum cylindrical mounting which had been preoutgassed in vacuum. A thermocouple measured the temperature of the molybdenum mounting which was heated by electron bombardment, and the crystal was heated by conduction through a good thermal contact. Optical pyrometer tests showed that the temperature of the crystal was less than 30°C lower than that of the mounting at 750°C. The control and determination of gas

---

* Assisted by the U. S. Army Office of Ordnance Research.

† Present address: Department of Physics, Wayne State Uni-ersity, Detroit 2, Michigan.

[1] R. E. Schlier and H. E. Farnsworth, Advances in Catalysis 434 (1957).

[2] H. E. Farnsworth and J. Tuul, J. Phys. Chem. Solids 9, 48 959).

[3] E. N. Clarke and H. E. Farnsworth, Phys. Rev. 85, 484 (1952).

[4] H. E. Farnsworth, R. E. Schlier, T. H. George, and R. M. Burger, J. Appl. Phys. 29, 1150 (1958).

[5] R. H. Fowler, Phys. Rev. 38, 45 (1931).

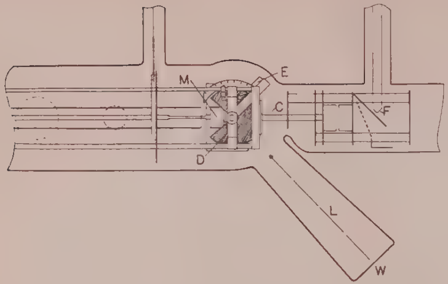

FIG. 1. Diagram of experimental tube. F is the gun filament; C is the collimator of the gun; M is the crystal mounting; D is the shielding drum; E is the electron collector; L is the direction of the incident ultraviolet light; W is a silica window attached to the Pyrex envelope with a graded seal.

pressure and the method of observation for different gas exposures were similar to those described previously.[2]

RESULTS AND DISCUSSION

Mechanism of Chemisorption

The results reported here, plus those obtained previously,[2] furnish strong evidence that adsorption of oxygen on the (100) nickel surface involves the following main features. Initial adsorption at room temperature occurs in an armorphous molecular form. Some of the adsorbed molecules diffuse over the surface to lattice-defect sites where they dissociate. The resulting atoms form in a lattice structure surrounding the defect site. With continued exposure to oxygen, a place exchange between some oxygen and nickel occurs to form an *s-s*, *s-s* structure with a slight increase in the lattice constant. This place exchange immediately preceeds the formation of the oxide structure of the rock-salt type.

Evidence for the molecular adsorption is the following:

(1) As oxygen adsorbs on the nickel surface, the intensity of the diffraction pattern from the nickel lattice decreases as a result of the low penetrating power of the electrons. The rate of decrease with increasing exposure is approximately the same for a surface which has been well annealed as for one which has received a "small" anneal after ion-bombardment cleaning. However, the diffraction patterns from the gas-lattice structures on the surface with the small anneal are much more intense than those from the gas-lattice structures on the well-annealed surface because of the different defect densities in the lattices. If the extinction of the pattern from nickel were a result of the presence of the gas-lattice structures, one would expect a greater rate of extinction for the surface having a small anneal. Since this is not the case, it appears that the major part of the extinction is the result of an amorphous structure on the surface which is independent of the defect density. Curves showing these relationships have been published previously.[2]

(2) Intensities of the diffraction patterns from ga lattices formed at 150°C are considerably greater tha those formed at 25°C. However, the rates of extinctio of diffraction patterns from the nickel lattices are approximately the same in the two cases. Thus, thes results lead to the same conclusion as in (1) above an the related curves are found in the previous publication

(3) Changes occur in diffracted beam intensity wit time of remaining in vacuum subsequent to variou oxygen exposures. Figure 2 shows several plots of pea diffraction beam current as a function of log of exposur The curves in sets 1 and 2 show increases I in beam intensities of gas structures which have occurred as result of conversion of the adsorbed amorphous molecular oxygen into atomic oxygen in a lattice structure. Th curves in set 3 show two increases and two decreases i intensity, marked I_1, I_2, and D_1, D_2, respectively. Th decrease D_1 and the increase I_1 represent a conversio from one lattice structure to another. The decrease D and increase I_2 represent a conversion from the plac exchange structure to the oxide structure. Tests we made which show that these changes were not th result of adsorption from the residual ambient. Earli observations[2] were less detailed and failed to note the changes in intensities with time in vacuum.[6]

In addition to the above general features, there a several details of significance. Using the method of observation and notation described previously,[2] Fig. shows plots of peak diffraction beam current as a fun tion of exposure for five different diffraction beams, t essential features of which are similar to those shown Fig. 2 of the previous report,[2] although there are so differences.

As has been shown previously, the lattice structur due to oxygen are much more pronounced for a surfa which has received only a small anneal subsequent ion bombardment. The *d-s*, *f-c* structure, which reach its maximum development at about 5×10^{-5} mm H min in Fig. 3, disappears rapidly with further exposu In some cases, depending on previous treatments a temperature of exposure, this structure is replaced by weak polycrystalline structure in the region indicat by the dotted curve.[7] The *s-s*, *s-s* structure appears pass through a weak maximum, then decreases wi further exposure until the intense *s-s*, *s-s* structure appears just preceding the oxide formation. Since this first weak maximum occurs at the same exposure as the maximum for the *d-s*, *f-c* structure, it appears probable that it is the result of diffraction from the *d-s*, *f-c* structure rather than the *s-s*, *s-s* structure [the surface grating spacings for these two structures are the same in the (100) azimuth]. As seen in Fig. 3, both of the beams from the nickel lattice pass through a maximum of intensity at the same exposure as for the case of the *s-s*, *s-s* beam. This behavior of the nickel beam in the (100) azimuth was previously attributed to the fact that the *s-s*, *s-s* structure has a surface lattice spacing in the (100) azimuth which is twice that of the nickel lattice in this azimuth. Hence, a second-order diffraction from the gas lattice coincides with the first-order diffraction from the nickel lattice. However, the intensity of the peak in the nickel curve of the (100) azimuth in Fig. 3 appears too great for a second-order reflection, which suggests that some portions of the surface may be composed of nickel atoms with the normal nickel spacing.

---

[6] Another result of a time delay was an increase in the to oxygen exposure necessary for the final peaking of the *s-s*, beam and the formation of the oxide. This also occurred if t first exposure to oxygen, following the ion-bombardment clean of the surface, was delayed for several hours. This phenomen was apparently not the result of an annealing effect since the placement also occurred in the case of the more complete anne There was also no detectable amount of contamination from ambient. It may be noted that a similar displacement tow higher exposure values was observed for the case of a nickel f deposited by evaporation onto a (100) face of a nickel cryst [H. E. Farnsworth and H. H. Madden, *Structure and Proper of Thin Films* (John Wiley & Sons, Inc., New York, 1959), p. 51 Further investigation is required to determine the origin of t displacement.

[7] As would be expected, beams from the polycrystalline str ture were independent of azimuth setting.

Curves 1 and 2 of Fig. 4 show that the electron energy, corresponding to the maximum development of the beams from the nickel lattice, changes with the amount of oxygen exposure. However, the diffraction angle also changes in such a way that the plane grating formula is satisfied without a change in the surface lattice spacing. This result indicates that the crystal inner potential is altered by the exposure to oxygen but the surface lattice spacing is unchanged.

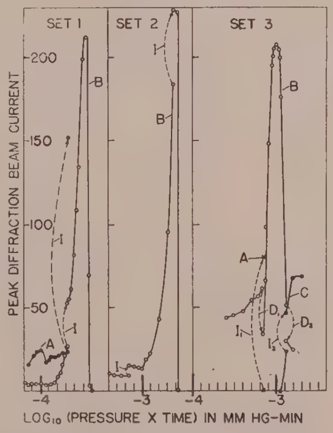

FIG. 2. Curves showing changes in beam intensity (indicated by the dashed lines) caused by allowing the crystal to remain in vacuum several hours subsequent to various exposures of oxygen. Multiply ordinate scales by 2 to obtain intensities of curves B. Curves A are for a 17-v diffraction beam in the (110) azimuth from a double-spaced face-centered structure. Curves B are for a 27-v diffraction beam in the (100) azimuth from a single-spaced simple-square structure. Curve C in set 3 is for a 22-v diffraction beam in the (110) azimuth from a NiO structure. The variation in the values of exposure corresponding to the maxima in the B curves is the result of varying intervals between times of cleaning the crystal and making the observations, as described in the footnote concerning time delay.

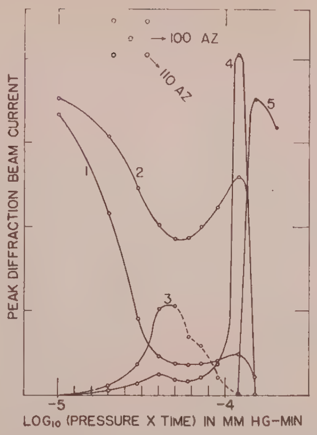

FIG. 3. Diffraction beam intensities as a function of oxygen exposure obtained after a small anneal of the crystal subsequent to ion-bombardment cleaning. Curve 1: Typical beam, in the (110) azimuth at about 28 v, from the clean nickel lattice. Multiply the ordinate scale by 2 to obtain intensity. Curve 2: Typical beam, in the (100) azimuth at about 58 v, from the clean nickel lattice. Multiply the ordinate scale by 6. Curve 3: Typical beam, in the (110) azimuth at about 17 v, from a double-spaced face-centered lattice. Curve 4: Typical beam in the (100) azimuth at about 27 v, from a single-spaced simple-square lattice. Multiply the ordinate scale by 2. Curve 5: Typical beam, in the (110) azimuth at about 22 v, from a nickel oxide lattice.

Place Exchange of Oxygen and Nickel Atoms

Curve 3 in Fig. 4 shows how the photoelectric work function φ of the crystal changes with exposure to oxygen over the range of exposures shown in Fig. 3. The initial rapid increase in φ resulting from adsorption is followed by a broad maximum and a subsequent rapid decrease as a result of oxide formation.[8] Because of the large value of φ in the region of the broad maximum, the accuracy is low. Although it is impossible to determine the exact exposure at which φ begins to decrease, this decrease occurs at exposures too small for the formation of the oxide.

The results of more precise observations over a small range of exposure, in the region just preceding oxide formation, are shown in Fig. 5. It is seen that φ is decreasing in the exposure range of the intense *s-s*, *s-s* structure which just precedes the formation of the oxide structure. This suggests that a place exchange occurs in the exposure range just preceding oxide formation and that the intense *s-s*, *s-s* structure is the result of this exchange. Additional evidence for this exchange is furnished by the observation that the lattice constant

---

[8] For the surface that had received the more complete anneal, φ did not decrease appreciably, from the high value, when the oxide was formed. Although the diffracted intensities from both the *s-s*, *s-s* and the oxide structures are lower for the more complete anneal, with similar exposures, even a small amount of oxide present on the surface for the small anneal dominates the photoelectric characteristics of the surface and causes a marked increase in photoelectric yield which is analyzed as an appreciable decrease in φ. Further discussion will be postponed until additional investigations have been made.

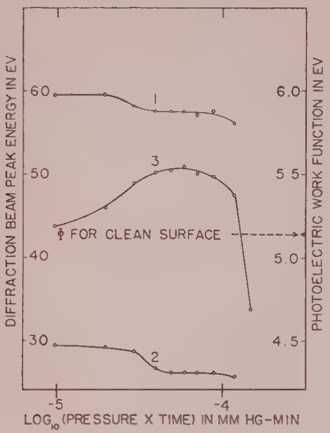

FIG. 4. Curves 1 and 2: Peak voltage for beams from nickel lattice vs $\log_{10}$ exposure (small anneal). Curve 3: Work function vs $\log_{10}$ exposure (small anneal).

of this structure is 2–5% greater than that of clean nickel. Although the accuracy of this determination was not great, the experimental values came within the indicated range. This increase in lattice constant was determined by plotting the colatitude angle as a function of primary voltage for the intense *s-s*, *s-s* structure, and noting the displacement of this curve from a similar curve for the weaker *s-s*, *s-s* structure that appears during smaller exposures.

Although the Fowler method of determining the work function does not apply to semiconductors, the experimental data fit the theoretical Fowler curve for all of the surface conditions preceding the oxide formation, thus indicating that for these observations the surfaces formed by both adsorption and place exchange exhibit the characteristics of a metal. These results are shown in Fig. 6. When nickel oxide forms, the data fail to fit the theoretical curve as would be expected for a semiconductor (see curve 3, Fig. 6). The estimated value of φ for the oxide was obtained by fitting the experimental points near the high-frequency end to the Fowler curve, since it was found previously in this laboratory[9] that the values of φ thus obtained for germanium and silicon were near those obtained by using the contact potential difference method. Although it is not intended that the indicated value of φ for the nickel oxide is more than approximate, we believe that the trend of the change in φ is reliable. The more accurate contact potential difference method for semiconductors will be incorporated in this apparatus for future measurements.

The question may be considered as to whether or not the *d-s*, *f-c* structure is also caused by place exchange rather than adsorption. The increasing work function in the exposure region where this structure appears indicates that the oxygen atoms are on the surface. Because of the relatively low intensity of the *d-s*, *f-c* beam, the test for a change in lattice constant has not furnished conclusive evidence on this question to date.

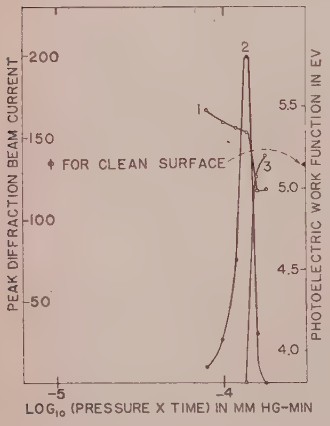

FIG. 5. Curve 1: Work function vs $\log_{10}$ exposure. Curve 2: Intensity of 27-v beam from single-spaced simple-square structure as a function of $\log_{10}$ exposure. Multiply the ordinate scale by 4. Curve 3: Intensity of 22-v beam from a nickel-oxide lattice as a function of $\log_{10}$ exposure.

Observations on CO Adsorption

Because one of the chief components of the residual ambient in an ultra-high vacuum, of the order of 10^{-10} mm Hg, is known to be CO,[10] some tests were made on the nickel crystal after controlled exposures of CO. The adsorption of CO by the clean crystal was found to be appreciably faster than the adsorption of O_2. The adsorbed CO as a result of an exposure of 3×10^{-5} mm Hg-min decreased the intensity of a 60-v diffraction beam from nickel to about 20%, and a weak half-integral-order beam appeared in the (100) azimuth. This beam remained weak even after an exposure of 10^{-4} mm Hg-min. Following an exposure of about 3.5×10^{-4} mm Hg-min, an extra diffraction beam appeared in the (110 azimuth which was associated with a polycrystalline structure on the surface. These results confirm the importance of avoiding the generation of CO by the presence of a hot tungsten filament where tests of its effect cannot be made.

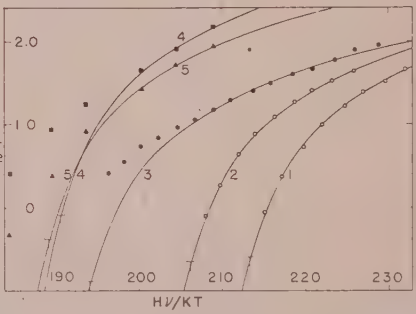

FIG. 6. Fowler curves. Solid lines are displaced theoretical curves; points are experimental values. Curve 1: Clean (100) nickel crystal surface after small anneal. $\varphi=5.135$ ev. Curve 2: Single-spaced simple-square structure on (100) nickel. $\varphi=5.34$ ev. Curve 3: Nickel oxide on (100) nickel. Curve 4: Clean (110) germanium. φ (photoelectric)$=4.88$ ev. φ (CPD)$=4.77$ ev. Curve 5: Clean (111) silicon. φ (photoelectric)$=4.83$ ev. φ (CPD)$=4.7$ ev.

---

[9] J. A. Dillon, Jr. (private communication).

[10] R. E. Schlier, J. Appl. Phys. **29**, 1162 (1958).

Work Function of Clean Nickel

The work function of the clean surface was found to depend on the type of anneal. The value obtained after argon ion bombardment was 5.08 ev. After the "small" anneal (described above), φ was 5.12 ev. After a more complete anneal, the value was 5.22 ev. For this anneal, the crystal was heated at 750°C (thermocouple reading) for 30 min or more, after which the heating power was reduced slowly to zero over a period of at least one hour. These results indicate that the lattice defects produced by ion bombardment result in a lower value of φ than that for the annealed surface. They are consistent with those for evaporated films.[3,11] The values of φ for evaporated films containing lattice imperfections were found to be less than those for the annealed solids.

Related papers have appeared recently. The general features of the results contained in a paper by Germer and Hartman[12] are in agreement with those we have published previously. A paper by Anderson and Klemperer[13] contains results for the photoelectric work function of polycrystalline nickel films after various exposures to oxygen and hence cannot be compared directly with our results for a single crystal. However, it may be noted that their data failed to fit a single theoretical Fowler curve after the smallest exposures to oxygen (less than one monolayer), whereas all of our data fit the theoretical curve except those obtained subsequent to the formation of a true nickel oxide. It thus appears that the polycrystalline nature of the film is responsible for this difference.

---

[11] C. F. Ying and H. E. Farnsworth, Phys. Rev. **85**, 485 (1952); I. L. Blackmer and H. E. Farnsworth, *ibid.* **77**, 826 (1950).

[12] L. H. Germer and C. D. Hartman, J. Appl. Phys. **31**, 2085 (1960).

[13] J. S. Anderson, E. A. Faulkner, and D. F. Klemperer, Australian J. Phys. **12**, 469 (1959); J. S. Anderson and D. F. Klemperer, Proc. Roy. Soc. (London) **258**, 350 (1960).

JOURNAL OF APPLIED PHYSICS VOLUME 32, NUMBER 10 OCTOBER, 1961

Attainment of Ultrahigh Vacua, Reduction in Surface Desorption, and the Adsorption of Hydrogen by Evaporated Molybdenum*

Angus L. Hunt, Charles C. Damm, and Earl C. Popp
University of California, Lawrence Radiation Laboratory, Livermore, California

(Received March 13, 1961)

Deposition of molybdenum by vaporization from simple hairpin filaments has been found to reduce pressures in both unbaked and moderately baked stainless steel vacuum systems to 4×10^{-10} mm Hg. A deposit of 300 mg from a single filament, 0.050 in. in diameter and 6 in. long, has maintained an unbaked 85-liter volume at pressures below 10^{-9} mm Hg for over 40 hr with the aid of a small well-trapped diffusion pump. For a substrate area of 8×10^{3} cm^2, the initial pumping speed of a molybdenum deposit was found to be as high as 10^{5} liters/sec for hydrogen and 8×10^{4} liters/sec for deuterium. The sticking probability for either hydrogen or deuterium on this deposit is estimated at 0.3.

A similar system, baked at 200°C for several days while pumped by an oil-free ion pump, attained 2×10^{-10} mm Hg with molybdenum evaporation. When the ion pump was valved off, the pressure in this 75-liter system remained at 2×10^{-10} mm Hg for two weeks with no external pumping.

INTRODUCTION

A MINIMUM rate of desorption from interior surfaces is an essential requirement for ultrahigh vacuum conditions in any experimental apparatus. For a given desorption rate, the ultimate pressure is proportional to the pumping speed available for the gaseous components evolved.

It has generally been considered necessary to bake large metal systems to at least 400°C to reduce the desorption rate to a level consistent with maintenance of ultrahigh vacuum. The attendant difficulties in mechanical design as well as the difficulty in maintaining integrity of large demountable seals under such thermal cycling make this procedure tedious and unreliable.

A fresh metallic film, deposited directly on the walls of the experimental chamber and covering the interior surfaces, could reduce the desorption rate and at the same time provide a pumping speed proportional to the deposited surface area for those gases adsorbed by the particular metal. The net result of these complementary effects could be a reduction in the ultimate pressure within the system without the necessity of a difficult baking cycle. The experimental achievement of low pressures by this method is the subject of this paper.

Several critical conditions must be met to assure success with this method. Initially, the surfaces must be sufficiently clean so the pressure during film deposition can be maintained at less than 10^{-7} mm Hg. Then the monolayer adsorption time is at least a few seconds and the rate of desorption low enough to prevent immediate film saturation. Second, the maximum surface area must be covered by the metallic film so that desorption

---

* Work performed under the auspices of the U. S. Atomic Energy Commission.

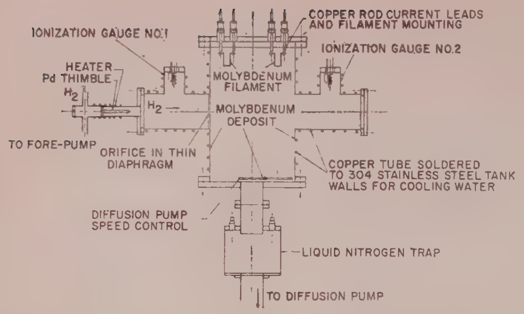
COPPER ROD CURRENT LEADS AND FILAMENT MOUNTING
IONIZATION GAUGE NO.1
IONIZATION GAUGE NO.2
HEATER
Pd THIMBLE
H_2
H_2
MOLYBDENUM FILAMENT
MOLYBDENUM DEPOSIT
TO FORE-PUMP
ORIFICE IN THIN DIAPHRAGM
COPPER TUBE SOLDERED TO 304 STAINLESS STEEL TANK WALLS FOR COOLING WATER
DIFFUSION PUMP SPEED CONTROL
LIQUID NITROGEN TRAP
TO DIFFUSION PUMP

FIG. 1. Eighty-five-liter vessel of type 304 stainless steel for Mo evaporation. Mounted on upper flange are 25 Mo filaments, 50 mils×6 in. long. Two Bayard-Alpert type ionization gauges are used. Pure H_2 or D_2 is diffused through the Pd thimble. The pressure differential across the orifice in the 30-mil-thick diaphragm gives the pumping speed. The orifice conductance is adjustable to 220 liters/sec or 285 liters/sec for H_2 at 300°K.

from the uncovered surface area will not immediately saturate the film. Third, the rate of deposition of the metallic film must exceed the rate of contamination by surface migration from adjacent uncovered areas. The rate of surface migration can be reduced by cooling the substrate. Finally, the deposited metallic film should adsorb a broad spectrum of gases so the deposit is effective in immobilizing the surface contamination and in adsorbing any specific gases that might be introduced into the experimental chamber.

Molybdenum was chosen for the metallic film, since it is generally known to be an active adsorber or getter of gases.[1] It has been established by quantitative gas-adsorption measurements that films of molybdenum deposited by evaporation have a much greater surface area and provide more efficient gettering systems than films of tungsten or tantalum deposited under comparable conditions.[2] Specifically, it was known that hydrogen was effectively adsorbed by molybdenum deposits evaporated by the electron bombardment technique.[3] A recent study of the interaction of hydrogen with molybdenum ribbon[4] has given impetus to the study of the molybdenum-hydrogen system, although one must use caution in comparing the results obtained for molybdenum ribbon cleaned by flashing and results obtained with the type of evaporated deposits described here. The hydrogen adsorption ability was essential to a projected application in which very high hydrogen pumping speeds were required. The comparative utility of metals other than molybdenum is not established by the present investigation.

PROCEDURE

The experimental procedure consisted in evaporating molybdenum from filaments to the cooled walls of an unbaked vessel which was simultaneously pumped by a small oil diffusion pump. The pressure history was followed with two ionization gauges. Pure hydrogen or deuterium was introduced at a known pressure differential through a known conductance and the pumping speed of this particular system determined. From the pumping speed an estimate is made of the sticking probability for hydrogen and deuterium on the molybdenum deposit.

After moderate baking, evaporations were also made in two similar systems. Each of these systems could be valved from the pump, so a rate of pressure rise could be determined as a function of the amount of molybdenum evaporated. One of these systems was pumped by an oil diffusion pump and the other by an oil-free ionic pump.

APPARATUS

A type 304 stainless steel vessel of about 85 liters volume was made so that 25 molybdenum filaments could be mounted on one flange. A schematic drawing of the assembled system is shown in Fig. 1. The upper flange assembly required 26 ceramic insulators, each with a coaxial copper rod $\frac{3}{8}$-in. in diameter. The insulator assemblies were inert-gas-welded into the top flange. Hairpin filaments were made from molybdenum wires, 0.050 in. in diameter and 6 in. long. Five hundred watts per filament were required to produce an appreciable evaporation rate at a temperature of about 2000°C. Repeated trials showed that an average of about 300 mg of molybdenum could be evaporated at this power level from each filament before destruction of the filament.

Two ionization gauges of the modern inverted structure[5] were installed in the arms of the tank. Under isothermal conditions, the two gauges always agreed within 20% and no inconsistent readings were observed. As an elementary check on each gauge, the gauge response at constant pressure was found to be linear with respect to electron emission.

Pure hydrogen was introduced through the palladium diffusion thimble shown at the extreme left of Fig. 1. The thin palladium thimble, 0.5 in. in diameter and 6 in. long, was heated by radiation from the stainless steel envelope which was wrapped with a heating cable. Hydrogen was admitted to the high-pressure side of the thimble at atmospheric pressure. To stop the flow of hydrogen it was necessary to exhaust the high-pressure side of the thimble, for at room temperature hydrogen was found to diffuse through Pd at an appreciable rate.

---

[1] I. Langmuir, J. Am. Chem. Soc. **37**, 1139 (1915); **41**, 167 (1919); S. Dushman, *Scientific Foundations of Vacuum Technique* (John Wiley & Sons, Inc., New York, 1949), p. 676; F. H. Healey, J. J. Chessick, and A. C. Zettlemoyer, J. Phys. Chem. **57**, 178 (1953); R. C. Abbott and A. M. Russell, AFOSR-TR-59-89, p. 9.

[2] J. W. Mitchell (private communication); E. B. Dorling, University of Bristol, Ph.D. thesis, 1953; P. A. Schroeder, University of Bristol, Ph.D. thesis, 1954.

[3] N. Milleron and E. C. Popp, *Transactions of the Fifth Vacuum Symposium, 1958* (Pergamon Press, New York, 1959), p. 153.

[4] R. A. Pasternak and H. U. D. Wiesendanger, 17th Meeting American Chemical Society, Cleveland, Ohio, April, 1960 (to be published in J. Chem. Phys., 1961).

[5] R. T. Bayard and D. Alpert, Rev. Sci. Instr. **21**, 571 (1950).

The orifice separating the hydrogen input arm from the main body of the tank was adjustable to 1 in. or to 1.125 in. in diameter with an external magnetic control. This orifice was cut in a thin stainless steel diaphragm 0.030 in. in thickness to provide two calculated conductances of 220 liters/sec and 285 liters/sec for hydrogen at 300°K.[6]

Calibration of the gauges with respect to hydrogen at 10^{-7} mm Hg was obtained by comparing the rate of hydrogen input at atmospheric pressure, as determined with a trapped oil manometer, with the rate of hydrogen input as obtained from the observed ionization gauge readings and the calculated conductances.

A small oil diffusion pump was connected to the tank through a liquid nitrogen trap of ultrahigh-vacuum design. This trap reduced the possibility of continual contamination with diffusion pump oil. A diffusion pump speed control, in the form of a loosely fitting stainless steel disk positioned magnetically from outside the system, was used to constrict the opening as an aid in establishing the pumping speed of the trapped diffusion pump. The walls of the tank and its two arms were cooled to about 10°C by water flowing through copper tubing soldered to the stainless steel exterior.

All demountable seals between the tank and the various flanges were of the all-metal step or pinch type[7] with 70/30 or 90/10 Cupronickel alloy gaskets.

Leak tests on the system were completed with a helium mass-spectrometric leak detector. The only leak located was the integrated leak through the 26 insulator units, involving over 100 welds or potential leak points. This leak (10^{-7} μl/sec) was reduced by a factor of 10^5 by covering the insulator flange with a differentially pumped chamber. A pressure of 10 μ in this chamber reduced the leak rate into the complete assembly to below the detectable limit. Evacuation of the system to below 10^{-7} mm Hg was always possible before deposition of any molybdenum.

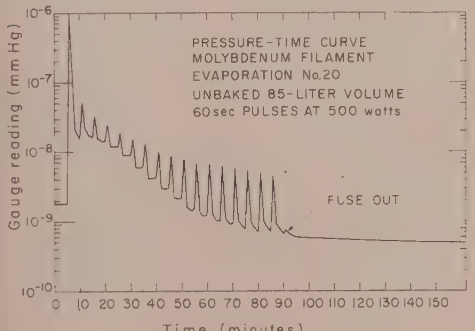

FIG. 2. Pressure history of evaporation. The filament is repetitively pulsed for 1 min at 5-min intervals. Ultimate pressure is 4×10^{-10} mm Hg.

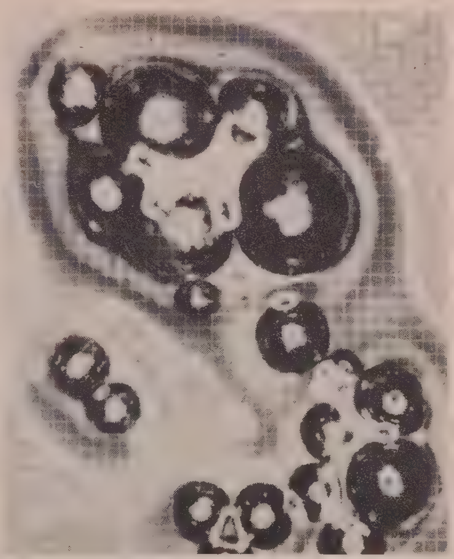

FIG. 3. Photomicrograph of larger molybdenum particles deposited on cooled wall of the vacuum vessel. Grid spacing is 25×10^{-4} cm.

PRESSURE DURING MOLYBDENUM EVAPORATION

Figure 2 shows the typical pressure changes in the unbaked 85-liter volume during one filament evaporation. Before evaporation, the filament was outgassed at a power input of 200 w. The pressure rise associated with this operation was due to degassing from the walls of the tank as well as from the filaments and its supports. The filament was repetitively pulsed with 500 w for 1 min at 5-min intervals. The envelope of maximum pressures decreased with each successive pulse as did the envelope of minimum pressures. The maximum ionization gauge readings were well in the 10^{-9}-mm Hg range near the end of the pulse series, and the minimum gauge readings were in the 10^{-10}-mm Hg range. After evaporation of the filament, the gauge readings remained below 10^{-9} mm Hg for over 40 hr, after which a gradual pressure rise occurred to the neighborhood of the initial pressure range of 10^{-8} mm Hg.

THE MOLYBDENUM DEPOSIT

The molybdenum deposit appears to be a grey powder. The deposit has little metallic luster except where the substrate is not cooled. Photomicrographs of samples removed from the cooled walls are reproduced as Figs. 3 and 4. The grid spacing on these photographs is 25×10^{-6} m. The deposit consists of two classes of particles. One class contains large particles of 100 to 300 μ in diameter which are almost spherical. The second class consists of smaller particles which, in turn, may be

---

[6] S. Dushman, *Scientific Foundations of Vacuum Technique* (John Wiley & Sons, Inc., New York, 1949), p. 92.

[7] W. J. Lange and D. Alpert, Rev. Sci. Instr. **28**, 725 (1957).

FIG. 4. Photomicrograph of smaller molybdenum particles deposited on cooled wall of the vacuum vessel. Grid spacing is 25×10^{-4} cm.

aggregates of much smaller particles. A deposit such as that illustrated is likely to have a large surface area.

ADSORPTION OF HYDROGEN AND DEUTERIUM

During early stages of experimentation with the apparatus of Fig. 1, a simple needle valve was used in place of the Pd diffusion thimble as a means of gas introduction. The computable conductance C for hydrogen through the orifice and the pressure difference across the orifice gave the pumping speed S for the molybdenum deposit and the diffusion pump according to the expression

$$S=(P_1-P_2)(C/P_2).$$

It was found that the indicated pumping speed for tank hydrogen decreased over a 20-min period under a constant hydrogen influx of 1.1×10^{16} molecules/sec. The indicated pressure increased in the main body of the tank from 8.7×10^{-9} mm Hg to 1.6×10^{-8} mm Hg during this 20-min interval. The base pressure before hydrogen admission was 7×10^{-10} mm Hg. When the major hydrogen impurity was found to be argon (0.5%), it was concluded from the measurements, and from the pumping speed of the diffusion pump, that the amount of argon adsorbed on the molybdenum deposit must have been small and that the hydrogen pumping speeds observed were conservative.

The hydrogen diffusion thimble shown in Fig. 1 was then installed to assure gas purity. When pure H_2 or D_2 was diffused directly into the system through the Pd thimble, the initial measured pumping speeds were found to be much higher. The initial speeds at room temperature were found to be 8×10^4 liters/sec for D_2 and 10^5 liters/sec for H_2. In contrast to the previou measurements, the diffusion thimble made possibl adjustment of the loading rate to 2×10^{10} molecules/cm sec. With this reduced hydrogen influx, indicated pressures of less than 10^{-9} mm Hg were maintained over th molybdenum deposit during the pumping speed measurements. Since the geometrical surface area of th substrate was about 8×10^3 cm^2, a sticking probabilit of about 0.3 was computed for H_2 and D_2 on a fres molybdenum deposit. The measured pumping spee decreased with the age of the deposit as well as with H or D_2 coverage. It can be assumed that the reduce speed was due to slow contamination by residual gas

Although the sticking probabilities or pumping speed for this type of molybdenum deposit might actually b higher than those found here, precise values probabl require the use of molecular beams. The large probabi ity that H_2 or D_2 molecules with thermal energies wi not survive a single encounter with a fresh molybdenur surface makes the measurement of pressure a functio of the relative positions of gas source, gauge, and adsorbing surfaces.

RATE OF PRESSURE RISE

In a second system, similar to that described abov it was possible to isolate the vacuum tank from th liquid-nitrogen trap and diffusion pumps with a larg all-metal, ultrahigh-vacuum valve. In this system, about 70 liters volume, a moderate baking at 200°C fo 12 hr reduced the initial pressure reading to 5×10 mm Hg, before evaporation of any molybdenum. B virtue of the valve in this system, it was possible t

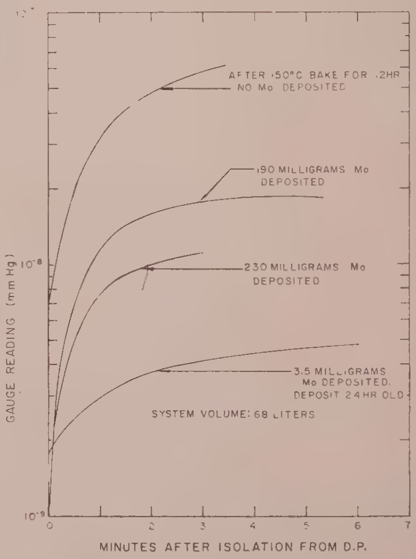

FIG. 5. Pressure rise after isolation from the diffusion pump as a function of amount of Mo deposited.

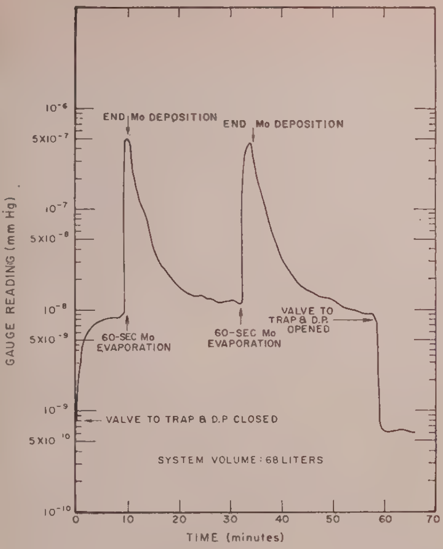

FIG. 6. Pressure changes during Mo evaporation. The system was initially isolated from the diffusion pump. Residual pressure indicates components not adsorbed by molybdenum, but pumped by diffusion pump.

measure the pressure increase as a function of time after valve closure.

Figure 5 shows the pressure rise with time, after isolating the system from the trap and diffusion pump, as a function of the quantity of molybdenum deposited. The upper curve is the pressure rise found for the cold system after baking and before any molybdenum was evaporated. That some of the components responsible for the pressure rise in the molybdenum system are inactive with respect to molybdenum is conclusively shown in Fig. 6, where two molybdenum deposits were completed with the system isolated from the liquid-nitrogen trap and diffusion pump. After closure of the valve at time zero, the usual pressure rise occurs. Two 1-min vaporizations of molybdenum did not reduce this pressure. Opening the valve to the diffusion pump and trap rapidly reduced the pressure below the initial value. Under similar conditions, but in a system which incorporated a mass spectrometer, it was found that the molybdenum filament interacts, probably with higher molecular weight hydrocarbons, to produce methane which is not rapidly adsorbed by the molybdenum deposit. It is therefore possible that one of the components which appears inactive with respect to molybdenum is methane.

A third system, largely oil-free, which was pumped by an ion pump[8] and a low-temperature sorption pump,[9] attained a lower pressure of 2×10^{-10} mm Hg under molybdenum gettering. This system, with a volume of about 75 liters, was baked at 200°C for 115 hr and on cooling showed a base pressure of 4×10^{-9} mm Hg. Evaporation of 1.235 g of molybdenum with the ion pump operating reduced the residual gas pressure to 2×10^{-10} mm Hg, as indicated by two independent ionization gauges. When the ion pump was valved from the system, the pressure remained at 2×10^{-10} mm Hg for two weeks with no external pumping of any kind. Gauge pumping was not responsible for the continued low pressure readings, as the gauges were inoperative for as long as 15 hr with no resulting pressure rise. No pressure bursts were observed as the gauge filaments were heated, indicating that the unknown residual gas was not adsorbed on the filaments. To some extent at least, the absence of positive rate of pressure rise in this third system can be attributed to the oil-free substrate and the attainment of an exceptionally tight system.

These pressure observations are consistent with the hypothesis that part of the function of a molybdenum deposit is to reduce the degassing rate of those gases which are inactive with respect to molybdenum. That is, the molybdenum deposit might reduce the conductance between the contaminated walls and the system and thereby reduce the rate at which ungetterable components reach the system. A similar covering action has been suggested for evaporated copper deposited on a glass substrate.[10]

In summary, it has been shown that deposition of fresh molybdenum by a simple technique on the cooled walls of large metal apparatus is an effective aid in obtaining ultrahigh vacuum conditions, especially where hydrogen or deuterium contamination is likely. The data suggests that the action of the molybdenum deposit might be both mechanical and chemical.

ACKNOWLEDGMENTS

The authors wish to acknowledge the assistance of John E. Omohundro who made many of the measurements. The photomicrographs were due to the cooperation of William B. Distler. The authors also wish to acknowledge many stimulating discussions with Richard F. Post concerning the methods and techniques of this work.

---

[8] Varian, 400-liter/sec Vacion pump.

[9] Varian, 2-liter Vacsorb pump.

[10] J. A. Allen, C. C. Evans, and J. W. Mitchell, *Structure and Properties of Thin Films*, edited by C. A. Neugebauer, J. B. Newkirk, and D. A. Vermilyea (John Wiley and Sons, Inc., New York, 1959), pp. 46–52, and Panel Discussion, pp. 533–538.

X-Ray Polarizer

H. COLE, F. W. CHAMBERS, AND C. G. WOOD
International Business Machines Corporation Research Center, Yorktown, New York

(Received May 15, 1961)

In the Borrmann effect, or the anomalous transmission, by diffraction, of x rays through perfect crystals, one state of polarization of the x-ray beam is preferentially absorbed. Since this happens in the "transmitted" as well as in the diffracted beam, a simple polarizer-monochromator is possible in the sense that insertion and rotation of the polarizer does not sensibly change the line of action of the x-ray beam. We have used as our "Borrmann crystal" a single-crystal slab of dislocation-free germanium approximately 30 mils thick and cut for symmetric Laue diffraction from the 220 planes. The details of the rotating crystal holder, an analysis of the polarization, comments on the double-crystal geometrical effects, and an example of the use of the polarizer-monochromator to study the polarization term in Bragg diffraction are presented.

INTRODUCTION

IN the Borrmann effect[1] the perfection of the crystal results in interactions, usually suppressed, between the diffracted beams and the incoming beams. The result of the interactions, for Laue diffraction through a crystal slab, is a net energy flow mostly along the atomic planes, and two standing wave patterns perpendicular to the flow. If the crystal structure is simple enough, the nodes of one standing wave pattern will coincide with atomic sites, and the normal photoelectric absorption will be inoperative for this part of the energy flow. The "anomalous transmission" of x rays results. However, even for this beam, the state of polarization with the electric vector in the plane of incidence, according to the theory, suffers considerable absorption with respect to the polarization state with the electric vector perpendicular to the plane of incidence. Thus, for example, if a single-crystal slab of dislocation-free germanium of ~1 mm thickness, cut to Laue diffract from the 220 planes, is oriented in the radiation from a copper-target x-ray tube so as to diffract Cu $K\alpha$ radiation, the only radiation leaving the crystal is expected to be essentially polarized Cu $K\alpha$ radiation. (See Fig. 1.) If now the crystal is rotated around th center line of the forward-diffracted (transmitte beam, the direction of the electric vector, in space, i the forward-diffracted beam can be made to take u any angle with respect to the plane of the drawin while the beam itself stays essentially fixed in spac Under these conditions, the diffracted beam traces o a cone in space, but this beam is not used.

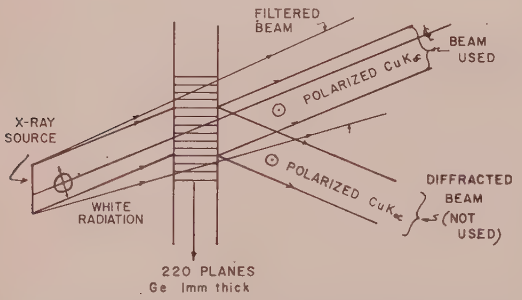

FIG. 1. Basic diffraction geometry for anomalous transmission of x rays (Borrmann effect). The 220 planes in a germanium crystal slab are used to produce the polarized and monochromated beams. The crystal is rotated around the center line of the forward diffracted beam, thereby turning the polarization vector in space.

I. POLARIZER-MONOCHROMATOR

Figure 2 is a drawing showing certain aspects of th rotatable crystal mounting. A 6° x-ray target take-o angle is used from a "spot focus" window to give 1- ×1-mm effective x-ray source size. The crystal hold consists of a cylinder turning inside a fixed cylind with angle marks inscribed on the rotatable cylind and with a locking screw which holds the two cylinde together during a measurement. A recessed groove the rotatable cylinder has a sloping bottom cut to gi approximately the correct 2θ for the 220 Ge Cu reflection. The crystal slab is cut with some accura etched, and mounted on a plate with a hole in it; t plate is pivoted on two points and its setting relative the sloping bottom can be adjusted with a 2θ adj screw. If some other radiation is desired, the sl should be properly chosen or the 2θ adjust given a larg swing.

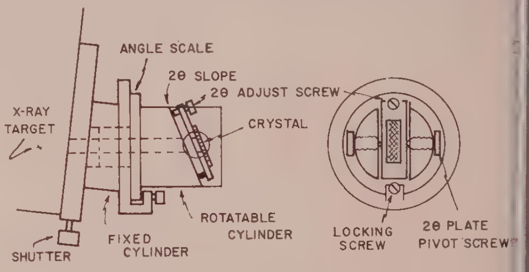

FIG. 2. Schematic representation of Borrmann crystal holder.

The 2θ adjust was necessary since neither the a of the cylinders nor the cutting of the crystal was go enough in this case to ensure the maintenance of t proper 2θ as the polarizer was turned. The polarizer was usually "tuned" at each setting and an I_0 count taken for normalization purposes. The diffracted beam was caught by a beam stop, and the hard radiation (very little) penetrating the crystal was discriminated against with a proportional detector and a pulse-height analyzer. Under these conditions, with the x-ray tube operating at 30 kv and 18 ma, and with a 1-mm² aperture just before the sample, an I_0 of 5000 counts/sec of polarized Cu $K\alpha_1$ and $K\alpha_2$ radiations was obtained. The total power in the forward-diffracted beam was considerably greater than this, but divergence considerations led to the 1-mm² aperture just before the sample and subsequent loss of total power.

---

[1] H. Cole and G. E. Brock, Phys. Rev. **116**, 868 (1959); G. Borrmann, Z. Krist. **106**, 109 (1954); **112**, 312 (1959); R. W. James, *Optical Principles of Diffraction of X Rays* (G. Bell and Sons, London, England, 1954).

II. VERIFICATION OF POLARIZATION IN THE BORRMANN EFFECT

The forward-diffracted beam from the polarizer crystal was used as an incident beam to study the 111, 333, and 444 Bragg reflections from another dislocation-free germanium crystal, cut to expose a 111 face and mounted in a standard Geiger-counter x-ray spectrometer. The 2θ for the germanium 333 reflection with Cu $K\alpha$ radiation is 90.05°; therefore, the integrated intensity of this reflection as a function of polarizer setting gives a check on the degree of polarization obtained by the polarizer. At the same time, the integrated intensities of the 111 and 444 reflections, as a function of $\sin\theta/\lambda$ and as a function of polarization of the incident beam, give two checks on the perfection of the second crystal.[2]

The integrated intensity as a function of polarization is given by

$$E\omega/I_0=R_p[\cos^2\varphi+\sin^2\varphi\,|\cos 2\theta|] \qquad (1)$$

for a perfect crystal with no absorption, and by

$$E\omega/I_0=R_M[\cos^2\varphi+\sin^2\varphi\,\cos^2 2\theta] \qquad (2)$$

for a perfect mosaic crystal, where φ is the polarizer angle and the other symbols have their usual x-ray meaning. 2θ is the Bragg angle of the reflection, E is the total count obtained in rocking through the reflection at a radian velocity ω, I_0 is the intensity of the incident beam involved in the diffraction process, and R_p and R_M are theoretical expressions giving the strength of the reflection. We have taken $\varphi=0$ when the electric vector is perpendicular to the plane of incidence. At the 333 setting, $2\theta=90.05°$, $\cos 2\theta=0$; therefore, for this reflection,

$$E\omega/I_0=R\cos^2\varphi, \qquad (3)$$

independent of the perfection of the second crystal.

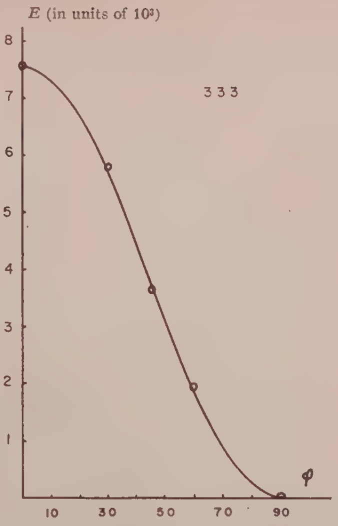

FIG. 3. Verification of polarization in the Borrmann effect. The forward diffracted beam is Bragg diffracted from a second crystal for which $2\theta=90°$; therefore, the integrated intensity of this reflection should follow a cos² law as a function of polarizer setting, if the polarization is complete. A plot of total rocking-curve count E vs polarizer setting φ is shown.

Figure 3 is a plot of E_{333} as a function of φ, and as can be seen, the experimental points follow the expected $\cos^2\varphi$ curve. The polarization, as obtained from the ratio of the integrated intensities for the two states of polarization, is at least 99% complete. No effort was made to define precisely the $\varphi=0°$ or 90° setting of the polarizer other than through the mechanical assembling of the parts and a slight tilt adjust on the second crystal. It is possible to observe a small 333 peak for $\varphi=90°$ if the second crystal is set properly with respect to rotation around its own diffraction vector so that simultaneous diffraction[3] (umweganregung) may occur. The "crossed polaroid" effect of the polarizer at $\varphi=90°$ on the 333 reflection permits suppression of the true 333 and thus opens the possibility of measuring simultaneous diffraction events.

III. GEOMETRICAL EFFECTS

A. Double Crystal Effect

When the polarizer is set such that the E vector is perpendicular to the plane of incidence of the diffraction from the second crystal, the atomic planes in the polarizer crystal and in the second crystal may approximate a "parallel" double-crystal arrangement, or an "antiparallel" arrangement. This is shown schematically in Fig. 4. For convenience, we will call $\varphi=0$ the "parallel" arrangement and $\varphi=180°$ the "antiparallel" case. If the 2θ of the Bragg reflection of the second crystal is less than the 2θ of the reflection being used in the polarizer, then, for the $\varphi=0$ setting, the normal α_1, α_2 angular positions in the rocking curve of the second crystal are reversed. For all other configurations, the curves look "normal," and, of course, the

---

[2] K. S. Chandrasekaran, Acta. Cryst. 12, 916 (1959).

[3] H. Cole, F. W. Chambers, and H. M. Dunn (to be published).

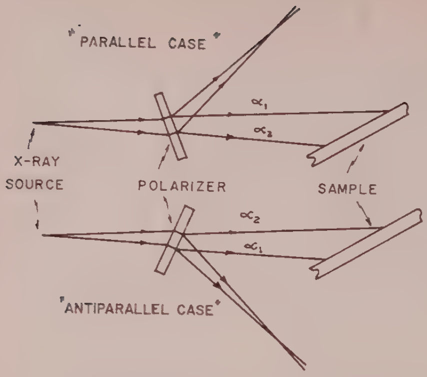

Fig. 4. Double-crystal geometry of the polarizer-sample crystal. Details are discussed in the text.

α_1, α_2 angular separation may be calculated from consideration of the geometry shown in Fig. 4.

It may be remarked that the different wavelengths in the diffracted beam (normally not used) of the polarizer are focused at a point equal to the distance of the polarizer crystal from the x-ray target; thus, an image of the target may be obtained if a film is placed at this point.

B. Divergences

For $\varphi=0°$ or 180°, as defined above, the rocking curves of the second crystal are as sharp as ordinary double-crystal rocking curves. In effect, the angular width of each wavelength component in the "horizontal" plane from the Borrmann crystal is only a few seconds wide; however, the "vertical" divergence is limited only by the slit system. When the polarizer is set at any other angle, and especially at $\varphi=90°$ or 270° where the "vertical" divergence becomes the "horizontal" divergence, each wavelength component may diffract over a considerable angular range during the rocking of the second crystal. The rocking curves then have the appearance of broad, triangular peaks. However, if all of the radiation diffracted from the second crystal is detected, the integrated intensities should not be affected.[4] We found that a 1×1-mm aperture just before the second crystal was adequate for divergence control.

IV. POLARIZATION TERM IN BRAGG DIFFRACTION

Referring to Eqs. (1) and (2), if integrated intensities are measured as a function of polarization angle φ, the perfection of the second crystal can be determined by comparing its behavior to these two theoretical extremes. A perfection parameter has been defined b Chandrasekaran[2] on this basis. A better estimate the perfect crystal case can be obtained if one ha available some additional data on the absorptio parameters. That is, the integrated intensity of perfect crystal, with absorption, is given by

$$R_p=\frac{\lambda^2(e^2/mc^2)N|F|e^{-M}}{\pi\sin 2\theta}\int R(k)dk, \qquad (4$$

where all the quantities have their usual x-ray meanin (see below), and have been calculated by Batterma for germanium and Cu $K\alpha$ radiation. The $\int R(k)d$ equals 8/3 for the perfect nonabsorbing crystal, an takes up such a value for the perfect mosaic crystal tha

$$R_M=\frac{\lambda^3(e^2/mc^2)^2N^2F^2e^{-2M}}{2\mu_l\sin 2\theta}. \qquad (5$$

The integral $\int R(k)dk$, in addition to its dependen upon wavelength λ, absorption μ_l, structure factor and Debye factor M, depends on the polarizatio state; therefore, Eq. (1) should be modified to read

$$E\omega/I_0=R_p[\cos^2\varphi+r\sin^2\varphi|\cos 2\theta|], \qquad ($$

where r is the ratio of $\int R(k)dk$ for the two polarizatio states, and is such as to make $r|\cos 2\theta|\rightarrow\cos^2 2\theta$.

Figures 5 and 6 are plots of total accumulated cou E for the 111 and 444 reflections of germanium vers φ, the polarization angle, for Cu $K\alpha$ radiation. $I_0=50$

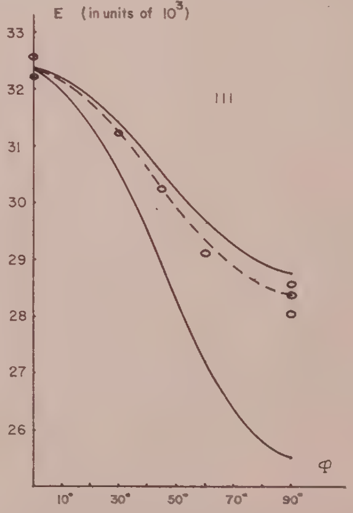

Fig. 5. Total rocking-curve count vs polarizer setting for 1 germanium Bragg reflection and Cu $K\alpha$ radiation. Upper curve expected variation for a perfect nonabsorbing crystal; lower cur is for an ideal mosaic crystal. Dotted curve represents correcti for absorption in perfect germanium. Circles represent expe mental points.

---

[4] Later studies have shown that if the "perfection" of the second crystal differs with respect to rotation around its surface normal, then the different divergence aspects of the different polarizer settings causes spurious results. In this case, the second crystal must also be rotated around its diffraction vector to present the same aspect to the beam.

[5] B. W. Batterman, J. Appl. Phys. **30**, 508 (1959).

counts/sec and $\omega = 0.05$ deg/min. The solid curves represent Eqs. (1), upper curve, and (2), lower curve, normalized to the observed E at $\varphi = 0$. The dotted curve represents Eq. (1) corrected to Eq. (6) using the value of r as evaluated by Batterman. The circles represent the measured values. Within the statistical accuracy of this experiment, this crystal would be judged quite perfect. The absolute, measured, integrated intensities are tabulated in Table I, and, for comparison, the theoretical values for a perfect crystal, as calculated by Batterman, are listed, as well as the values to be expected for a perfect mosaic crystal, obtained from Batterman's numbers by

$$R_M = \frac{\sin 2\theta}{2\lambda\mu_l}\left[\frac{\pi R_p}{\int R(k)dk}\right]^2. \qquad (7)$$

As can be seen, the agreement here is quite good although perhaps not as good as the polarization measurements would lead one to expect; however, a great many factors are fed into the calculation of the theoretical numbers, so it is not surprising to find somewhat less good agreement.

V. COMMENTS ON THE THICKNESS OF THE BORRMANN POLARIZER CRYSTAL

The four wave fields[1] inside the crystal which make up the description of dynamical diffraction effects are each modified by its own average absorption term, of the form

$$\exp[-\mu_l t(1 \pm K\epsilon)], \qquad (8)$$

where K is the polarization term ($K = 1$ or $|\cos 2\theta|$) and ϵ is a parameter whose value lies between 0 and 1 and which varies inversely as the spatial extent of the atomic absorption [$\epsilon \sim (F_{hkl}''/F_{000}'')$, where F'' is the imaginary part of the structure factor]. Hunter[6] has measured ϵ for the 220 reflection of germanium with Cu $K\alpha$ radiation and found it to be approximately 0.95. μ_l is the normal photoelectric absorption coefficient ($\mu_l \sim 350$ cm^{-1}), and t is the thickness of the crystal seen by the radiation. Since the forward-diffracted beam is being used in the polarizer, the crystal must be its own filter for those wavelengths of and near the one of interest which are not diffracted through the crystal. The absorption of these rays is given by the ordinary $e^{-\mu_l t}$. The relative absorption terms for the case considered here are then of the form

(1) $e^{-\mu_l t}$: normal filtering;
(2) $e^{-\mu_l t(0.05)}$: wave with nodes at Ge sites, polarization perpendicular to plane of incidence;
(3) $e^{-\mu_l t(0.328)}$: wave with nodes at Ge sites, polarization in plane of incidence;
(4) $e^{-\mu_l t(1.95)}$: wave with antinodes at Ge sites, perpendicular polarization;
(5) $e^{-\mu_l t(1.67)}$: wave with antinodes at Ge sites, parallel polarization,

where the second term is obviously associated with the usable radiation coming through the polarizer. If one assumes that of all the Cu $K\alpha$ radiation falling on the polarizer from the x-ray tube only 10^{-4} or so is involved in the diffraction process, then, even if the second-term exponent were zero, $e^{-\mu_l t}$ should be of the order of 10^{-6} for proper filtering. This implies that the thickness should be about 0.5 mm. If the crystal is very thin, the filtering is poor and the diffraction weak; if the crystal is very thick, the filtering is excellent, but the finite exponent in the second term above results in small transmission again. There is apparently a very broad maximum around $\mu_l t \sim 10$, or $t \sim 0.5$ mm. The thicker the crystal, of course, as long as I_0 is still a usable number, the cleaner the system.

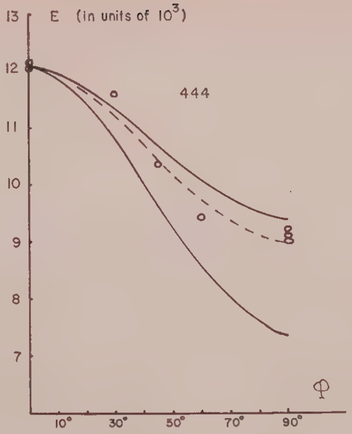

FIG. 6. Same as Fig. 5, except for 444 reflection.

TABLE I. Comparison of measured and calculated integrated intensities for germanium reflections and Cu $K\alpha$ radiation. R_p = Batterman's values for perfect absorbing crystal; R_M = values for ideal mosaic crystal; R_{obs} = observed. Polarization state perpendicular to plane of incidence.

Reflection	$R_p \times 10^4$	$R_M \times 10^4$	$R_{\text{obs}} \times 10^4$
111	0.8722	5.527	0.9417
333	0.2083	0.8095	0.2211
444	0.3671	1.4996	0.3636

---

[6] L. P. Hunter, IBM J. Research Develop. 3, 106 (1959).

Alternating Current Magnetohydrodynamic Generator

P. R. Smy
Physics Department, University of British Columbia, Vancouver 8, B. C., Canada

(Received June 12, 1961)

The design criteria of a proposed ac magnetohydrodynamic (mhd) generator are discussed. It is found that electrical losses to the moving fluid are serious unless the duct length-to-width ratio is greater than about 30. Two developments of such a generator are suggested. The first would provide a solution to the problem of power output from a segmented-electrode generator. The second development, that of capacitive power transfer at the electrode-fluid interface, would have many benefits, but its application is found to be severely restricted by the limited dielectric strength of materials.

INTRODUCTION

In recent years the problem of magnetohydrodynamic power generation has attracted much attention. Various workers such as Kantrowitz and Sporn,[1] and Thring, have suggested that this method of converting heat energy to electrical energy might be developed to give a higher efficiency than that attainable with the present turbine-generator systems. The experimental characteristics of several pilot magnetohydrodynamic (mhd) generator systems have already been described.[2–5]

In a simple mhd generator, an electrically conducting fluid is driven along the channel between two parallel electrodes (E and E') which are connected by an external impedance Z. A magnetic field is applied to the electrode system such that the magnetic lines of force are parallel to the surfaces of the electrodes and are perpendicular to the velocity of the fluid. (See Fig. 1.)

The motion-induced electric field produces an emf in the circuit EZE', $V=2x_0uB$ volts, where u=plasma velocity (m/sec), $2x_0$=electrode separation (m), and B=magnetic induction per unit area (webers/m^2). The emf drives a current through Z and thus supplies electrical power to an external impedance. The current i, in conjunction with the applied magnetic field, also produces a retarding force which reduces the enthalpy of the fluid. In this way, electrical power is generated at the expense of the enthalpy of the fluid.

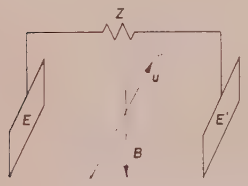

FIG. 1. mhd electrode assembly.

A disadvantage of such a generator is that it provides dc electrical power. Harris[6] reports that the inversion equipment necessary to convert this dc power to ac power would almost double the cost of such a generato In this paper, the design criteria of a proposed ac mh generator are discussed, together with some possib developments of such a generator.

PROPOSED ac mhd GENERATOR

An ac output would be obtained from the simple d generator described above by replacing the stead applied magnetic field with a sinusoidally time-varyi applied field $B_0 \sin\omega t$. The electrical circuit now b comes that shown in Fig. 2.

POWER LOSSES TO THE FLUID

For efficient power production, the ohmic heating the fluid (resistance R_p) must be much less than th power delivered to the external impedance, i.e

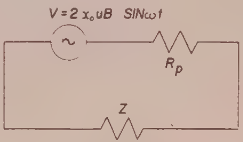

FIG. 2. Equivalent circuit of an mhd generator.

$\langle i^2\rangle_{\text{av}} R_p \ll \langle i^2\rangle_{\text{av}} Z$; therefore

$$R_p \ll Z, \qquad ($$

where $\langle i^2\rangle_{\text{av}}$=mean square current.

Also, the eddy current power loss in the fluid must much less than the power delivered to the extern impedance. For a given volume of conductor, edd current losses can be minimized by severely restricti one of the two dimensions of the conductor which a perpendicular to the direction of the applied tim varying magnetic field.

In the following calculation, fluid of conductivity is considered to be contained between 'nonconductin electrodes of length l and depth d, and a distance 2 apart. The dimension $2x_0$ is assumed to be

(a) much less than the skin depth $1/(\omega\mu_0\sigma)^{\frac{1}{2}}$, whe $2\pi\omega$=frequency of applied field;

(b) much less than l.

As a result of (a), the magnetic field at every point the fluid can be taken as $B_0 \sin\omega t$. As a result of (b) w can neglect nonuniform effects at each end of t electrode region. (See Fig. 3.)

---

[1] A. Kantrowitz and P. Sporn, Power 103, 62 (1959).
[2] R. J. Rosa, J. Appl. Phys. 31, 735 (1960).
[3] R. J. Rosa, Phys. Fluids, 4, 182 (1961).
[4] H. J. Pain and P. R. Smy, J. Fluid Mech., 10, 51 (1960).
[5] P. R. Smy, Ph.D. thesis, University of London, 1960.
[6] L. P. Harris, General Electric Corporation Rept. No. 60-RL2515G.

Maxwell's laws applied to the moving fluid give

$$\nabla\times(\mathbf{E}-\mathbf{u}\times\mathbf{B})=-d\mathbf{B}/dt,$$

where $\mathbf{E}$=total electric field at any point in the fluid. The solution to this equation if (a) and (b) apply is

$$\mathbf{E}=uB\mathbf{x}-x(dB/dt)\mathbf{y}.$$

The E_x component is the usual $\mathbf{u}\times\mathbf{B}$ motion induced electric field, and the E_y component is the term responsible for eddy currents. The consequent eddy current heating per unit volume is

$$\sigma E_y^2\ \mathrm{w/m^3}=\sigma x^2(dB/dt)^2.$$

The time averaged eddy current loss in the electrode region is

$$2ld\int_0^{x_0}\sigma x^2(dB/dt)^2=\tfrac{2}{3}ld\sigma x_0^3(dB/dt)^2$$

$$=\tfrac{1}{3}ld\sigma x_0^3\omega^2B_0^2\ \text{watts},\qquad(2)$$

which is the usual expression for the eddy current loss in a long thin conductor.

To avoid substantial electrical heating of the fluid, these two criteria must be satisfied:

(a) $R_p\ll Z$,
(b) $\frac{1}{3}ld\sigma x_0^3\omega^2B_0^2\ll$power output;

where the power output

$$=\langle V^2\rangle_{\mathrm{av}}Z/(R+Z)^2\rightarrow u^2B_0^2 2x_0^2/Z,$$

(a) and (b) reduce to

$$2x_0\ll\sigma ldZ\ll 6u^2/(x_0\omega^2).\qquad(3)$$

If the fractional power loss is to be less than 10% in each case, then

$$200x_0\lesssim 10\sigma dlZ\lesssim 6u^2/(x_0\omega^2).\qquad(4)$$

A typical proposed mhd generator[6] has these characteristics:

$u\sim10^3$ m/sec,
Input pressure $P_i\sim5$ atm$=5\times10^5$ newtons/m^2,
Exit pressure $P_0\sim1$ atm$=10^5$ newtons/m^2,
Temperature $\sim$2 500°K,
Density $\rho\sim0.5$ kg/m^3.

The time-varying current and field result in a time-varying magnetic retarding force. It is undesirable that this force should generate large fluctuations in the velocity of the fluid since irreversible shock heating of the plasma might occur. It is shown later, on the basis of a very simple model, that the velocity of the plasma will be constant within 6% if

$$l/(4\pi)\gtrsim u/\omega,\qquad(5)$$

i.e., that fluid in passing through the length of electrode region suffers several successive retarding impulses. The energy lost in electrically heating the fluid is not completely wasted since a substantial fraction of this heat energy may be recovered downstream by a conventional generator.

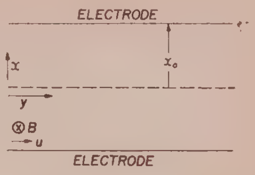

FIG. 3. Coordinate system.

Conditions (4) and (5) lead to a minimum value of the duct length-to-width ratio

$$l/(4\pi)\gtrsim u/\omega\gtrsim(200/6)^{\frac{1}{2}}x_0;$$

therefore

$$l/(2x_0)\gtrsim 2\pi(200/6)^{\frac{1}{2}}\sim35.\qquad(6)$$

If the duct length-to-width ratio is too great, viscous and heat transfer effects will reduce the efficiency of the generator. Estimates of the consequent upper limit of the above ratio are usually about 30.[3,6] This quantity, in conjunction with (6), shows that the duct length-to-width ratio of such an ac generator will be restricted to a value

$$l/(2x_0)\sim30.\qquad(7)$$

An efficient generator, then, must satisfy relations (4) and (7). An ac frequency of 50 cps is chosen, as this would fit in with existing power distribution networks. With $f\sim50$ cps, i.e., $\omega\sim300$ rad/sec, $u=10^3$ m/sec, $l=40$ m [from relation (5)], $x_0=\frac{2}{3}$ m [from relation (7)]; relation (4) becomes

$$40/3\lesssim\sigma dlZ\lesssim30/3;$$

therefore

$$\sigma dlZ\sim10.\qquad(8)$$

FACTORS AFFECTING MAGNETIC FIELD INTENSITY

For an efficient (constant velocity) generator which abstracts a substantial fraction of the enthalpy of the moving fluid, the pressure drop across the generator will be of the same order of magnitude as the inlet pressure, i.e., pressure drop across generator $\sim P_i$; therefore, the magnetic retarding force exerted on the fluid is

$$iB2x_0\sim P_id2x_0.$$

Now $i=V/Z=2x_0uB/Z$; therefore

$$P_id=2x_0u\langle B^2\rangle_{\mathrm{av}}/Z=x_0uB_0^2/Z;$$

thus

$$B_0=[ZdP_i/(x_0u)]^{\frac{1}{2}},\qquad(9)$$

which with (8) gives

$$B_0[10P_i/(\sigma lx_0u)]^{\frac{1}{2}}.\qquad(10)$$

Hall effects may become important if $B_0>1$ weber/m^2. Also it would be difficult to construct coils of this size to withstand intensities $B_0>5$ webers/m. It is apparent from these facts that B_0 should be kept to a minimum, which by relation (10) requires that σ should be a maximum. The maximum conductivity obtainable with seeding techniques is generally given as $\sigma\sim10^2$ mhos/m.[2,6] Thus, from (10) the minimum value of B_0 is

$$\sim\left(\frac{10\times5\times10^5}{0.7\times10^3\times10^2\times40}\right)^{\frac{1}{2}}=1.3 \text{ webers/m}^2.$$

Rosa[3] reports that Hall current effects are observed under rather similar conditions to those envisaged above with a field strength of 1.4 webers/m². However, Rosa also showed experimentally that segmented electrodes could be used to counteract the Hall effect, a concept put forward by R. M. Patrick.[7] The use of segmented electrodes is discussed later.

A field strength of $B_0=1.3$ webers/m² will generate a voltage $V \sin\omega t$ across the external impedance where

$$V=2x_0uB_0\doteq\tfrac{4}{3}\times10^3\times1.3=1700 \text{ volts.}$$

In short, this ac generator would operate on a moving fluid whose conductivity was kept close to 10^2 mhos/m. The duct dimensions would be: length $l=40$ m, width $2x_0=\frac{4}{3}$ m, height $d=1$ m (say). The output voltage 1700 v (50 cps) would act across an external impedance of $Z=10/(\sigma ld)$ [relation (8)], i.e., $Z=(1/400)\Omega$ which is equivalent to a power output of $(400\times1.7^2\times10^6)/2=10^9/2$ watts.

USE OF A SERIES-WOUND FIELD COIL

The alternating applied magnetic field can be conveniently supplied by a field coil wound in series with the external impedance. The effect of the considerable circuit inductance introduced in this way can be offset by also including in the circuit a series capacitance such that the resonant frequency of the circuit is 50 cps, i.e., if L=inductance of field coil and C=series capacitance, then $100\pi=1/(LC)^{\frac{1}{2}}$. We can write $V=2x_0uB=ki$, where k is a constant which is a function of the field coil configuration.

If k is initially greater than Z it can be shown that oscillations of charge, current, and field will increase in amplitude until the magnetic retarding force $iB2x_0$ is sufficient to reduce u and hence k, so that $z-k=0$. Under these conditions, the current through the circuit will oscillate sinusoidally at 50 cps. The criterion that $k>z$ initially, allied with the fact that for low power loss $z\gg R_p$, leads to the relation that $V/i\gg R_p$ which was determined before. Considering the use of such a field coil with the generator described above, the inductive energy periodically stored in coil

$$\int_v\frac{B^2}{2\mu_0}dv=\frac{(1.3)^2}{2\times10^{-6}}\times40\times\tfrac{4}{3}\sim4\times10^7 \text{ joules.}$$

At 50 cps, this corresponds to a reactive power circulation $\sim4\times10^9$ w or roughly 8 times the power output This power ratio is a significant parameter; if it i $\lesssim1$, the small periodic fluctuations in the fluid velocity will distort the output voltage of the generator. If the ratio is $\gg1$, then stress and insulation problems wil arise.

The peak current in the generator$=V/Z=400\times170$ $=7\times10^5$ amp. The inductive energy$=\frac{1}{2}Li^2=4\times10$ joules; therefore

$$L=\frac{2\times4\times10^7}{5\times10^{11}}\sim2\times10^{-4}h, \qquad (11$$

which corresponds to a coil having two turns aroun the electrode assembly. The circuit capacitance would b

$$C=\frac{1}{2\times10^{-4}\times10^4\times\pi^2}=\frac{1}{20}f. \qquad (12$$

The peak inductance-condenser voltage can be foun from the equation $\frac{1}{2}CV_0^2=4\times10^7$, i.e.,

$$V_0=(8\times10^7\times20)^{\frac{1}{2}}=4\times10^4 \text{ v.} \qquad (13$$

ASSUMPTIONS MADE IN DERIVING THE ABOVE EQUATIONS

1. Nonconducting Electrodes

In deriving the expression for eddy current powe loss, it was assumed that the electrodes were non conducting, that is, that eddy currents could not pas along the electrodes. (See Fig. 4.) In practice, th electrodes would be made of a substantial thickness o metal, and so appreciable longitudinal electrod currents would flow and lead to a prohibitive increas in eddy current losses. For instance, in the circu $ABCD$, the full induced emf E_{ABCD} would be operativ over AD and BC only; hence the joule heating in thes regions would increase by a larger factor.

This situation can be remedied by replacing eac electrode with a series of segmented electrodes, wit each opposing segment pair connected through the own isolated series capacitor and load. (See Fig. 5.)

If $y_1\sim y_2\ll2x_0$, the longitudinal electrode curren will be reduced to negligible proportions, and the flui resistance R_p will not be appreciably increased. The ver strong inductive coupling between the individu circuits should ensure that their respective curren are in phase.

2. Negligible Heat Losses in the Coil Material

The coil windings must have a resistance R_c which less than the resistance of the fluid; otherwise conside able energy will be wasted. Also, eddy current losses the coil material must be kept low.

Consider a typical segment electrode generator, which segment length y_2=segment separation$=y_1=$ cm; then $N=40$ m/10 cm$=400$ segments. The flu

---

[7] R. M. Patrick, Ph.D. thesis, Cornell University, June, 1956.

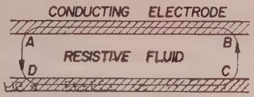

FIG. 4. Effect of conducting electrodes.

resistance applicable to a circuit involving one segment pair is $R_p=$ (solid electrode R_p)$\times$number of segments in the new electrode assembly,

$$\sim\frac{1}{4000}\times 400\sim\tfrac{1}{10}\Omega.$$

If the windings are made of copper and are two turns per coil, then the length of a winding l is $\sim$200 m. At room temperatures, σ(copper)$\sim10^8/2$ mhos/m. If R_c is to be $\sim(1/100)\Omega$, then $R_c\sim10^{-2}\sim(2\times10^{-8}\cdot2\times10^2)/x'$; therefore $x'=4\times10^{-4}$ m, where x' is the required thickness of conductor of width 1 m. The field coil then consists of many long strips of conductor, all of which are subject to a time-varying magnetic field. The strength of this magnetic field will be B/μ_0 at the inner coil windings (adjacent to the fluid) and will decrease to a much lower value at the outer windings. We can obtain a somewhat exaggerated estimate of the eddy current power loss in the coil by considering all the windings to be immersed in a uniform magnetic field B/μ_0. From Eq. (2), the eddy current loss in a sample of conductor $[(l\times2x_0\times d)$, conductivity $\sigma]$ is $\alpha lx_0^3\sigma d$. We know that the eddy current loss with $l=40$ m, $x_0=\frac{2}{3}$ m, $\sigma=10^2$ mhos/m, $d=1$ m, is 10% of the total power output. So with $x_0=x'/2=2\times10^{-4}$ m, $\sigma=10^8/2$ (mhos/m), $l=200$ m, $d=1$ m, the eddy current loss in the 400 coil windings will be

$$400\times\left(\frac{2\times10^{-4}}{0.66}\right)^3\times\frac{200}{40}\times\frac{10^8}{2}\times\frac{10}{10^2}\%$$

of power output, $=0.27\%$, which is negligible.

3. Constant Flow Velocity

Earlier in this paper it was stated that to obtain steady flow it is necessary that the fluid suffer several complete impulses in passing through the electrode assembly. With the above 'tuned circuit' assembly, we can assume that current and field will be in phase and will oscillate sinusoidally,

$$\text{i.e.,}\quad i=i_0\sin\omega t;\quad B=B_0\sin\omega t.$$

If the plasma velocity is everywhere the same and is $u(t)$, and ρ is the density of the fluid, we can write

$$d(P_i-P_0)=i_0B_0\sin^2\omega t+dl\rho(du/dt). \qquad (14)$$

Time-averaging this equation $\langle du/dt\rangle_{\text{av}}=0$, and so $i_0B_0/(2d)=P_i-P_0$ and Eq. (14) becomes

$$(P_i-P_0)\cos2\omega t=l\rho(du/dt),$$

and

$$u=u_0+(P_i-P_0)\sin2\omega t/(2\omega l\rho).$$

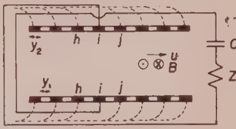

FIG. 5. Segmented electrode assembly.

Thus, the fractional variation in velocity=

$$\Delta u/u=(P_i-P_0)/(2\omega l\rho u). \qquad (15)$$

If $P_i=5\times10^5$ newtons/m^2, $P_0=10^5$ newtons/m^2, $\omega=300$ rad/sec, $l=40$ m, $\rho=0.5$ kg/m^3, $u=10^3$ m/sec, then

$$\frac{\Delta u}{u}=\frac{4\times10^5}{2\times3\times10^2\times4\times10\times0.5\times10^3}=\frac{1}{30}.$$

Thus, the behavior of this simple model predicts a total velocity variation of less than 6% if $l/(4\pi)\geqslant u/\omega$, i.e., the fluid suffers at least four complete retarding impulses in passing through the electrode region.

In general, in mhd work, $u\sim c$, the velocity of sound in the fluid, which is $\sim[(P_i-P_0)/\rho]^{\frac{1}{2}}$ [since $c\sim(P/\rho)^{\frac{1}{2}}$]. Thus, from (15)

$$\frac{\Delta u}{u}\sim\frac{1}{2\omega}(u^2)\frac{1}{lu}=\frac{u}{2l\omega},$$

for $\Delta u/u$ small $l\gg u/(2\omega)$.

TWO DEVELOPMENTS OF THIS ac mhd GENERATOR

1. The Use of a Secondary Coil Winding to Remove Electrical Power from the System

If, as seems likely, it becomes necessary to use segmented electrodes in an operational mhd generator, (ac or dc), then one is faced with the inconvenience of having to feed electrical power into many external impedances which must be kept insulated from each other. This problem might be solved by removing electrical power from the generator via a secondary coil winding. Such a step would bring a much needed flexibility to the internal impedance of the generator, i.e., for a given generator power the output voltage could be altered by varying the number of windings in the secondary coil. In this way, the generator could be matched to transmission lines, transformers, etc.

The primary circuit would contain an ac voltage source (V volts), a capacitor (C farads), and a coil consisting of n_1 turns around the electrode assembly. The emf of the voltage source$=V=uB2x_0=u\phi/l$, where ϕ is the flux through each of the turns comprising the primary coil. The secondary coil (coincident with the primary) consists of n_2 turns about the electrode assembly connected across an external impedance Z.

For the primary circuit we can write

$$n_1\frac{d\phi}{dt}=\frac{u}{l}\phi-\frac{1}{C}\int_0^t i_1dt, \qquad (16)$$

and for the secondary

$$-n_2(d\phi/dt)=i_2Z$$

$$\frac{d}{dt}(16)\cdots n_1\frac{d^2\phi}{dt^2}=\frac{u}{l}\frac{d\phi}{dt}-\frac{i_1}{C}. \tag{17}$$

Now $\phi=(n_1i_1+n_2i_2)L$, where L is the inductance of a single turn around the electrode assembly. Substituting for i_1 and i_2 in the above expression we obtain

$$-\frac{\phi}{L}=n_1^2C\frac{d^2\phi}{dt^2}-n_1C\left(\frac{u}{l}\right)\frac{d\phi}{dt}+\frac{n_2^2}{Z}\frac{d\phi}{dt},$$

and therefore

$$n_1^2C\left(\frac{d^2\phi}{dt^2}\right)+\frac{d\phi}{dt}\left[\frac{n_2^2}{Z}-Cn_1\left(\frac{u}{l}\right)\right]+\frac{\phi}{L}=0.$$

As before, current, field, and voltage oscillations build up until u is reduced, in this case to satisfy

$$Cn_1(u/l)=n_2^2/Z,$$

and the frequency of the oscillations $(2\pi\omega)$ satisfies $\omega=1/(n_1^2LC)^{\frac{1}{2}}=1/(L_1C)^{\frac{1}{2}}$, where L_1 is the inductance of the primary coil when the secondary circuit is open. Thus, under steady-state conditions the current, field, and voltage oscillations in the circuit are at the resonant frequency of the unloaded primary circuit.

2. Capacitive Power Transfer from the Fluid

To exploit the full electronic conductivity of the working fluid, one must ensure sufficient electron emission from the electrode surface. Recent work by Rosa[3] has shown that this may not be such a difficult problem as previously imagined. Results obtained with an mhd generator working under rather unusual conditions[4,5] showed that at large current densities, substantial electron emission certainly occurred. However, this state of affairs was always accompanied by a very rapid loss of plasma heat energy to the electrodes. It was deduced that these very large currents only flowed in the absence of the usual thermally (and electrically) insulating boundary layer.

An interesting development of the ac continuous electrode mhd generator is one which would eliminate conduction at the electrode surface. The electrodes would be covered with a thin layer of dielectric, and the circuit capacitance C would comprise the two series capacitances at each electrode-fluid 'interface'. This system would also avert the necessity of using segmented electrodes to prevent longitudinal electrode currents.

If we take the generator dimensions used in all previous calculations, then the capacity at each electrode-fluid interface $2C\sim10^{-11}ldK/S$, where S $=$thickness of dielectric (dielectric constant$=K$). A reasonable thickness of dielectric $S\sim1$ cm, K for glass ~10, and thus

$$C\sim\frac{40\times10\times10^{-11}}{2\times10^{-2}}f=2\times10^{-7}f.$$

To be efficient, the generator must satisfy relation (4). The power output (force×velocity)$\sim(P_i-P_0)2x_0du$ and is also $\sim iV=\omega CV_02x_0uB$. Now $P_i-P_0\sim P_i$ fo substantial enthalpy removal, and therefore

$$P_i2x_0du\sim V\omega C2x_0uB,$$

and

$$V_0\sim P_id/(\omega CB). \quad (18$$

From relation (4) we have $200x_0\leqslant6u^2/(x_0\omega^2)$; therefor

$$\omega\leqslant u/(6x_0). \quad (19$$

From Eqs. (18) and (19),

$$V_0\geqslant6P_idx_0/(BCu). \quad (20$$

The duct length-to-width ratio $D=l/(2x_0)$. Substi tuting for C we obtain from (20) that the peak dielectri stress

$$T=\frac{V_0}{2S}>\frac{1.5\times10^{10}P_i}{DBu}.$$

Thus, with $P_i\sim5\times10^5$ newtons/m², $P=35$, $B=$ weber/m², and $u=10^3$ m/sec,

$$T>\frac{7.5\times10^5\times10^{10}}{35\times1\times10^3}=2\times10^5\text{ kv/mm.}$$

In practice, the upper limit of dielectric strength materials, even at room temperatures, is only $\sim2\times1$ kv/mm. Hence, capacitive removal of power from th above mhd generator is highly improbable with th magnetic field strengths, fluid velocities, and linea dimensions at present envisaged. It should also be note that stipulation of a minimum dielectric thickness say 1 mm will involve the generation of transien voltages $\sim10^8$ v, resulting in extensive insulatio problems.

CONCLUSIONS

From these considerations, it seems that such a ac mhd generator could be reasonably efficient. Mor over, a secondary coil winding might be used to ove come the problems inherent in the use of segmente electrodes.

Capacitive power removal does not appear to be feasible proposition with the fluid velocities ar pressures envisaged at present

It is to be expected that any experimental generator constructed on the lines proposed in th paper would in fact require more sophisticated fie oil windings. Firstly, no account has been taken of ny variation in channel cross section. To maintain onstant flow velocity in the fluid, any pressure decrease r the fluid must be accompanied by an increase in the hannel cross section. Secondly, to avoid secondary ddy current effects, the field coils should be designed o provide a more uniform distribution of magnetic ux in the electrode assembly.

ACKNOWLEDGMENTS

The author is one of a group of research workers in the Physics Department at the University of British Columbia who received a grant from the National Research Council of Canada in aid of plasma physics research. The author would also like to acknowledge the advice and encouragement given by Dr. D. W. Allan now at Yerkes Observatory.

OURNAL OF APPLIED PHYSICS VOLUME 32, NUMBER 10 OCTOBER, 1961

On the Wear of Sapphire

R. P. Steijn*
E. I. du Pont de Nemours & Company, Wilmington, Delaware

(Received May 8, 1961)

The wear resistance of single crystals of sapphire was determined as a function of crystallographic orientation with respect to plane of wear and rubbing direction. Distinct anisotropy was found. Evidence of plastic flow at the wear surface on both basal and prismatic slip systems was obtained. In bulk deformation tests, these systems do not become operative until a temperature of 1000°C is reached for basal slip, 1800°C for prismatic slip. The resistance against wear correlates in a qualitative way with the relative ease of operation of the two slip systems involved. When the orientation is such that both basal and prismatic slip are blocked, a brittle type of wear occurs that is characterized by conchoidal fracture. All results confirm that plastic flow during rubbing is a governing factor in, if not an integral part of, the wear process for even such a hard material as sapphire.

I. INTRODUCTION

IN the extensive literature on wear, little prominence is given to the possible effect of crystal orientation n the rate of wear. It has long been known, however, hat such an effect exists in the case of certain marials. Gwathmey *et al.*[1,2] studied the friction and urface damage of large single crystals of copper dermed by sliding and scratching along certain crystalographic planes. The highly directional wear of diaond has been described by Schultink, Spier, and ander Wagt,[3] and more recently by Wentorf.[4] Certain echanical properties customarily related to wear restance have also been found to depend strongly on ystal orientation. Attinger[5] and Stern[6] noted large ifferences in the microhardness of sapphire, depending n the plane of indentation, while Albrecht[7] observed orresponding differences in grindability.

Purely from the standpoint of wear research, these henomena, if properly studied, hold great promise of evealing details on the mechanism of wear and the rmation of loose wear particles. While most wear studies have been concerned with the macroaspects of wear and the formulation of empirical laws to predict the effects of such external variables as load, sliding distance, rubbing velocity, temperature, etc., the fact is often forgotten that, basically, wear is a microfracture process. Some of the details of this process, which are difficult to observe in fine polycrystalline materials, could be gleaned from wear experiments on large, suitably oriented single crystals.

This paper gives the initial results of quantitative wear determinations on a number of prominent crystal planes of sapphire. In addition, some microstructural aspects are described that are considered of prime importance to an understanding of the wear mechanism, notably the evidence of plastic flow on the conventional slip systems during a relatively mild rubbing action.

II. EXPERIMENTAL WORK

A. Materials

The experimental work was conducted on single crystals of synthetic corundum (α-Al_2O_3 or "white sapphire") procured from the Linde Company. This material was selected for a number of reasons. In the first place, sapphire is one of the hardest natural minerals (9 on the Mohs' scale) and possesses outstanding wear resistance. This is primarily why sapphire, both natural and synthetic, is being used for jewel bearings in fine instruments and watches. In the second place, sapphire is a high-temperature material of ex-

---

* Research associate, Mechanical Research Laboratory.

[1] A. T. Gwathmey, H. Leidheiser, and G. P. Smith, Proc. oy. Soc. (London) **A212**, 464 (1952).

[2] J. M. Gailey and A. T. Gwathmey, Symposium Am. Chem. c. Symposia No. 4A, **3**, A25 (1958).

[3] L. Schultink, H. L. Spier, and A. J. Vander Wagt, Philips ech. Rev. **16**, No. 3, 91 (1956).

[4] R. H. Wentorf, J. Appl. Phys. **30**, 1765 (1959).

[5] C. Attinger, Ind. Diamond Rev. **12**, 136 (1952).

[6] W. Stern, Ind. Diamond Rev. **12**, 137 (1952).

[7] F. Albrecht, Z. Krist. **106**, 183 (1954).

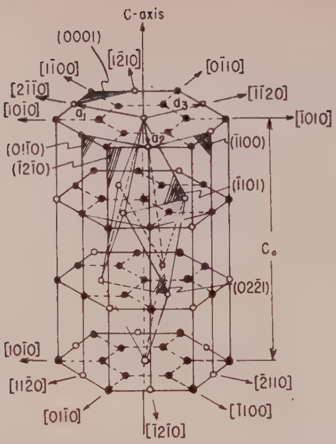

FIG. 1. Sapphire. Aluminum-ion distribution and empty aluminum-ion sites (after Kronberg, reference 10).

ceptional chemical stability. This too is well known. The dissociation pressure of Al_2O_3 at 1000°K is listed at 1.5×10^{-24} psi. Preliminary rubbing tests showed that sapphire, in wear, remains a single crystal, which cannot be said for many otherwise attractive metals and alloys. Finally, the crystal structure of sapphire is well established, and a considerable body of information on its physical, mechanical, and optical properties exists in the technical and scientific literature.

B. Crystal Structure

Sapphire, or α-Al_2O_3, crystallizes in the corundum structure. In its simplest form, this may be considered as a hexagonal close-packed lattice of oxygen atoms with the aluminum ions located at the octahedral interstices of the oxygen framework. To satisfy the valency requirements, one out of every three octahedral sites is empty. Thus, each aluminum ion is surrounded by 6 oxygen ions, while each oxygen ion is surrounded by 4 aluminum ions. The morphological unit cell of sapphire, with only the aluminum ions showing and with the prominent planes and directions, is depicted in Fig. 1. For details on the corundum structure, the reader is referred to more extensive treatises on the subject.[8]

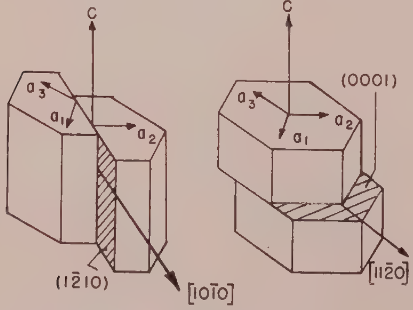

FIG. 2. Sapphire slip systems (from Scheuplein-Gibbs, reference 12). Prismatic slip is shown at left; basal slip at right.

The mechanisms by which plastic deformation in sapphire is known to occur are slip and twinning. There are two systems of slip: basal and prismatic. The basal slip system appears to be the more common of the two and has been observed by Wachtman and Maxwell[9] in static tensile loading. It takes place at the (0001) planes in the $[11\bar{2}0]$ direction at temperatures as low as 900°C. Kronberg[10] confirmed this slip system for dynamic tensile testing in the temperature range of 1300° to 2000°C. The observation of a second slip system on the $(\bar{1}2\bar{1}0)$ planes in the $[\bar{1}010]$ direction is credited to Klassen-Neklyudova[11] who deformed sapphire above 2000°C. Apparently, the prismatic slip system operates at considerably higher temperatures than the basal slip system. Scheuplein and Gibbs,[12] in a recent study on dislocations in sapphire, obtained evidence of prismatic slip in bend tests in the flame of an oxygen-gas torch, presumably 1800° to 2000°C. A schematic illustration of the basal and prismatic slip system is given in Fig. 2.

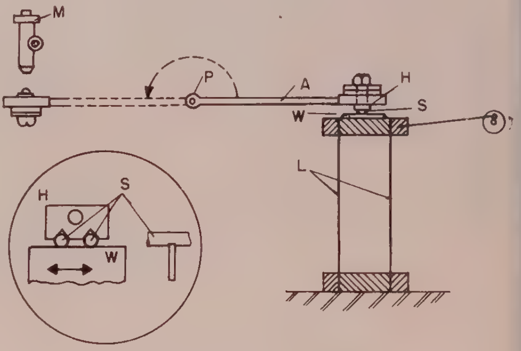

FIG. 3. Wear-test apparatus (schematic).

C. Wear Apparatus

The wear apparatus used in the investigation is simple reciprocating device shown schematically in Fig. 3. The specimen holder H with the sapphire specimen S is securely held in a weighted lever arm A. The lever arm pivots around point P and is adjusted to horizontal position at the beginning of each test. The sapphire rests on the wear plate W which, mounted between the two vertical spring leaves L, is the reciprocating part of the tester. It moves horizontally with a short stroke of 6.25 mm and is driven by an off-center pulley on the shaft of a $\frac{3}{16}$-hp variable-speed electric motor. All tests were run at 1000 rpm. The vertical load of 1500 g was measured at the point of contact between specimen S and wear plate W and was adjustable by putting weights on either side of pivot point P. After preliminary experimentation, satisfactory wear plates were found in the form of sintered tungsten carbide blanks ground to a 20-μin. rms finish. All tests were conducted in air and at room temperature.

---

[8] A. F. Wells, *Structural Inorganic Chemistry* (Clarendon Press, Oxford, England, 1950), 2nd ed., p. 364.

[9] J. B. Wachtman and L. H. Maxwell, J. Am. Ceram. Soc. 37, No. 7, 291 (1954).

[10] M. K. Kronberg, Acta Met. 5, No. 9, 507 (1957).

[11] M. V. Klassen-Neklyudova, J. Tech. Phys. (U.S.S.R.) 1 519 (1942).

[12] R. Scheuplein and P. Gibbs, J. Am. Ceram. Soc. 43, 4 (1960).

The general procedure was to determine wear as a function of time. This was done by flipping the lever arm 180° around the pivot and measuring the flat wear scar on the specimen under a microscope M with a Filar measuring eyepiece. Using $\frac{3}{16}$-in.-diam sapphire balls as specimens, we could easily calculate the volume of the worn-off cap. As expected, the relation between sliding distance and corresponding wear was found to be perfectly linear.[13] The slope of the wear-vs-distance line is the wear rate in cm^3/linear cm of sliding distance for the particular load used. A typical example of basal wear in sapphire is given in Fig. 4.

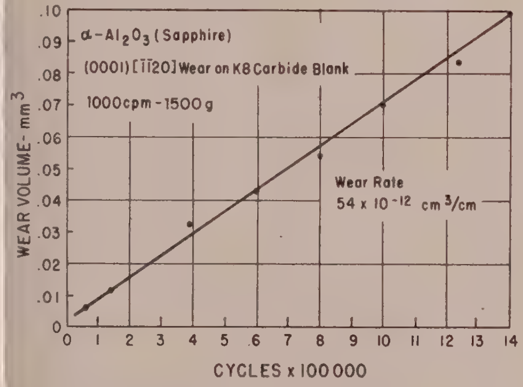

FIG. 4. Typical wear-vs-distance curve.

D. Sliding Direction

Early in the investigation, it was found that rubbing on the prismatic planes in a direction parallel to the C axis invariably resulted in such severe chipping and conchoidal fracturing of the wear surface that valid wear determinations were nearly impossible. Figure 5 shows a prismatic wear surface that had been rubbed first along the [$2\bar{1}\bar{1}0$] direction and then along the [0001] direction. During rubbing along the [$2\bar{1}\bar{1}0$], a smooth wear surface was obtained; however, during rubbing along the [0001], this smooth wear surface then chipped and fractured on many points. For this reason, sliding on all prismatic and pyramidal planes was done in a direction perpendicular to the *C* axis. By so doing, smooth, well-defined, and accurately measurable wear scars were obtained. As a rule, no chipping or conchoidal fracturing was encountered during testing on the basal planes (see Fig. 6).

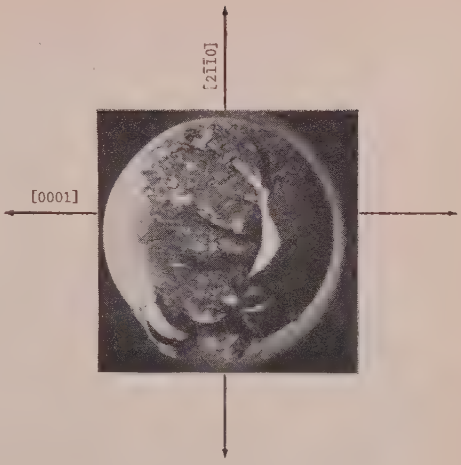

FIG. 5. ($01\bar{1}0$) wear scar. 30×.

In addition to the testing of $\frac{3}{16}$-in.-diam balls, a few experiments were carried out on $\frac{1}{8}$-in.-diam sapphire rods. Sliding was carried out on the cylindrical surface in a direction perpendicular to the rod axis by the narrow edge of a tungsten carbide blank. By mounting two rods side by side (see inset of Fig. 3), the wear resistance of one rod relative to the other could be obtained directly. A comparison between basal and prismatic wear could also be made by using rods grown with the *C* axis parallel and perpendicular to the rod axis, and by ensuring proper orientation.

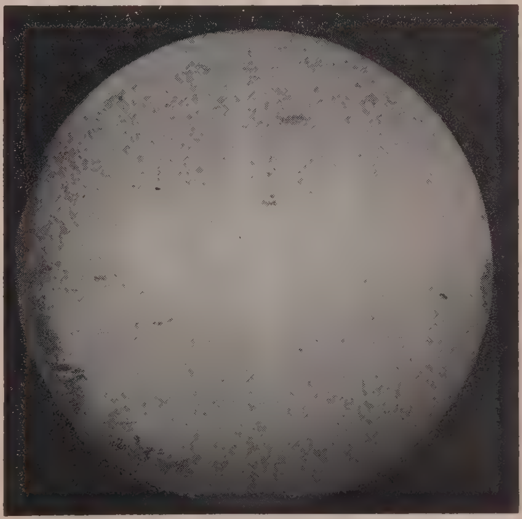

FIG. 6. Basal wear scar. 60×.

---

[13] J. F. Archard and W. Hirst, Proc. Roy. Soc. (London) **A236**, 397 (1956).

TABLE I. Wear rates in cm³/cm×10⁻¹².[a]

Wear plane	Wear direction	$\frac{3}{16}$-in.-diam spheres; α-Al_2O_3						$\frac{1}{8}$-in. diam rods; α-Al_2O_3 C axis		Ti_2O_3	α-Fe_2O_3	Cr_2O
		α	β	ϵ	ζ	η	γ	⊥ rod	∥ rod	ψ	χ	δ
(0001)	$[10\bar{1}0]$	71	140	...	...	216	...	...	...	135.0	930	...
	$[\bar{1}\bar{1}20]$	54	90	154	66	240	...	...	...	...	...	2100
	random	...	...	68	...	...	107	36	...	...	...	...
$(\bar{1}100)$	$[11\bar{2}0]^b$	3.5	1.8	1.7	...	...	...	...	1.3	2.7	...	2100
	$[0001]$	44.0	25.0	...	...	...	...	...	...	...	...	...
$(\bar{1}2\bar{1}0)$	$[10\bar{1}0]^b$	5.1	...	...	...	...	...	...	...	...	800	...
$(\bar{3}4\bar{1}0)$	$[5\bar{2}\bar{7}0]^b$ (20° off)	5.4	...	...	...	...	...	...	...	...	...	...
$(\bar{1}101)$	$[11\bar{2}0]^b$	2.2	...	...	...	...	...	...	...	...	...	...
$(\bar{2}201)$	$[11\bar{2}0]^b$	3.5	...	...	...	...	...	...	...	...	...	...
$(1\bar{1}02)$	$[11\bar{2}0]^b$	10.4	...	...	13.6	...	...	...	...	...	...	...

[a] Except for Cr_2O_3, all wear tests were run against Kennametal K-8 ground blanks. The Cr_2O_3 tests were run against sintered boron carbide.
[b] All directions so marked are perpendicular to the C axis.

E. Orientation Determination

The orientation of the sapphire specimen was determined by standard x-ray-reflection Laue techniques[14] and the angular distance chart for sapphire prepared by Winchell.[15] With the aid of an Astro-Compass, the crystal was then rotated into the desired orientation and mounted with an epoxy cement in the specimen holder H, which can be rotated in the lever arm L so that any axis in the wear plane can be made the rubbing direction. Details of the orientation and mounting procedure with the Astro-Compass will be published elsewhere.[16]

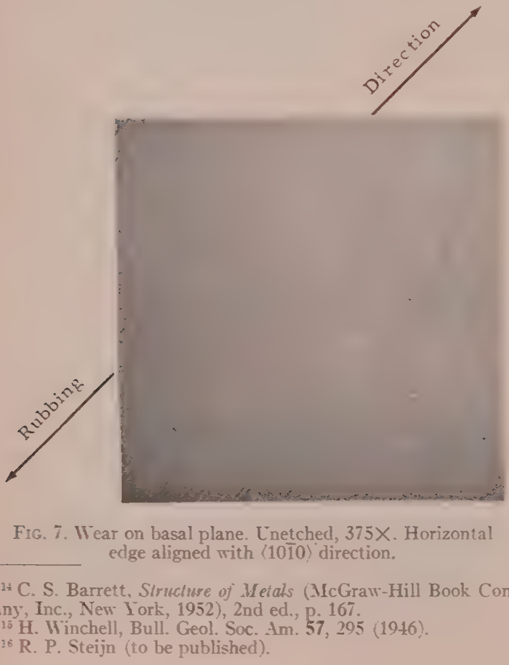

FIG. 7. Wear on basal plane. Unetched, 375×. Horizontal edge aligned with ⟨10$\bar{1}$0⟩ direction.

III. DISCUSSION OF RESULTS

Table I lists the results of all wear tests on $\frac{3}{16}$-in. diam spheres and $\frac{1}{8}$-in.-diam rods of sapphire.

From these results, it can be seen that the wear o sapphire is strongly orientation dependent. The thre important findings are as follows.

(1) On the prismatic planes, two distinctly differen modes of wear, a "smooth" and a "chipping" type, ar encountered. The direction of rubbing determines whic mode will be operative.

(2) When rubbed along the direction that favor "smooth" wear (perpendicular to the *C* axis), the wea resistance of the prismatic and pyramidal planes c sapphire is 50 to 80 times better than that found fo the basal planes.

(3) The wear of the basal plane is, for all practica purposes, independent of the rubbing direction. Smoot well-defined wear scars are formed.

From a broader standpoint, it would be interestin to see if the large differences in wear resistance reporte here for sapphire (α-Al_2O_3) could also be claimed fo other members of the corundum structure such a Cr_2O_3, α-Fe_2O_3, and Ti_2O_3. We therefore procured few crystals of Ti_2O_3, Cr_2O_3, and natural α-Fe_2O which could be broken up into small fragments an oriented in the same manner as the sapphire ball After mounting in the specimen holder, the rough an irregularly shaped crystals were then lapped to a 6 semiapex cone to provide a geometry suitable fo making wear determinations. For the titanium sesqu oxide, we found that the wear resistance of the bas plane was 30 times lower than that of the prismat plane, which follows in the same pattern as the α-Al_2 crystals. However, the wear resistances on the bas and prismatic planes of α-Fe_2O_3 and Cr_2O were foun to be approximately equal (see Table I).

Thus, having established that a pronounced anis tropy in wear behavior exists for sapphire (α-Al_2O_3), we were then faced with the question of what factor makes the wear process orientation dependent.

---

[14] C. S. Barrett, *Structure of Metals* (McGraw-Hill Book Company, Inc., New York, 1952), 2nd ed., p. 167.
[15] H. Winchell, Bull. Geol. Soc. Am. 57, 295 (1946).
[16] R. P. Steijn (to be published).

In trying to answer this from the standpoint of considering wear as basically a fracture process, we strongly suspected that the mechanism of plastic flow is a governing factor in the orientation dependence of wear. In the first place, the two distinctly different types of wear on the prismatic planes, depending on whether the rubbing direction is parallel or perpendicular to the *C* axis, appear to suggest a "brittle" and a "ductile" fracture process on the wear plane. In the second place, present-day research on the fracture mechanism of crystalline solids strongly implies that plastic deformation plays an all-important role in fracture. Some theories even go so far as to claim that plastic flow is a prerequisite to so-called brittle fracture. Finally, plastic flow in sapphire is of a crystallographic nature and occurs (outside twinning) by slip on both the basal and prismatic planes, although very high temperatures apparently are necessary.

Perhaps it seems a bit preposterous to expect high-temperature slip systems to work in simple, room-temperature rubbing tests under a normal load of less than $3\frac{1}{2}$ lb. Yet, that plastic flow in sapphire occurs during ordinary microhardness testing is a matter of fact,[17] and those familiar with the field of friction and wear are not surprised at what can happen on a sliding surface. Bowden and Tabor,[18] who have done so much to clarify the problem of friction and lubrication, showed quite clearly that on a microscale very high stresses and temperatures can be reached when solids rub together. Also, the stress system under which asperities meet in sliding is considered hydrostatic in nature by some workers, thus permitting otherwise inconceivable yield phenomena to occur.[19]

On this basis, it is perhaps less surprising but nevertheless significant that we have found microscopic evidence of slip on both the established slip systems of sapphire. The first indication that plastic deformation might take place on the wear surface comes from the peculiar etch-pit pattern that is revealed when the wear scar is etched in boiling phosphoric acid after the method of Scheuplein and Gibbs.[12] It should be pointed out that these wear scars are metallographically smooth, and no surface preparation, such as polishing with assorted diamond pastes, is required for microscope examination.

Figure 7 is a typical view of a basal wear scar seen under oblique illumination. The abrasion marks, which run parallel to the rubbing motion, delineate shallow steps on the surface. It was shown under a two-beam interferometer that these steps are about 3 to 5 μin. in height.

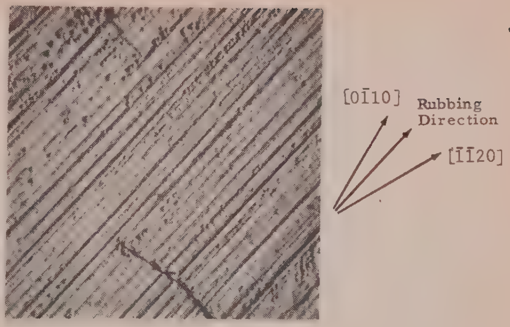

FIG. 8. Wear on basal plane. Etched, 180×. Horizontal edge aligned with ⟨10$\bar{1}$0⟩ direction.

Careful etching of these basal wear scars in phosphoric acid at 300°C reveals an etch-pit pattern in which the pits are clearly arranged along the direction of sliding (see Figs. 8 and 9). After etching away up to 25 to 50 μ, the markings of sliding direction are gradually lost, the pit distribution becomes random, and the pit density decreases by two orders of magnitude. When, for brief periods of time, a (1$\bar{1}$02) surface is rubbed consecutively along three different directions and then etched, etch-pit arrays are brought out which clearly follow these same sliding directions (see Fig. 10). It appears, therefore, that the pits on these planes are uniquely associated with the sliding process.

While the foregoing constitutes no positive proof that plastic deformation takes place on the surface, we have felt sufficiently encouraged to conduct a further investigation. Without going into the nature of these pits (we prefer to call them "solution-etch pits"), it is obvious to us that they indicate some sort of surface damage, that this damage is finite in depth, and that the damage corresponds directionally to the mechanical rubbing process to which the surface is exposed. The

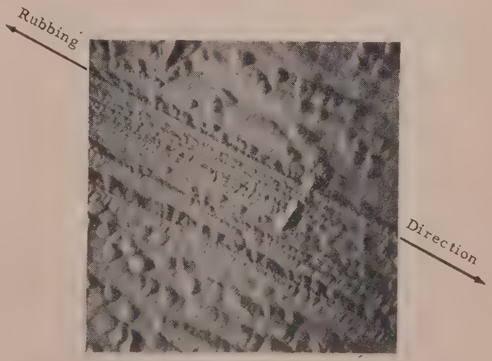

FIG. 9. Wear on basal plane. Etched 318×.

---

[17] H. Palmour, III and W. W. Kriegel, N. Carolina State Coll. Dept. Eng. Study Rept., under contract (1961).

[18] F. P. Bowden and D. Tabor, *The Friction and Lubrication of Solids* (Oxford at the Clarendon Press, Oxford, England, 1950).

[19] R. F. King and D. Tabor, Proc. Roy. Soc. (London) **A223**, 225 (1954).

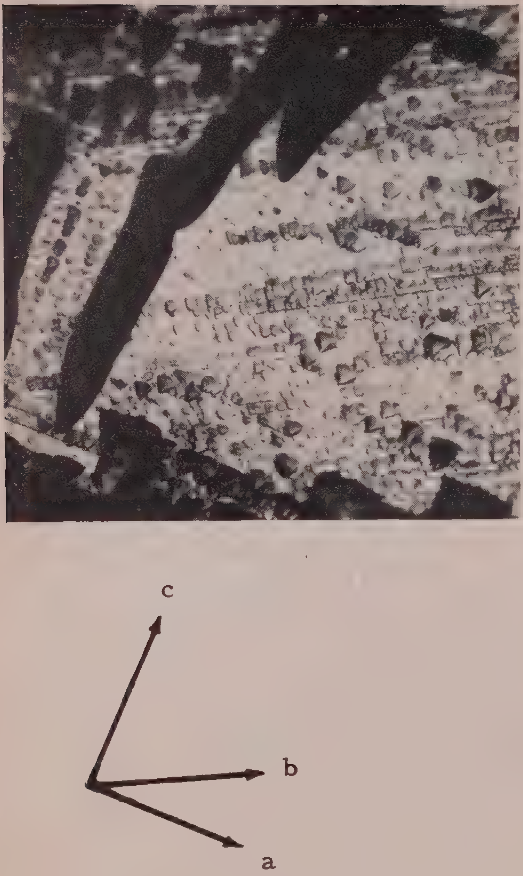

FIG. 10. Rubbing on $(1\bar{1}02)$ plane along directions *a*, *b*, *c*. Etched, 300×.

same question which Faust,[20] working with abraded germanium has raised before, namely, whether these pits are caused by irregularities produced by the abrasion process or by mechanically induced dislocations, must remain unanswered until further work is done.

Yet, the fact that some plastic flow takes place on both slip systems has become apparent from further microscopic examinations of etched and unetched wear surfaces. Since for both slip systems the slip direction lies in the basal plane (see Fig. 2), it follows that the relative displacements of the slipped segments will not show up as steps on an unetched basal plane. However, it was thought that very careful etching might bring them out, especially if care were taken not to obliterate them by abrasion marks. This was done by putting the rubbing direction at an oblique angle from the crystallographic slip direction. Thus, wear testing was carried out on the basal plane in the $\langle 11\bar{2}0\rangle$ direction, which is 30° from the $\langle 10\bar{1}0\rangle$ glide direction of the prismatic slip system. Etching was done by immersing the sapphire in orthophosphoric acid and raising the temperature with a Bunsen burner until it reached 270°C, after which the flame was turned off instantly. Upon careful examination on a metallograph, fine slip markings in the form of short arrays of triangular etch pits are observed which run 30° from the sliding direction and are believed to be the traces of $\langle 11\bar{2}0\rangle$ prismatic slip planes (see Fig. 11). The depth of this deformation is almost entirely restricted to the surface, as the slightest amount of overetching removes these slip bands permanently. Very likely, the affected layer is not deeper than 5 to 10 μ.

To find evidence of slip on the basal system, a single crystal of sapphire was oriented on the wear-testing apparatus so that a $(3\bar{4}10)$ prismatic plane became the wear plane. This plane was selected because, ideally flow on the basal plane would cause slip steps on it unless the simultaneous rubbing action eliminated these as they were formed. To distinguish such slip lines from abrasion markings, the sliding direction was purposely put 20° from the expected slip traces. After the test the $(3\bar{4}10)$ wear surface was examined in the unetched condition and, indeed, fine slip markings were found in particular near the periphery of the wear scar. Ligh

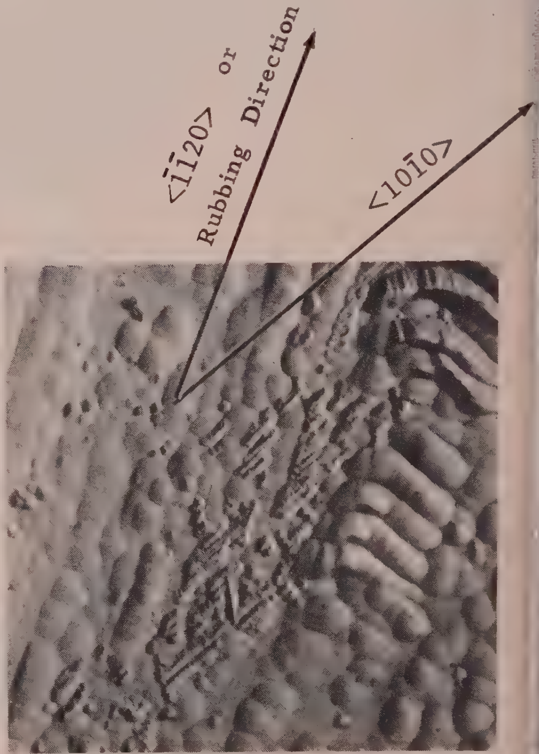

FIG. 11. Wear on basal plane showing short slip bands in $\langle 10\bar{1}0\rangle$ direction. Etched, 740×.

---

[20] J. W. Faust, Jr., *The Surface Chemistry of Metals and Semiconductors*, edited by H. C. Gatos (John Wiley & Sons, Inc., New York, 1960), p. 163.

etching accentuated these markings, and under oblique illumination a host of traces, believed to be basal slip lines, became visible 20° from the imposed rubbing direction (see Fig. 12).

A similar procedure was followed for a $(20\bar{2}1)$ wear plane rubbed in a direction 20° from the traces of the basal planes. This plane was selected because, according to Scheuplein and Gibbs,[12] the $(20\bar{2}1)$ plane is the favored etching plane for basal dislocations. After etching the wear scar in phosphoric acid at 260°C, a dense distribution of triangular etch pits was brought out (see Fig. 13). However, the interesting point is that, in contrast to our experience with rubbing basal planes, these pits do not line up along the sliding direction, but instead form short arrays along the traces of the basal planes at 20° from the rubbing direction. This is also taken as further evidence that we are dealing here with original slip-band traces of the basal slip system.

While these observations strongly suggest that basal and prismatic slip occur on a microscale during rubbing, positive proof of this is not easy to furnish. A conclusive answer requires that the slip plane be defined by traces measured on more than one plane of intersection. In the case of sapphire, which has to be cut with diamond wheels, the preparation of such a plane would either destroy the evidence we are looking for or introduce its own slip.

The above observations shed some light on the final results of the wear experiments. In the first place, the type of wear characterized by conchoidal fracture pits and chipping and encountered on the prismatic planes when the rubbing direction is parallel to the C axis can now be explained. The obvious reason is that the resolved shear stress along the slip direction is zero and, therefore, none of the slip systems can become operative, so that brittle fracture will ensue. How "absolutely" brittle this fracture is, is not known at this time. The qualitative result, however, is quite interesting. It gives further emphasis to the notion that the "easy" wear of the basal plane might be a wholly ductile fracture process of the friction junctions akin to the familiar cup and cone shear fracture in ductile metals tested in tension. Another substantiating point might be that the wear debris is amorphous. Neither x-ray nor electron diffraction has been able to show crystallinity in a sample of loose wear particles collected from a basal plane.

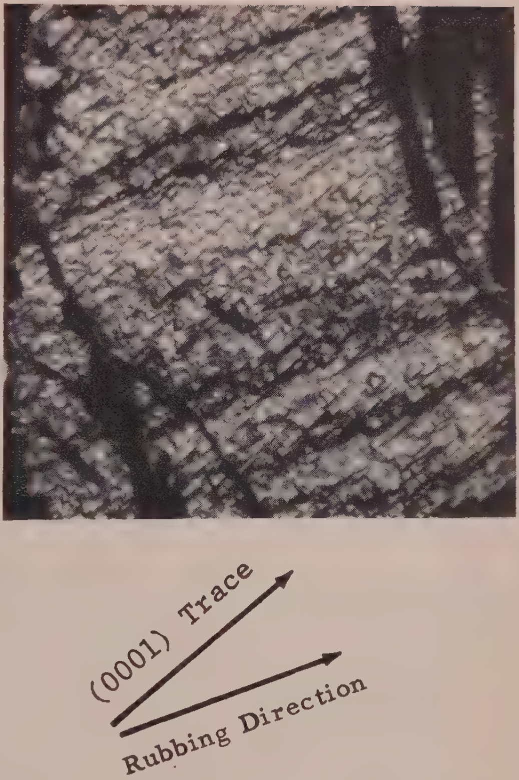

FIG. 13. $(20\bar{2}1)$ wear face. Etched, 1000×.

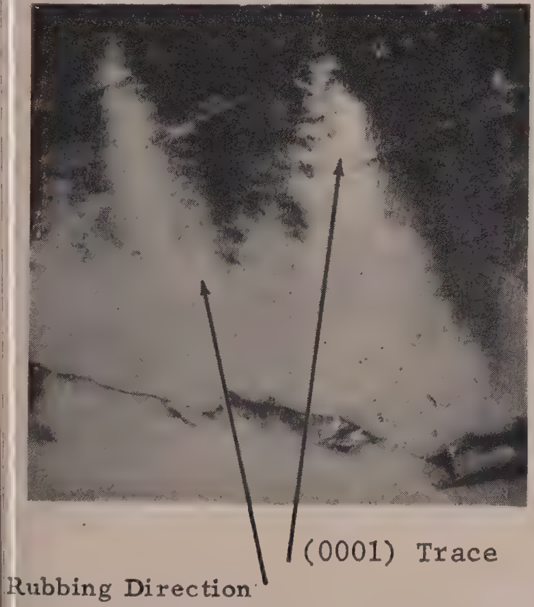

IG. 12. Slip lines on $(3\bar{4}10)$ plane. 500×. Blackish area is stain that clouds the face progressively during etching.

On the question of why the basal plane has the lowest wear resistance—in fact, 50 to 80 times lower than that of the prismatic and rhombohedral planes—no completely satisfactory answer can be advanced at this time. It is felt, however, that slip on the basal plane is the "easy" slip in sapphire and that wear on the basal plane is a matter of predominantly basal slip. To say this with certainty would require a detailed understanding of the complex stress system that exists at the asperities in contact. Green's work[21] on the deformation and fracture of friction junctions using Plasticene models gives reason to believe that such junctions shear off uniformly in the center. Thus, it is conceivable that, in the case of sapphire, the friction junctions would fail by shear fractures along the (0001) planes, since these are the favorably oriented planes of easy glide. Some accompanying shear along prismatic planes may be expected.

IV. SUMMARY AND CONCLUSIONS

The following points were established experimentally.

(1) For sapphire, or α-Al_2O_3, resistance against wear depends strongly upon orientation. The basal plane is by far the weakest crystal face to support sliding or rubbing action.

(2) When the rubbing direction is perpendicular to the *C* axis, very high wear resistance is exhibited on the prismatic and rhombohedral crystal faces.

(3) When the rubbing direction is parallel to the *C* axis, however, a "brittle" type of wear occurs that is characterized by chipping and conchoidal fracture pits on the surface.

(4) The loose wear particles produced by rubbing on the basal planes were found to be amorphous by x-ray and electron diffraction.

(5) Sapphire undergoes plastic deformation in room-temperature rubbing tests. Both basal and prismatic slip systems become operative. In conventional deformation tests, these slip systems do not operate until very high temperatures (1000°C for basal slip, 1800°C for prismatic slip) are reached.

Based on the above, the following tentative picture of the wear of sapphire is suggested.

(1) During the rubbing of sapphire, surface conditions are created that induce plastic flow on a microscale through the participation of both the basal and prismatic slip systems.

(2) This plastic deformation is in some way related to microfracture of the friction junctions (the "welded contact points between sliding surfaces) and is th same problem as flow and fracture in bulk solids, whic still remains unsolved.

(3) The experimental findings strongly suggest tha plastic deformation introduces shear failures in th friction junctions. It is even believed that, for rubbin on the basal plane, breaking of the friction junctions i entirely ductile and that plastic deformation is actuall part of the wear process itself.

(4) Since basal slip is considered to be the easy glid system compared with prismatic slip, it will be muc more difficult to shear off the friction junctions assoc ated with wear along the prismatic planes than alon the basal planes. This could be the reason why the wea resistance on the prismatic planes is so much highe than on the basal planes.

(5) When the rubbing direction is parallel to th *C* axis or, in other words, perpendicular to the sli direction of both systems, plastic flow by slip is difficul if not impossible, to achieve, and a brittle type o fracture will occur.

Although far from complete, the above picture tri to explain the wear process in terms of flow and fra ture of crystalline solids; the experimental finding seemed to dictate this approach. Plastic deformation a significant, if not a controlling, factor in wear behavio

It is believed that wear and sliding experiment despite the complex and undefined nature of the im posed stress system, might open a new and fruitful wa to study the fundamental aspects of flow and fractu in brittle solids.

ACKNOWLEDGMENTS

The author is indebted to N. E. Glueck, who d signed the wear tester used in this investigation, an to H. A. Selz, who gave skillful assistance with th experimental work.

---

[21] A. P. Green, Proc. Roy. Soc. (London) **A228**, 191 (1955).

JOURNAL OF APPLIED PHYSICS VOLUME 32, NUMBER 10 OCTOBER, 1961

Partial Rotation in Permalloy Films

S. METHFESSEL, S. MIDDELHOEK, AND H. THOMAS
International Business Machines Corporation, Research Laboratory, Zurich, Switzerland

(Received June 22, 1960)

Magnetization reversal at an angle to the easy direction has been studied on Permalloy films with different values of coercive force H_c and anisotropy field H_K. The hysteresis properties show that "inverted" films ($H_c>H_K$) do not represent a special case, but that every film exhibits inversion in a certain sector of field direction. In the inversion sector, two critical field values are observed. The corresponding Bitter patterns make it evident that the lower critical field is due to a partial rotation process which is accompanied by a splitting of the film into many fine domains, whilst the higher one is due to wall motion. The observed processes can be understood qualitatively if the dispersion of the local values of the anisotropy field and anisotropy direction, as well as the internal exchange and stray field coupling are taken into account.

INTRODUCTION

MAGNETIZATION reversal in thin films of soft magnetic material with uniaxial anisotropy can take place by rotation or by wall motion processes.

A characteristic field value for rotation processes is the anisotropy field $H_K=2K/M$. (K=anisotropy constant, M=saturation magnetization.) If the film retains its single domain structure at all stages of magnetization reversal (coherent rotation), an irreversible rotation jump is expected at a critical field $\mathbf{H}_r$. The magnitude of the critical field is a function of the angle between this field and the easy direction. According to the Stoner-Wohlfarth theory,[1] the locus of the point of the $\mathbf{H}_r$ vector in the H_x,H_y plane ("critical curve") is an asteroid with its vertices at $H_x=\pm H_K$; $H_y=0$ and $H_x=0$; $H_y=\pm H_K$ (x and y are in the plane of the film parallel to the easy and hard direction, respectively (see Fig. 4).

The irreversible process actually observed in a quasistatic experiment is, however, of a different kind, because the film loses its single domain structure. Usually, magnetization reversal takes place by wall motion at a critical field $\mathbf{H}_w$, before the critical field for coherent rotation is reached, and a critical curve for wall motion can be obtained experimentally.[2] The easy direction coercive force H_c actually observed can, therefore, (in this normal case $H_c<H_K$) be taken as a characteristic field value for this wall motion process.

It is, however, possible to prepare permalloy films which still possess a uniaxial anisotropy, but reverse their magnetization in the easy direction by wall motion at a field $H_c>H_K$ when subjected to a field parallel to the easy direction. Such films have been termed "inverted,"[3] and the question has arisen, why does magnetization reversal not take place by coherent rotation at H_K?

In order to study this question, we have investigated the magnetization changes and the domain configurations occurring during the quasistatic magnetization reversal in 80–20 permalloy films with different H_c/H_K ratios. The uniaxial anisotropy was induced by evaporation in a magnetic field[4] or at an oblique angle.[5] The dependence of the characteristic field values H_K and H_c on the evaporation conditions allowed a wide range of values for H_c/H_K to be obtained.

CRITICAL CURVES

We observed the 50-cps hysteresis loops of the films with the ac driving field at an angle to the easy direction, or with the driving field in the easy direction employing a dc bias field in the hard direction. Since we are mainly interested in "critical" fields, where sudden irreversible magnetization changes occur, the dM/dt versus H curves were also observed.

The H_K values were obtained from the slope of the hard direction loop for small field amplitudes. This hard direction loop showed a reversible, linear relation $M_y/M=H_y/H_K$ even in the inverted films for all field amplitudes $H_y\lesssim 0.8H_K$. This behavior indicates that for all investigated films, including the inverted ones, the deviations from a single uniaxial anisotropy are small, and that the method of the H_K measurement is applicable.

Figure 1(a) shows the hysteresis loop and Fig. 1(b) the dM/dt versus H curve of an inverted film with the driving field at an angle of 30° to the easy direction. The magnetization process clearly occurs in two distinct steps. The peak at the higher field in the dM/dt curve displays a Barkhausen spectrum typical for wall motion processes and defines by its center of gravity the critical field for wall motion H_w. The other peak at the lower field corresponds to a smooth change of the magnetization. In order to study the magnetization processes occurring at this peak, a dc bias field was superimposed parallel to the ac driving field. The loops obtained by this method (Fig. 2) show that irreversibilities begin to occur at a field value, which corresponds closely to the steepest slope of the loop. Therefore, we introduce this field value as the critical field H_p for this irreversible process, which will be identified as a partial rotation process.

---

[1] E. C. Stoner and E. P. Wohlfarth, Phil. Trans. Roy. Soc. (London) **A240**, 599 (1948).

[2] E. M. Bradley and M. Prutton, J. Electronics and Control **6**, 81 (1959).

[3] D. O. Smith, E. E. Huber, Jr., M. S. Cohen, and G. P. Weiss, J. Appl. Phys. **31**, 295S (1960).

[4] M. S. Blois, Jr., J. Appl. Phys. **26**, 975 (1955).

[5] D. O. Smith, J. Appl. Phys. **30**, 264S (1959).

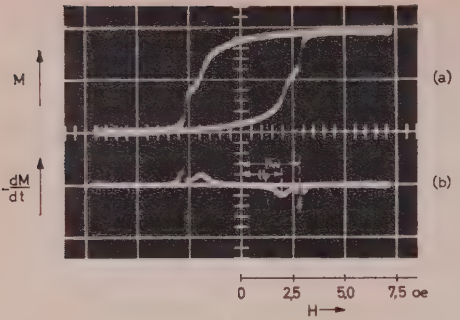

FIG. 1. Hysteresis loop (a) and dM/dt versus H curve (b) of an inverted film ($H_C=3.25$ oe, $H_K=2.4$ oe) with the field at an angle of 30° to the easy direction. H_p and H_w are the critical field values for partial rotation and wall motion, respectively.

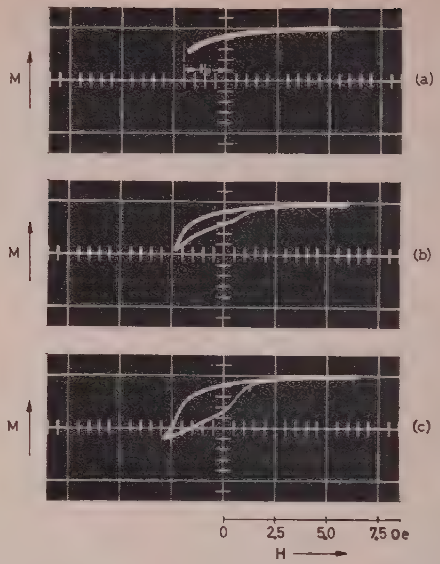

FIG. 2. Minor loops of the film of Fig. 1 with an asymmetric field at an angle of 30° to the easy direction.

The critical curves representing the angle dependence of H_w and H_p in the H_x,H_y plane can be obtained from a series of dM/dt curves measured at various angles to the easy direction, or by using an ac field of constant amplitude in the easy direction $H_x^{(ac)}$ and various dc bias fields in the hard direction $H_y^{(dc)}$.

As long as only reversible magnetization changes occur, the magnetization state of the film at a certain moment will depend exclusively on the total field, but will be independent of the manner in which it is applied. Since, up to the lower critical field H_p, only reversible rotation takes place, the critical curve for H_p will be the same for both methods of measurement. The higher critical field H_w may, in principle, depend on the point where the lower critical curve is crossed, and strictly speaking, the term "critical curve" will lose its meaning in this case. Experimentally, however, the difference is hardly observable, so that this difficulty does not seem to be significant.

Figure 3 shows the dM_x/dt versus H_x curves of thre films with different H_c/H_K ratios for bias fields $H_y^{(dc)}$ $=0$ to $2H_K$. The curves calculated for an ideal film which reverses its magnetization according to the Stoner-Wohlfarth theory, are given in Fig. 3(a). Com parison with the curves for the actual films in Fig. 3(c and (d) indicates that the smooth peak at H_p evolve from the reversible rotation peak at $H_x^{(ac)}=0$ fo $H_y^{(dc)}>H_K$. The Barkhausen peak at H_w develops fron the wall motion peak at $H_x^{(ac)}=H_c$ for $H_y^{(dc)}=0$. Thi behavior suggests that the reversal process occurring a

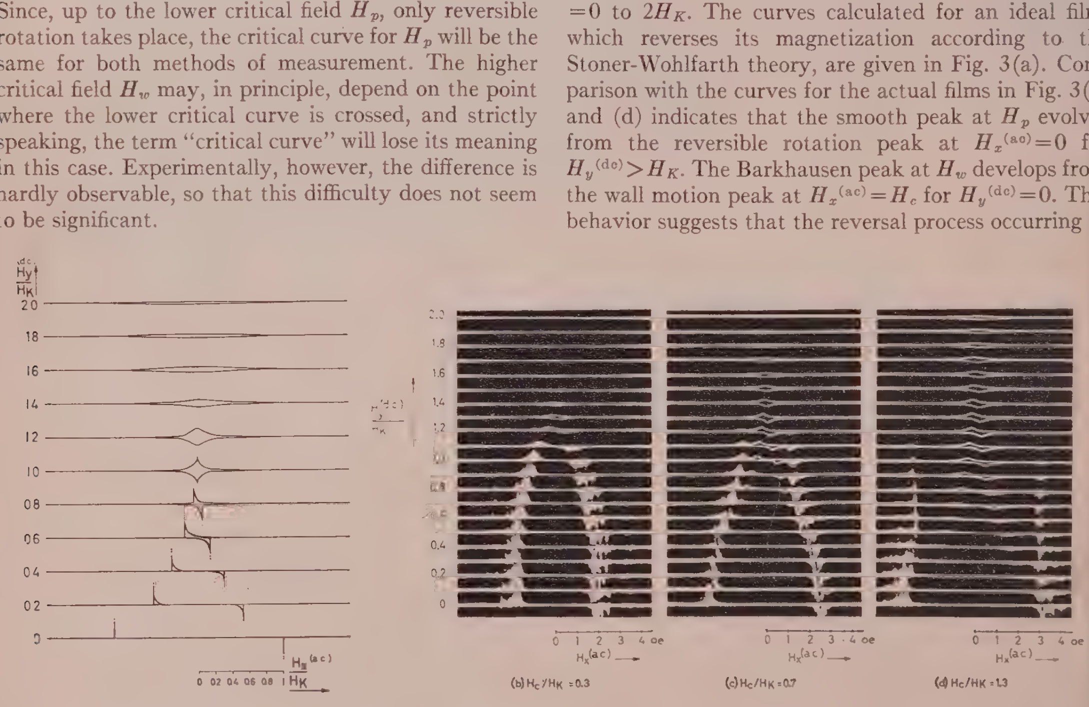

(a) (b) (c) (d)

FIG. 3 (a) Theoretical dMx/dt versus H_x curves of the Stoner-Wohlfarth model with the ac field $H_x^{(ac)}$ in the easy direction and d bias fields $H_y^{(dc)}=0$ to H_K in the hard direction. (b)–(d) Experimental dM/dt versus H_x curves with the ac field $H_x^{(ac)}$ in the eas direction and dc bias fields $H_y^{(dc)}=0$ to H_K in the hard direction: (b) $H_c=1.9$ oe, $H_K=10.0$ oe, film thickness $D=1100$ A, (c) $H_c=2.6$ o $H_K=3.8$ oe, film thickness $D=510$ A, (d) $H_c=3.25$ oe, $H_K=2.4$ oe, film thickness $D=380$ A. The ac field amplitude was 5 oe.

H_p is a rotation process, which, however, does not lead to complete reversal, but leaves the film in some intermediate state. We call it a "partial rotation process." The reversal is completed by a wall motion process taking place at H_w.

The critical curves corresponding to H_p and H_w derived from these experiments, as well as the H_r curve of the Stoner-Wohlfarth model, are plotted for these three films in Fig. 4. The diagrams show, first of all, that in "normal" films with $H_c/H_K<1$, the H_w curves and the H_r curves cross, so that, consequently, every film can be called "inverted" in a sector above a certain angle to the easy direction, where $H_w>H_r$, and this angle decreases with increasing the H_c/H_K ratio of the film. No irreversible rotation occurs at the field H_r in the inversion sector. The H_p curve is roughly parallel to the H_r curve, but displaced a certain amount to higher field values.

From these observations, the following questions arise: What stabilizing effect prevents the magnetization from rotating at the field H_r? What is the nature of the intermediate state after partial rotation at H_p, and what keeps the film in this state until wall motion occurs at H_w?

DOMAIN OBSERVATIONS

In order to study these questions, we observed the domain configurations of the films at various steps of the magnetization reversal, using the Bitter technique.

Figure 5 shows the domain configurations observed in an inverted film. First the film was saturated in the easy direction, and then a slowly increasing dc field was applied at an angle of 135° to this direction. In agreement with the hysteresis loop observations, nothing happens in the Bitter picture when the field becomes equal to the critical field H_r of the Stoner-Wohlfarth model. As soon as the field reaches the H_p value, long-shaped domains appear all over the film [Fig. 5(a)]. The direction of their long axes depends on the angle of the applied field and is always perpendicular to the equilibrium direction of the magnetization immediately before the domains appear. Therefore, the form of the domains is certainly not caused by the existence of needle-shaped regions of different magnetic behavior with fixed positions in the film, but must be due to magnetostatic reasons. These domains do not grow continuously from small nuclei, but suddenly appear in their final form, which changes very little by further increasing the field. This indicates that they are created by a rotation process.

When the field is further increased, at the critical field strength H_w, domain walls start at the film edges and remove the fine structure by a motion parallel to the easy direction [Fig. 5(b)]. At the end of this process, the film is again in a single domain state, and the magnetization rotates reversibly into the reverse easy direction when the field is decreased to zero.

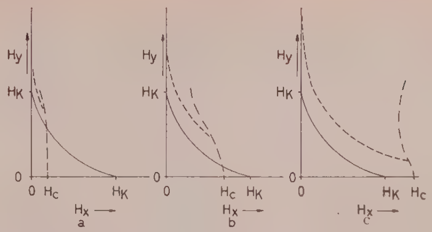

Fig. 4. Critical curves for coherent rotation (theoretical): ———, wall motion (experimental): —·— and partial rotation (experimental): – – – for the three film samples of Fig. 2.

When, on the other hand, the field is reduced to zero after exceeding the H_p value but before reaching the H_w value, the film does not regain its single domain state. Figure 6(a) shows the film before, Fig. 6(b) after decreasing the field to zero. The large domains are subdivided into smaller ones with their long axes parallel to the easy direction, obviously in order to reduce the large stray field resulting from the discontinuity of the normal component of the magnetization at the domain boundaries.

DISCUSSION

For the interpretation of the reversal processes observed, the following situation must be considered:

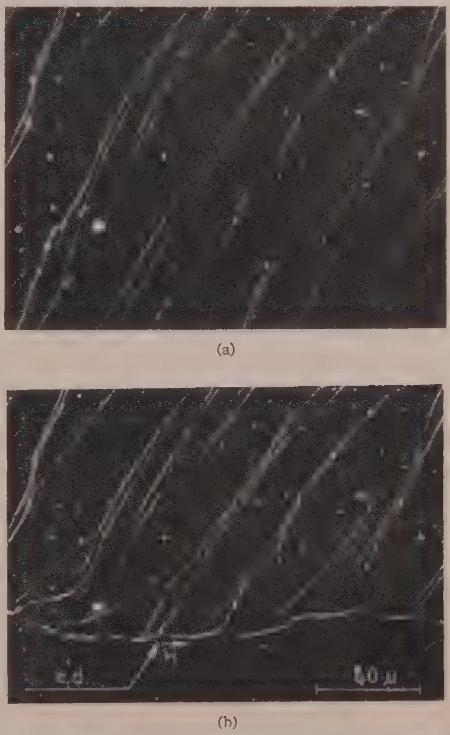

Fig. 5. Bitter patterns of an inverted film at two stages of the reversal process: (a) $H_p<H<H_w$, (b) $H=H_w$.

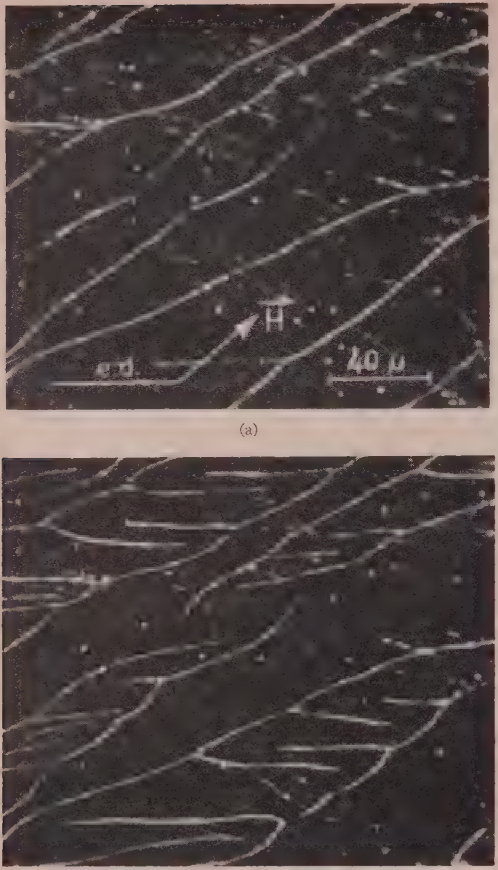

(a)

(b)

FIG. 6. Bitter patterns of an inverted film. (a)$H_p < H < H_w$; (b) field reduced to zero.

(a) The critical curve for coherent rotation of the Stoner-Wolhfarth model is calculated under the assumption that the magnetic behavior of the film is determined exclusively by the existence of a homogeneous uniaxial anisotropy. Such an "ideal" film ought to be free from all disturbances causing deviations of the magnetization from homogeneity, such as additional anisotropies, holes, scratches, thickness variations, etc. In this case, the coercive force for wall motion (ignoring nucleation problems) would be zero.

Real films always have a certain amount of disturbances produced by internal microstress,[6] deviations in alloy composition,[7] crystal anisotropy,[8] etc., the effect of which can be described by assuming a distribution of the local values of anisotropy field and anisotropy direction. Since the coercive force H_c in the easy direction is a characteristic field value for wall motion, it is correlated with the local variations of the anisotropy. The average uniaxial anisotropy is given by the anisotropy field H_K. Therefore, the ratio H_c/H_K is a measure of the relative deviation of the film from the coherent rotation model.

As a first step towards a description of the hysteresis behavior of real films, the single critical curve of an ideal film could be replaced by the multitude of critical curves corresponding to the local values of the anisotropy. This would be equivalent to the individual particle model of the Stoner-Wohlfarth theory.[1] For an average distribution of the additional anisotropies, the remanence, for instance, would approach the value 0.637 for $H_c/H_K \rightarrow \infty$, i.e., for isotropic films with the magnetization restricted to the film plane.

(b) This model, however, assumes independent behavior of the individual anisotropy regions in the film, and neglects the internal exchange and stray field coupling. The "stiffness" of the magnetization caused by the exchange coupling results in a finite "resolving power" for anisotropy variations, which is of the order of the domain wall thickness. Thus, to a considerable extent, the magnetization will average over all Fourier components of the anisotropy variations with wavelengths smaller than this resolving power, especially over the contributions of the crystal anisotropy in the crystallites, in contrast to large-grained bulk material.

The response of the magnetization to the remaining anisotropy variations with longer wavelengths, on the other hand, is partly restricted by the stray field coupling, which is particularly effective in soft magnetic material with $K \ll 2\pi M^2$. Since a wave-like variation of the magnetization direction with the wave-normal perpendicular to the average magnetization ("lateral magnetization ripple") gives rise to a higher stray field energy than a variation with the wave-normal parallel to the average magnetization ("longitudinal magnetization ripple") with the same amplitude, the magnetization will respond preferably to those anisotropy variations producing a longitudinal ripple. Such a longitudinal ripple [cf. Fig. 7(a)] has been observed by Fuller and Hale[9] in Permalloy films using an electron-optical method.

Thus, the internal exchange and stray field coupling causes a magnetization more homogeneous than that resulting from the individual particle model. Even in isotropic films, the remanence, for instance, may be almost equal to the saturation magnetization.

With this situation in mind, we can now proceed to interpret the reversal processes in qualitative terms which are suggested by the effects of the exchange and stray field coupling.

When a slowly increasing field is applied at an obtuse angle to the magnetization in the easy direction the magnetization ripple rearranges itself around the successive equilibrium positions of the average mag netization [Fig. 7(b)]. If the field direction is in the sector of normal behavior ($H_w<H_r$), the magnetization reverses simply by a wall motion process at $H=H_w$.

---

[6] R. S. Smith, IBM J. Research Develop. **4**, 205 (1960).

[7] W. W. L. Chu, J. E. Wolfe, and B. C. Wagner, J. Appl. Phys. **30**, 272S (1959).

[8] S. Middelhoek, Z. angew. Physik **13**, 151 (1961).

[9] H. W. Fuller and M. E. Hale, J. Appl. Phys. **31**, 238 (1960)

If, however, the field direction is in the inversion sector ($H_w>H_r$), the film will react approximately as if it were composed of alternating bands perpendicular to the average magnetization, with critical fields $H_r^{(1)}$ and $H_r^{(2)}$ ($H_r^{(1)}<H_r^{(2)}$) equal to the average values in the corresponding bands. Without stray field coupling between the bands, the magnetization in the odd-numbered bands would rotate at $H=H_r^{(1)}$ irreversibly into the reverse equilibrium direction. But, actually, as soon as this rotation starts, large stray fields arise, preventing the continuation of the rotation process in the odd-numbered bands, and the field must be increased to a higher value $H=H_p$, until the rotation process becomes irreversible. Thus, instead of the sudden rotation jump of an ideal film at H_r, we have a continuous rotation in the odd-numbered bands, indicated by the smooth signal at $H=H_p$ in Fig. 1(b). The stray fields will also have some influence on the magnetization in the even-numbered bands, which may result in a backward rotation in these bands.

During the rotation process in the odd-numbered bands, the boundaries between the bands have become real domain walls. Since the field is too small to move these walls, the magnetization cannot rearrange itself to a more favorable configuration, so that an intermediate state with the odd-numbered bands reversed, the even-numbered bands not reversed, is frozen in. The domain walls between the bands indicate the rippling pattern of the film immediately before the rotation process started in the odd-numbered bands [Fig. 7(c)].

This intermediate state is accompanied by large stray fields perpendicular to the bands, which have a stabilizing effect on the magnetization in the even-numbered bands. In order to reverse the magnetization in these bands by a rotation process, the external field would have to be increased to considerably higher values. Therefore, the magnetization reversal is completed by domain wall motion at $H=H_w$ [Fig. 7(d)].

The magnitude of the stray field in a band of a width of $20\,\mu$ can be estimated for a Permalloy film of 400-A thickness to be of the order of 10 oe.

The existence of large stray fields in the intermediate state becomes evident when the external field is reduced to zero before the magnetization reversal is completed by wall motion. In this case, the stray field causes the magnetization in the already reversed odd-numbered bands to rotate back to its original direction, leaving only narrow reversed regions with a largely reduced stray field [Fig. 7(e)].

The reversal processes described occur in a sector of field directions, which is determined by two conditions:

(a) The angle of the field to the easy direction must be larger than a certain limiting angle, which is indicated by the amplitude of the magnetization ripple in zero external field. If, on the other hand, the field angle

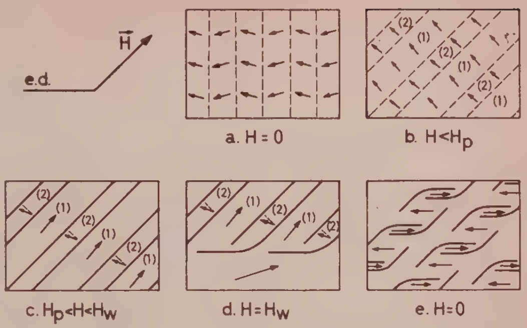

a. $H=0$ b. $H<H_p$ c. $H_p<H<H_w$ d. $H=H_w$ e. $H=0$

FIG. 7. Proposed magnetization state at the various steps of magnetization reversal (schematic).

to the easy direction is less than this limiting angle, the magnetization initially rotates clockwise in some regions, and counter-clockwise in others, which apparently leads to a "locked" state, so that the whole reversal takes place by wall motion. This process has been observed by Fuller and Rubinstein[10] and Smith *et al.*[3]

(b) The angle of the field to the hard direction must be larger than a second limiting angle, which is determined by the amplitude of the magnetization ripple at $H_x=0$; $H_y=H_K$. If the field angle to the hard direction is smaller than this limiting angle, the magnetization rotates only in some regions to the reverse direction, but in other regions back to the original direction, when the field decreases to zero after saturation. Therefore, the film does not resume its single domain state after each half-period, but splits into many fine domains. The hysteresis processes in this case have been studied by Middelhoek.[11]

CONCLUSIONS

The reversal processes observed can be understood qualitatively if the internal exchange and stray field coupling are taken into account. Since the partial rotation process is a consequence of the magnetization ripple produced by the anisotropy variations, and since these anisotropy variations are responsible for the wall motion coercive force, coherent rotation reversal in inverted films seems to be impossible in a quasistatic experiment.

From the discussion of the reversal processes, it seems appropriate to generalize the definition of inversion from the criterion of $H_c/H_K\gtrless 1$ to the criterion of $H_w/H_r\gtrless 1$, i.e., to that of whether or not the external field is able to break up the internal coupling before domain wall motion starts. Since the torque of the applied field on the magnetization increases, and the pressure on a domain wall decreases with increasing angle between the field and the easy direction, a sector of inversion should always exist in real films.

---

[10] H. W. Fuller and H. Rubinstein, J. Appl. Phys. **30**, 84S (1959).

[11] S. Middelhoek, Helv. Phys. Acta **33**, 519 (1960).

JOURNAL OF APPLIED PHYSICS VOLUME 32, NUMBER 10 OCTOBER, 1961

Specific Heat of Superparamagnetic Particles

J. D. Livingston and C. P. Bean
General Electric Research Laboratory, Schenectady, New York

(Received May 8, 1961)

The specific heat of an assembly of independent superparamagnetic particles has been calculated with the methods of statistical mechanics. The cases of isotropic particles in an applied field and anisotropic particles in the absence of a field have been considered. The specific heat calculated is temperature dependent and is of the order of k per particle at low temperatures. A smaller contribution varying linearly with temperature can also appear, thereby affecting the linear temperature coefficient of specific heat usually associated with the electronic specific heat. Conditions are discussed under which these effects should be experimentally observable.

RECENTLY, low-temperature specific heat measurements on TiFe have been interpreted by Schröder and Cheng[1] as having a large contribution due to the randomization of the direction of magnetization in superparamagnetic particles that they suggest exist in this alloy. However, we find their theoretical considerations of the specific heat of superparamagnetic particles unclear and seemingly at variance with our own.[2] We present, therefore, a brief analysis of the specific heat of such particles, both isotropic and anisotropic.

The general method we use is that common in statistical mechanics. For a system with energy levels ϵ_n, the energy U is given by $U=[\sum\epsilon_n \exp(-\epsilon_n/kT)]/\sum \exp(-\epsilon_n/kT)$ and the specific heat at constant volume C_v is by definition $C_v\equiv\partial U/\partial T$. Here k is Boltzmann's constant and T is the absolute temperature. The denominator in the energy expression is known as the partition function Z.

The first case we treat is that of an isotropic particle in a magnetic field. The energy levels are the eigenstates of a particle of total angular momentum $S\hbar$ subjected to the Hamiltonian $\mathcal{H}=-g\beta\mathbf{S}\cdot\mathbf{H}$, where g is the spectroscopic splitting factor, β the Bohr magneton, and H the magnetic field. There are $2S+1$ such energy levels, spaced $g\beta H$ apart. For the case $S=1$ for example we obtain three levels with energies $-g\beta H$, O, $g\beta H$. The specific heat calculated using the equations above is shown in Fig. 1 for $S=1$ and $S=\frac{5}{2}$. It is plotted as a function of $kT/\mu H$, where μ is $g\beta S$. For a large superparamagnetic particle, we assume $S=\infty$ and employ a classical treatment. The sums in the energy expression above are replaced by integrals, the partition function in this case being $Z=2\pi\int_0^\pi \exp(-\mu H \cos\theta/kT) \sin\theta d\theta$. In this expression, μ is the magnetic moment of the particle and θ is the polar angle between the field direction and the magnetization direction. The result of this calculation also appears in Fig. 1.

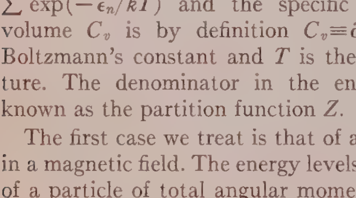

FIG. 1. Specific heat per particle of isotropic paramagnetic particles of magnetic moment μ in a magnetic field H.

The low-temperature limit with this classical treatment is seen to be $C_v=k$. At low temperatures, the magnetization is nearly parallel to the field, and in its small excursions from the field direction it resembles a classical two-dimensional harmonic oscillator[3] with an average energy of $kT/2$ per degree of freedom. Hence it has a specific heat per particle of k near absolute zero. In any real case, the quantum number S will not be infinite, and, in agreement with Nernst's theorem, the specific heat will fall to zero at absolute zero. By the preceding quantum mechanical method the low-temperature limit of the specific heat of a particle of any S is $C_v=k(g\beta H/kT)^2 \exp(-g\beta H/kT)$. This exponential specific heat resulting from the finite separation of the lower levels will only be important at temperatures less than $g\beta H/k$. For a field of 10^4 oe, this temperature is approximately 1.3°K.

We turn now to the case that is physically mor interesting, that of the anisotropic superparamagneti particle in the absence of an applied field. The Hamiltonian that we employ to represent a uniaxial anisotrop for finite spin S is $\mathcal{H}=-a(S_z^2-\mathbf{S}^2/3)$. Here, S_z is a operator with eigenvalues $-S, -S+1, \ldots, S$, and $\mathbf{S}$ is an operator with the eigenvalue $S(S+1)$ for all $2S+$ states. The constant a is a measure of the anisotrop energy. For the case $S=1$, we obtain two levels wit energy $-a/3$ and one level with energy $2a/3$. Th calculated specific heats for $S=1$ and $S=\frac{5}{2}$ are show for positive a in Fig. 2 and for negative a in Fig. 3. The are plotted as a function of kT/KV, where KV is th energy difference between the lowest and the highe levels, this difference being aS^2 for S integral an $a(S^2-\frac{1}{4})$ for S half-integral. Here V represents th volume of the particle and K the anisotrop energy per unit volume. A large particle we again treat classically, employing as our partition function $Z=2\pi\int_0^\pi \exp(-KV\sin^2\theta/kT)\sin\theta d\theta$. The specific heat for this case is derived to be $C_v/k=\frac{1}{2}-(e^b/4I)(1-2b+e^b/I)$, where $b=KV/kT$ and $I=\int_0^1 \exp bt^2 dt$. Employing tabulated values[4] of the integral I, specific heat curves were calculated and are shown in Fig. 2 for K positive and in Fig. 3 for K negative. Positive K or a values correspond to particles whose low energy or "easy" directions of magnetization are along the axis of symmetry of the particles, such as rodlike particles in the case of shape anisotropy. For negative values of K or a, the high energy or "hard" directions of magnetization are along the symmetry axis, as for platelike particles.

---

[1] K. Schroder and C. H. Cheng, J. Appl. Phys. **31**, 2154 (1960).

[2] We also have serious reservations concerning their interpretation of the magnetic data for this alloy.

[3] The analogy is inexact. The Hamiltonian for the classic harmonic oscillator requires both kinetic and potential energ terms, and leads to a specific heat of k per degree of freedom. this magnetic case, only a potential energy term appears in t Hamiltonian, and a specific heat of $k/2$ per degree of freedo appears as the low-temperature limit.

For $S=\infty$, the low-temperature limits for the specific heat are k for positive K and $k/2$ for negative K. For positive K, at low temperatures the magnetization stays nearly parallel to the symmetry axis and resembles, as in the above case with the applied field, a classical two-dimensional harmonic oscillator. For negative K, at low temperatures the magnetization is nearly confined to the plane perpendicular to the symmetry axis. Only excursions out of this plane increase the energy of the particle, and hence this resembles a classical *one*-dimensional harmonic oscillator and has a low-temperature specific heat of only $k/2$. (It should be pointed out that this result is valid only if all directions normal to the symmetry axis are *exactly* equivalent.) An interesting special case is that of an ideal platelike particle with a magnetic field applied exactly along the symmetry axis. The low-temperature specific heat limit here remains at $k/2$ for fields less than the anisotropy field $2KV/\mu$, above which this limit abruptly becomes k since the low-energy position for the magnetization is along the symmetry axis for this and higher fields. Again, these nonzero specific heats at zero temperature are a result of the approximation of infinite quantum number. If one takes into account as before the finite separation of the lower levels, the specific heat again approaches zero exponentially as the temperature approaches zero. The form of this exponential drop, for large S and positive K, is identical to that given above for the isotropic particle in a field H, except that for H must be substituted the anisotropy field $2KV/\mu$. For usual values of this field, this correction to the specific heat will be unimportant for temperatures above a few tenths of a degree. For negative K, such a correction will not be necessary until even much lower temperatures, since here the lower energy levels are much more closely spaced.

Calculation of the specific heat curves for particles with anisotropies other than uniaxial has not been attempted. It may be remarked, however, that in the approximation of infinite quantum number the low-temperature, specific heat limit of particles with positive or negative cubic anisotropy is k per particle, since in these cases the magnetization fluctuations about the easy directions will again resemble classical two-dimensional oscillators.

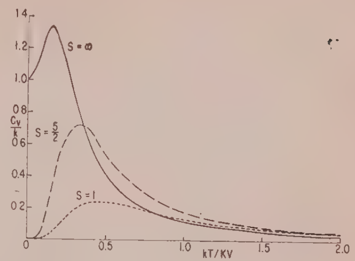

FIG. 2. Specific heat per particle of paramagnetic particles with a positive uniaxial anisotropy energy KV.

The above treatment of superparamagnetic particles predicts the temperature-dependent specific heat per particle shown in Figs. 1–3. For most particles with uniaxial anisotropy, the curves for $S=\infty$ should be a close approximation to the expected behavior (except for the required exponential drop to zero specific heat at zero temperature, which would usually be expected to occur below $T=1°K$). Although it is not entirely clear that the measurements on TiFe[1] were associated with this effect, it does seem that, under appropriate conditions, the specific heat of superparamagnetic particles could be measured experimentally. At low temperatures, this specific heat will be roughly k per particle. For an alloy with an atomic fraction f of precipitated or clustered ferromagnetic atoms and an average number N of such atoms per particle, the particles should contribute a specific heat of roughly Rf/N per mole of the alloy, where R is the gas constant. In an earlier review of superparamagnetism,[5] magnetization data was shown for a copper—2% cobalt alloy that had been heat treated to produce particles about 8 A in radius containing about 200 atoms per particle. At k per particle, these particles would contribute to the sample a specific heat of about $2\cdot 10^{-4}$ cal deg^{-1} mole^{-1}. The specific heat of copper[6] at 2°K is about 3.8×10^{-4} cal deg^{-1} mole^{-1}, so that the specific heat of the superparamagnetic particles in this copper-cobalt specimen should be measurable at these low temperatures. Their contribution could be made more prominent by in-

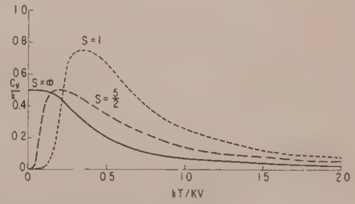

FIG. 3. Specific heat per particle of paramagnetic particles with a negative uniaxial anisotropy energy KV.

---

[4] E. Jahnke and F. Emde, *Tables of Functions* (Dover Publications, New York, 1945). Further tables for positive values of b are given by H. M. Terrill and L. Sweeney, J. Franklin Inst. **237**, 495 944); **238**, 220 (1944).

[5] C. P. Bean and J. D. Livingston, J. Appl. Phys. **30**, 120S (1959).

[6] J. A. Rayne, Australian J. Phys. **9**, 189 (1956).

creasing the volume fraction of precipitate or by decreasing the average particle size.

For positive K in the approximation of $S=\infty$, we derive $C_v=k(1+kT/KV)$ per particle for $T\ll KV/k$. Thus, superparamagnetic particles under optimum conditions might also make a measurable contribution to γ, the linear temperature coefficient of the specific heat.

It should be noted that the above treatment has neglected the effects of any interaction between particles.

Note added in proof. An article on this subject has recently appeared[7] in which anisotropy has been represented approximately by an effective field. For the case of large S and $kT\ll\mu H$, it is shown there that the exponential drop of specific heat as $T\rightarrow 0$ takes the form o the Einstein specific heat function.

ACKNOWLEDGMENT

Prior to the appearance of the paper by Schröder and Cheng, this problem had been called to our attention by N. Kurti, who had also raised the question in discussion at the 1958 International Magnetism Conference.[8]

---

[7] K. Schröder, J. Appl. Phys. 32, 880 (1961).

[8] N. Kurti, J. phys. radium 20, 221 (1959).

JOURNAL OF APPLIED PHYSICS VOLUME 32, NUMBER 10 OCTOBER, 196

Effect of Electron Bombardment on the Near-Infrared Fluorescence of Single-Crystal CdS

B. A. Kulp
Aeronautical Research Laboratory, Wright-Patterson Air Force Base, Ohio

(Received April 24, 1961)

Under electron bombardment at 40°C, two fluorescence bands in the near infrared are observed in many CdS crystals. The bands are at about 8500 A and 1.05 μ. The 8500-A band is reduced in intensity by electron bombardment at 100 and 275 Kev and by exposure to x radiation. The 1.05-μ band is not greatly affected by these irradiations. Heat treatment for $\frac{1}{2}$ hr at 200°C partially restores the 8500-A band. The effect is interpreted as a redistribution of electrons over the existing defects. The defect responsible for the 8500-A band is believed to be copper in a particular ionization state. The 1.05-μ band is observed to appear after heat treatment at 200°C if it is not present originally. This fact makes the origin of this latter band uncertain.

INTRODUCTION

THE use of an energetic electron beam to produce defects in CdS has produced some interesting results concerning edge emission and another fluorescence band in CdS. Collins[1] produced edge emission with a 200-kev beam of electrons, and on the basis of the effect of heat treating in a sulfur atmosphere, concluded that edge emission was a result of sulfur vacancies. Kulp and Kelley,[2] on the other hand, measured the threshold for the production of edge emission by electron bombardment as being 115 kev, and proposed that edge emission was a result of sulfur interstitials. Further, the latter authors proposed that sulfur vacancies are the center for a fluorescence band at 7200 A at 77°K. Kulp and Kelley[3] have observed that the 1.4-μ quenching band is reduced in intensity following electron bombardment at 100 kev of thin platelet-type crystals of CdS. On this basis and the effect of temperature on quenching and on edge emission, they propose that the center, or at least part of it, for the 1.4-μ quenching band is the sulfur interstitial. While the conclusions reached by analyzing the results of electr bombardment of CdS may be classified as somewh speculative, nontheless, electron bombardment repr sents a new approach to the problem of identifying t centers responsible for the many and varied fluoresce and photoconductive properties of CdS.

EXPERIMENTAL

Platelet-type single crystals 25 to 250 μ thick, gro by vapor-phase deposition by Greene according to t methods commonly used in this laboratory,[4] were us throughout the experiments described here. The pla lets were from several crystal growing runs. While intentional doping agents were added, spectrograp analysis showed copper, aluminum, magnesium, a calcium present in concentrations of 1 to 10 ppm and s con and iron in smaller concentrations. The crystals w bombarded with 275-kev electrons from a Van Graaff accelerator and with 100-kev electrons fro Cockroft-Walton type accelerator at a dc level of 0 to 10 μa/cm^2.

The fluorescent spectra were taken with a Perk Elmer glass-prism spectrometer with a PbS detec

---

[1] R. J. Collins, J. Appl. Phys. 30, 1135 (1959).

[2] B. A. Kulp and R. H. Kelley, J. Appl. Phys. 31, 1057 (1960).

[3] B. A. Kulp and R. H. Kelley, J. Appl. Phys. (to be published).

[4] D. C. Reynolds and S. J. Czyzak, Phys. Rev. 79, 1957 (1

RESULTS

A. Spectra Under Electron-Bombardment Excitation

Figure 1 shows the fluorescence spectrum typical of a group of CdS crystals as a function of electron-beam current. The intensity of the 8500-A fluorescence increases much more rapidly than the 1.05-μ band as the current is increased. Figure 2 shows the behavior of the fluorescence spectrum of these crystals under electron bombardment, 275 kev, 2.5 μa/cm^2 at 40°C after 1×10^{17}, 2.5×10^{17}, 7×10^{17}, and 5×10^{18} electrons/cm^2, respectively. The elimination of the band at 8500 A is clearly observed while the band at 1.05 μ increases somewhat in intensity. Generally, the 8500-A band is reduced in intensity by a factor of 10 after bombardment by about 10^{18} electrons/cm^2.

In another crystal the resistivity was measured using sputtered platinum electrodes and a voltage gradient of 100 v/cm. The dark resistivity increased from 3×10^4 to 5×10^9 ohm-cm after 10^{18} electrons/cm^2 struck the crystal. The 8500-A band was removed and the 1.05-μ band decreased slightly during this bombardment. Similar increases in dark resistivity were observed in other crystals as the 8500-A band was removed.

The 8500-A and the 1.05-μ bands have been found in several batches of platelets and some bulk crystals grown with no intentional doping. The dark resistivity of these crystals is in the range of 10^4 to 10^7 ohm-cm. The 8500-A band was not found in a batch grown with 0.01% CuS added to the charge. The resistivity of these crystals was about 10^{11} ohm-cm. The 1.05-μ band was found in these crystals at room temperature. The 8500-A band was likewise not observed in silver-doped platelets, but was observed in a large crystal which showed both silver and copper impurities. Crystals grown from ultra-pure powder did not have either of the fluorescence bands mentioned here. The resistivity of the silver-doped platelets was 10^9 ohm-cm. That of the ultra-pure crystal was 10^7 ohm-cm.

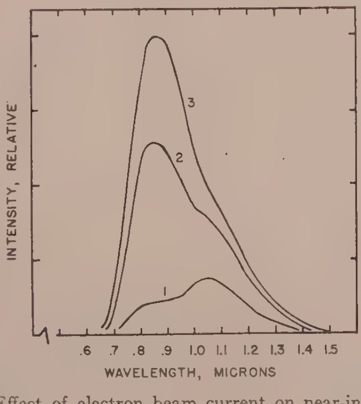

FIG. 1. Effect of electron beam current on near-infrared fluorescence of CdS. Spectra taken with (1) 0.5 μa/cm^2; (2) 2.5 μa/cm^2; and (3) 5 μa/cm^2, 275-kev electron excitation.

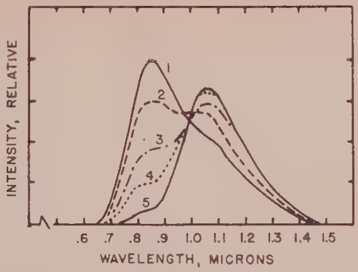

FIG. 2. Effect of electron bombardment on the near-infrared fluorescence of CdS. Spectra taken with 275-kev 2.5 μa/cm^2 electron excitation. (1) Original; (2), after 10^{17} electrons/cm^2; (3) after 2.5×10^{17}; (4) after 6×10^{17}; and (5) after 5×10^{18} electrons/cm^2.

The decrease in intensity of the 8500-A fluorescent band under irradiation has been observed to take place with 100-kev electrons and with exposure to x rays from a tungsten target FA60 tube for 20 hr at 50 kv, 40 ma. The phenomenon was observed in all crystals having the broad peak at 8500 A regardless of the intensity of the 1.05-μ band. There was variation in the time required to produce the effect. One group of crystals required about 10 times as much radiation to produce the effect as those shown in Fig. 2. In rare cases, the 1.05-μ band decreased as fast as the 8500-A band for the first 5×10^{17} electrons; subsequent bombardment, however, reduced the 8500-A band with no further decrease in the 1.05-μ band.

B. Spectra Under Band-Gap Light Excitation

Figure 3 shows the fluorescence spectrum of a crystal taken with band-gap light excitation (a 100-w Sylvania Zr arc lamp through a CuSO$_4$ solution filter which cut off at 6200 A) before and after bombardment with 10^{18} electrons/cm^2 at 100-kev energy. Figure 4 shows the spectra with band-gap light excitation and with electron excitation taken after the 8500-A band had been reduced by a factor of 10 by bombardment by 10^{18} electrons/cm^2 at 275 kev. There is a definite difference in the spectra depending on the nature of the exciting radiation. Dependence of spectra on exciting radiation has been previously noted by Leverenz[5] and others. In the case of band-gap light there are peaks at 7400 and 6900 A which become quite intense following electron bombardment. These peaks are not observed in these crystals before bombardment or while under electron bombardment in the current range 0.25 to 10 μa/cm^2. In other groups of crystals not showing the 8500-A band, however, the 7400-A and the 6900-A peaks have been observed under electron bombardment. The 6800- and 7400-A bands have been previously observed under electron bombardment at room temperature by Bleil and Snyder.[6]

---

[5] H. W. Leverenz, *Luminescence of Solids* (John Wiley & Sons, Inc., New York, 1950), e.g., p. 197.

[6] C. E. Bleil and D. D. Snyder, J. Appl. Phys. **30**, 1799 (1959).

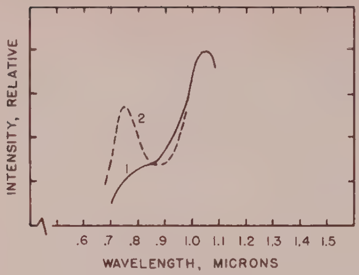

FIG. 3. Effect of electron bombardment on the fluorescence spectrum when excited by light, (1) before; (2) after 10^{18} electrons/cm² at 100-kev energy.

DISCUSSION

Two possible mechanisms for the disappearance of a fluorescence band can be readily postulated: (1) actual removal of the fluorescence center, and (2) insertion of a competing center which would poison the fluorescence, for example, nickel in CdS.[6] The removal of the fluorescence could be accomplished in several ways: (1) by removing the atom or impurity from the lattice site it occupied, (2) by removing impurity atoms from the crystal altogether, or (3) by changing the character of the impurity by adding or removing an electron. Radiation damage by high-energy electrons is capable of doing all three of the above, however, 100-kev electrons and especially x rays would be capable of performing only the third type of damage. Further evidence that this is the mechanism comes from the fact that the cross section for the process is very large—about 10^{-18} cm² compared to $\sim 10^{-22}$ to 10^{-23} cm² for displacement of an atom from a lattice point with electrons.[7]

The actual mechanism for the irreversible (under isothermal conditions) redistribution of electrons over the existing impurity levels could be explained as follows: It is assumed that one or more impurities in the crystals can exist in several ionization states. Such a model has been proposed by Woods and Wright[8] for sulfur and cadmium vacancies, and for Cl and Cu occupying sulfur and cadmium lattice sites, respectively. In addition, Woodbury and Tyler[9] have established that gold and copper impurities in germanium introduce a series of levels in which the impurity center has charges which may vary from $+1$ to -3 electronic charges. Schockley and Last[10] have shown that the probability of such an impurity being in a particular charge state depends upon the position of the Fermi level. Thus, if the Fermi level is below one of the levels A characteristic of one charge state of a many charge-state impurity, then A will have essentially unit probability of occupancy while level B nearer the conduction band will have small probability of occupancy. As the Fermi level moves up, the probability of occupancy will shift continuously according to a Fermi function until level B has unit probability of occupancy when the Fermi level is several kT above level A.

In this case, since it was observed that the dark resistivity of the crystal increased as the level was being emptied, it is necessary to consider that the impurity involved is a hole-trapping impurity. Using the model of Rose[11] in which he proposes a steady-state hole Fermi level and a hole-demarcation level under excitation, it can be seen that a redistribution of the holes can take place under deeply penetrating radiation. There are, of course, many trapping centers in addition to the one responsible for the 8500-A fluorescence band which are important in establishing the properties of the crystals. It can take an appreciable length of time before steady-state conditions are reached. Such long time buildup or decay of photoconductivity and fluorescence is common in CdS. Upon removal of the ionizing radiation, the tendency of the crystal to return to the original state is prevented because the levels are too widely separated for thermal transitions to take place. Thus, the crystal is now in a state where the impurity has one less hole trapped at it than originally. The net result is that the 8500-A fluorescence band is no longer detectable and the crystal has a higher dark resistivity than originally. Whether there is a fluorescence band farther in the infrared which is due to the second level is not known since the wavelength limit of the equipment presently available is 2.75 μ.

The appearance of one or two shorter wavelength fluorescence bands after bombardment when the crystals are excited with light indicates that there has been a redistribution of the electrons over several levels. It would seem that if these bands were associated with the 8500-A band, they should be observed under electron bombardment. One is tempted to suggest that the 6900- and 7400-A bands are the result of surface states or states near the surface which would be strongly excited by the light, but only weakly excited by penetrating radiation. However, in many crystals these

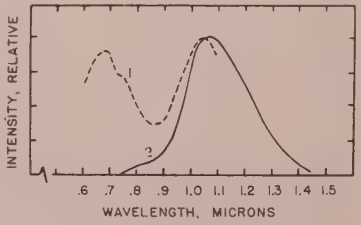

FIG. 4. Effect of exciting radiation on fluorescence of CdS crystal after electron bombardment. (1) light; (2) 275-kev 2. μa/cm² electrons.

---

[6] H. W. Leverenz, *Luminescence of Solids* (John Wiley & Sons, Inc., New York, 1950), p. 333.

[7] F. Seitz and J. S. Koehler, *Solid State Physics* (Academic Press, Inc., New York, 1956), Vol. 2, p. 332.

[8] J. Woods and D. A. Wright, *Solid State Physics, Brussels Conference* (Academic Press, Inc., London, 1960), Vol. 2, Part 2, p. 880.

[9] H. H. Woodbury and W. W. Tyler, Phys. Rev. **205**, 84 (1957).

[10] W. Schockley and J. T. Last, Phys. Rev. **107**, 392 (1957).

[11] A. Rose, Phys. Rev. **97**, 322 (1955).

bands are observed under electron excitation and hence the difference in the spectra under light and electron excitation must be attributed to a difference in occupation of states brought about by the difference in ionization densities of the two types of exciting radiation. Light causes very intense ionization in a thin layer, while electrons cause more uniform but not so intense ionization throughout the crystal.

It would seem that the results shown in Fig. 1 are contrary to the model; however, since the temperature of the crystal increases as the electron beam increases in intensity, there is a tendency for the effect of the increased ionization on the steady-state Fermi level to be neutralized by the rise in temperature.

HEAT TREATMENT

If the above model is correct, one might expect that heating the crystal to a few hundred degrees Centigrade would return the crystal to its original state. Figure 5 shows the spectrum with electron excitation of a crystal before and after bombardment and after heat treatment for $\frac{1}{2}$ hr at 200°C in air. The partial recovery of the 8500-A band is shown. The intensity of this band was subsequently reduced to its value before heat treatment by bombardment with 3×10^{17} electrons/cm^2. Heat treatment of a similar crystal which had not been bombarded caused a slight decrease in the 8500-A band and no change in the 1.05-μ band. While the heat-treatment experiment is not conclusive, it is consistent with the model proposed.

It should be noted here that heat treatment for $\frac{1}{2}$ hr at 200° and at 300°C has been observed to produce the 1.05-μ fluorescence band in many crystals which do not have it. In the case of the crystal in Fig. 5, the intensity of the 1.05-μ band is sufficiently high before heat treatment so that no change in its intensity is observed. Figure 6, however, shows the effect of the same heat treatment on another crystal in which the 8500-A band had been reduced in intensity by x radiation. The appearance of the 1.05-μ band after heat treatment is very evident as is the recovery of the 8500-A band. When crystals with spectra similar to that shown in Fig. 6 are heat treated before bombardment, the 1.05-μ band appears strongly and the 8500-A band decreases somewhat in intensity. The reason for the appearance of the 1.05-μ band is not known at the present.

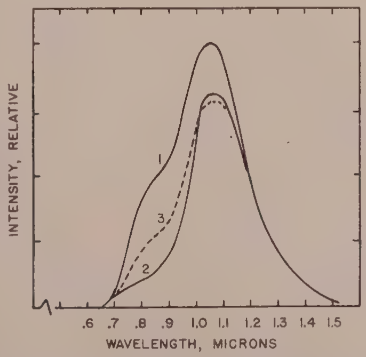

FIG. 5. Effect of heat treating on fluorescence of CdS after bombardment. (1) Original; (2) after 10^{18} electrons/cm^2 at 275 kev; (3) after $\frac{1}{2}$ hr at 200°C. Spectra taken with 275-kev 2.5 μa/cm^2 electron excitation at 40°C.

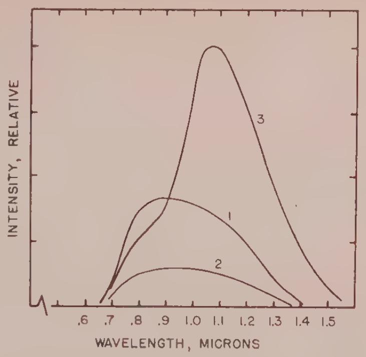

FIG. 6. Effect of heat treating. (1) Original; (2) after prolonged exposure to x rays; (3) after $\frac{1}{2}$ hr at 200°C. Spectra taken with 275-kev 2.5 μa/cm^2 electron excitation at 40°C.

DEFECT RESPONSIBLE FOR THE 8500-A BAND

Fluorescence bands at 8200 A and 1.02 μ in copper-activated CdS phosphors have been reported by Grillot and Guintini[12,13] and confirmed by Garlick and Dumbelton.[14] Grillot and Guintini found that, depending on the method of preparation, the 8200-A and/or the 1.02-μ bands are found in CdS:Cu at room temperature. Avinor[15] has found that with an excess of coactivator (indium or gallium) over the copper activator, two bands appear at about 8300 A and 1.01 μ. With small amounts of coactivator the 1.01-μ band appears alone.

The bands observed here are quite broad and their shape and the position of the peaks depend on the relative intensities of the two bands. It seems reasonable to say that the band at 8500 A is a copper band. The appearance of the 1.05-μ band upon heat treatment indicates that the origin of this band needs further investigation.

ACKNOWLEDGMENTS

The author wishes to thank L. C. Greene, of this Laboratory, for supplying the crystals used in this investigation, and to R. G. Schulze for making the resistivity measurements and for discussions concerning the manuscript.

---

[12] E. Grillot and P. Guintini, Compt. rend. **236**, 802 (1953).

[13] E. Grilliot and P. Guintini, Compt. rend. **239**, 419 (1954).

[14] G. F. J. Garlick and M. J. Dumbleton, Proc. Phys. Soc. (London) **B67**, 442 (1952).

[15] M. Avinor, thesis, University of Amsterdam, 1959.

JOURNAL OF APPLIED PHYSICS VOLUME 32, NUMBER 10 OCTOBER, 1961

Influence of the Hall Effect upon the Transverse Magnetoresistance in Indium Antimonide

Charles A. Simmons
Burroughs Corporation Research Center, Paoli, Pennsylvania

(Received January 9, 1961)

A detailed experimental investigation of the influence of the specimen geometry on the transverse magnetoresistance has been made. Differentiation between the bulk properties and the geometrical contributions has been accomplished. It was found that the enhancement of the magnetoresistance effect in rectangular elements is due to the Hall effect rather than to its absence and that the bulk property has an H^2 relationship while the geometry effect is linear with H and inversely proportional to the length-to-width ratio.

INTRODUCTION

THERE have been several investigations of the galvanomagnetic effects in InSb.[1–3] The results of these investigations indicate a strong dependence of the Hall and magnetoresistance effects upon the geometry of the test specimen. Because of this, it has been difficult to determine clearly bulk physical properties. To minimize the geometric effects, the specimen usually is made long and narrow, but even for this case the absence of the saturation of the magnetoresistance effect at high fields that should occur theoretically is thought to be due to sample geometry.

The usual theory[1] for the geometrical influence is based on the assumption that the enhancement of the magnetoresistance effect in rectangular elements is due to a decrease or an elimination of the Hall voltage. At the current electrodes, which cover the entire end surfaces of the sample, the Hall field is reduced to zero ($E_y=0$). The Hall voltage reaches its full value at some distance from these ends. Isenberg *et al.*[4] and Volger[5] have made calculations of E_y as a function of the length-to-width ratios for germanium. They determined that this ratio has to be four or larger before the true Hall voltage can be realized.

In the end-effect areas, where there is a reduction in the Hall voltage, the total current no longer exists in the length direction of the slab, but there is an appreciable transverse current component ($J_y>0$) present; hence, the charge carriers travel a longer path, resulting in a magnetoresistance larger than the value given by the conventional expression. It has been assumed[1,3] that this increase is greater by an amount that is proportional to μ^2H^2, where μ is the mobility and H is the externally applied magnetic field, and it has also been assumed[1,3] that the Hall voltage reduction in the end-effect areas in some manner contributes to the transverse current by an increasing amount as the sample length-to-width ratio grows smaller.

The Corbino disk configuration gives a very large magnetoresistance enhancement, and to account for this fact it has been assumed that in this particular geometrical configuration there is no Hall voltage present. Welker and Weiss[2] have suggested an alternate method for obtaining a zero Hall field. This method involves doping the material so that a zero Hall coefficient ($R_H=0$) is obtained. However, Harmon *et al.*[6] have demonstrated theoretically that the Hall field is always present when the magnetoresistance is a maximum.

A detailed experimental study of the geometrical influence upon the transverse galvanomagnetic effects in InSb, using an improved probing technique, has been made. The results of these studies differ considerably from the above prevailing theories. Conclusive experimental proof will be given that the geometrical enhancement of the magnetoresistance effect is due to the presence of the Hall field rather than its absence.

Table I. Material characteristics at 25°C.

Material code	Hall coefficient, R_H	Resistivity	Hall mobility (R_H/ρ_0)
InSb-5N	303 cm^3/coul	3.915×10^{-3} ohm/cm	77 400 cm^2/v-sec

EXPERIMENTAL PROCEDURES

Rectangular polycrystalline InSb specimens were cut perpendicular to the direction of freezing in the zone refining process. Typical characteristics of the material are given in Table I.

Potentials, dc, were probed over the samples using conventional instrumentation techniques. Rectangular slabs, with their ends entirely electroded, were used throughout. The magnetic field was produced by a magnet giving a uniform field over a volume which was larger than that occupied by the specimen. The field was measured with a Gerhard K. Hennig gauss meter. The current in the specimen was determined by the voltage drop across a precision resistor. All dc potentials were measured with a L & N type K potentiometer.

---

[1] H. P. R. Frederikse and W. R. Hosler, Phys. Rev. **108**, 1136 (1957).

[2] H. Welker and H. Weiss, Solid State Phys. **3**, 1–78 (1956).

[3] Beer *et al.*, "Research and Development Work on Semiconducting Materials of Unusually High Electron Mobility." Batelle Memorial Institute for the Wright Air Development Center, WADC Tech. Rept. 55–307.

[4] I. Isenberg, B. R. Russell, and R. F. Greene, Rev. Sci. Instr. **19**, 685 (1948).

[5] J. Volger, Phys. Rev. **79**, 1023 (1950).

[6] T. C. Harman, R. K. Willardson, and A. C. Beer, Phys. Rev **95**, 699 (1954).

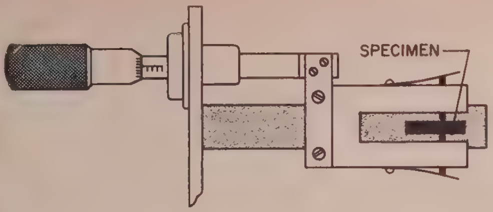

FIG. 1. Specimen holder.

The specimen holder consisted of a phenolic beam with a movable yoke, as shown in Fig. 1. Each arm of the yoke contained a gold-plated probe which was spring loaded such that point contacts were made on opposite edges of the specimen. The yoke, hence the probes, could be positioned with respect to the length dimension of the slab with a micrometer adjustment. With this arrangement, potential measurements could be made continuously from one end of the specimen to the other.

When the Hall voltage is plotted as a function of distance along a rectangular slab of InSb, a Hall profile is obtained as shown in Fig. 2. A profile, which has proved to be more useful than the Hall profile in the study of the galvanomagnetic effects, is the potential profile shown in Fig. 3. This profile was obtained by plotting the potential distribution along the two edges of the specimen with respect to one of the current electrodes. This type of profile contains all the necessary information pertaining to both the Hall and magnetoresistance effects while also permitting observation of the end effects. The end effects are present in the areas where the Hall voltage deviates from its true value. The Hall voltage at any point on the specimen is determined by taking the potential difference between the two profile curves indicated in Fig. 3. At zero magnetic field, the two curves are coincident and linear. In both the Hall and potential profiles, inhomogeneities, if present, would be shown as departures from these standard forms; hence, homogeneous specimens could be selected. To illustrate, a potential profile of a specimen that contained both impurity gradients and an inclusion of an indium-rich alloy is shown in Fig. 4 with a micrograph of the ingot from which the specimen was taken.

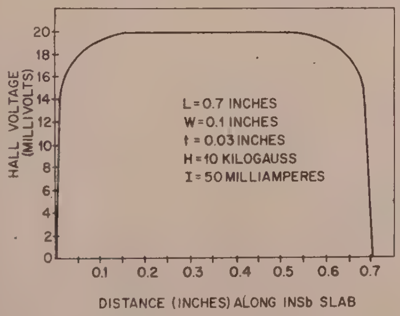

FIG. 2. Hall voltage profile obtained by plotting the Hall voltage as a function of position on a rectangular slab of InSb.

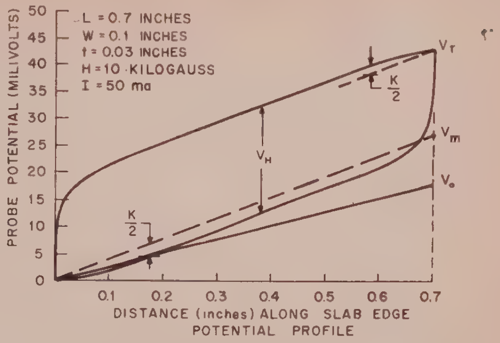

FIG. 3. Potential profile—the potential distribution around the periphery of a rectangular slab.

The magnetoresistance is determined conventionally by potential measurements between the current electrodes, or—in order to avoid junction and geometry effects—between two probes placed on the specimen at some distance from the current electrodes.

The total magnetoresistivity [hereafter referred to as $(\Delta\rho/\rho_0)_T$] is defined by

$$(r_H-r_0)/r_0=\Delta r/r_0=(\Delta\rho/\rho_0)_T, \tag{1}$$

where r and ρ are, respectively, resistance and resistivity and the subscripts H and 0 refer to their value in a magnetic field H and magnetic field zero; $\Delta\rho$ is the change in resistivity. The end-to-end measurements of potential determine $(\Delta\rho/\rho_0)_T$. It will be shown later that from the latter measurements[7] the true bulk magnetoresistivity of the material, termed here physical magnetoresistivity and designated by $(\Delta\rho/\rho_0)_P$ can be obtained. Identical results can also be obtained from the potential profiles, Fig. 3, for $(\Delta\rho/\rho_0)_T=(V_T-V_0)/V_0$ and for $(\Delta\rho/\rho_0)_P=(V_m-V_0)/V_0$.

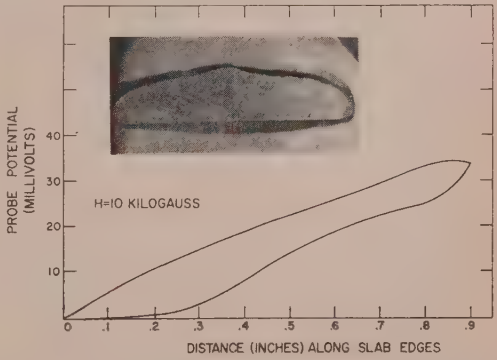

FIG. 4. Potential profile of a rectangular element that contained both inclusions and impurity gradients. Inset shows a photograph of the ingot from which the element was taken.

---

[7] The current electrodes to InSb at room temperature almost always form ohmic contacts.

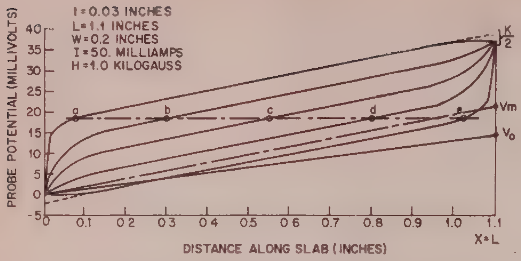

FIG. 5. Potential profiles taken on the two edges and on the body of a rectangular slab. Points a, b, c, d, and e are equipotential points and are used to establish an equipotential line on the slab.

EXPERIMENTAL RESULTS

From Fig. 3 it can be seen that the difference between the voltage due to total and physical magnetoresistance is due to the Hall effect. While it is true that the Hall voltage is zero at the current electrodes and reaches a maximum value some distance away, nevertheless the voltage increase due to the Hall effect is still present in the total magnetoresistance. If the end effects are making a contribution to the physical magnetoresistance term, it is not readily apparent in this profile.

To specify the end effects, an equipotential plot of a specimen was obtained by first making a potential profile along its edges and a similar plot at known distances from the edges, as shown in Fig. 5. A line, when drawn parallel to the abscissa, will intersect the profiles at equipotential points a, b, c, d, and e. On transposing these points to a scaled drawing of the element, and connecting, an equipotential line is established. This procedure is followed until the entire face of the slab is mapped, as shown in Fig. 6. It is seen that the equipotential lines tend to converge at points near diagonal corners. These are the regions corresponding to the steep potential gradients of the profiles of Fig. 5. The steepness is a consequence of the large Hall angle (79° at 10 kgauss) which causes the current lines to make an angle of 11° with the equipotential electrodes at which the current enters and exits the element.

The geometric contribution (effect of the W/L ratio) on the total magnetoresistivity is determined as follows:

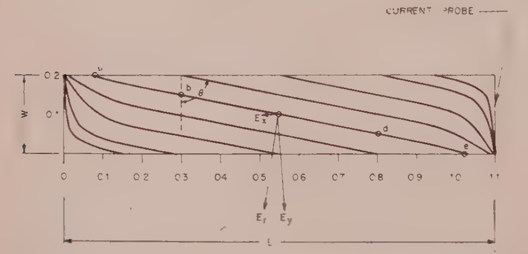

FIG. 6. A scale drawing of a rectangular slab showing the equipotential lines. $E_y/E_x=\tan\theta$, where θ is the Hall angle.

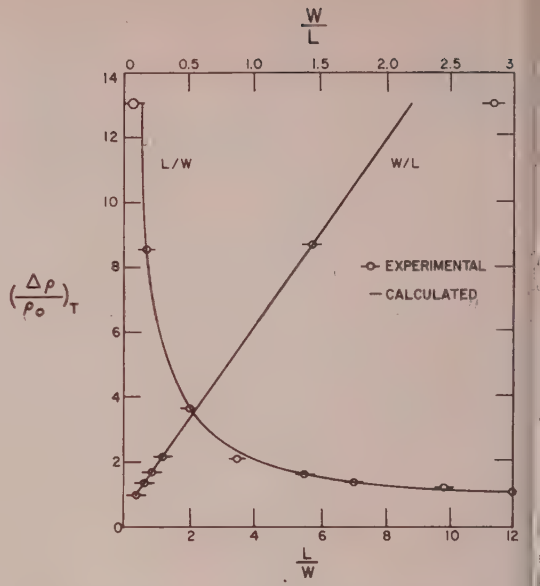

FIG. 7. $(\Delta\rho/\rho_0)_T$ as a function of the L/W and W/L ratios.

From Fig. 3, it is seen that

$$(\Delta\rho/\rho_0)_T=(V_T-V_0)/V_0=[(V_m+V_H-K)-V_0]/V_0$$
$$=(V_m-V_0)/V_0+V_H/V_0-K/V_0, \qquad (2$$

and subsequently by substitution

$$(\Delta\rho/\rho_0)_T=(\Delta\rho/\rho_0)_P+(\mu_0H\times10^{-8})/(L/W)-(Kt/\rho_0I)/(L/W), \qquad (3$$

or

$$(\Delta\rho/\rho_0)_T=(\Delta\rho/\rho_0)_P+(\Delta\rho/\rho_0)_G, \qquad (4$$

where the subscripts P and G indicate the physical an

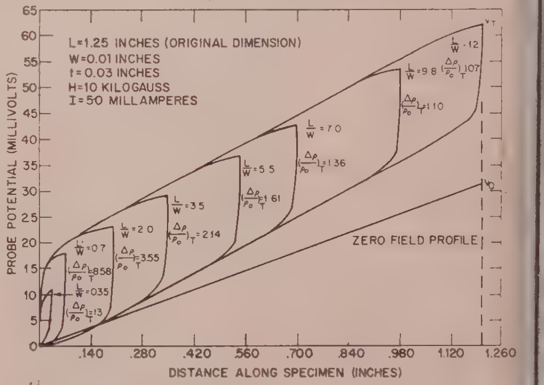

FIG. 8. Potential profiles of a long element and successive shorter length of the same element showing $(\Delta\rho/\rho_0)_T$ for t different L/W ratios.

geometrical[8] contributions to the total magnetoresistivity. The voltage difference K is required to adjust for the deviation from linearity of the low potential gradient portion of the voltage profile[9] as indicated by the dashed lines in the figure. V_m is the "physical" magnetoresistivity voltage. It is the ordinate at $x=L$ of a line passing through the origin parallel to the linear portion of the profile curves, Figs. 3 and 5. The other yet undefined symbols are: μ, mobility: I, specimen current; W, width; L, length (Fig. 6); and t, thickness of the specimen.

Curves, solid lines, calculated from (3) of the total magnetoresistivity, $(\Delta\rho/\rho_0)_T$, versus both W/L and L/W are shown in Fig. 7. The experimental points (circles) derived from the family of curves in Fig. 8 fall essentially on the calculated curve showing nearly perfect agreement. It should be noted that for small[10] L/W ratios $(\Delta\rho/\rho_0)_T$ is indeterminant by (3) since the Hall voltage term decreases below a certain critical L/W ratio.

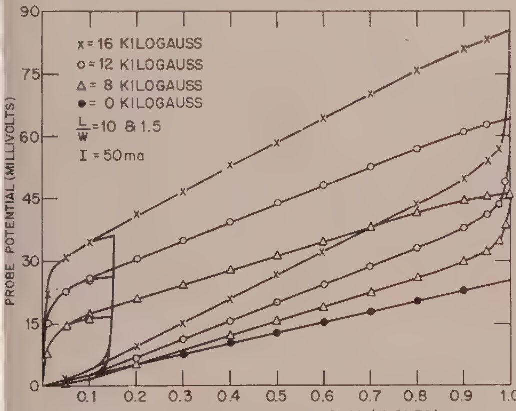

FIG. 9. Representative potential profiles of a slab with $L/W=10$ and the same slab cut to an $L/W=1.5$.

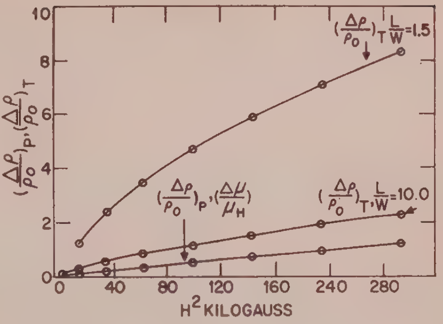

FIG. 10. $(\Delta\rho/\rho_0)_P$, $(\Delta\rho/\rho_0)_T$, and $(\Delta\mu/\mu_H)$ versus H^2. (These quantities were determined on the long specimen.)

EXPERIMENTAL CONFIRMATION

Experimental confirmation of (3) and (4) by geometry potential profiles of an element with L/W ration of 10 and 1.5 (the latter was cut from the former) were taken with magnetic fields ranging from 2 to 16 kgauss. Representative plots are shown in Fig. 9. The profiles were then used to determine the following quantities: by potential ratios, Eq. (2)—$(\Delta\rho/\rho_0)_T$, $(\Delta\rho/\rho_0)_P$, and $(\Delta\rho/\rho_0)_{GH}$ (see footnote 9); by resistivity and Hall measurements—$(\Delta\mu/\mu_H)$, μ_H, and $\tan\theta$. The first two of these and $(\Delta\mu/\mu_H)$ have been plotted against H^2, Fig. 10, and the remainder against H, Fig. 11. An examination of the various curves demonstrate the following: the physical magnetoresistivity $(\Delta\rho/\rho_0)_P$ and the fractional magnetic variation of mobility $(\Delta\mu/\mu_H)$ are equal and lie on a curve which is linear in H^2. The geometric contribution[8] to the total magnetoresistivity, $(\Delta\rho/\rho_0)_{GH}$ is linear in H in agreement with (3). The total magnetoresistivity $(\Delta\rho/\rho_0)_T$ shows a curvature that decreases with L/W and apparently approaches $(\Delta\rho/\rho_0)_P$ in the limit of very large L/W. Tanθ, θ is the Hall angle, tends to saturation at high magnetic fields.

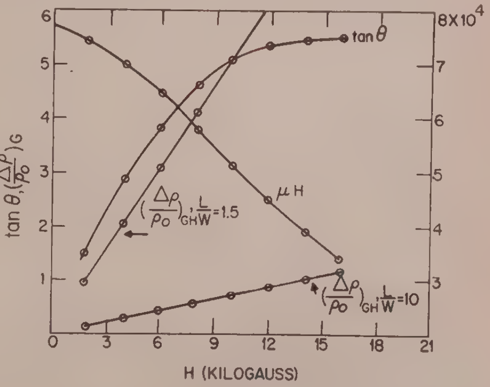

FIG. 11. Tanθ, μ_H, and $(\Delta\rho/\rho_0)_G=\rho_H/\rho_0\mu_H H\times10^{-8}$ versus H. (These quantities were determined on the long specimen.)

---

[8] Observe that the geometric contribution to the total magnetoresistivity constitutes the last two terms of (3) and that one is magnetic field dependent, namely $(\Delta\rho/\rho_0)_{GH}=V_H/V_0 = (R_HH)/[\rho_0(L/W)]=(\mu_0H\times10^{-8})/(L/W)$, and the other current dependent, namely $(\Delta\rho/\rho_0)_{GI}=(Kt/\rho_0I)/(L/W)$, where R_H is the Hall constant. R_H is not necessarily a constant at higher magnetic fields—in fact, the results of this paper show that R_H is essentially constant for InSb, which is interesting in view of the fact that the Hall angle is not linear in H.

[9] It has been observed that for the same material, K is independent of length for $L/W\geq0.7$, Fig. 7, independent of W beyond certain minimum width yet undetermined, and dependent on the current density, Figs. 3 and 5.

[10] It has been pointed out by Dr. Milton Green of this laboratory (also see reference 11, pp. 327–8) that in the limit of L/W going to zero $(W/L\rightarrow\infty)$ the total magentoresistance should become equal to that of a Carbino disk, namely, $(\Delta\rho/\rho_0)_T = (\Delta\rho/\rho_0)_P+\rho_H/\rho_0\tan^2\theta$. For the experimental conditions for which the data of Fig. 7 were obtained, $(\Delta\rho/\rho_0)_P=0.49$, $\rho_H/\rho_0=1.49$, $\tan\theta=5.1$ giving, limit $L/W\rightarrow0$, $(\Delta\rho/\rho_0)_T=39.3$. The experimental points of Fig. 7 are too remote from this limiting point for an accurate extrapolation as to compare theory and experiment. We have found values of $(\Delta\rho/\rho_0)$ for Corbino disks of the same material and same conditions of 22 and 24.

TABLE II. Comparison μ_0/μ_H versus H.

Magnetic field kgauss	2	4	6	8	10
μ_0/μ_H (Weiss & Walker[11])	1.05	1.14	1.25	1.36	1.48
μ_0/μ_H (This paper)	1.04	1.10	1.20	1.34	1.49

There is no evidence of saturation of $(\Delta\rho/\rho_0)_P$ as implied by some theories. Finally a comparison of values of $\rho_H/\rho_0=\mu_0/\mu_H$ determined from the curves of Fig. 9 are in good agreement with the values of Weiss and Welker[11] which were measured on a long thin rod (Table II).

COMPARISONS OF EXPERIMENTAL RESULTS

It has been shown that the total magnetoresistance in rectangular slabs of InSb consists of two components, the physical or bulk property term $(\Delta\rho/\rho_0)_P$ and the geometry term $(\mu_0 H\times 10^{-8})/(L/W)$. The physical effect is shown to be linear in H^2, while the geometry term is linear in H.

Wick,[12] in his analysis of the germanium gyrator, showed a fractional resistance change $\Delta R/R_0$ in terms of the Hall effect and the geometry of the test specimen. He defined ΔR as the increase in resistance over the zero magnetic field value R_0. ΔR is then equivalent to (V_T-V_0) as shown in Fig. 3. Therefore, $\Delta R/R_0$ is equal to $(\Delta\rho/\rho_0)_T$. The expression for $\Delta R/R_0$ and $(\Delta\rho/\rho_0)_T$ contains two terms, the physical or bulk property term which is linear in H^2 and the geometry term which is linear in H.

Drabble and Wolfe[13] extended Wick's work to include the case of measurements made between probes symmetrically placed at various distances from the current electrodes. The specific case where the measurements are made between the current electrodes is identical to Wick and in good agreement with the results of this paper. Their "ideal resistance R," the resistance present in the absence of end effects, can be expressed as V_m/I, where V_m is the physical magnetoresistance voltage shown in Figs. 3 and 5 and I is the current. By referring to Fig. 6, it is seen that this can be expressed simply and accurately as

$$V_m/I=(V_H L)/(IW\mu_H H\times 10^{-8}), \tag{5}$$

and as seen in Fig. 3, their Hall resistance term ΔR, the increase in resistance over the "ideal resistance," can be expressed as V_H/I with an error of $-K/I$, on substituting these quantities into their Eq. (4.1) and solving for the total magnetoresistance effect an equation identical to Eq. (3) of this paper is obtained.

$$(\rho_m-\rho_0)/\rho_0=(\Delta\rho/\rho_0)_T=[(\rho_H-\rho_0)/\rho_0]_P+\{[(\rho_H/\rho_0)\mu_H H\times 10^{-8}]/(L/W)\}-K/\rho_0, \tag{6}$$

where $(\rho_H/\rho_0)\mu_H=\mu_0$. and ρ_m is the resistivity determined by end-to-end measurements.

It is also seen that the Hall resistance is zero if the probes are placed at sufficient distance from the current electrodes which is in agreement with their results. Wick shows that his term ΔR is *nearly* independent of the L/W ratio for $L/W>1$ (see reference 12, Fig. 13). If the resistance due to the bulk effect is eliminated from this term, then it would be completely independent of the L/W ratio for $L/W>1$ and would agree with the results shown in Fig. 8 where the Hall resistance is approximately equal to V_H/I. Also, it is seen in Fig. 8 that the Hall resistance term decreases below V_H/I for $L/W<0.7$ which is in good agreement with his work. Therefore, Eq. (3) would give inaccurate results for $(\Delta\rho/\rho_0)_T$ in those slabs with $L/W<0.7$. Some recent experimental work on slabs with very small L/W ratios shows that $(\Delta\rho/\rho_0)_T$ becomes independent of the L/W ratio for $L/W<0.2$, but is dependent on L, in a way yet to be determined.

The feasibility of using V_m as the physical magnetoresistance voltage is verified by the comparison of the results obtained in this paper to those of Welker and Weiss, Table II. Although V_m can be expressed in terms of the Hall voltage and Hall angle, one should be careful not to confuse the two effects present. Physical magnetoresistance as shown in Figs. 11 and 12 is a consequence of a decrease in mobility with increasing magnetic field. The physical effect in InSb is generally expressed as[1]

$$=a\mu^2H^2\times 10^{-16}=a\tan^2\theta \qquad (7$$

for small fields and thought to saturate at high fields. Tanθ was observed to approach saturation for $H>1$ kgauss. No direct relationship was found to exist between the measured values of tanθ or tan$^2\theta$ and $(\Delta\rho/\rho_0)_P$. $(\Delta\rho/\rho_0)_P$ was found to be quadratic in H up to 16 kgauss.

The close correlation between the results of this pape and the reference work gives a clear indication of th accuracy of the experimental methods and reliability o the results. Since homogeneous specimens were selecte for the study, the homogeneity effects as described b Herring[14] were completely absent or negligible. On thi basis it is stated that separation of the bulk propertie from the geometry effects has been accomplished, an that the total magnetoresistance effect is adequatel described by Eq. (3) for those homogeneous InS specimens with $L/W>0.7$.

ACKNOWLEDGMENTS

The technical assistance of R. G. White, in th collection of part of the data presented herein, is greatl appreciated. The contribution of Dr. Milton Green in reviewing and reorganizing the manuscript is gratefull acknowledged.

---

[11] H. Weiss and H. Welker, Z. Physik **138**, 329 (1954).

[12] R. F. Wick, J. Appl. Phys. **25**, 741 (1954).

[13] J. R. Drabble and R. Wolfe, J. Electronics and Control **3**, 259 (1957).

[14] C. Herring, J. Appl. Phys. **31**, 1939 (1960).

JOURNAL OF APPLIED PHYSICS VOLUME 32, NUMBER 10 OCTOBER, 1961

Use of Idealized Relaxation Spectra in the Interpretation of Experimental Results Concerning Polymer Solutions

K. Walters
Department of Applied Mathematics, University College of Wales, Aberystwyth, England

(Received March 20, 1961)

The usefulness of a new representation of the relaxation spectrum for elasticoviscous liquids is discussed, and an idealized form of this spectrum is used to interpret experimental results concerning polymer solutions.

1. THE RELAXATION SPECTRUM

IN recent years, various authors[1–4] have discussed the extension from a generalized Maxwell model to a relaxation spectrum. Without exception, they define the relaxation spectrum by considering the rigidity of the individual Maxwell elements as distributed over a continuous range of relaxation times. Such a representation of the spectrum is suitable for studies involving viscoelastic *solids*, but it has disadvantages when employed in the study of elasticoviscous *liquids*, the main disadvantage being that the classical Newtonian liquid cannot be represented pictorially on the spectrum. This difficulty is overcome if a new representation is given to the relaxation spectrum involving a distribution function of the viscosity, instead of the rigidity.[5] The new distribution function $N(\tau)$ is related to the distortional stress tensor p_{ik}' and the rate of strain tensor $e_{ik}^{(1)}$ by the equation

$$p_{ik}'=2\int_0^\infty \frac{N(\tau)}{\tau}d\tau\int_{-\infty}^{t} e^{-(t-t')/\tau}e_{ik}^{(1)}(t')dt', \qquad (1)$$

and to the dynamic viscosity η' and dynamic rigidity G' by the equation

$$\eta'-\frac{iG'}{\omega}=\int_0^\infty \frac{N(\tau)d\tau}{(1+i\omega\tau)}, \qquad (2)$$

where ω is the angular frequency.

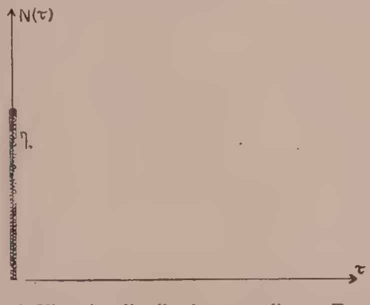

FIG. 1. Viscosity distribution according to Eq. (4).

This representation of the relaxation spectrum has the immediate advantage that some real significance can be given to the area under the curve which represents the spectrum graphically. In slow steady motion, Eq. (1) reduces to

$$p_{ik}'=2\int_0^\infty N(\tau)d\tau e_{ik}^{(1)}, \qquad (3)$$

and the area under the curve can therefore be identified with the limiting viscosity at small rates of shear η_0. Since η_0 is measured in many experiments, a normalizing condition is immediately imposed on the relaxation spectrum.

The main advantage of defining the distribution function in terms of the viscosity arises from the fact that the classical Newtonian liquid can now be represented pictorially on the spectrum. If η_0 is the constant Newtonian viscosity coefficient (having, of course, the same significance as the η_0 defined above, without the restriction on the rate of shear), the Newtonian liquid has a relaxation spectrum of the form

$$N(\tau)=\eta_0\delta(\tau), \qquad (4)$$

where δ is Dirac's δ function (Fig. 1). Any concentration of viscosity at relaxation times greater than $\tau=0$ will now represent elastic behavior.

In an earlier paper,[5] it was shown how idealized forms of the relaxation spectrum could be used to interpret experimental results concerning elasticoviscous liquids (notably the dilute polymer solutions investigated in the elastoviscometer of Oldroyd,

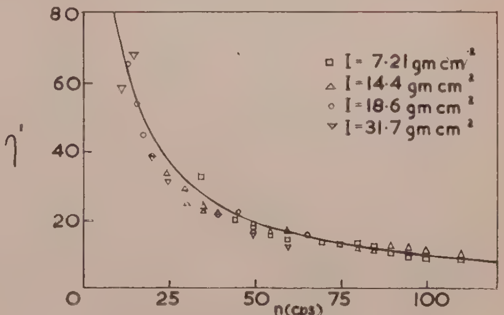

FIG. 2. Frequency dependence of η'. Theoretical curve for idealized spectrum (full line).

---

[1] R. Simha, J. Appl. Sci. 13, 201 (1942).
[2] R. Sips, J. Polymer Sci. 5, 69 (1950).
[3] D. Ter Haar, Physica 16, 719 (1950).
[4] A. J. Staverman and F. Schwarzl, *Die Physik der Hockpolymeren* (Springer-Verlag, Berlin, Germany, 1956), Vol. 4, Chap. 1.
[5] K. Walters, Quart. J. Mech. Appl. Math. 13, 444 (1960).

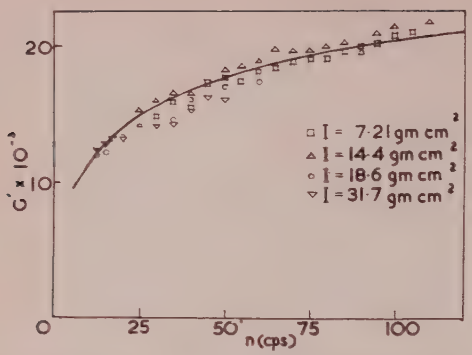

FIG. 3. Frequency dependence of G'. Theoretical curve for idealized spectrum (full line).

Strawbridge, and Toms[6]). This interpretation was complicated by the lack of phase lag results,[5,7] and the actual procedure involved the laborious comparison of families of theoretical amplitude ratio-frequency curves with the experimental curve. In the present paper, it is shown how this procedure is avoided and the interpretation of the experimental results greatly simplified when phase lag results are also available and it is possible to derive the dynamic viscosity and rigidity immediately from the experimental results.[7,8]

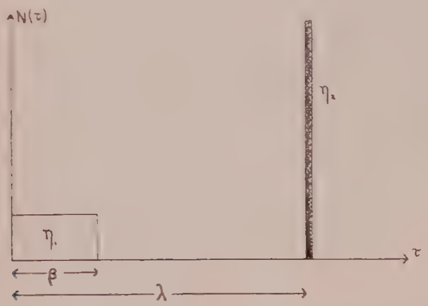

FIG. 4. Viscosity distribution according to Eq. (6).

2. INTERPRETATION OF EXPERIMENTAL RESULTS BY MEANS OF IDEALIZED RELAXATION SPECTRA

We consider a set of published experimental results for a 12.8% solution of Vistanex polyisobutylene B-140 in tetralin, of density 0.96 gm/cc.[9] The solution was investigated in the elastoviscometer of Markovitz and his collaborators in four experimental setups, corresponding to four different moments of inertia of the inner cylinder. No consideration was given to the motion resulting from steady rotation of the outer cylinder (cf. Oldroyd *et al.*[6]), and the limiting viscosity η_0 has to be determined from independent experiments. The lack of experimental results at low frequencies makes it impossible to determine η_0 from the slope of the amplitude ratio-frequency curve at the origin,[10] or by extrapolating the dynamic viscosity graph to zero frequency. However, η_0 can be identified with the falling ball viscosity, since this is obtained in what is essentially a zero shear-rate experiment. Using a $\frac{1}{32}$-in. stainless steel ball, Markovitz *et al.* obtained the value 14 900 poises for the solution in question in this type of experiment. This value can be used in the normalizing condition for the relaxation spectrum

$$\eta_0=\int_0^\infty N(\tau)d\tau. \qquad (5)$$

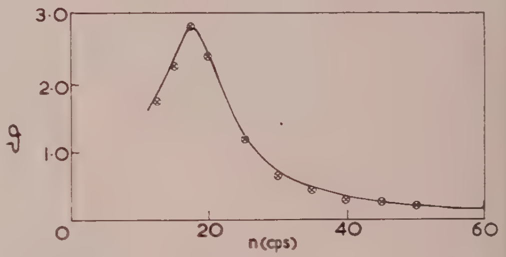

FIG. 5. Predicted (full line) and observed (⊗) relations between ϑ and n. ($I=18.6$ g cm²; $L=4.31$ cm; $K=140$ d cm/rad.)

In principle, it is possible to deduce the relaxation spectrum immediately from the dynamic data (Figs. 2 and 3), but the transformations involved require mathematical expressions for the experimental curves,[1 which is rarely possible in practice. However, the available dynamic viscosity and rigidity curves afford an excellent guide to the general shape of the relaxation spectrum.

Inspection of Figs. 2 and 3 reveals a considerable drop in the dynamic viscosity at quite low frequencies. Indeed, the value falls from 14 900 poises at zero frequency to approximately 80 poises at 10 cps. At the

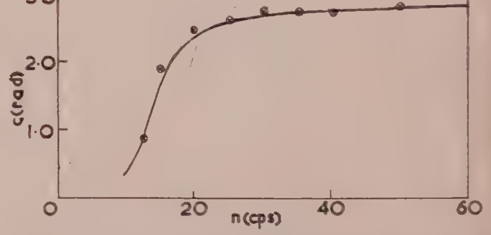

FIG. 6. Predicted (full line) and observed (⊗) relations between and n. ($I=18.6$ g cm²; $L=4.31$ cm; $K=140$ d cm/rad.)

---

[6] J. G. Oldroyd, D. J. Strawbridge, and B. A. Toms, Proc. Phys. Soc. (London) **B64**, 44 (1951).

[7] K. Walters, Quart. J. Mech. Applied Math. (to be published).

[8] H. Markovitz, J. Appl. Phys. **23**, 1070 (1952).

[9] H. Markovitz, P. M. Yavorsky, R. C. Harper, Jr., L. J. Zapas, and T. W. De Witt, Rev. Sci. Instr. **23**, 1070 (1952).

[10] B. A. Toms, *Rheology*, edited by F. R. Eirich (Academic Press Inc., New York, 1958), Vol. 2, Chap. 12.

[11] B. Gross, *Theories of Viscoelasticity* (Hermann & Cie, Paris France, 1953), p. 30.

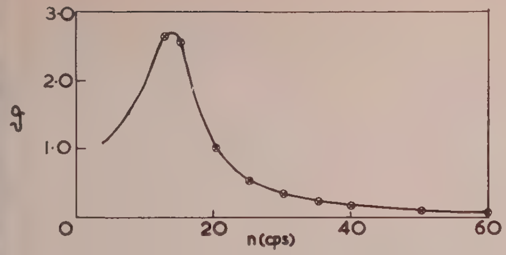

FIG. 7. Predicted (full line) and observed (⊗) relations between ϑ and n. ($I=31.7$ g cm^2; $L=4.60$ cm; $K=140$ d cm/rad.)

same time, the dynamic rigidity rises abruptly in the same frequency range and reaches a value of approximately 12 000 d/cm^2 at 10 cps. In terms of the relaxation spectrum, this implies that the majority of the viscosity is included in elements at a considerable distance along the time scale.

Further inspection of the dynamic data reveals a steady rise in dynamic rigidity at high frequencies and a corresponding decrease in dynamic viscosity. This implies at least one secondary element close to the origin of the relaxation spectrum contributing much less to the viscosity than the long time elements. Furthermore, the steady decrease in dynamic viscosity even at very high frequencies implies the absence of a significant Newtonian element at the origin of the relaxation spectrum.

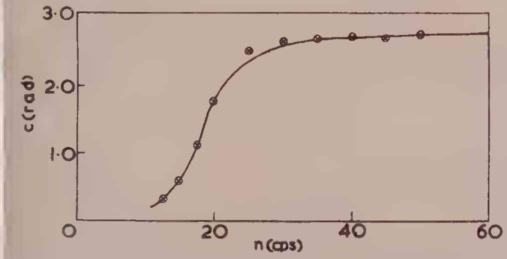

FIG. 8. Predicted (full line) and observed (⊗) relations between c and n. ($I=31.7$ g cm^2; $L=4.60$ cm; $K=140$ d cm/rad.)

With the above considerations as a guide, we are led to consider a spectrum consisting of a rectangle stretching from the origin in the (N,τ) diagram, and a Maxwell element at some distance along the time scale. Four constants $(\eta_1,\eta_2,\beta,\lambda)$ are needed to specify this spectrum, three only being independent on account of the normalizing condition. We take

$$\left.\begin{aligned}N(\tau)&=\eta_1/\beta\,(0\leqslant\tau\leqslant\beta),\\ N(\tau)&=\eta_2\delta(\tau-\lambda)\,(\tau>\beta),\end{aligned}\right\}\qquad(6)$$

where $\lambda\gg\beta$ (Fig. 4).

The values of the parameters corresponding to the solution under consideration can be chosen by plotting dynamic viscosity and rigidity curves for a series of values of the parameters and then comparing these graphs with the corresponding curves derived from experiment (Figs. 2 and 3). For the relaxation spectrum (6), the dynamic viscosity and rigidity are given by

$$\eta'=\eta_1\tan^{-1}\omega\beta/\omega\beta+\eta_2/(1+\omega^2\lambda^2),\qquad(7)$$

$$G'=\eta_1\log(1+\omega^2\beta^2)/2\beta+\eta_2\omega^2\lambda/(1+\omega^2\lambda^2);\qquad(8)$$

and, making the comparisons, the following values have to be assigned to the spectrum parameters to give agreement between theory and experiment for the solution under consideration:

$$\left.\begin{aligned}\eta_1&=130\text{ poises},\quad \eta_2=14\,700\text{ poises},\\ \beta&=0.0325\text{ sec},\quad \lambda=1.75\text{ sec}.\end{aligned}\right\}\qquad(9)$$

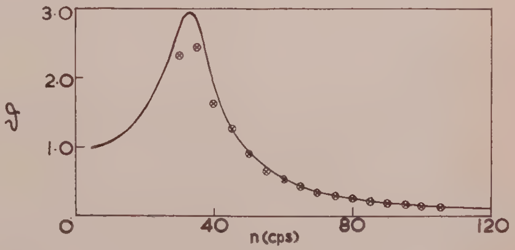

FIG. 9. Predicted (full line) and observed (⊗) relations between ϑ and n. ($I=7.21$ g cm^2; $L=4.80$ cm; $K=140$ d cm/rad.)

With these values, the limiting viscosity η_0 is given by

$$\eta_0=\int_0^\infty N(\tau)d\tau=14\,830\text{ poises},\qquad(10)$$

which is in satisfactory agreement with the falling ball viscosity (14 900 poises).

Figure 2 and 3 indicate the agreement between the theoretical dynamic viscosity and rigidity curves and those deduced from the experimental results. Having obtained this agreement, (ϑ,n) and (c,n)[12] curves can now be constructed from the proposed spectrum [(6) and (9)] and compared with the experimental curves, in order to illustrate formally that the spectrum is an alternative interpretation of the experimental

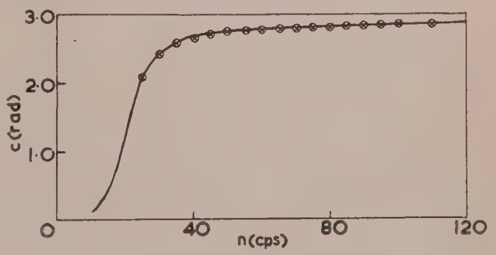

FIG. 10. Predicted (full line) and observed (⊗) relations between c and n. ($I=7.21$ g cm^2; $L=4.80$ cm; $K=140$ d cm/rad.)

---

[12] ϑ and c are the amplitude ratio and phase lag, respectively, and n is the frequency in cycles/sec. In Figs. 3–10, I is the moment of inertia the inner cylinder about its axis, L is the length of the annular gap, and K the restoring constant of the torsion wire.

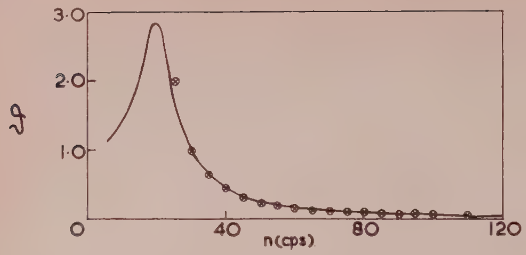

FIG. 11. Predicted (full line) and observed (⊗) relations between ϑ and n. ($I=14.4$ g cm^2; $L=4.08$ cm; $K=140$ d cm/rad.)

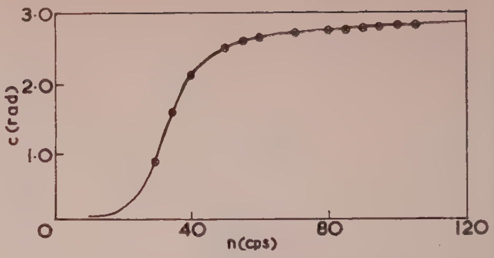

FIG. 12. Predicted (full line) and observed (⊗) relations between and n. ($I=14.4$ g cm^2; $L=4.08$ cm; $K=140$ d cm/rad.)

results. Figures 5–12 illustrate the excellent agreement between the predicted curves and the observed results for both amplitude ratio and phase lag in four different experiments. The agreement between theory and experiment is thought to be well within experimental accuracy, estimated from the variation in the original dynamic viscosity and rigidity results (Figs. 2 and 3).

Although the idealized spectrum shows agreement with experiment in respect of both amplitude ratio and phase lag (cf. Walters[5]), the interpretation is not free from ambiguity. No experimental results were available for frequencies less than 10 cps, and as a consequence, the long time end of the spectrum cannot be defined with any precision. The most we can say is that, at a point on the relaxation time scale near $\tau=1.75$ sec there is a large concentration of viscosity, which, a far as the experiments of Markovitz *et al.* are concerned is adequately described by a Maxwell element. Thi lack of resolution in the spectrum is due entirely to th limited frequency range which was observed.

ACKNOWLEDGMENT

The author wishes to express his gratitude to Dr. H Markovitz for allowing him access to his experimenta results.

JOURNAL OF APPLIED PHYSICS VOLUME 32, NUMBER 10 OCTOBER, 196

Calculations of the Thermoelectric Parameters and the Maximum Figure of Merit for Acoustical Scattering

LOUIS R. TESTARDI
The Franklin Institute Laboratories, Philadelphia, Pennsylvania

(Received May 3, 1961)

The calculations of Chasmar and Stratton [R. P. Chasmar and R. Stratton, J. Electronic and Control **7**, 52 (1959)] for the determination of the maximum thermoelectric figure of merit are extended for the case of acoustical scattering. Graphical data are presented for the determination of the material parameter, the optimum values of several quantities, and the degradation of the figure of merit for nonoptimum conditions. The variations of the Seebeck coefficient and the electrical conductivity computed from exact statistics are compared with experimental results for several alloys of thermoelectric interest. Good agreement is found except for high electrical conductivities. Other anomalies are noted.

INTRODUCTION

THE maximization of the performance of a thermoelectric device from thermodynamic principles shows that, for a thermoelement at the operating temperature, the quantity $z=S^2\sigma/\kappa$ should be as large as possible.[1] The Seebeck coefficient S, the electrical conductivity σ, and the thermal conductivity κ, are not, however, internally constrained in any way from thermodynamics alone. Semiconductors now represent the principal searching ground for materials of higher figure of merit z. In part, their merit lies in that th parameters S, σ, and κ can be varied by the additio of impurities (doping agents) thereby allowing a optimization of z for a given material. In practice, thi additional latitude gives rise to the necessity of dopin studies to establish the maximum figure of merit fo the material; in principle, the maximum figure of meri is formally determined on writing the constrain relations among the thermoelectric parameters fro transport theory. For an extrinsic semiconducto numerical solutions of the transport equations can b obtained if specific assumptions are made for the for of the relation between energy and wave vector an between relaxation time and wave vector for the charge carriers. The maximum figure of merit on doping can then be related to parameters characterizing the nondegenerate properties of the material, and the sets of S, σ, and κ for the material at any extrinsic doping level can be generated from these parameters by varying the position of the Fermi level. Under the above assumptions, the material parameters can be determined from a single known set of S, σ, and κ for an extrinsic semiconductor in an unknown state of doping. It thus results that the knowledge of the thermoelectric parameters of one specimen determines its complete, extrinsic, doping behavior insofar as the method by which the Fermi level is varied in practice does not affect a breakdown of the conditions initially assumed to make the solution tractable.

---

[1] A. F. Ioffe, *Semiconductor Thermoelements and Thermoelectric Cooling* (Infosearch, London, 1957).

THE TRANSPORT EXPRESSIONS

We consider the case of an extrinsic semiconductor with spherical-constant energy surfaces whose charge carriers have a relaxation time τ of the form $\tau \propto \epsilon^{-\frac{1}{2}}$ (acoustical scattering), where ϵ is the kinetic energy. For this case, it can be shown that[2]

$$S=(\pm)\frac{k}{e}\left[\frac{2F_1(\eta)}{F_0(\eta)}-\eta\right], \tag{1}$$

$$\sigma=ne\mu, \tag{2}$$

$$\mu=\frac{\pi^{\frac{1}{2}}F_0(\eta)}{2F_{\frac{1}{2}}(\eta)}\mu_0, \tag{3}$$

$$n=4\pi^{-\frac{1}{2}}(2\pi m^*kT/h^2)^{\frac{3}{2}}F_{\frac{1}{2}}(\eta), \tag{4}$$

$$\kappa=\kappa_g+\Lambda\sigma T, \tag{5}$$

$$\Lambda=\frac{3F_0(\eta)F_2(\eta)-4F_1^2(\eta)}{F_0^2(\eta)}\left(\frac{k}{e}\right)^2, \tag{6}$$

where n is the carrier concentration, m^* the density of states effective mass, e the electronic charge, μ and μ_0 the conductivity mobilities in the actual and nondegenerate states, respectively, κ_g the lattice thermal conductivity, Λ the Lorenz number, and T the absolute temperature. $F_r(\eta)$ is the Fermi-Dirac integral of order r and η is the Fermi level in units of kT measured from the band edge and taken as negative in the energy gap and positive in the band. The assumptions of spherical energy surfaces and acoustical scattering have entered into Eqs. (1), (3), (4), and (6) while Eq. (5) assumes further that the thermal conductivity is composed of lattice and Lorenz electronic contributions only.

The thermoelectric figure of merit z may then be expressed in the form

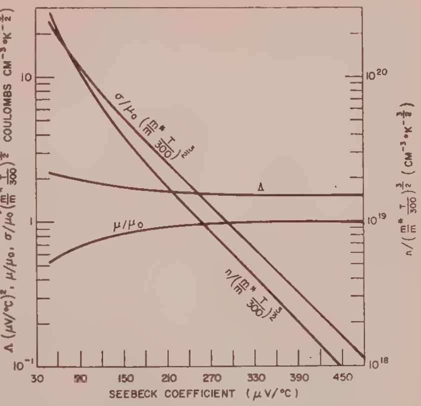

FIG. 1. Curves for obtaining material parameter and other quantities from Seebeck coefficient.

$$z\left(\frac{T}{300}\right)=\frac{S^2(\eta)}{[2eM(2\pi mk300/h^2)^{\frac{3}{2}}F_0(\eta)]^{-1}+300\Lambda}. \tag{7}$$

The figure of merit is a function of the material parameter $M=\mu_0(m/m^*)^{\frac{3}{2}}(T/300)^{\frac{5}{2}}/\kappa_g$ and the reduced Fermi level η, while the maximum figure of merit $z_{\max}$, is determined by M alone. For various values of η, Eqs. (1), (3), (4), (6), and (7) (here, also for various M) have been solved numerically with an electronic computer, and the results are given in Figs. (1) and (2).

DISCUSSION OF CALCULATIONS

Chasmar and Stratton,[3] departing from a material parameter[4] similar to M, have obtained the maximum figure of merit for a number of scattering laws. For the case of acoustical scattering, the value of the Seebeck coefficient uniquely determines the quantities Λ, and $\sigma/\mu_0(Tm^*/300m)^{\frac{3}{2}}$ according to Fig. 1. Thus, from the measurements of S, σ, κ and T in the extrinsic state, and Eq. (5), one can obtain the values for $\mu_0(m^*/m)^{\frac{3}{2}}(T/300)^{\frac{5}{2}}$ and κ_g from which $z_{\max}$ can be determined using Fig. 2.

The solution of Eq. (7) for $z_{\max}$ also gives the values of S and η at $z_{\max}$ and these are presented in Fig. 3. The optimum value of η also determines the ratio $n/(Tm^*/300m)^{\frac{3}{2}}$ at $z_{\max}$ and this quantity appears in Fig. 2. Since, in the as-grown state, the ratio $n/(Tm^*/300m)^{\frac{3}{2}}$ is determined by the value of the Seebeck coefficient (see Fig. 1), the fractional change in the carrier concentration to reach optimum doping can be computed.

In the preparation of thermoelectric materials by slow directional freezing, the thermoelectric parameters

---

[2] A. H. Wilson, *The Theory of Metals* (Cambridge University Press, New York, 1953), 2nd ed., pp. 12, 196–204.

[3] R. P. Chasmar and R. Stratton, J. Electronics and Control **7**, 52 (1959).

[4] The material parameter of Chasmar and Stratton $\beta=0.8952\times10^{-5}M$.

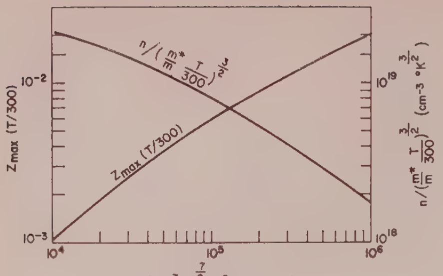

FIG. 2. $z_{max}(T/300)$ and optimum value of $n/(Tm^*/300m)^{\frac{3}{2}}$ vs material parameter $M=\mu_0(m^*/m)^{\frac{3}{2}}(T/300)^{\frac{5}{2}}/K_g$.

are often markedly dependent upon the position along the ingot and the exact optimum conditions may prevail only for a vanishingly short segment. Figure 4, obtained from the numerical solution of Eq. (7), indicates what fractional departure is S or n from their optimum values will reduce the z to $0.9z_{max}$. The degradation of z on the degenerate and nondegenerate sides of optimum doping are approximately symmetrical for the case chosen. The very slow fall in z as S or n departs from the optimum value, of course, allows a greater portion of an inhomogeneous ingot to be utilized, but also indicates that the detrimental effects of minority carriers (through ambipolar diffusion and the reduction of the Seebeck coefficient) may be reduced by lowering the Fermi level down the degenerate side of optimum doping. With all nondegenerate properties given for a particular material, the magnitude of the minority carrier effects depends only on the position of the Fermi level. By operating at the $z=0.9z_{max}$ point, the increase in η (computed from Fig. 3) leads to an exponential reduction in the number of minority carriers and it may then be determined if the actual z has been improved.[3]

For acoustical scattering, the maximum value of $S^2\sigma$ occurs for $\eta\approx+0.65$. At this point,

$$S\approx167\ \mu v/°C,\quad n/(Tm^*/300m)^{\frac{3}{2}}\approx3.1\times10^{19}/cm^3$$

and $\sigma\approx4.3\mu_0(Tm^*/300m)^{\frac{3}{2}}$. For maximum heat pumping capacity the optimum doping level may more nearly coincide with that giving the maximum value in $S^2\sigma$ than z_{max}. Figure 4 shows the fractional reduction in z from the value at z_{max} which occurs for the operation at $(S^2\sigma)_{max}$. The curve also indicates the importance of a sensitive as well as accurate method for the measurement of the thermal conductivity.

Note added in proof. For $M\rightarrow\infty$, z is limited by the minority carrier reduction of S and ambipolar diffusion. Setting $E_g/kT=E_g'$ (reduced energy gap) and $r=(\mu_0m^{*\frac{3}{2}})_p/(\mu_0m^{*\frac{3}{2}})_n$, an approximate (∼5%) expression for z_{max} in this case is

$$z_{max}\left(\frac{T}{300}\right)=10^{-3}[0.115E_g'^{2.25}+1]\left[1+\frac{7.5(1-r)^2}{E_g'}\right]^{\mp1}$$

(+ and − for p- and n-type thermoelements, respec tively) in the range $5\leq E_g'\leq80$ and $1\leq r\leq10$.

APPLICATION OF THE CALCULATIONS

The procedure outlined above for the determinatio of the maximum figure of merit bears, of course, severa shortcomings. For a new material one generally wi not know the scattering law, the band structure, c whether the specimen under test is truly extrinsic. Th inhomogeneity along the ingots of present day materia may often be used to determine the latter, and, in th case of extrinsic conduction, may also lead to a know edge of the scattering law when the above calculation are extended to other scattering laws. Band structure other than simple spherical, need not alter the validit of the calculations based on a simple spherical band the expressions for S and Λ can be reduced to the form given in Eqs. (1) and (6) and the functional dependen on η of Eq. (2) is not changed; though in anisotrop materials the calculations will pertain to the crystallin direction in which M was obtained.

The solution of Eq. (7) by numerical methods al leads to sets of S and z which, themselves, unique determine z_{max} and M. Thus, it is possible from measurement of S and z in an extrinsic semiconductor deduce z_{max} directly, without obtaining the materi parameter. The factor $\mu_0(m^*/m)^{\frac{3}{2}}$, however, ca generally be obtained with greater accuracy and ea than κ_g. In addition, ambipolar diffusion may invalida Eq. (5) before appreciable reductions in the Seebe coefficient from mixed conduction are observed. T separate determinations of $\mu_0(m^*/m)^{\frac{3}{2}}$ and κ_g should gi a more lucid indication of the validity of the assum tions in this analysis and a better estimate of t maximum figure of merit.

The calculations have been applied to p-type co positions in the $Bi_2Te_3-Sb_2Te_3$ pseudo-binary all system. The temperature dependences of S and observed in this laboratory have been found to be satisfactory accord with the assumptions of acousti scattering and a band structure of the type propos by Drabble[5] for Bi_2Te_3. The behavior of the therm electric properties with doping at room temperatu has been studied for several compositions. The resu

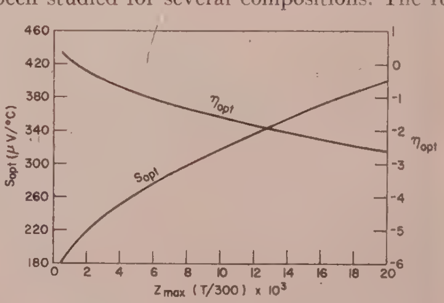

FIG. 3. Optimum values of S and η vs $z_{max}(T/300)$.

---

[5] J. R. Drabble, Proc. Phys. Soc. (London) **72**, 380 (1958).

r the alloy $70\%Sb_2Te_3+30\%Bi_2Te_3$ shown in Fig. 5[6] gree substantially with the variations predicted by Eqs. (1)–(4) for a material with the factor $\mu_0(m^*/m)^{\frac{3}{2}}$ = 325 cm²/v sec. (Within the experimental error, the observed thermal conductivities were also in agreement with predicted behavior). The discrepancy for $S<110$ v/°C may arise as the effects of a band structure which is more complicated than the simple form ssumed. With the large density of states effective mass usually required for a good thermoelectric material, the tates of partial degeneracy are reached only with the inclusion in the sample of large numbers of impurities or defects. The possibility of consequent new scattering mechanisms or impurity band conduction increases and the analysis may not be adequate here.

The substitution of the inhomogeneity along a owered ingot for otherwise discriminately doped amples has been found successful, at least in the case when adjacent samples have Seebeck coefficients which differ by about 10%–15%. In this manner, it is possible o observe variations in the factor $\mu_0(m^*/m)^{\frac{3}{2}}$ of ingots grown in different manners. Smaller variations in this actor (~5%–10%) are also found in ingots prepared n (ostensibly) identical manners.

The calculated value of $z_{\max}$ for the p-type alloy $0\%Sb_2Te_3+30\%Bi_2Te_3$ is found to be $2.4\times10^{-3}(°K)^{-1}$ o $2.6\times10^{-3}(°K)^{-1}$ which is in good agreement with xperimental observations.

The measured values values of S and σ for the n-type lloy $70\%Bi_2Te_3+30\%Bi_2Se_3$ are also shown in Fig. 5. Although the iodine doped alloys of this composition eemed to exhibit acoustical scattering, the substitution of Cu_2Br_2 for the iodine led to several anomalies. nitially, the figures of merit obtained with the Cu_2Br_2 doping agent were higher than those obtained with odine, but the variations of the thermoelectric arameters were not consistent with acoustical scatterng and the parameters were later found to be markedly unstable on aging. Other anomalous behaviors have been reported for this composition.[7,8] Figure 5 also shows the theoretical variations of S and σ for the scattering laws $\tau\propto\epsilon^{-\frac{3}{2}}$, $\tau\propto\epsilon^{-\frac{1}{2}}$, and $\tau\propto\epsilon^{+\frac{1}{2}}$. At least on the degenerate side of optimum doping, the variations in S and σ over the experimental range are reasonably distinct in the three cases.

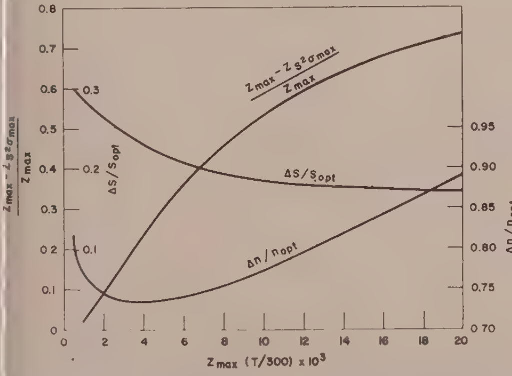

FIG. 4. Curves of degradation in z for nonoptimum conditions. $\Delta S/S_{\rm opt}=|S_{\max}-S0.9z|_{\max}/Sz_{\max}$, $\Delta n/n_{\rm opt}=|nz_{\rm opt}\delta-n0.9z_{\max}|/$ $z_{\max}$.

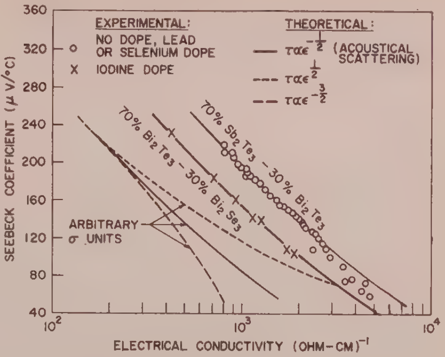

FIG. 5. Doping curves of Seebeck coefficient and electrical conductivity for two alloys.

CONCLUSIONS

The use of exact statistics to calculate a maximum figure of merit from a known set of thermoelectric parameters of an extrinsic semiconductor may be of limited utility without a knowledge of the band structure or scattering mechanism. Plausibility arguments established from other material properties may be substituted in lieu of this ignorance, and it may also occur that the result is not too sensitive to some variation of the unknown parameters. In practice, several samples in different states of degeneracy will generally be prepared (or available from an inhomogeneous ingot) and it can be determined if the calculations are applicable for a given scattering law. The results from several alloys of thermoelectric interest have been found to confirm the assumptions on which our calculations have been based if the specimens are not too degenerate. In this case the calculations may be of further use in the comparison of thermoelectric materials prepared in different manners and different as-grown states of degeneracy, and in providing some information of the processes involve in aging, irradiation, or diffusion in these materials.

ACKNOWLEDGMENTS

The author is indebted to Dr. F. J. Donahoe for his advice and review of the manuscript, G. Mc Connell for assistance in the measurements, and the sponsors of The Thermoelectric Effects Program for their financial support.

---

[6] Measurements made with the current flowing in the cleavage lanes.

[7] N. Fuschillo, J. N. Bierly, and F. J. Donahoe, J. Phys. Chem. Solids **8**, 430 (1959).

[8] I. G. Austin and A. Sheard, J. Electronics **3**, 236 (1957).

JOURNAL OF APPLIED PHYSICS VOLUME 32, NUMBER 10 OCTOBER, 196

Experimental Study of the Interrelation between the Theory of Dislocations in Polycrystalline Media and Finite Amplitude Wave Propagation in Solids

JAMES F. BELL
The Johns Hopkins University, Baltimore 18, Maryland

(Received April 10, 1961; in final form, June 19, 1961)

By use of experimental data from a large number of free flight impact tests involving diffraction grating measurement of strain, a detailed and very close experimental verification is given for the G. I. Taylor theory of dislocations in polycrystalline annealed aluminum. Applying the finite amplitude wave theory, with a theoretical parabolic stress-strain curve obtained from dislocation theory, experimental and theoretical correlations within approximately 1% are obtained for the velocities of strain propagation, maximum strain, largest distance of penetration of maximum strain, dynamic stress levels in the first diameter, time of contact, coefficient of restitution, mushrooming in the first diameter, and an energy balance before and after impact. Variations in the plastic wave development and dynamic stress behavior below the Karman critical velocity are considered theoretically and experimentally in terms of a difference in the initial elastic reflection behavior below the critical velocity. Plastic deformation is found to be independent of strain rate, even at experimentally determined values of 2000 in./in./sec. Initial shock fronts exceeding the dilatational velocity are experimentally identified near the impact face. The subsequent development of dispersive plastic wave fronts following the passage of the initial shock, also are found to be in accordance with predictions based upon dislocation theory. The equipartition of energy in the vicinity of the impact face has been found to be related to the reflection behavior of these initial shock fronts at the lateral surface of the rod.

INTRODUCTION

DURING the last two years, this writer has carried out over 400 free flight compression impact tests in several metals, nearly 300 of these tests having been in annealed aluminum. The majority of the measurements have involved the writer's diffraction grating method[1–3] for the determination of strain and surface angle. Other tests using a different optical method have included the measurement of time of contact, coefficient of restitution, and particle velocity versus time at many positions along the specimen (including the free end), and load bar measurements of the stress at the impact face. Low level strain measurements have been made in the vicinity of the free end of the struck specimen, using wire resistance strain gauges.

The reason for conducting such a large number of diffraction grating measurements at each of many positions along the entire length of the specimen has been that, although maximum strains are very closely reproducible for a given impact velocity, variations in strain arrival time are observed from one test to another. In a recent paper,[4] it has been shown that these variations are connected with the development of the dispersive plastic wave from nondispersive wave fronts in the immediate vicinity of the impact face. The close correlation between experiment and theory, reported upon in the present paper, is a consequence of the averaging of this large amount of data.

In a recent series of papers,[4–6] this writer has shown experimentally that the finite amplitude theory of one-dimensional wave propagation may be used for th
study of plastic wave propagation in annealed alum
num. Velocities of strain propagation are found to b
constant, as predicted, and relatively close to valu
obtained from the slopes of the static stress-strain curv
Using these experimental propagation velocities, a
excellent check has been obtained for the theoretic
maximum strain for several different impact velociti
Recently it has been shown[4] that the dynamic stre
levels first experimentally observed by others[7–9] ma
be computed directly from a nondispersive shock theo
using the static stress-strain curve. It was furth
shown[4] that this initial nondispersive front develops
two sections from an equipartition of energy into t
deviatoric and dilatational components. The prese
writer also has shown[6] that the time of contact, c
efficient of restitution, and an energy balance dete
mined from the strain rate independent finite amplitu
wave theory were in excellent agreement with expe
mental results.

In a paper recently submitted for publication, th
writer has extended E. H. Lee's[10] theoretical treatme
of the progressive absorption of the initial reflect
elastic front, to cover some aspects of the entire u
loading phenomenon, so that times of contact, c
efficients of restitution, and particle displacement m
be determined theoretically. All these latter results ha
been verified experimentally, including an earlier[6]
perimental correlation with the prediction of the a
sorption of the initial elastic reflected front.

The purpose of the above review of the experimen
results recently obtained by this writer is to show th
the essential order which had been observed step by s

---

[1] James F. Bell, J. Appl. Phys. 27, 10 (1956).

[2] James F. Bell, Proceedings of the 3rd U. S. National Congress of Applied Mechanics (June, 1958).

[3] James F. Bell, Proc. Soc. Exptl. Stress Anal., 17, No. 2 (1959), pp. 51–64.

[4] James F. Bell, J. Appl. Phys. 31, 12 (1960).

[5] James F. Bell, J. Appl. Phys. 31, 2 (1960).

[6] James F. Bell, J. Mech. and Phys. Solids 9, 1 (1961).

[7] J. E. Johnson, D. S. Wood, and D. S. Clark, J. Appl. Me
20, 4 (1953).

[8] J. D. Campbell, J. Mech. and Phys. Solids 1 (1952–53).

[9] E. T. Habib, J. Appl. Mech. 15, 3 (1948).

[10] E. H. Lee, Quart. Appl. Math. 10, 4 (1953).

is found to stem from the applicability of a parabolic stress-strain law developed from dislocation theory in 1934 by Sir Geoffrey Taylor.[11]

THE PARABOLIC STRESS-STRAIN LAW

From a series of experiments on single crystals in the early 1930's Taylor proposed a theory of dislocations as the underlying mechanism of plastic deformation. This theory, which was developed for the fcc single crystals of aluminum, copper, and gold, predicted that the shear stress-shear strain relation along the slip plane would be parabolic.

$$\tau=\beta_s\gamma^{\frac{1}{2}}, \tag{1}$$

where β_s was determined from single crystal measurements. For aluminum, Taylor obtained

$$\tau=5.51\times10^3\gamma^{\frac{1}{2}}\text{ psi}. \tag{2}$$

For the single crystal, the normal stress σ and increment of normal strain $d\epsilon$ are related to the corresponding shear stress τ and increment of shear strain $d\gamma$ by

$$\sigma/\tau=m=d\gamma/d\epsilon, \tag{3}$$

where m is a factor depending upon the orientation of the slip plane upon which the shear stress τ acts. For a polycrystalline aggregate made up of randomly oriented single crystals, Taylor has obtained a relation

$$\sigma/\tau=\bar{m}=d\gamma/d\epsilon, \tag{4}$$

where $\bar{m}$ now includes the summation for the polycrystalline aggregate. Taylor's value for $\bar{m}$ for aluminum is 3.06. Bishop and Hill,[12] who have treated this problem from the point of view of the theory of plasticity, also have obtained a value of $\bar{m}$ of 3.06.

From Eqs. (4) and (2), we have

$$\sigma=\bar{m}\times5.51\times10^3(\bar{m}\epsilon)^{\frac{1}{2}}\text{ psi} \tag{5}$$

or

$$\sigma=\bar{m}^{\frac{3}{2}}\times5.51\times10^3\epsilon^{\frac{1}{2}}\text{ psi}. \tag{6}$$

Substituting the value of $\bar{m}$, this equation is

$$\sigma=2.98\times10^4\epsilon^{\frac{1}{2}}\text{ psi}. \tag{7}$$

In order to see whether this writer's experimental results would give agreement with the Taylor theory, the velocities of strain propagation

$$c_p=\left(\frac{\partial\sigma}{\partial\epsilon}\bigg/\rho\right)^{\frac{1}{2}} \tag{8}$$

were experimentally determined by averaging propagation times for a very large number of diffraction grating tests between one and four diameters, where, as has been shown earlier,[5] the finite amplitude theory of wave propagation applies.

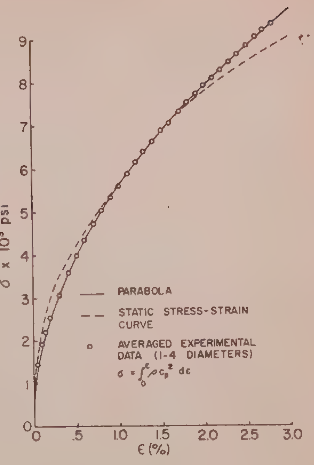

FIG. 1. A comparison of the experimental parabola and the static stress-strain curve.

Having these c_p's, the stress-strain relation may be determined by Eq. (9)

$$\sigma=\int_0^\epsilon\rho c_p{}^2d\epsilon. \tag{9}$$

In Fig. 1 is shown a stress-strain curve calculated from the experimental data, using Eq. (9). A parabolic fit to this experimental stress-strain curve was found. It is given by Eq. (10):

$$\sigma=5.60\times10^4\epsilon^{\frac{1}{2}}\text{ psi}, \tag{10}$$

which is numerically different from Taylor's curve for polycrystalline aluminum of Eq. (7).

One interesting aspect of Eq. (10) is its close fit to the data. It is not possible to change the power of $\frac{1}{2}$ by ±0.01, or to change the coefficient by as much as ±0.05 and obtain a fit over the length of the curve between 0.2%–2.8% strain.

If Eq. (10) is compared with Eq. (7) of Taylor for the single crystal, $\bar{m}$ is found to be 4.65 instead of the Taylor value of 3.06. In Fig. 2, a dynamic parabolic

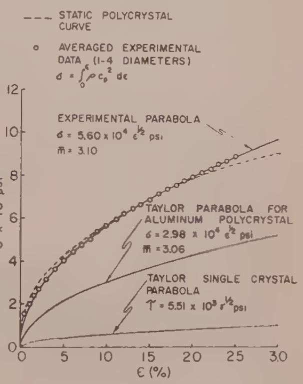

FIG. 2. The single-crystal and polycrystalline parabolas for annealed aluminum.

---

[11] *The Scientific Papers of Sir Geoffrey Ingram Taylor*, edited by G. K. Batchelor (Cambridge University Press, New York, 1958), Vol. 1, Nos. 21, 22, 27, 41.

[12] J. F. W. Bishop and R. Hill, Phil. Mag. **XLII**, 414 and 1298 (1951).

polycrystalline stress-strain curve is compared with the static polycrystalline stress-strain curve and with the experimental values of Fig. 1, as well as with the Taylor parabolas for polycrystalline aluminum, Eq. (7), and for single crystals of aluminum, Eq. (2).

If the experimental single-crystal parabola of Taylor is used as a basis for determining the theoretical polycrystalline stress-strain curve, it is necessary to make the unlikely assumption that all polycrystalline grains deform by single slip. Pond and Harrison[13] have studied the compression of aluminum single crystals including the phenomenon of duplex slip, a phenomenon more likely to be present in the polycrystalline situation. Figure 3 reproduces the Pond and Harrison stress-strain curve for their test No. 2–15. The initial 2.5% of strain is a region of single slip; the abrupt change of slope, and subsequent higher stress levels, inaugurates a region of duplex slip. The solid line of Fig. 3 is a parabola fitted to these data by the present writer.

Since Pond and Harrison have given the x-ray diffraction data on this test, the resolved shear stress and shear strain curve may be determined. The curve determined from the x-ray diffraction data from Eq. (3) is shown in Fig. 4, where

$$m=1/(\cos\phi\,\cos\lambda), \qquad (11)$$

where ϕ is the angle between the specimen axis and the normal to the slip plane, and λ is the angle between the specimen axis and the direction of slip on the slip plane. The parabola fitted to the resolved shear stress-strain curve, shown as the solid line in Fig. 4, is given in Eq. (12).

$$\tau=9.80\times10^3\gamma^{\frac{1}{2}}. \qquad (12)$$

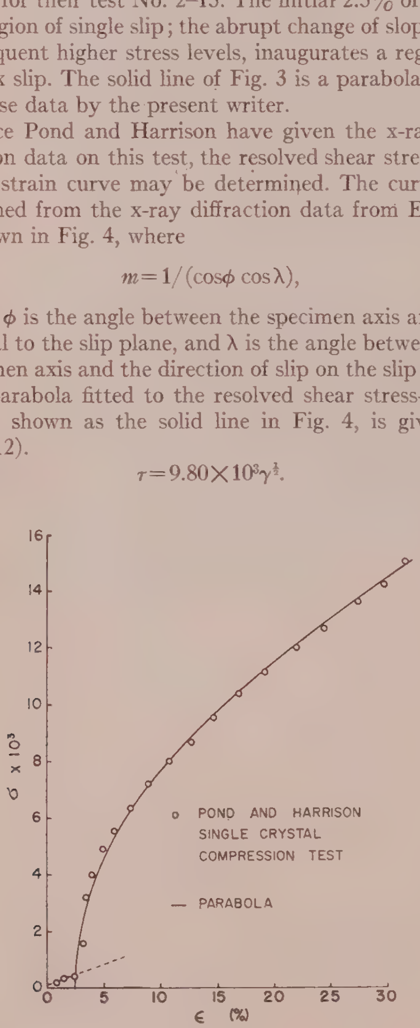

FIG. 3. Pond and Harrison compression test for single crystal of aluminum (purity: 99.99+).

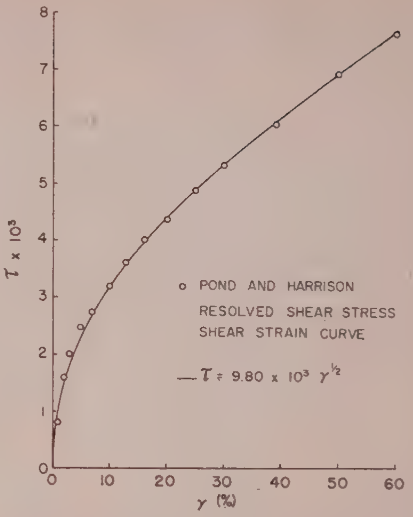

FIG. 4. Resolved shear stress-shear strain determined from singl crystal compression test of Pond and Harrison.

Thus, in place of Eq. (6) for the Taylor data, we hav

$$\sigma=\bar{m}^{\frac{3}{2}}\times9.80\times10^3\epsilon^{\frac{1}{2}}. \qquad (13$$

A comparison of Eq. (13) with the experimental polycrystalline parabola of Eq. (10) gives an $\bar{m}$ of 3.18 This result, which is in good agreement with th Taylor[11] and Bishop and Hill[12] upper bound of $\bar{m}=3.06$ indicates that the Taylor theory of the polycrystallin aggregate may be used to determine a theoretica dynamic polycrystalline stress-strain curve, providin the single-crystal experimental data is obtained from the parabola associated with duplex slip.

It should be emphasized at this point that the experimental verification of the Taylor theory given her is between single-crystal measurements and *dynami* plastic measurements. The static polycrystalline stress strain curve (as may be seen in Fig. 5) follows th theoretical polycrystalline parabola to about 2% strai and then, probably due to a developing anisotropy moves over to the theoretical polycrystalline parabol derived from single slip, single-crystal measurements Although the present writer's static polycrystallin curve of Fig. 5 is for strains up to only 7.5%, at highe strain levels the experimental results of Taylor hav indicated that the polycrystalline curve crosses th lower parabola at approximately 15% strain. As shown later, in Fig. 12, the dynamic data follows th parabola and not the static stress-strain curve, at leas to strains to 3.5%.

It has been found empirically that, in both anneale aluminum and annealed copper it is possible to determine the polycrystalline dynamic stress-strain parabol from single crystal, single slip tests of the type give by Taylor,[11] by Schmid and Boaz,[14] or by a compression stress-strain curve in a one-inch diameter, three-inch long single crystal test of the present writer. These single crystal stress-strain curves are in fair numerical agreement, and all may be represented by parabolic curves.

---

[13] R. B. Pond and Eleanor Harrison, Trans. Am. Soc. Metals **50**, 994 (1958).

It is pointed out above that, in the determination of $\bar{m}$ from the comparison of Eqs. (6) and (10) from the Taylor single crystal data, $\bar{m}$ was 4.65; 4.65 is $\frac{3}{2}\times 3.10$, or $\frac{3}{2}\bar{m}$, where, here, $\bar{m}$ no longer represents the value of 4.65 but is equal to 3.10. It would seem significant that in copper, with different numerical values, a comparison of a polycrystalline parabola determined from dynamic measurements, with single crystal, single slip data, also gives a value of $\frac{3}{2}\bar{m}$, if $\bar{m}$ is considered to be 3.10 instead of 4.65.

All these measurements are for the situation of uniaxial stress, for which one would have an axial deviatoric stress component of $\frac{2}{3}\sigma_x$ with lateral deviatoric stress components of $-\frac{1}{3}\sigma_x$ combined with a hydrostatic state of stress with components $\sigma_x/3$. It has seemed to the present writer that one would have to add an effective hydrostatic component if one were comparing the polycrystalline aggregate with the single crystal, single slip measurements in which the slip plane extended across the entire cylindrical specimen. It would not be necessary to introduce this hydrostatic component for single crystal measurements involving duplex slip. For duplex slip measurements, the uniaxial stress situation experimentally contains the hydrostatic component since the acting slip planes terminate in a complex fashion in the interior of the specimen. If this assumption for the situation of single slip, single crystal measurements is made, then the σ of Eq. (4) is replaced by the deviatoric component $\frac{2}{3}\sigma$ and the γ of Eq. (4) is replaced by $\frac{2}{3}\gamma$, and Eq. (5) becomes

$$\sigma=(\tfrac{3}{2}\bar{m})^{\frac{3}{2}}\times 5.51\times 10^{3}\epsilon^{\frac{1}{2}}, \qquad (14)$$

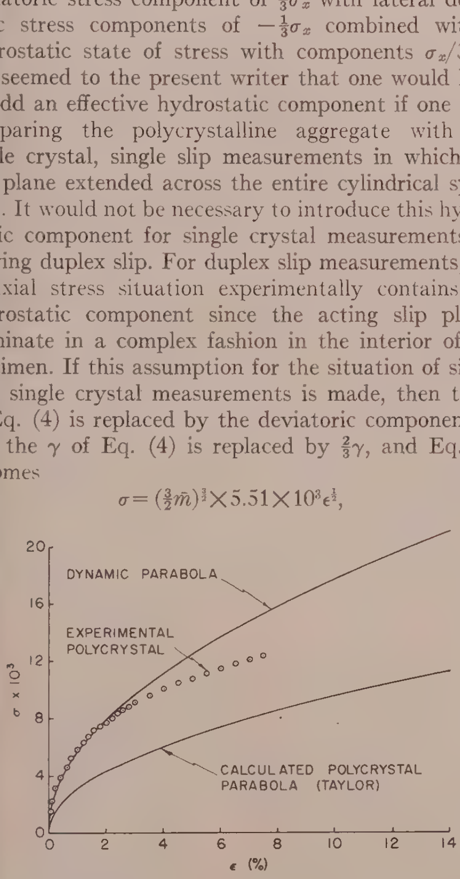

FIG. 5. Dynamic parabola (upper solid line) which agrees with theoretical curve determined from duplex slip, and parabola for polycrystalline aggregate (lower solid line) determined from single slip data, both compared with static stress-strain curve of polycrystalline aggregate (circles).

which for $\bar{m}=3.10$ gives the experimentally determined polycrystalline parabola of Eq. (10). As was pointed out above, similar results have been obtained in annealed copper.

Thus, the duplex slip parabola of Eq. (12) may be determined from the single slip parabola by adding a hydrostatic component to Eq. (2) in the form of Eq. (14).

A complete energy treatment should note that the actual axial strain ϵ is given by $\epsilon_x=e_x+\Delta/3$, where Δ is the dilatation and e_x is the axial deviatoric strain. The dilatational energy may be obtained from the bulk modulus of the material. For an impact velocity of 800 in/sec, for example, it constitutes approximately 0.3% of the total energy for the situation of uniaxial stress, with 99.7% of the energy in the deviatoric plastic strain. The axial strain component $\Delta/3$ corresponds to 85 μ in./in., which is very small when compared to the maximum strain of 22 000 μ in./in. for this impact velocity.

Thus it has been shown that a polycrystalline stress-strain parabola, developed from the Taylor theory, is in remarkably close agreement with experimental predictions from a large number of diffraction grating tests. In what follows it will be shown, further, that the Taylor parabola may be used to provide a very close check between experiment and finite amplitude wave theory for all of the many details of plastic wave propagation presented earlier by Bell.[4–6]

FINITE AMPLITUDE WAVE PROPAGATION

An important aspect of the correlation shown above between the theoretical and the experimental stress-strain curves in polycrystalline aluminum, is the complete absence of any strain rate effects. Between one and four diameters, the experimental velocities of strain propagation used in Eq. (9) have been shown earlier[5] to be constant. In fact, as was shown in the earlier paper,[5] all of the detail of the plastic wave propagation was in very good agreement with the strain rate independent finite amplitude wave theory of von Karman,[15] Taylor,[16] Rakhmatulin,[17] and White.[18] This theory, developed from the one-dimensional wave equation

$$\partial^2 u/\partial t^2=c_p{}^2(\partial^2 u/\partial x^2), \qquad (15)$$

has a solution for the situation of constant velocity impact.[19] This solution provides that the velocities of propagation c_p are constant and are given from the slopes of some governing stress-strain curve, Eq. (8), and predicts a relation between particle velocity and strain

---

[14] E. Schmid and W. Boas, *Plasticity of Crystals* (F. A. Hughes, London, 1950), pp. 156–157.

[15] T. von Karman, NDRC Rept. A 29, OSRD 365 (1942).

[16] G. I. Taylor, British Official Report RC 329 (1942).

[17] K. A. Rakhmatulin, Appl. Math. and Mech. **9**, 91–100 (1945).

[18] M. P. White and L. Griffis, NDRC Report A72, OSRD 742 (1942).

[19] H. Kolsky, *Stress Waves in Solids* (Oxford University Press, London, 1953).

$$v=\int_0^{\epsilon} c_p d\epsilon. \qquad (16)$$

The theory does not prescribe that the stress-strain curve for strain rate independence should necessarily be the static stress-strain curve. Hence, if one were to find higher stresses, it would not necessarily imply a departure from strain rate independence. As a matter of fact, however, as was shown earlier,[5] the relation between maximum strain and the impact velocity found experimentally is very close to that predicted from the slopes of the static stress-strain curve.

Using the theoretical parabola of Eq. (10) instead of the static stress-strain curve, an even closer correlation has been found, not only for impact velocity versus strain, but for every other parameter which this investigator has reported, although departures are found for the dynamic stresses of Johnson, Wood, and Clark[7] below the Karman critical velocity. This difference will be discussed below.

In Fig. 6, the solid line is the impact velocity versus maximum strain curve given by the theoretical parabola from Eq. (16); the circles are a few of the experimental maxima shown earlier.[5]

This work in aluminum has involved the study of many impact velocities. However, one velocity $v_0=66.5$ ft/sec (hitter velocity, 133 ft/sec) has been chosen for particularly intensive study. Well over half the total number of tests in aluminum have been at this impact velocity. For this impact velocity, the average experimental maximum of a very large number of tests is 2.20%, where the average experimental impact velocity in inches per second is 798 in./sec. The value of impact velocity at the strain of 0.022 in./in., calculated from the theoretical parabola is 800.5 in./sec. The agreement between the theoretical parabola and the stress obtained from the square of the c_p's in Eq. (9) indicates the closeness of these velocities of strain propagation between one and four diameters, to values determined from the slopes of the theoretical parabol from Eq. (8).

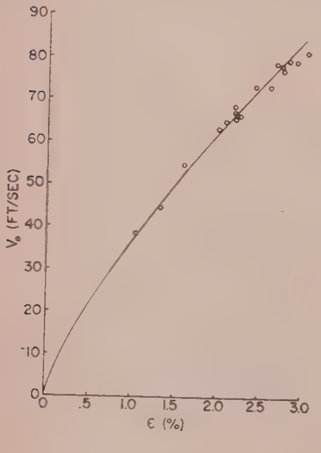

Fig. 6. Impact velocity vs maximum strain. The solid line is that computed from theoretical parabola.

In a recent paper[4] in which initial conditions wer studied, this writer found that the dynamic stress level obtained by Johnson, Wood, and Clark,[7] and Campbell from load bar tests in annealed aluminum could b predicted theoretically by assuming that a nondispersive shock front was present immediately following impact. If P is the dynamic stress level, and ϵ_0 is the strai level from the static stress-strain curve correspondin to an energy of deformation per unit volume equal t the initial kinetic energy per unit volume prior to impac T_0, then it was shown that

$$\tfrac{1}{2}P\epsilon_0=\int_0^{\epsilon_0} \sigma_x d\epsilon = T_0, \qquad (17$$

where σ_x and ϵ were static stress and strain. If the theoretical parabola of Eq. (10) is introduced into the integral of Eq. (17), we may compute P. Values of P thu computed are shown in Fig. 7 as circles. The upper an lower solid lines of Fig. 7 are the dynamic stress level given by Johnson, Wood, and Clark,[7] the upper on being the $(\sigma-v)$ curve in which the strain was determined from velocity considerations, and the lower on being the $(\sigma-\epsilon)$ curve in which the strain was determined from final strain measurements. For the mos studied impact velocity, that of 66.5 ft/sec, the theoretical P is 9677 psi. This writer has conducted experiments (two values of which are shown as stars in Fig. 7 similar to Johnson, Wood, and Clark's for this and othe impact velocities and has obtained an average experimental value for 66.5 ft/sec. impact velocity of 9700 Below the Karman critical velocity, however, th dynamic stress levels determined from Eq. (17) ar those given by the static stress-strain curve and not b the theoretical parabola. Above the Karman critica velocity, fair agreement is found between the predictions from the theoretical parabola and the experimental results of Johnson, Wood, and Clark, to th largest value of strain for which they made measurements, i.e., 5% strain. As will be shown below, thi

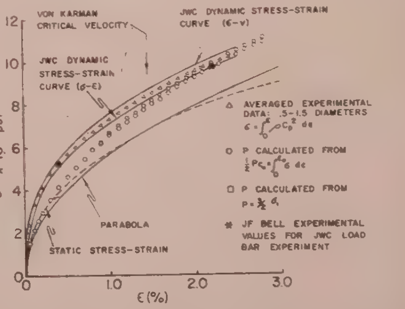

Fig. 7. Johnson, Wood, and Clark dynamic stress-strain curve The circles and squares are values computed from theoretica parabola.

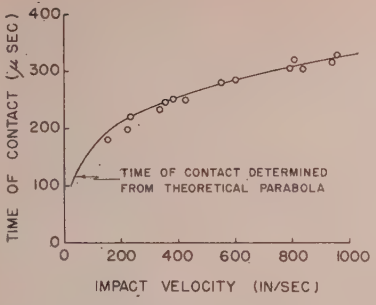

FIG. 8. Time of contact vs impact velocity.

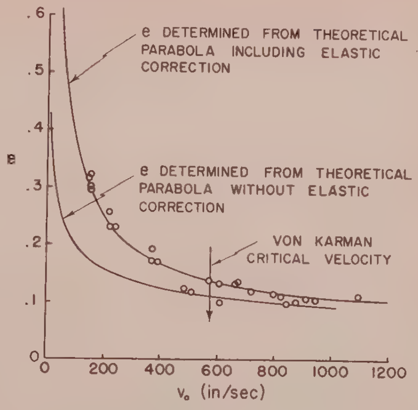

FIG. 9. Coefficient of restitution vs impact velocity.

agreement with the static stress-strain curve for lower impact velocities is thought to be related to a difference in the development of plastic deformation in the first diameter.

In the paper on initial conditions,[4] this writer observed that dynamic stress levels also might be computed from experimental observations from the observed strain ϵ_1 which corresponded to the maximum of the surface angle. It was pointed out that ϵ_1 could be determined by two methods, one in which the strain corresponding to the surface angle maximum was averaged from many different tests; and the second, in which the time of surface angle maxima was used to compute the velocity of propagation. The strain corresponding to this velocity of propagation was ϵ_1. The first procedure for 66.5 ft/sec gave $\epsilon_1=1.35\%$ strain, and the second gave 1.38% strain when a large number of tests were averaged. It was shown that ϵ_1 depended upon the impact velocity and was always the value corresponding to the point on the static stress-strain curve for which the energy of deformation was $\frac{1}{2}$ that of the energy of deformation at the maximum strain, and for which the stress level σ_1 was invariably $\frac{2}{3}$ of the dynamic stress P. Since the energy of deformation per unit volume is given by

$$U=\int_0^{\epsilon_{\max}} \sigma_x d\epsilon_x, \tag{18}$$

the theoretical parabola of Eq. (10) may be used to determine the value of ϵ_1 and the corresponding σ_1 from which the dynamic stress P then can be determined. The squares in Fig. 7 correspond to the calculated values of P thus obtained, where similar experimental agreement with the static stress-strain curve is observed below the Karman velocity. For 66.5 ft/sec, P determined in this fashion is 9888 psi, and ϵ_1, which may be compared to the values given above, is 1.38% strain.

In a recent paper[6] dealing with unloading phenomenon in constant velocity impact, the present writer has shown that it is possible to determine the time of contact and the coefficient of restitution from the static stress-strain curve. Experimental values of the time of contact and coefficient of restitution were obtained by an optical method discussed in that paper. The predicted times of contact were given by the time required for a stress level of $\frac{1}{2}$ the maximum stress to propagate from the impact face to the free end of the specimen with a velocity $c_p(\sigma/2)$ given by Eq. (8), at $\frac{1}{2}$ the maximum stress σ, plus the time required for an unloading wave to return to the impact face with an elastic velocity. Thus, for the time of contact T_c we have

$$T_c=\frac{L}{c_p(\sigma/2)}+\frac{L}{c_0}, \tag{19}$$

where L is the bar length, and $c_0=(E/\rho)^{\frac{1}{2}}$, the elastic velocity.

It also was assumed that the coefficient of restitution was given by the elastic unloading of this stress level of $\frac{1}{2}$ the maximum stress. This coefficient of restitution e was given by

$$e=v_f/v_0=c_0\sigma/(2Ev_0), \tag{20}$$

where E is Young's modulus, v_f is the final velocity after impact, and v_0 is the impact velocity.

In Figs. 8 and 9, experimental values of time of contact and coefficient of restitution, shown as circles, are compared with theoretical values (solid lines) computed from Eqs. (19) and (20) using the theoretical parabola of Eq. (10). The average experimental value of the time of contact for 66.5 ft/sec is 306 μsec. The value calculated from the theoretical parabola is 308 μsec.

The determination of the coefficient of restitution from Eq. (20), using the theoretical parabola, is shown as the lower solid line in Fig. 9. In a recent paper dealing with the unloading phenomenon,[6] the present writer showed that the coefficient of restitution determined from Eq. (20) using the static stress-strain curve was also not in too good agreement below an impact velocity of 400 in./sec. As a matter of fact, in that earlier paper[6] it was shown that the coefficient of restitution was in closer correspondence with results predicted from the dynamic stress-strain curve for low impact velocities. The use of Eq. (20) for the determination of the coefficient of restitution, however, implies that the unloading particle velocity is that associated with the unloading of $\frac{1}{2}$ the maximum stress. The reflection of the initial elastic front involves particle velocities determined from the elastic stress level itself and not from $\frac{1}{2}$ this level. Thus, the disagreement between the experimental data and the coefficient of restitution at lower impact velocities determined from either the parabola or the static stress-strain curve could be related to the omission of the elastic component of the final velocity.

The static strain at the elastic limit, as averaged from several stress-strain curves, is 110×10^{-6} in./in. As was shown in Fig. 7 of an earlier paper[5] on wave propagation in aluminum, or in Fig. 5 of a paper on the unloading phenomenon in aluminum,[6] the dynamic elastic limit is approximately the same as the static value, i.e., 110×10^{-6} in./in.

Figure 10 shows a comparison of the elastic particle velocity for a Young's modulus of 10.8×10^6 psi, determined by the present writer for the aluminum used, with the impact velocity v_0 calculated from Eq. (20) for the parabola, and with the final velocity v_f determined from the unloading of $\frac{1}{2}$ the stress levels of the parabola. The difference between the elastic velocity for which the reflected component is that of the entire elastic stress, and the velocity determined from the parabola for $\frac{1}{2}$ the stress, is shown as a bracket at the strain level of 110×10^{-6} in./in., i.e., the static or dynamic elastic limit. Thus Eq. (20) becomes

$$e=\sigma c_0/(2Ev_0)+(v_e-v_p)/v_0, \tag{21}$$

where v_e is the elastic particle velocity at the elastic limit and v_p is the particle velocity determined from the parabola from the elastic unloading of $\frac{1}{2}$ the maximum stress at the same strain of the elastic limit. For annealed aluminum, $v_e-v_p=17$ in./sec. The upper solid line in Fig. 9 shows the excellent agreement between experimental results and values of the coefficient of restitution determined from Eq. (21). The experimental data of Fig. 9 contains a number of new tests in the low velocity region. A careful analysis was made of the coefficient of restitution determined from the averaging of 75 measurements at 66.5-ft/sec impac velocity for which the hitter velocity and final specime velocity had been measured using electronic counters The average value obtained for e was 0.117. The predic tion from Eq. (21) for this impact velocity is 0.120, or difference of 2.5%.

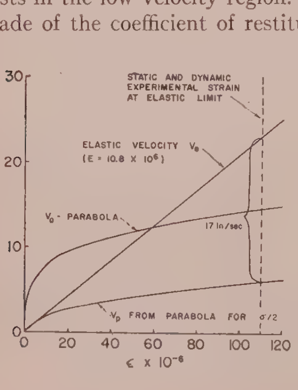

FIG. 10. Comparison of particle velocities below the elastic limit of 110×10^{-6} in./in., from linear elasticity and from parabola.

Thus, both the coefficient of restitution and the tim of contact are shown to be in excellent agreement wit the predictions obtained from the introduction of th parabolic stress-strain law into the strain rate inde pendent finite amplitude wave theory.

Returning to Fig. 7 and Eqs. (17) and (18) for th determination of the initial dynamic stresses in th vicinity of impact, it should be pointed out that, in a earlier paper,[4] the calculation of dynamic stresses fro these equations using the static stress-strain curve wer in very good agreement over the entire strain range wit the Johnson, Wood, and Clark[7] experimental curv shown in the present Fig. 7.

The averaged experimental data between $\frac{1}{2}$ and 1 diameters, shown as triangles in Fig. 7, bear out thi correspondence between theory and experiment. If however, one calculates from the parabola the dynami stresses from Eqs. (17) and (18), the circles and square shown in Fig. 7 are obtained. These do not agree wit the experimentally determined initial dynamic stres levels. A correction for the elastic limit is required similar to that given for the coefficient of restitutio but based upon the difference in energies. A simpl correction of the type suggested for the coefficient o restitution has not been found for these dynamic stresse unless it is presumed that the difference between th parabola and the static stress-strain curve in this lo strain region is in itself the correction. The energie under the static stress-strain curve in this low strai region, when substituted into Eqs. (17) and (18), d give the experimental dynamic stresses. Above th strain of 2%, they are given by the parabola and not b the static stress-strain curve.

Using the static stress-strain curve, for an impac velocity of 66.5 ft/sec, an energy balance of 2% wa obtained[6] before and after impact and at the time th elastic front reached the free end of the rod. Simila results are obtained when the parabolic stress-strai law, Eq. (10), is used.

Using the arrival times of all strain levels at positio between one and four diameters to determine the strai at one diameter, as if the plastic wave had been initiate from an infinite step at the impact face, a compariso may be made with the theoretical parabola (solid lin Fig. 11). The actual experimental strain-time curve of course, involve the delays in the arrival of the highe strain levels discussed in earlier papers.[4–6] However, the very low strain levels of the parabola and the ind vidual tests are brought into coincidence, nearly a individual tests give close agreement in strain time wit the theoretical parabola up to the strain of the mea energy which does appear to propagate from an almos infinite step at the origin. Hence, Fig. 11 not only is the average from many tests, but it is also typical of individual tests between the impact face and the first four diameters if the origin of the parabola is located at the point of initiation of plastic deformation.

To provide a check on whether dynamic results follow the parabola or the static stress-strain curve for impact velocities producing strains above 2%, where the two curves separate, tests were run at an impact velocity of 90 ft/sec. Results of such a test are shown in Fig. 12. A comparison is made between the experimental results and those predicted by the parabola. The theoretical arrival times are given by Eq. (22) and the theoretical maximum by Eq. (23).

$$c_p = (\beta/2\rho)^{\frac{1}{2}}\epsilon^{-\frac{1}{4}}, \tag{22}$$

$$\epsilon_{\max} = (9v_0^2\rho/8\beta)^{\frac{2}{3}}, \tag{23}$$

where β is the coefficient of the polycrystalline parabola. Equation (22) is obtained by substitution of the parabola in Eq. (8); and Eq. (23), by a substitution of the parabola in Eq. (16). At this impact velocity, the static stress-strain curve and the parabola have separated by a stress of nearly 1000 psi and a strain of nearly 0.3%, indicating that the dynamic results are following the parabola at higher impact velocities.

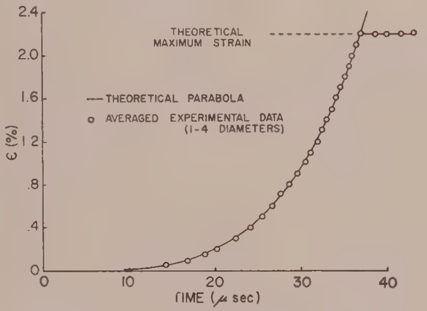

FIG. 11. Strain-time experimental results compared with computations from theoretical parabola.

The strain-time behavior after the first diameter thus is found to be very closely given by the theoretical parabola, providing one can account for the development of the plastic wave in the region near the impact face. This development of the dispersive plastic wave from initial shock fronts, from elastic reflection theory, and from the applicability of the theoretical parabola under conditions of high strain rate is considered immediately below.

THE INITIAL SHOCK FRONT

In a recent report[20] the present writer made an analysis of the developing elastic wave in the first few diameters, using what might be referred to as a "seismological" treatment of the initial wave development. Fair theoretical and experimental agreement was obtained in that study. One of the purposes of the work, which had extended over several years, was to consider whether or not one might successfully employ Huygen's principle from optics for an examination of the wave development, particularly in the first diameter. It seemed to be a possible method for investigating the experimentally observed mushrooming effect of the plastic wave in the first diameter. The experimental and theoretical study of the elastic strain pulse was confined to the point loading at the center of one end of a cylindrical rod.

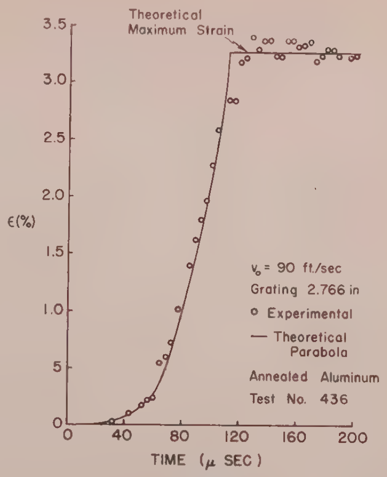

FIG. 12. Experimental strain-time results for an impact velocity of 90 ft/sec (circles) compared with predicted results (solid line) from theoretical parabola.

If each point on the impact face is considered as a point of origin, the strain-time history at a point on the lateral surface of the rod at some fixed distance from the impact face will have a delay in strain arrival, owing to the difference in the distance which must be traveled by each of the developing spherical wavelets. In Fig. 13 is shown the contribution (assuming an axial impact) from that diameter at the impact face which lies in the plane containing the point of interest. The earliest information which could arrive with zero amplitude is that from the point at the edge of the impact face closest to the point of measurement, and the longest arrival time would be that from the opposite end of this diameter.

Side wall reflections also would make contributions to developing strain. This type of wave development is seen to be very sensitive to the degree of axiality. In Fig. 14 are shown two tests at $\frac{1}{4}$ diameter, (a) and (b), and one test at $\frac{1}{2}$ diameter (c). Figures 14(a) and 14(c) are thought to be axial impacts. The arrival time t_D is that of the shock front directly along the lateral surface, and t_2 is the computed arrival time for a wavelet which

---

[20] James F. Bell, "The initial development of an elastic strain pulse propagating in a semi-infinite bar," Tech. Report No. 6, U. S. Army, BRL (November, 1960).

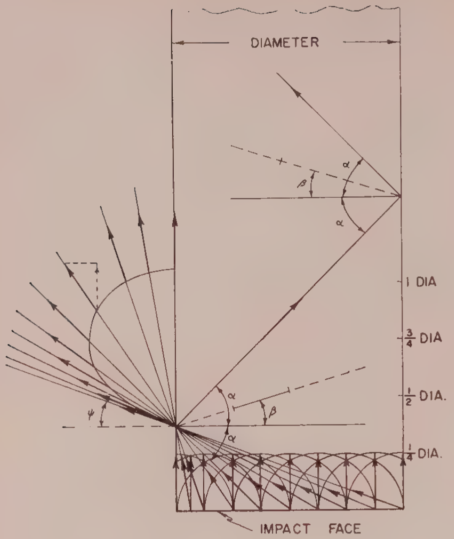

FIG. 13. Initial development at $\frac{3}{8}$ diameter from shock wave contribution along one diametral line of impact face.

has traveled with the shock velocity D from the far side of the impact face. Figure 14(b) is for a nonaxial impact, in which it is thought that the first contact occurred at the far side of the impact face so that the first arrival time occurs at t_2 and the abrupt change in strain slope is seen to occur at a time of approximately $t_2+(t_2-t_D)$. Figure 14(c) is an axial test at $\frac{1}{2}$ diameter. The t_D and t_2 occur at different times, but the behavior is similar to that of Fig. 14(a) at $\frac{1}{4}$ diameter. The mor rapid rise for an axial impact at $\frac{1}{2}$ diameter suggests that the intensity of the spherical fronts decreases wit angle. Tests of the type 14(a) and 14(c) have the earliest arrival times observed. From a study of many tests in the first half-diameter, it has been possible t identify a number of nonaxiality conditions.

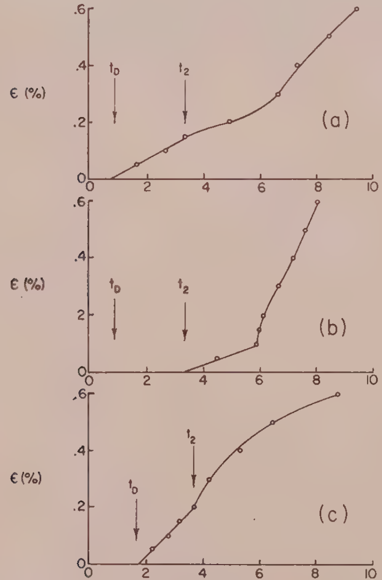

FIG. 14. Initial strain development at $\frac{1}{4}$ diameter (a), (b), and $\frac{1}{2}$ diameter (c).

If one is sufficiently close to the impact face, the plan front which would develop would be similar to that fo a plane front propagating into a semi-infinite solid. I this were correct at the positions of experimental measurement in the vicinity of the impact face, the stress obtained from

$$P=\int_0^{\epsilon} \rho D_e^2 d\epsilon \quad (24$$

must be equal to the stress level determined from shoc wave theory. In Eq. (24), P is the stress, ϵ the strain ρ the mass density, and D_e is the velocity of propagatio

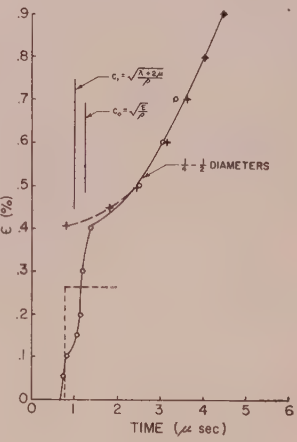

FIG. 15. Strain tim obtained from averagin tests at $\frac{1}{4}$ and $\frac{1}{2}$ diameters. The crosses are th plastic strain from th theoretical parabola.

of each level of strain determined from the arrival time When a number of tests are made at each of two adjacent points in the vicinity of the impact face, tim averages at each point eliminate axiality effects. Th determination of the time for each level of strain t travel between the two points in question, then provide strain-time detail.

In Fig. 15 is shown the result of such a computatio for an impact velocity of 66.5 ft/sec, where seven test at $\frac{1}{4}$ diameter are time-averaged and compared wit seven tests at $\frac{1}{2}$ diameter. It will be observed that a initial front is obtained which exceeds the dilatationa velocity. If this initial velocity D is introduced into th mass and momentum conservation equations, a valu of stress and of strain may be determined since th shock velocity D is known experimentally, and th particle velocity v behind the front is the impact ve locity v_0. The strain-time front of this computed shoc wave is shown as the dotted line in Fig. 15, which he wave front which is presumed to have produced he experimental strain distribution observed. The nock velocity D is 7.6 mm/μsec, which is considerably igher for a 4-kilobar pressure than the dilatational veocity of 6.3 mm/μsec.

In Fig. 16 is shown a stress-strain curve computed rom Eq. (24) using the experimental arrival times hown in Fig. 15. The stress level of the shock front is 4 kilobars, or 60 000 psi. The stress computed from the bserved data is 60 250 psi. This agreement suggests he validity of the calculated initial shock front and the nterpretation using Huygen's principle.

Dr. Joseph Sperrazza[21] of the Aberdeen Proving round, in preliminary experiments at the same impact elocity, has obtained extremely short duration stress eaks of approximately 55 000 psi, using quartz crystals emented to the impact face of annealed aluminum pecimens provided by this writer. The elastic limit of he material is less than 1000 psi; the theoretical maxinum stress from the finite amplitude wave theory is 8100 psi; and the dynamic stress of Johnson, Wood, nd Clark[7] is 9700 psi for this impact velocity. This ast-named dynamic stress is the experimental value btained after plastic deformation has commenced on he free surface of the specimen. It is produced by the ombination of the stress levels associated with the lastic deformation and the remaining hydrostatic omponent, which then drops (as is shown in a manucript recently submitted for publication) to the theoetical value of 8100 psi after an interval of over 100 μsec.

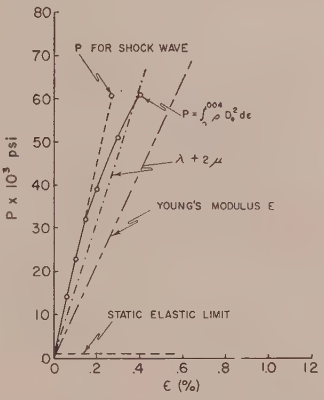

FIG. 16. Stress-strain determined from shock front and from integration of experimental strain-time data.

Plastic deformation in the first diameter has been hown earlier[4] to involve an equipartition of energy etween the deviatoric, or shear, component and the ilatational component. The reflection of the elastic hock front at the free surface will involve a dilatational omponent and a deviatoric component in order to atisfy the free stress boundary condition. In Fig. 17 he energies of these reflected waves, calculated from elastic reflection theory for a Poisson's ratio of $\frac{1}{3}$, are shown as a function of the angle of incidence α. If one integrates from $\alpha=90°$ back to $\alpha=0°$, it is found that an equipartition of energy between the dilatational and deviatoric reflection fronts is obtained. This is similar to the situation which is present on the side wall of the rod near the impact face which is receiving incident strain from all angles. In the energy partition at the free surface, however, the material is unable to support a reflected elastic deviatoric component. Hence, the deviatoric portion of the energy is converted into plastic deformation.

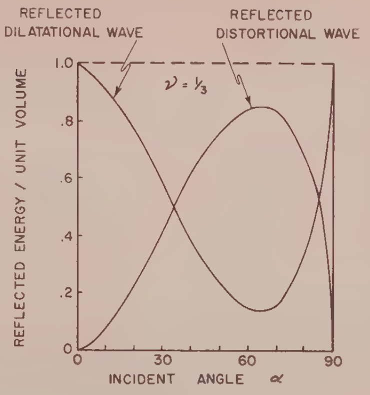

FIG. 17. Reflected energy per unit volume for varying angles of incidence α.

In Fig. 18 the total strain-time history between $\frac{1}{4}$ and $\frac{1}{2}$ diameter is shown for 66.5 ft/sec. It is found that the amount of plastic strain, $\Delta\epsilon=1.38\%$, is that shown earlier[4] to correspond to the deviatoric stress level and half the energy of deformation. When the strain level of approximately 1.8% is reached, an unstable hydrostatic situation is encountered. As may be seen from Fig. 18, above 1.8% there is at first an increase in velocity, and then there is a long interval of 15 μsec in which the strain reaches the theoretical value, following which, in an additional 10 μsec, the mushrooming occurs. The amount of mushrooming may be deter-

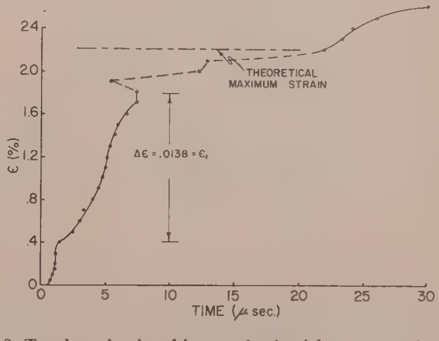

FIG. 18. Total strain-time history obtained from averaging data at $\frac{1}{4}$ diameter and $\frac{1}{2}$ diameter from impact face.

---

[21] Private communication.

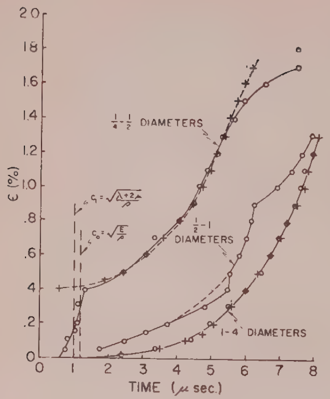

FIG. 19. Strain time obtained from averages between the indicated distance from the impact face.

mined. Thus the delays in the development of the higher strain levels commented upon earlier[4–6] are accounted for.

In Fig. 19 is shown the strain-time behavior averaged at ¼ to ½ diameters, ½ to one diameters, and one to four diameters. The crosses in this figure, as well as those in Fig. 15, correspond to the predicted strain-time behavior from the theoretical parabola. The behavior between ¼ and ½ diameter and between one and four diameters is found to be in excellent agreement. The behavior between ½ and one diameter, however, indicates the changes produced by the process of eliminating the shock front. Individual tests at one diameter itself are in very good agreement with the theoretical parabola up to the strain of the mean energy. The integrated average behavior at ½ to one diameter shown in Fig. 19, is observed in the lack of reproducibility in diffraction grating measurements of strain at ¾ diameter.

In earlier papers,[4,6] it has been shown that below the Karman critical velocity of 48.5 ft/sec in annealed aluminum, the first diameter behavior of the developing plastic wave is markedly different from that above this velocity. After leaving the first diameter, the velocity of propagation, etc., are identical with those obtained above the Karman critical velocity. These first diameter effects are exhibited in a large delay in the development of strain,[4] in a lack of mushrooming, a lack of reproducibility in the data in the immediate vicinity of the impact face, and (from results recently submitted for publication) a more rapid rise of particle displacement at the free end of the specimen.

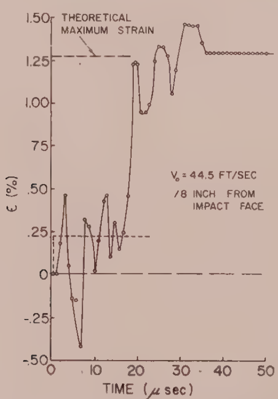

FIG. 20. Strain time below the Karman critical velocity from a single diffraction grating measurement at ⅛ diameter from impact face. The dashed step is the equivalent elastic front from elementary theory.

In Fig. 20 is shown a test at 44.5 ft/sec, which contains the Pochhammer-Chree type oscillations preceding the initiation of plastic deformation. Furthermore, the final strain level, as is characteristic of tests below the Karman critical velocity, is very close to the theoretical value, i.e., no mushrooming is observed The theoretical maximum strain shown in Fig. 20 is that computed from the theoretical parabola.

If it is assumed that below the Karman critical velocity it is possible to reflect a deviatoric elastic wave due to surface conditions in either the oxide coating on in dislocation fields near the free surface, then an apparent delay time for plastic deformation would occur after the deviatoric wave had been reflected. The Karman critical velocity determined from static tension tests conducted by Professor Robert Pond[22] of the Johns Hopkins University, is exactly the same as that determined from these dynamic compression tests. The determination of the Karman critical velocity in the static tension tests at the point where necking begins also may be related to a surface stability phenomenon For example, there is considerable difference between the value of the Karman critical velocity determined from specimens machined from annealed material when compared with those of materials annealed *afte* machining. The values given here are those for th latter situation, since static specimens were treated i precisely the same fashion as the dynamic specimens i.e., annealed after machining.

SUMMARY AND CONCLUSIONS

In this paper it has been shown that the theoretica stress-strain curve for polycrystalline aluminum ob tained by Taylor[11] from dislocation theory and exper ments on aluminum single crystals, are in agreemen with the present writer's dynamic experimental result tained by Taylor[11] from dislocation theory and exper ments on aluminum single crystals, are in agreemen with the present writer's dynamic experimental result

The theoretical $\bar{m}$ of Taylor, which is the ratio the normal stress of the polycrystalline aggregate, t the shear stress tangential to the slip plane of the sing crystal, was given by Taylor as $\bar{m}=3.06$. Bishop an Hill,[12] who also have considered the problem of th polycrystalline aggregate, obtained a value of $\bar{m}=3.0$ In the present writer's dynamic plastic wave exper ments, $\bar{m}$ has been found to be in agreement with the predicted value.

---

[22] Private communication.

During the several years in which this work has been in progress, the present writer has been finding an increasing order in the plastic wave propagation in aluminum, as manifested in a number of numerical relations which have been established. This underlying order obviously has been that of the governing parabola from dislocation theory. A nearly completed study of annealed copper has shown that the Taylor theory also agrees with the dynamic data for this metal. It should be pointed out that the theoretical parabolic stress-strain curve

$$\sigma=\beta\epsilon^{\frac{1}{2}} \tag{25}$$

may be introduced into the wave equation (1), giving

$$\rho\frac{\partial^2 u}{\partial t^2}=\frac{\beta\partial^2 u/\partial x^2}{[2(\partial u/\partial x)^{\frac{1}{2}}]}, \tag{26}$$

where $\epsilon=\partial u/\partial x$, from which solutions for cases other than constant velocity impact might be given.

In the present paper, experimental evidence has been provided for high stress level shock waves, even in the low velocity impact of a dead soft material. It has been shown that the parabola from Taylor's dislocation theory may be fitted to the plastic deformation time data occurring after the passage of the initial shock front. Although plastic strain rates of 2000 in./in./sec are involved, no strain rate effects are observed. Thus it may be concluded that in annealed aluminum, strain rate is not a first-order factor in plastic wave propagation. This latter conclusion is consistent with all of the present writer's experimental observations in annealed aluminum.

In a nearly completed study of incremental wave propagation in annealed aluminum, indications are that the incremental loading wave, which a number of years ago was discovered by the present writer to travel at elastic velocities,[23] also is amenable to a strain rate independent treatment, providing the incremental stress level is sufficiently high to again trigger plastic deformation.

In the earlier[5] comparison with the static stress-strain curve, it had been observed that some departures were present in stress levels in the vicinity of the elastic limit. At that time, these were thought to be possibly attributable to experimental inaccuracies. It is in this very region, however, that the theoretical parabola departs the most from the static stress-strain curve in the strain levels considered. Experimental results in this low region have been found to be in very good agreement with predictions from the theoretical parabola.

As yet unfinished work in other fcc metals indicates dynamic results similar to those given here for annealed aluminum. One interesting possibility is that apparent strain rate sensitivity of some metals at low machine rates may be caused by their being tested in a region where time for slip plane rotation is of the order of that of the test, while for other metals, such as aluminum, much higher rates would have to be used to obtain these strain rate effects. In all situations, however, the 100-μsec region would involve the hydrostatic parabola.

Although impact velocity measurements from 100–500 ft/sec currently are being made, the experimental results considered here have been limited to impact velocities up to 90 ft/sec, corresponding to maximum strain levels of approximately 3.2%. Experiments also are in progress up to 600°C in aluminum. Impact studies are being conducted in one-inch diameter, ten-inch long single crystals with varying orientation, to compare these with the static results given earlier by G. I. Taylor. One would expect that these latter comparisons would be very close, in view of the polycrystalline agreement; nevertheless, there is some interest in comparing the behavior at much higher strain levels.

In the present paper, a further study is made of differences in wave development below the von Karman critical velocity. An interpretation based upon elastic reflection theory is given, which is consistent with the observed experimental behavior.

In the present paper, too, it has been shown that the details of plastic wave propagation, including maximum strain, distance of penetration of maximum strain, dynamic stress levels in the first diameter, initial shock fronts, unloading detail including time of contact and coefficient of restitution, equipartition of energy near the impact face, and an energy balance may all be determined with remarkable accuracy from the introduction into the finite amplitude theory of plastic wave propagation, of the theoretical parabola obtained from dislocation theory by G. I. Taylor for a polycrystalline aggregate.

ACKNOWLEDGMENTS

This work was sponsored by the U. S. Air Force Office of Scientific Research. The author would like to express his appreciation to his invaluable assistant John Suckling. He would like to thank Patricia Jones who carried out most of the computations. He also would like to thank the many graduate student research assistants who have worked in his laboratory at one time or another in the last several years.

---

[23] James F. Bell, Tech. Report No. 5, U. S. Navy, ONR (June, 1951).

JOURNAL OF APPLIED PHYSICS VOLUME 32, NUMBER 10 OCTOBER, 196

Power Output Characteristics of a Ruby Laser

MALCOLM L. STITCH
Hughes Aircraft Company, Culver City, California

(Received November 7, 1960; in final form, June 14, 1961)

The theoretical power output of a ruby laser is examined under certain idealized operating conditions, and it is found that there are two principal regions of operation. These are the regions of strong oscillation characterized by the condition $p\tau_2/A \gg h\nu_{13}/\sigma_{13}$ and the region of saturation in which $p\tau_3/A \gg h\nu_{13}/\sigma_{13}$. Here p/A is the "pumping" illumination within the absorption band of ruby, τ_2 is a charactersitic relaxation time of fluorescence in ruby, τ_3 is a characteristic thermal relaxation time from the excited U band, ν_{13} is the pumping frequency, and σ_{13} is the cross section for interaction between pumping radiation and Cr^{3+} ions in ruby. Efficiency of operation is examined under two limiting conditions.

INTRODUCTION

THE recent achievement of T. H. Maiman[1,2] in obtaining stimulated emission of sizable power at optical frequencies from a ruby crystal and additional confirmation by R. J. Collins and co-workers[3] raise the interesting question of how much power can be obtained under limiting conditions from a ruby laser. We ask the question in this form: "When is saturation reached?" We also examine starting and intermediate conditions of operation.

THREE-LEVEL ANALOGY

We consider first an idealized three-level quantum system with state population densities of N_1, N_2, N_3 per unit volume and corresponding energies E_1, E_2, E_3, such that $E_3 > E_2 > E_1$. This system is made somewhat analogous to the appropriate levels of a ruby system by spacing the energy levels so that[2,4,5] $(E_3-E_1)/hc \approx 18\times10^3$ cm^{-1} and $(E_2-E_1)/hc \approx 14.4\times10^3$ cm^{-1}. These energies correspond to radiation at 5600 A (green) and 6940 A (red), respectively. As in the case of ruby, the following conditions hold for relaxation processes:

(1) Relaxation from state No. 3 occurs most rapidly by thermal relaxation to state No. 2. This process takes place so much more rapidly than other competitive processes that it determines the characteristic lifetime of this state. This lifetime is given by[4] $\tau_3 \approx 5\times10^{-8}$ sec.

(2) Relaxation from state No. 2 occurs predominantly by spontaneous emission to state No. 1 with a characteristic lifetime given by[2,6] $\tau_2 \approx 3\times10^{-3}$ sec. This situation corresponds to fluorescent radiation in ruby.

Pumping radiation at frequency $\nu_{13} = [(E_3-E_1)/h]$ applied to the system gives rise to an induced transition probability per unit time between states No. 1 and No. 3 of W_{13}. The resultant emission from state No. 2 at a frequency $\nu_{12} = [(E_2-E_1)/h]$ gives rise to an induced transition probability per unit time between states No 1 and No. 2 of W_{12}. This entire system has a quantum efficiency of unity.[4] This means that, for every photon at frequency ν_{13} absorbed, one photon is emitted at frequency ν_{12}. The population distribution among the three states is then determined by the following relations at steady state:

$$dN_3/dt = W_{13}(N_1-N_3) - N_3/\tau_3 = 0, \qquad (1)$$

$$dN_2/dt = W_{12}(N_1-N_2) - N_2/\tau_2 + N_3/\tau_3 = 0, \qquad (2)$$

and by the conservation condition

$$N_1+N_2+N_3 = N_0. \qquad (3)$$

We solve (1), (2), and (3), use the condition $\tau_2 \gg \tau_3$, and obtain

$$\frac{N_2-N_1}{N_0} = \frac{W_{13}\tau_2 - 1}{W_{13}\tau_2[1+W_{21}(3\tau_3+2/W_{13})]+1}. \qquad (4)$$

From (4), it is evident that a necessary though not sufficient condition for the existence of stimulated emission is

$$W_{13}\tau_2 > 1. \qquad (5)$$

To evaluate W_{13} in terms of macroscopic quantities, we consider the process described by (1) as a scattering process. This means that we consider a stream of photons normally incident on a rectangular slab of area A and thickness d containing a homogeneous distribution of sites. At each of these sites a particle is subject to the states and conditions of the three-level of quantum system discussed above. The sites have a density of N_0 per unit volume (of which N_1 per unit volume have particles in state No. 1, etc.). There is a collision cross section of σ_{13} between the incident photons of frequency ν_{13} and particles either in state No. 1 or in No. 3. A "collision" between such a photon and particle drives the particle into the other of the two states (No. 1 and No. 3). Then, at steady state, we equate the rate at which particles are driven into state No. 3 by the incident flux of n photons per second normal to the surface with the rate at which they decay from state No. 3 with a relaxation time τ_3.

---

[1] T. H. Maiman, Nature **187**, 493 (1960).

[2] T. H. Maiman, Brit. Commun. & Electronics **7**, 674 (1960).

[3] R. J. Collins, D. R. Nelson, A. L. Shawlow, W. Bond, C. G. B. Garrett, and W. Kaiser, Phys. Rev. Letters **5**, 303 (1960).

[4] T. H. Maiman, Phys. Rev. Letters **4**, 564 (1960).

[5] McClure, Solid State Phys. **9**, 399 (1959); S. Sugano and Y. Tanabe, J. Phys. Soc. Japan **13**, 880 (1958).

[6] F. Varsanyi, D. L. Wood, and A. L. Schawlow, Phys. Rev. Letters **3**, 544 (1959).

That is,

$$N_3Ad/\tau_3=n(N_1-N_3)\sigma_{13}d \tag{6}$$

or

$$N_3=(n/A)\tau_3(N_1-N_3)\sigma_{13}.$$

Equations (1) and (6) describe the same process from two points of view. If we solve each equation for $N_3/(N_1-N_3)$ and equate, we get the relation

$$W_{13}=n\sigma_{13}A^{-1}=(p/A)\sigma_{13}h^{-1}\nu_{13}^{-1}. \tag{7}$$

In (7), we have made use of $E=nh\nu$ so that p is the energy flow per unit time (i.e., the power) of the incident photon flux. It should be recognized that (6) is valid only if the condition of "optical thinness" holds, that is if

$$\beta\equiv(N_1-N_3)\sigma_{13}\ll 1. \tag{8}$$

Likewise, the use of a uniform value for W_{13} in (1) implies condition (8). To make condition (8) hold in general, d must be replaced by a differential, and then (7) and (2) hold for each infinitesimal slab at depth d from the front surface when p_0 is incident on it. It is evident that, in general,

$$p_d=p_0\exp(-)\int_0^d(N_1-N_3)\sigma_{13}dx,$$

where (N_1-N_3) is usually a function of depth.

RUBY SYSTEM

We now go from the idealized three-level quantum system to the quantum system for ruby as illustrated in Fig. 1. The fact that state No. 3 is now actually a band of states has no effect on the arguments thus far presented except that the pumping radiation may occupy a bandwidth of the order of 20% of the center frequency instead of being a sharply defined frequency. As a result, we rewrite σ_{13} as a function of frequency, $\sigma_{13}(\nu)$. If we make the reasonable assumption that our absorption spectra has a Lorentzian shape, then the effective value of p for an incident flux with a uniform frequency distribution is obtained by assuming an effective bandwidth of $(\pi/2)\Delta_{\frac{1}{2}}$, where $\Delta_{\frac{1}{2}}$ is the bandwidth between half-value points of $\sigma_{13}(\nu)$. We use the maximum value of a $\sigma_{13}(\nu_0)$ at the center of the band. A good value of $\Delta_{\frac{1}{2}}$ for ruby is 800 A.[5] The first complication is due to the presence of two neighboring levels, $\bar{E}(^2E)$ and $2\bar{A}(^2E)$, 870 kMc apart rather than the single No. 2 state in the idealized case. These give rise to the fluorescent doublet, R_1 and R_2. At 6943 A, the R_1 line is the one that builds up to laser emission when the sufficient conditions for emission are met.

Maiman has published some evidence[2] that indicates that the population shifts to the $\bar{E}$ level from the $2\bar{A}$ level under laser operating conditions. One explanation offered by Maiman is that thermal relaxation processes between these two states occur very rapidly at room temperature (with a Boltzmann ratio of the order of unity). As a result, "the population ratio of the two states is kept constant, but since $\bar{E}$ decays much faster, almost the entire initial population of the two states decays through R_1 emission". Thus τ_2 really refers to the relaxation time into levels $2\bar{A}$ and $\bar{E}$ combined with the relaxation time from $2\bar{A}$ to $\bar{E}$.

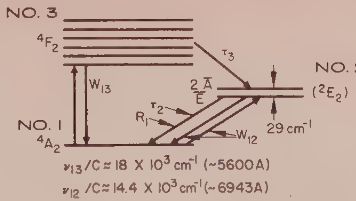
NO. 3
$^4F_2$
τ_3
NO. 2
$(^2E_2)$
W_{13}
$2\bar{A}$
$\bar{E}$
τ_2
R_1
NO. 1
$^4A_2$
W_{12}
29 cm^{-1}
$\nu_{13}/C\approx 18\times 10^3$ cm^{-1} (~5600A)
$\nu_{12}/C\approx 14.4\times 10^3$ cm^{-1} (~6943A)

FIG. 1. Pertinent energy levels of ruby employed in laser action.

The implication here is that, under certain conditions at least, one might treat state No. 2 as if only the $\bar{E}$ level existed. It should be noted that under saturation conditions and, if τ_3 is much shorter than the relaxation between $2\bar{A}$ and E levels, laser action could occur simultaneously at both the R_1 and R_2 frequencies. In this case, the equivalent τ_3 would be somewhat smaller than the value used in the strong oscillation condition. For simplicity, we err on the side of pessimism by neglecting any change and use the same value for τ_3.

IDEALIZED SLAB LASER

We particularize now to a simple physical embodiment to continue the argument. Consider the ruby crystal in Fig. 2, which is strain free and homogeneous, and has a Cr ion density of N_0 per unit volume. The two partially reflecting optically flat surfaces at the ends are parallel to each other, normal to the longitudinal axis, and comprise the end plates of a Fabrey-Perot interferometer.

If we follow the course of the growing wave corresponding to the normal mode which grows at a fractional rate of $\alpha=(N_2-N_1)\sigma_{12}$ per unit length through two reflections, we find that the condition for build-up of oscillation is

$$e^{2\alpha L}r_1r_2>1. \tag{9}$$

As the amplitude builds up and depletes N_2, α decreases until at steady state the inequality in (9) is replaced by an equality. Expanding and making use of the assumption that r_1, r_2 are nearly unity, we see that the condition of oscillation build-up is approximately

$$(N_2-N_1)\sigma_{12}L\geq\tfrac{1}{2}(1-r_1r_2) \tag{10}$$

and the equality holds for steady state.

Ideally, we permit all the output to come out of one end by letting, say, $r_2\rightarrow 1$, and we obtain unity circuit efficiency by having no absorption by the end reflectors; hence, the transmission is equal to $1-r_1$.

Provided that the ruby is uniformly illuminated [i.e., (8) holds], the laser power output is now given by

$$P_0=W_{21}(N_2-N_1)Ladh\nu_{21}. \tag{11}$$

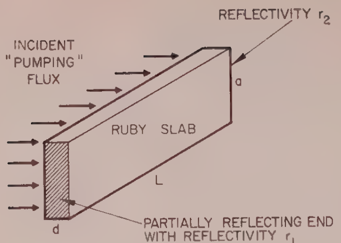

FIG. 2. Ruby slab laser suitable for idealized design computations.

We define and will later justify two regions as follows:

(1) Strong oscillation—here the condition of operation is

$$W_{13}\tau_2 \gg 1 \gg W_{13}\tau_3. \tag{12}$$

(2) Saturation—here the condition of operation is

$$W_{13}\tau_3 \gg 1. \tag{13}$$

We now evaluate (11) under these two conditions of operation.

Strong Oscillation

With the aid of (4), (7), (10), (12), and $r_2=1$, Eq. (11) becomes

$$P_0=\frac{1}{2}\left(\frac{N_0 2\sigma_{12}L}{1-r_1}-1\right)\left(\frac{1-r_1}{2\sigma_{12}L}\right)\left(\frac{\nu_{21}}{\nu_{13}}\right)(\sigma_{13}d)p, \tag{14}$$

where p now refers to the incident pumping power within the absorption band which has an effective width of approximately 1260 A. We later will justify that under certain conditions

$$N_0 2\sigma_{12}L/(1-r_1) \gg 1. \tag{15}$$

Then (14) becomes

$$P_0=\tfrac{1}{2}N_0\sigma_{13}d(\nu_{21}/\nu_{13})p. \tag{16}$$

Now, under ideal conditions when quantum efficiency is unity, and when spontaneous emission is small compared to stimulated emission, the amount of power absorbed from the incident radiation is given by $(\nu_{13}/\nu_{12})P_0$. Therefore, from (16), the fraction of the incident power which is absorbed is given by $\beta=\frac{1}{2}N_0\sigma_{13}d$. Thus, the condition of optical thinness (8) now becomes

$$\tfrac{1}{2}N_0\sigma_{13}d \ll 1, \tag{17}$$

and $N_1-N_3 \approx N_0/2$.

When (15) and (17) are satisfied simultaneously, it follows that

$$\tfrac{1}{2}(\sigma_{13}/\sigma_{12})dL^{-1}(1-r_1) \ll N_0\sigma_{13}d \ll 2. \tag{18}$$

Equation (18) serves to specify some dimensional ratios and the Cr ion density of the ruby. An approximate value[7] for the ratio σ_{13}/σ_{12} is 4; a more accurate value[7] for σ_{13} is 10^{-19} cm^2.

Saturation

With the aid of (4), (10), (13), (15), and $r_2=1$, Eq. (11) becomes

$$P_0=\tfrac{1}{3}N_0Lad[(h\nu_{21}/\tau_3)/p]p. \tag{19}$$

By the same argument that gave us (17), the condition of optical thinness now becomes

$$\tfrac{1}{3}N_0Lad[(h\nu_{21}/\tau_3)/p](\nu_{13}/\nu_{12}) \ll 1. \tag{20}$$

To satisfy (7), (13), (15), and (20) simultaneously, the following conditions must hold:

$$\frac{\sigma_{13}}{\sigma_{12}}\frac{(1-r_1)d}{2L} \ll N_0\sigma_{13}d \ll 3\frac{\nu_{13}}{\nu_{12}}\left(\frac{p}{A}\right)\frac{h\nu_{13}}{\tau_3\sigma_{13}},$$

and

$$(p/A)(h\nu_{13}/\tau_3\sigma_{13})^{-1} \gg 1. \tag{21}$$

DETAILS AND INTERPRETATION OF OPERATING CONDITIONS

In order to demonstrate how the conditions for strong oscillation and saturation, i.e., (12) and (13), were arrived at, we solve (11) more exactly by use of (4). Then, we have

$$P_0=N_0Y(x)(Lad)(h\nu_{12}/\tau_2), \tag{22}$$

where

$$Y(x)=\left(\frac{N_2-N_1}{N_0}\right)W_{12}\tau_2=\frac{(1-a)x-(1+a)}{3(\tau_2/\tau_3)x+2}, \tag{23}$$

$$x=W_{13}\tau_2,$$

and

$$a=(N_2-N_1)/N_0=\tfrac{1}{2}(1-r_1)/N_0\sigma_{12}L. \tag{24}$$

The optical thickness can also be written in terms of

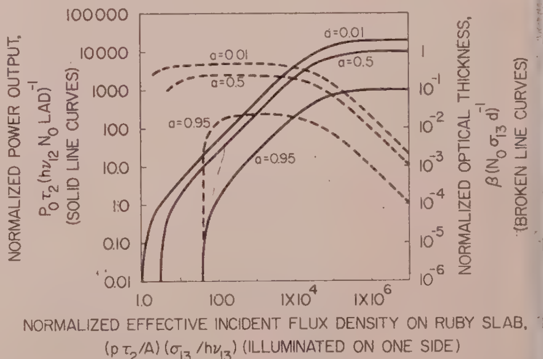

FIG. 3. Calculated normalized power output and optical thickness as a function of normalized "pumping" flux density. This relation is valid as long as N_0d is so adjusted that $\beta \ll 1$. If the ruby is within an illuminated enclosure, the curves of normalized power output are still valid if, in reading the abscissa, the indicated flux density values are halved.

---

[7] T. H. Maiman (private communication).

the normalized functions $Y(x)$ as follows:

$$\beta \equiv (N_1 - N_3)\sigma_{13} d = N_0 \sigma_{13} d Y(x)/x. \tag{25}$$

The relations

$$Y(x) \equiv P_0 \tau_2 (N_0 L a d h\nu_{12})^{-1}$$

and

$$Y(x)/x = (N_1 - N_0)/N_0 = \beta / N_0 \sigma_{13} d$$

are plotted as functions of x in Fig. 3 for several values of the parameter a. We have used the ratio of τ_2 to τ_3 appropriate for ruby, although the relations would hold generally for any "three-level" system with a quantum efficiency of one in which $\tau_2 \gg \tau_3$.

The curves of normalized power output $Y(x)$ and normalized optical thickness $Y(x)/x$ can be used to predict the performance of a laser under specified operating conditions as well as to demonstrate how the operating conditions depend on the regions specified by conditions (12) and (13). At $Y(x)=0$, the oscillation threshold is reached and then oscillation builds up rapidly as the optical pumping power in normalized units x is increased until x reaches a value of τ_2/τ_3 (which is equivalent to saying that $W_{13}\tau_3 = 1$). Beyond this point, $Y(x)$ approaches an asymptotic value and the system saturates. From an examination of the $Y(x)/x$ curve and a knowledge of the value of σ_{13}, one can determine the maximum value of $N_0 d$ consistent with a desired optical thinness or fractional absorption of pumping power. It is seen that when x is within the range

$$(1+a)/(1-a) \ll x \ll \tau_2/\tau_3, \tag{26}$$

the function $Y(x)/x$ describes a broad plateau. This is the region which we called "strong oscillation," and it is seen that for reasonable values of a, such that $a \ll 1$, relation (26) is equivalent to condition (12), while in the region of saturation, where condition (13) holds, $Y(x)/x$ decreases and it is permissible (and indeed necessary) to increase $N_0 d$ in order to increase the power output.

With the help of (7), Eq. (12) can be rewritten in the form

$$p\tau_2/A \gg h\nu_{13}/\sigma_{13} \gg p\tau_3/A. \tag{27}$$

This can be interpreted to mean that in order for strong oscillation to occur, the incident power flux density (within the absorption band) must be so high that within the lifetime of the (metastable) fluorescent state, the energy intercepted by a typical ion at its site must be much greater than that necessary to cause an absorbing transition. This would have the effect of putting most of the ions in fluorescent state No. 2 if the effective lifetime τ_2 were not markedly decreased by stimulated emission.

Thus, for pulsed operation, on evaluating (27) we find that for strong oscillation a pumping pulse of duration τ_2 or less must have an energy flux density (within the absorption band) given by

$$p\tau_2/A \gg 3.54 \text{ joules/cm}^2, \tag{28}$$

and this corresponds to a pulse power (within the absorption band) of

$$P/A \gg 1200 \text{ w/cm}^2, \tag{29}$$

provided that the pulse is of τ_2 duration. If the pulse is shorter than τ_2, p/A must be proportionately greater.

If the ruby slab is excited from both sides rather than from one side as assumed above and *provided that it is optically thin*, then in (7) n becomes $2n$ and hence (7) becomes

$$W_{13} = 2(p/A)\sigma_{13}(h\nu_{13})^{-1}, \tag{7'}$$

where p/A still means the power flux density at each surface. Equation (27) becomes

$$p\tau_2/A \gg \tfrac{1}{2} h\nu_{13}/\sigma_{13} \gg p\tau_3/A; \tag{27'}$$

Eqs. (28) and (29) become

$$p\tau_2/A \gg 1.77 \text{ joules/cm}^2 \tag{28'}$$

and

$$p/A \gg 600 \text{ w/cm}^2. \tag{29'}$$

For the optically thin case treated above, it is apparent, on considering the photometric illumination at an arbitrary imaginary differential surface within the crystal, that (7′) describes the relation between W_{13} and p/A not only for the thin slab excited on both sides, but for a crystal of any shape, provided that it is within a luminous enclosure, and that the incident flux at any area on the surface is given by the same value of p/A. Under these circumstances, one halves all values on the abscissa of Fig. 3 as indicated there.

A similar treatment for the saturation case (13) within an enclosure gives as a condition for operation that a pumping pulse of duration τ_3 or less must have an energy flux density (within the absorption band) of

$$p\tau_3/A \gg \tfrac{1}{2} h\nu_{13}/\sigma_{13} \ (=1.77 \text{ joules/cm}^2). \tag{30}$$

Equation (30) can be interpreted to mean that, at saturation, the incident power flux density (within the absorption band) must be sufficient that within the lifetime of the excited state No. 3 most of the ions are driven into this state before they have a chance to relax into the fluorescent state. This corresponds to a pulse power (within the absorption band) given by

$$p/A \gg 3.5 \times 10^7 \text{ w/cm}^2. \tag{31}$$

This value of flux density is considerably in excess of that currently available from a spectral source.

EFFICIENCY

If we use the initially stated assumption that the laser operates with a quantum efficiency of unity and the concept of optical thickness, we find in general

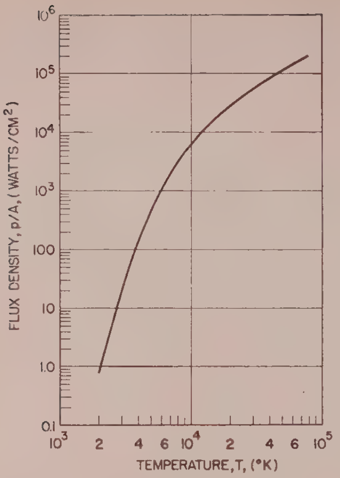

FIG. 4. Equivalent incident "pumping" flux density within the effective laser action absorption bandwidth of ruby as a function of the temperature of a blackbody source as determined by Eq. (35) of the text.

that

$$P_0=\beta(\nu_{21})/(\nu_{13})p. \tag{32}$$

Equation (32) holds provided that β, the optical thickness, obeys the thinness condition (8), provided that p is taken to mean the total incident pumping flux (within the absorption band), and provided the geometry is such that a common value of β can be used to describe the absorption process (such as, for example, our narrow slab, or a cylindrical rod).

Let us examine the efficiency of energy conversion. It would appear from (32) and the thinness condition that the efficiency is quite low. That this is not necessarily so, and that the efficiency depends rather on the nature of the pumping source is illustrated by the following two (idealized) examples.

Case I

Let the thin ruby slab be illuminated by a spectral source in the form of a sheet of intensely luminous gas placed against the broad wall of the slab. Assume that the emission occurs over a band covering the absorption band of the ruby, and that the gas behaves as a blackbody over this bandwidth and is transparent outside this band. Now, let the gas have an equivalent emission temperature of T_1 such that it emits light flux of a total radiant emittance p/A on each side. Then, the emittance from the back side is lost into space and that from the side next to the ruby slab is transmitted through the ruby with an absorption of $\beta(p/A)$. In order to keep the gas at constant temperature, power equivalent to $2p/A$ per unit area of the sheet must be supplied to the gas. For simplicity, we have assumed 100% conversion of this power into light flux within the desired band. Then the efficiency is given by

$$\epsilon_{\mathrm{I}}=\beta(p/A)/2(p/A)=\beta/2, \tag{33}$$

which, as mentioned above, must be quite low.

Case II

We have the arrangement of Case I with the addition of a reflecting sheet on the side of the ruby slab farthest from the gas sheet. Let the sheets have a reflection coefficient of R within the radiation bandwidth. Then we sum up the power which must be supplied to the gas to keep it at the same equivalent emission temperature T_1 as in Case I. Neglecting any temperature rise of the reflecting sheets (since they could be cooled) and disregarding end effects, the net loss of flux per unit area from the gas sheet is $(p/A)(1-R)$ from the back side and $(p/A)[1-(1-\beta)^2R]$ from the side next to the ruby slab. The ruby slab now absorbs a fraction of the radiation entering from the side of the gas sheet, still at equivalent temperature T_1, at the rate $\beta(p/A)$, and a fraction of the reflected flux entering from the side of the reflector at the rate $\beta(p/A)(1-\beta)R$. The efficiency is thus

$$\epsilon_{\mathrm{II}}=\frac{\nu_{12}}{\nu_{13}}\,\frac{\beta[1+(1-\beta)R]}{2-[1+(1-\beta)^2]R}. \tag{34}$$

Note that when

$$R\rightarrow 1,\quad \epsilon_{\mathrm{II}}\rightarrow \nu_{12}/\nu_{13}. \tag{34'}$$

Implicit in the discussion is that the heat generated in the ruby crystal, which represents $(\nu_{13}-\nu_{12})/\nu_{13}$ or 20% of the absorbed pumping flux, is dissipated in some manner. If the heat cannot be dissipated, one is restricted to pulse operation.

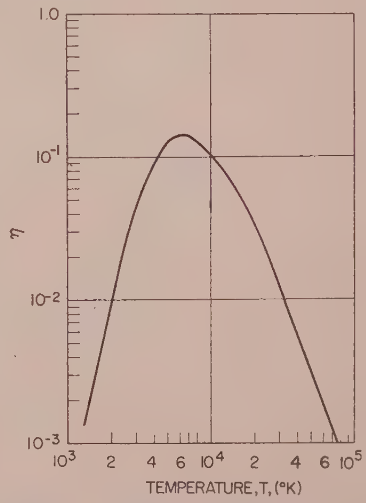

FIG. 5. Fraction of the total blackbody radiation which is effective in "pumping" a ruby laser as determined by Eq. (35) of the text.

SOURCE TEMPERATURE

If, in an effort to get enough power density, the radiant gas source is put under sufficient pressure, the lines become so broad that the output resembles black-body radiation. For this reason, it was considered interesting to examine p/A as a function of T for ruby pumped by black-body radiation under conditions of optical thinness and a Lorentzian shape for the absorption band with a half-width of 800 A. The relation

$$p/A=\eta\sigma T^4, \tag{35}$$

where

$$\eta\equiv\frac{15}{\pi^4}\int_0^{\infty}\frac{(1/400)^2}{(1/\lambda-1/\lambda_0)^2+(1/400)^2}\frac{x^3}{e^x-1}$$

and $x=hc/\lambda kT$ has been computed for a range of T. The flux density p/A has been plotted as a function of the temperature T in Fig. 4 and the fraction of the total radiation effective in exciting the ruby, η, is plotted versus T in Fig. 5.

While admittedly the preceding discussion has been limited to idealized cases, it should serve as a guide in determining the design parameters of solid-state lasers where power is a consideration.

ACKNOWLEDGMENTS

The author wishes to thank Dr. T. H. Maiman for several illuminating discussions. This work is strongly influenced by his concept of laser action. The author also wishes to acknowledge that his interest in the field was aroused by the piquant paper of Schawlow and Townes[8] which first examined the possibility of stimulated emission of optical radiation.

---

[8] A. L. Schawlow and C. H. Townes, Phys. Rev. **112**, 1940 (1958).

JOURNAL OF APPLIED PHYSICS VOLUME 32, NUMBER 10 OCTOBER, 1961

Birefringence due to Dislocations in Glide Bands of Rocksalt Single Crystals

S. Mendelson*
Columbia University, New York, New York

(Received March 3, 1961)

Birefringence techniques which emphasize the difference in stress on each side of a slip plane having edge dislocations of one sign are described. The principal stresses due to edge dislocations in a glide band are found to be parallel and perpendicular to the Burgers vector. The opposite stressed regions on both sides of a slip plane produce opposite retardations in the phase of light passing through the slip plane. When this light is retarded in phase by an amount equal to the advancement from the compressive region (or advanced by an amount equal to the retardation from the tensive region), a birefringence band forms which is, for instance, dark on the compressive side, light on the tensive side in a background having an intensity halfway between these two shades. These asymmetrically shaded birefringence bands are observed when viewed both normal and parallel to the Burgers vector and this is shown to be a direct consequence of the edge dislocations in the slip planes and to be independent of screws. The asymmetry of the band permits a determination of the sign of the dislocations in the slip plane and the apparent position of its source. The magnitude of the principal stress parallel to the Burgers vector was computed from the measured retardations and found to be in good agreement with that computed from the dislocation stress fields.

INTRODUCTION

THE phenomenon of stress polarization is well known and the principle of artificial birefringence is the basis of photoelastic methods used in stress analysis.[1,2] It has also been used by many European and Russian researches[3] since the early nineteen hundreds in studies of flow in alkali halide crystals. The use of this effect in the study of dislocations in single crystals of transparent materials is, on the other hand, a relatively new technique and only recently has been used for this purpose.[4–7]

Obreimow and Schubinokoff[8] were first to show that slip planes in NaCl are planes of double refracting material. These authors found a compressive stress on one side of a glide band and a tensive stress on the other. Nye[4] first pointed out that the birefringence observed in glide bands of deformed silver chloride crystals is a direct consequence of the presence of a majority of one sign edge dislocations. Kear and Pratt[5] found asymmetrically colored birefringence bands in

---

* Part of a thesis submitted in partial fulfillment of the requirements for the degree of Doctor of Philosophy at Columbia University, 1961.

[1] E. G. Coker and L. N. G. Filon, *Photoelasticity* (Cambridge University Press, Cambridge, England, 1957).

[2] H. T. Jessop, Encyclopedia of Physics **6**, 127 (1958).

[3] E. Schmid and W. Boas, *Plasticity of Crystals* (F. A. Hughes and Company, Ltd., London, 1950).

[4] J. F. Nye, Proc. Roy. Soc. (London) **A198**, 190 (1949).

[5] B. K. Kear and P. L. Pratt, Acta Met. **6**, 457 (1958).

[6] W. L. Bond and J. Andrus, Phys. Rev. **101**, 1211 (1956).

[7] R. Bullough, Phys. Rev. **110**, 620 (1958).

[8] I. W. Obreimow and L. W. Schubnikoff, Z. Physik **41**, 907 (1927).

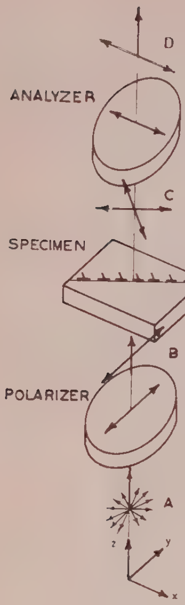

FIG. 1. Optical system. Light from source "*A*" passes through the polarizer and is plane polarized "*B*". Passing through the stressed region of an isotropic crystal (shown here as an array of edge dislocations) it is polarized parallel to the principal stresses "*C*". This beam has a component in phase with the optic axis of the analyzer which is at right angles to that of the polarizer and passes to the eyepiece. Light passing through the unstressed region is extinguished at the analyzer.

the interior of quenched NaCl crystals when the optical system included a sensitive tint plate. The asymmetry of color on each side of the slip plane was shown to be associated with the presence of edge dislocations of a particular sign. Bond and Andrus[6] made the significant observation that the birefringence pattern around a single edge dislocation in silicon is the same as the stress pattern predicted from elasticity theory.

Theoretical treatments of this phenomenon[9,10] consider anisotropy of the Lorentz-Lorenz and Coulomb forces between ions, changes in overlap of ions and the anisotropy of ionic refractions. The treatment given here is phenomenological and in terms of an application of the principle to studies of dislocations in slip planes of simple crystals. No attempt will be made to interpret the results in terms of the theoretical aspects of the phenomenon of stress polarization.

PHENOMENOLOGICAL THEORY

The stressed region of an optically isotropic material behaves as an anisotropic crystal and becomes double refracting. Described in terms of strains, the lattice spacing parallel to the compressive stress is decreased and that normal to the stress increased, thus producing a tetragonal structure and, hence, a double refracting material. In terms of stress, the Neumann-Maxwell law states that "Light passing through the stressed region is polarized parallel to the directions of the principal stresses in the plane of the wave-front at that point." Both of these approaches give equivalent effects and have been used by many workers to interpret birefringence due to elastic deformation.

When an optically isotropic material is viewed between crossed polarizers the system is at extinction and no light passes to the eyepiece. On the other hand, when an internal stress exists in the material such as an array of edge dislocations in a slip plane (see Fig. 1), the light passing through this region is polarized parallel to the principal stresses "*C*". The resulting wave, depending upon the orientation of the crystal, will have a component rotated in phase parallel to the analyzer and will thus produce a birefringence. The two rays leaving the stressed region, designated as ordinary and extraordinary rays, have different refractive indices and travel with different velocities and wavelengths. This results in a retardation in phase and consequently a birefringence. The combination of the two waves results in a radius vector which sweeps clockwise or counterclockwise, depending on the manner in which the waves, which vibrate in the mutually perpendicular planes, combine, i.e., whether the retardation is positive or negative. The retardation is positive for a tensile stress and negative for a compressive stress (this is reversed in some alkali halide crystals) and to a first approximation is proportional to and a direct measure of the stress in the solid.

RESULTS AND DISCUSSION

A. Principal Stresses

The intensity of light transmitted through a crystal between crossed polarizers is given by

$$T=a^2\sin^2(2\gamma)\sin^2(\delta/2), \tag{1}$$

where δ is the phase difference in the two principal directions at any point. a is the amplitude of the incident plane polarized light, and γ is the angle between the incident plane polarized light vector (polarizer) and a principal direction. β as defined by Bullough,[7] is the angle between the polarizer and the slip direction and is given by

$$2\gamma=2\theta+2\beta, \tag{2}$$

where $\theta=\frac{1}{2}\tan^{-1}[(y^2-x^2)/2xy]$, and x and y are the coordinates from the origin at the core of the dislocation.

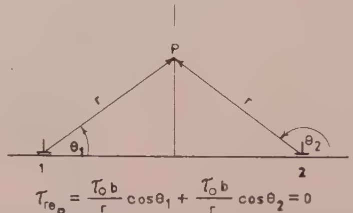
P
r
r
θ_1
θ_2
1
2
$\tau_{r\theta_P}=\frac{\tau_0 b}{r}\cos\theta_1+\frac{\tau_0 b}{r}\cos\theta_2=0$

FIG. 2. The shear stress at a point P midway between two edge dislocations vanishes. The shear stress from 1 is of equal magnitude but opposite sign to that from 2.

---

[9] H. Mueller, Physics **6**, 179 (1935); Phys. Rev. **47**, 947 (1935).

[10] R. S. Krishnan, *Progress in Crystal Physics* (Central Art Press, Chetput, Madras, India, 1958).

When a uniform closely spaced array of dislocations forms in a stressed NaCl crystal, a birefringence band appears at the slip plane when viewed normal to the Burgers vector while between crossed Nicols. The intensity of this band is found to be a maximum when the slip plane is 45° to the polarizers. Equation (1) also gives a maximum intensity when the principal directions make an angle of 45° with the polarizers. Thus the above observation indicates that $\beta=\gamma$ and $\theta=0$, i.e., a principal axis is parallel to the slip direction for an array of closely spaced equal sign edge dislocations.

The stress state between edge dislocations in a slip plane is such that the principal stress planes are parallel and perpendicular to the Burgers vector, i.e., in this region the major components of shear stress[11] $\tau_{r\theta}=(\tau_0 b/r)\cos\theta$ for equally spaced edge dislocations cancel each other. The shear stress will vanish midway between any symmetric array of edge dislocations; this is shown for two edge dislocations in Fig. 2. On the other hand, at positions near the end of an array the shear stress should be finite. Observations of the ends of glide bands at $\gamma=45°$ show birefringence up to within a few dislocations of the end. It is therefore likely that the shear stress at any point along the dislocation array is only significant for the few nearest dislocations. The principal stresses can be expressed in terms of τ_x and τ_y[11] [see Figs. 3(a) and (b)], parallel and perpendicular to the Burgers vector for a single edge dislocation. Both are compressive in the upper part and tensive in the lower part of the slip plane. This is shown schematically in Fig. 3(c).

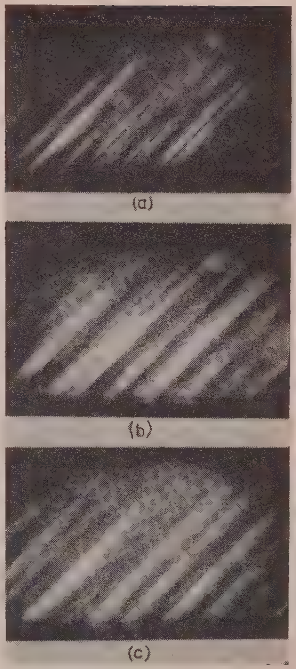

FIG. 4. Birefringence from glide bands viewed normal to the Burgers vector. (a) between crossed polarizers. (b) Light leaving the specimen is advanced in phase by an amount equal to the retardation from the tensive region. (c) Light leaving the specimen is retarded in phase by an amount equal to the advancement from the compressive region.

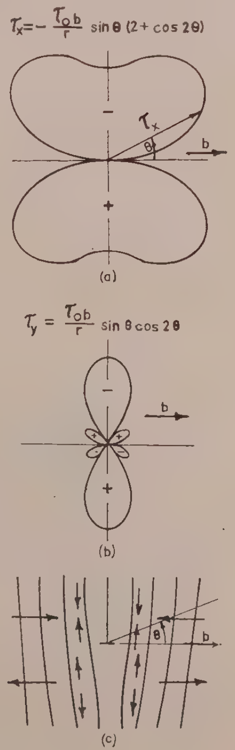
$\tau_x = -\frac{\tau_0 b}{r}\sin\theta\,(2+\cos 2\theta)$
−
τ_x
θ
b
+
(a)
$\tau_y = \frac{\tau_0 b}{r}\sin\theta\cos 2\theta$
−
b
+
(b)
θ
b
(c)

FIG. 3. Stress field around an edge dislocation. (a) Plot of stress parallel to the Burgers vector as a function of θ. (b) Plot of stress normal to the Burgers vector as a function of θ. (c) Schematic of the principal stresses around an edge dislocation in a slip plane.

The principal stress normal to the Burgers vector, τ_{py}, is the same as that for a single edge dislocation whereas that parallel to the Burgers vector τ_{px} is due to the stress fields of all dislocations in the array. The principal stresses are therefore given by

$$\tau_{py}=-\tau_0 b/y \tag{3}$$

and

$$\tau_{px}=-\sum_{n=1}^{n}\tau_0 b/x_n, \tag{4}$$

where $\tau_0=G/[2\pi(1-\nu)]$ and x_n is the x coordinate of the nth dislocation in the slip plane.

Thus the material on each side of the slip plane containing edge dislocations of one sign should behave as a double refracting material with the principal stresses parallel and perpendicular to the Burgers vector. Since these stress intensities are not equal for an array of edge dislocations in a slip plane, the optical properties on the two principal planes will be different and the two rays will travel with different velocities and wavelengths. This results in a phase difference between these components as they emerge from the crystal and this will be negative in the compressive (upper) part of the slip plane and positive in the tensive (lower) part.

---

[11] A. H. Cottrell, *Dislocations and Plastic Flow in Crystals* (Oxford University Press, London, 1956).

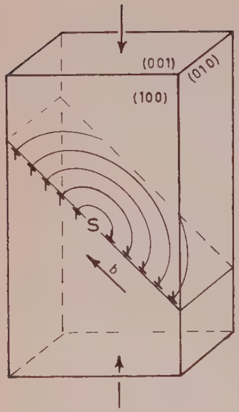

FIG. 5. Schematic of a deformed specimen for which a source is activated in the central region. Opposite sign edge dislocations extend from the source in opposite directions.

B. Distinction Between Compressive and Tensive Stresses on the Two Sides of a Glide Band

The retardation from each side of a slip plane results in a birefringence and since each side is oppositely retarded in phase, the asymmetry of the birefringence should be pronounced. When a deformed crystal is viewed between crossed Nicols the background intensity vanishes (unstressed region) and both retardations from the two sides of a slip plane appear as increases in intensity. An example of this is shown in Fig. 4(a). Each side of a glide band shows relatively equal intensities. This birefringence therefore does not distinguish between compressive and tensive stresses. This can be accomplished by the following two methods.

1. Use of Tint Plate

The full wave plate is called a tint plate because although it may be a full wave plate for green light, it is less than a full wave plate for red, and more than full wave plate for blue light. If a tint plate is placed between crossed Nicols so that white plane polarized light from the first Nicol strikes it at 45° then the green component of the white light will be extinguished by the analyzer Nicol, but the red and blue components will penetrate it, giving transmitted light of a color tint. The variations in color are emphasized when a positive or negative increment of retardation comes into play. Positive retardation changes the color toward blue; negative retardation changes it toward red. The tint plate thus serves to exaggerate the effects of slight retardations. Coloration depends on the stress in the band, and ranges from, for example, blue in the tensive side of the band to red in the compressive side. Color distribution also depends on the azimuth of the tint plate so that a given color distribution can be reversed by simultaneously rotating the crossed polarizers with respect to the crystal by 90°. Kear and Pratt[5] were first to observe this effect in studies of quenching stresses in ionic crystals.

2. By Retardation of the Light Leaving the Specimen

Another method to emphasize the difference in stress on both sides of the slip plane is to retard the phase of light leaving the crystal by an amount equal to the advancement from the compressive region (or to advance the light by an amount equal to the retardation from the tensive region).[12] The resulting birefringence band is, for instance, dark on the compressive side, light on the tensive side, in a background having an intensity halfway between these two shades. This is shown in Figs. 4(b) and (c). In (b) the light leaving the specimen was advanced in phase, whereas in (c) the light leaving the specimen was retarded. The bands in both (b) and (c) now have an asymmetric shading. In (b) the lower part of a band is dark and the upper part light, while the reverse is true in (c).

C. Birefringence from Slip Planes Having Different Sign Edge Dislocations

1. Viewed Normal to Burgers Vector

When a Frank-Read source is activated in the central region of a NaCl crystal the dislocation morphology may be illustrated schematically as in Fig. 5. The source generates dislocations in the form of concentric loops with opposite sign dislocations moving in opposite directions. The birefringence from each half of these bands when viewed normal to the Burgers vector should be oppositely shaded or colored. This is shown in Fig. 6. It is significant to note the difference in shading between the two sides of a band; dark areas above the slip plane on the left-hand side and below the slip plane on the right-hand side. This is a reflection of opposite sign stresses in the two sides and is exactly what we would expect if a Frank-Read source operated between them.

The intensity of birefringence increases as the depth of focus increases until the depth of the band extends from one surface to the other.[13] In these specimens the

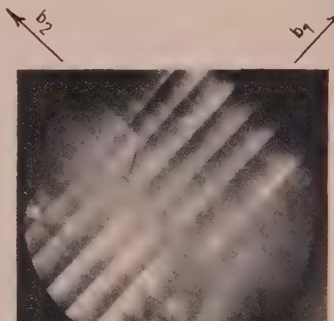

FIG. 6. Birefringence from glide bands in a deformed specimen with sources in the central region. 6.6×. The microscope axis lies in the slip plane and is normal to the Burgers vector. b_1 is the Burgers vector of the most active slip system.

---

[12] S. Mendelson, Bull. Am. Phys. Soc. 6, 23 (1961).

[13] S. Mendelson, J. Appl. Phys. (to be published).

birefringence is sharpest when the optical system is focused about halfway through the thickness. This probably is a reflection of the greater edge component on the dislocation loops at this position. When these crystals are etched[14] edge dislocation etch pits are observed in the slip planes of the glide bands and they generally appear on a few closely spaced slip planes in each band (see Fig. 7). The bands broaden slowly with increasing stress.[13] Figure 8 is an example of etch pits in broader bands.

2. *Viewed Parallel to Burgers Vector*

Light passing through the stressed region parallel to the Burgers vector should also experience a stress polarization due to edge dislocations in a slip plane. In this view the light rays pass normal to a lattice which has principal stresses $\tau_{px}=0$ and $\tau_{py}=-\tau_0 b/y$. Since these are not equal, the light will again be retarded in phase and result in a birefringence. τ_{py} is compressive in the upper half and tensive in the lower half of the slip plane [see Fig. 3 (b)]. Thus an asymmetric birefringence band should also appear when viewed parallel to the Burgers vector and should reverse coloration when the stress reverses. This is shown in Fig. 9; (a), (b), and (c) illustrate birefringence bands formed during progressive stages in deformation when viewed normal to the Burgers vector. (d) and (e) are views of the deformed crystal in (c) parallel to the Burgers vector. (d) was taken for the optical system focused in the upper half (i.e., point nearest the objective lens) while (e) is for the optical system focused in the lower half of the specimen. These show a reversal in stress birefringence halfway through the crystal as the optical system is adjusted to various depths of focus. The reversal in shading is merely a reflection of a reversal in the state of stress in the two parts of the band. Both types of birefringence observations (i.e., parallel and perpendicular to the Burgers vector) indicate that the dislocations generated are in the form of concentric loops with the sources in the center of the bands.

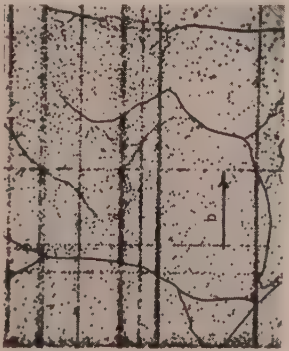

FIG. 7. Etch pits in glide bands of NaCl crystals. 30×.

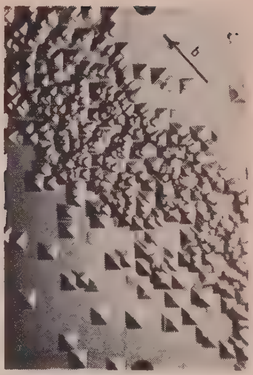

FIG. 8. Etch pits in a glide band after broadening during flow. 310×.

D. Birefringence Due to Screw Dislocations

The state of stress for a screw dislocation parallel to the Burgers vector is one of pure shear (see Fig. 10). Mueller[9] points out that optical anisotropy in sodium chloride is largely due to changes in the Cl-Cl distance. In NaCl the Cl ions are in contact with each other because the Na ions are much smaller than the Cl ions. Under shear strains the Cl-Cl distance remains unchanged and thus shear should make a small contribution to birefringence. Expressed in another way, Burstein and Smith[15] suggest that since "central forces" predominate between the ions in ionic crystals, shear strains should not cause large effects.

Suzuki[16] also observed birefringence bands when deformed KCl crystals were viewed parallel to the Burgers vector. He assigns this birefringence to the screw dislocations present in the slip plane. However, the traction around a screw dislocation perpendicular to the Burgers vector is zero and screws should make no contribution to the birefringence when viewed parallel to the Burgers vector. His observations, as the ones in the present work, are a direct consequence of the edge dislocations in the glide bands and not of screws as suggested.[16]

E. Magnitude of Principal Stresses

The principal stresses in a glide band can be computed from the measured retardations and appropriate piezo-optical coefficients. The retardations on each side of the slip plane can be determined by measuring the angular phase difference required to cancel the advancement or retardation from each region. This was accomplished in this work with a quarter wave plate. The retardation due to this plate is zero when it is parallel to the polarizer optic axis and $\lambda/4$ when at 45° to it. The relative retardation at any angle is given by

$$\Delta=\lambda/4\sin 2\phi, \qquad (5)$$

---

[14] S. Mendelson, J. Appl. Phys. **32**, 1579 (1961).

[15] E. Burstein and P. L. Smith, Phys. Rev. **74**, 229 (1948).

[16] T. Suzuki, *Dislocations and Mechanical Properties of Crystals* (John Wiley & Sons, Inc., New York, 1957), p. 215.

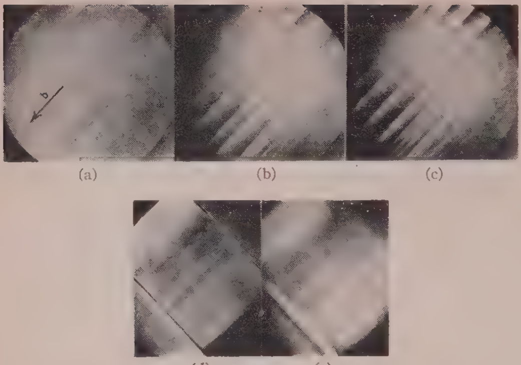

(a) (b) (c)

(d) (e)

FIG. 9. Birefringence from glide bands viewed normal and parallel to the Burgers vector. (a), (b), and (c) are progressive stages in the flow processes when viewed normal to the Burgers vector. (d) and (e) are views of the deformed crystal in (c) parallel to the Burgers vector. (d) was taken for the optical system focused in the upper half (i.e., point nearest the objective lens) while (e) is for the optical system focused in the lower half of the specimen.

where λ is the wavelength of the incident light. For the specimen in Fig. 4, $\phi=3°$ for both retardation and advancement. Taking the average wave length of white light as 550 mμ the retardation is 1.44×10^{-6} cm. The piezo-optical coefficients have been tabulated for ionic crystals by Nye[17] for sodium D light. Use of these values in these computations will not cause serious errors (i.e., the refractive index changes very slowly with wavelength in this range).

For cubic crystals of class (m3m) in uniaxial tension along a cube axis the birefringence for light traveling normal to the principal axis is given by[17]

$$n_{\parallel}-n_{\perp}=-(1/2)n_0^3(\pi_{11}-\pi_{12})\tau, \tag{6}$$

where $n_{\parallel}$ and $n_{\perp}$ are the refractive indices along the principal planes and π_{11} and π_{12} are the piezo-optical coefficients. The relative retardation is given by

$$\Delta=(n_{\parallel}-n_{\perp})t \tag{7}$$

and the stress in terms of this is

$$\tau=-2\Delta/[n_0^3(\pi_{11}-\pi_{12})t]. \tag{8}$$

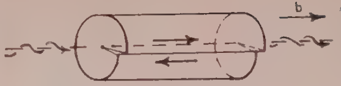

FIG. 10. Schematic of a screw dislocation. State of stress is pure shear.

Substituting $t=1$ cm (thickness in Fig. 4), $n_0=1.544$ and $(\pi_{11}-\pi_{12})=-1.21\times10^{-13}$ cm^2/d, $\tau=65$ g/mm^2. This is a measure of the difference in the principal stresses (i.e., $\tau=\tau_{px}-\tau_{py}$). The observed birefringence normal to the Burgers vector is about 3 times as intense as that parallel to b for equal depths of focus. Therefore $\tau_{px}-\tau_{py}\simeq3(\tau_{py})$ and the principal stresses are $\tau_{py}=22$ g/mm^2 and $\tau_{px}=87$ g/mm^2.

The glide bands form in avalanches or bursts of flow under an applied stress of $\sim$50 g/mm^2.[13] The computed value of τ_{px} is of the correct order of magnitude although somewhat larger. This may be due to the more dense dislocation morphology in "dynamic bands" as opposed to those which form under "static" conditions.

The stress in the glide band can also be evaluated from the elastic fields of the dislocations within the band. This can be approximated by assuming the glide band as a single slip plane. This stress will be on the high side due to the neglected stress field relaxations from dislocations on parallel slip planes. For an array of like sign dislocations in a slip plane d cm apart, the stress along the slip plane can be expressed as

$$\sum_{n=1}^{n}\tau_0 b/x_n\simeq\int_0^n(\tau_0 b/d)dn/n\simeq(\tau_0 b/d)\ln n.$$

For $d=7$ μ and $n=400$ (average number of dislocations in a plane), $\tau_{px}=94$ g/mm^2. This is in good agreement with that computed from the measured retardations.

The observed birefringence due to dislocations in slip planes suggests an interesting new approach to studies of photoelastic properties of transparent crystals as well as their plastic properties. Similar observations have also been made in MgO, LiF, KCl, KBr, and KI.[18]

ACKNOWLEDGMENTS

The author wishes to thank Dr. E. S. Machlin of Columbia University and Dr. W. G. Johnston of The General Electric Research Laboratories, Schenectady, New York, for their advice and interest in this work.

---

[17] J. F. Nye, *Physical Properties of Crystals* (Oxford University Press, London, 1957).

[18] S. Mendelson (to be published).

JOURNAL OF APPLIED PHYSICS VOLUME 32, NUMBER 10 OCTOBER, 1961

Fast-Risetime Excitation Scheme to Achieve Nonequilibrium and Amplifying Carrier Distributions

GEORGE C. DOUSMANIS
RCA Laboratories, Radio Corporation of America, Princeton, New Jersey

(Received March 24, 1961)

A technique is suggested for creating anisotropic and emissive carrier distributions in semiconductors or other crystals at low temperatures. As an example, application of the technique in the re-entrant (negative-mass) regions of heavy holes in germanium and silicon, in conjunction with cyclotron resonance using circularly polarized microwaves, is discussed. These distributions are expected to be short-lived (of order 0.2 to 5 mμsec), but more anisotropic than those obtained so far in these regions by applying steady-state optical excitation alone. The nonequilibrium distributions would be created by excitations (pulsing, for example) with risetime shorter than the carrier-phonon scattering time. Recently, the increasing purity of materials and speed of electronic instruments have approached the theoretical requirements of this method.

THE purpose of this note is to suggest a fast-risetime pulsing method for achieving strongly nonequilibrium, orientation dependent, and amplifying carrier distributions in crystals. The basic feature of the scheme is the requirement that the pulse risetime Δt be shorter than the carrier-(electron or hole) lattice scattering time τ. The fast-rising pulse can throw the carrier distribution into particular regions of momentum space, and strongly nonequilibrium distributions, including emissive ones, can be obtained for short time intervals of order τ. The short life of such distributions is, of course, the result of strong phonon emission processes that will "thermalize" them, so that the fast-risetime excitation has to be repetitive. The pulse width and interval between pulses are, in principle, not significant in this scheme.

The discussion here will be mainly concerned with the re-entrant contours of Ge and Si, where nonequilibrium distributions and cyclotron resonance negative-mass effects have been recently the subject of considerable work.[1-6] The technique, however, can in principle be used in other crystals for basic transport and carrier relaxation studies and possible use of effects of this type in both positive and negative-mass regions of holes or electrons.

Consider the requirement $\Delta t < \tau$. At present, high-quality Ge crystals, even if doped to 20 ohm-cm, can yield τ's of about 0.3 mμsec at temperatures near 1.5°K. The speed of existing oscilloscopes (and pulsers) is 0.25 to 0.4 mμsec. Thus, this requirement is barely satisfied in Ge. In Bi and some other materials, $\tau > 1$ mμsec, and the requirement is well met. From these numbers one concludes that such short-lived nonequilibrium distributions can be produced in crystals.

The detection or possible utilization of the transport effects arising from these carrier distributions is at present difficult. Use of this technique in conjunction with cyclotron resonance, preferably with circularly polarized microwaves, offers optimum conditions since one gains from resonance spectral separation of various carriers and a factor of $(1+\omega^2\tau^2)$ in sensitivity. Use of the combined scheme would necessitate abandonment of narrow banding in cyclotron spectrometers. The cavity relaxation or "ringing" time Q/ω also has to be shorter than Δt. The requirement $f\Delta t > 1$, i.e., the rf has to go through a few cycles during the risetime, is easily met.

We consider, as a specific example, application of the fast-rising field along the main axis [(100)] of the negative mass regions of heavy holes in Ge and Si with cyclotron resonance using circular microwaves [$E_{\text{rf}} \perp$ (100) axis] and H parallel to that axis (see Fig. 1 and reference 2 and 3). In the idealized case shown, the entire distribution is thrown inside the re-entrancy, and would be amplifying the rf signal for particle transitions $\perp$ (100) axis (see diagram of energy levels and relevant rf transitions in Fig. 1). For initial experimentation, the system may consist of microwave signal source, appropriate waveguides, magnet, cavity, diode detector, and high-speed oscilloscope. A feasibility estimate has been made on the basis of the performance of cyclotron spectrometers, with the modifications required by the present scheme. The values used are $Q_{\text{cavity}} = 40$, total density of holes (generated by infrared light from acceptors) of $5 \times 10^{10}/\text{cm}^3$, effective filling factor of 1/50,

---

[1] H. Krömer, Phys. Rev. **109**, 1956 (1958); *Progress in Semiconductors* (Heywood and Company, Ltd, London, 1959), Vol. 4, p. 1.

[2] G. C. Dousmanis, Phys. Rev. Letters **1**, 55 (1958).

[3] G. C. Dousmanis, R. C. Duncan, Jr., J. J. Thomas, and R. C. Williams, Phys. Rev. Letters **1**, 404 (1958); *Proceedings of the Conference on Semiconductor Physics, Prague, 1960* (Publishing House, Czech. Acad. Sci., Prague, 1961), p. 603; for more recent work see also RCA Laboratories Report, under contract, March 25, 1961 (unpublished).

[4] B. Lax and J. G. Mavroides in *Solid State Physics*, edited by F. Seitz and D. Turnbull (Academic Press, Inc., New York, 1960), Vol. 11, p. 261 (see this review paper for further discussion and a comprehensive list of references on this subject); G. C. Dousmanis in *Quantum Electronics*, edited by C. H. Townes (Columbia University Press, New York, 1960), p. 458; H. Krömer, *Paper Digest* (Solid State Circuit Conference, University of Pennsylvania, 1960), p. 84; B. Rosenblum and R. C. Duncan, Jr., *Proceedings of the Conference on Semiconductor Physics, Prague, 1960* (Publishing House, Czech. Acad. Sci., Prague, 1961), p. 606.

[5] C. Kittel, Proc. Nat. Acad. Sci. **45**, 744 (1959).

[6] D. O. North (private communication); R. C. Williams and F. Herman, *Proceedings of the Conference on Semiconductor Physics, Prague, 1960* (Publishing House, Czech. Acad. Sci., Prague, 1961), p. 599; D. C. Mattis, Phys. Rev. **122**, 52 (1960); Yu. Kagan, J. Exptl. Theoret. Phys. (USSR) **38**, 1854 (1960), translation: Soviet Phys.—JETP **11**, 1333 (1960).

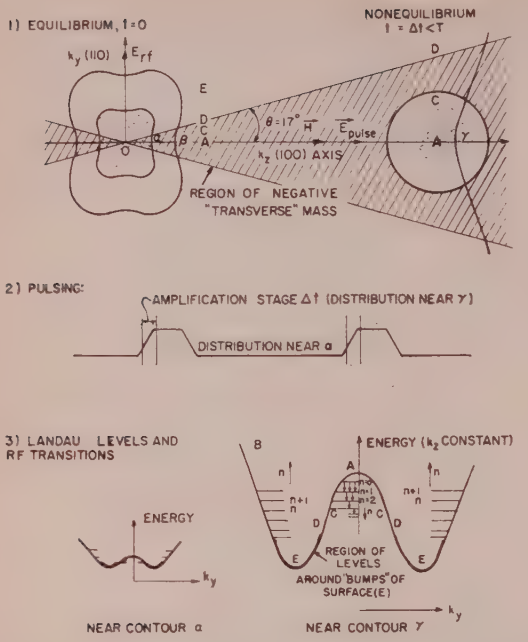

FIG. 1. Schematic representation of use of fast-risetime excitation in conjunction with resonance, in the negative-mass regions of warped energy surfaces. Upper part (1) shows the energy contours of heavy holes in Ge and Si and the distribution at equilibrium (or between pulses) extending up to contour α, and after time Δt when it has been thrown near the high-energy contour γ and inside the re-entrant (negative-mass) region. Part (2) shows the type of pulsing and the amplification period Δt. In (3) the Landau levels and the three branches of the energy spectrum are schematically shown for two values of k_z (point A for contours near α and γ). The rf cyclotron transitions of interest are between the overpopulated low quantum number levels (A) and the lower energy states (C) in the m^- region (near contour γ). Note the inverted nature of the levels, the small quantum numbers, and the small number of equally-spaced levels in the m^- region, even near the higher energy contour γ.

rf signal frequency of 17 kMc and power in the range of 15 to 150 μw. The maximum value of E_{pulse} is less than 4 v/cm, which is the impact ionization field for Ge, and would accelerate the particles to energies lower than those of optical photons, starting with a *main* distribution[7] in the helium range of T (1.5° to 4.5°K). In cases where impact ionization does not occur or is helpful, larger fields may be used.

At present, this evaluation, even with the use of somewhat optimistic values for some of the parameters above, predicts marginal performance. However, the efficiency of the technique is being progressively enhanced by the increasing purity of materials (larger τ's) and speed of electronic instruments (shorter Δt's). Development of high-frequency amplifiers (to be interposed between detector and oscilloscope) with short response times would make the initial phases of such work much easier. The Q's required for this scheme will depend on frequency and Δt, but in general must be low. Thus, traveling wave structures might be used in place of the microwave cavity. This is particularly so since the semiconductor materials themselves provide considerable slowing factors.

Detection of an amplified resonant signal *in time of order* Δt, in the example above, and its decay with time, would yield information on the relaxation processes following carrier excitation in the narrow re-entrancy and at energies quite high by comparison to T_{lattice}. If this type of pulse is applied along other directions of the warped surface, equally interesting physical information would be obtained from such distributions as a result of sudden large changes in positive-mass conductance as well as in that of the harmonics. Some information, albeit crude, could be obtained on the relaxation processes of the Landau levels associated with the "bumps" of the energy surface (Fig. 1). The simplest case to consider in principle is the speedy displacement of carriers from the low-energy Landau levels of a simple narrow band towards those near the inflection point, in which case the microwave absorption (and rf conductance) would change from a large positive value to one close to zero.

Once a strongly nonequilibrium, direction-dependent carrier distribution has been established, it will decay by emitting phonons, since it consists of "hot" carriers (40° to 400°K) in an extremely cold lattice (1.5° to 4.2°K). The maximum fractional energy loss per collision of a single carrier is given by[8]

$$\frac{\Delta \mathrm{E}}{\mathrm{E}} \sim 4\left[\frac{m^* s^2}{2\mathrm{E}} + \left(\frac{m^* s^2}{2\mathrm{E}}\right)^{\frac{1}{2}}\right],$$

where m^* is the carrier effective mass and s the sound velocity. We compute that despite the reduction of τ with increasing E (τ is proportional to $\mathrm{E}^{-\frac{1}{2}}$ rather than $\mathrm{E}^{-\frac{3}{2}}$ in our case), a substantial number of collisions with acoustic phonons is required before the carrier gets rid of its energy (E is assumed to be smaller than that of optical phonons). This implies that the nonequilibrium distribution will be at high energies for an appreciable time. It does not, in general, guarantee any significant confinement of the distribution to the region of **k** space into which it was originally thrown. The spreading is a result of collisions involving large changes in momenta. Confinement after the time Δt, although very helpful is not essential here.

Since the carriers are thrown into specific regions of anistropic bands, they may require excitation of specific lattice modes to be brought back to a distribution that is a function of E alone. Such new nonequilibrium phonon excitations are difficult to estimate and may be small, but their existence in semiconductor cyclotron resonance using the present or other excitation schemes should not be overlooked. The occurrence of nonequilibrium phonons has been recently of considerable interest in the area of electron spin resonance in paramagnetic crystals.[9]

---

[7] An optically excited initial distribution would have some anisotropies in momentum space under the above conditions (see references 3, 4, 6) but may be considered as a function of energy alone for our present purposes.

[8] J. M. Ziman, *Electrons and Phonons* (Oxford University Press, New York, 1960), p. 432.

The main advantage of the resonance-fast risetime technique discussed here is that it would create and yield information on extremely anisotropic, direction-dependent carrier distributions. Whereas under optical excitation in warped (and possibly other) energy surfaces anisotropic distributions can be obtained,[3,4,6] no large anisotropies of the type discussed here have so far been achieved by steady-state resonance and optical excitation alone. This, of course, does not imply that the negative-mass emission in Ge cannot be enhanced by further improvements in the steady-state resonance-optical excitation work.[3]

Electric pulsing in conjunction with cyclotron resonance is not the only excitation where the present considerations apply. Any excitation process, such as optical, rf, etc., that satisfies the requirement $\Delta t<\tau$ may be considered. The case of rf excitation does not necessarily imply that one has to pulse the rf with such high speeds. The steep part of a continuous rf wave, of frequency much smaller than that of the signal, may play the role of the rising part of the pulse.

We may compare this technique for achieving nonequilibrium distributions with that proposed by Krömer.[1] Aside from the resonance embodiment, the present scheme differs fundamentally from the previous one in that it relies on "beating" the acoustic phonon scattering time to obtain intermittent conductivity variations, including microwave amplification. In Krömer's case, a steady state was to be established by use of the optical phonon "barrier" to confine the particles in particular directions of momentum space. This requirement alone, in view of the detrimental effects of acoustic phonons in this case, is much more difficult to satisfy by comparison to those of the fast risetime-cyclotron resonance techniques discussed here.

Note added in proof. Whereas, as discussed above, the creation of these new distributions, and the detection of transport effects arising from them are *at present* difficult, the progress both in speed of electronic instruments and in material purification should not be underestimated. For example, the risetime of high-speed oscilloscopes (corresponding to Δt), has been decreased by about a factor of 2 since the above material was written. The present speed is in the range of 0.10 to 0.25 mμsec.

At the same time, further improvements in semiconductor material purification increases the scattering time, so that it tends towards the phonon limit. Improvements in this area are the more significant since they allow some distribution confinement after Δt and do not reduce sensitivity, i.e., there is obvious advantage, once the basic requirement ($\Delta t<\tau$) is satisfied, in using both Δt and τ large.

The low value of cavity Q (40) used in the example above is connected with the use, in that calculation, of a low microwave frequency (17 kMc). Work at higher microwave frequencies and mm wavelengths allows use of higher Q's in the range of 200 to 4000. For a given frequency, of course, a large τ allows use of larger Δt's and higher Q's.

We make some further remarks on Fig. 1: In part (1), point B (not shown) lies high above point E. It is interesting to note that the branch of the energy spectrum associated with the eight "bumps" of the energy surface (protrusions along the (111) and equivalent axes) occupies a *large* fraction of momentum space (30 to 45% of the total in Ge). This, of course, applies to volume in momentum space occupied at equilibrium, and should not be taken as an accurate representation of the particle distribution in the presence of applied fields or under nonequilibrium conditions.

ACKNOWLEDGMENTS

The author is indebted to Mr. R. C. Duncan, Jr., Mr. E. O. Johnson, Mr. R. M. Josephs, Dr. D. O. North, and Miss M. D. Stebbins of these Laboratories for their interest and several discussions on this subject. In particular, I am obliged to Dr. B. W. Faughnan for his extensive comments, and for his critical reading of the manuscript.

---

[9] See, for example, *Quantum Electronics*, edited by C. H. Townes (Columbia University Press, New York, 1960).

JOURNAL OF APPLIED PHYSICS VOLUME 32, NUMBER 10 OCTOBER, 1961

Semiconducting Stress Transducers Utilizing the Transverse and Shear Piezoresistance Effects

W. G. Pfann and R. N. Thurston
Bell Telephone Laboratories, Inc., Murray Hill, New Jersey

(Received May 5, 1961)

Principles of a varied group of new semiconducting, piezoresistive stress and strain transducers are outlined. These devices have in common the utilization of the transverse or shear piezoresistive effect. One group of devices consists of gauges in the form of a thin rectangular sheet which is bonded to the test piece, and whose resistance change can be expressed as a simple function of the principal stresses in the gauge. Two special gauges in this group are described. In one, the resistance change is proportional to the sum of the principal biaxial stresses for any orientation of the gauge on the test piece. In the other, the resistance change is proportional only to longitudinal stress components, being independent of transverse stress components. Also described are: a four-terminal gauge for complete determination of biaxial stresses, full-bridge gauges made from a single crystal, load cells of low compliance, new torque transducers, and diffusion techniques for making some of the foregoing. The devices are illustrated in terms of germanium and silicon but extension to other semiconductors is straightforward.

1. INTRODUCTION

THE literature on semiconducting stress and strain gauges published since C. S. Smith measured the piezoresistance coefficients of germanium and silicon[1] deals almost exclusively with the *longitudinal* piezoresistance effect. However, the *transverse* and *shear* effects are also large, and can be utilized to increase the sensitivity and versatility of semiconducting stress or strain transducers. A variety of examples are given in this paper. In the remainder of this section we discuss the pertinent piezoresistive constants, the many-valley model and the general behavior of wire, foil, and semiconducting strain gauges under transverse strain.

Following Mason and Thurston,[2] we define a *longitudinal piezoresistance constant* π_{11}', by[3]

$$\Delta\rho/\rho_0=\pi_{11}'\sigma, \tag{1}$$

where $\Delta\rho=\rho-\rho_0$ is resistivity change ($\rho_0=$zero stress resistivity) for the case in which the electric field, the current, and a simple tensile stress σ are in the same direction. The value of π_{11}' depends on the direction in the crystal. For crystals of the diamond-cubic or zinc-blende structure, π_{11}' is given by

$$\pi_{11}'=\pi_{11}-2(\pi_{11}-\pi_{12}-\pi_{44})(l_1^2m_1^2+l_1^2n_1^2+m_1^2n_1^2), \tag{2}$$

where l_1, m_1, and n_1 are direction cosines of the current direction with respect to the crystallographic axes, and π_{11}, π_{12}, and π_{44} are the fundamental piezoresistance coefficients of the crystal.

The *transverse piezoresistance constant* π_{12}', is defined by an equation similar to Eq. (1). However, the simple tensile stress is now normal to the current. For diamond-cubic and zinc-blende structures, π_{12}' is given by

$$\pi_{12}'=\pi_{12}+(\pi_{11}-\pi_{12}-\pi_{44})(l_1^2l_2^2+m_1^2m_2^2+n_1^2n_2^2), \tag{3}$$

where one of the subscripts refers to the current direction and the other to the stress direction. The derivation of Eq. (3) is analogous to that of Eq. (2).[2]

We distinguish two kinds of *shear piezoresistance constants*, depending on whether the electric field and current involved are in the same direction or in mutually perpendicular directions. When the electric field and current are in the same direction, say the 1′ direction, a shear stress (τ_{12}', for example) may affect the resistance through the coefficient π_{16}'. On the other hand, the same shear stress, τ_{12}', affects the ratio of the field in the 1′ direction to the current density in the 2′ direction through the coefficient π_{66}'. For the first kind, in which field and current are in the same direction, the first subscript will be 1, 2, or 3, while for the second kind, both subscripts will be greater than 3.

When referred to crystallographic axes in the classes of cubic symmetry O_h, T_d, and O,[4] all of these shear coefficients vanish except $\pi_{66}=\pi_{55}=\pi_{44}$.[1,2] However, the remaining coefficients may take on large values for other orientations. For general orientations in these crystal classes, π_{16}' is

$$\pi_{16}'=2\pi_{61}'=2(\pi_{11}-\pi_{12}-\pi_{44})(l_1^3l_2+m_1^3m_2+n_1^3n_2), \tag{4}$$

and π_{66}' is

$$\pi_{66}'=\pi_{44}+2(\pi_{11}-\pi_{12}-\pi_{44})\times[(l_1l_2)^2+(m_1m_2)^2+(n_1n_2)^2]. \tag{5}$$

Orientations for extremal values are indicated in Appendix B, Table IV.

A nonzero value of a coefficient like π_{61}' shows that a tensile stress in the 1′ direction affects the ratio of the elctric field in the 1′ direction to the current density in the 2′ direction.

---

[1] C. S. Smith, Phys. Rev. **94**, 42 (1954).

[2] W. P. Mason and R. N. Thurston, J. Acoust. Soc. Am. **29**, 1096 (1957).

[3] The π's, being derived from the components of a fourth-order tensor, properly have four subscripts, of which the first refers to the electric field component, the second to the current density component, and the last two to the stress component involved. In the two subscript π's, each subscript has replaced two of the original four subscripts according to the scheme 11 → 1, 22 → 2, 33 → 3, 23=32 → 4, 31=13 → 5, 12=21 → 6.

[4] Hermann-Mauguin symbols $m3m$, $\bar{4}3m$, and 432, respectively.

The Many-Valley Model

The symmetry of the piezoresistance effects in germanium and silicon can be visualized readily in terms of the many-valley model of Herring.[5] In the ⟨100⟩-valley model, which applies to electrons in silicon, the conduction electrons are imagined as lying in three equal groups, or valleys, aligned with the three ⟨100⟩ directions.[6] For any valley, the mobility is lowest in the valley direction (i.e., ⟨100⟩) and highest normal to that direction, but the average mobility for all the valleys is isotropic. Tension in a valley direction removes electrons from that valley and transfers them to valleys lying normal to the tension. Hence, the average mobility becomes higher in the direction of tension (longitudinal effect) and lower in directions transverse to the axis of tension (transverse effect). Compression has the opposite effect. The largest coefficient is π_{11}, which is negative for tension. Note that if the crystal is stressed in a ⟨111⟩ direction, or if the resistance change is measured in a ⟨111⟩ direction, there is a negligibly small effect, because this direction is symmetrical to the three valleys.

Electrons in germanium obey the ⟨111⟩-valley model. Here the electrons are imagined as lying in four valleys, one along each ⟨111⟩ direction. Hence the maximum longitudinal effect is in a ⟨111⟩ direction. In both models the transverse effect, for current in the valley direction, is closely equal to minus one-half the longitudinal effect.

For holes in germanium and silicon, the symmetry of the piezoresistance coefficients is that of a ⟨111⟩-valley material, even though the many-valley model does not hold. However, the sign of the large coefficient π_{44} is opposite that for electrons, being positive for tension in the "valley" direction. The approximate values of the coefficients of germainum and silicon are listed in Table I. For clarity, only the large values are listed. Among the 3–5 compounds, all coefficients are small for GaAs, but some of the coefficients in InSb and GaSb, for example, are large.[7,8] Longitudinal and transverse piezoresistance coefficients for the principal crystal directions, obtained using Eqs. (2) and (3) are listed in Table II. For all these orientations, π_{16}' is zero.

TABLE I. Approximate piezoresistance coefficients at room temperature.[a]

Material	Resistivity (ohm cm)	π_{11}	π_{12}	π_{44}
		(10^{-12} cm^2/dyne)		
n-Ge	$\sim$1	···	···	-138
p-Ge	$\sim$1	···	···	$+97$
n-Si	$\sim$12	-102	$+53$	···
p-Si	$\sim$8	···	···	$+138$

[a] From reference 2, Table I.

TABLE II. Longitudinal and transverse piezoresistance coefficients for various directions in cubic crystals.

Longitudinal direction, 1	Longitudinal coefficient, π_{11}'	Transverse direction, 2	Transverse coefficient, π_{12}'
001	π_{11}	010	π_{12}
001	π_{11}	110	π_{12}
111	$\frac{1}{3}(\pi_{11}+2\pi_{12}+2\pi_{44})$	$1\bar{1}0$	$\frac{1}{3}(\pi_{11}+2\pi_{12}-\pi_{44})$
111	$\frac{1}{3}(\pi_{11}+2\pi_{12}+2\pi_{44})$	$11\bar{2}$	$\frac{1}{3}(\pi_{11}+2\pi_{12}-\pi_{44})$
$1\bar{1}0$	$\frac{1}{2}(\pi_{11}+\pi_{12}+\pi_{44})$	111	$\frac{1}{3}(\pi_{11}+2\pi_{12}-\pi_{44})$
$1\bar{1}0$	$\frac{1}{2}(\pi_{11}+\pi_{12}+\pi_{44})$	001	π_{12}
$1\bar{1}0$	$\frac{1}{2}(\pi_{11}+\pi_{12}+\pi_{44})$	110	$\frac{1}{2}(\pi_{11}+\pi_{12}-\pi_{44})$
$1\bar{1}0$	$\frac{1}{2}(\pi_{11}+\pi_{12}+\pi_{44})$	$11\bar{2}$	$\frac{1}{6}(\pi_{11}+5\pi_{12}-\pi_{44})$
$11\bar{2}$	$\frac{1}{2}(\pi_{11}+\pi_{12}+\pi_{44})$	$1\bar{1}0$	$\frac{1}{6}(\pi_{11}+5\pi_{12}-\pi_{44})$
$1\bar{1}0$	$\frac{1}{2}(\pi_{11}+\pi_{12}+\pi_{44})$	$22\bar{1}$	$\frac{1}{9}(4\pi_{11}+5\pi_{12}-4\pi_{44})$
$22\bar{1}$	$\pi_{11}-16(\pi_{11}-\pi_{12}-\pi_{44})/27$	$1\bar{1}0$	$\frac{1}{9}(4\pi_{11}+5\pi_{12}-4\pi_{44})$

Transverse Sensitivity of Other Gauges

The metal wire and foil-type gauges, and the semiconductive strain gauges in the form of thin rods of squarish cross section, in general, are sensitive only to those components of strain in the body to which they are bonded that are parallel to the gauge length. Such gauges have low sensitivity to transverse strains in the body primarily because such strains are not effectively transmitted to the gauge.

In this paper we discuss a quite different type of semiconducting gauge, one in which, we assume, transverse and shear strains are faithfully transmitted to the semiconductor. This assumption is felt to be reasonable, especially for gauges made by the diffusion technique discussed in a later section.

2. RESPONSE OF GAUGES HAVING TRANSVERSE AND SHEAR SENSITIVITY

Consider a thin, rectangular, single-crystal sheet of semiconductor, for example silicon, of arbitrary orientation, bonded to a massive body of comparable elastic modulus. If the crystal is thin enough and wide enough, and the adhesive is strong enough, the crystal will experience, in planes parallel to the body, the same elastic strain as the body, except at its very edges. The stresses in the body are related to those in the gauge through the elastic constants of the gauge and body.

Consider such a crystal, with metallic end-electrodes, subject to normal stresses σ_1' and σ_2' and shear stresses τ_{12}', as shown in Fig. 1. The relative resistance change $\Delta R/R_0$ for current in the $1'$ direction, neglecting the

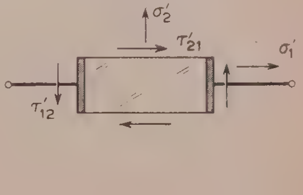

FIG. 1. Semiconductor strain gauge with current in the $1'$ direction, subjected to a longitudinal stress σ_1', a transverse stress σ_2', and a shear stress $\tau_{12}'=\tau_{21}'$.

---

[5] C. Herring, Bell System Tech. J. 34, 237 (1955).

[6] Actually there are six valleys, one for each positive and negative ⟨100⟩ direction, but for our purposes it is sufficient to imagine three.

[7] L. E. Hollander, G. I. Vick, and T. J. Diesel, Rev. Sci. Instr. 31, 323 (1960).

[8] R. W. Keyes and M. Pollak, Phys. Rev. 118, 1001 (1960).

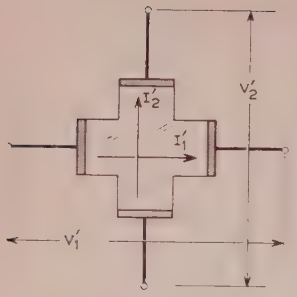

FIG. 2. Semiconductor gauge for complete measurement of biaxial stress (or strain).

effect of dimensional changes, will be

$$\Delta R/R_0=\pi_{11}'\sigma_1'+\pi_{12}'\sigma_2'+\pi_{16}'\tau_{12}'. \quad (6)$$

The relative resistance change in terms of *strain* is described in Appendix A for a gauge aligned with the cube axes.

Since any system of biaxial stress can be resolved into two principal normal stresses, σ_a and σ_b, which are orthogonal, it is appropriate to consider the response of a semiconducting gauge like that of Fig. 1 to such a stress system. Let θ be the angle between σ_a and the long direction of the gauge. The longitudinal components are $\sigma_a\cos^2\theta$ and $\sigma_b\sin^2\theta$; the transverse components are $\sigma_a\sin^2\theta$ and $\sigma_b\cos^2\theta$; the shear stress is $\frac{1}{2}(\sigma_a-\sigma_b)\sin 2\theta$. The resistance change is

$$\Delta R/R=\pi_{11}'(\sigma_a\cos^2\theta+\sigma_b\sin^2\theta)$$
$$+\pi_{12}'(\sigma_a\sin^2\theta+\sigma_b\cos^2\theta)+\tfrac{1}{2}\pi_{16}'(\sigma_a-\sigma_b)\sin 2\theta. \quad (7)$$

A complete measurement of the biaxial stress can be obtained in principle from three measurements using a single gauge. For example, referring to Fig. 2, we can measure the quantities

$$(V_1'/I_1')_{I_2'=0},\quad (V_2'/I_2')_{I_1'=0},\quad (V_2'/I_1')_{I_2'=0}.$$

From Appendix B, the equations for the corresponding field quantities (electric field and current density) are

$$(E_1'/\rho_0 i_1')_{i_2'=0}=1+\pi_{11}'\sigma_1'+\pi_{12}'\sigma_2'+\pi_{16}'\tau_{12}',$$
$$(E_2'/\rho_0 i_2')_{i_1'=0}=1+\pi_{21}'\sigma_1'+\pi_{22}'\sigma_2'+\pi_{26}'\tau_{12}', \quad (8)$$
$$(E_2'/\rho_0 i_1')_{i_2'=0}=\pi_{61}'\sigma_1'+\pi_{62}'\sigma_2'+\pi_{66}'\tau_{12}'.$$

These relations (or similar ones based on an experimental calibration) provide three equations for the three unknowns σ_1', σ_2', and τ_{12}', and hence the state of stress (or strain) can be found from three measurements on a single semiconductor gauge.

The existence of the transverse piezoresistance effect also makes possible gauges in which the current is perpendicular to the plane of the gauge. One possible advantage of such an arrangement is that the semiconducting gauge can be bonded to a metal piece with a conducting metallic bond.

The resistivity in the 3′ direction can be obtained from the general equation (B7) of Appendix B:

$$\rho/\rho_0=E_3'/(\rho_0 i_3')=1+\pi_{31}'\sigma_1'+\pi_{32}'\sigma_2'+\pi_{33}'\sigma_3'$$
$$+\pi_{34}'\tau_{23}'+\pi_{35}'\tau_{13}'+\pi_{36}'\tau_{12}'. \quad (9)$$

If we consider plane stress in the plane of the gauge [(1′,2′) plane], Eq. (9) reduces to

$$E_3'/(\rho_0 i_3')=1+\pi_{31}'\sigma_1'+\pi_{32}'\sigma_2'+\pi_{36}'\tau_{12}'. \quad (10)$$

In general, the response depends on all three plane stress components (or on the two principal stresses and the angle θ), but special orientations can be found which have special properties.

For the ⟨111⟩-valley model, the gauge responds only to a stress in the 1′ direction if the 1′ and 3′ directions are ⟨110⟩ and 2′ is ⟨100⟩. For this case, π_{36}' is precisely zero, and π_{32}' is small in comparison with π_{31}'. The resistivity equation becomes

$$E_3'/(\rho_0 i_3')=1+\tfrac{1}{2}(\pi_{11}+\pi_{12}-\pi_{44})\sigma_1'+\pi_{12}\sigma_2'. \quad (11)$$

Orientations for which both π_{36}' and π_{32}' vanish precisely can be found by choosing the direction cosines as

$$\begin{bmatrix} l_1 & m_1 & n_1 \\ l_2 & m_2 & n_2 \\ l_3 & m_3 & n_3 \end{bmatrix}=\begin{bmatrix} -\dfrac{1}{\sqrt{2}} & \dfrac{1}{\sqrt{2}} & 0 \\ \dfrac{\sin\alpha}{\sqrt{2}} & \dfrac{\sin\alpha}{\sqrt{2}} & \cos\alpha \\ \dfrac{\cos\alpha}{\sqrt{2}} & \dfrac{\cos\alpha}{\sqrt{2}} & -\sin\alpha \end{bmatrix}. \quad (12)$$

Then referring to Table III of Appendix B we see that π_{36}' vanishes for all α, and π_{32}' and π_{31}' become

$$\pi_{32}'=\pi_{12}\left(1-\frac{3}{8C}\sin^2 2\alpha\right);$$
$$\pi_{31}'=\pi_{12}\left(1-\frac{1}{2C}\cos^2\alpha\right). \quad (13)$$

where

$$C=-\pi_{12}/(\pi_{11}-\pi_{12}-\pi_{44}). \quad (14)$$

We then choose $\sin^2 2\alpha=8C/3$, which is possible for $0\leq C\leq\frac{3}{8}$. This condition is met in n-Ge, p-Ge, and n-Si. The resulting value of π_{31}' is, taking 2α in the first quadrant,

$$\pi_{31}'=(\pi_{11}-\pi_{12}-\pi_{44})\{-C+\tfrac{1}{4}[1+(1-8C/3)^{\frac{1}{2}}]\}. \quad (15)$$

(This also vanishes if $C=\frac{1}{3}$, but in that case, we can take 2α in the second quadrant to obtain a nonzero value of π_{31}', using a minus sign before the radical.)

We could also choose $\cos^2\alpha=2C$, which is possible for $0\leq C\leq\frac{1}{2}$, in which case π_{31}' vanishes and the resulting value of π_{32}' is

$$\pi_{32}'=(\pi_{11}-\pi_{12}-\pi_{44})(2C-6C^2). \quad (16)$$

If a large shear coefficient π_{36}' is desired, we may take

$$\begin{bmatrix} l_1 & m_1 & n_1 \\ l_2 & m_2 & n_2 \\ l_3 & m_3 & n_3 \end{bmatrix} = \begin{bmatrix} \frac{1}{2} & \frac{1}{2} & \frac{1}{\sqrt{2}} \\ \frac{1}{2} & \frac{1}{2} & -\frac{1}{\sqrt{2}} \\ \frac{1}{\sqrt{2}} & -\frac{1}{\sqrt{2}} & 0 \end{bmatrix}. \tag{17}$$

Then $\pi_{36}'=\frac{1}{2}(\pi_{11}-\pi_{12}-\pi_{44})$, and $\pi_{31}'=\pi_{32}'=(\frac{1}{4}-C)\times(\pi_{11}-\pi_{12}-\pi_{44})$. It is not unlikely that a material of proper purity or doping can be found to give the value $C=\frac{1}{4}$, in which case the only response would be to the shear stress τ_{12} through the coefficient π_{36}'.

3. GAUGES HAVING ZERO TRANSVERSE STRESS SENSITIVITY

The value of π_{12}' can be made zero (or close to it) by choosing for the transverse direction a crystal direction symmetrical to the valleys, e.g., ⟨111⟩ for a ⟨100⟩-valley material, ⟨100⟩ for a ⟨111⟩-valley material. Examples are shown in Figs. 3(a) and 3(b). The resistance change, in terms of principal stresses, is

$$\Delta R/R=\pi_{11}'(\sigma_a \cos^2\theta+\sigma_b \sin^2\theta). \tag{18}$$

In other words, the gauge responds only to longitudinal normal stresses. It is independent of transverse stresses, in contrast with wire, foil, and rod-type gauges, even though transverse stress is actually transmitted to the gauge. A price paid for this important advantage is a longitudinal gauge factor somewhat lower than the best for the material in question.

The above approximate statements are based on the idealization that $\pi_{12}=0$ for the ⟨111⟩-valley model and $\pi_{11}=-2\pi_{12}$, $\pi_{44}=0$ for the ⟨100⟩-valley model. However, as shown in Appendix B, we can take the fundamental coefficients just as they come in an actual material, and find orientations such that π_{12}' is *precisely* zero in that material, the only restriction being $0\leq C\leq\frac{1}{2}$. This condition is satisfied in n-Ge, p-Ge, and n-Si. (Smith's data[1,2] yield $C\doteq-0.0084$ for 7.8 ohm cm p-Si.)

FIG. 3. Stress gauges insensitive to transverse stresses.

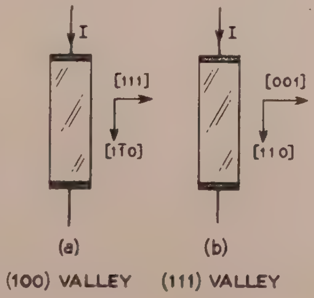

FIG. 4. Stress gauge which measures sum of principal stresses regardless of their direction.

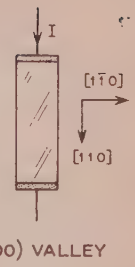

Suppose, for example,

$$\begin{pmatrix} l_1 & m_1 & n_1 \\ l_2 & m_2 & n_2 \end{pmatrix} = \begin{pmatrix} 1/\sqrt{2} & 0 & 1/\sqrt{2} \\ \cos\psi/\sqrt{2} & \sin\psi & -\cos\psi/\sqrt{2} \end{pmatrix}. \tag{19}$$

Then, referring to Eq. (3) or Table III, we find

$$\begin{aligned}\pi_{12}'=\pi_{21}'&=\pi_{12}[1-C^{-1}(l_1^2l_2^2+m_1^2m_2^2+n_1^2n_2^2)]\\ &=\pi_{12}[1-\cos^2\psi/(2C)].\end{aligned} \tag{20}$$

An orientation for which $\pi_{12}'=0$ then results from choosing ψ such that $\frac{1}{2}\cos^2\psi=C$.
Since both

$$(l_1^3l_2+m_1^3m_2+n_1^3n_2) \quad \text{and} \quad (l_1l_2^3+m_1m_2^3+n_1n_2^3)$$

are zero for this orientation, π_{16}' and π_{26}' are also both zero for this orientation (Table III). Thus, this orientation leads to particularly simple equations for the complete measurement of biaxial stress from three measurements using a single gauge, as explained in the previous section, and illustrated in Fig. 2. In this case, only σ_1' would affect the resistance in the 1′ direction, only σ_2' would affect the resistance in the 2′ direction, and only τ_{12}' would affect the transfer impedance $(E_2'/\rho_0 i_1')_{i_2'=0}$.

4. GAUGES INSENSITIVE TO STRESS ORIENTATION

Inspection of Eq. (7) reveals that a gauge of the form of Fig. 1, for which $\pi_{11}'=\pi_{12}'$ and $\pi_{16}'=0$ would be independent of θ, in other words, of the orientation of the principal stresses. Such a gauge could be made, for example, from an ideal ⟨100⟩-valley material, if the longitudinal and transverse directions were [110] and [1$\bar{1}$0] (see Fig. 4). The relative resistance change would be

$$\Delta R/R_0=\pi_{11}'(\sigma_a+\sigma_b)=0.25\pi_{11}(\sigma_a+\sigma_b). \tag{21}$$

An n-type silicon crystal approximates ideal ⟨100⟩-valley behavior, except for a small nonzero π_{44}.

Three other approaches can be used to obtain a gauge whose response is independent of θ. In the first approach, the effect of nonzero π_{44} is compensated by changing the orientation from [110], [1$\bar{1}$0] so as to obtain an orientation in which the longitudinal coefficient π_{22}', and the transverse coefficient π_{12}' are precisely equal. From Table III [or from Eqs. (2) and (3)],

$$\pi_{22}'=\pi_{11}-2(\pi_{11}-\pi_{12}-\pi_{44})(l_2^2m_2^2+m_2^2n_2^2+n_2^2l_2^2),$$

$$\pi_{12}'=\pi_{12}+(\pi_{11}-\pi_{12}-\pi_{44})(l_1^2l_2^2+m_1^2m_2^2+n_1^2n_2^2).$$

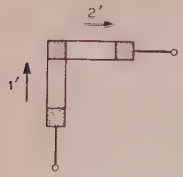

FIG. 5. *L*-form stress gauge which measures sum of principal stresses regardless of their direction.

Now define

$$D=\pi_{11}/[2(\pi_{11}-\pi_{12}-\pi_{44})].$$

By substitution,

$$\pi_{22}'=2(\pi_{11}-\pi_{12}-\pi_{44})[D-(l_2^2m_2^2+m_2^2n_2^2+n_2^2l_2^2)],$$

$$\pi_{12}'=(\pi_{11}-\pi_{12}-\pi_{44})[-C+(l_1^2l_2^2+m_1^2m_2^2+n_1^2n_2^2)].$$

Equating π_{22}' to π_{12}' leads to the equation

$$2D+C=(l_1^2l_2^2+m_1^2m_2^2+n_1^2n_2^2)+2(l_2^2m_2^2+m_2^2n_2^2+n_2^2l_2^2).$$

Since the right member is non-negative, the condition can be satisfied exactly only for $2D+C\geq 0$, i.e., only for $(\pi_{11}-\pi_{12})$ of the same sign as $(\pi_{11}-\pi_{12}-\pi_{44})$, or zero.

Considering as an example, the direction cosines specified in Sec. 3 (Eq. 19), for which the shear coefficient π_{26}' vanishes identically, we are led to the equation

$$3\cos^4\psi-5\cos^2\psi+2(2D+C)=0, \qquad (22)$$

which has real solutions for $0\leq(2D+C)\leq 25/24$. This condition is satisfied in *n*-Ge, *p*-Ge, and possibly also for some dopings in *n*-Si. (For 11.7 ohm cm *n*-Si, Smith's data[1,2] yields $2D+C=1.095$).

In the second approach, which leads to a larger range of permissible crystal orientations and materials, the gauge is made in the form of an ell, having equal resistances in the two perpendicular arms, as shown in Fig. 5. If 1′ and 2′ denote the directions of the arms, the gauge will be independent of the orientation of the principal stresses if

$$\pi_{11}'=\pi_{22}',\quad \pi_{12}'=\pi_{21}',\quad \text{and}\quad \pi_{16}'+\pi_{26}'=0;$$

where π_{11}' and π_{22}' are given by Eq. (1) with appropriate subscripts, π_{12}' and π_{21}' are given by Eq. (3), and π_{26}' is given by Eq. (4) with the subscripts of the direction cosines reversed.

These conditions are met by an ell in the (100) or (111) plane. It is readily shown that, for any orientation of the ell in the (100) plane,

$$\Delta R/R_0=[(\sigma_a+\sigma_b)/2](\pi_{11}+\pi_{12}); \qquad (23)$$

and for any orientation in the (111) plane

$$\Delta R/R_0=[(\sigma_a+\sigma_b)/6](2\pi_{11}+4\pi_{12}+\pi_{44}). \qquad (24)$$

Furthermore, the effects of the normal components of σ_a and σ_b, parallel and normal to the 1′ and 2′ directions, on the dimensional changes and hence on the resistance of the gauge, even though small compared to the piezoresistive effects, are also independent of θ.

In the third approach, which provides the greatest sensitivity of all, the current is in the 3′ direction and the gauge is in the 1′–2′ plane. The shape of the gauge in the 1′–2′ plane is immaterial. From Eq. (10) it can be seen that, if $\pi_{31}'=\pi_{32}'$ and $\pi_{36}'=0$, the relative resistance change will be independent of the orientation of the principal stresses. These conditions are met if the gauge lies in the (100) plane or in the (111) plane. For the (100) plane

$$\Delta R/R_0=\pi_{31}'(\sigma_a+\sigma_b)=\pi_{12}(\sigma_a+\sigma_b). \qquad (25)$$

For the (111) plane,

$$\Delta R/R_0=\pi_{31}'(\sigma_a+\sigma_b)=\tfrac{1}{3}(\pi_{11}+2\pi_{12}-\pi_{44})(\sigma_a+\sigma_b). \qquad (26)$$

An example of such a gauge is shown in Fig. 6. The upper face contains a metallic contact of limited area; the lower face may be entirely metallized. If the thickness is small compared to the diameter of the upper contact, the current will flow primarily in the 3′ direction.

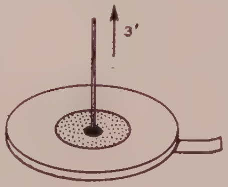

FIG. 6. Stress gauge utilizing current normal to plane of gauge, which measures sum of principal stresses regardless of direction.

Since these direction-independent gauges do not respond to shear stresses (because for these $\sigma_a+\sigma_b=0$), they could be used, for example, to indicate the tensile stress, only, in a rod subject to both tension and torsion.

5. FULL-BRIDGE GAUGES

A number of important advantages can be gained by having a gauge in the form of a hollow square. Two examples are shown in Fig. 7. Firstly, the gauge represents a complete Wheatstone bridge; external resistors are unnecessary. Secondly, the gauge is reliably compensated against changes in resistance with temperature; all arms change alike. Thirdly, all arms are active and hence the output signal is enhanced by a factor of three over the best that can be done with a single arm in a conventional Wheatstone bridge with either type of semiconductor. Fourthly, the balance of the full-bridge gauge is unaffected by homogeneous plane strain, whether produced by differential thermal expansion between gauge and test material, or by hydrostatic compression of the gauge itself or of the test material on which the gauge is mounted (if isotropic), or by contraction of the bonding agent. Lastly, the simplicity, accuracy, and ruggedness of construction are advantages, about which more will be said in Sec. 6.

In the gauges shown in Fig. 7, the resistance changes for a given stress are opposite in adjacent arms, because

π_{11}' and π_{12}' are opposite in sign. Hence, they are additive in the bridge output ΔV. The output of the gauge of Fig. 7(a), for a uniaxial stress σ_a at angle θ to the ⟨100⟩ arm is, since $\pi_{12}\cong -\frac{1}{2}\pi_{11}$,

$$2\Delta V_{cd}/V_{ef}\cong -1.5\pi_{11}\sigma_a(\cos^2\theta-\sin^2\theta). \qquad (27)$$

For the orientation of Fig. 7(b),

$$2\Delta V_{cd}/V_{ef}=-\pi_{44}\sigma_a(\cos^2\theta-\sin^2\theta).$$

An orientation equivalent to Fig. 7(b), for a ⟨111⟩-valley material is ⟨111⟩, ⟨1$\bar{1}$0⟩ or ⟨111⟩, ⟨11$\bar{2}$⟩.

A general expression for the output of a full-bridge gauge in response to principal stresses σ_a and σ_b, and assuming $\pi_{16}'=0$ is

$$-2\Delta V_{cd}/V_{ef}=(\pi_{11}'-\pi_{21}')(\sigma_a\cos^2\theta+\sigma_b\sin^2\theta) \\ -(\pi_{22}'-\pi_{12}')(\sigma_a\sin^2\theta+\sigma_b\cos^2\theta), \qquad (28)$$

where subscripts (1) and (2) refer to the vertical and horizontal arms, respectively, of Fig. 7.[9]

For the gauge of Fig. 7(a) Eq. (28) reduces to

$$2\Delta V_{cd}/V_{ef}\cong -1.5\pi_{11}(\sigma_a-\sigma_b)(\cos^2\theta-\sin^2\theta). \qquad (29)$$

For the gauge of Fig. 7(b), Eq. (28) reduces to

$$2\Delta V_{cd}/V_{ef}\cong -\pi_{44}(\sigma_a-\sigma_b)(\cos^2\theta-\sin^2\theta). \qquad (30)$$

A full-bridge gauge having zero sensitivity to transverse stresses can be made by adapting the orientations of Fig. 3 to the hollow square form, as shown in Fig. 8. For these gauges, π_{12}', π_{22}', and π_{21}' are zero. The output is

$$2\Delta V_{cd}/V_{ef}\cong -\pi_{11}'(\sigma_a\cos^2\theta+\sigma_b\sin^2\theta). \qquad (31)$$

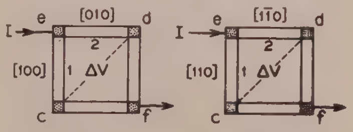

Fig. 7. Full-bridge stress gauges.

(a) [100] VALLEY

(b) [111] VALLEY

For the gauge of Fig. 8(a), Eq. (31) reduces to

$$-2V_{cd}/V_{ef}\cong 0.25\pi_{11}(\sigma_a\cos^2\theta+\sigma_b\sin^2\theta). \qquad (32)$$

For the gauge of Fig. 8(b), Eq. (31) reduces to

$$-2\Delta V_{cd}/V_{ef}\cong 0.5\pi_{44}(\sigma_a\cos^2\theta+\sigma_b\sin^2\theta). \qquad (33)$$

Advantages would be that the output is twice that of a single arm gauge of the orientation of arm (1) in a bridge circuit, and the full bridge is compensated against the effects of uniform temperature changes on the resistances of the arms.

6. DIFFUSION TECHNIQUES

We digress here to describe a mask-diffusion technique for making piezoresistive devices because this technique is used in the load cells and torque transducers of the following sections. While the gauge forms of Figs. 1, 5, and 7 can readily be cut from germanium or silicon by a supersonic vibrator, the so-called "cookie cutter," this technique may introduce microcracks, which must be removed by deep etching. But deep etching is inconsonant with accurate control of dimensions. Furthermore, when such a gauge is glued to a test piece, there is some uncertainty, especially in the transverse dimension, as to how much of the strain in the body is transmitted to the gauge, as we have discussed above.

A way around these difficulties, which has other advantages as well, is to produce, by mask-diffusion techniques, a gauge of the desired shape in the surface of a somewhat larger thin blank of high resistivity semiconductor, which is then bonded to the test piece. The diffused layer experiences perfect transmission of longitudinal and transverse strains that appear in the blank, no matter how fine the dimensions of the layer. For reasonable dimensions and resistivities, almost all of the current can be confined to the high-conductivity diffused layer. Moreover, if desired, it can be confined there by reverse-biasing the junction between a *p*-type diffusion layer and *n*-type blank, by a circuit isolated from the Wheatstone bridge circuit. Going a step further, the change in resistance of the *p*-*n* junction itself can be used as an indicator of stress or strain.

A diffusion technique can also be used to make an improved version of a cantilever force or displacement transducer. The principal of operation is like that already described,[2] but the cantilever arm is made of a single piece of high resistivity material, with high conductivity diffused layers on top and bottom where the strain is greatest. The simpler construction of the single-piece device should make it more suitable for applications in accelerometers, microphones, etc.

The cross-like form of Fig. 2 might well be made by mask-diffusion.

7. LOAD CELLS

A simple, low-compliance load cell, which utilizes the transverse piezoresistive effect is shown in Fig. 9. A very thin slice of semiconductor is placed between compression members. Current flows in the plane of the slice

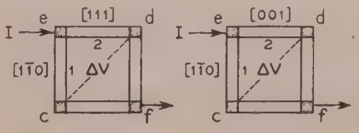

(a) [100] VALLEY

(b) [111] VALLEY

Fig. 8. Full-bridge stress gauges sensitive only to stress components parallel to arms "1."

---

[9] As an alternative to the full-bridge gauges of Fig. 7, one might use four parallel arms, two of *n*-type and two of *p*-type silicon or germanium. The orientation of maximum longitudinal piezoresistive coefficient could be used for each arm. Such an array could be wired into a full-bridge setup. It would have somewhat greater output than the gauges of Fig. 7, but disadvantages would be the difficulty of aligning the arms accurately and making electrical connections, and the difficulty of finding *n*- and *p*-type materials having identical temperature coefficients of resistance.

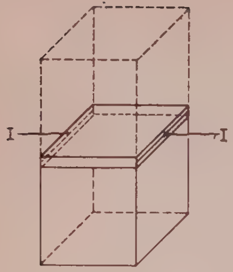

FIG. 9. Low-compliance load cell for compression using transverse piezoresistive effect.

between two line-contacts at opposite edges. The value of the transverse coefficient π_{12}', obtainable from Eq. (3), can be fairly large.

Suitable orientations are: plane of gauge, for a ⟨100⟩-valley material, {001}; for a ⟨111⟩-valley material, {110}. The direction of the current is immaterial in a square or rectangular gauge. For definiteness, one may wish to use [100] for the ⟨100⟩-valley material, and [1$\bar{1}$0] for the ⟨111⟩-valley material. The values of π_{12}' are $+\pi_{12}$ for the gauge in the (001) plane and $-\frac{1}{2}\pi_{44}$ for the gauge in the (110) plane.

A load cell like that of Fig. 9 will read the average pressure over its area if the deviations in pressure are not large enough to alter substantially the flow pattern of the current. Hence, moderate deviations from perfect squareness of the compression members and the wafer can be tolerated.

The advantages of a full-bridge gauge can be realized in load cells using only the transverse effect. An example is shown in Fig. 10. An orientation suitable for both ⟨100⟩- and ⟨111⟩-valley materials is: plane of gauge—(110); arms—[001] and [1$\bar{1}$0]. For *n*-Si (using values of Table I),

$$\pi_{12}'=\pi_{12}=+53 \qquad \text{(for the [001] arms)},$$

$$\pi_{12}'\cong\tfrac{1}{2}(\pi_{11}+\pi_{12})\cong-25 \qquad \text{(for the [1}\bar{1}\text{0] arms)}.$$

Adjacent arms change in opposite senses, and the bridge output voltage ΔV will be three times that for a single [001] arm used in the transverse manner.

For *n*-Ge, *p*-Si, or *p*-Ge, the change in the [001] arms will be negligible, because that direction is symmetrical to ⟨111⟩, while the value of π_{12}' in the [1$\bar{1}$0] arms will be $(-\frac{1}{2})(\pi_{44})$, or $\sim|70|$; ΔV will be twice that for a bridge having only one active arm.

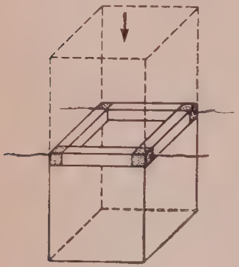

FIG. 10. Full-bridge low-compliance load cell using transverse piezoresistive effect.

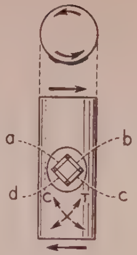

FIG. 11. Full-bridge diffusion-type gauge bonded to cylinder to measure torque.

Should the hollow shape be undesirable, for example, when the load cell is in contact with the test piece, a more uniform distribution of compressive stress in the test piece can be obtained either by inserting a flat plate between load cell and test piece or by using mask-diffusion to produce a hollow square in one surface of a solid wafer of semiconductor.

The longitudinal piezoresistance effect can also be utilized in load cells. For example, contacts might be plated on the upper and lower faces of the gauge of Fig. 9. The device would have lower impedance, and larger sensitivity than a transverse cell of the same dimensions. Of course, the plated contacts need not cover the entire area of the large faces. The impedance could be raised by using small, opposed contacts. There would be minor difficulties with edge effects and in making contact to the active parts of the contact area.

We should also mention that load cells arranged as in Fig. 9 can be oriented so as to respond to thickness shear (say τ_{12}' or τ_{13}' where 1′ is along the thickness) through coefficients such as π_{25}' or π_{26}' with current in the plane of the gauge, or through π_{15}' or π_{16}' with current perpendicular to the plane of the gage. The response to face shear (τ_{23}') has been described in Secs. 2 and 3 (with appropriate permutation of subscripts).

8. TORQUE TRANSDUCERS

The full-bridge semiconducting gauge lends itself admirably to the measurement of torque. It is common practice to use a full-bridge arrangement of foil-type gauges for this purpose, in a square array at 45° to the length of the rod being twisted. The full-bridge semiconducting gauge having transverse sensitivity, however, is doubly effective because it measures both the compressional and tensile components of the torsional shear stress in each arm.

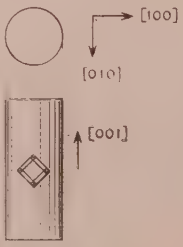

FIG. 12. Full-bridge diffusion-type gauge integral with round semiconducting rod for measuring torque.

This is illustrated by Fig. 11 in which a square gauge of ⟨111⟩-valley material, having ⟨110⟩ arms is bonded to a round rod, which is under torsional strain. (When made thin enough, semiconducting gauges can be bonded to cylinders of small radius. The bending should not affect the response.)

The gauge is made by mask-diffusion in a larger blank of high resistance semiconductor, as this structure is especially suited for picking up transverse strains. The shear stresses are shown resolved into a tension and a compression parallel to the gauge arms. For each arm, $\pi_{11}'\cong+\frac{1}{2}\pi_{44}$ and $\pi_{12}'\cong-\frac{1}{2}\pi_{44}$. Arms *a* and *c* experience a longitudinal tension and an equal transverse compression. Arms *b* and *d* experience a longitudinal compression and an equal transverse tension. The effects of tension and compression are additive in a given arm, but the signs of the resistance change are opposite in adjacent arms so they are additive in the bridge output. Since the shear stress τ is equal in magnitude to the compression or tension, the response of the gauge is

$$\Delta V/V=\pi_{44}\tau. \tag{34}$$

Other suitable orientations for the arms are [100], [010] for *n*-silicon, [111], [1$\bar{1}$0] for *n*- and *p*-germanium, and *p*-silicon.

Bonding problems can be avoided by making the torsion rod itself of semiconductor and constructing the gauge on the rod by diffusion, epitaxy, or similar technique. Figures 12–14 show examples suitable for a ⟨111⟩-valley semiconductor. In Fig. 12 the rod is round, and the arms of the gauge lie approximately in ⟨110⟩ directions, more accurately so the smaller the gauge. In Fig. 13 the arms lie exactly in ⟨110⟩ directions, but the strain is not pure shear. In either case, however, the response will be proportional to the torque.

In Fig. 14, the arms lie in ⟨110⟩ directions but are not coplanar. In all these arrangements, current leads are placed at one pair of opposite arm-intersections and voltage leads at the other pair. In all designs, Figs. 11 through 14, the response is independent of longitudinal tension or compression of the bar, or of bending.

A mask-diffusion technique can also be used to construct an improved torque transducer based on the same principle as the one described by Mason and Thurston.[2] For example, diametrically opposite layers subtending angles of about 150° can be diffused into the surface to carry the current. This leaves two undoped (high resistivity) diametrically opposite 30° sectors where the voltage output electrodes are to be placed. An advantage over a homogeneous cylinder is that the current is confined to the surface layer of the cylinder where the strain is greatest. This permits higher current density for a given heating effect, resulting an increased sensitivity. Moreover, the resistance and resistivity can be controlled independently by controlling the depth of and impurity concentration in the diffused layer.

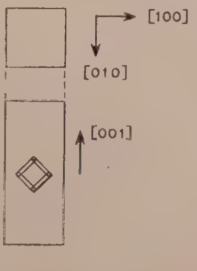

Fig. 13. Full-bridge diffusion-type gauge integral with square semiconducting rod for measuring torque.

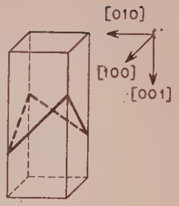

Fig. 14. Full-bridge, nonplanar, diffusion-type gauge integral with semiconducting rod for measuring torque.

Mason and Thurston proposed to put the axis of the transducer along a ⟨100⟩ direction in Ge, thus exploiting the large value of π_{44}. We see from Table III that π_{44}' can exceed π_{44} only when π_{44} and $(\pi_{11}-\pi_{12}-\pi_{44})$ are of the same sign, or $\pi_{44}=0$ and hence there are no more sensitive orientations in Ge or in *p*-Si. However, in *n*-Si, we can have, for 2′ and 3′ along ⟨110⟩ directions,

$$\pi_{44}'=2(\pi_{11}-\pi_{12})>\pi_{44},$$

as may be verified from Appendix B and the values cited by Smith.[1,2] Thus, if such a transducer were to be made from *n*-Si, or any other material having π_{44} and $(\pi_{11}-\pi_{12}-\pi_{44})$ of the same sign, or $\pi_{44}=0$, the cylinder axis and the voltage output electrodes should be along ⟨110⟩ directions to obtain the maximum sensitivity.

A torque gauge can also be based on the use of shear coefficients such as π_{16}' or π_{15}'. Figure 15 shows a cylinder of high resistivity semiconducting material with diametrically opposite diffused layers (top and bottom in Fig. 15). One end of the cylinder is covered with a continuous metal electrode. A torque about the cylinder axis 1′ results in shear stresses τ_{13}' which are of opposite sign in the upper and lower layers. Therefore, the resistance in the 1′ direction, proportional to $E_1'/\rho_0 i_1'$, is affected oppositely, in the upper and lower layers, through the term $\pi_{15}'\tau_{13}'$. This differential change can be detected in a bridge circuit connected as illustrated.

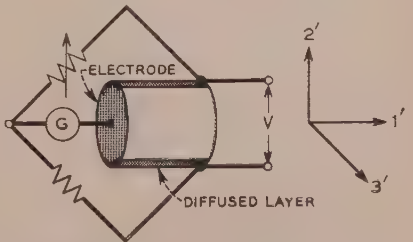

Fig. 15. Torque gauge utilizing the shear piezoresistance coefficient π_{15}'.

The maximum value of π_{15}' is 0.562 $(\pi_{11}-\pi_{12}-\pi_{44})$, and the corresponding orientation can be obtained from the entry opposite the third expression in Table IV (upon replacing the subscript 2 by 3). Such a gauge could also be made of a homogeneous semiconductor, but the sensitivity would be less.

ACKNOWLEDGMENTS

We are pleased to acknowledge helpful discussions with J. P. Guerard, G. R. Gohn, C. Herring, A. R. Hutson, W. P. Mason, M. Pollak, G. F. Weissmann, I. V. Williams, and R. Wolfe. We are grateful to E. N. Gilbert for proving that the extremal values of the 2nd and 3rd expressions of Table IV are as indicated, and to K. E. Benson and J. T. Nelson for experimental assistance in the preliminary verification of certain of the concepts reported here.

APPENDIX A. GAUGE FACTOR EXPRESSED IN TERMS OF STRAIN

The relative change in resistivity $\Delta\rho/\rho_0$, can be expressed in terms of the longitudinal and transverse strains ϵ_1 and ϵ_2, respectively, produced by stresses σ_1 and σ_2 in the plane of the gauge, by using the following expression (Mason[10]):

$$E_1/\rho_0=i_1+m_{11}i_1\epsilon_1+m_{12}i_1(\epsilon_2+\epsilon_3)+m_{44}(i_2\epsilon_6+i_3\epsilon_5), \tag{A1}$$

where E_1 is the field in the 1 direction, i_1 is the current density, and the m's are elastoresistance constants which are given in terms of piezoresistance constants π and elastic constants c by

$$\begin{aligned} m_{11}&=\pi_{11}c_{11}+2\pi_{12}c_{12},\\ m_{12}&=\pi_{11}c_{12}+\pi_{12}(c_{11}+c_{12}),\\ m_{44}&=\pi_{44}c_{44}. \end{aligned} \tag{A2}$$

For simplicity let the 1, 2, and 3 directions be cube axes. Let the current be in the 1 direction, so that i_2 and i_3 are zero. Then Eq. (A1) becomes

$$E_1/\rho_0=i_1[1+m_{11}\epsilon_1+m_{12}(\epsilon_2+\epsilon_3)]. \tag{A3}$$

Following Mason and Thurston,[2] if $E_1/i_1=(\rho_0+\Delta\rho_1)$ is the resistivity under strain, then the fractional change in resistivity under strain is, from Eq. (A3),

$$\Delta\rho_1/\rho_0=m_{11}\epsilon_1+m_{12}(\epsilon_2+\epsilon_3). \tag{A4}$$

If it is assumed that $\sigma_3=0$, then the strain ϵ_3 normal to the plane of the gauge is not independent, but can be expressed in terms of ϵ_1 and ϵ_2 by eliminating σ_1 and σ_2 from the following equations for the three strains:

$$\begin{aligned} \epsilon_1&=Y^{-1}(\sigma_1-\nu\sigma_2),\\ \epsilon_2&=Y^{-1}(\sigma_2-\nu\sigma_1),\\ \epsilon_3&=-\nu Y^{-1}(\sigma_1+\sigma_2), \end{aligned} \tag{A5}$$

where Y denotes Young's modulus along the cube axis, and ν denotes Poisson's ratio. The result is

$$\epsilon_3=-\nu(\epsilon_1+\epsilon_2)/(1-\nu). \tag{A6}$$

Substituting Eq. (A6) in Eq. (A4) we obtain

$$\frac{\Delta\rho_1}{\rho_0}=\epsilon_1\left[m_{11}-\frac{\nu}{1-\nu}m_{12}\right]+\epsilon_2\frac{(1-2\nu)}{(1-\nu)}m_{12}. \tag{A7}$$

For stress in the cube direction, ν is $c_{12}/(c_{11}+c_{12})$. Hence, $(\Delta\rho_1/\rho_0)$ is expressed in terms of ϵ_1, ϵ_2, and known constants.

For a simple tension, σ_1 only, $\sigma_2=0$ and $\epsilon_2=-\nu\epsilon_1$. Equation (A7) reduces to

$$\Delta\rho_1/\rho_0\cong\epsilon_1(m_{11}-2\nu m_{12}). \tag{A8}$$

The coefficient of ϵ_1 is equal to $\pi_{11}Y=m_l$, where Y is Young's modulus in the cube direction, which is to be expected.

It may be more useful to express Eq. (A7) in terms of π's and c's. By substituting Eq. (A2) in Eq. (A7) we obtain

$$\Delta\rho_1/\rho_0=\epsilon_1[A\pi_{11}+B\pi_{12}]+\epsilon_2[B\pi_{11}+A\pi_{12}], \tag{A9}$$

where

$$A=c_{11}-c_{12}^2/c_{11},\quad B=c_{12}-c_{12}^2/c_{11}. \tag{A10}$$

Since, for a (100)-valley material (which would be used for a gauge aligned with the cube axes), $\pi_{12}\cong-0.5\pi_{11}$, Eq. (A9) can be written

$$\Delta\rho_1/(\pi_{11}\rho_0)\cong\epsilon_1[A-0.5B]+\epsilon_2[B-0.5A]. \tag{A11}$$

APPENDIX B. PIEZORESISTANCE COEFFICIENTS FOR ARBITRARY ORIENTATIONS

Introduction

For arbitrary orientations, piezoresistance coefficients in addition to the longitudinal coefficient and the shear coefficient π_{44} employed in previously published applications of semiconductor stress or strain transducers[2,1 are of interest. For symmetry classes O_h, T_d, and O of the cubic system, the matrix of the 2-subscript piezoresistance coefficients, *referred to the crystallographic axes* has the form shown below.[1]

$$\begin{matrix} \pi_{11} & \pi_{12} & \pi_{12} & 0 & 0 & 0\\ \pi_{12} & \pi_{11} & \pi_{12} & 0 & 0 & 0\\ \pi_{12} & \pi_{12} & \pi_{11} & 0 & 0 & 0\\ 0 & 0 & 0 & \pi_{44} & 0 & 0\\ 0 & 0 & 0 & 0 & \pi_{44} & 0\\ 0 & 0 & 0 & 0 & 0 & \pi_{44}. \end{matrix} \tag{B1}$$

However, all 36 of the coefficients may be nonzero when referred to a Cartesian system of *arbitrary orientation* relative to the crystallographic axes.

In materials like Ge and Si, in which the piezoresist

---

[10] W. P. Mason, *Physical Acoustics and the Properties of Solids*, (D. Van Nostrand Company, Inc., Princeton, New Jersey, 1958), p. 351.

[11] F. T. Geyling and J. J. Forst, Bell System Tech. J. 39, 70 (1960).

TABLE III. Piezoresistance coefficients for rotated axes.

Coefficient	Expression	Analogous coefficients
π_{11}'	$=\pi_{11}-2(\pi_{11}-\pi_{12}-\pi_{44})[(l_1m_1)^2+(m_1n_1)^2+(n_1l_1)^2]$	π_{22}', π_{33}'
$\pi_{12}'=\pi_{21}'$	$=\pi_{12}+(\pi_{11}-\pi_{12}-\pi_{44})[(l_1l_2)^2+(m_1m_2)^2+(n_1n_2)^2]$	$\pi_{13}'=\pi_{31}'$; $\pi_{23}'=\pi_{32}'$
$\pi_{16}'=2\pi_{61}'$	$=2(\pi_{11}-\pi_{12}-\pi_{44})(l_1^3l_2+m_1^3m_2+n_1^3n_2)$	$\pi_{24}'=2\pi_{42}'$; $\pi_{35}'=2\pi_{53}'$ $\pi_{26}'=2\pi_{62}'$; $\pi_{34}'=2\pi_{43}'$ $\pi_{15}'=2\pi_{51}'$
$\pi_{36}'=2\pi_{63}'$	$=2(\pi_{11}-\pi_{12}-\pi_{44})(l_1l_2l_3^2+m_1m_2m_3^2+n_1n_2n_3^2)$	$\pi_{14}'=2\pi_{41}'$; $\pi_{25}'=2\pi_{52}'$
$\pi_{46}'=\pi_{64}'$	$=2(\pi_{11}-\pi_{12}-\pi_{44})(l_1l_2^2l_3+m_1m_2^2m_3+n_1n_2^2n_3)$	$\pi_{54}'=\pi_{45}'$; $\pi_{65}'=\pi_{56}'$
π_{66}'	$=\pi_{44}+2(\pi_{11}-\pi_{12}-\pi_{44})[(l_1l_2)^2+(m_1m_2)^2+(n_1n_2)^2]$	π_{44}', π_{55}'

ance effect is highly anisotropic, any of the coefficients can be made large by choosing an appropriate orientation. Knowledge of these additional coefficients and the orientations for which they take on large values opens up new possibilities for strain gauges, dynamometers, and accelerometers. For example, a shear can be measured directly from the change of resistance between a single pair of electrodes, instead of requiring the voltage to be measured at right angles to the current, as in the torque meter described earlier.[2]

In this Appendix, we indicate expressions for the piezoresistance coefficients for arbitrary orientations, and mention orientations for which they take on large values.

Derivation Procedure

Expressions for the coefficients π_{ij}', referred to arbitrarily oriented axes, may be obtained formally in either of two ways: One may convert to the 4-subscript coefficients, apply the usual transformation rule for 4th-order tensors, and then reconvert to the 2-subscript coefficients. Or, one may proceed by writing down the piezoresistance equations referred to crystallographic axes, then transform the current density and stress to a new, arbitrarily oriented system of axes, and finally, by expressing the electric field in the new system, obtain piezoresistance equations referred to the new axes, but in which only the coefficients referred to the crystallographic axes appear. The coefficients π_{ij}', referred to the arbitrary orientation, then appear as the expressions which are the coefficients of various current density and stress components in the new equations. For example, π_{36}' is the coefficient of $i_3'\tau_{12}'$ in the expression for E_3'/ρ_0.

Let quantities without primes be referred to the crystallographic axes, and primed quantities to a Cartesian system whose orientation is specified by the transformation matrix

$$\begin{array}{cccc} & 1 & 2 & 3 \\ 1' & l_1 & m_1 & n_1 \\ 2' & l_2 & m_2 & n_2 \\ 3' & l_3 & m_3 & n_3. \end{array} \tag{B2}$$

That is, the x_i' axis has the direction cosines l_i, m_i, n_i with respect to the crystallographic axes $i=1, 2, 3$. The current density components in the crystallographic system are given by

$$\begin{aligned} i_1&=l_1i_1'+l_2i_2'+l_3i_3', \\ i_2&=m_1i_1'+m_2i_2'+m_3i_3', \\ i_3&=n_1i_1'+n_2i_2'+n_3i_3'. \end{aligned} \tag{B3}$$

The stress components in the crystallographic system are[12]

$$\begin{aligned} \sigma_1&=l_1^2\sigma_1'+l_2^2\sigma_2'+l_3^2\sigma_3'+2(l_2l_3\tau_{23}'+l_1l_3\tau_{13}'+l_1l_2\tau_{12}'), \\ \tau_{23}&=m_1n_1\sigma_1'+m_2n_2\sigma_2'+m_3n_3\sigma_3'+(m_2n_3+m_3n_2)\tau_{23}' \\ &\quad+(m_1n_3+m_3n_1)\tau_{13}'+(m_1n_2+m_2n_1)\tau_{12}'. \end{aligned} \tag{B4}$$

The equations for σ_2 and σ_3 are of the same form as the first of this pair, and those for τ_{31} and τ_{12} are of the same form as the second. The electric field components in the rotated system are given by equations like the inverses of (B3):

$$\begin{aligned} E_1'&=l_1E_1+m_1E_2+n_1E_3, \\ E_2'&=l_2E_1+m_2E_2+n_2E_3, \\ E_3'&=l_3E_1+m_3E_2+n_3E_3. \end{aligned} \tag{B5}$$

Now the piezoresistance equations, referred to crystallographic axes are

$$\begin{aligned} E_1/\rho_0&=i_1[1+\pi_{11}\sigma_1+\pi_{12}(\sigma_2+\sigma_3)] \\ &\quad+\pi_{44}(i_2\tau_{12}+i_3\tau_{13}), \\ E_2/\rho_0&=i_2[1+\pi_{11}\sigma_2+\pi_{12}(\sigma_1+\sigma_3)] \\ &\quad+\pi_{44}(i_1\tau_{12}+i_3\tau_{23}), \\ E_3/\rho_0&=i_3[1+\pi_{11}\sigma_3+\pi_{12}(\sigma_1+\sigma_2)] \\ &\quad+\pi_{44}(i_1\tau_{13}+i_2\tau_{23}). \end{aligned} \tag{B6}$$

By substituting (B3) and (B4) into (B6), and the resulting expressions for E_1, E_2, and E_3 into (B5), we obtain equations of the form

$$\begin{aligned} E_1'/\rho_0=i_1'(1&+\pi_{11}'\sigma_1'+\pi_{12}'\sigma_2'+\pi_{13}'\sigma_3' \\ &+\pi_{14}'\tau_{23}'+\pi_{15}'\tau_{13}'+\pi_{16}'\tau_{12}') \\ &+i_2'(\pi_{61}'\sigma_1'+\pi_{62}'\sigma_2'+\pi_{63}'\sigma_3' \\ &+\pi_{64}'\tau_{23}'+\pi_{65}'\tau_{13}'+\pi_{66}'\tau_{12}') \\ &+i_3'(\pi_{51}'\sigma_1'+\pi_{52}'\sigma_2'+\pi_{53}'\sigma_3' \\ &\quad+\pi_{54}'\tau_{23}'+\pi_{55}'\tau_{13}'+\pi_{56}'\tau_{12}'), \end{aligned}$$

---

[12] A. E. H. Love, *A Treatise on the Mathematical Theory of Elasticity* (Dover Publications, New York, 1944), 4th ed., p. 80.

TABLE IV. Extremal values of the expressions in the direction cosines.

Expression	Extremal values	Example of orientation for extremum $\begin{bmatrix} l_1 & m_1 & n_1 \\ l_2 & m_2 & n_2 \end{bmatrix}$
(1) $(l_1m_1)^2+(m_1n_1)^2+(n_1l_1)^2$	0	$\begin{bmatrix} 1 & 0 & 0 \\ \multicolumn{3}{c}{\text{Any} \perp \text{dir.}} \end{bmatrix}$
	$\frac{1}{3}$	$\begin{bmatrix} \frac{1}{\sqrt{3}} & \frac{1}{\sqrt{3}} & \frac{1}{\sqrt{3}} \\ \multicolumn{3}{c}{\text{Any} \perp \text{dir.}} \end{bmatrix}$
(2) $(l_1l_2)^2+(m_1m_2)^2+(n_1n_2)^2$	0	$\begin{bmatrix} 1 & 0 & 0 \\ \multicolumn{3}{c}{\text{Any} \perp \text{dir.}} \end{bmatrix}$
	$\frac{1}{2}$	$\begin{bmatrix} \frac{1}{\sqrt{2}} & \frac{1}{\sqrt{2}} & 0 \\ \frac{1}{\sqrt{2}} & -\frac{1}{\sqrt{2}} & 0 \end{bmatrix}$
(3) $l_1^3l_2+m_1^3m_2+n_1^3n_2$	±0.281	$\begin{bmatrix} \mp 0.3055 & \mp 0.3055 & \mp 0.9022 \\ \mp 0.638 & \mp 0.638 & \mp 0.432 \end{bmatrix}$
(4) $l_1l_2l_3^2+m_1m_2m_3^2+n_1n_2n_3^2$	±0.25	$\begin{bmatrix} \pm\frac{1}{2} & \pm\frac{1}{2} & \pm\frac{1}{\sqrt{2}} \\ \mp\frac{1}{2} & \mp\frac{1}{2} & \pm\frac{1}{\sqrt{2}} \end{bmatrix}$

$$\begin{aligned} E_2'/\rho_0 = {} & i_1'(\pi_{61}'\sigma_1'+\pi_{62}'\sigma_2'+\pi_{63}'\sigma_3' \\ & +\pi_{64}'\tau_{23}'+\pi_{65}'\tau_{13}'+\pi_{66}'\tau_{12}') \\ & +i_2'(1+\pi_{21}'\sigma_1'+\pi_{22}'\sigma_2'+\pi_{23}'\sigma_3' \\ & +\pi_{24}'\tau_{23}'+\pi_{25}'\tau_{13}'+\pi_{26}'\tau_{12}') \\ & +i_3'(\pi_{41}'\sigma_1'+\pi_{42}'\sigma_2'+\pi_{43}'\sigma_3' \\ & \qquad +\pi_{44}'\tau_{23}'+\pi_{45}'\tau_{13}'+\pi_{46}'\tau_{12}'), \end{aligned}$$

$$\begin{aligned} E_3'/\rho_0 = {} & i_1'(\pi_{51}'\sigma_1'+\pi_{52}'\sigma_2'+\pi_{53}'\sigma_3' \\ & +\pi_{54}'\tau_{23}'+\pi_{55}'\tau_{13}'+\pi_{56}'\tau_{12}') \\ & +i_2'(\pi_{41}'\sigma_1'+\pi_{42}'\sigma_2'+\pi_{43}'\sigma_3' \\ & +\pi_{44}'\tau_{23}'+\pi_{45}'\tau_{13}'+\pi_{46}'\tau_{12}') \\ & +i_3'(1+\pi_{31}'\sigma_1'+\pi_{32}'\sigma_2'+\pi_{33}'\sigma_3' \\ & \qquad +\pi_{34}'\tau_{23}'+\pi_{35}'\tau_{13}'+\pi_{36}'\tau_{12}'). \qquad \text{(B7)} \end{aligned}$$

Expressions for the Coefficients

The actual expressions obtained for the primed coefficients are summarized in Table III.

Orientations for Maximum Coefficients

The above expressions involve the direction cosines in four fundamentally different ways. The factors multiplying $(\pi_{11}-\pi_{12}-\pi_{44})$ are zero for certain orientations, for example, for the crystallographic axes. The extremal values, and the orientations for which they occur, are indicated in Table IV.

Possibility of Zero Coefficients

For certain uses, it is useful to know whether it is possible to choose orientations such that certain of the coefficients are precisely zero. In the first place, all coefficients which are zero in the original array (B1) vanish for the crystallographic axes, and also for certain other orientations.

Since the first expression in Table IV ranges between 0 and $\frac{1}{3}$, the coefficient π_{11}' or the analogous coefficients π_{22}' and π_{33}' can be made to vanish if

$$0 \leq \pi_{11}/[2(\pi_{11}-\pi_{12}-\pi_{44})] \leq \tfrac{1}{3}. \qquad \text{(B8)}$$

Since the second expression ranges between 0 and $\frac{1}{2}$, the coefficient π_{12}' or its analogs can be made to vanish if

$$0 \leq -\pi_{12}/(\pi_{11}-\pi_{12}-\pi_{44}) \leq \tfrac{1}{2}. \qquad \text{(B9)}$$

Similarly, π_{66}' or its analogs can be made to vanish if

$$0 \leq -\pi_{44}/[2(\pi_{11}-\pi_{12}-\pi_{44})] \leq \tfrac{1}{2}. \qquad \text{(B10)}$$

The situation for Ge and Si, based on the measurements of Smith[1,2] can be summarized as follows:

Condition	Satisfied In
(B8)	*p*-Ge
(B9)	*p*-Ge, *n*-Ge, *n*-Si
(B10)	*p*-Ge

Except in the case of π_{16}', etc., which vanish exactly for crystallographic axes, the orientations which give precisely zero values will depend on the actual values of π_{11}, π_{12}, and π_{44} in the material under consideration.

Elastoresistance Coefficients for Arbitrary Orientations

Elastoresistance coefficients m_{ij} may be defined by equations of the same form as (B7) with the stress components replaced by the corresponding engineering strain components.[10] Since the transformation formulas for the engineering strains differ slightly from (B4), factors of two are absent from certain terms in the expressions for the coefficients referred to rotated axes. It turns out that Table III holds for m's if every π whose *second* subscript is 4, 5, or 6 is replaced by *twice* the m having the same subscript, and the remaining π's are replaced by the corresponding m's. For example,

$$m_{66}'=m_{44}+(m_{11}-m_{12}-2m_{44})(l_1^2l_2^2+m_1^2m_2^2+n_1^2n_2^2)$$

and

$$m_{16}'=m_{61}'=(m_{11}-m_{12}-2m_{44})(l_1^3l_2+m_1^3m_2+n_1^3n_2).$$

JOURNAL OF APPLIED PHYSICS VOLUME 32, NUMBER 10 OCTOBER, 1961

Majority Carrier Magnetosurface Effect

ROBERT D. LARRABEE
RCA Laboratories, Princeton, New Jersey

(Received April 6, 1961)

In semiconductors with extremely low majority carrier densities, the conductivity of the surface space charge region can be very different from the conductivity of the bulk. This paper demonstrates that the conductivity of this surface space charge region can be materially altered by the application of a magnetic field which is perpendicular to the direction of current flow. A tentative prototype model of this effect is presented which not only illustrates the mechanisms of importance, but also is sufficiently accurate to enable one to estimate the order of magnitude of the effect for certain experimental conditions. This model suggests that this effect may find application in magnetoresistance and/or negative resistance devices and might prove useful in the measurement of surface parameters.

INTRODUCTION

SEMICONDUCTORS with extremely low majority carrier density have many interesting properties.[1] In particular, the width of the surface space charge region becomes quite large and may approach or even exceed the sample dimensions. The total integrated charge on the exposed free surface areas of the specimen may be comparable or greater than the charge on the ionized, uncompensated impurities in the bulk. It is not surprising, therefore, that the surface can have a profound effect upon the electrical properties of specimens constructed from such material.

Semiconductors with extremely low majority carrier density are easily prepared by deionizing a deep impurity level at an appropriate temperature. For the case of deionized gold-doped germanium at 77°K, majority carrier densities in the range of 10^8 holes/cm^3 are easily obtainable. It is quite apparent that any charges on the surface of reasonable sized specimens of such deionized material will have a large effect on the net conductance of these specimens.

If the current is mainly flowing in the surface space charge regions of a specimen, then most of the surface effects will become predominant, and, in turn, will affect the conductivity of the specimen. Amith[2] has considered the effect of a magnetic field in enhancing the relative importance of surface scattering and its effect on the mobility of the carriers in the surface space charge region.[3] This paper is concerned with the effect of a magnetic field in changing the number of carriers in the surface space charge region. It will be shown that this effect can be quite large and can give rise to large changes in the net conductivity of a specimen.

Shockley and Pearson[4] attempted to influence the surface layer conductance by means of an externally applied voltage to a condenser plate in close proximity to the surface in question. The charge added to the sample to compensate for the charge on the condenser plate was assumed to reside in the surface space charge region and thus would be mobile and would modulate the conductivity. Unfortunately, it was found that a large portion of the added charge resided in the immobile surface states, and consequently, the modulation of the conductivity by the voltage applied to the condenser plate was very much lower than was otherwise expected.

---

[1] For some interesting properties that are not mentioned in this paper, see V. I. Stafeev, Soviet Phys.—Solid State **1**, 763 (1959).

[2] A. Amith, J. Phys. Chem. Solids **14**, 271 (1960).

[3] J. N. Zemel, Phys. Rev. **112**, 762 (1958).

[4] W. Shockley and G. L. Pearson, Phys. Rev. **74**, 232 (1948).

This very same bulk-surface interaction which was so detrimental to the Shockley field effect[4] is also responsible for a very interesting magnetic effect. The application of a magnetic field in a direction transverse to the net flow of current tends to concentrate (or deplete) the majority carrier density at the surface, just as did the voltage applied to the condenser plate in the Shockley experiment. However, in the present case, the application of a magnetic field does not directly add or subtract any electrical charge from the sample. However, since there will be a redistribution of charge between the immobile surface states and the bulk, the application of this magnetic field will modulate the net conductivity of the specimen.

It is this magnetically induced redistribution of charge between the bulk and surface that has been termed the majority carrier magnetosurface effect and will be discussed in greater detail in this paper.

The following discussion presents a mathematical description of the magnetosurface effect, which is sufficiently accurate to enable one to evaluate the order of magnitude of the conductivity changes expected. The mathematical development is followed by a discussion of the application of this theory to the semiconductor germanium. Unfortunately, the present technology of surfaces has not advanced to the point where it is possible to prepare samples with the surface properties required for the effective utilization of the magnetosurface effect. Therefore, it has been virtually impossible to design experiments to illustrate the basic ideas of this theory.

DEVELOPMENT OF A MODEL OF THE MAGNETOSURFACE EFFECT

The general procedure utilized in the following section of this paper to derive a mathematical description of the magnetosurface effect involves a combination of the carrier transport equation with Poisson's equation to obtain a differential equation for the majority carrier density[5] as a function of position in the specimen. This equation is integrated and the boundary conditions imposed by the surface are applied, so that an explicit relationship between carrier density and position is obtained. The net conductivity of the specimen as a function of magnetic field (and the other experimental parameters) are derived from this relationship.

The nature of the surface presents a formidable problem if the most general surface conditions are assumed. For mathematical reasons, only two types of surface states have been recognized in this analysis. One of these states is assumed to be charged positively when occupied by a hole and the other is assumed to be charged negatively when occupied by an electron. Both of these states are assumed to be located in energy far from the Fermi level so that Boltzmann statistics can be utilized. It is also assumed that, on any particular surface, only one of these states is present and will give rise to an accumulation or a depletion surface depending upon its electrical charge.

It is also assumed that the sample is thick enough so that the space charge channels of two opposite surfaces do not overlap. This is an important assumption since it implies that each surface space charge region is independent of the other and assures that there will be no interaction between them. This assumption is made for mathematical reasons, and it is felt that some interesting physics may have been lost by its introduction. However, this assumption does greatly simplify the mathematics and enables one to solve the problem without any further drastic assumptions.

MATHEMATICAL ANALYSIS OF THE MAGNETOSURFACE EFFECT

Assume a semi-infinite slab of semiconductor material with a surface at $Z=0$ as shown in Fig. 1. It will be assumed that this material is a p-type semiconductor. A uniform electric field is applied in the Y direction through contacts (at infinity) that are "ohmic" to the valence band. A uniform magnetic field is applied in the X direction.

Let:

p_0 = the extrinsic thermal equilibrium bulk hole density,
p = the hole density in the space charge region,
N_s' = the thermal equilibrium density of charge on surface states,
N_s = the density of charge in surface states under arbitrary conditions—both N_s and N_s' carry the sign of the charge on the surface states,
μ = the hole mobility (assumed to remain constant),
e = the electronic charge,
$V_T = kT/e$ = the voltage equivalent of the temperature,
$D = \mu V_T$ = the diffusion constant of holes,
ϵ = the permittivity of the semiconductor material,
E = the applied electric field (in the Y direction),
B = the applied magnetic field (in the X direction).

The mks system of units will be utilized throughout this analysis.

A. Transport Equation

Under steady-state conditions, the current density of holes toward the surface (i.e., the Z direction) will be equal to zero. Consequently, the sum of the components of current due to electric fields, Lorentz forces, and

---

[5] The temperature is assumed sufficiently low so that the thermal equilibrium density of minority carriers can be neglected. The mobility of the majority carriers is assumed constant and independent of position and field strengths.

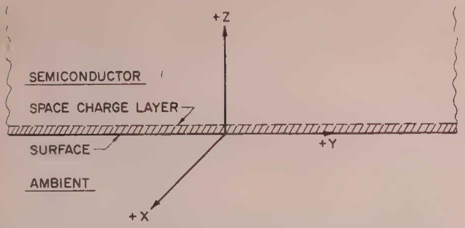

FIG. 1. Schematic representation of the coordinate system used in the mathematical development of the magnetosurface effect.

diffusion must vanish. Consequently,

$$p\mu E_z - p\mu^2 EB - D(dp/dz) = 0, \tag{1}$$

where E_z represents the electrical field in the Z direction.

B. Poisson's Equation

Poisson's equation relates the space charge and the electrical field in the Z direction in the following way:

$$dE_z/dz = e(p-p_0)/\epsilon. \tag{2}$$

Equation (2) can be solved for p and this value inserted into Eq. (1), with the following result:

$$\left\{p_0 + \frac{\epsilon}{e}\frac{dE_z}{dz}\right\}\{E_z - \mu BE\} - \frac{\epsilon V_T}{e}\frac{d^2E_z}{dz^2} = 0.$$

This equation is simplified by the substitution

$$S = E_z - \mu BE \quad \text{and} \quad dS = dE_z. \tag{3}$$

Consequently,

$$\frac{d^2s}{dz^2} - \frac{s}{V_T}\frac{ds}{dz} - \frac{p_0 e}{\epsilon V_T} S = 0.$$

A first integral of this equation is obtained by use of the substitution

$$\frac{ds}{dz} = P \quad \text{and} \quad \frac{d^2s}{dz^2} = \frac{dP}{dz} = P\frac{dP}{ds}.$$

By utilizing this substitution, the first integral of the above differential equation can be written in the following form:

$$\frac{p}{p_0} - \ln\frac{p}{p_0} = \frac{\epsilon}{2p_0 eV_T} S^2 + A,$$

where A is a constant of integration. By substituting the value for S given in Eq. (3), this equation can be expressed in the following form:

$$E_z = \mu BE \pm \left(\frac{2p_0 eV_T}{\epsilon}\right)^{\frac{1}{2}} \left(\frac{p}{p_0} - A - \ln\frac{p}{p_0}\right)^{\frac{1}{2}}. \tag{4}$$

C. Boundary Conditions Imposed by the Bulk.

It will be assumed that the specimen is thick enough so that the surface space charge regions from opposite surfaces do not overlap one another. In this way, the solution of the present problem for two opposite surfaces will be independent of one another and the initial assumption of a semi-infinite slab is reasonable. There will be a region near the middle of a specimen (or for large Z values in the semi-infinite slab) where there will be no space charge (i.e., $p = p_0$). In these regions the electric field must equal the familiar Hall field given by the relation $E_{\text{Hall}} = \mu BE$. Since Eq. (4) is valid throughout the semiconductor, this condition implies that A must equal unity.

E_z can be eliminated from Eq. (4) by utilizing the relationship expressed in Eq. (1) to yield the following differential equation for the majority carrier density p:

$$\frac{dp}{dz} = \pm\frac{p}{V_T}\left(\frac{2p_0 eV_T}{\epsilon}\right)^{\frac{1}{2}} \left(\frac{p}{p_0} - 1 - \ln\frac{p}{p_0}\right)^{\frac{1}{2}}. \tag{5}$$

The integration of Eq. (5) to obtain an explicit relationship for the hole density as a function of Z is very difficult. Two special cases for which the mathematics is relatively simple will be considered. For accumulation surfaces, $p > p_0$ and the term involving $\ln p/p_0$ is small compared to the remaining terms under the square root sign of Eq. (5), and will be neglected. For depletion surfaces, $p < p_0$ and the converse is true. In this way, Eq. (5) can be solved for these two special cases by neglecting the appropriate terms under the square root sign.

1. Accumulation Solution

Equation (5) can be expressed in the following form for accumulation surface conditions:

$$\frac{dp}{p(p-p_0)^{\frac{1}{2}}} = -\left(\frac{2e}{\epsilon V_T}\right)^{\frac{1}{2}} dz.$$

The negative sign is necessary since, for accumulation surfaces, dp/dz is negative. This equation can be immediately integrated to yield

$$p = p_0\left\{1 + \tan^2\left[\left(\frac{ep_0}{2\epsilon V_T}\right)^{\frac{1}{2}}(z - z_0)\right]\right\}, \tag{6a}$$

where z_0 is a constant of integration which represents the width of the space charge layer.

2. Depletion Solution

Equation (5) can be expressed in the following form for depletion surface conditions:

$$\frac{dp}{p[\ln(p_0/p)]^{\frac{1}{2}}} = +\left(\frac{2ep_0}{\epsilon V_T}\right)^{\frac{1}{2}} dz.$$

The positive sign is necessary since, for depletion surfaces, dp/dz is positive. This equation can be immediately integrated to yield

$$p=p_0 \exp\left[-\frac{ep_0}{2\epsilon V_t}(z-z_0)^2\right], \quad (6b)$$

where z_0 is a constant of integration which represents the width of the space charge layer.

D. Boundary Conditions Imposed by the Surface

The electrical charge in the immobile surface states is given by the relation: Charge in surface states $=eN_s$ coul/m^2 (N_s carries the sign of the charge). Gauss' theorem relates the charge density in the surface states to the electric field produced by these charges. Consequently, if there is no electric field external to the semiconductor and its surface, Gauss' theorem implies that

$$E_z]_{z=0}=+eN_s/\epsilon.$$

Combining this equation with Eq. (4) evaluated at $Z=0$ (i.e., the surface), one obtains

$$N_s=\frac{\epsilon}{e}\mu BE\pm\left(\frac{2p_0\epsilon V_T}{e}\right)^{\frac{1}{2}}\left(\frac{p(0)}{p_0}-1-\ln\frac{p(0)}{p_0}\right)^{\frac{1}{2}}, \quad (7)$$

where $p(0)$ is the value of p at $Z=0$.

It is now necessary to specify the nature of the surface states which comprise the N_s charge. It will be assumed that there are two kinds of surface states, one of which gives rise to an accumulation surface and one that gives rise to a depletion surface. The case where more than one kind of surface state is simultaneously present on the same surface will not be considered. The type of surface state that will give rise to an accumulation surface on p-type material will be assumed to possess a negative charge when occupied by an electron. Similarly, the other type of surface state that gives rise to a depletion surface on p-type material will be assumed to carry a positive charge when occupied by a hole. Both of these surface states will be assumed to lie sufficiently far in energy from the Fermi level that Boltzmann statistics is a valid approximation under all experimental conditions.

1. Accumulation Surfaces

The density of negative charge residing in surface states is related to the thermal equilibrium density of charge (designated by N_s') and to the change in surface potential (ΔV) caused by the application of the applied electric and magnetic fields by the Boltzmann relation

$$N_s=N_s'e^{-\Delta V/V_T}.$$

The density of carriers in the space charge region adjacent to the surface $p(0)$ is related to the thermal equilibrium density of majority carriers at the surface $p'(0)$ and the change in surface potential (ΔV) by a similar Boltzmann relation

$$p(0)=p'(0)e^{\Delta V/V_T}.$$

Combining these last two equations,

$$p(0)=N_s'p'(0)/N_s.$$

However, from Eq. (7) (neglecting the ln term as discussed previously) it is apparent that

$$\frac{2p_0\epsilon V_T}{e}\left\{\frac{p(0)}{p_0}-1\right\}=\left\{N_s-\frac{\epsilon}{e}\mu BE\right\}^2.$$

By setting $E=0$ in this expression, a relationship involving the thermal equilibrium majority carrier density at $Z=0$ [i.e., $p'(0)$] is obtained as follows:

$$p'(0)=p_0+\frac{e}{2\epsilon V_T}(N_s')^2.$$

Combining the last three equations reveals that

$$-N_s=\left\{\left(\frac{2\epsilon V_T}{e}\right)\left[\left(\frac{N_s'}{N_s}\right)\times\left(p_0+\frac{e}{2\epsilon V_T}N_s'^2\right)-p_0\right]\right\}^{\frac{1}{2}}-\frac{\epsilon\mu BE}{e}.$$

Let

$$R=N_s/N_s',\ \alpha=\epsilon V_T p_0/(eN_s'^2),\ \beta=-\epsilon\mu BE/(eN_s'). \quad (8)$$

By utilizing these substitutions, the previous equation becomes

$$R^3+2\beta R^2+(\beta^2+2\alpha)R-(2\alpha+1)=0. \quad (9a)$$

The parameter R is a measure of the change in the surface charge density N_s (measured in terms of N_s') when an electric and a magnetic field are applied to the specimen so that thermal equilibrium conditions are no longer valid. Alpha is a dimensionless parameter that does not depend upon the magnitude of the applied electric and magnetic fields, but rather depends mainly upon the uncompensated impurity density p_0 and the equilibrium density of surface states N_s'. Beta is a dimensionless parameter that depends upon the magnitude of the applied electric and magnetic fields and upon the equilibrium density of surface states. Beta is positive when the Lorentz force tends to concentrate the holes against the surface in question and negative when it tends to deplete the hole density at the surface. Therefore, Eq. (9a), is a relationship for the number of charged surface states under any arbitrary experimental condition as specified by alpha and beta. Figure 2 represents a graph of the relationship expressed by Eq. (9a) in which R is plotted as a function of beta for different alpha values, over the range of beta where the assumptions of the present analysis are valid.

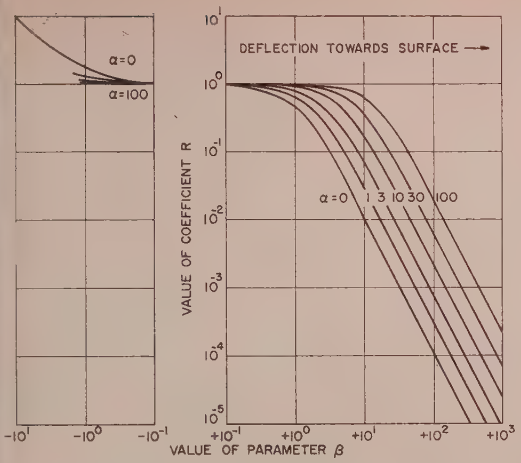

FIG. 2. Graphical representation of the number of charged surface states R as a function of the experimental conditions α and β, for the case of an *accumulation* surface [this is a graph of the relationship expressed in Eq. (9a)]. The right side of the graph corresponds to deflection towards surface and the left side of the graph to deflection away from the surface.

2. *Depletion Surfaces*

The procedure used in the derivation of an equation analogous to Eq. (9a) but appropriate for depletion surfaces proceeds in the same fashion as in the derivation of Eq. (9a) except that the surface state that is charged positive when occupied by a hole is assumed and the ln term of Eq. (7) is assumed to dominate over the remaining terms under the square root sign. In this way, the following equation appropriate for depletion surfaces is obtained:

$$R^2+2R\beta-2\alpha\ln(1/R)+\beta^2-1=0, \qquad (9b)$$

where the values of alpha and beta are given by Eq. (8). The relationship expressed by Eq. (9b) is shown in Fig. 3 in which R is plotted as a function of beta for several alpha values, over the range of beta consistent with the assumptions employed in the present analysis.

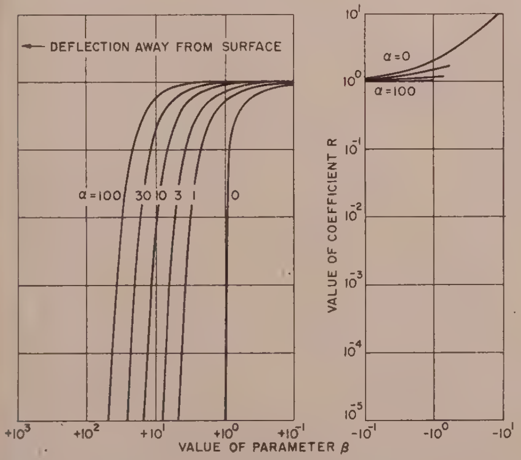

FIG. 3. Graphical representation of the number of charged surface states R, as a function of the experimental conditions α and β, for the case of a *depletion* surface [this is a graph of the relationship expressed in Eq. (9b)]. The right side of the graph corresponds to deflection towards surface and the left side of the graph to deflection away from the surface.

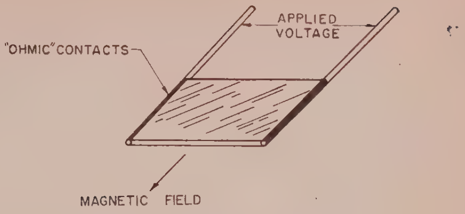

FIG. 4. Wafer sample consisting of a semiconductor material provided with two "ohmic" contacts to the majority carrier band suitable for studies of the magnetosurface effect.

E. Calculation of the Net Conductance of a Semiconductor Specimen

The total net positive charge per unit surface area in a p-type wafer sample such as illustrated in Fig. 4 is given by

Total positive charge/unit surface area

$$=\int_0^w p\,dz+N_s]_{\text{depletion}},$$

where w = the sample thickness and $N_s]_{\text{depletion}}$ is the surface charge density on any depletion surfaces.

The total net negative charge per unit surface area in the wafer sample is given by

Total negative charge/unit surface area

$$=-p_0w+N_s]_{\text{accumulation}}.$$

Since the sample plus surface is electrically neutral, the above two expressions can be combined to give

$$\int_0^w p\,dz=p_0w-N_s]_{\text{accumulation}}-N_s]_{\text{depletion}}.$$

Since the mobility of the mobile charge carriers will be assumed to be constant over the cross section of the specimen, the conductivity of the complete sample will not be dependent upon the spacial dependence of the density in the z direction, but rather upon the integrated density as given above. Therefore, the equivalent conductivity of the specimen as a whole can be expressed in the following form:

$$\sigma=p_0e\mu-\left\{\frac{N_s}{w}\bigg|_{\text{accumulation}}+\frac{N_s}{w}\bigg|_{\text{depletion}}\right\}e\mu, \qquad (10)$$

($N_s]_{\text{accumulation}}$ is a negative quantity). Consequently, by inserting the values for the surface charge densities as determined by Eqs. (9a) and/or (9b) (Figs. 2 and/or 3) into Eq. (10), the total equivalent conductivity of the specimen can be found for any arbitrary experimental condition. An example of this procedure will be illustrated in a subsequent section of this paper.

F. Calculation of the Width of the Surface Space Charge Layers

It has been assumed that the sample is thicker than the sum of the space charge regions of the two opposite surfaces of the specimen. It is of interest to compute these space charge thicknesses so that one can be sure that this assumption is fulfilled in any particular application of this model.

1. Accumulation Surfaces

If Eq. (6a) is evaluated at the surface (i.e., $Z=0$) and then solved for the width of the space charge layer z_0, one obtains

$$z_0=\left(\frac{2\epsilon V_T}{ep_0}\right)^{\frac{1}{2}}\tan^{-1}\left(\frac{p(0)-p_0}{p_0}\right)^{\frac{1}{2}}.$$

By utilizing the relationships derived above, this equation can be expressed in the following form:

$$z_0=\left(\frac{2\epsilon V_T}{ep_0}\right)^{\frac{1}{2}}\tan^{-1}\left\{\frac{R+\beta}{(2\alpha)^{\frac{1}{2}}}\right\}. \tag{11a}$$

Consequently, the width of the space charge layer of an accumulation surface can be found by substituting the values of alpha, beta, and R appropriate for the existing conditions. Notice that z_0 is bounded by an upper bound given by

$$z_0\leq\frac{\pi}{2}\left(\frac{2\epsilon V_T}{ep_0}\right)^{\frac{1}{2}}.$$

2. Depletion Surfaces

If Eq. (6b) is evaluated at the surface ($Z=0$) and then solved for the width of the space charge layer z_0, one obtains

$$z_0=\left(\frac{2\epsilon V_T}{ep_0}\right)^{\frac{1}{2}}\left\{\ln\frac{p_0}{p(0)}\right\}^{\frac{1}{2}}.$$

Utilizing the relationships derived above, this equation can be expressed in the following form:

$$z_0=N_s'(R+\beta)/p_0. \tag{11b}$$

Notice that the width of a depletion layer does not possess an upper bound as was the case for an accumulation surface. Instead, as beta increases, the width of the depletion layer increases without limit. Consequently, Eqs. (11a) and (11b) serve as convenient equations to determine the thickness of the space charge layers of either an accumulation [Eq. (11a)] or a depletion [Eq. (11b)] surface.

G. Review of the Assumptions of this Model

Since there have been a number of assumptions made in the development of this model, it is instructive to summarize them at this point.

It has been assumed that the density of minority carriers is low enough that they never contribute an appreciable conductivity. This assumption is valid at sufficiently low temperatures where the intrinsic density is well below the actual majority carrier density present.

The assumption of a constant mobility throughout the sample is valid if the width of the space charge layer is not too small[2,3] so that surface scattering is not an important parameter, if the electric field is not so high as to give rise to any appreciable high field effects,[6] and if the effects of the applied magnetic field on the mobility can be neglected.

The assumptions regarding the nature of the surface states is valid if these surface properties can be produced experimentally. Of course, the analysis will not be valid for surfaces with properties different from those assumed.

The assumptions regarding the expression

$$[p/p_0-1-\ln(p/p_0)]$$

in Eq. (5) were made for mathematical convenience and should not give rise to appreciable errors within the range where this approximation is valid.

The assumptions made regarding the thickness of the specimen can be easily satisfied. However, it is quite probable that some interesting effects which are not predicted by the present model will occur when the two space charge regions overlap so as to interact with one another.

In view of these considerations, it is felt that the present model is a first approximation to the solution of this problem and is not a completely rigorous analysis of all the interactions possible.

H. Generalization of the Model to *n*-Type Material

The results of the previous analysis [Eqs. (9a), (9b), (10), (11a), (11b), and Figs. 2 and 3] can be generalized to represent either *n*-type or *p*-type material in the following way. Equations (9a), (11a), and Fig. 2 are valid for accumulation surfaces and Eqs. (9b), (11b), and Fig. 3 are valid for depletion surfaces (regardless of the nature of the bulk semiconductor). p_0 and μ are assumed positive and taken to represent the majority carrier equilibrium density and mobility, respectively. Beta is taken as positive if the Lorentz force is of such a direction as to push majority carriers towards an accumulation or away from a depletion surface. Notice that α and R are positive definite in terms of the above definitions.

---

[6] R. D. Larrabee, J. Appl. Phys. **30**, 857 (1959).

APPLICATION OF THE MODEL TO GERMANIUM

Perhaps it would be appropriate at this point to apply the results of this model to specific examples involving the semiconductor germanium. Consider first, the value of the parameter α for a specimen of n-type germanium with an uncompensated impurity density of 10^{14} donors/cm^3 and a surface charge density of 10^{11} charges/cm^2 at room temperature. Under these conditions, α is approximately 2×10^{-3}. It is apparent from the definition of α [Eq. (8)] that unless p_0 is very large (an uninteresting case since it minimizes the surface effects of interest) or unless N_s' is very small, α for germanium will be much less than unity. Assuming an electron mobility of 3600 cm^2/v sec for germanium, and subjecting this material to an electric field of 100 v/cm and a magnetic field of 10^4 gauss, one finds that the value of β will be approximately 3×10^{-3}. Notice that unless E or B is very large or unless N_s' is very small, β for germanium will be much less than unity. Referring to Figs. 2 and 3, one can readily see that the present model predicts small changes in conductivity (i.e., R) for β values much less than unity. It is felt that this is the reason why large conductivity changes due to the magnetosurface effect have not been observed in the past.

It is constructive to compute the conductivity change predicted for a thin wafer sample of germanium such as illustrated in Fig. 4. It will be assumed that the two large surface areas are in an identical state of accumulation. The $\alpha=0$ curve of Fig. 2 [i.e., Eq. (9a)] can be expanded in a Maclaurin Series about $\beta=0$ to give

$$R\approx1-\frac{2}{3}\beta+\frac{1}{9}\beta^2+\frac{2}{81}\beta^3+\cdots.$$

In the application of this series approximation to the thin wafer sample, it is necessary to notice that β will be positive for one surface and negative for the other. With this fact in mind, one can substitute this series approximation into Eq. (10) and retain only terms to the second order. In this way, the equivalent conductivity of the wafer sample is found to be

$$\sigma=p_0e\mu+\frac{2e\mu}{w}\left\{N_s'+\frac{1}{9N_s'}\left(\frac{\epsilon\mu BE}{e}\right)^2\right\}.$$

The first two terms in the above expression represent the equivalent conductivity of the bulk and surface under thermal equilibrium conditions, while the last term represents the change in the equivalent conductivity due to the magnetosurface effect. This equation states that for moderate values of electric and magnetic fields (e.g., 100 v/cm and 10^4 gauss), the equivalent conductivity of a thin wafer sample of germanium with two identical accumulation surfaces will increase quadratically with an increase in either B or E. It is interesting to notice that the conductivity changes predicted by this equation are generally small and may be of the same magnitude as other magnetoresistive effects, such as the variation of mobility with magnetic field. In fact, it is possible that the magnetosurface effect has caused some of the errors and uncertainty in the past magnetoresistive measurements of the variation of μ with B, since both effects can have about the same effect on the observed conductance of a specimen, and to a first approximation, they both vary with the square of the applied magnetic field.

In order to make the magnetosurface effect large, β must be about equal to or greater than unity. Since large electric and magnetic fields are generally not attractive, one is forced to employ surfaces with low densities of charged surface states. If the value of N_s' required is low, then p_0 will also have to be a low value so that the bulk conductivity does not dominate over the surface conductivity for samples of reasonable dimensions. If one is interested in optimizing the effect in germanium, one can utilize germanium with low majority carrier densities (such as deionized gold-doped germanium at reduced temperatures) and should employ surface treatments that do not produce a large number of charged surface states. It will be necessary to control the density and the electric properties of the surface states so as to obtain the desired characteristics. It is unfortunate that, at the present time, the technology of surfaces has not advanced to the point where the degree of control, reproducibility, and stability of surfaces that one would like to achieve in order to utilize the magnetosurface effect, can be easily realized.

SOME IMPLICATIONS OF THE MODEL

Notice that the curves of Figs. 2 and 3 indicate that β must be equal to or greater than unity for an appreciable magnetosurface effect. This implies that at low electric and magnetic field strengths and for surfaces with a large equilibrium surface charge density, the effect of β on the specimen conductivity will be small. These considerations suggest that there will be an optimum surface treatment (i.e., N_s') for obtaining the maximum effect. If N_s' is too large, there will be a large surface conductance, but the β values for reasonable values of E and B will be small, and the net effect will be small. For small values of N_s', the β values will be sufficiently large to give rise to an appreciable change in the parameter R, but, unfortunately, the conductivity of the specimen will be dominated by the bulk conductivity and the net effect of a change in the specimen conductance will be small. Therefore, it is necessary to adjust the density of the surface states to an optimum value in order to effectively utilize the magnetosurface effect. This optimum value of N_s' will depend upon the sample geometry, p_0, the highest values of B and E that can be used, etc.

Notice that, if an accumulation surface to which the carriers are deflected (i.e., the surface with a positive beta) has a slightly smaller density of charged surface states than the opposite accumulation surface (see Fig. 4), its beta value will have a slightly larger absolute magnitude for a given E and B. This situation could result in a voltage-controlled negative resistance characteristic if the magnetic field is held constant and the electric field (voltage) is varied. This negative resistance arises since the accumulation surface with a negative beta can be adjusted so that its charge density does not change greatly over the range of B and E of interest. However, the charge on the surface with a positive beta can be made to decrease greatly over the same range of B and E, thus leading to a net decrease in the surface charges (and thus current) with an increase in voltage. One can, in fact, produce a variety of characteristics by altering the magnitude and/or sign of the charges on these two surfaces.

SOME LIMITATIONS OF THE PRESENT MODEL

Several of the assumptions which have been made in the development of the present model of the magnetosurface effect limit the applicability of the model. It has been assumed, for example, that the specimen is thick enough so that the space charge layers of opposite surfaces do not overlap, and thus the surfaces behave independently. It would be interesting to theoretically and/or experimentally determine the nature of the interactions if this were not the case.

It was assumed that only one kind of surface state was present and that it was located far from the Fermi level so that Boltzmann statistics could be utilized. The simultaneous presence of two or more kinds of surface states would give rise to some interesting characteristics, particularly if they were located in energy so that one or more of them could pass through the Fermi level as β was varied. The relatively sudden change in the probability of occupancy of these surface states as they passed through the Fermi level would produce some very interesting characteristics.

CONCLUSION

A new magnetosurface effect has been described in which the number of mobile carriers in a specimen can be altered by virtue of a magnetically induced redistribution of charge between the bulk and the surface states. A tentative model of the basic mechanism has been developed for certain types of surfaces. This model not only illustrates the physical nature of the effect, but also is sufficiently accurate to aid the experimenter in the design of samples and/or devices. The model suggests that this phenomenon may find use not only as a tool for measuring surface properties, but also suggests new magnetoresistive and negative resistance device applications for the phenomenon. Certainly, when it becomes experimentally possible to prepare suitable, controlled, reproducible, and stable surfaces on semiconductors and insulators, more work to extend the range of validity of the present model would probably be required. It appears to the author that the magnetosurface effect presents intriguing problems to both the theorist and the experimentalist and that the solution of these problems should prove extremely interesting.

ACKNOWLEDGMENTS

The author wishes to express his appreciation for the comments and criticisms of K. H. Zaininger, H. S. Sommers, Jr., A. Rose, A. Amith, G. C. Dousmanis, and A. M. Goodman.

JOURNAL OF APPLIED PHYSICS VOLUME 32, NUMBER 10 OCTOBER, 1961

Preparation of Monocrystalline Cuprous Oxide*

YUKIKO EBISUZAKI
Chemical Laboratory, Indiana University, Bloomington, Indiana

(Received May 11, 1961)

A method is described for preparing large single crystals of cuprous oxide by oxidation of monocrystalline copper. The initial oxidation is performed slowly at low oxygen pressure and temperature, to promote oriented growth of the oxide film. The cuprous oxide crystals obtained from the oxidation process showed subgrain boundaries which were removed by subsequent annealing.

INTRODUCTION

CUPROUS oxide may be considered the prototype of the series of oxides whose properties as a semi-onductor are governed by the stoichiometric excess of xygen. Since the numerous investigations have all een performed on polycrystalline specimens, it is ighly desirable to have monocrystalline samples of igh purity available for such studies.

There have been several attempts to grow single rystals of cuprous oxide.[1–4] Although in rare individual ases fairly large crystals were obtained, the methods vere not consistently successful and usually yielded nly coarse-grained polycrystalline oxide. Recently, oth, Kilkson, and Trivich[5] have described a method f growing thin sections of large monocrystalline cuprous xide by the annealing of polycrystalline samples pre-ared by oxidation of copper.

A method has been developed in this laboratory to repare thick single crystals of cuprous oxide, of large urface area.

EXPERIMENTAL PROCEDURE

A monocrystalline 99.999% copper rod, grown by he Bridgman technique with the [111] axis of the rystal parallel to the cylinder axis, was obtained from he Virginia Institute for Scientific Research. Disks of .5 mm thickness were cut from the rod and, after hemical removal of strained areas, they were me-hanically polished to a mirror finish on emery paper nd polishing alumina. Then they were electrolytically olished in orthophosphoric acid,[6] washed in distilled ater, and dried in nitrogen.

When a disk was placed in the furnace, it was main-ained under a low oxygen pressure while the tempera-ure of the furnace was gradually raised from 22–980°C. his low oxygen pressure was provided by the im-urities in tank nitrogen (about 0.2% oxygen). After -6 hr of slow oxidation, the oxygen pressure was increased and oxidation continued for 8.5 days in a flowing mixture consisting of oxygen (3.1 mm Hg) and tank nitrogen. Then the cuprous oxide crystal was allowed to cool in a stream of tank nitrogen.

By this method copper disks of thickness about 1.8 mm were converted into cuprous oxide crystals approximately 3.2 mm thick and 18 mm in diameter. The maximum thickness obtained was 5 mm. Since the oxide crystals had slightly rounded surfaces and a void in the central region corresponding to the central plane of the original metal, they were split into halves and the porous central regions removed with fine-grained emery paper. Finally, the crystal surfaces were etched quite deeply in acid solution (17% HNO_3, 41.5% H_3PO_4 and 41.5% HOAc by volume) at 38°C to remove any strain introduced by the mechanical treatment.

The cuprous oxide crystals thus obtained had shiny smooth surfaces and a translucent red color. A typical sample is seen in Fig. 1, which shows one-half of a crystal after splitting.

Transmission Laue x-ray photographs of the oxide crystals were taken using a tungsten-target tube operated at 40 kv and 20 ma. The crystal to film distance was set at 5 cm and an aluminum foil (2.5×10^{-2} mm) was employed for screening the fluorescent radiation.

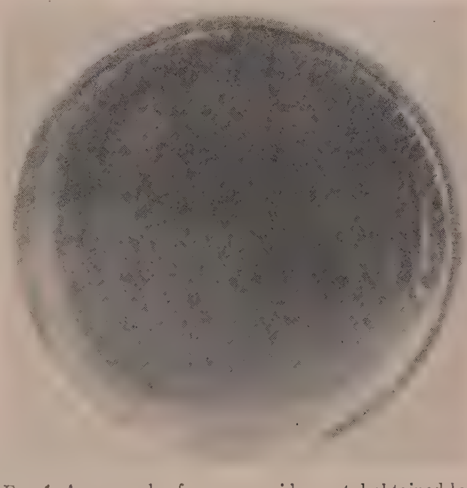

FIG. 1. An example of cuprous oxide crystal obtained by oxidation of single-crystal copper.

---

* Work sponsored by the U. S. Atomic Energy Commission.

[1] N. Takahashi and J. J. Trillat, Acta Met. **4**, 201 (1956).

[2] A. L. Rvachev, Zhur. Tekh. Fiz. **28**, 45 (1958).

[3] G. Blankenburg and K. Kassel, Ann. Phys. **10**, 201 (1952).

[4] Y. I. Gritsenko, Izvest. Akad. Nauk. S.S.S.R. Ser. Fiz. **21**, 53 (1957).

[5] R. S. Toth, R. Kilkson, and D. Trivich, J. Appl. Phys. **31**, 117 (1960).

[6] W. J. McG. Tegart, *Electrolytic and Chemical Polishing of etals* (Pergamon Press, New York, 1956).

Crystals used for these studies were 0.6–0.8 mm thick and the exposure time was between 5 and 10 hr.

An unannealed cuprous oxide crystal gave a transmission photograph such as that in Fig. 2. Each Laue spot is split into a packed multiplet, showing the existence of subgrain boundaries. After annealing at temperatures ranging from 1050–1080°C, the Laue spots became sharper, as shown in Fig. 3. Figure 4, taken after annealing a crystal, 0.8 mm thick, for 96 hr at 1080°C, shows a low angle-of-misfit grain boundary.

Usually the subgrain boundaries disappeared completely to produce a distortion-free single crystal as shown in Fig. 5, taken using a 0.6-mm thick crystal which had been annealed at 1050°C for 65 hr. Similar photographs, all showing the same orientation, were obtained from different portions of an annealed crystal.

DISCUSSION

The most critical phases in these operations probably lie in insuring that the copper disks are smooth, free from any traces of discoloration due to oxide films or contaminants, and that slow nucleation was achieved. These conditions have been shown by Young, Cathcart, and Gwathmey,[7] and Harris, Ball, and Gwathmey[8] to be the requirements for the formation of oriented oxide nuclei.

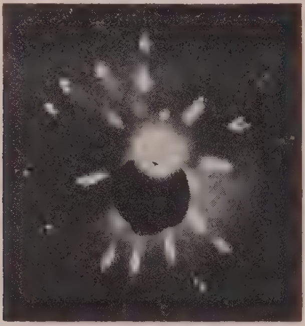

Fig. 2. A typical Laue transmission photograph of an unannealed cuprous oxide crystal (0.8 mm thick).

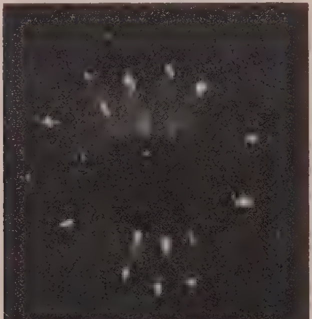

Fig. 3. Transmission Laue photograph of the crystal shown in Fig. 2 after annealing for 17.5 hr at 1080°C.

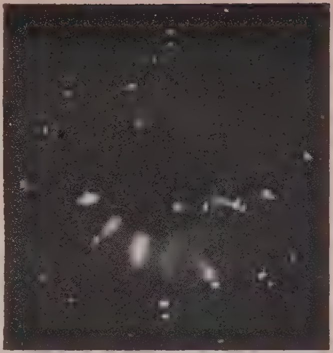

Fig. 4. Laue photograph of the crystal shown in Fig. 2 after annealing for 96 hr.

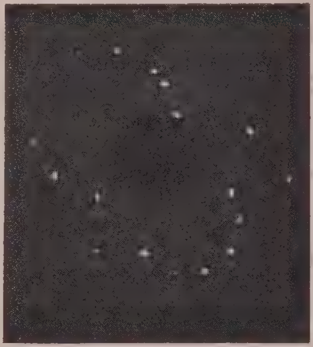

Fig. 5. A typical Laue photograph of single-crystal cuprous oxide.

The subgrain boundaries seen in the x-ray films were probably introduced owing to a polygonization process.[9] A strain was introduced into the oxide film as the oxidation proceeded at the edge and both surfaces of the disk. The resulting curvature and the central hollow zone shaped like a double convex lens show that bending of the crystal took place. Since the strain was introduced at a sufficiently high temperature (980°C), polygonization resulted. The subgrain boundaries could be removed by the annealing process, although there was also some tendency to form crystallites, separated by a low angle-of-misfit grain boundary. Perhaps the annealing could be made to occur during the oxidation process, if the cuprous oxide crystals were grown at higher temperatures.

This method of growing single crystal cuprous oxide may be considered successful and has the advantage of yielding large crystals.

ACKNOWLEDGMENTS

The author wishes to acknowledge helpful discussions with Professor W. J. Moore and Dr. J. J. Lander.

---

[7] F. W. Young, J. V. Cathcart, and A. T. Gwathmey, Acta Met. 4, 145 (1956).

[8] W. W. Harris, F. L. Ball, and A. T. Gwathmey, Acta Met. 5, 574 (1957).

[9] A. Guinier, *Imperfections in Nearly Perfect Crystals*, edited by W. Shockley, J. Hollomon, R. Maurer, and F. Seitz (John Wiley & Sons, Inc., New York, 1952).

OURNAL OF APPLIED PHYSICS VOLUME 32, NUMBER 10 OCTOBER, 1961

Conductivity of Seeded Atmospheric Pressure Plasmas

L. S. Frost
Westinghouse Research Laboratories, Pittsburgh 35, Pennsylvania

(Received February 27, 1961)

The electrical conductivity is calculated for some typical seeded gases of magnetohydrodynamic interest. The electron density is obtained using Saha's equation. A method is developed for calculating electron mobility in gas mixtures, taking account of the variation of the scattering cross section with energy. Scattering by ions is also considered. Results are presented for several gases seeded with small amounts of Cs or K in the temperature range from 2000° to 4000°K.

INTRODUCTION

THE increasing interest in magnetohydrodynamic (MHD) generation of electrical power[1,2] and in he electrical properties of flames has emphasized the eed for a better understanding of the conductivity of he hot gases involved. This paper presents data, ethod of calculation, and results for several gases and edings in the temperature range from 2000° to 000°K.

The conductivity of a gas depends on the density of lectrons in the gas and on their mobility

$$\sigma = en_e\mu. \tag{1}$$

he electron density in presently postulated systems sults from seeding with alkali metal compounds. It ill be given by Saha's equation and is considered in ec. I below. The dc electron mobility depends on the um of momentum transfer collision frequencies for all omponents of the gas mixture, including the ions when eir scattering is significant. This calculation, together ith our conductivity results, is presented in Secs. II d III. In Sec. IV a method is presented for combining e conductivities due to molecular scattering alone and e to ion and electron scattering alone to get the true nductivity, which should be useful for extending the esent results to other cases of interest.

I. ELECTRON DENSITY

Consider a gas of possible MHD interest at a pressure one atmosphere. In general, it will have negligible nductivity when heated to 2000° to 4000°K. If a essure of $\mathcal{E}$ atmospheres of an alkali metal is added, eful conductivities may be obtained in this temperare range. The total pressure is thus $1+(1+f)\ \mathcal{E}$ mospheres, where f is the fraction of the alkali atoms hich are ionized. Generally, it is expected that $\mathcal{E}\ll 1$, though this restriction is not necessary.

The equilibrium constant for ionization of atoms with nization potential V, at temperature T°K, is given by the Saha equation[3]

$$K_1 = \frac{n_e n_i}{n_0} = \frac{2g_i}{g_0}\frac{(2\pi mkT)^{\frac{3}{2}}}{h^3}e^{-\frac{eV_i}{kT}}. \tag{2}$$

Here the n's are densities per cubic centimeter, the g's are statistical weights, and the subscripts e, i, and 0 denote electrons, ions, and neutral atoms, respectively. For the alkali metals, $g_i/g_0=\frac{1}{2}$. We shall consider the alkali metals K and Cs, with V_i equal to 4.34 and 3.893 ev, respectively.

Solving Eq. (2) for n_e, noting that space-charge neutrality requires $n_i=n_e$ to a high degree of approximation, we have

$$n_e = (K_1N_a)^{\frac{1}{2}}[(1+K_1/4N_a)^{\frac{1}{2}} - (K_1/4N_a)^{\frac{1}{2}}], \tag{3}$$

where

$$N_a = n_0 + n_e = 7.335\times 10^{21}\mathcal{E}/T\ \text{cm}^{-3} \tag{4}$$

is the total density of alkali metal particles, atoms, and ions present.

The calculated electron density for three values of Cs seeding and one of K seeding is shown as a function of temperature in Fig. 1. Note that Cs yields a greater electron density than K, as expected from its smaller ionization potential. Also note that for 0.001 atm of Cs f is approaching unity at 4000°K, as evidenced by the flattening (and eventual turning down) of this curve.

In general, the electron density is independent of the nature of the main gas, as long as it contributes negligible ionization. In the case of flame gases, however, the presence of a considerable concentration of the hydroxyl radical OH reduces the electron density by forming negative hydroxyl ions and by forming alkali hydroxide molecules. These effects are discussed in Appendix A.

II. MOBILITY OF ELECTRONS SCATTERED BY NEUTRAL MOLECULES ONLY

The electron mobility with no magnetic field is given by[4]

$$\mu = (4\pi e/3m)\int_0^\infty F(v)(d/dv)(v^3/\nu_t)dv, \tag{5}$$

---

[1] S. Way and R. L. Hundstad, *Eighth Symposium (International) Combustion, Pasadena, California, August 28–September 2, 1960* o be published).

[2] L. Steg and G. W. Sutton, Astronautics **5**, 22 (August, 1960).

[3] Saha, Phil. Mag. **40**, 472 (1920). For an application to this problem, see H. Belcher and T. M. Sugden, Proc. Roy. Soc. (London) **A202**, 17 (1950).

[4] W. P. Allis, *Handbuch der Physik* (Springer-Verlag, Berlin, Germany, 1956), Vol. XXI, p. 413.

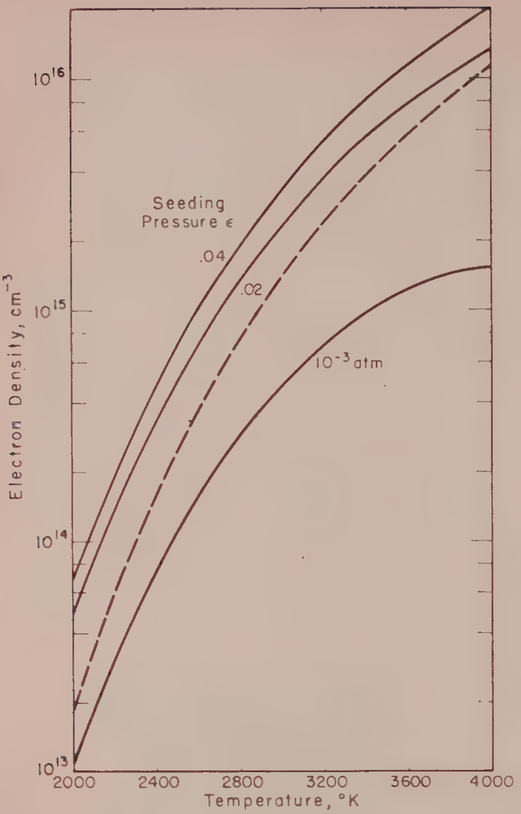

FIG. 1. Electron density vs temperature as given by Saha's equation. Solid curves: Cs seeding. Dashed curve: K seeding.

where e, m, v, and ν_t are the electronic charge, mass, velocity, and total collision frequency, respectively, and $F(v)$ is the velocity distribution function for the electrons.[5] With a magnetic field B the mobility is unchanged in the field direction while being reduced in the transverse direction by electron cyclotron effects by the approximate factor[6]

$$\mu_\perp/\mu=[1+(\omega_b/\nu_t)^2]^{-1}=(1+B^2\mu^2)^{-1}, \qquad (6)$$

where $\omega_b=eB/m$ is the electron cyclotron angular frequency.

The collision frequency for momentum transfer is given by

$$\nu_c=vNQ_d, \qquad (7)$$

where N is the molecular density and Q_d is the momentum transfer cross section of the molecular species considered. We denote by ν_0 the total collision frequency with neutral molecules; it is the sum of ν_c's for all molecular species present. In high-conductivity plasmas Coulomb scattering is also important. Defining ν_{ei} as the effective collision frequency of electron scattering by ions, including effects of electron-electron interactions, the total collision frequency to be used in Eq. (4) is

$$\nu_t=\nu_0+\nu_{ei}. \qquad (8)$$

In this section we consider neutral scattering only, i.e., mobility at low electron densities.

From a review of the literature on momentum transfer cross sections, we have arrived at the approximate expressions for ν_c/N as a function of the electron energy in electron volts u, given in Table I for various gases of interest here. These expressions are chosen to represent the experimental data primarily in the range of 0.05 to 1 ev, which contains nearly all electrons in equilibrium with gases at practicable temperatures (below 5000°K). Uncertainties arising from (1) discrepancies between the results of different investigators; (2) sparse evidence in the energy range of interest; and (3) errors involved in making a simple analytic representation, limit the accuracy to perhaps ±30%.

In an open-cycle MHD generator, the main gas may be composed of the products of combustion of fuel oil and oxygen. We have calculated the equilibrium combustion products for the composition $CH_2+\frac{3}{2}O_2$ at one atmosphere, using data of Lewis and von Elbe.[7,8] The

TABLE I. Approximate analytic expressions for ν_c/N in MHD gases.

Gas	$10^8\nu_c/N$, sec⁻¹ cm⁻³	References
H_2O	$10u^{-\frac{1}{2}}$	a
CO_2	$1.7u^{-\frac{1}{2}}+2.1u^{\frac{1}{2}}$	b,c
CO	$9.1u$	b,c
O_2	$2.75u^{\frac{1}{2}}$	d,e
O	$5.5u^{\frac{1}{2}}$	d
H_2	$4.5u^{\frac{1}{2}}+6.2u$	f,g
H	$42u^{\frac{1}{2}}-14u$	h
OH	$8.1u^{-\frac{1}{2}}$	a,i
N_2	$12u$	f
He	$3.14u^{\frac{1}{2}}$	c
Ne	$1.15u$	j
K, Cs	160	k

[a] S. Altshuller, Phys. Rev. **107**, 114 (1957). For experimental data se S. Takeda and A. A. Dougal, J. Appl. Phys. **31**, 412 (1960).
[b] R. H. Healey and J. W. Reed, *The Behavior of Slow Electrons in Gase* (Amalgamated Wireless, Ltd., Australia, 1941).
[c] S. C. Brown, *Basic Data of Plasma Physics* (John Wiley & Sons, Inc. New York, 1959).
[d] See reference 27.
[e] V. A. J. van Lint, E. G. Winkler, and D. L. Trueblood, Rept. N TRS9-43 (August 31, 1959), General Atomic Division of General Dynamic Corporation, San Diego, California (unpublished). We have used the mea of the experimental data discussed in this paper.
[f] R. W. Crompton and D. J. Sutton, Proc. Roy, Soc. (London) **A215**, 46 (1952).
[g] G. Bekefi and S. C. Brown, Phys. Rev. **112**, 159 (1958).
[h] E. Gerjuoy and N. A. Krall, Phys. Rev. **119**, 705 (1960).
[i] K. P. Madden and W. S. Benedict, J. Chem. Phys. **23**, 408 (1955).
[j] A. L. Gilardini and S. C. Brown, Phys. Rev. **105**, 31 (1957).
[k] A. V. Phelps (private communication). The original analysis of pub lished cesium positive column data has been corrected using revised electro densities. See C. Boeckner and F. L. Mohler, Bur. Standards J. Researc **10**, 357 (1933); **17**, 849 (1936).

---

[5] The conductivity formula used by Lin, Resler, and Kantrowitz (see reference 6) uses the reciprocal of the sum of average cross sections, instead of correctly averaging the reciprocal of the sum of collision frequencies according to Eq. (5).

[6] S. C. Lin, E. L. Resler, and A. Kantrowitz, J. Appl. Phys. **26**, 95 (1955).

[7] B. Lewis and G. von Elbe, *Combustion, Flames and Explosion of Gases* (Academic Press, Inc., New York, 1951), p. 742.

[8] R. von Stein, Rept. No. F-TS-93GRE, Wright Field, Dayton Ohio (unpublished), gives equilibrium products for a similar pre combustion mixture.

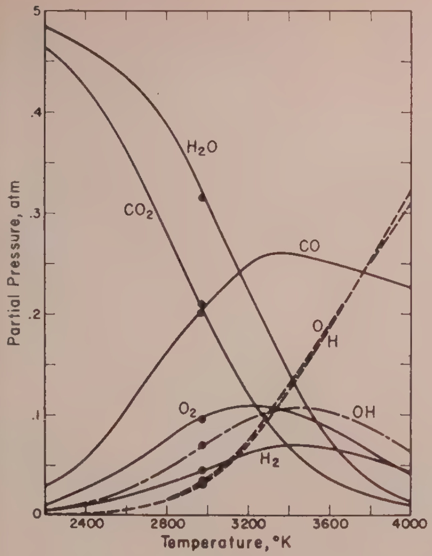

FIG. 2. Equilibrium combustion products of $CH_2+\frac{3}{2}O_2$ at one atmosphere pressure. Points are from reference 9.

results are shown in Fig. 2, plotted against temperature. The points represent a calculation by Gaydon and Wolfhard[9] for the same gas composition; the agreement is good.

To compute the collision frequency of electrons in the combustion products at a given temperature, we multiply the fractional composition, given in Fig. 2, for a given gas by its ν_c/N from Table I, and add for all gases present. The results are given in analytic form in Table II for five temperatures. In a similar manner, ν_c/N for helium, neon, or argon, plus a seeding ratio of K or Cs, as might be used in closed MHD cycles, can be obtained. For argon, use is made of a curve of momentum transfer cross section recently obtained by Frost and Phelps.[10]

There are some microwave determinations of collision frequency in flames in the literature, calculated assuming that ν_0 is independent of energy. Hofmann, Kohn, and Schneider[11] obtained $\nu_0=20\times10^{10}$ sec^{-1} in an acetylene air flame at 2500° and 2750°K; our calculated value using their published[12] gas composition is about 15×10^{10} sec^{-1} at both temperatures. Kuhns[13] measured a value $\nu_0=19\times10^{10}$ sec^{-1} for a propane-air flame of 2200°K; our calculated value assuming stoichiometric ratio and complete equilibrium is about 20×10^{10} sec^{-1}, in excellent agreement. Hofmann *et al.*[11] also measured a propane-air flame at 2100°K, obtaining a value $\nu_0=27\times10^{10}$ sec^{-1}. Belcher and Sugden[14] obtained a relatively low value, $\nu_0=8.8\times10^{10}$ sec^{-1}, for a coal-gas/air flame at 2000°K. Since it is not expected that the composition of these flame gases will differ sufficiently to produce much change in collision frequency, this value appears to be low.

We wish to evaluate the mobility for electrons in equilibrium with the gas at temperature T°K so that their energy distribution is Maxwellian. If the reciprocal of the collision frequency can be expressed as a power series,

$$\frac{N}{\nu_t}=\sum_{-b}^{n} a_i u^i, \quad b<\tfrac{5}{2}, \tag{9}$$

then the integration in Eq. (5) can be accomplished analytically and the mobility can be evaluated by a method derived by Pack and Phelps[15]:

$$\mu N=\frac{e}{m}\sum_{-b}^{n}\frac{\Gamma(\frac{5}{2}+i)}{\Gamma(\frac{5}{2})}a_i\left(\frac{kT}{e}\right)^i. \tag{10}$$

The quantity kT/e is the gas temperature expressed in electron volts.

It is clear that in general the mobility in a mixture of gases cannot be obtained directly from the mobilities of the components. Rather, the component collision frequencies must first be added up, an analytic expression found for the reciprocal of the total collision frequency, and the mobility obtained by use of Eq. (10).

We have evaluated the electron mobility for several seeded gases using the data of Tables I and II, and Eq. (10); the results are plotted as a function of temperature in Fig. 3. The combustion products give the smallest mobility, primarily due to the large scattering cross sections of water vapor and of atomic hydrogen. Argon with light seeding gives the greatest mobility, due to the very small cross section at the Ramsauer minimum.[10] This advantage decreases with increasing seeding pressure as scattering by alkali metal atoms becomes dominant; with $\mathcal{E}=0.01$ atm, the mobility in Ne is about the same as that in Ar. It can be shown that for small fractional ionization of the alkali metal atoms,

TABLE II. ν_0/N for the gas mixtures of Fig. 2.

	$10^8\nu_0/N=160\,\mathcal{E}+Bu^{-\frac{1}{2}}+Cu^{\frac{1}{2}}+Du$		
Temperature °K	B	C	D
2000	5.78	1.044	0.125
2800	4.73	1.648	1.461
3200	3.22	4.18	1.652
3500	1.991	8.05	0.591
4000	0.654	15.63	−2.22

---

[9] A. G. Gaydon and H. G. Wolfhard, *Flames* (Chapman and Hall, Ltd., London, England, 1960), p. 287.

[10] L. S. Frost and A. V. Phelps, Bull. Am. Phys. Soc. Ser. II, 5, 371 (1960).

[11] F. W. Hofmann, H. Kohn and J. Schneider, Duke Univ. Microwave Lab. Rept. No. 28, November 1, 1959–February 1, 1960, under contract (unpublished).

[12] J. Schneider and F. W. Hofmann, Phys. Rev. **116**, 244 (1959).

[13] Quoted in reference 9; original reference, P. W. Kuhns, National Advisory Committee for Aeronautics, Lewis Laboratory, Cleveland, Ohio, Tech. Note 3254 (1954).

[14] H. Belcher and T. M. Sugden, Proc. Roy. Soc. (London) **A201**, 480 (1950).

[15] J. L. Pack and A. V. Phelps, Phys. Rev. **121**, 798 (1961).

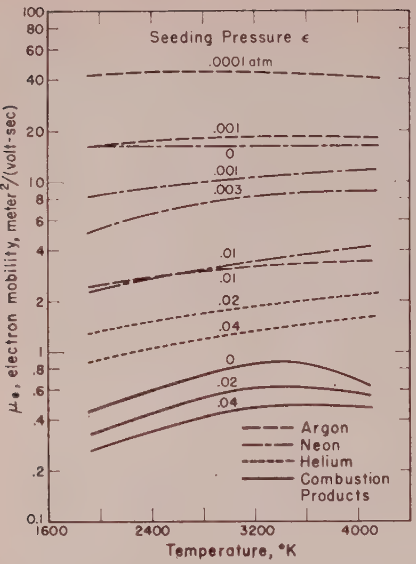

FIG. 3. Electron mobility in seeded gases vs temperature at $1+\mathcal{E}$ atmospheres pressure. "Combustion products" refers to the composition shown in Fig. 2.

(and neglecting hydroxyl effects, Appendix A), the conductivity has a maximum with respect to varying $\mathcal{E}$, occurring at about that value of $\mathcal{E}$ which gives equal effective scattering of electrons by the main gas and by the seeding atoms. This condition obtains at about $\mathcal{E}=0.001$ atm in Ar, and $\mathcal{E}=0.003$ atm in Ne.

Combining the electron density results of Sec. I with these mobility values according to Eq. (1), we obtain the calculated conductivity for neutral scattering only, which we designate σ_0 and shall make use of in Sec. IV.

III. MOBILITY INCLUDING ELECTRON SCATTERING BY IONS

At electron densities great enough to yield sufficiently high conductivity for MHD applications, Coulomb scattering of electrons by positive ions is important and must be considered. The mobility must be recalculated including Coulomb scattering appropriate to the electron density occurring at a given seeding ratio, alkali metal, and temperature.

Spitzer and Harm[16] have worked out the theory of Coulomb interaction in a completely ionized gas. Their expression for conductivity, which we denote by subscript *ei* to indicate the ion scattering limit, is

$$\sigma_{ei}=\frac{4\sqrt{2}\gamma_E(4\pi\epsilon_0)^2}{\pi^{\frac{3}{2}}em\ln\Lambda}=1.913\times10^4\frac{(kT/e)^{\frac{3}{2}}}{\ln\Lambda}\frac{\text{mhos}}{\text{m}}. \qquad (11)$$

γ_E is a factor expressing the effect of electron-electron collisions and is equal to 0.582 for ions of unit charge, the case of interest here. Λ is a cutoff parameter applied to an integration over impact parameter and is equal to the ratio of Debye shielding distance to the impact parameter for a 90° scattering by an ion; it is given by Eq. (23) in Appendix B. The theory breaks down for small Λ, and may be in error by an amount of the order of $1/\ln\Lambda$; i.e., from 15 to 30% for the range of variables covered in this paper.

An expression for ν_{ei}, the effective frequency of momentum transfer collisions with ions including the effects of electron-electron interaction, is developed in Appendix B. It yields the correct conductivity, Eq. (11), in the completely ionized limit, and is consistent with Hwa's[17] calculations of combined neutral and ion scattering. This expression is

$$\nu_{ei}=0.476K\eta^{-1}, \qquad (12)$$

where K is given in Appendix B and η is the dimensionless energy variable eu/kT. Using this expression in Eq. (8) to get the total collision frequency ν_t, we have evaluated the electron mobility with electron-ion collisions by the method of Eqs. (9) and (10).

In Fig. 4 are shown the calculated conductivities of the gases included in the mobility plot, Fig. 3, at various seedings over the temperature range 2000° to 4000°K. The wide range of conductivities suggested by the

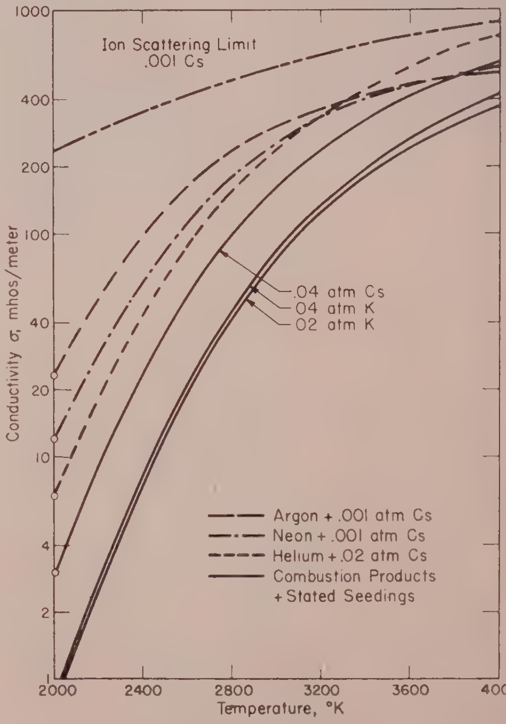

FIG. 4. Conductivity of seeded gases including electron scattering by ions at $1+\mathcal{E}$ atmospheres pressure.

---

[16] L. Spitzer and R. Harm, Phys. Rev. **89**, 977 (1953).

[17] R. C. Hwa, Phys. Rev. **110**, 307 (1958); R. C. Hwa and L. Goldstein, Univ. Illinois Rept. AFCRC-TN-57-780.

mobility curves of Fig. 3 does not materialize except at low temperatures, near 2000°K. The curves of Fig. 4 show the strong influence of electron scattering by ions, especially above 2800°K.

The small gain in conductivity in going from 0.02 to 0.04 atm of K in combustion products suggests that the optimum seeding is in this range, corresponding to about equal electron scattering by the main gas and the alkali metal atoms, as discussed in Sec. II. The seeding values given for the noble gases are chosen to approximate this condition.

Electron attachment and alkali hydroxide formation can be taken into account if desired using the factors given in Appendix A. Electron-ion interaction would be enhanced by the presence of negative ions since Coulomb scattering does not depend on the sign of the scatterer; however, there is an appreciable concentration of negative ions only at the lower temperatures, while electron-ion interaction is effective at the higher temperatures, so that these two effects do not interact appreciably.

Way and Hundstad[1] have measured the conductivity of combustion products seeded with 1.5% K in several MHD generator test runs, and compared with our predicted value. As an example, test 6/29/60 at 2877°K gave a measured conductivity of 24.0 mhos/m; our calculated value is either 35.5 or 22.5 mhos/m, depending on whether we take 2.1 or 2.65 ev for the electron affinity of OH. The agreement is within the calculated and experimental errors. No conclusion as to which electron affinity is better appears to be justified on the basis of these experiments.

IV. ALTERNATIVE METHOD FOR COMPUTING CONDUCTIVITY

It is desirable to have a way of combining the conductivities due to neutral scattering alone with the Spitzer conductivity due to ion scattering. Let us denote by σ_{add} the conductivity according to the usual law of adding conductances in series:

$$\sigma_{\text{add}}=\left(\frac{1}{\sigma_0}+\frac{1}{\sigma_{ei}}\right)^{-1}. \tag{13}$$

Suppose that the neutral collision frequency ν_0 can be expressed as a single power term,

$$\nu_0=Au^m. \tag{14}$$

If $m=-1$, the energy dependence is the same as that of ν_{ei}, Eq. (12), so that $\sigma=\sigma_{\text{add}}$. We solve analytically in Appendix B the cases $m=0$, $m=1$, and interpolate for $m\approx\frac{1}{2}$. $\sigma/\sigma_{\text{add}}$ for these cases is plotted in Fig. 5 vs σ_0/σ_{ei}. The correctly computed points obtained above for seeded argon and combustion products are plotted, showing by reasonably small scatter the good accuracy that can be obtained by this method. These data cut across the calculated curves in a manner predictable by the changing effective m value as the temperature changes.

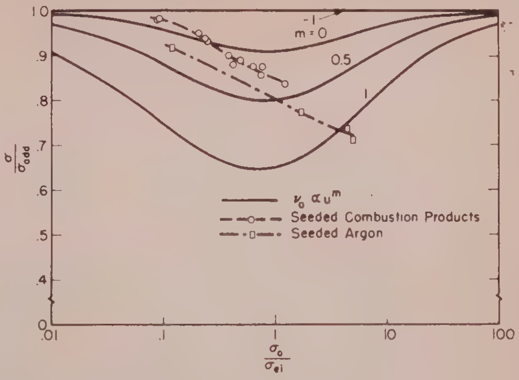

FIG. 5. Ratio of true conductivity to that obtained by the law of addition of conductivities in series.

Thus, the alternative method for computing conductivity is as follows: Calculate σ_0 using the electron density data of Sec. I and mobility either from Fig. 3 or calculated by means of Eqs. (9) and (10), with $\nu_t=\nu_0$, the total collision frequency by neutral molecules. Find the exponent m, Eq. (13), best fitting ν_0 for electrons with energy centered about kT/e. Compute σ_{ei} by the Spitzer and Harm relation, Eq. (11). Read Fig. 5 for this m and ratio σ_0/σ_{ei} to obtain $\sigma/\sigma_{\text{add}}$. This factor multiplied by σ_{add}, Eq. (13), gives the desired conductivity. The method appears to have as good accuracy as is meaningful in view of uncertainties in input data and in Coulomb interaction theory.

V. CONCLUSIONS

The conductivities calculated here are believed to be accurate within the error limits of the cross section data used and uncertainties in the theory of Coulomb scattering. An empirical rule for combining the effects of electron scattering by neutrals and by ions has been presented. It is hoped that these results will be useful in a wide range of experiments dealing with partially ionized high temperature plasmas.

ACKNOWLEDGMENTS

The author is pleased to acknowledge the assistance of A. V. Phelps in many stimulating discussions, and to thank S. Way for suggesting the problem.

APPENDIX A. EFFECT OF THE HYDROXYL RADICAL

The situation in the case of the combustion products is complicated by the considerable concentration of the hydroxyl radical, OH. This radical reduces the electron concentration by two mechanisms: electron attachment and by formation of the undissociated KOH or CsOH molecule. Using square brackets enclosing a symbol to

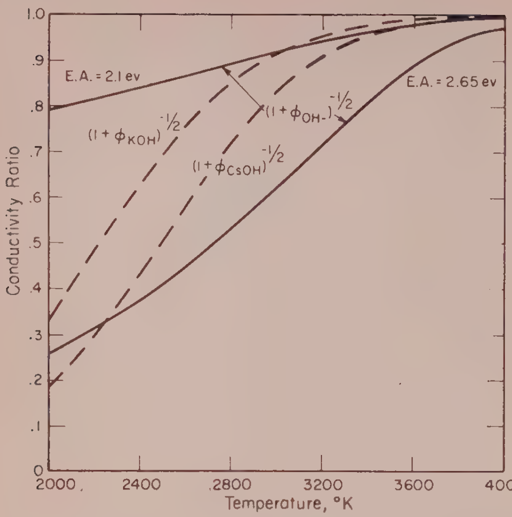

FIG. 6. Conductivity reduction effect of electron attachment to OH and of formation of alkali hydroxides in the combustion products of Fig. 2.

express its partial pressure in atmospheres, the following reactions with their constants are involved where A for alkali stands for either K or Cs:

$$A \rightleftharpoons A^+ + e, \quad K_1 = \frac{[A^+][e]}{[A]}$$

$$\log_{10} K_1 = -\frac{5050}{T} V_i + \frac{5}{2} \log_{10} T - 6.48; \quad (15)$$

$$\mathrm{OH}^- \rightleftharpoons \mathrm{OH} + e, \quad K_2 = \frac{[\mathrm{OH}][e]}{[\mathrm{OH}^-]}$$

$$\log_{10} K_2 = \frac{5050}{T} E + \frac{5}{2} \log_{10} T - 5.58; \quad (16)$$

$$A\mathrm{OH} \rightleftharpoons A + \mathrm{OH}, \quad K_3 = \frac{[A][\mathrm{OH}]}{[A\mathrm{OH}]}$$

$$\log_{10} K_3 = -\frac{5050}{T} V_{A\mathrm{OH}} + \frac{5}{2} \log_{10} T - \mathrm{const},$$

$$\simeq \frac{5050}{T} (V_{\mathrm{H_2O}} - V_{A\mathrm{OH}}) + \log K_{\mathrm{H_2O}} - 0.716. \quad (17)$$

Here E is the electron affinity of OH, published values of which range from 2.1 ev[18] to 2.65 ev.[19] $V_{A\mathrm{OH}}$, $V_{\mathrm{H_2O}}$ are the energies of dissociation of AOH into A+OH and H_2O into H+OH, and are equal to 3.74 ev for KOH,[15] 3.96 ev for CsOH[20] and 5.16 ev for H_2O.[21]

The constant in Eq. (17) depends on the unknown partition functions of KOH and CsOH; it can be estimated from recent data by Hofman, Kohn, and Schneider[22] at 2500°K. To allow approximately for variation of the partition functions with temperature, we have computed K_3 from published[7] values of $K_{\mathrm{H_2O}}$ using the last line of Eq. (17).

Two other relations are needed to solve for the electron concentration: conservation of charge and of total alkali concentration. Solution of this system of simultaneous equations gives the electron concentration in the form

$$[e]^2 = \frac{K_1 \mathcal{E}}{(1+\phi_2)(1+\phi_3+K_1/[e])}, \quad (18)$$

where

$$\phi_2 = \frac{[\mathrm{OH}^-]}{[e]} = \frac{[\mathrm{OH}]}{K_2}, \quad (19)$$

$$\phi = \frac{[A\mathrm{OH}]}{[A]} = \frac{[\mathrm{OH}]}{K_3}. \quad (20)$$

The term $K_1/[e]$ arises from depletion of the neutral alkali atom density as a result of ionization; it is only appreciable at 3500°K and above, where the equation must be solved as a quadratic equation. It is seen that OH attachment and AOH formation reduce the electron density (and therefore the conductivity) by $(1+\phi_2)^{\frac{1}{2}}$ and $(1+\phi_3)^{\frac{1}{2}}$, respectively. These factors are shown in Fig. 6. The alkali hydroxide formation has considerable effect below about 2800°K. Attachment to the hydroxyl radical reduces the electron density appreciably over the whole temperature range if we take 2.65 ev for the electron affinity of OH, while the reduction is not more than 21% if we take for the electron affinity the smaller value, 2.1 ev. The lower affinity value is favored by the microwave conductivity measurements of Schneider, Hofmann, and Kohn[22,23] and the mass spectrometric investigation of Knewstubb and Sugden,[24] both groups finding no evidence of important attachment effects in seeded flames. These factors have not been included in the conductivity values shown in Fig. 5 because of the uncertainties in the electron affinity of OH and the partition functions of KOH and CsOH; they may be applied by the reader if desired.

---

[18] J. Goubeau and W. Klemm, Z. physik Chem. **B36**, 362 (1937).

[19] F. M. Page and T. M. Sudgen, Trans. Faraday Soc. **53**, 1092 (1957).

[20] H. Smith and T. M. Sugden, Proc. Roy. Soc. (London) **A219**, 204 (1953).

[21] A. G. Gaydon, *Dissociation Energies* (Chapman and Hall, Ltd., London, England, 1953), pp. 200 and 237.

[22] F. W. Hofmann and H. Kohn, Duke Univ. Tech. Rept. 14, (September 15, 1960), under contract; F. W. Hofman, H. Kohn, and J. Schneider, *ibid.*

[23] J. Schneider, F. W. Hofmann, and H. Kohn, Duke Univ. Microwave Lab. Rept. No. 28, see reference 11.

[24] P. F. Knewstubb and T. M. Sugden, Proc. Roy. Soc. (London) **A255**, 520 (1960). These authors quote an even lower value for the electron affinity of OH from L. Branscomb and S. Smith (private communication), 1.73 ev.

APPENDIX B. ELECTRON-ION COLLISION FREQUENCY INCLUDING EFFECT OF ELECTRON-ELECTRON INTERACTION

As Hwa[17] has pointed out, electron-electron collisions ave a complex effect on electron scattering through hanges in the velocity distribution, and cannot be presented rigorously by means of a collision frequency. However, for the present application, an approximation an be made which appears on the basis of the rather mited evidence available, to represent the effect with ufficient accuracy.

Two expressions for electron-ion collision frequency hich attempt to include the effect of electron-electron nteraction have appeared in the literature. Heald[25] has iven an expression based on Spitzer's 90° deflection ime. In the fully ionized limit, it yields a conductivity bout 14% below that of the Spitzer and Harm value, q. (11). Heald's value, in mks units unless specified herwise, is

$$\nu_{ei}=K/\eta^{\frac{3}{2}}, \quad \eta=eu/kT, \tag{21}$$

$$=\frac{2\pi n_e e^2 \ln\Lambda}{(4\pi\epsilon_0)^2}\left(\frac{2e}{m}\right)^{\frac{1}{2}}\left(\frac{e}{kT}\right)^{\frac{3}{2}}$$

$$=7.75\times10^{-6}\frac{n_e(\mathrm{cm}^{-3})\ln\Lambda}{(kT/e)^{\frac{3}{2}}}, \tag{22}$$

$$\Lambda=\frac{3}{(2\pi n_e)^{\frac{1}{2}}}\left(\frac{4\pi\epsilon_0 kT}{e^2}\right)^{\frac{3}{2}}=1.550\times10^{10}\frac{(kT/e)^{\frac{3}{2}}}{n_e^{\frac{1}{2}}}. \tag{23}$$

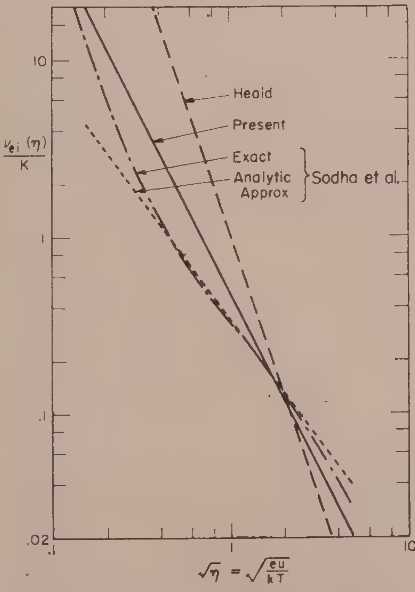

FIG. 7. Frequency of electron-ion collisions, including the effect electron-electron interaction as assumed by different authors. he abscissa is proportional to electron velocity.

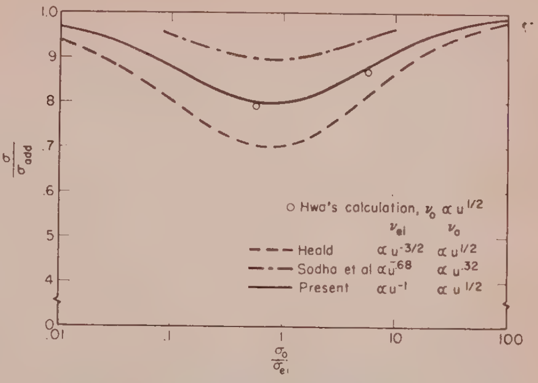

FIG. 8. Ratio of true to additive conductivities for three different ν_{ei}'s and Hwa's rigorous solutions.

Sodha and Varshni[26] and Shkarofsky, Bachynski, and Johnston[27] have derived an equivalent electron-ion collision frequency from Spitzer and Harm's distribution function solution in the completely ionized case. This may be written, using the constant K defined above,

$$\nu_{ei}=KA\eta^{\frac{1}{2}}/2D(\eta), \tag{24}$$

where the function $D(\eta)/A$ is tabulated in Spitzer and Harm. This value is plotted in Fig. 7 along with Heald's value, Eq. (21). A single power fit to Eq. (24), useful in analytic integrations below, is also shown; it yields the correct Spitzer and Harm conductivity in the limit of complete ionization. It is

$$\nu_{ei}=0.34K/\eta^{0.68}. \tag{25}$$

Hwa[17] has solved the complete Boltzmann-Fokker-Planck equation on a high-speed digital computer to obtain the effect of electron-electron interactions on cyclotron resonance in two cases including constant cross-section scattering by neutral molecules. At resonance the results are applicable to the present dc case, and may be used as a standard, presumably correct solution against which the above expressions for the electron-ion collision frequency may be evaluated. A convenient comparison can be made in terms of the conductivity ratio $\sigma/\sigma_{\mathrm{add}}$, σ_{add} being defined in Eq. (13). This ratio is plotted in Fig. 8 vs σ_0/σ_{ei}, the ratio of conductivities (or mobilities) in the two limits of low and high electron density. The integral in Eq. (5) can be expressed in terms of functions given by Dingle, Arndt, and Roy[28] when the exponents of energy dependence of ν_0 and ν_{ei} differ by one of the integers 1, 2, or 3.

Examination of Fig. 8 shows that neither the Heald nor the Sodha *et al.* expressions for electron-ion collision frequency, including the effect of electron-electron interaction, is correct, although the errors are not large since none of the conductivities differ from σ_{add} by more than 30%. It appears that an expression giving an energy dependence intermediate between the two would fit Hwa more closely than either of these expressions. Choosing an inverse first power in energy, we obtain the expression given in Eq. (12) and shown in Fig. 7, with the constant determined by requiring it to yield the correct limiting conductivity, σ_{ei} of Eq. (11). $\sigma/\sigma_{\mathrm{add}}$ for this expression and ν_0 proportional to $u^{\frac{1}{2}}$ is also shown in Fig. 8; the agreement with Hwa is good. This curve was obtained by interpolating between the ν_0 constant and $\nu_0 \propto u$ solutions, both of which can be expressed in terms of the functions of Dingle *et al.*, and are shown in Fig. 5.

---

[25] M. A. Heald, Project Matterhorn Rept. MATT-17, Princeton niversity, Princeton, New Jersey (August 26, 1959).

[26] M. S. Sodha and Y. P. Varshni, Phys. Rev. **111**, 1203 (1958).

[27] I. P. Shkarofsky, M. P. Bachynski, and T. W. Johnston, RCA Research Rept. 7-801, December 5, 1959 (unpublished).

[28] R. B. Dingle, D. Arndt, and S. K. Roy, Appl. Sci. Research **6B** 144, 155, 245 (1957).

JOURNAL OF APPLIED PHYSICS VOLUME 32, NUMBER 10 OCTOBER, 1961

Effect of Hydrostatic Pressure on the High-Temperature Steady-State Creep of Lead*

B. M. Butcher and A. L. Ruoff
Cornell University, Ithaca, New York

(Received May 15, 1961)

The activation energy and activation volume for the creep of high-purity lead were obtained by the method of rapidly varying the temperature and pressure. The activation energy was found to be 1.18±0.03 ev and the activation volume was found to be $(24.2\pm0.6)\times10^{-24}$ cc or 0.80 atomic volume.

INTRODUCTION

THE results of experiments by Dorn[1] and Weertman[2] indicate that, at temperatures greater than half the absolute melting temperature, the creep behavior of high-purity lead is controlled by a single thermal activation process whose activation energy appears to be somewhat greater than the self-diffusion activation energy.

The work presented in this paper was designed to investigate the effect of hydrostatic pressure on creep. If we infer from the near agreement of the activation energies that creep is diffusion-controlled, then we would expect the activation volume for creep to be somewhat greater than that for self-diffusion. On the other hand, if the agreement of the two activation energies are fortuitous, we would expect the activation volumes to differ. The activation volume for creep was determined by measuring the creep rate at different pressures and a comparison with the value for self-diffusion[3] shows good agreement.

APPARATUS AND PROCEDURE

The lead used in these experiments was 99.9999% pure polycrystalline lead wire 1 mm in diameter. All specimens were annealed for one hour at 110°C in silicon oil. Early determinations of the complete creep curve showed that the quasi-linear portion of the secondary creep region is between strains of 3.5% and 14 to 16%. Consequently, all measurements were made in this range.

The measurement of deformation with respect to time under constant stress was accomplished using the device shown schematically in Fig. 1. If the initial extension of the linear spring is made approximately equal to the initial length of the specimen, as was the case in these experiments, the stress is maintained quite constant during the entire test, i.e., it is independent of the strain. There are a number of other factors, however, which can cause the stress to change. These will be discussed later in this paper. As is clear from Fig. 1, the deformation is measured by a potentiometric technique; the sensitivity is at least 5×10^{-5} in. Further

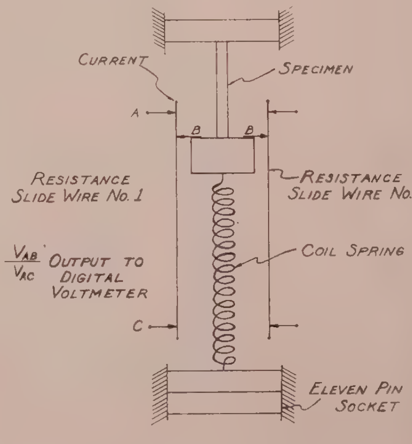
Current
Specimen
A
B
B
Resistance Slide Wire No. 1
Resistance Slide Wire No. 2
$\frac{V_{AB}}{V_{AC}}$ Output to Digital Voltmeter
Coil Spring
C
Eleven Pin Socket

Fig. 1. Sketch of creep jig.

---

* This work was sponsored by the Atomic Energy Commission and the Advanced Research Projects Agency.

[1] C. D. Wiseman, O. D. Sherby, and J. E. Dorn, J. Metals **9**, 58 (1957).

[2] J. Weertman, Trans. Am. Inst. Mining, Met., Petrol., Engrs. **218**, 207 (1960).

[3] N. H. Nachtrieb, H. A. Resing, and S. A. Rice, J. Chem. Phys. **31**, 135 (1959).

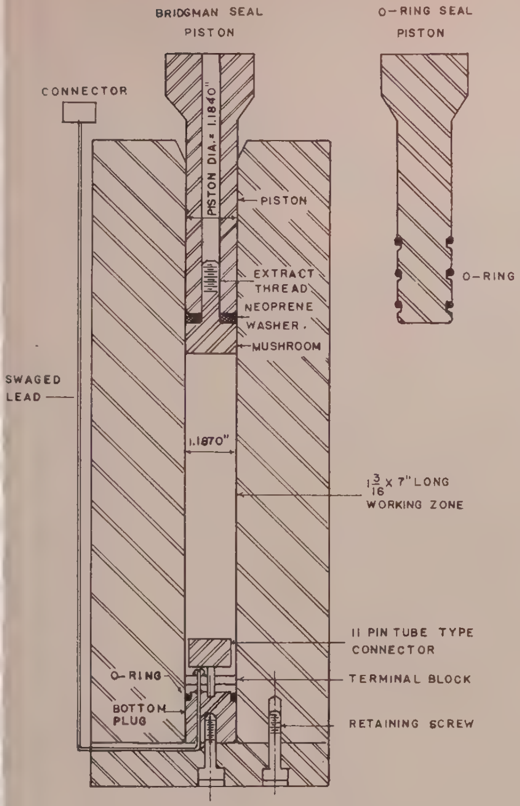

FIG. 2. A pressure vessel for creep studies.

hysical details of the creep jig and the measuring ystem will be found elsewhere.[4]

A pressure vessel for creep studies which is applicable or work to 10 kbar is shown in Fig. 2. Silicon oil was sed as the pressure-transmitting media. For these ests the pressure vessel was enclosed in a thermally ontrolled bath so that the temperature in the working one was held to ±0.05°C. As the creep jig can be eadily placed in or removed from the pressure vessel with electrical connection as shown), the same jig may e used for both pressure and temperature studies, lthough, in the latter, tests are usually made directly constant-temperature silicon oil baths. Further deails of the electrical lead-in system of the pressure essel are described elsewhere.[5]

Temperature studies were made primarily to check he agreement with past results. The steady-state reep rate $\dot{\epsilon}_1$, under constant stress at atmospheric ressure, was measured at temperature T_1, the temerature then rapidly changed to T_2, and the new teady-state creep rate determined. The activation energy E_c is obtained from the relation

$$\frac{\dot{\epsilon}_1}{\dot{\epsilon}_2}=\exp\left[\frac{-(E_c+PV_c)}{k}\left(\frac{1}{T_1}-\frac{1}{T_2}\right)\right], \tag{1}$$

where V_c is the activation volume, and P is the pressure (at a pressure of one atmosphere the PV_c term can be neglected). In general, about ten such ratios were obtained per specimen using a temperature difference of about 10°C at each temperature range. The advantages of determining activation energies by this method are discussed elsewhere.[1]

A similar technique was used to obtain the activation volume; in this case a pressure difference of about 1 kbar was used at all pressures. The specimen was held at one pressure until the strain rate was determined; the pressure was then changed, and the measurements repeated. The activation volume is determined from the relation

$$\frac{\dot{\epsilon}_1}{\dot{\epsilon}_2}=\exp\left[\frac{V_c(P_2-P_1)}{kT}\right]. \tag{2}$$

RESULTS AND CONCLUSIONS

The partial results of a creep experiment in which the temperature was cycled are given in Fig. 3. The value obtained for the activation energy for creep is 1.18±0.03 ev based on 21 determinations. The agreement with the work of other investigators is shown in Table I. Figure 4 shows typical results of a creep test in which the pressure was varied. The activation volume, based on 40 determinations, is determined to be $(0.80\pm0.02)\Omega_0$, where Ω_0 is the atomic volume of lead $(30.3\times10^{-24}$ cc).

The following corrections were considered in the calculation of the activation energies and volumes given above. Those changing the stress under which the specimen was being tested are:

(1) The variation of the spring constant of the tension spring with respect to temperature and pressure.

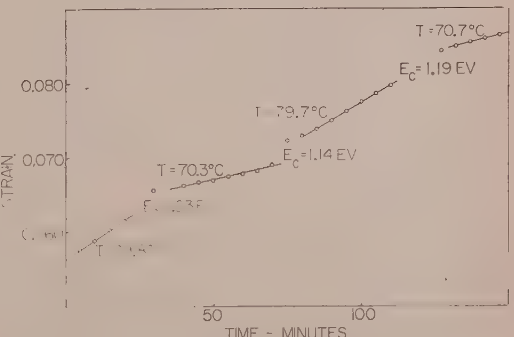

FIG. 3. Partial creep curve showing the effect of cycling the temperature, at atmospheric pressure, of a 1-mm diameter polycrystalline 99.9999% pure lead specimen under a tensile stress of 58.1 bars. The specimen was annealed at 110°C for 1 hr.

---

[4] R. H. Cornish, Ph.D. thesis to be submitted to Cornell University, September, 1961.

[5] R. H. Cornish and A. L. Ruoff, Rev. Sci. Instr. 32, 639 (1961).

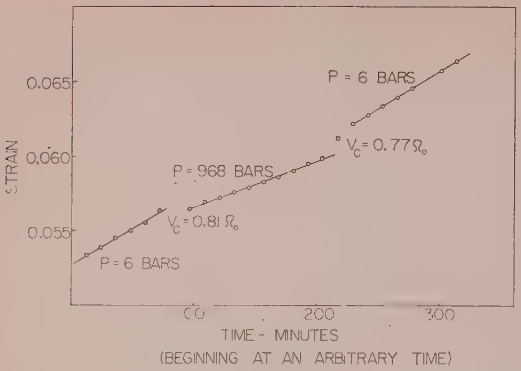

FIG. 4. Partial creep curves of 1-mm diameter polycrystalline 99.9999% pure lead at 70°C, at a tensile stress of 58.1 bars, showing the effect of cycling the pressure. The specimen was annealed at 110°C for 1 hr.

The spring constant varies because the shear modulus changes with temperature[6] and pressure[7] and because the dimensions of the spring change.

(2) The buoyancy effect of the pressurizing media[8] on the movable lower specimen grips.

(3) The effect of dimensional changes of the specimen and the frame of the testing jig, due to pressure and temperature changes, which results in a net change in the extension of the spring.

Corrections were calculated using the stress dependence of the creep rate reported by Weertman.[2] These corrections were nearly negligible. A strain correction due to changes in distance between knife edges A and C on the creep jig as the temperature or pressure was changed was also considered.

TABLE I. A comparison between the creep and self-diffusion activation energies and volumes of lead.

E_c ev	E_d ev	V_c Ω_0	V_d Ω_0
1.18		0.80	
1.13[a]	1.051[c]		0.71[d]
1.21[b]	1.13[e]		0.87[d]
Ω_0 based on an atomic volume of 30.3×10^{-24} cc			

[a] See reference 1.
[b] See reference 2.
[c] N. H. Nachtrieb and G. S. Handler, J. Chem, Phys. **23**, 1569 (1955).
[d] See reference 3.
[e] B. Okkerse, Phys. Rev. **103**, 1246 (1956).

In Table I a comparison is made between the values presented above and some of the more recent self-diffusion data. The values given for the activation volume for self-diffusion[3] were obtained at two temperatures; from the quoted values of the standard deviation, we conclude that these results do not imply a variation with temperature in the activation volume. Hence, if the average value of the two self-diffusion values is used, there is close agreement of the creep and self-diffusion activation volumes. However, since the standard deviation of the $0.71\Omega_0$ value is smaller than for the $0.87\Omega_0$ value, a greater weight should perhaps be given to the smaller value. In this case the activation volume for creep would be somewhat larger than that for self-diffusion, a situation which appears to be analogous to that for the activation energies.

The activation energy for creep in pure metals, when it is controlled by the climb of dislocations under near-equilibrium conditions (equilibrium concentration of vacancies), is equal to or greater than the activation energy of self-diffusion.[9] The present results, therefore, show beyond any reasonable doubt that self-diffusion is the rate-controlling process in creep in lead.

ACKNOWLEDGMENT

The authors wish to express their gratitude to R. H Cornish for many helpful discussions.

---

[6] F. Garofalo, P. R. Malenock, and G. V. Smith, ASTM Special Publication **129**, 10 (1952).
[7] F. Birch, J. Appl. Phys. **8**, 129 (1937).
[8] P. W. Bridgman, Proc. Am. Acad. Arts Sci. **77**, 129 (1949).
[9] J. Lothe, J. Appl. Phys. **31**, 1077 (1960).

OURNAL OF APPLIED PHYSICS VOLUME 32, NUMBER 10 OCTOBER, 1961

Emission Fluctuations of Tungsten-Based Barium Dispenser Cathodes

I. Brodie
Westinghouse Electric Corporation, Electronic Tube Division, Elmira, New York

(Received May 25, 1961)

Emission fluctuations in five different types of tungsten-based barium dispenser cathodes have been measured as functions of both frequency and current density. Two of the cathodes were of the *L* variety and the remainder of the "impregnated" variety. The *L* cathode spectra show that the emission fluctuations are caused by fluctuations in the number of adsorbed atoms on the tungsten emitting surface. The amplitude of the fluctuations is governed by the average surface coverage and theoretical studies indicate that the shape of the spectra is governed by the diffusion processes by which the surface is replenished.

The results from the impregnated cathodes indicate that the contribution of the impregnant in the pore ends to the total noise is only significant when the pore ends supply an appreciable fraction of the total emission from the cathode, the majority of the surface, which is barium activated tungsten, behaving as an *L* cathode surface.

1. INTRODUCTION

THE true flicker effect has been defined as random fluctuations in the emission of a thermionic athode. This effect can be measured unambiguously n a saturated diode where, as Bell[1] has shown, current luctuations due to fluctuations in the cathode resist-nce and disturbance of the space charge by ions are liminated.

The fluctuations are conveniently described by giving he mean square current fluctuation $\langle i_F^2\rangle_{av}$ in a small requency range Δf about a given frequency f.

In general,

$$\langle i_F^2\rangle_{av}=A.W(f,\bar{J})\Delta f, \qquad (1)$$

here A = cathode area, $\bar{J}$ = average current density eing drawn from the cathode, and W = noise intensity istribution function.

In order to compare the flicker noise properties of ifferent kinds of cathodes, the magnitude of W and s variation with f and $\bar{J}$ have to be determined for ach cathode.

2. THE CATHODES INVESTIGATED

Five different kinds of tungsten-based barium dis-enser cathodes were examined; two were of the *L* ype first described by Lemmens *et al.*[2] and three were f the "impregnated" variety containing barium-alcium aluminates.[3,4] The constructional details of hese cathodes are given below.

Type (*i*). *L* cathode as shown in Fig. 1 (a). The avity in the cathode was filled with barium and stron-ium carbonates in equimolar proportions which, during he processing of the tube, were broken down to the xides. The porous tungsten disk which closed the avity and formed the emitting surface was of 45% orosity, 1 mm thick and 3 mm in diameter.

Type (*ii*). *L* cathode as above except that the porous tungsten barrier was of 25% porosity.

Type (*iii*). Impregnated cathode mounted as shown in Fig. 1 (b). The tungsten pellet was 1 mm thick, 3 mm diameter, of 45% porosity and impregnated with barium-calcium aluminate in which the molar ratio of the oxides were $\frac{1}{2}$CaO:3BaO:Al$_2$O$_3$.

Type (*iv*). Impregnated cathode as above except that the tungsten porosity was 25%.

Type (*v*). Impregnated cathode[5] as shown in Fig. 1 (b). In this case, the tungsten porosity was 17% and the molar ratio of the oxides in the impregnant was $1\frac{1}{2}$CaO:$2\frac{1}{2}$BaO:Al$_2$O$_3$.

The cathodes were mounted in modified A.S.T.M. reference planar diodes[6] shown in Fig. 2, the cathode-anode spacing being 1 mm. The tubes, which were of lead glass, were processed by baking at 400°C for an hour on a mercury diffusion pump with liquid-nitrogen trap. The anode and cathode shield, which were made of pure nickel, were outgassed by eddy current heating

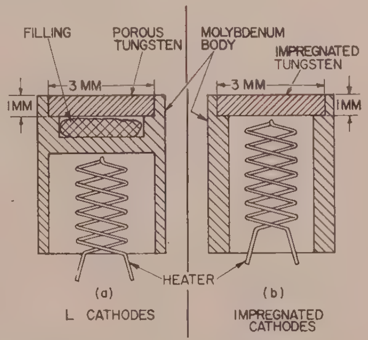

Fig. 1. The cathode studied: (a) *L* cathodes, type (i) tungsten porosity 45%, filling BaCO$_3$·SrCO$_3$, type (ii) tungsten porosity 25%, filling BaCO$_3$·SrCO$_3$; (b) impregnated cathodes, type (iii) tungsten porosity 45%, impregnant $\frac{1}{2}$CaO·3BaO·Al$_2$O$_3$, type (iv) tungsten porosity 25%, impregnant $\frac{1}{2}$CaO·3BaO·Al$_2$O$_3$, type (v) tungsten porosity 17%, impregnant $1\frac{1}{2}$ CaO·3BaO·Al$_2$O$_3$.

---

[1] D. A. Bell, *Electrical Noise* (D. Van Nostrand Company, Inc., rinceton, New Jersey, 1960), Chap. 8, p. 167.

[2] H. J. Lemmens, M. J. Jansen, and R. Loosjes, Philips Tech. ev. **11**, 341 (1950).

[3] R. Levi, J. Appl. Phys. **26**, 639 (1955).

[4] I. Brodie and R. O. Jenkins, J. Appl. Phys. **27**, 417 (1956).

[5] Cathodes of type (v) were supplied by Dr. R. Levi of Philips Metalonics.

[6] American Society for Testing Materials Specification Number F11-60T.

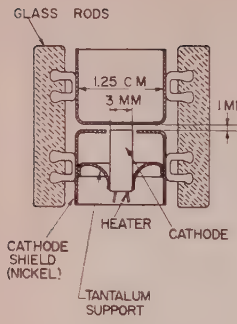

FIG. 2. The modified A.S.T.M. reference planar diode.

to 900°C for 10 min. The cathodes were outgassed and activated and 20 ma of emission was drawn from each cathode before the tubes were sealed from the pump and gettered. The tubes were aged by drawing 10–15 ma saturated emission from the cathode with 400-v PD applied between cathode and anode, this power being somewhat larger than the maximum at which the tube is tested for noise. Aging was continued in about 50-hr intervals until repeatable noise measurements were obtained, the total time necessary for this being usually between 100 and 300 hr. It was also found that if a tube was left unused for a week or more, it became much noisier and had to be re-aged for a few hours to bring it back to its original condition.

3. NOISE MEASUREMENT APPARATUS

The technique used for the measurement of the emission fluctuations was fairly conventional[7] and was chosen for its simplicity of use and availability of the apparatus. The principle of measurement may be explained by reference to Fig. 3. The tube under test (T.U.T.) was run as a temperature-limited diode and the current drawn from it controlled by regulating the heater power. The fluctuating component of the diode current divides equally at the point 0 in the circuit as the impedance to ac on both sides of the circuit had been arranged to be the same over the frequency range used. On the measurement side the noise current passed through an 8-μf blocking capacitor and through a 10 000-ohm resistor. The fluctuating voltage developed across this resistor was amplified by the low-level preamplifier and fed into a heterodyne wave analyzer with a 4-cps bandwidth and a linear diode detector. It must be appreciated that, in noise work, the rms noise current at a given frequency itself fluctuates with time, containing all frequencies within the passband, and its mean value must be determined by averaging over a suitable period of time. To carry out the averaging, the output from the wave analyzer was fed through a low-frequency filter, which removed frequencies above 0.5 cps, into a recorder from which the final averaging was carried out. Bennett and Fulton[8] have shown that, if the noise has a normal distribution and a uniform spectral density, and a square-law detector is used, then the length of time T over which the averaging must take place to ensure that the measured mean has a 95% certainty of lying within P% of the true mean is given by

$$T=(4\times10^4)/P^2\Delta f. \tag{2}$$

In this work, averaging times of about three to five minutes have been used. In the present circumstances, although the conditions for applying the above equation are not strictly adhered to, it might nevertheless be expected that P would be less than 5%. This method of measuring noise and the use of a linear detector have been discussed in the literature[7,9] and it is recognized that certain errors may arise at the lowest frequencies when the bandwidth becomes comparable with the center frequency and breakthrough of the carrier frequency becomes possible. However, spot comparison tests using ordinary filters and a square-law detector (thermocouple meter) showed that the apparatus could be used for noise measurements down to 15 cps without serious error using the correction factor obtained for sinusoidal input. The direct current through the tube under test was monitored by measuring the voltage across a 1000-ohm resistor in the circuit using the second channel of the recorder so that any direct current drift while noise measurements were being taken could be easily detected.

The background noise in the system was made as small as possible by using only low-noise metal film resistors and oil-filled capacitors, and taking care with the electrical connections. The noise generated by the dry batteries driving the saturated diode was reduced to a negligible amount by placing a large inductance (28 h) in series with them and a large capacitor (50 μf) in parallel with them. All sections of the noise circuit were contained within grounded metal boxes set on vibration isolating mountings.

The frequency indications on the wave analyzer were

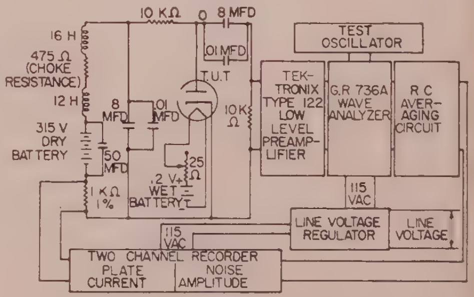

FIG. 3. The noise measurement equipment.

---

[7] D. A. Bell, *Electrical Noise* (D. Van Nostrand Company, Inc., Princeton, New Jersey, 1960), Chap. 14, p. 302.

[8] R. R. Bennett and A. S. Fulton, J. Appl. Phys. 22, 118 (1951).

[9] A. van der Ziel, *Noise* (Prentice-Hall, Inc., Englewood Cliffs, New Jersey, 1954), Chap. 13, p. 341.

ot judged to be sufficiently accurate, especially at the ow-frequency end of the spectrum, and to obtain these eadings accurately the wave analyzer was tuned to the tandard oscillator.

In order to see whether the background noise in the ystem was a function of the direct current, the tube nder test was replaced with low-noise metal film reistors. Under these conditions direct currents of up to 0 ma were drawn without any detectable increase in he background noise.

4. CALIBRATION

First the frequency response of the system was obained, and it was found that, for sinusoidal input, orrection factors were required at the low and high nds of the frequency range to reduce the wave anayzer readings to the same arbitrary scale of readings s the midspectrum points.

The calibration of the apparatus for noise was chieved by plotting the corrected mean wave analyzer eading squared against the total diode current, using cathode at a frequency at which the shot noise ominated. Let $\bar{N}$ = mean wave analyzer reading, then

$$\langle i^2\rangle_{\mathrm{av}} = K\bar{N}^2 = \langle (i_S + i_B)^2\rangle_{\mathrm{av}},$$

here K = calibration factor, i_S = shot noise, i_B = backround noise. Now $\langle (i_S+i_B)^2\rangle_{\mathrm{av}} = \langle i_S^2\rangle_{\mathrm{av}} + \langle i_B^2\rangle_{\mathrm{av}}$ since and i_B are uncorrelated; hence

$$K\bar{N}^2 = 2eI\Delta f + \langle i_B^2\rangle_{\mathrm{av}}, \tag{3}$$

sing the well-known shot noise relation, I = total urrent, e = electronic charge.

It was found that graphs of $\bar{N}^2$ against I were linear ith the same slope at all frequencies over which shot oise dominated, and by using diodes with pure tungen cathodes, frequencies down to 40 cps were checked. he fact that the plots were linear again demonstrates hat $\langle i_B^2\rangle_{\mathrm{av}}$ was independent of I and that $\bar{N}^2 \propto \langle i^2\rangle_{\mathrm{av}}$. he fact that the slope of each plot was independent frequency was as expected since the method of easurement ensures that Δf is independent of f. The omparison tests mentioned in Sec. 3 above showed hat the same calibration could be used down to 15 ps with sufficient accuracy. Figure 4 shows a typical librating plot.

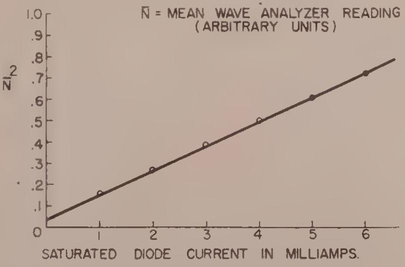

FIG. 4. A typical calibrating plot. Thoriated tungsten filament at 1000 cps.

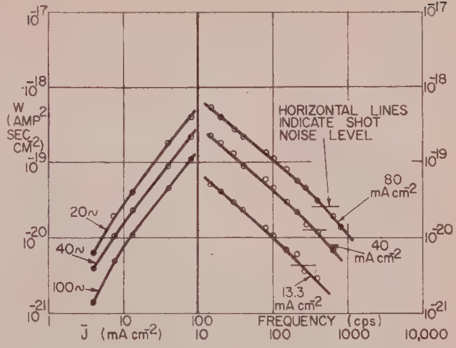

FIG. 5. Intensity distribution for the emission fluctuation component of the total noise for a cathode of type (i) (the 45% porous L cathode).

5. MEASUREMENT OF THE EMISSION FLUCTUATIONS

The measured mean square current fluctuations $\langle i^2\rangle_{\mathrm{av}}$ is composed of three parts; that due to the background noise, $\langle i_B^2\rangle_{\mathrm{av}}$ that due to the discrete nature of the electron, that is the shot noise $\langle i_S^2\rangle_{\mathrm{av}}$, and that due to emission fluctuations at the cathode $\langle i_F^2\rangle_{\mathrm{av}}$. These are related by the equation

$$\begin{aligned}\langle i^2\rangle_{\mathrm{av}} &= \langle (i_F+i_S+i_B)^2\rangle_{\mathrm{av}}\\ &= \langle i_F^2\rangle_{\mathrm{av}} + \langle i_S^2\rangle_{\mathrm{av}} + \langle i_B^2\rangle_{\mathrm{av}}\end{aligned}$$

since i_F, i_S, and i_B are uncorrelated; hence,

$$\langle i_F^2\rangle_{\mathrm{av}} = \langle i^2\rangle_{\mathrm{av}} - (\langle i_S^2\rangle_{\mathrm{av}} + \langle i_B^2\rangle_{\mathrm{av}}). \tag{4}$$

The procedure adopted was to measure $\bar{N}$ for various currents through the diode at frequencies between 15 cps and about 10 kcps. The lower frequency limit was set by the wave analyzer and the upper frequency limit was set for any individual cathode by the frequency at which the flicker noise became small compared with the shot noise. At 16 kcps, for all cathodes tested, the flicker noise was insignificantly small. It was also found that the background noise was small and virtually independent of frequency, hence the 16-kcps reading was taken to give the background and shot noises. Thus

$$\begin{aligned}\langle i_F^2\rangle_{\mathrm{av}} &= K(\bar{N}^2 - \bar{N}_{16\,\mathrm{kcps}}^2),\\ &= A.W(f,\bar{J})\Delta f. \qquad (1)\end{aligned}$$

Hence,

$$W(f,\bar{J}) = (K/A\Delta f)(\bar{N}^2 - \bar{N}_{16\,\mathrm{kcps}}^2). \tag{5}$$

In practice, emission fluctuation noise levels less than about half the shot noise level could not be measured with any accuracy. By way of comparison, the value of the shot noise intensity $(2e\bar{J})$ has been indicated on the subsequent graphs of W vs f. The total diode noise level for the cathode being considered will be given, of course, by the sum of these two components.

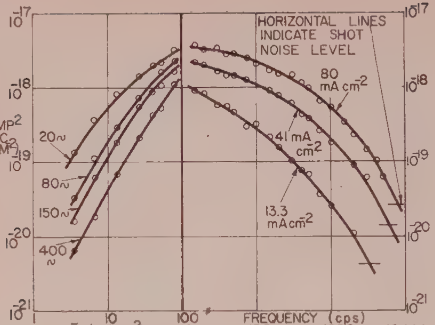

Fig. 6. Intensity distribution for the emission fluctuation component of the total noise for a cathode of type (ii) (the 25% porous L cathode).

6. EXPERIMENTAL RESULTS FOR *L* CATHODES

Several diodes containing both types of L cathode were studied. It was found that measurements on tubes with similar cathodes agreed fairly closely and observations on any given tube were repeatable, within the experimental error, provided they had been aged according to the schedule given in Sec. 2.

Figure 5 shows W as a function of frequency and current density for a typical L cathode of type (i) (45% porosity). Figure 6 shows W as a function of frequency and current density for a typical L cathode of type (ii) (25% porosity).

It will be seen that there is a remarkable change in the character of the noise as the tungsten porosity is decreased from 45% to 25%. The 45% porous cathode is considerably quieter than the 25% porous cathode and its spectra at the current densities measured show approximately an $f^{-0.86}$ variation. Although the variation of noise with current density shows some evidence of deviation at current densities below 10 ma cm^{-2}, over the rest of the range measured it varies as $\bar{J}^{1.23}$ at all frequencies.

On the other hand, the 25% porous cathode shows an unusual tendency towards saturation both in its noise spectra and the variation of noise with current density. The shape of the spectra depends on the current density and the shape of the noise variations with current density depends on the frequency. Such noise characteristics are somewhat unusual and confirm some earlier preliminary studies by van der Ziel[10] which indicated the existence of a relaxation effect in L cathodes.

7. EXPERIMENTAL RESULTS FOR IMPREGNATED CATHODES

Again several diodes containing each of the three types of impregnated cathode were studied. It was found that measurements on tubes with similar cathodes agreed fairly closely with each other and the observations on each tube were repeatable provided they had been aged according to the schedule given in Sec. 2.

Plots of W as a function of frequency and current density are shown in Figs. 7–9 for typical cathodes of types (iii), (iv), and (v), respectively.

It will be seen that type (v) is the noisiest of this group, although it is about one-fifth that of type (ii) (the 25% porous L cathode). It is of interest that it also shows some evidence of saturation both in its frequency and current density plots although they are not so marked as in the case of the 25% porous L cathode.

On the other hand, the other types of impregnated cathodes [types (iii) and (iv)] do not show any evidence of saturation. The cathode made from the more porous tungsten, type (iii), is noisier than that made from the less porous tungsten. For both cathodes, the noise intensity distribution function W can be written in the form

$$W(f,\bar{J})=B\bar{J}^{\alpha}f^{-\beta}. \tag{6}$$

When i and $\bar{J}$ are measured in amp cm^{-2} and f in cps, then for cathode of type (iii), $B=1.45\times10^{-15}$, $\alpha=1.63$, $\beta=1$, and for cathode of type (iv), $B=1.16\times10^{-16}$, $\alpha=1.35$, $\beta=0.72$, compared with cathode of type (i) for which $B=1.21\times10^{-16}$, $\alpha=1.23$, $\beta=0.86$, approximately.

It will be seen that the noise properties of the 25% porous impregnated cathode [type (iv)] are fairly close to the 45% L cathode [type (i)], whereas the 45% porous impregnated cathode [type (iii)] is markedly noisier than both due mainly to its larger α and B terms.

8. DISCUSSION OF RESULTS FOR THE *L* CATHODES

The first point that arises is the very large increase in noise that is observed when the porosity of the tungsten is decreased. This appears to be most likely

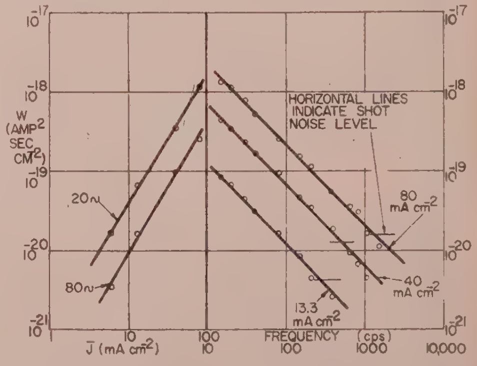

Fig. 7. Intensity distribution for the emission fluctuation component of the total noise for a cathode of type (iii) (the 45% porous impregnated cathode, impregnant $\frac{1}{2}CaO\cdot 3BaO\cdot Al_2O_3$).

---

[10] A. van der Ziel, *Noise in Electron Devices*, edited by L. D. Smullin and H. A. Haus (The Technology Press, M.I.T., and John Wiley & Sons Inc., New York, 1959), Chap. 2, p. 69.

related to the rate of supply of barium to the emitting surface. Previous measurements by Brodie and Jenkins[11] have shown that the evaporation rate of barium from a 45% porous tungsten *L* cathode, at any given temperature, is about seven times that from a 25% porous cathode of the same thickness. Now if, as a result of the lower rate of supply of barium, the number of activating atoms in the adsorbed monolayer on the tungsten surface of the low porosity cathode did not correspond with complete surface coverage, then fluctuations in the number of adsorbed atoms would give rise to larger emission fluctuations than if the monolayer were complete. This can be readily seen by referring to Fig. 10 which shows the typical form of a plot of emission versus surface density (n) for barium on tungsten (after Becker[12]). The emission passes through a maximum at optimum monolayer coverage where $n=n_0$; hence, fluctuations in n close to this point would give rise to smaller fluctuations in the emission than would occur at lower values of n. Evidence that the monolayer is not complete in the case of the low porosity *L* cathodes when run under dc operating conditions has been given by Brodie[13] who showed that the dc emission from such *L* cathodes is a little lower than that obtained under microsecond pulsed conditions due to removal of part of the activating monolayer by gas or ions liberated at the anode or by ions formed in the anode-cathode space.

This being so it would be expected, with a saturated diode at a fixed current and frequency, that the emission fluctuations would depend on the anode dissipation, i.e., in this case the applied voltage. Figure 11 shows the relation between the 150-cycle noise at 40 ma cm^{-2} and voltage for the cathodes under examination. It will be seen that, in the case of the 25% *L* cathode, the noise increases with increasing voltage until a saturation level is reached at about 200 v, after which the noise becomes independent of frequency. For the 45% *L* cathode, the same pattern is observed but the increase in noise with increasing voltage is not so marked. Since no reduction in the shot noise occurred in either cathode at the same time, the effect cannot be attributed to a patchy emitting surface.

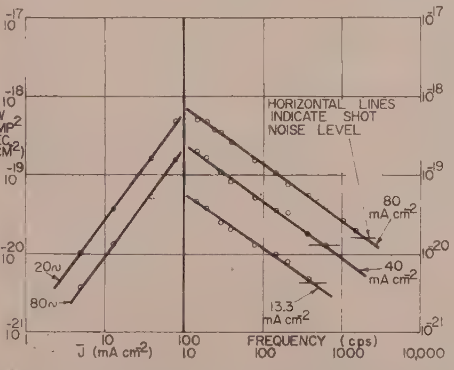

FIG. 8. Intensity distribution for the emission fluctuation component of the total noise for a cathode of type (iv) (the 25% porous impregnated cathode, impregnant $\frac{1}{2}$CaO·2BaO·Al$_2$O$_3$).

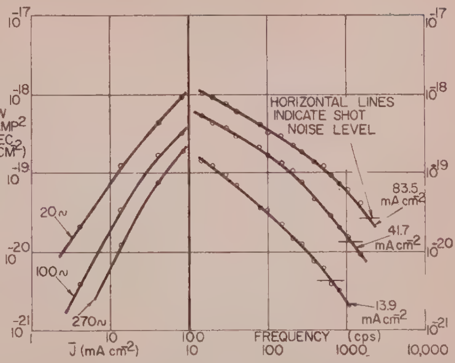

FIG. 9. Intensity distribution for the emission fluctuation component of the total noise for a cathode of type (v) (the 17% porous impregnated cathode, impregnant $1\frac{1}{2}$CaO·$2\frac{1}{2}$BaO·Al$_2$O$_3$).

From this discussion it will be seen that the hypothesis that the emission fluctuations in *L* cathodes are due to fluctuations in the number of activating atoms adsorbed on the tungsten surface rests on a fairly sound foundation. The Schottky[14] theory for emission fluctuations is based on precisely this concept and, by assuming that each activating atom spends a mean time τ_0 on an active site before it is removed, Schottky predicted

$$W(f,\bar{J}) \propto \bar{J}^2\tau_0(1+4\pi\tau_0^2 f^2)^{-1}. \qquad (7)$$

It will be seen that *L* cathodes do not follow the predictions of this theory. However, van der Ziel[15] has extended Schottky's theory by assuming that a number of different values of τ_0 exist with a distribution function for the number of absorbed atoms having mean adsorption time between τ_0 and $\tau_0+d\tau_0$ given by $g(\tau_0)d\tau_0$. Thus,

$$W(f,\bar{J}) \propto \int_{\tau_0=0}^{\infty} \frac{g(\tau_0)\tau_0 d\tau_0}{1+4\pi\tau_0^2 f^2}. \qquad (8)$$

To make this integrable, van der Ziel chose a distribution function of the form

$$\begin{aligned} g(\tau_0)&=0 && \text{for} \quad \tau_1>\tau_0>\tau_2, \\ g(\tau_0)&=(\tau_0 \ln\tau_2/\tau_1)^{-1} && \text{for} \quad \tau_1<\tau_0<\tau_2, \\ &&& \qquad \tau_1<\tau_2. \end{aligned} \qquad (9)$$

The choice of this distribution function was justified by considering that the mean adsorption time is related

---

[11] I. Brodie and R. O. Jenkins, J. Electronics **2**, 457 (1957).
[12] J. A. Becker, Trans. Am. Electrochem. Soc. **A180**, 225 (1929).
[13] I. Brodie, Proc. Phys. Soc. (London) **B68**, 1146 (1955).

[14] W. Schottky, Phys. Rev. **26**, 74 (1926).
[15] A. van der Ziel, Physica **16**, 359 (1950).

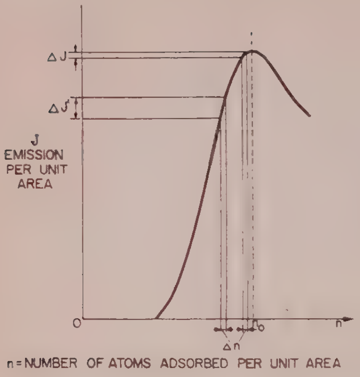

Fig. 10. Proposed mechanism for increase of noise with decreasing surface density of adsorbed barium.

to the temperature by the relation

$$\tau_0=\tau_{00}\exp[\phi_0/kT],\qquad(10)$$

where ϕ_0 is the activation energy for adsorption in electron volts when Boltzmann's constant k is given in electron volts per degree. This means that the chosen distribution function in τ_0 is equivalent to a simple distribution function in ϕ_0 in which all activation energies between ϕ_1 and ϕ_2 are equally probable and all ϕ_0 outside these limits have zero probability. Application of these assumptions gives

$$W(f,\bar{J})\propto\bar{J}^2f^{-1}(\tan^{-1}2\pi f\tau_2-\tan^{-1}2\pi f\tau_1).\qquad(11)$$

By writing $\tau_2/\tau_1=a$ and $2\pi f\tau_1=x$, numerical solutions of the equation

$$W(x)=(\tan^{-1}ax-\tan^{-1}x)x^{-1}\qquad(12)$$

were obtained for various values of a. Some of these solutions are shown in Fig. 12. By choosing a value for a and a matching point on each spectrum, it was found that for the 25% porosity cathode, remarkably good fits for each current density could be obtained. The best fit results are given in Table I together with the time constants calculated from them.

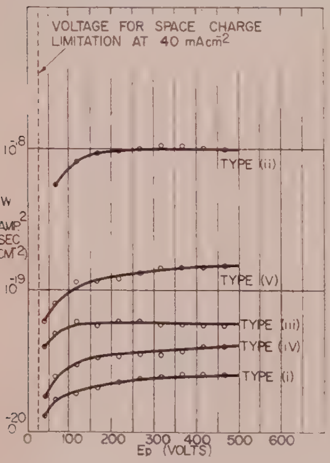

Fig. 11. 150-cps noise as a function of anode voltage, at constant current for the cathodes studied.

It will be seen that the time constants decrease with increasing emission. If it is supposed that the time constants vary with temperature according to the usual exponential form

$$\tau_1=\tau_{01}\exp[\phi_1/kT],\quad \tau_2=\tau_{02}\exp[\phi_2/kT],\qquad(13)$$

and since, over a limited range,

$$\bar{J}=J_0\exp[-\phi_e/kT],\qquad(14)$$

where $\phi_e=\phi_{0e}+k(T_1+T_2)$, ϕ_{0e}=work function obtained from Richardson's equation, k=Boltzmann's constant, and T_1 and T_2 are the end points of the temperature range being considered,[16] then graphs of $\log\tau_1$ and $\log\tau_2$ versus $\log\bar{J}$ should be straight lines with slopes proportional to ϕ_1/ϕ_e and ϕ_2/ϕ_e, respectively. Figure 13 shows such plots of τ_1 and τ_2 as a function of $\bar{J}$ and they appear reasonably linear. Using the result of Rittner *et al.*[17] for the work function of the L cathode as 1.67 ev and assuming a temperature range of operation of 1000–1200°K, the activation energy for the lower time constant calculates to be 0.7 ev and for the higher to be 2.2 ev.

It is interesting to speculate what physical processes in the L cathode could give rise to such activation energies. Rittner *et al.*[17] measured, as a function of temperature, the mean adsorption time and the mean migration length of the evaporation products from an L cathode on an oxygenated tungsten surface. From these results they calculate an activation energy for adsorption of 2.13 ev for a well-covered surface, and an activation energy for surface migration of 0.73 ev. It will be seen that these activation energies correspond remarkably well to the energies calculated for the end-point time constants using van der Ziel's theory. A discrepancy, however, arises in trying to correlate the actual times estimated here and those for adsorption and migration observed by Ritter *et al.* Extrapolation of the latters' results to 1000°K shows that, in a time of about 8250 hr, a barium atom would migrate a linear distance of 0.32 cm before evaporating. J. H. de Boer[18] has shown that there are close to 10^7 active sites for barium on a centimeter length on a tungsten surface, hence there would be 3.2×10^6 active sites in the migration length before evaporation. Assuming each barium atom moves in a random walk, it would on average visit about $(3.2\times10^6)^2$ sites in 8250 hr before evaporating and, hence, neglecting the time taken to move from one site to the next, would remain an average of 2.9×10^{-6} sec on each site. This compares with the value of 7×10^{-5} sec using the van der Ziel theory (saturated $\bar{J}$ at 1000°K ~ 10 ma cm⁻²). Considerably less favorable is the comparison of the adsorption

---

[16] W. B. Nottingham in *Handbuch der Physik*, edited by S. Flügge (Springer-Verlag, Berlin, 1956), Vol. 21, p. 1.

[17] E. S. Rittner, R. H. Ahlert, and W. C. Rutledge, J. Appl. Phys. **28**, 156 (1957).

[18] J. H. deBoer, *Electron Emission and Adsorption Phenomen* (Cambridge University Press, New York, 1935).

TABLE I. Matching theory with experiment for the 25% porosity L cathode.

Current density	$a=\tau_2/\tau_1$	x	f	W_{calc}	W_{obs}	τ_1 (sec)	τ_2 (sec)
13.3 ma/cm²	90	0.01	22.8	7.2×10^{-19}	7.3×10^{-19}		
		0.1	228	1.35×10^{-19}	1.35×10^{-19}	7×10^{-5}	6.3×10^{-3}
		1.0	2280	7.7×10^{-21}	8.0×10^{-21}		
40 ma/cm²	30	0.01	35	1.5×10^{-18}	1.6×10^{-18}		
		0.1	350	5.72×10^{-19}	5.5×10^{-19}	4.55×10^{-5}	1.37×10^{-3}
		1.0	3500	3.81×10^{-20}	4.0×10^{-20}		
80 ma/cm²	10	0.01	45	2.4×10^{-18}	2.7×10^{-18}		
		0.1	450	1.2×10^{-18}	1.1×10^{-18}	3.54×10^{-5}	7.08×10^{-4}
		1.0	4500	9.1×10^{-20}	9.1×10^{-20}		

time before evaporation. This was calculated above by extrapolating the results of Rittner *et al.* to 1000°K and gave 8250 hr compared with the estimate from the theory of 8×10^{-3} sec!

These results might be reconciled if it is assumed that the time constants involved in the theory do not refer to the mean times an atom remains on a site before being removed, but refer to the mean times which it takes for a barium atom to be *replaced* by a migration or evaporation process after it has been removed. Such a substitution in the theory would not alter its formal predictions, in which case the τ_1 and τ_2 in the van der Ziel theory would be related to the mean time it takes for a site to be reactivated by a migration and an evaporation mechanism, respectively, and that all times between τ_1 and τ_2 are allowed with a probability distribution of the form chosen.

Another point concerning the theory is the spectrum of the 45% porosity cathode which, over the frequency range examined, shows little evidence of relaxation. This implies that τ_1 and τ_2 are much further apart in this cathode, probably due to a greater decrease in τ_1 than τ_2 as the barium supply rate is increased.

Despite the conceptual difficulties imposed and the necessary choice of a simple distribution function for τ_0, the van der Ziel theory closely predicts the behavior of the 25% L cathode and must be judged in the light of this result.

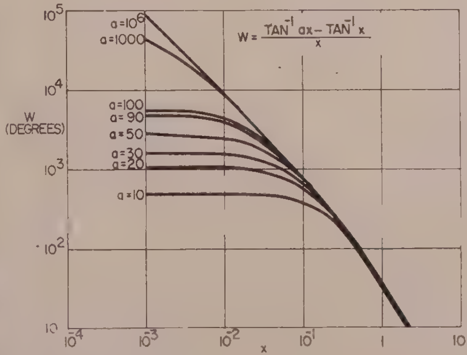

FIG. 12. Plots of $W(x)=x^{-1}(\tan^{-1}ax-\tan^{-1}x)$ vs x for various a.

9. DISCUSSION OF RESULTS FOR THE IMPREGNATED CATHODES

The emitting surface of the impregnated tungsten cathode consists of patches of impregnant at the pore ends surrounded by barium activated tungsten. When the impregnant is barium-calcium aluminate, the pore ends contribute significantly to the total emission from the cathode.[19] Hence, it would be expected that, as the porosity of the tungsten is reduced, the total current from the cathode would become largely that from the activated tungsten portion and that the noise would tend to be similar to that from an L cathode with a corresponding barium supply rate. The results from the impregnated cathodes tested here seem to confirm this hypothesis. The cathode of type (v) has the lowest porosity (17%) and the barium evaporation rate has been reduced as much as possible by both increasing the calcium oxide content and decreasing the barium oxide content in the impregnant. The noise from this cathode is about four times that from the 45% porous L cathode [type (i)] and about one-fifth that from the 25% porous L cathode [type (ii)]. The strongest indications that L type emission dominates are: firstly, the tendency towards saturation that exists both in its

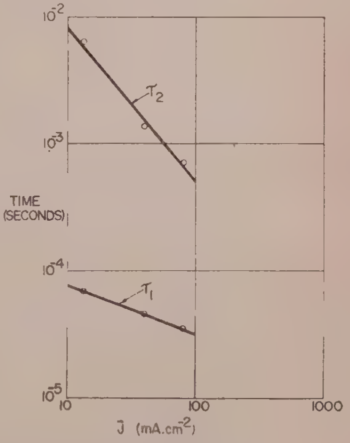

FIG. 13. Time constants as a function of $\bar{J}$ for cathode of type (ii) (the 25% porous L cathode).

---

[19] I. Brodie and R. O. Jenkins, Brit. J. Appl. Phys. 8, 27 (1957).

spectrum and its noise variation with current density (see Fig. 9), and secondly, the greater variation of noise with anode dissipation (see Fig. 11). Both of these effects, though not as definite as in the 25% porous *L* cathode, are nevertheless well marked.

The impregnated cathode of type (iii) (45% porous tungsten) is about twice as noisy as the 45% porous *L* cathode and there is no evidence of saturation either in its spectrum or its current density variation. This is despite the fact that it has been shown[11] that the barium evaporation rate from this cathode is about the same as that from the 45% porous *L* cathode at an operating temperature of 980°C. On the other hand, the cathode of type (iv) [25% porous tungsten, same impregnant as type (iii)] is less noisy than type (iii) over most of the frequency range examined, although the noise decreases less rapidly with increasing frequency than in any of the other cathodes. All the impregnated cathodes showed some decrease in noise with decreasing anode dissipation as shown in Fig. 11.

It is obvious from these results that the physical processes governing the emission fluctuations in these cathodes must be very complex depending as they do on the tungsten porosity, type of impregnant used, barium supply rate (which is known to vary with time of operation of the cathode[20]) and other possible variables. It may, however, be inferred from the present work that the noise is composed of two parts, that from the activated tungsten controlled by the barium supply rate, and that from the pore ends controlled by their size.

10. CONCLUSIONS

The emission fluctuations that occur in barium dispenser cathodes under dc conditions appear to be related to the rate of supply of barium to the emitting surface and hence the surface coverage. The greater the barium supply rate the better the surface coverage and hence the smaller the emission fluctuations. In the case of the *L* cathode with a low barium supply rate, the spectra show relaxation effects which follow the predictions of van der Ziel's extension of the Schottky theory. The time constants calculated by applying the theory appear to be related to the adsorption and migration characteristics of barium on an oxygenated tungsten surface.

For the impregnated cathodes it seems that when the fraction of the emitting surface which is comprised of pore ends is large enough to make an appreciable contribution to the emission then it also makes an appreciable contribution to the emission fluctuations. On the other hand, when the fraction of the surface that is pore ends is too small to contribute significantly to the emission then the cathode behaves as the simpler *L* cathode. The details of the mechanisms controlling the emission fluctuations in the impregnated cathode are extremely complex.

ACKNOWLEDGMENTS

Thanks are due Professor C. Dalman of Cornell University and Mr. J. P. Sackinger of our laboratory for many useful discussions. The technical assistance given by Mr. P. Carpentier also is acknowledged. This work was carried out during a research program partly supported by the Bureau of Ships.

---

[20] I. Brodie, R. O. Jenkins, and W. G. Trodden, J. Electronics and Control **6**, 149 (1959).

Letters to the Editor

Electron Emission from Reverse-Biased *p*-*n* Junctions in SiC

Lyle Patrick
Westinghouse Research Laboratories, Beulah Road, Churchill Borough, Pittsburgh 35, Pennsylvania

(Received May 11, 1961)

THE purpose of this note is to question some of the conclusions proposed by Gleichauf and Ozarow in a recent letter[1] about electron emission from reverse-biased SiC junctions. Gleichauf and Ozarow reported on the energy distribution of emitted electrons, measured by a retarding voltage technique. There are three points which we think were not properly taken into account. The first two would require corrections in the numbers reported. The third is a more fundamental criticism of the experimental arrangement. (1) The SiC electron affinity appears to have been neglected in calculating the energy requirement of electrons collected. As shown in Fig. 1, the necessary electron energy above the bottom of the conduction band is $W_c = eV_c + W_\varphi - \Delta E$. (2) The internal voltage drop of the junction V_i should be added to the external voltage V_j in calculating the energy available to an electron in the conduction band on the *p* side of the junction. (3) The collector voltage V_c is measured with respect to the *n*-type SiC, and therefore applies only to electrons which emerge from that side of the junction. There is nothing in the experimental arrangement, however, to prevent electrons from emerging from a point in the junction itself, at which point the voltage with respect to the collector may be quite different. The current collected at high apparent retarding voltage may be due to electrons collected from portions of the junction surface whose true retarding voltage is very small.

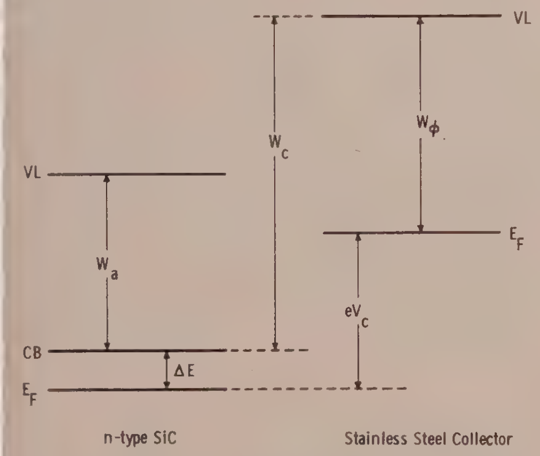

FIG. 1. Energy level diagram for calculating the energy W_c measured from the bottom of the conduction band in SiC, which an electron must have to reach the stainless steel collector biased by a retarding voltage V_c. E_F and VL, respectively, are the Fermi and the vacuum levels in the two systems. CB is the bottom of the SiC conduction band, and W_a is its electron affinity. W_φ is the work function of the stainless steel collector and V_c is its retarding voltage bias. ΔE is the (small) energy difference between E_F and CB in *n*-type SiC. As indicated, $W_c = W_\varphi + eV_c - \Delta E$.

The corrections required under (1) and (2) are comparable in size but opposite in sign. No quantitative evaluation is needed, however, in view of the criticism in (3). We may conclude, from the data of Gleichauf and Ozarow, that there was an electron emission current of 10^{-14} amp due to electrons which had lost only 3 or 4 ev to the SiC crystal; but is is not known how much of the junction those electrons traversed before emerging from the crystal, nor can one assume that they lost any energy in hole-electron pair production during the time they were being accelerated within the SiC crystal. Indeed, it is likely that the high-energy electrons collected were those which began as minority carriers on the *p*-type side, and were accelerated in the portion of the junction bordering the *p*-type material until they had enough energy to overcome the electron affinity and escape into the lossless vacuum. It does not therefore seem possible to draw any conclusions about the energy required for an ionizing collision in SiC.

---

[1] P. H. Gleichauf and V. Ozarow, J. Appl. Phys. **32**, 549 (1961).

Corbino Disk

Milton Green
Burroughs Laboratories, Paoli, Pennsylvania

(Received February 9, 1961)

A SOLUTION of Corbino-disk[1] behavior has recently been approximated. The results show that the resistance of the disk in the applied magnetic field depends on the direction of current flow into the disk, i.e., a slight rectification should be present. In an article which appeared in the July, 1961 issue of this Journal entitled "Corbino disk magnetoresistivity measurements on InSb," we reported just such an experimental observation and explained its cause. We attributed it, as does reference 1 below, to the magnetic field of the circulating component, I_θ, of the current of the Corbino disk. This field adds *both* constructively and destructively to the applied magnetic field (*not just one or the other*, as indicated in the analysis of reference 1). However, the net effect of the disk current is to produce, as stated in reference 1, an increased magnetoresistance when the radial component of the current is inward and a decrease for the outward flow. In our article we give the following expression (derivation not given) for the approximate change, ΔR, in the magnetoresistance:

$$\Delta R = -\frac{dR}{dH}\frac{\mu H^{HI}}{2d}\left[\left(\frac{\rho^2+1}{\rho^2-1}\right)\ln\rho - 1\right]10^{-9}, \tag{1}$$

where dR/dH is the slope of the resistance vs H curve at magnetic field H, μH is the carrier mobility (single carrier) of the disk at field H, d is the thickness of the disk, and ρ is the ratio of the external to the internal radius. Calculations, using the above equation, are in rough agreement with experimental observations. The change ΔR is about 0.2% for 0.8 amp and 18 kg at 296°K, and about 0.4% for 0.65 amp and 18 kg at 203°K. The experimental measurements included other effects, such as contact injection and a slight amount of joule heating. Although the experimental conditions were such as to minimize the latter two effects, it is difficult to eliminate them completely. Hence, we considered the agreement between the calculated and observed results as quite satisfactory.

The solution offered by Kleinman and Schawlow[1] in Eq. (12), for the steady state and for their condition is incorrect because their boundary condition is incorrect. The correct boundary condition for $r_1 < r < r_2$ is given by their Eq. (42), namely,

$$\int_{r_1}^{r_2} H_Z r dr = \text{const} = (r_2^2 - r_1^2) H_0, \tag{2}$$

where

$$H_Z = H_0 (b/r)^B, \quad r_1 < b < r_2, \tag{3}$$

and b is a radius to be determined from (2). It is the radius at which $H_{ZI} = 0$, where $H_Z = H_0 + H_{ZI}$. When B is positive, hence I positive, H_{ZI} adds *constructively* in the interval $0 \leq r \leq b$ and destructively in the interval $b \leq r < \infty$; the converse is true for B negative.

While the solution (3) is a perfectly good one, physically it is difficult to realize, since it corresponds to a cylinder for which the height is infinite and the conductivity along the Z axis is zero;

otherwise $I_Z \neq 0$ and $H_r \neq 0$. For a long, thin cylinder the effect of a nonvanishing I_Z cannot be neglected because it also contributes a "geometrical effect" to the magnetoresistivity. For a flat, thin Corbino disk, however, I_Z can be neglected. This is the case for which (1) is an approximate solution.

The mathematical solution for a Corbino disk geometry is admittedly quite complicated. However, with certain simplifying assumptions, some cases of reasonable accuracy are soluble. A paper dealing with this subject is now in preparation by this correspondent.

[1] D. A. Kleinman and A. L. Schawlow, J. Appl. Phys. **31**, 2176 (1960).

On the Interpretation of Internal Friction Experiments on Strain Aging of Iron

J. C. Swartz

Edgar C. Bain Laboratory For Fundamental Research, United Steel Corporation Research Center, Monroeville, Pennsylvania

(Received April 26, 1961)

DEFORMATION induced changes in the internal friction of iron at the temperature of the carbon peak have been interpreted as establishing the rate of segregation of carbon to dislocations and the quantity of carbon which is redissolved upon repeated deformation.[1–8] Generally, it is assumed that changes in the background damping during strain aging are negligible, despite the observation[9] of the Köster effect in room temperature deformed iron. To assess the validity of this assumption, damping experiments which distinguish the changes in the peak and background damping components have been undertaken.

Wire specimens of 99.9% iron containing small quantities of carbon were solution treated and quenched. Damping measurements were made with an inverted torsion pendulum.[10] The specimens were deformed a few percent in torsion in the pendulum.

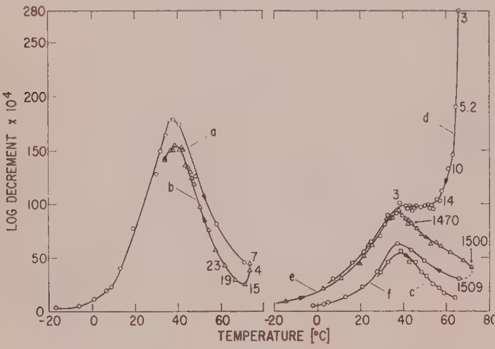

FIG. 1. Temperature dependences of damping during strain aging. In the as-quenched condition, the carbon peak decrement of this specimen was 190×10^{-4}. Subsequent data are as follows: (a) after 1 hr quench aging at 77°C; (b) immediately after straining 5% at 74°C; (c) following a brief anneal at 200°C; (d) after an additional 5% strain; (e) and (f) after 19 hr at −195°C with temperature rising and falling, respectively. The numbers refer to the time (min) from the preceding deformation.

A typical experiment is described in Fig. 1. The results of this and several similar experiments can be summarized as follows:

(1) Deformation of a specimen when the carbon peak is still relatively high does not appear to alter the background damping when measurements are started several minutes after deformation.

(2) When the carbon peak is low due to aging, deformation can cause a large and readily observable increase in the background.

(3) There is no indication that a ≤5% deformation increases the carbon peak. An increase in the peak decrement of 10^{-3} could have been detected.

(4) The transient background damping introduced by deformation is initially a strong function of temperature, such as shown in Fig. 1(d).[11]

(5) The rate of decay of the transient background damping is related to the height of the carbon peak just prior to the deformation. The smaller this peak the slower is the decay of the transient background.

In view of observation (1), the strain-aging experiments[1–6] determining the rate of carbon segregation to dislocations are probably without error due to background changes. On the other hand, those experiments[7,8] which have been interpreted as evidence for dissolution of carbon atmospheres upon deformation are probably confused by changes in the background damping. If the data of the latter experiments are reinterpreted as representing changes in the background rather than the peak component, they indicate the transient background is sensitive to the total carbon concentration in the strain-aged condition.

The dissolution of carbon atmospheres upon deformation of strain-aged iron has also been inferred by Cottrell and Churchman[12] from their observations of electrical resistance. According to their analysis, more than 8×10^{-4} wt % carbon returned to solution during deformation. Our internal friction experiments predict $<3 \times 10^{-4}$ wt % carbon dissolves (assuming the peak decrement/π = wt % interstitial carbon).[13] Even allowing for differences in deformation, the proposed conclusions of these experiments disagree. Since the internal friction method is more specific for interstitial carbon than is the resistance method, we conclude that there is no evidence for dissolution of carbon atmospheres during deformation.

[1] S. Harper, Phys. Rev. **83**, 709 (1951).
[2] W. R. Thomas and G. M. Leak, J. Iron Steel Inst. (London) **180**, 155 (1955).
[3] W. Pitsch and K. Lucke, Arch. Eisenhüttenw. **27**, 45 (1956).
[4] W. Wepner, Acta Met. **5**, 703 (1957).
[5] R. H. Doremus, Acta Met. **6**, 674 (1958).
[6] T. Suzuki and Y. Tomono, J. Phys. Soc. Japan **14**, 597 (1959).
[7] F. W. Kunz, Acta Met. **3**, 126 (1955).
[8] F. W. C. Boswell, Can. J. Phys. **37**, 1474 (1959).
[9] W. Köster, Arch. Eisenhüttenw. **14**, 271 (1940).
[10] J. C. Swartz, Rev. Sci. Instr. **32**, 335 (1961).
[11] Other results on the transient background damping in deformed iron will be described in a forthcoming report.
[12] A. H. Cottrell and A. T. Churchman, J. Iron Steel Inst. (London) **162**, 271 (1949).
[13] L. Dijkstra, Trans. Am. Inst. Mining, Met., Petrol. Engrs. **185**, 252 (1949).

Electron Spin Resonance in Powders

Gerald Burns

International Business Machines Corporation, Research Center, Yorktown, New York

(Received April 17, 1961)

THE use of powders for electron spin resonance measurements rather than single crystals is pointed out and demonstrated. As an example, the values of g and D for the spin Hamiltonian $g\beta\mathbf{H}\cdot\mathbf{S}+D[S_z^2-\frac{1}{3}S(S+1)]$ for Cr^{3+} and Mn^{2+} in two compounds are measured. The convergence of the equations to third order in D is good and so is the agreement with published single-crystal work.

When measuring electron spin resonance (ESR) in compounds that have angular dependent spectra, one normally uses single crystals.[1] However, for a Hamiltonian equal to $g_{\parallel}\beta H_zS_z + g_{\perp}\beta(H_xS_x+H_yS_y)$, it has been shown how one can interpret the resulting spectra when a powder is used.[2] More recently the powder pattern for the Hamiltonian having three nonequal g values [i.e., $(g_xH_xS_x+g_yH_yS_y+g_zH_zS_z)\beta$] has been investigated.[3]

The object of this paper is to point out and demonstrate the usefulness in measuring ESR in powders for materials with more general Hamiltonians. To interpret the data, the results of perturbation calculations for high field electric quadrupole experiments are borrowed.[4] This is possible since the form of the Hamiltonian, including nuclear magnetic resonance (NMR) and nuclear quadrupole resonance (NQR) terms, is the same as that encountered in many ESR Hamiltonians.

In the case of Cr^{3+} $(S=\frac{3}{2})$, for example, the spin Hamiltonian in an axial crystalline field is

$$\mathcal{H}=g\beta \underline{H}\cdot S+D[S_z^2-\tfrac{1}{3}S(S+1)]. \tag{1}$$

Normally, g and D are obtained by measuring the ESR in oriented single crystals.[1] However, as will be demonstrated below, one can obtain these results from powders, thus making the determination faster and easier.

Feld and Lamb[5] describe the powder pattern that results when an axial nuclear quadrupole interaction, eQq/h, is considered to first order in an NMR experiment. Their results are shown in Fig. 1 for a nuclear spin, I, of $\frac{3}{2}$. To this pattern, one must add line-broadening effects such as the magnetic dipole-dipole effects.

The extremes in the absorptions $\nu_0\pm\nu_1$ and $\nu_0\pm\nu_2$ are due to the crystallites, whose angle between the external applied field H and the symmetry axis is 90° and 0°, respectively, as can be seen from the formula

$$\nu=\nu_0\pm\tfrac{1}{4}(eQq/h)(3\cos^2\theta-1). \tag{2}$$

The equation describes the frequency of resonance for any single crystallite for the transition $\pm\frac{3}{2}\leftrightarrow\pm\frac{1}{2}(I=\frac{3}{2})$, where θ is the angle between the principal axis of the field gradient tensor and the external magnetic field.

The Hamiltonian that describes an NMR plus an eQq/h interaction has the same form as the ESR Hamiltonian in Eq. (1) with D replacing $[3/4I(2I-1)](eQq/h)$, and the equations worked out for quadrupole resonance can be applied to ESR and vice versa. Thus, the powder pattern in Fig. 1 also describes the results of an ESR experiment in a powder, for $S=\frac{3}{2}$, to first order in D. The result to higher order in D will be discussed below.

In the NMR case, the small signal to noise ratio (S/N) usually limits the usefulness of the powder methods to samples in which eQq/h is small.[6] This is because the area under the absorption curve must remain constant as one turns up the perturbation, eQq/h. Thus, the magnitude of the absorption will decrease as eQq/h increases. However, in the ESR case one often deals with spectra that have large S/N. On the other hand, the splittings involved are large. Conveniently, the large S/N more than makes up for the large splittings. Figure 2 shows the powder ESR of the alum, $NH_4(99\,Al+1\,Cr)(SO_4)_2\cdot 12\,H_2O$ run with an integrating time of 0.3 sec. Thus, the S/N could easily be made 10 times larger. The two small outer lines are at $\nu_0\pm\nu_2$. The larger ones are at $\nu_0\pm\nu_1$ and the two strongest center lines correspond to the $\frac{1}{2}\leftrightarrow-\frac{1}{2}$ transition which is split by second-order effects. (For this transition the first-order splitting is zero.) The powder pattern for the $\frac{1}{2}\leftrightarrow-\frac{1}{2}$ transition has been discussed in the NMR case[4] and one can use the results for the ESR case by replacing $[3/4I(2I-1)](eQq/h)$ by D as mentioned before. One can get values of D and g from the $\frac{1}{2}\leftrightarrow-\frac{1}{2}$ transition but the results from the other transitions should be more accurate since the splittings are larger.

Thus, one can see that the measured result in Fig. 2 is just the derivative of the expected powder pattern where the lines at $\nu_0\pm\nu_1$ and $\nu_0\pm\nu_2$ are clearly visible. Second-order splitting of the main line is also quite distinct. To make the powder method useful one must understand the pattern to higher powers of D/ν_0. For example, in the alums $D\sim 1000$ gauss and $\nu_0(=g\beta H/h)\sim 3400$ gauss at X band. Also, one must know what points on the experimental curve correspond to $\nu_0\pm\nu_1$, etc.

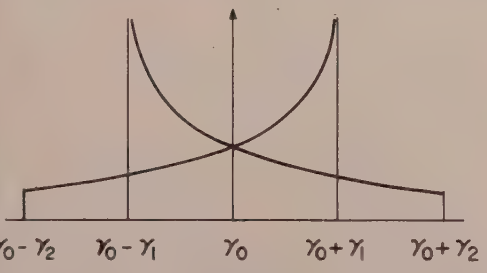

FIG. 1. The powder absorption pattern for an NMR line showing quadrupole effects to first order for $I=\frac{3}{2}$.[5] The line at ν_0 is not shown since it is unaffected by eQq/h to first order.

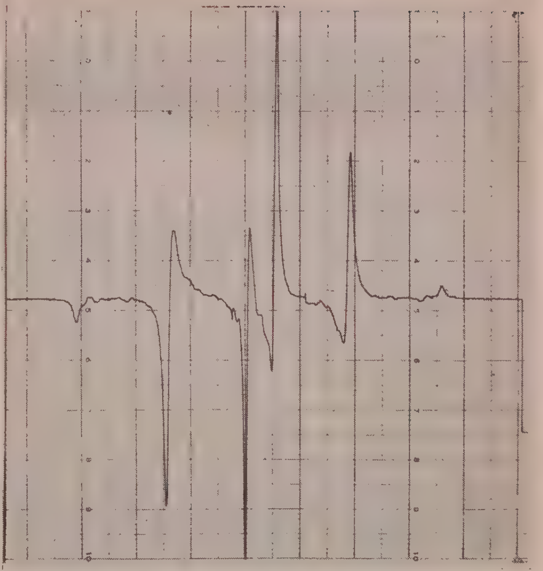

FIG. 2. ESR of Cr^{3+} at X band in powdered $NH_4(1\,Cr+99\,Al)SO_4\cdot 12H_2O$. The sweep is ~150 gauss per division. The integrating time constant is 0.3 sec, and the temperature 24°C.

One can extend Eq. (2) to third order by using the general relations in the literature.[7] The result, which must be added to Eq. (2), is

$$+6\cos^2\theta(1-\cos^2\theta)\frac{(D)^2}{\nu_0}$$
$$\pm\tfrac{3}{8}(1-3\cos^2\theta)(1-\cos^2\theta)(1+15\cos^2\theta)\frac{D^3}{\nu_0^2} \tag{3}$$

for $S=\frac{3}{2}$. For this value of S, one gets the equivalent NQR equation by substituting $4D=eQq/h$. Note that the total splitting, Eqs. (2) and (3), still has extrema at $\theta=0$ deg and 90 deg for reasonable D/ν_0. One will observe an infinite peak in the powder pattern whenever the ν vs θ relation has extrema, except at $\theta=0$. Thus, the separation between the lines at $\nu_0\pm\nu_2$, which is due to crystallites with $\theta=0$ deg, is $4D$; the separation between the lines at $\nu_0\pm\nu_1$, which is due to crystallites with $\theta=90$ deg, is $2D-\frac{3}{4}[D^3/(g\beta H/h)^2]$.

The theoretical powder pattern has infinite slopes at $\nu_0\pm\nu_1$ and $\nu_0\pm\nu_2$. It is not clear if the addition of other broadening effects will cause the line to have a very large or a zero slope at these points. This question was answered by the experimental measurements. The result for D of Cr^{3+} in $NH_4(99\,Al+1\,Cr)(SO_4)_2\cdot 12H_2O$ at 24°C is 0.0498 cm^{-1} from the maximum slope of the lines at $\nu_0\pm\nu_1$. The third-order term contributes ~1%. If the zero slope position were used, the value would be ~4% smaller. From the lines at $\nu_0\pm\nu_2$, $D=0.0495$ cm^{-1} is obtained.[8] The values of g obtained are 1.978 and 1.977, respectively.[8] Thus, the values are in agreement with careful single-crystal work.[1]

Mn^{2+}. The Mn^{2+} resonance is powdered $(98\,Zn+2\,Mn)SiF_6\cdot 6H_2O$ was observed to test the use of powder work for $S=\frac{5}{2}$. A main line, four large satellites corresponding to $\theta=90$ deg, and two small satellites corresponding to $\theta=0$ deg, are expected.[5] However, due to nuclear magnetic hyperfine interaction, each of the satellites is composed of six lines. The result is a very congested pattern but with the above knowledge, it can be made

useful. Assuming that the D splitting is very much larger than the cubic field splitting, which is the case for Mn^{2+}, $D=0.0170$ cm^{-1} was obtained which is in agreement with recent careful single-crystal work.[1]

The use of powders for ESR should permit the study of a number of groups of compounds that can be prepared in single-crystal form only with great difficulty (for example, the high temperature ferroelectric oxides). For the case of axial symmetry, the powder pattern will have a discontinuity whenever the ν vs θ relation has extrema. Thus, the method should be useful for a number of other paramagnetic ions. One drawback of the method is the smaller S/N that results. Another is that the observed lines are wider for the powdered sample than for the single crystal. Thus, any of the fine details of the spectra that require measurements more accurate than a linewidth will be lost. For example, one would not be able to measure the difference between $g_\perp$ and $g_{\parallel}$ for Cr^{3+} using a powder.[8] The powder work should also be useful when a rhombic term, $E(S_x^2-S_y^2)$, is added to the spin Hamiltonian since the ν vs θ relation has been worked out for the quadrupole case[4] and the ESR case.[4]

It is a pleasure to thank Dr. R. S. Title for the use of his spectrometer.

[1] For a review of the measured ESR results, see B. Bleaney and K. W. H. Stevens, Rept. Progr. in Phys. **16**, 108 (1953); K. D. Bowers and J. Owen, *ibid.* **18**, 304 (1955); J. W. Orton, *ibid.* **22**, 204 (1959).

[2] R. H. Sands, Phys. Rev. **99**, 1222 (1955); B. Bleaney, Proc. Roy. Soc. (London) **A63**, 407 (1950).

[3] F. K. Kneubuhl, J. Chem. Phys. **33**, 1074 (1960).

[4] For a review of quadrupole effects in NMR, see M. H. Cohen and F. Reif, in *Solid-State Physics*, edited by F. Seitz and D. Turnbull (Academic Press, Inc., New York, 1957), Vol. 5. For a calculation of the effects of a D and E term on the ESR to second order, see W. Low, *ibid.*, Suppl. 2.

[5] B. T. Feld and W. E. Lamb, Phys. Rev. **67**, 15 (1945).

[6] For example, the lines at $\nu_0\pm\nu_2$ have not been observed. Recently in one favorable case, Li Ta O_3, these lines have been seen (G. Burns, to be published).

[7] R. V. Pound, Phys. Rev. **79**, 685 (1950); R. Bersohn, J. Chem. Phys. **20**, 1505 (1952); and G. M. Volkoff, Can. J. Phys. **31**, 820 (1953). See G. Becker, Z. Physik **130**, 415 (1951) for the second-order effect for $I=\frac{3}{2}$.

[8] If $g_{\parallel}\neq g_\perp$, the effect on the D values is very small. One still obtains extrema at $\theta=0$, 90 deg. The separation between the lines at $\nu_0\pm\nu_1$ is still $2D$ to first order, independent of $g_{\parallel}/g_\perp$. The second-order corrections become $D^2/g_\perp\beta H$ but they are zero for $S=\frac{3}{2}$ (but not for $S=\frac{5}{2}$). Presumably, the third-order corrections would become $D^3/g_\perp\beta H$ but this cannot be ascertained since the ν vs θ relation has not been worked out for $g_{\parallel}\neq g_\perp$ to third order. [See B. Bleaney, Phil. Mag. **42**, 411 (1951).] The separation between the lines at $\nu_0\pm\gamma_2$ is $4D$ independent of $g_{\parallel}/g_\perp$. By adding the fields for the lines at $\nu_0\pm\nu_2$, one obtains $2g_{\parallel}$. From the $\nu_0\pm\nu_1$ lines, $2g_\perp$ is obtained with the first possible correction term being $\propto D^4/\nu_0$. (The D^2/ν_0 term is zero for $S=\frac{3}{2}$. For $S=\frac{5}{2}$, the correction term to $2g_\perp$ is $-2D^2/g_\perp\beta H$ from the $M=\frac{5}{2}$ transition.) However, for Cr^{3+} the difference between $g_{\parallel}$ and $g_\perp$ is probably too small to be obtained from the powder results.

Stress Dependence of the Piezoresistance Effect

Donald Long
Honeywell Research Center, Hopkins, Minnesota
(Received April 26, 1961)

THE recent increased emphasis on the use of semiconductors as strain or stress sensors[1] has led to a desire for a better understanding of their properties. This note deals with a comparison of the stress dependences of the piezoresistance in lightly- and heavily-doped crystals.

Consider a general situation in which the piezoresistance effect arises from stress-induced relative shifts of certain energy levels in which electrons (or holes) have different mobilities, and a resultant statistical redistribution of the electrons over them such that the average mobility changes thereby giving an over-all change of resistivity. This mechanism is believed to be the main contributor to the piezoresistance in many materials.[2] The energy shifts can occur when an applied nonhydrostatic stress destroys the crystal symmetry. Our approach is to consider only the statistics of the electron redistribution, assuming that the energy shifts are known from some other experiment or theory. We assume also that the total concentration of conduction electrons is constant, as in an extrinsic semiconductor.

If N_i is the electron concentration in a group of states small enough that the mobility can be represented by a single value μ_i (which is itself not explicitly dependent on stress), the piezoresistance fractional resistivity change for the entire assembly of such groups is

$$\Delta\rho/\rho_0=(N_0\mu_0/\Sigma_i\, N_i\mu_i)-1, \tag{1}$$

where $N_0=\Sigma_i\, N_i$, and the subscript zeros refer to the unstressed situation.

For classical statistics, such as would apply to a relatively highly purified semiconductor, we have

$$N_i\mu_i/N_{i0}\mu_i=e^{\eta-\eta_0}e^{-\beta_i S} \tag{2}$$

for the ratio of the electron conductivities in the ith group of states under finite and zero stresses S. Note that η represents the Fermi level divided by kT, and that β_i represents the energy shift per unit stress of the ith group, also divided by kT. Solution for $\eta=\eta(S)$ with subsequent substitution of (2) into (1) leads to the following equation, where $\beta_i S\ll 1$ as will be true in practice,[2] and the effect is expanded through terms in S^2.

$$\begin{aligned}\frac{\Delta\rho}{\rho_0}\cong-\frac{1}{N_0\mu_0}\Big\{&\mu_0\ \Sigma_i\, N_{i0}\beta_i S-\Sigma_i N_{i0}\mu_i\beta_i S+\tfrac{1}{2}\ \Sigma_i\, N_{i0}\mu_i\beta_i^2S^2\\&-\tfrac{1}{2}\mu_0\ \Sigma_i\, N_{i0}\beta_i^2S^2-\frac{1}{N_0\mu_0}(\Sigma_i\, N_{i0}\mu_i\beta_i S)^2\\&+\frac{1}{N_0}(\Sigma_i\, N_{i0}\beta_i S)(\Sigma_i\, N_{i0}\mu_i\beta_i S)\Big\}.\end{aligned} \tag{3}$$

For highly degenerate statistics, as in a very heavily-doped semiconductor, and an approximately parabolic band,[2] we have

$$N_i\mu_i/N_{i0}\mu_i=(\eta-\beta_i S)^{(\frac{3}{2}+p_i)}/\eta_0^{(\frac{3}{2}+p_i)}, \tag{4}$$

where we have allowed for an energy dependence of the mobility relaxation time τ_i of the form $\tau_i\propto\epsilon^{p_i}$. This is somewhat restrictive approximation, but it does permit a tractable consideration of at least some qualitative consequences of an energy dependent τ. An energy dependence of τ has no explicit influence on the classical result. Following essentially the same procedure as before, we find that the piezoresistance for fully degenerate statistics is given to terms in S^2 by

$$\begin{aligned}\frac{\Delta\rho}{\rho_0}\cong-\frac{1}{2N_0\mu_0}\Bigg\{&\left(\frac{\Sigma_i\, N_{i0}\beta_i S}{N_0\eta_0}\right)\Sigma_i\, N_{i0}\mu_i(3+2p_i)\\&-\Sigma_i\, N_{i0}\mu_i(3+2p_i)\frac{\beta_i S}{\eta_0}-\frac{1}{4}\left(\frac{\Sigma_i\, N_{i0}\beta_i^2S^2}{N_0\eta_0^2}\right)\Sigma_i\, N_{i0}\mu_i(3+2p_i)\\&+\frac{1}{4}\left(\frac{\Sigma_i\, N_{i0}\beta_i S}{N_0\eta_0}\right)^2\Sigma_i\, N_{i0}\mu_i(3+2p_i)\\&+\tfrac{1}{4}\ \Sigma_i\, N_{i0}\mu_i(3+2p_i)(1+2p_i)\frac{\beta_i^2S^2}{\eta_0^2}\\&+\frac{1}{4}\left(\frac{\Sigma_i\, N_{i0}\beta_i S}{N_0\eta_0}\right)^2\Sigma_i\, N_{i0}\mu_i(3+2p_i)(1+2p_i)\\&-\frac{1}{2}\left(\frac{\Sigma_i\, N_{i0}\beta_i S}{N_0\eta_0}\right)\Sigma_i\, N_{i0}\mu_i(3+2p_i)(1+2p_i)\frac{\beta_i S}{\eta_0}\\&-\frac{1}{2N_0\mu_0}\left(\frac{\Sigma_i\, N_{i0}\beta_i S}{N_0\eta_0}\right)^2[\Sigma_i\, N_{i0}\mu_i(3+2p_i)]^2\\&-\frac{1}{2N_0\mu_0}\left[\Sigma_i\, N_{i0}\mu_i(3+2p_i)\frac{\beta_i S}{\eta_0}\right]^2\\&+\frac{1}{N_0\mu_0}\left(\frac{\Sigma_i\, N_{i0}\beta_i S}{N_0\eta_0}\right)[\Sigma_i\, N_{i0}\mu_i(3+2p_i)]\\&\times\left[\Sigma_i\, N_{i0}\mu_i(3+2p_i)\frac{\beta_i S}{\eta_0}\right]\Bigg\}.\end{aligned} \tag{5}$$

Equations (3) and (5) are both complicated, but they show several interesting features. The first-order (in S) classical effect in (3) is proportional to the energy shifts and to $(kT)^{-1}$, both of which are included in the β_i, and the S^2 effect is proportional to their squares. The degenerate case of (5) has temperature independent first- and second-order effects since $\beta_i/\eta_0 \neq f(T)$. The first-order effect in a degenerate material is thus smaller by $\sim 1/\eta_0$ than that in a classical material for the same energy shifts[2] since $\eta_0 \gg 1$. Of most interest here is the additional fact that the S^2 effect in a degenerate material is smaller than that in a classical material by $\sim 1/\eta_0^2$, so that $\Delta\rho/\rho_0$ should be more nearly linear with S up to a given S in the degenerate material. These last conclusions may be modified, however, according to the values of the p_i, since they also affect the degenerate case. In general, the nature of the scattering mechanism has a more direct and pronounced influence in the degenerate case than in the classical. Expressions for $\Delta\rho/\rho_0$ vs S for materials in which the energy band structures and qualitative energy shifts are known, like n-type Si and Ge, can be derived directly from Eqs. (3) and (5).

Our principal conclusion is that the piezoresistance linearity is usually improved by statistical degeneracy, the amount of improvement depending somewhat on the p_i, or more generally on the nature of the scattering mechanism. Thus, heavily-doped semiconductor stress sensors should generally exhibit better linearity than lightly-doped ones. There is some experimental evidence for this conclusion.[3]

Thanks are due to Dr. O. N. Tufte for helpful discussions.

---

[1] See, for example, F. T. Geyling and J. J. Forst, Bell System Tech. J. 39, 705 (1960).

[2] R. W. Keyes, Solid State Physics 11, 149 (1960).

[3] Mason, Forst, and Tornillo, Instrument Society of America Conference Preprint No. 15-NY60, September, 1960.

Spherical Lenses for Infrared and Microwaves

G. TORALDO DI FRANCIA
Centro Microonde, Firenze, Italy

(Received May 19, 1961)

THE mathematical problem of finding all possible lenses of the Luneberg type has been solved quite generally[1] and yields a great variety of solutions. Later, but independently, similar solutions were given by Morgan.[2] A particularly important class of lenses for which numerical tables were published[3] is formed by lenses with an outer spherical shell of constant refractive index n_1 and an inner core of variable refractive index $n_2(r)$. It is found in this case that the higher the value of n_1, the smaller is the variation of n_2 as a function of the radial coordinate r. It therefore occurred to me that by using a very high value of n_1, it might be possible to find a very good approximation to a perfect lens, even with a constant n_2. Indeed, this turns out to be the case with n_1 in the range $3<n_1<4$. Such values of the refractive index, which are quite unrealistic in the case of visual optics, are not at all fantastic in the case of infrared optics. For instance, it is known that the refractive index of germanium has the value $n=4.1$.

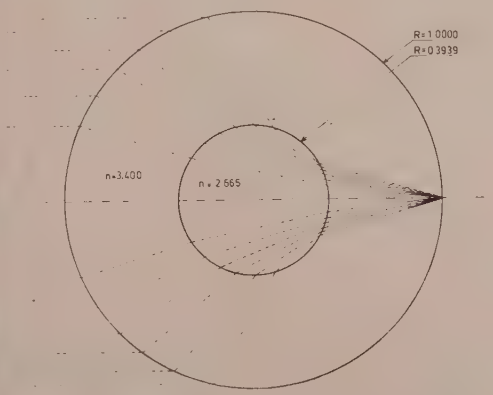

FIG. 1. Spherical lens which images a point at infinity on its outer surface.

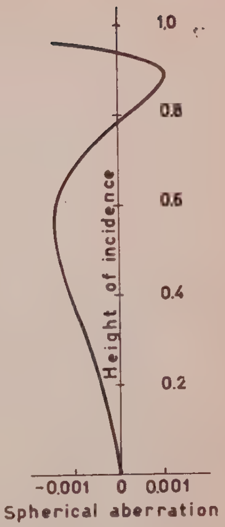

FIG. 2. Spherical aberration (abscissa) of lens represented in Fig. 1, plotted as a function of the height of incidence of the rays from infinity (ordinate).

As an example, the lens represented in Fig. 1 has $n_1=3.400$, $n_2=2.665$ (very close to the refractive indices of silicon and of TiO_2, respectively[4]). If the radius of the outer sphere is assumed equal to unity (focal length $f=1$), the radius of the core for this lens is $r=0.3939$. Some rays are traced in Fig. 1 for an object at infinity. The longitudinal spherical aberration is represented in Fig. 2 (abscissas) as a function of the height of incidence of the incoming rays (ordinates). The striking feature is the double correction of spherical aberration with very little zonal errors. As a microscope objective for infrared, this lens would be practically perfect up to a numerical aperture very close to unity. Of course, we have not taken into account chromatic aberration, and the radiation should be filtered. Moreover, a surface coating would be needed to reduce the otherwise large loss by reflection.

Alternatively, such lenses may serve as microwave collimators, provided the high values of the refractive index can be attained by suitably loaded dielectrics. For instance, a sphere of unit radius, with $n_1=3.600$, $n_2=2.750$, and the radius of the core $r=0.3863$, would collimate the rays from a point source located on its surface with a maximum angular error of only 2 min of arc up to a diameter of the beam equal to 0.9 times the diameter of the whole sphere. As a consequence, the error would be masked by diffraction even if the diameter of the beam were 1000 times the wavelength.

---

[1] G. Toraldo di Francia, Ann. Mat. 44, 35 (1957); J. Opt. Soc. Am. 47, 566 (1957).

[2] S. P. Morgan, J. Appl. Phys. 29, 1358 (1958).

[3] G. Toraldo di Francia and M. T. Zoli, Publs. Inst. Nazl. Ottica, No. 827 (1958).

[4] H. L. Hackforth, *Infrared Radiation* (McGraw-Hill Book Company, Inc., New York, 1960), p. 109.

Crystal Structure of Photoelectric Films of Cesium Antimonide

W. H. McCARROLL
RCA Laboratories, Princeton, New Jersey

(Received April 17, 1961)

THE observation has been made that normal valence alkali antimonides of high photoelectric sensitivity also have crystal structures based on cubic symmetry.[1,2] However, such a correlation suffers from the fact that all previous work on the crystal structure of alkali antimonides utilized materials synthesized under conditions which differ radically from those used to prepare photocathodes. Moreover, the use of such materials prevented the measurement of photoelectric properties which could be used to relate crystal structure to photoemission. The work presented here describes such measurements as well as the observation of the crystal structure of material taken from a photocathode. Although the work with Cs_3Sb is only part of a more general program to study photocathode structures, it was felt that presentation of the results to date for this compound would be of interest since there have been some questions raised as to the composition of the sensitive photocathode[3] as well as to the degree of ordering in the crystal structure.[4–6]

The results are based on data obtained from the x-ray powder diffraction patterns of material taken from photocathodes of known sensitivities in microamperes relative to a standard tungsten lamp. A specially designed tube containing a flat Pyrex plate with TIC electrodes on it was used for the preparation of samples. This plate serves as the substrate on which cathodes were prepared by treating an evaporated antimony layer with cesium until a cathode of maximum sensitivity was obtained. Processing was carried out at 125°C in the usual manner.[7] However, in some cases cathodes were purposely prepared with low sensitivity in order to observe the structural and composition differences. To prepare the most sensitive cathodes, it was necessary to process the cathode so that it did not contain an excess of cesium. Those cathodes of low sensitivity were prepared in such a manner that their cesium content would be much less than the ideal Cs:Sb ratio of 3:1. In this way cathodes ranging in sensitivity from 6 to 38 μa/lu were prepared. Cesium antimonide formed on the glass substrate was removed by peeling or scraping with a razor blade which was attached to a shaft fitted to a Monel bellows. The motion of the bellows was controlled externally. The sample material was removed from the cathode in the form of a coarse powder and was collected in a Pyrex capillary situated below the cathode substrate. The capillaries used in these experiments had wall thicknesses of 0.02 mm and a maximum diameter of 0.4 mm. Filtered copper radiation was used for x-ray photography.

An interesting correlation between the powder diffraction patterns of the samples and the photoemission of the original cathode was noted. In all cases the main lines of the pattern corresponding to Cs_3Sb were observed which are indicative of simple body-centered cubic structure with a lattice constant of 4.56 A. In addition, lines of other phases, believed to be lower antimonides, were also found. However, as the sensitivity of the cathode increased, the relative intensity of lines corresponding to Cs_3Sb also increased until, in the most sensitive cathodes (above 30 μa/lu), the lines attributable to other phases were either absent or just barely visible.

Although small crystallite size and highly strained lattices are to be expected in films prepared at the temperatures used in these experiments, it is often possible to eliminate these defects by annealing. Several of the samples sealed in the capillaries used for x-ray diffraction studies were heated at 200° to 210°C for 24 hr. Two principal effects were observed which depended upon the homogeneity of the sample. When multiphase samples were annealed the lines of the powder pattern were sharpened, but the lines corresponding to Cs_3Sb decreased in relative intensity or, in some cases, were not observed. This behavior is attributed to Cs_3Sb reacting with the other phases present to form lower valent antimonides. According to Klemm[8] seven different compounds exist, so that the possibilities for reactions to occur are numerous.

In the relatively pure (high sensitivity) samples, annealing sharpened the principal lines of the powder pattern of Cs_3Sb considerably. In addition, superlattice lines were observed which are evidence for the partially ordered sodium thallide type of structure found for Cs_3Sb by Jack and Wachtel.[4] This superlattice formation also results in the doubling of unit cell length. Unfortunately, the data obtained are not sufficient to distinguish between a phase transition and slow annealing out of gross crystalline defects. No lines of the type $h+k+l=4n+2$, which are indicative of a completely ordered DO_3 type of structure, were found. Although these lines are inherently weak, one would expect to see them if ordering had occurred. Gnutzmann[6] claims that such a structure exists for Cs_3Sb by analogy with his results for Cs_3Bi and Rb_3Bi. Annealing of a freshly prepared sample in the sealed capillary for 65 hr at 130°C sharpened the x-ray pattern, but no superlattice lines were observed. The sharpening of the pattern was considerably less than that observed after annealing at 200°C.

These experiments produced no evidence for an ordered structure in the photocathode. It now appears that this type of experiment could not be expected to yield such information because of the poor crystallinity of the samples. However, they do show conclusively that the sensitive cesium antimonide photocathode is homogeneous and has a cubic structure. It also appears that no stable compound containing cesium in considerable excess of the normal stoichiometric ratio exists in the sensitive cathodes, as has been suggested by Miyake.[3] On the other hand, we find no evidence to contradict Sommer's conclusion[9] that the sensitive photocathode is deficient in cesium to the extent that the cathode has *p*-type conductivity.

[1] W. H. McCarroll, J. Chem. Phys. Solids **16**, 31, (1960).
[2] W. E. Spicer, J. Appl. Phys. **31**, 2077 (1960).
[3] K. Miyake, J. Appl. Phys. **31**. 76 (1960).
[4] K. H. Jack and M. M. Wachtel, Proc. Roy. Soc. (London) **A239**, 46 (1957).
[5] J. J. Scheer and P. Zalm, Philips Research Repts. **14**, 143 (1959).
[6] G. Gnutzmann, dissertation, Münster, Germany (1953).
[7] A. H. Sommer and W. E. Spicer, *Methods of Experimental Physics 6B*, edited by K. Lark-Horovitz and V. A. Johnson (Academic Press, Inc., New York, 1959), p. 376 ff.
[8] W. Klemm, J. Chem. Soc. **1958**, 329.
[9] A. H. Sommer, J. Appl. Phys. **29**, 1568 (1958).

On the Theoretical Limitation of a Radio Telescope in Determining the Sky Temperature Distribution

Y. T. Lo
Department of Electrical Engineering, University of Illinois, Urbana, Illinois

(Received May 29, 1961)

In 1954 Bracewell and Roberts published their well-known paper[1] on a theoretical investigation of the limitation of an antenna in mapping the sky temperature distribution. They concluded that due to the finiteness of the antenna aperture, the antenna behaves like a low-pass filter which possesses a cutoff spatial frequency such that any information of the temperature distribution containing spatial frequency higher than the cutoff is completely lost and unrecoverable. Their conclusion has been often quoted and generally accepted. Since then Bracewell and others have published numerous papers[2] following the same argument. About three years ago this author took a refined look at their analysis and reached a somewhat different conclusion. Only recently this author had an opportunity to exchange his point of view rather briefly with Professor R. M. Chisholm of Queens College who happens to have conducted a similar investigation and seems to have reached a similar conclusion from a different approach. Also lately this author observed that some investigations have been made in an attempt to restore the exact sky distribution without considering noise and thereby reached some sort of wishful-thinking conclusions. This prompts this author to write such a short note to the editor.

Briefly, the analysis of Bracewell *et al.* is to solve the following equation by Fourier transform:

$$T_a(\theta)=\int A(\theta-\alpha)T(\alpha)d\alpha, \tag{1}$$

where α, θ are angular displacements measured from some convenient axes, $T(\theta)$ is the actual temperature distribution in the sky, $T_a(\theta)$ is the measured antenna temperature when the antenna is beamed at θ, and $A(\theta)$ is the antenna power pattern function.

The limits of the integral should be from 0 to 2π; since for large antenna the beam is very narrow, they reasoned that the limits can be replaced by $-\infty$ to ∞. By using Fourier transform, one obtains

$$\bar{T}_a(s)=\bar{A}(s)\bar{T}(s), \tag{2}$$

where the bar denotes the transform of the associated function. Now

$$A(\theta)=\int_{-\infty}^{\infty}\bar{A}(s)\exp i2\pi\theta s d\theta=E(\theta)E^*(\theta), \tag{3}$$

where $E(\theta)$ is the antenna field intensity pattern function, $E^*(\theta)$ its complex conjugate. It is related to the antenna illumination function $f(x)$ by

$$E(\theta)=\int_{-\infty}^{\infty}f(x)\exp i2\pi x\sin\theta dx\approx\int_{-\infty}^{\infty}f(x)\exp i2\pi x\theta dx, \tag{4}$$

where it is assumed that θ and $\sin\theta$ are nearly equal.[3] From (3) and (4) one obtains

$$\bar{A}(s)=f\bigstar f'^*, \tag{5}$$

where $\bigstar$ signifies the convolution integral, and $f'(x)=f(-x)$. Since for practical antenna $f(x)$ is aperture-limited, $\bar{A}(s)=0$ for s greater than a certain value s_c. It follows from (2) that $\bar{T}_a(s)=0$ for $s>s_c$, even if $\bar{T}(s)\neq0$ there. Therefore they conclude that part of spatial distribution $\bar{T}(s)$ is lost and cannot be recovered.

It appears that in the above analysis, θ and $\sin\theta$ (denoted by u from here on), are used indistinguishably. In what follows we propose to make a distinction between the two by defining the following two different scanning schemes: (1) Electrical scanning where the scan is achieved by a progressive phase shift; namely, the phase factor $\exp i2\pi xu$ in (1) is replaced by $\exp i2\pi x(u-v)$. It may be noted that the antenna pattern, in general, changes during scan since it is only a truncated function of the Fourier transform of $f(x)$; (2) Mechanical scanning, which is achieved merely by rotating the whole antenna or by the daily drift of the heavenly bodies. In this case the phase factor $\exp i2\pi x\sin\theta$ is replaced by $\exp i2\pi x\sin(\theta-\alpha)$ and it is also clear that the antenna pattern remains unchanged except for a rotation of the axis.

(1) Electrical scan. The measured antenna temperature in terms of u is

$$T_a(u)=\int_{-1}^{1}A(u-v)T(v)dv,$$

which can be rewritten as

$$T_a(u)=\int_{-\infty}^{\infty}A(u-v)T_b(v)dv, \tag{6}$$

if we define

$$\begin{aligned}T_b(u)&\equiv T(u)\quad\text{as}\quad|u|\leq1,\\&\equiv0\quad\text{as}\quad|u|>1.\end{aligned} \tag{7}$$

Evidently, to determine $T(u)$ is the same as determining $T_b(u)$. As before, by using Fourier transform,

$$\bar{T}_a(s)=\bar{A}(s)\bar{T}_b(s). \tag{8}$$

Since

$$A(u)=\int_{-\infty}^{\infty}\bar{A}(s)\exp i2\pi su ds=E(u)E^*(u)$$

with

$$E(u)=\int_{-\infty}^{\infty}f(x)\exp i2\pi xu dx,$$

one obtains as before

$$\bar{A}(s)=f\bigstar f'^*. \tag{9}$$

Although it appears that we obtain the same relations as before, we have made no assumption that $\sin\theta\approx\theta$, and the most important difference is that $T_b(u)$, $\bar{A}(s)$, and $\bar{T}_a(s)$ are "band-limited" functions, namely each equal identically to zero outside a finite range of its argument. By invoking a well-known powerful theorem due to Wiener-Paley[4] their transforms $\bar{T}_b(s)$, $A(u)$, $T_a(u)$ are entire functions. Now using the functional analyticity property, $\bar{T}_b(s)$ [as well as $T_a(u)$] can be, in principle, completely determined by its value over an infinite set of points on s, in particular by its value over some interval of s as given by (8) (using such as analytic continuity or some other methods). In short, $\bar{T}_b(s)$ for $s>s_c$ cannot be anything as Bracewell and Roberts implied since $T_b(u)$ is a band-limited function and $\bar{T}_b(s)$ must be analytic.

(2) *Mechanical scan.* In this case $A(\theta)$, $T(\theta)$ are periodic functions. Our aim is to solve the following integral equal for $T(\theta)$:

$$T_a(\theta)=\int_0^{2\pi}A(\theta-\alpha)T(\alpha)d\alpha. \tag{10}$$

A general procedure for solving this equation is to use a set of functions $\{\phi_n\}$ over $0\leq\theta<2\pi$ and to look for a solution in this functional space. In the present case, evidently, we may use $\phi_n=\exp in\theta$ since it is both complete and orthogonal. Now taking the Hermitian scalar product of both sides of (10) with ϕ_n, one obtains

$$\begin{aligned}2\pi\bar{T}_a(n)&=\int_0^{2\pi}\int_0^{2\pi}A(\theta-\alpha)T(\alpha)\exp(-in\theta)d\alpha d\theta\\&=\int_0^{2\pi}T(\alpha)\exp(-in\alpha)\int_0^{2\pi}A(\theta-\alpha)\\&\qquad\qquad\times\exp[-in(\theta-\alpha)]d\theta d\alpha\\&=(2\pi)^2\bar{T}(n)\bar{A}(n),\end{aligned} \tag{11}$$

where $\bar{T}_a(n)$, $\bar{T}(n)$, and $\bar{A}(n)$ are the Fourier coefficients with respect to ϕ_n. Thus

$$\bar{T}_a(n)=2\pi\bar{A}(n)\bar{T}(n),$$

which is in fact a convolution integral theorem corresponding to (2) but for a finite transform. Then the solution to (10) is

$$T(\theta)=\sum_{-\infty}^{\infty}\bar{T}(n)\exp in\theta=\frac{1}{2\pi}\sum_{-\infty}^{\infty}\frac{\bar{T}_a(n)}{\bar{A}(n)}\exp in\theta. \tag{13}$$

It is known that if the above series diverges, there exists no solution of $T(\theta)$ of class L_2. If it is convergent, since $\{\phi_n\}$ is complete in $(0,2\pi)$, (13) is the unique solution[5] except for a function of measure zero which is of no practical interest.

It is easy to show that even for a simple two element interferometer there exists no N such that $\bar{A}(n)=0$ for $n>N$ although $\bar{A}(n)\rightarrow0$ as $n\rightarrow\infty$. For an array with

$$A(\theta)=\sum_{m=-M}^{M}\exp im\beta d\sin\theta=1+2\sum_{m=1}^{M}J_0(m\beta d)+4\sum_{n=1}^{\infty}A_n\cos2n\theta,$$

where

$$A_n=\sum_{m=1}^{M}J_{2n}(m\beta d).$$

For $2n\gg m\beta d$,

$$J_{2n}(m\beta d)\approx\frac{1}{2(\pi n)^{\frac{1}{2}}}\left(\frac{m\beta de}{4n}\right)^{2n}$$

and

$$A_n\approx\frac{1}{2(\pi n)^{\frac{1}{2}}}\left(\frac{\beta de}{4n}\right)^{2n}\sum_{m=1}^{M}(m)^{2n},$$

which is never identically equal to zero although it may approach zero fast as $n\rightarrow\infty$.

So far we have shown that on a purely theoretical ground a unique solution $T(\theta)$ can be determined by a finite antenna, without even considering a theoretical possibility of super gain. However, we must agree with Bracewell and Roberts in the conclusion that the exact temperature distribution cannot be determined in practice but, due to a different factor, namely the noise which has not been taken into consideration in their analysis. As a result of the unavoidable noise contribution (here the term noise is used in a wide sense including, besides the thermal noise of the system, also the fluctuation of the medium, the nonzero tolerance of various designing parameters and their fluctuations, etc.) the measured temperature is not exactly given by (6) and (10); instead, there should be terms due to noise and random variations of both A and T functions. This will set a limit of the uncertainty of the measured T_a, or $\bar{T}_a(n)$. Also this uncertainty will render the analytic continuity of $\bar{T}_a(s)$ for large s almost impossible. Therefore, we conclude that there does exist a practical limit in mapping the details of the sky temperature distribution which is determined by both the noise and the antenna pattern function. In this respect it seems that the limitation of the radio telescope is not basically different from many other systems of measurements commonly seen, and it is not an intrinsic shortcoming of the antenna as generally thought to be.

---

[1] R. N. Bracewell and J. A. Roberts, Australian J. Phys. **7**, 615 (1954).

[2] R. N. Bracewell, Australian J. Phys. **9**, 297 (1956); A. E. Covington and N. W. Broten, IRE Trans. on Antennas and Propagation **AP-5**, 247 (1957); A. E. Covington and G. A. Harvey, Can. J. Phys. **37**, 1216 (1959).

[3] It is seen that this assumption is not compatible with the previous one on the limits of the integral in Eq. (1).

[4] R. E. A. C. Paley and N. Wiener, Trans. Am. Math. Soc. **35**, 348 and 761 (1933), which has been used so convincingly to prove the nonexistence of an upper limit in the directive gain of an antenna of finite size. For the latter, one may refer to C. J. Bouwkamp and N. G. DeBruigin, Philips Research Repts. **1**, 135 (1948) which bears a great similarity to the present argument, although it is a completely different problem. Also N. I. Achieser, *Theory of Approximation* (Frederick Ungar Publishing Company, New York), p. 134.

[5] F. G. Tricomi, *Integral Equations* (Interscience Publishers, Inc., New York, 1957).

Probabilities for the Neon Laser Transitions

G. F. Koster
Massachusetts Institute of Technology, Cambridge, Massachusetts
AND
H. Statz
Raytheon Company, Research Division, Waltham, Massachusetts

(Received June 14, 1961)

THE successful operation of a neon laser was reported some time ago.[1] Use was made of transitions between the four $2s$ states and the ten $2p$ states (Paschen notation) of NeI. There are three factors determining the strength of the laser oscillation, namely, the population inversion, the Q of the cavity which is related to the reflection coefficient of the Fabry-Perot plates at the considered frequency, and the transition probability between the considered states. While it is easy to determine the reflection coefficient, the degree of population inversion is more difficult because it depends upon details of collision processes between the Ne atoms and He metastable atoms as well as on relaxation processes of the $2p$ states. In order to learn more about the latter mechanisms and to understand the laser action better, we have made an approximate calculation of the transition probabilities.

In these calculations we make use of an observation of Racah[2] according to which the excited states of certain atoms including neon are describable in a j-l coupling scheme. Expressed in different language, this means that we can obtain an approximate wave function of neon if we couple the angular momentum l of the running electron, which for our case is in either a $3p$ or $4s$ state, to the angular momentum j of the core. The resultant angular momentum we designate by k. To K we then couple the spin angular momentum S to give a total angular momentum J. The values of j, K, and J for neon are tabulated in reference 3. By building up the wave function in the above described way using Clebsch-Gordon or 3-j coefficients, the wave function is not antisymmetric in the coordinates of the running electron ($3p$ or $4s$) with respect to those of the core. It may be shown, however, that for orthogonal one-electron wave functions, the transition probability is identical whether fully-symmetrized wave functions are utilized or not.

According to the outline we make up the final wave function with angular momentum J and z component J_z from the above described wave function having angular momentum K, and the spin wave function with angular momentum $S=\frac{1}{2}$. In the standard way [see reference 4, Eq. (1.15)] we obtain

$$|KSJJ_z\rangle=(-1)^{S-K-J_z}\sum_{m_k m_s}(2J+1)^{\frac{1}{2}}\begin{pmatrix} K & S & J \\ m_k & m_s & -J_z \end{pmatrix}|Km_kSm_s\rangle. \tag{1}$$

In Eq. (1) m_k and m_s are the z components of K and S, respectively. The symbol $|KSJJ_z\rangle$ stands for a wave function described by the four quantum numbers K, S, J, and J_z. Similarly $|Km_kSm_s\rangle$ represents the product of the wave function characterized by K and m_k and the spin wave function with angular momentum $S=\frac{1}{2}$ and z component m_s. Also introduced into the equation are the 3-j symbols.[4]

In order to calculate transition probabilities, we have to evaluate matrix elements of the electric dipole operator $p=e\mathbf{r}$ between two states which we distinguish by using subscripts 1 and 2. The above introduced vector $\mathbf{r}$ stands for $\sum_i \mathbf{r}_i$. If we designate the coordinates of the running electron by 1 we can restrict the sum to $\mathbf{r}_1$ since the other terms give no contribution. Instead of calculating the matrix elements of x, y, and z, we calculate those of z, $x\pm iy$ and we call this operator T_{pq}; where $p=1$ and $q=0, \pm 1$. In calculating matrix elements between two functions of the type (1) we are led to matrix elements of the form $\langle K_1m_{k1}l_1j_1|T_{pq}(1)|K_2m_{k2}l_2j_2\rangle$, where T_{pq} acts only on the coordinates of the running electrons (l_1 and l_2). According to Rose[5] we obtain

$$\langle K_1m_{k1}l_1j_1|T_{pq}(1)|K_2m_{k2}l_2j_2\rangle=(-1)^{-m_{k1}+j_2+p-2l_2-2K_2-l_1}$$
$$\times(2K_1+1)^{\frac{1}{2}}(2K_2+1)^{\frac{1}{2}}\delta(j_1j_2)\begin{pmatrix} K_1 & pK_2 \\ -m_{k1} & qm_{k2} \end{pmatrix}\begin{Bmatrix} l_2 & K_2 & j_2 \\ K_1 & l_1 & p \end{Bmatrix}$$
$$\times\langle l_1\|T_p(1)\|l_2\rangle. \tag{2}$$

In Eq. (2) the brace indicates a 6-j symbol,[4] and the remaining matrix element is a so-called reduced matrix element depending only on l_1 and l_2 which are fixed for the considered transitions. From (2) and (1) the final matrix element may be written. Some

TABLE I. Probabilities for NeI $2s \rightarrow 2p$ transitions and reported laser oscillations.[a]

Transition	$\lambda(\mu)$	Relative probability	Laser oscillations (Javan[a])
$2s_2 \rightarrow 2p_{10}$	0.88677	0	
$2s_3 \rightarrow 2p_{10}$	0.89910	0	
$2s_4 \rightarrow 2p_{10}$	0.94893	1/18	
$2s_5 \rightarrow 2p_{10}$	0.96681	5/18	
$2s_2 \rightarrow 2p_9$	1.01239	0	
$2s_3 \rightarrow 2p_9$	1.02850	0	
$2s_2 \rightarrow 2p_8$	1.02982	0	
$2s_3 \rightarrow 2p_8$	1.04649	0	
$2s_2 \rightarrow 2p_7$	1.06236	0	
$2s_3 \rightarrow 2p_7$	1.08010	0	
$2s_2 \rightarrow 2p_6$	1.08475	0	
$2s_4 \rightarrow 2p_9$	1.09422	0	
$2s_3 \rightarrow 2p_6$	1.10325	0	
$2s_4 \rightarrow 2p_8$	1.11461	1/2	
$2s_5 \rightarrow 2p_9$	1.11806	7/9	1.118
$2s_5 \rightarrow 2p_8$	1.13936	1/18	
$2s_2 \rightarrow 2p_5$	1.14123	1/9	
$2s_2 \rightarrow 2p_4$	1.15259	5/9	1.153*
$2s_4 \rightarrow 2p_7$	1.15282	5/18	
$2s_2 \rightarrow 2p_3$	1.16047	0	
$2s_3 \rightarrow 2p_5$	1.16173	2/9	1.160
$2s_3 \rightarrow 2p_4$	1.17351	0	
$2s_2 \rightarrow 2p_2$	1.17700	2/9	
$2s_4 \rightarrow 2p_6$	1.17923	1/18	
$2s_5 \rightarrow 2p_7$	1.17931	1/18	
$2s_3 \rightarrow 2p_3$	1.18168	0	
$2s_3 \rightarrow 2p_2$	1.19882	1/9	1.199
$2s_5 \rightarrow 2p_6$	1.20696	1/2	1.207
$2s_4 \rightarrow 2p_5$	1.24628	0	
$2s_4 \rightarrow 2p_4$	1.25984	0	
$2s_4 \rightarrow 2p_3$	1.26927	1/9	
$2s_5 \rightarrow 2p_5$	1.27730	0	
$2s_4 \rightarrow 2p_2$	1.28907	0	
$2s_5 \rightarrow 2p_4$	1.29156	0	
$2s_5 \rightarrow 2p_3$	1.30146	0	
$2s_5 \rightarrow 2p_2$	1.32229	0	
$2s_2 \rightarrow 2p_1$	1.52349	1/9	
$2s_3 \rightarrow 2p_1$	1.56025	0	
$2s_4 \rightarrow 2p_1$	1.71666	0	
$2s_5 \rightarrow 2p_1$	1.77608	0	

[a] See reference 1.

simplification is obtained by observing that a sum over three 3-j symbols may be reduced to a product of a 3-j and a 6-j symbol according to Eq. (2.20) of reference 4. Since the transition probability depends only on the square of the matrix element,

$$|\langle K_1S_1J_1J_{z1}|T_{pq}(1)|K_2S_2J_2J_{z2}\rangle|^2$$
$$=(2J_1+1)(2J_2+1)(2K_1+1)(2K_2+1)\delta(j_1j_2)\begin{pmatrix} J_1 & J_2 & p \\ -J_{z1} & J_{z2} & q\end{pmatrix}^2$$
$$\times\begin{Bmatrix} J_1 & J_2 & p \\ K_2 & K_1 & S_1\end{Bmatrix}^2\begin{Bmatrix} l_2 & K_2 & j_2 \\ K_1 & l_1 & p\end{Bmatrix}^2|(l_1\|T_p(1)\|l_2)|^2. \quad (3)$$

Finally summing over all orientations, i.e., all J_{z1} and J_{z2}, and using the values of $l_1=0$, $l_2=1$, $p=1$, $K_1=j_1$, $S_1=S_2=\frac{1}{2}$, we obtain with Eqs. (1.13) and (2.12) of reference 4

$$\sum_{J_{z1}J_{z2}}|\langle K_1S_1J_1J_{z1}|T_{pq}(1)|K_2S_2J_2J_{z2}\rangle|^2$$
$$=\frac{1}{9(2j_1+1)}(2J_1+1)(2J_2+1)(2K_1+1)(2K_2+1)\delta(j_1j_2)$$
$$\times\begin{Bmatrix} J_1 & J_2 & 1 \\ K_2 & K_1 & \frac{1}{2}\end{Bmatrix}^2|(l_1\|T_p(1)\|l_2)|^2. \quad (4)$$

We see that the final result is independent of the polarization of the stimulating light. Equation (4) has been evaluated and the resulting relative transition probabilities are listed in Table I. We have also indicated the approximate positions of the reported laser oscillations.[1] In this connection it should be noted that the maximum reflection of the Fabry-Perot plates occurred in the vicinity of 1.16 μ, falling off toward both sides in the wavelength scale. The strongest observed line is marked with an asterisk. From Table I, one may see that for uniform population inversion between the 2s and 2p levels there should have been at least two more observed lines. At the positions of the $2s_4\rightarrow 2p_7$ and $2s_2\rightarrow 2p_4$ transitions, there is only one reported emission line, and the same is true for the $2s_3\rightarrow 2p_5$ and $2s_2\rightarrow 2p_2$ transitions.

We wish to thank Miss W. Doherty for help in the calculations and Dr. C. F. Luck for contributions to the communication.

---

[1] A. Javan, W. R. Bennett, Jr., and D. R. Herriot, Phys. Rev. Letters 6, 106 (1961).

[2] G. Racah, Phys. Rev. 61, 537(L) (1942).

[3] C. E. Moore, "Atomic energy levels, Vol. 1," Circ. of the National Bureau of Standards, June 15, 1949.

[4] M. Rotenberg, R. Bivins, N. Metropolis, and J. K. Wooten, Jr., *The 3-j and 6-j Symbols* (Technology Press, Cambridge, Massachusetts, 1959).

[5] M. E. Rose, *Elementary Theory of Angular Momentum* (J. Wiley & Sons, Inc., New York, 1957), p. 119.

Electron Beam Excitation of a Fabry-Perot Interferometer*

Murray D. Sirkis, Robert J. Strain, and William E. Kunz
Ultramicrowave Group, Electrical Engineering Research Laboratory, University of Illinois, Urbana, Illinois

(Received May 1, 1961)

THE Fabry-Perot interferometer, the familiar physical optics device which has proven its utility in maser research,[1,2] has been shown in this study also to be a practical resonator for the generation of short microwaves by electron beam techniques. An interferometer, with dimensions of many free space wavelengths, has been used to extract energy from a megavolt, bunched electron beam at the tenth, eleventh, twelfth, and thirteenth harmonics of the beam's S-band fundamental frequency. The source of the beam was a Rebatron.[3] At the highest of these harmonics, 36.9 kMc (8.15 mm), approximately 150 mw were produced by a beam with an average current of 14 ma.

This experiment contrasts with conventional electron beam experiments because the beam interacted with the transverse rather than the longitudinal electric field.[4] This is, of course, necessary in a device which is so large that plane wave behavior is approximated.

The coupling of a bunched electron beam with a Fabry-Perot resonator may be readily analyzed using a plane wave approximation. Consider two perfectly conducting planes of area A located at $z=\pm d/2$ as shown in Fig. 1. The region between the plates is filled with a dielectric having permittivity ϵ. A bunched electron beam crosses the structure at an angle θ with respect to the z axis, with its trajectory in the y-z plane. Assume a plane standing wave with the electric field in the y direction inside the dielectric described by

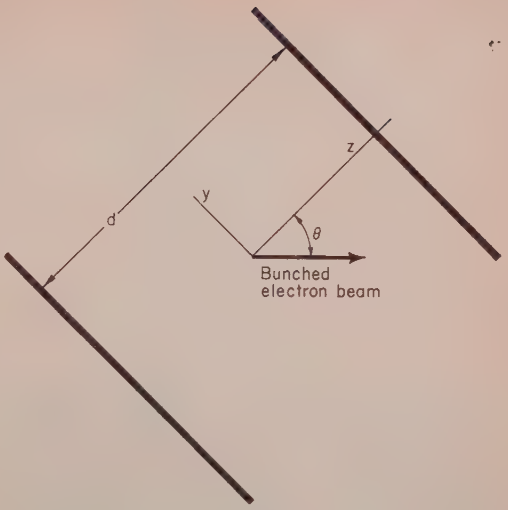

FIG. 1. The geometry of the plane-wave analysis of the Fabry-Perot interferometer-electron beam interaction. The electric field is in the y direction, and the magnetic field is perpendicular to the plane of the drawing.

$$\mathbf{E}=\hat{j}E\sin\left[\frac{\omega}{v_p}\left(z-\frac{d}{2}\right)\right]e^{i\omega t},$$

where $v_p=(\epsilon\mu)^{-\frac{1}{2}}$ is the phase velocity of the plane wave, and $\omega d/v_p=n\pi$, where n is an integer. The driving current is given by

$$\mathbf{I}=Ie^{i\omega(t-s/v)}(\hat{k}\cos\theta-\hat{j}\sin\theta),$$

where s is the distance measured along the beam trajectory starting from the origin of coordinates and v is the electron speed. The power delivered by the beam to the electromagnetic field is

$$P=-\frac{1}{2}\,\mathrm{Re}\int_{-d(2\cos\theta)^{-1}}^{d(2\cos\theta)^{-1}}\mathbf{I}\cdot\mathbf{E}^*ds.$$

This power must be equated to the sum P_D+P_L of the power lost in the dielectric and the power delivered to any external load. If the loss in the end plates is neglected, the power loss is

$$P_D=\frac{1}{2}\omega\epsilon\tan\delta\int\mathbf{E}\cdot\mathbf{E}^*dV.$$

The greatest power output is achieved when $v\cos\theta=v_p$, i.e., when there is synchronism between the electron beam and the forward traveling wave. The value of this maximum is

$$P_L=\tfrac{1}{16}(I^2d\tan^2\theta/\omega\epsilon A\tan\delta).$$

The validity of the plane-wave assumption used in this analysis has been checked by considering the exact solution for a dielectric rod waveguide.[5] For the geometry used in this experiment, the longitudinal interaction is less than 4% of the transverse interaction.

The experimental interferometer, which is shown in Fig. 2, is a Teflon cylinder 76 mm in diameter and 125 mm in length which has flat reflecting surfaces at each end. One of the reflecting surfaces has a number of parallel slits to allow radiation of power from the resonator. In order to achieve synchronism between the 0.88-Mev bunched electron beam and one traveling-wave component of the electromagnetic field, the electron beam was passed through the interferometer at an angle of 42° with respect to its axis for a distance of approximately 11 cm.

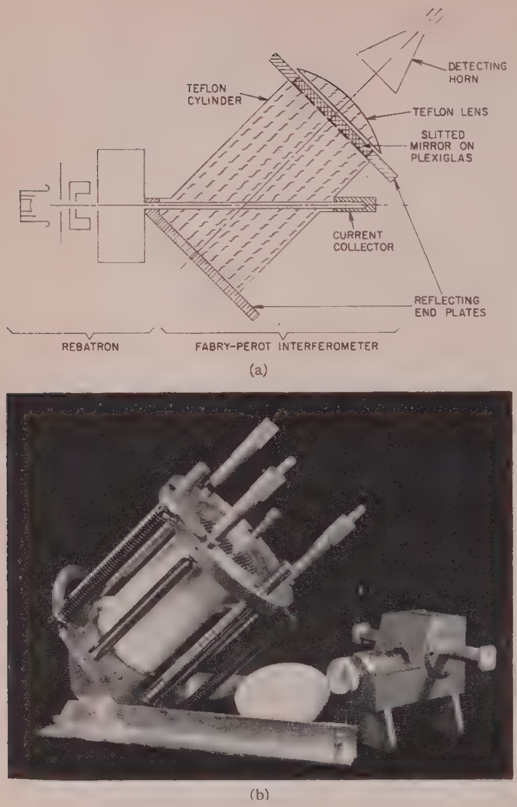

FIG. 2. (a) A drawing of the experimental interferometer. (b) The same unit photographed with the lens removed. The commercial unit is an 8-mm precision attenuator.

The parameters of importance in this experiment are: $I \approx 14$ ma, $d \approx 8.5$ cm, $\omega/2\pi = 36.9$ kMc, $\epsilon/\epsilon_0 = 2.08$, $\theta = 42°$, $\tan\delta = 3\times10^{-4}$, $A = 46$ sq cm. If these numerical values are substituted into the power expression derived above, the theoretical result is 150 mw, which corresponds well with the results observed during the experiment. The harmonic current I has been taken to be equal to the average beam current, in accordance with earlier theoretical and experimental work.[6]

The dielectric Fabry-Perot resonator has thus been shown to provide a large and easily predicted interaction with a high energy, bunched electron beam. Furthermore, its large size provides a practical means of circumventing the fabrication difficulties encountered in longitudinal field structures at short wavelengths, and the quasi-plane wave output is well adapted to systems utilizing optical techniques for the transmission of microwave radiation.

The authors wish to thank Professor Paul D. Coleman for the stimulating discussions during which this experiment was conceived and Richard J. Kenyon, also of the Ultramicrowave Group, for his assistance and the use of his Rebatron, without which the experimental data would have been far more elusive.

---

* Work supported by the United States Air Force.

[1] A. Javan, W. R. Bennett, Jr., and D. R. Herriott, Phys. Rev. Letters **6**, 106 (1961).

[2] W. Culshaw, IRE Trans. on Microwave Theory and Techniques **MTT9**, 135 (1961).

[3] P. D. Coleman, J. Appl. Phys. **28**, 927 (1957).

[4] H. Wilhelmsson, R.L.E. Report No. 32, Trans. Chalmers University of Technology, No. 155 (1954).

[5] S. A. Schelkunoff, *Electromagnetic Waves* (D. Van Nostrand Company, Inc., Princeton, New Jersey, 1943), pp. 425–428.

[6] I. Kaufman, University of Illinois, Urbana, Illinois, thesis, 1956; U. S. Air Force Office of Scientific Research, Tech. Note 57-7.

Far Infrared and Microwave Detector

D. W. GOODWIN AND R. H. JONES
Royal Radar Establishment, Great Malvern, England
(Received June 9, 1961)

CURRENTLY available detectors for the far infrared cover a wide range of wavelengths. Their detectivity is limited by 300°K radiation noise to a value[1] of 2×10^{10} w^{-1}. If the signal source is confined to a narrow wavelength band the detectivity can be increased by the use of cooled filters and radiation shields with a subsequent loss in flexibility.

A possible method for confining detection to a narrow tunable band involves the use of cyclotron resonance absorption in solids.[2] The absorption coefficient (k) of a semiconductor can be increased at the cyclotron resonance frequency (ω_c) provides that the momentum relaxation time (τ_m) is greater than ω_c^{-1}. The radiation power absorbed will raise the electron temperature and, provided that τ_m is energy dependent, the static electrical conductivity will be changed.

In order to assess the performance of this type of detector, measurements have been made on n-type germanium at a temperature of 4.2°K with a radiation source at a frequency of 34 kMc. Because of the small absorption coefficient at resonance (10^{-3} cm^{-1}) the specimen is placed in a conventional microwave cavity at a position of maximum electric field strength, with its $\langle 100\rangle$ axis parallel to and its $\langle 110\rangle$ axis at right angles to the magnetic field. Under these conditions a single resonance line is observed corresponding to an effective mass of $0.13m_e$.

The power absorbed (P_A) by a specimen of Q_s when placed in a microwave cavity with input coupling coefficient (Q_1) is given by[3]

$$P_A = P_0\cdot[4Q_1Q_s/(Q_1+4Q_s)^2], \tag{1}$$

where P_0 is the incident power, assuming that the cavity is matched to the input waveguide. The rate of loss of energy from the electrons to the lattice can be expressed in terms of an energy relaxation time[4] (τ_ϵ) and if τ_m is limited by impurity scattering at 4.2°K it can be shown that the differential change in voltage across the specimen given by

$$\frac{\Delta V}{V} = \frac{P_0}{A}\cdot\frac{8\pi Q_1\mu\tau_\epsilon F}{\epsilon\epsilon_0\omega t}\left(\frac{e}{kT},\right)\frac{1+\omega^2\tau_m{}^2+\omega_c{}^2\tau_m{}^2}{(1+\omega_c\tau_m{}^2-\omega\tau_m{}^2)^2+4\omega^2\tau_m{}^2}, \tag{2}$$

where A is the detector area, t the thickness, μ the electron mobility, F the cavity filling factor, and ω the microwave frequency, provided that $Q_1 < Q_s$. Thus Eq. (2) can be used to estimate τ_ϵ from the magnitude of the signal at resonance and τ_m from the shape of the resonance line.

A conventional circuit comprising a battery and load resistance is used to determine the change in static resistance of the specimen. Microwave power from a reflex klystron is modulated at 1 kc and the change in voltage across the specimen as the magnetic field is swept through resonance detected using a phase sensitive amplifier. The static electric field strength across the specimen is kept below 1 v cm^{-1} to avoid impact ionization.

The responsivity for a specimen of area 2 mm^2 when placed in a cavity of $Q_1 = 5\times10^3$ was 2×10^4 μv/μw. Measurement of noise power at 1 kc showed that excess noise was comparable with Johnson noise, hence the normalized detectivity (D^*) for 1 cm^2 and unit cycle bandwidth is 10^{11} w^{-1}.

On the assumption that the major contribution to energy loss is through acoustic phonon scattering, then[5]

$$\tau_\epsilon/\tau_m = kT/m^*u^2, \tag{3}$$

when u is the velocity of sound. At 4.2°K, τ_ϵ/τ_m should be approximately 27. The ratio measured using Eq. (2) is 20 and thus indicates within the limits of experimental accuracy the preponderance of acoustic phonon scattering. Because of the characteristics of the microwave cavity used for these experiments only 6% of the incident power was absorbed in the specimen. The use of a more efficient resonant cavity and material having high electron mobility should result in D^* not exceeding 10^{14} w^{-1}.

The speed of response of the detector is limited by the value of τ_ϵ which, for this specimen, is $(6\pm2)\times10^{-10}$ sec.

The resolving power of the detector $(2\pi c_0\tau_m/\lambda)$ is 20 at 34 kMc and will increase as the detector is used at higher frequencies. The possible extension to the far infrared depends on the development of suitable resonant structures and magnetic fields. A superconducting magnet of niobium-tin[6] would enable detection at wavelengths from approximately 200 μ upwards using the resonance line of electrons in germanium.

The authors wish to acknowledge the help of Dr. A. F. Gibson who suggested the possibilities of this detector a year ago. This letter is published by kind permission of the Controller, H. B. M. Stationary Office.

[1] R. L. Petritz, Proc. Inst. Radio Engrs. **47**, 1458 (1959).
[2] H. J. Zeiger, C. I. Rauch, and M. E. Behrmdt, J. Phys. Chem. Solids **8**, 496 (1959).
[3] C. R. Ditchfield (private communication).
[4] A. F. Gibson, J. W. Granville, and E. G. S. Paige, J. Phys. Chem. Solids (to be published).
[5] H. Frohlich and B. V. Paranjape, Proc. Phys. Soc. (London) **69B**, 21 (1956).
[6] J. E. Kunzler, E. Buchler, F. S. L. Hsu, and J. H. Wenick, Phys. Rev. Letters **6**, 89 (1961).

Impurity Striations in Unrotated Crystals of InSb

H. C. Gatos, A. J. Strauss, M. C. Lavine, and T. C. Harmon
Lincoln Laboratory, Massachusetts Institute of Technology, Lexington 73, Massachusetts*

(Received May 15, 1961)

PERIODIC variations in impurity concentration (striations) along the growth axis have frequently been observed in semiconductor single crystals, pulled from the melt by a rotating seed-holder (Czochralski method). We have observed the occurrence of similar transverse striations in Se-doped InSb crystals pulled from the melt without rotation. The transverse striations which have been reported previously[1,2] were observed in metal ingots solidified horizontally. Transverse striations are to be distinguished from the longitudinal striations[2] which have been shown to be associated with cellular structure.

Impurity striations have been detected in rotated crystals of Ge (by electroplating,[3,4] autoradiography,[5] resistivity measurements,[5] infrared absorption,[5] and indium alloying[6]), Si (by etching[7]), and InSb (by autoradiography[8] and etching[8]). The spacing of the striations (d) is found to be equal to the distance which the crystal grows vertically during one rotation: $d=r_1/r_2$, where r_1 is the macroscopic growth rate and r_2 is the rotation rate. These striations are generally attributed to the fact that the temperature distribution at the solid-liquid interface is not radially symmetric.[3,9] Consequently, as the crystal rotates the microscopic growth rate and therefore the impurity concentration incorporated into the crystal vary with angular position. The surfaces of constant impurity concentration in the resulting crystal are helical, and striations are formed by the intersection of these surfaces with the plane of any longitudinal section.

In the present study, the distribution of Se in InSb single crystals was investigated at a concentration of approximately 10^{18} cm^{-3}. The rotation rate was varied during crystal growth without changing the pull rate, and portions of some crystals were grown without rotation. An etched longitudinal section of one of these crystals, is shown in Fig. 1. The usual relationship between striation spacing and rotation rate is observed. A high Se concentration core associated with the presence of a $\langle111\rangle$ facet at the growth interface[10] is also observed. Closely spaced striations are present in the unrotated portion of this crystal, although they are not distinct in the photograph. More widely spaced striations are clearly visible in the unrotated portion of a second crystal shown in Fig. 2. In some unrotated crystals, on the other hand, no striations could be detected. No correlation between the presence of striations and the macroscopic conditions of crystal growth has been established; this is not surprising in view of the strong dependence of the crystal growth process on external conditions and particularly on temperatures and temperature gradients about the interface.

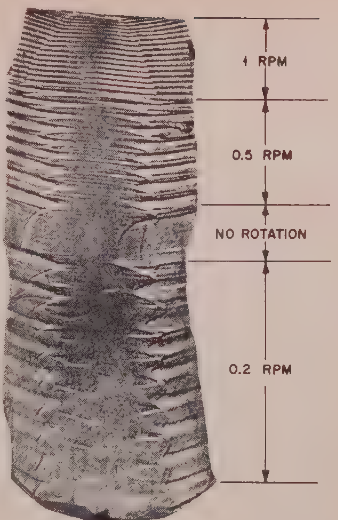

FIG. 1. Longitudinal section of an InSb single crystal doped with Se at a concentration of approximately 10^{18}/cm^3, and etched with dilute CP4. The rate of rotation was varied during growth as indicated. Impurity striations are present in both the rotated and the unrotated portions of the crystal. Note core with increased impurity concentration. Pulling rate 1 in./hr; 2×.

It is believed that the observed impurity striations in unrotated crystals, like those in rotated crystals, result from changes in the microscopic rate of crystal growth. The variation in growth rate, however, is brought about by different causes in the two cases. In rotated crystals, the growth rate differs with position due to rotation as pointed out above. In the unrotated crystals, on the other hand, the growth rate is essentially the same at all points on the interface at a given instant but changes periodically. This pulsating growth must be associated with periodic changes in temperature and/or impurity concentration at the interface which might be expected to occur in the following manner.

A certain degree of supercooling is required in order to initiate growth from the melt. When this is attained and crystallization begins, latent heat of fusion is liberated and impurity atoms are rejected from the growing crystal into the liquid layer adjacent to the growth interface (if the impurity distribution coefficient is less than unity). The resulting increase in temperature and in impurity concentration in the liquid layer decreases the degree of supercooling and therefore the rate of crystal growth. If the rate of heat dissipation and/or the rate of transfer of impurity atoms from the liquid layer into the remainder of the melt is sufficiently small, growth will be arrested until the degree of supercooling required to initiate growth is once again established and the cycle begins again (cf. reference 11). This type of periodicity could be superimposed on the striations due to rotation but its detection may be outside the limits of the commonly employed experimental techniques.

Whether the striations which were observed in unrotated crystals were caused solely by phenomena of the type just de-

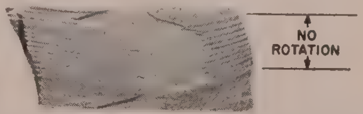

FIG. 2. Longitudinal section of an InSb crystal etched with dilute CP4. Striations in the unrotated portion of this crystal are spaced further apart; 2.8×.

scribed cannot be unambiguously decided on the basis of the present data. A quantitative study of these striations—for example, their dependence on macroscopic vertical growth rate, thermal gradients in the vicinity of the growth interface, orientation, and thermal conductivity of the material—should lead to a better understanding of the mechanism of crystal growth from the melt.

---

* Operated with support from the U. S. Army, Navy, and Air Force.

[1] M. T. Stewart, R. Thomas, K. Wauchope, W. C. Winegard, and B. Chalmers, Phys. Rev. **83**, 657 (1951).

[2] J. W. Rutter and B. Chalmers, Can. J. Phys. **31**, 15 (1951).

[3] P. R. Camp, J. Appl. Phys. **25**, 459 (1954).

[4] J. A. M. Dikhoff, Solid-State Electronics **1**, 202 (1960).

[5] J. A. Burton, E. D. Kolb, W. P. Slichter, and J. D. Struthers, J. Chem. Phys. **21**, 1991 (1953).

[6] A. C. English, J. Appl. Phys. **31**, 1498 (1960).

[7] W. D. Edwards, Can. J. Phys. **38**, 439 (1960).

[8] W. P. Allred and R. T. Bate, J. Electrochem. Soc. **108**, 258 (1961).

[9] E. Billig, Proc. Roy. Soc. (London) **229**, 346 (1955).

[10] K. F. Hulme and J. B. Mullin, Phil. Mag. **4**, 1286 (1959).

[11] A. I. Landau, Fiz. Metal. i Metalloved. **6**, 1948 (1956).

Stress Optical Constants of Germanium

K. J. Schmidt-Tiedemann
Philips Research Laboratory Hamburg, Hamburg, Germany

(Received June 5, 1961)

GERMANIUM becomes birefringent under the action of stress. The effect is described by a set of stress optical constants Q defined as follows:

$$R = QXd, \tag{1}$$

where R is the relative retardation of the two light waves in the crystal, measured in degrees of arc, X the magnitude of an applied uniaxial stress in kg/cm², and d the thickness in cm of the sample in the direction of the light beam.

The value of Q depends, in general, on the direction n of the wave normal of the incident beam and the direction s of the uniaxial stress.[1] Cubic symmetry cuts down the number of independent constants to two as far as relative phase shifts are concerned. Commonly, the following constants are considered to be the basic ones:

$$\begin{aligned} &Q_1: s=\langle 100\rangle, \quad n\perp s\\ &Q_2: s=(1/\sqrt{3})\langle 111\rangle, \quad n\perp s. \end{aligned} \tag{2}$$

The experimental arrangement consisted of a xenon arc light source, an interference filter for the wavelength range 2.2±0.05 μ, a calcite Glan-Thompson prism as polarizer, the combination of a quarter wavelength plate and a second Glan-Thompson prism as analyzer (Senarmont compensator[2]), and a PbS photoresistor as detector. Light was chopped at 300 cps and the output signal detected by a tuned amplifier.

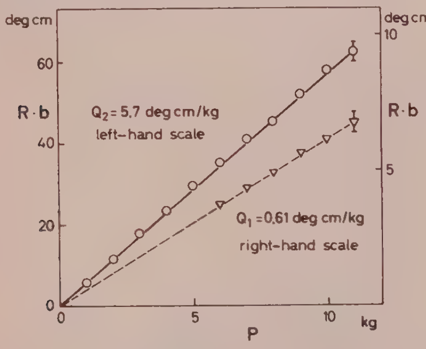

FIG. 1. Phase shift times sample width vs load for undoped Ge at $\lambda = 2.2\mu$. Stress optical constants Q_i are given by the slope of the straight lines. Direction of uniaxial stress ⟨100⟩ and ⟨111⟩ for Q_1 and Q_2, respectively. Wave normal of light wave perpendicular to stress direction. Experimental points are average values of 15 measurements on 8 different samples. Mean square deviation of experimental scatter is also indicated.

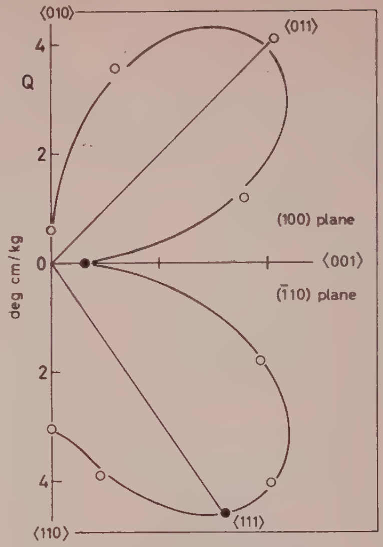

FIG. 2. Polar coordinate plot of stress optical constant Q vs direction of uniaxial stress. The curves have been calculated by means of tensor transformation rules from Q_1 and Q_2 which are represented by full dots.

The samples were cut from monocrystals, perpendicular to the growth axis, and oriented optically to within about one degree. They were rectangular bars of 2.5 cm length and a cross section $b\times d$ of 0.5×0.1 cm² or 0.5×0.2 cm², and the light traveled along the smallest dimension. At both ends they were sealed into closely fitting copper cups by means of a two-component polymeric adhesive. One cup was rigidly fixed; at the other, the tensile stress was applied through a torsion-free nylon string of 1 mm in diameter carrying a variable load P at the other end. Stresses up to 200 kg/cm² were applied.

The surfaces of the sample were chemically (by CP4 etch) or mechanically polished. The etched surfaces sometimes showed a wavy structure, but no significant differences of the stress-optical properties between both types of treatment have been found.

The results are given by Fig. 1. Since in our case $X = P/b\cdot d$ and hence $b\cdot R = Q\cdot P$ by using Eq. (1), a plot of bR vs P should give a straight line with slope Q. We obtained

$$Q_1 = 0.61 + 0.05 \text{ deg cm/kg},$$
$$Q_2 = 5.7 \pm 0.2 \text{ deg cm/kg}.$$

The value of Q_1 is in fair agreement with $Q_1 = 0.57 \pm 0.06$ deg cm/kg found by Desvignes,[3] who used a bending technique to apply the stress and deduced the Q value from the observed fringe pattern. Q_2 has also been measured with the same apparatus[4] and yielded 5.35±0.4 deg cm/kg.

The accuracy in determining the phase shift was, in our experiments, about one degree of arc. The observed scatter of the experimental points which is up to ten times this value must be ascribed to other sources, probably mainly to stress inhomogeneities in the sample. Scanning the sample with a light spot of 0.1×0.2 cm² showed slight variations of phase shift over the sample area. This seems to confirm the above-made tentative assumption.

When Q_1 and Q_2 are known, the stress optical constant for arbitrary direction of stress can be calculated. Figure 2 shows the calculated curves which have been checked by experiment for the stress directions ⟨130⟩, ⟨113⟩, ⟨331⟩, and ⟨110⟩. Observed and predicted values agree within the experimental error.

The temperature has been varied between 300° and 80°K. Observations seem to indicate a slight increase in Q of about 3 percent when the sample is cooled down, but the effect lies within the limit of experimental accuracy and may not be true.

The author is greatly indebted to Miss I. Ruether for excellent experimental assistance and to A. Hauptmann who prepared the crystals. It is a pleasure to acknowledge the helpful cooperation of F. Desvignes, Laboratoires d'Electronique et Physique Appliquées (LEP), Paris.

[1] F. Pockels, *Lehrbuch der Kristalloptik* (B. G. Teubner, Leipzig, Germany, 1906), pp. 467 ff.

[2] See H. T. Jessop, "Photoelasticity," in *Encyclopedia of Physics* (Springer-Verlag, Berlin, Germany, 1958), p. 154.

[3] C. Grandjean and F. Desvignes, Compt. rend. **250**, 1183 (1960).

[4] F. Desvignes and K. J. Schmidt-Tiedemann, LEP Report No. 181/60 (1960), unpublished.

Effect of Frequency Modulation on Subsidiary Resonance in Ferrites

J. F. Ollom and H. L. Goldstein
Bell Telephone Laboratories, Murray Hill, New Jersey

(Received June 12, 1961)

RECENT experiments by Gyorgy and Hagedorn[1] have shown that the subsidiary resonance which appears in ferrimagnets because of high-power instability can be suppressed by reversing the flux in a sample. Experiments reported by Hartwick, Peressini, and Weiss[2] indicate that the same result can be achieved by modulating the applied dc magnetic field. Stern and Mangiaracina in an earlier paper[3] describe a similar effect which occurs at the main resonance. The work reported here shows that modulation of the microwave source frequency, instead of modulation of the biasing magnetic field, will also suppress subsidiary absorption. This effect has been predicted by Suhl[4] who has worked out a detailed theory for the case of field modulation. Our measurements indicate that optimum suppression is obtained when the modulation index m (ratio of maximum frequency excursion Δf to modulating frequency f_m) is near the first root of the Bessel function $J_0(m)$. When the theory is adapted for frequency modulation it leads to a similar conclusion, although quantitative agreement between theory and experiment has not yet been established.

The measurements were taken on a single-crystal yttrium iron garnet sphere 0.04 in. in diameter and located in the center of a TE_{102} cavity with a loaded Q of 1000. The cavity was excited at its resonant frequency of 9670 Mc by a klystron oscillator, which was frequency modulated by applying a sinusoidal voltage to its reflector. The biasing magnetic field was applied parallel to the microwave magnetic field at the sample, and swept over the value of 1650 oe where subsidiary resonance occurred. The latter was observed on a scope from the resulting dip in the cavity output.

Figure 1 shows the minimum Δf required to suppress subsidiary absorption as a function of f_m, for three values of relative microwave amplitude h/h_c, where h_c is the threshold amplitude for subsidiary resonance without modulation. The curves have a minimum near $m=2.4$, the first root of $J_0(m)$. When at a given modulation frequency, Δf is increased beyond the point where subsidiary absorption is suppressed this absorption does not reappear.

The theory which was derived for the case of dc field modulation can be readily adapted for microwave source modulation. This is done by replacing $2f/v$ in Eqs. (5) and (6) of reference 4 by the modulation index m. The resulting equation is

$$A_0=\eta_k/P_kJ_0(m), \qquad (1)$$

where A_0 is the threshold value of the applied microwave magnetic field below which complete suppression of the subsidiary resonance is obtained. η_k is the relaxation frequency of the kth spinwave which is responsible for the instability and P_k is a coefficient which measures the strength of the coupling between the applied microwave field and the kth spinwave. According to Eq. (1) the subsidiary absorption should be suppressed when $J_0(m)=0$, regardless of power level. However, the results shown in Fig. 1 do not support this statement. When the power level is raised and f_m is kept constant, Δf must be increased to suppress the absorption. As Suhl has stated, Eq. (1) is based upon relatively crude approximations in the theory. It is expected that more refined approximations will result in better agreement with experiment. Applications of frequency modulation to suppress high-power instability in microwave devices are being investigated.

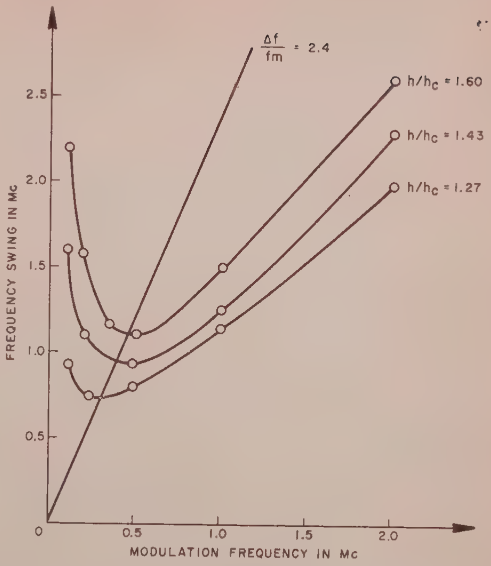

FIG. 1. Minimum frequency excursion Δf required to suppress subsidiary absorption vs modulating frequency f_m, for different relative microwave field amplitudes h/h_c.

We are indebted to E. G. Spencer for helpful advice and for providing the YIG sample, to L. G. Van Uitert, who called the results of Gyorgy and Hagedorn to our attention, and to W. H. von Aulock for stimulating discussions and his interest, which made this study possible. We also wish to thank J. P. Hart and W. A. Hove for assistance in the measurements.

[1] E. M. Gyorgy and F. B. Hagedorn, J. Appl. Phys. **31**, 1775 (1960).

[2] T. S. Hartwick, E. R. Peressini, and M. T. Weiss, Phys. Rev. Letters 6, 176 (1961).

[3] E. Stern and R. S. Mangiaracina, IRE Trans. on Microwave Theory and Techniques **MTT-7**, No. 1, 11 (1959).

[4] H. Suhl, Phys. Rev. Letters 6, 174 (1961).

Thermionic Emission from Spherical Metallic Particles*

M. S. Sodha
Physics Division, Armour Research Foundation, Chicago 16, Illinois

(Received May 18, 1961)

AN expression for thermionic emission from a charged particle has been obtained. This expression has been used to study the charging of a particle due to thermionic emission in absence of any surrounding space charge.

In this communication the author has derived an expression for the rate of thermionic emission from a charged spherical metallic particle (where the free electron theory is applicable). This expression has been used to investigate the charging of particles when no space charge is present around the particles.

The number of electrons per unit volume inside a metal at a temperature T, having velocity components between v_x and v_x+dv_x, v_y and v_y+dv_y, v_z and v_z+dv_z is given by

$$dN=\frac{2m^3}{h^3}\left[1+\exp\left\{\frac{m}{2kT}(v_x^2+v_y^2+v_z^2)-\frac{\alpha}{kT}\right\}\right]^{-1}dv_xdv_ydv_z, \qquad (1)$$

where m is the electronic mass, h is Planck's constant, k is Boltzmann's constant, and α is the Fermi energy. The velocity distribution of electrons, leaving a small element of the surface, per unit time per unit area inside the surface is given by

$$\begin{aligned} dn&=0 \quad \text{for} \quad v_x<v_0, \\ dn&=v_x dN \quad \text{for} \quad v_x>v_0, \end{aligned} \tag{2}$$

where $(\frac{1}{2})mv_0{}^2=\psi$, the energy required by an electron to overcome the barrier and x axis is along the normal.

If u_x, u_y, and u_z represent the velocity components of electron velocity, just outside the surface we have

$$u_y=v_y,\ u_z=v_z, \quad \text{and} \quad \tfrac{1}{2}mu_x{}^2=\tfrac{1}{2}mv_x{}^2-\psi. \tag{3}$$

From Eqs. (1), (2), and (3) one obtains

$$dn=\frac{2m^3}{h^3}\left[1+\exp\left\{\frac{m}{2kT}(u_x{}^2+u_y{}^2+u_z{}^2)+\frac{\varphi}{kT}\right\}\right]^{-1}u_x du_x du_y du_z, \tag{4}$$

with $u_x>0$ and $\varphi=\psi-\alpha$ the work function.

Making the usual assumption that the exponential term is much greater than unity, Eq. (4) can be simplified to

$$dn=\frac{2m^3}{h^3}\cdot u_x \exp(-\varphi/kT) \cdot\exp\left[-\frac{m}{2kT}(u_x{}^2+u_y{}^2+u_z{}^2)\right]du_x du_y du_z. \tag{4a}$$

If the charge on the spherical particle of radius r is Be, the condition[1] for the electrons to escape is $(\frac{1}{2})mu^2>(Be^2/r)$ [not $(\frac{1}{2})mu_x{}^2>(Be^2/r)$]. Hence the number of electrons n escaping per unit area per unit time can be obtained by integrating (4a) so that the above condition is always satisfied.

Putting $u_x=(2kT/m)^{\frac{1}{2}}X$, $u_y=(2kT/m)^{\frac{1}{2}}Y$, and $u_z=(2kT/m)^{\frac{1}{2}}Z$, the integral can be expressed as follows [provided we integrate over only those regions where $X^2+Y^2+Z^2>\zeta=(Be^2/rkT)$]:

$$n=\frac{2m^3}{h^3}\left(\frac{2kT}{m}\right)^2\exp\left(-\frac{\varphi}{kT}\right)\int_0^{\infty}\int_{-\infty}^{+\infty}\int_{\infty}^{+\infty} \times X\exp(-X^2-Y^2-Z^2)dXdYdZ. \tag{5}$$

Dividing the integrations into two regions where $Y^2+Z^2<\zeta$ and $Y^2+Z^2>\zeta$, the above triple integral can be expressed as

$$I=\iint\limits_{Y^2+Z^2<\zeta}\left[-\tfrac{1}{2}\exp(-X^2-Y^2-Z^2)\right]_{x^2=\zeta-Y^2-Z^2}^{x^2=\infty}dYdZ + \iint\limits_{Y^2+Z^2>\zeta}\left[-\tfrac{1}{2}\exp(-X^2-Y^2-Z^2)\right]_{x^2=0}^{x^2=\infty}dYdZ.$$

Putting $Y=R\cos\theta$ and $Z=R\sin\theta$, $Y^2+Z^2=R^2$ and

$$dYdZ=\begin{vmatrix}\frac{\partial Y}{\partial R} & \frac{\partial Z}{\partial R}\\ \frac{\partial Y}{\partial \theta} & \frac{\partial Z}{\partial \theta}\end{vmatrix}dRd\theta=RdRd\theta=\frac{d\theta}{2}dR^2,$$

$$I=\int_0^{\zeta}\int_0^{2\pi}\tfrac{1}{4}\exp(-\zeta)dR^2d\theta+\int_{\zeta}^{\infty}\int_0^{2\pi}\tfrac{1}{4}\exp(-R^2)dR^2d\theta$$

$$=\frac{\pi}{2}\left[\{R^2\exp(-\zeta)\}_0^{\zeta}+\{-\exp(-R^2)\}_{\zeta}^{\infty}\right]=\frac{\pi}{2}(1+\zeta)\exp(-\zeta).$$

Thus

$$n=A(1+Be^2/rkT)T^2\exp\left[-\left\{\frac{\varphi}{kT}+\frac{Be^2}{rkT}\right\}\right] \tag{5a}$$

or

$$(n/n_0)=(1+\zeta)\exp(-\zeta), \tag{5b}$$

where $A=4\pi mk^2/h^3$, and n_0 is the rate of thermionic emission for neutral particles. It may be restated that $\zeta=Be^2/rkT$ is the dimensionless charge parameter of the particle.

In the absence of space charge around the particles the rate of ionization of the particles is given by

$$dB/dt=4\pi r^2 n, \tag{6}$$

which on integration and using Eq. (5) gives

$$\tau=\int_1^{\zeta+1}\frac{\exp(\beta)}{\beta}d\beta=\overline{Ei}(\zeta+1)-\overline{Ei}(1), \tag{7}$$

where

$$\overline{Ei}(W)=\int_{-\infty}^{W}\frac{\exp(w)}{w}dw$$

is a tabulated function,[2]

$$\tau=(16\pi^2\epsilon re^2mkT/h^3)\cdot\exp(-\varphi/kT)\cdot t,$$

$\epsilon=2.718$ and $B=0$ at $t=0$.

TABLE I. Variation of dimensionless charge parameter ζ with time parameter τ.

τ	ζ
0.000	0.0
0.272	0.1
0.547	0.2
0.826	0.3
1.102	0.4
1.406	0.5
2.027	0.7
3.059	1.0
4.706	1.4
7.391	1.9
12.030	2.5
20.682	3.2
38.290	4.0
84.095	5.0
189.610	6.0
438.485	7.0
1035.980	8.0

Table I gives the variation of the dimensionless charge parameter ζ of the particle with the dimensionless parameter τ of time. It is hoped that the table in this form will be most useful.

---

* Work supported by Armour Research Foundation, Chicago, Illinois.

[1] L. Page, *Introduction to Theoretical Physics* (D. Van Nostrand Company, Inc., Princeton, New Jersey, 1935), p. 88.

[2] E. Jahnke and F. Emde, *Tables of Function* (Dover Publications, New York, 1945), pp. 6–9.

Presence of Carbon in Gallium Phosphide Crystals

C. J. Frosch, M. Gershenzon, and L. Derick
Bell Telephone Laboratories, Murray Hill, New Jersey

(Received June 15, 1961)

INGOTS of GaP prepared in graphite boats by lengthwis solidification at 1500°C and at a phosphorus pressure of 2 atm[1] are usually highly polycrystalline even after several slo molten-zone traverses. Hall effect data reveal the presence o 2×10^{17} to 5×10^{18} atoms cc^{-1} of an acceptor whose level lie 0.035 ev above the valence band.[2] This center is somewhat compensated by the presence of a donor.[2] It is, however, unaffecte by repeated passes of the molten zone. When bars cut from thes ingots are recrystallized by a single pass of a floating zone a 1500°C and in 20–25 atm of phosphorus, larger crystals ar usually immediately evident, the total acceptor concentratio drops to 10^{14}–10^{16} atoms cc^{-1}, and a solid film forms on the coole walls (1000°C) of the quartz envelope. The film is formed b vapor transport—not splattering—from the hot zone. Althoug much of the film is GaP, a considerable portion of it is opaqu insoluble in aqua regia, and has been identified as carbon. Whe a bar that has been subjected to a single floating zone pass remounted in a clean tube, subsequent floating zone passes longer yield this film.

On the basis of these observations it was then supposed that (carbon from the graphite boat dissolves in the GaP, (2) the carbo prefers the phosphorus substitutional sites, behaving as a acceptor (some carbon on gallium sites could be the observe compensating donor), (3) some precipitation of a second phas containing carbon prevents the growth of large GaP crystals, ar

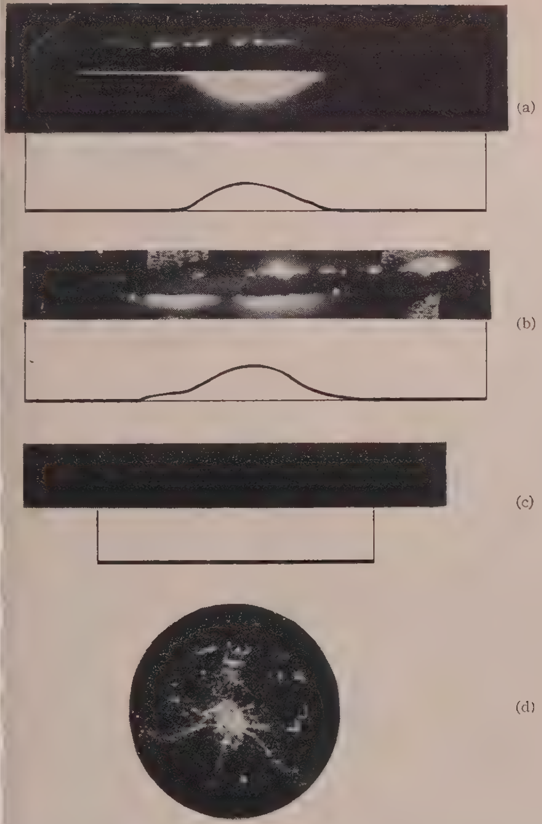

FIG. 1. Radioautographs of C^{14} in GaP and their optical densitometer tracings. (a). Longitudinal section of a 6-in. ingot and the C^{14} labeled graphite boat in which it was grown. Exposure: 20 min. Only the C^{14} remaining on the surface of the boat is evident here. (b). Section of ingot removed from boat. Exposure: 30 days. Here the C^{14} in the body of the ingot appears as well as some minute specks adhering to the surface. (c). Section of ingot after a single floating-zone pass. Exposure: 30 days. No trace of C^{14} is detected. (d). Film deposited on walls of floating-zone chamber. Exposure: 20 min.

(4) the floating zone almost completely removes the carbon, probably by the vapor phase transport of a carbon-phosphorus species.

A radioactive tracer technique was employed to verify some of these assumptions. 1 mg of C^{14} in the form of acetylene was cracked onto the central portion of a graphite boat heated by induction to 900–1000°C. The extent of the reaction was monitored by noting the hydrogen-acetylene ratio by condensing the acetylene periodically during the course of the reaction. An ingot of GaP was then prepared in this boat in the usual manner.[1] Radioautographs were made of a longitudinal section of the ingot plus the boat [Fig. 1(a)] and of the ingot alone [Fig. 1(b)]. A mean penetration depth of the soft C^{14} β rays in GaP of $\sim 2\,\mu$ was obtained by radiographically measuring the absorption as a function of the sample thickness. Using calibrated plates it was then possible to estimate a total ingot carbon content of 10^{18}–10^{19} atoms cc^{-1} if it was assumed that only carbon originating from the acetylene entered the crystal lattice. A bar cut from this ingot was then purified by a single floating zone pass. Its radioautograph shown in Fig. 1(c) indicates a reduction in carbon content to $<10^{17}$ atoms cc^{-1}. A radioautograph of the film deposited on the outer walls of the floating-zone chamber is shown in Fig. 1(d).

The large amounts of carbon detected in the C^{14} ingot suggested the applicability of direct chemical analysis for carbon without the use of a radioactive tracer. Samples from ingots prepared in boats and from bars recrystallized by the floating-zone method (1-g charges) and samples of the film deposited from the vapor were oxidized in oxygen at $\sim$1500°C and the carbon dioxide formed was collected in a $Ba(OH)_2$ solution, which was analyzed conductometrically to determine the amount of carbon dioxide absorbed.[3] The results indicate that the ingots grown in boats contain 1×10^{18} to 2×10^{19} carbon atoms per cc while the floating zone rods contain $\lesssim 4\times10^{17}$ atoms cc^{-1}. The carbon removed during floating-zone processing is quantitatively recovered in the film.

It was noted that the total carbon concentration in the ingots was more than the density of acceptors revealed by the Hall measurements, even assuming that as much as half of the carbon was on donor sites. It was previously concluded, however, from microautoradiograms of ingots containing C^{14}, that some of the total carbon is present as part of a second phase.[4] Moreover, this second phase is absent after the passage of a floating zone. It is therefore deduced that the removal of the carbon, as by the floating zone, is a necessary condition for the production of large crystals of GaP.

[1] C. J. Frosch and L. Derick, J. Electrochem. Soc. **108**, 251 (1961).
[2] M. Gershenzon and R. M. Mikulyak (to be published).
[3] We are indebted to F. W. Ryan for these determinations.
[4] M. Gershenzon, C. J. Frosch, and R. M. Mikulyak, Electrochemical Society, Spring Meeting, Indianapolis, Indiana, Abstract 53 (1961).

Erratum: A Theory for the Cathode Mechanism in Metal Vapor Arcs

[J. Appl. Phys. **32**, 917 (1961)]

T. H. LEE AND ALLAN GREENWOOD
General Electric Company, Philadelphia, Pennsylvania

EQUATIONS (3d) and (3e) in the paper, "A theory for the cathode mechanism in metal vapor arcs" by Lee and Greenwood [J. Appl. Phys. **32**, 917 (1961)] are incorrect. The correct equations are·

$$u=\frac{q}{\rho c(\pi k)^{\frac{1}{2}}}\left[\left(\frac{\pi}{k}\right)^{\frac{1}{2}} a\,\mathrm{erfc}\frac{a}{2(kt)^{\frac{1}{2}}}+2(t)^{\frac{1}{2}}(1-\epsilon^{2/4kt})\right] \tag{3d}$$

$$u_\infty=qa/\rho ck=qa/K. \tag{3e}$$

Books Reviewed

Prompt, noncritical reviews appear in this column. Critical reviews of many of the books described here will appear in Physics Today, The Review of Scientific Instruments, *or* American Journal of Physics.

Basic Concepts of Physics. ARTHUR BEISER. Pp. 341. Addison-Wesley Publishing Company, Inc., Reading, Massachusetts, 1961. Price $7.75.

This new text offers a straightforward introduction to physics. It is designed especially for use in one-semester college courses, and is written in a clear and interesting manner. No prior knowledge of physics or chemistry is assumed, and no more than the simplest mathematics is employed. A brief review of the mathematics used in the text is included in an appendix.

Cybernetics or Control and Communication in the Animal and the Machine. NORBERT WIENER. Pp. 212. The M.I.T. Press, Cambridge, Massachusetts and John Wiley & Sons, Inc., New York and London, 1961. Price $6.50.

This new, revised second edition has been completely re-edited and contains two new chapters and a new introduction by Dr. Wiener. Dr. Gordon Raisbeck of the Bell Telephone Laboratories is technical editor of this new edition.

Microwave Ferrites. P. J. B. Clarricoats. Pp. 260. John Wiley & Sons, Inc., New York, 1961. Price $8.00.

This book is intended primarily for the microwave engineer engaged in research and development work on waveguide devices employing ferrites. It contains a comprehensive account of the theory of electromagnetic wave propagation through ferrite-loaded waveguides together with a critical survey of the operation, performance, and design of ferrite devices. There are chapters describing the general properties and intrinsic microwave properties of ferrites, and the subject of magnetic losses is dealt with in some detail. These latter topics will be of interest to physicists engaged in fundamental studies involving ferromagnetic materials.

Books Received

Introduction to Theoretical Physical Chemistry. Sidney Golden. Pp. 307. Addison-Wesley Publishing Company, Inc., Reading, Massachusetts, 1961. Price $9.75.

Advances in Electronics and Electron Physics. Vol. 14. L. Marton, Editor. Pp. 341. Academic Press Inc., New York and London, 1961. Price 88s.

High Speed Testing, Vol. 2. Second Annual Symposium held at Boston, Massachusetts, January 27, 1961. A. G. H. Dietz and Frederick R. Eirich, Editors. Interscience Publishers, Inc., New York, 1961. Price $4.50.

Satellite Environment Handbook. Francis S. Johnson, Editor. Pp. 155. Stanford University Press, Stanford, California, 1961. Price $5.50.

Plasmas and Controlled Fusion. David J. Rose and Melville Clark, Jr. Pp. 493. The M.I.T. Press, Cambridge Massachusetts and John Wiley & Sons, Inc., New York, and London, 1961.

Quantum Mechanics. John I. Powell and Bernd Crasemann. Pp. 495. Addison-Wesley Publishing Company, Inc., Reading, Massachusetts, 1961. Price $9.75.

The Plasma State. E. J. Hellund. Pp. 197. Reinhold Publishing Corporation, New York, 1961. Price $6.50.

Fuel Element Fabrication, Vol. 2. Edited by the International Atomic Energy Agency. Pp. 384. Academic Press Inc., New York and London, 1961. Price $10.

Proceedings of an International Conference on Instrumentation for High-Energy Physics. C. E. Mauk, A. H. Rosenfeld, and R. K. Wakerling, Editors. Pp. 321. Interscience Publishers, Inc., New York and London, 1961. Price $10.

Announcements

1959 Digest of Literature on Dielectrics

Volume 23 of this series is now available from Printing and Publishing Office, National Academy of Sciences, National Research Council, 2101 Constitution Avenue, Washington 25, D. C. at $8 per copy.

NEW NON-DESTRUCTIVE CHEMICAL ANALYSIS

PARTS PER MILLION TRACINGS— WITH FANTASTIC ACCURACY AND SPEED

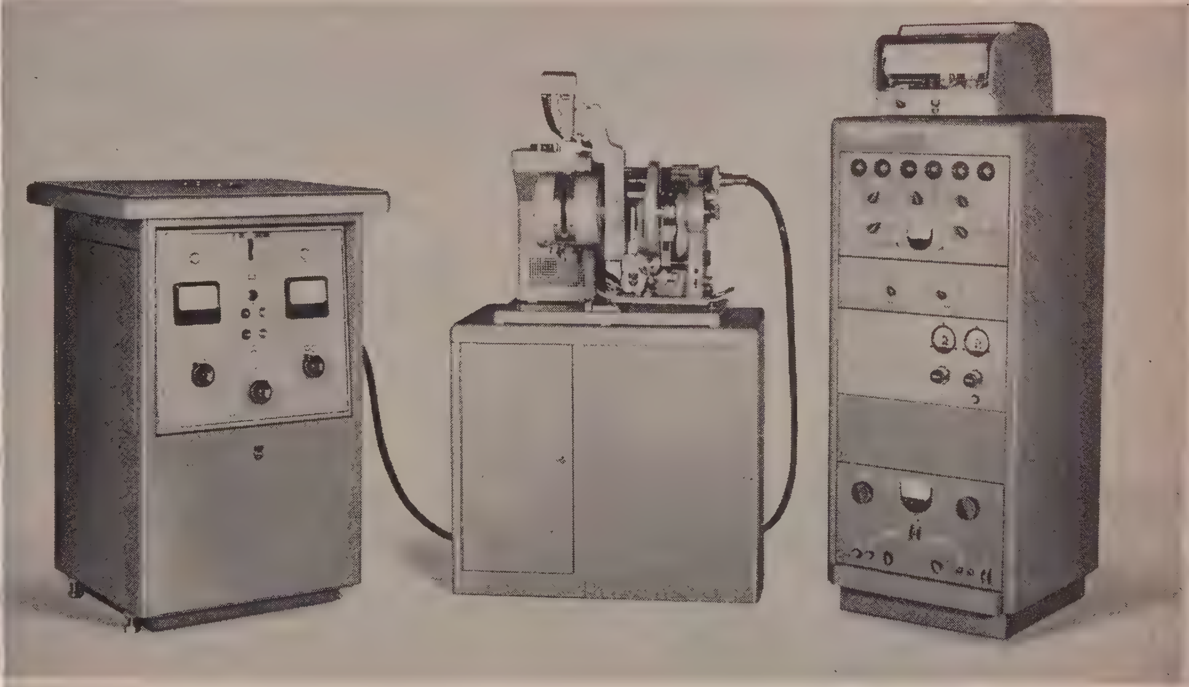

ecent developments have widened the scope of an canny instrumental chemical sleuth. Now, besides pplying quantitative data with exceptional accuracy, is Norelco Spectrograph conserves the valuable time the chemist by automatically providing analytical ta on samples in a fraction of the time otherwise quired. Data are obtained from an instrument which nctions unattended—once the prepared sample has en positioned.

irting through a prescribed arc, detectors and sociated electronic circuitry integrate the whole of radiated sample's characteristic spectra, supplying ear and/or logarithmic data on a chart in terms of both identity *(qualitative)* and intensity *(quantitative)*.

Abundant with interesting features, a new Norelco high capacity generator and X-ray tube combination plus new integrating electronics, unquestionably qualifies the Norelco Spectrograph as having the highest resolution and greatest intensity with better signal-to-noise ratios when compared to any other equipment in the market place.

Why Norelco is the best and how it can serve to improve your products and profits is understandable. Want us to tell you? Call or write today. Go ahead and ask us why. We are enthusiastic about all such opportunities. Well? Wouldn't you be?

HILIPS
ECTRONIC
STRUMENTS
Norelco

For more information and specifications on this remarkable Norelco instrument, write today on your letterhead to:

PHILIPS ELECTRONIC INSTRUMENTS
A Division of Philips Electronics and Pharmaceutical Industries Corp.
750 South Fulton Avenue, Mount Vernon, N. Y.
In Canada: Research & Control Instruments • Philips Electronics Industries Ltd. • 116 Vanderhoof Avenue • Leaside, Toronto 17, Ont.

MH COLLEGE DIVISION

PEACETIME USES OF OUTER SPACE

Edited by SIMON RAMO, Thompson Ramo-Wooldridge, Inc. 295 pages, $6.95.

This remarkable volume brings together outstanding scientists, educators, politicians, and businessmen for an examination of the coming space age. Emphasizing the peacetime, non-military aspects of space technology, the book seeks to heighten public responsiveness to the full impact of science and technology in shaping our future.

ELEMENTARY QUANTUM FIELD THEORY

By ERNEST M. HENLEY, University of Washington; and WALTER THIRRING, University of Vienna. *McGraw-Hill International Series in Pure and Applied Physics.* Available in March, 1962.

A second year graduate book presenting an extension and expansion of the material covered in the last third of Schiff's QUANTUM MECHANICS. The important features of quantum field theory are examined on a level that students can follow *after a standard quantum mechanics course.*

SYNTHESIS OF OPTIMUM CONTROL SYSTEMS

By SHELDON S. L. CHANG, New York University. 381 pages, $11.75.

A second-year-graduate-level text bridging the gap between a standard text on the subject and the current literature on optimum control.

PRINCIPLES AND APPLICATIONS OF ELECTROMAGNETIC FIELDS

By ROBERT PLONSEY and ROBERT E. COLLIN, Case Institute of Technology. *McGraw-Hill Series in Electronics and Electrical Engineering.* Available in October, 1961.

A thorough and complete treatment of basic electromagnetic fundamentals, with a detailed and broad coverage of applications.

FOUNDATIONS OF FUTURE ELECTRONICS

Edited by DAVID LANGMUIR, Ramo-Wooldridge Company; and W. D. HERSHBERGER, University of California, Los Angeles. *The University of California Engineering Extension Series.* Available in November, 1961.

This work is a collection of articles written by a number of distinguished authorities, each well qualified to present theory, techniques, and potential applications in his particular field.

THERMAL REGIMES OF COMBUSTION

By L. A. VULIS; translated from the Russian by GLENN WILLIAMS, Massachusetts Institute of Technology, and others for the project SQUID, Princeton, N. J., 299 pages, $7.50.

Of primary interest to chemical and mechanical engineers and to chemists and physicists interested in kinetics, this timely translation offers a detailed mathematical discussion of the consequences of applying simple thermal combustion theory and simplified (first order) kinetics to over-all combustion problems.

DESIGN MANUAL FOR TRANSISTOR CIRCUITS

By JOHN M. CARROLL, *Electronics,* McGraw-Hill Pub. Co. 376 pages, $9.50.

A selected group of articles from *Electronics* magazine showing an engineer how to design circuits using transistors and other semiconductor devices.

McGraw-Hill Book Company, Inc.
330 W. 42nd St.
New York 36,
New York

MH SEND FOR COPIES ON APPROVAL

The first number of the new review

PHYSICA STATUS SOLIDI

has just come out.

Editors: K. W. Böer, Berlin; W. Franz, Hamburg; P. Görlich, Jena; E. Grillot, Paris; R. Kaischew, Sofia; P. T. Landsberg, Cardiff; A. Piekara, Posnania; N. Riehl, Munich; A. Seeger, Stuttgart; O. Stasiw, Berlin; M. Steenbeck, Jena; F. Stöckmann, Karlsruhe; G. Szigeti, Budapest; J. Tauc, Prague.

Editorial staff: K. W. Böer, Berlin-Spandau Schnepfenreuther Weg 27 a

This new monthly review will publish as quickly as possible, original researches from the entire field of the physics of solid bodies.

Each number will carry concise reports, original essays, and short original information. It will include both previous announcements of titles and extracts from original works soon to be published in this Monthly and also in the Soviet review "Fizika Tverdogo Tela" (this one in the English language).

Each number will be approx. 80 pages, and illustrated. Price: $1.43 a single copy.

Orders through any bookseller.

For particulars, prospectus and specimen copy apply direct to:

THEORIA CUM PRAXI

AKADEMIE—VERLAG GMBH
BERLIN
Berlin W 8, Leipziger Strasse 3–4.
German Democratic Republic

SCIENTISTS
ENGINEERS
CALIFORNIA

offers you and your family

- A world center of the electronics-missile-space industries for CAREER ADVANCEMENT
- The High Sierra and the Pacific Ocean for RECREATION
- And for your children some of the nation's FINEST PUBLIC SCHOOLS
- World Famous Universities for ADVANCED STUDY
- MAJOR CULTURAL CENTERS

while living in such places as

Exciting San Francisco
Fabulous Southern California
Cultural Palo Alto

Companies pay interview, relocation and agency expenses

Submit resume in confidence to:

PROFESSIONAL and TECHNICAL RECRUITING ASSOCIATES
(a Division of the Permanent Employment Agency)
Suite A
825 San Antonio Road
Palo Alto, Calif.

**Challenging Career
Opportunities in IBM**

PHYSICAL OPTICS

IBM's Data Systems Division is engaged in challenging programs in its Technical Development Laboratory that are concerned with the interaction between optical systems and computer technology. Inquiries are invited from scientists with experience in photo-materials, optical systems engineering, and optical physics.

Scientists participating in these studies will receive extensive technical and scientific support in a professionally stimulating atmosphere. The results of their efforts are expected to have a significant impact on data processing techniques and communications.

Requirements—Ph.D. in Physics or Optics and/or appropriate creative experience in relevant areas.

Assignments are in Poughkeepsie, New York, a pleasant, non-metropolitan environment just 80 miles from New York City. All applicants will be considered without regard to race, creed, color, or national origin. Excellent schools and housing. Extensive employee benefits program.

Please write, outlining your experience and interests, to . . .

**Mr. H. J. Cooke, Dept. 579K
IBM Development Laboratory
Box 390
Poughkeepsie, New York**

IBM

International Business Machines Corporation

CENCO® HYVAC

GAS BALLAST PUMPS

For vacuum applications plant and laboratory. Eliminates use of oil separators, centrifuges, refrigerated traps. Wide range of capacities.

No. 91506-1 rated displacement, 70.0 liters per min. . . .$284.25

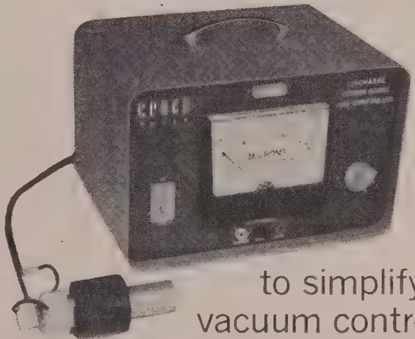

to simplify
vacuum control . . .

NEW CENCO DISCHARGE GAGE AND CONTROLLER

A gage and automatic controller that continuously reads from 0.001 to 20 microns total pressure of all condensable vapors and gases in your system. Starts instantly at any pressure. Controller provides automatic on-off switching at pre-set pressures—transistorized amplifier opens or closes contacts of relay to control up to 1 amp.

No. 94183 $249.50

cenco
Quality since 1889

CENTRAL SCIENTIFIC
A Division of Cenco Instruments Corporation
1700 Irving Park Road • Chicago 13, Illinois
Mountainside, N. J. Montreal Santa Clara
Somerville, Mass. Toronto Los Angeles
Birmingham, Ala. Ottawa Vancouver Houston
Cenco S.A., Breda, The Netherlands Tulsa

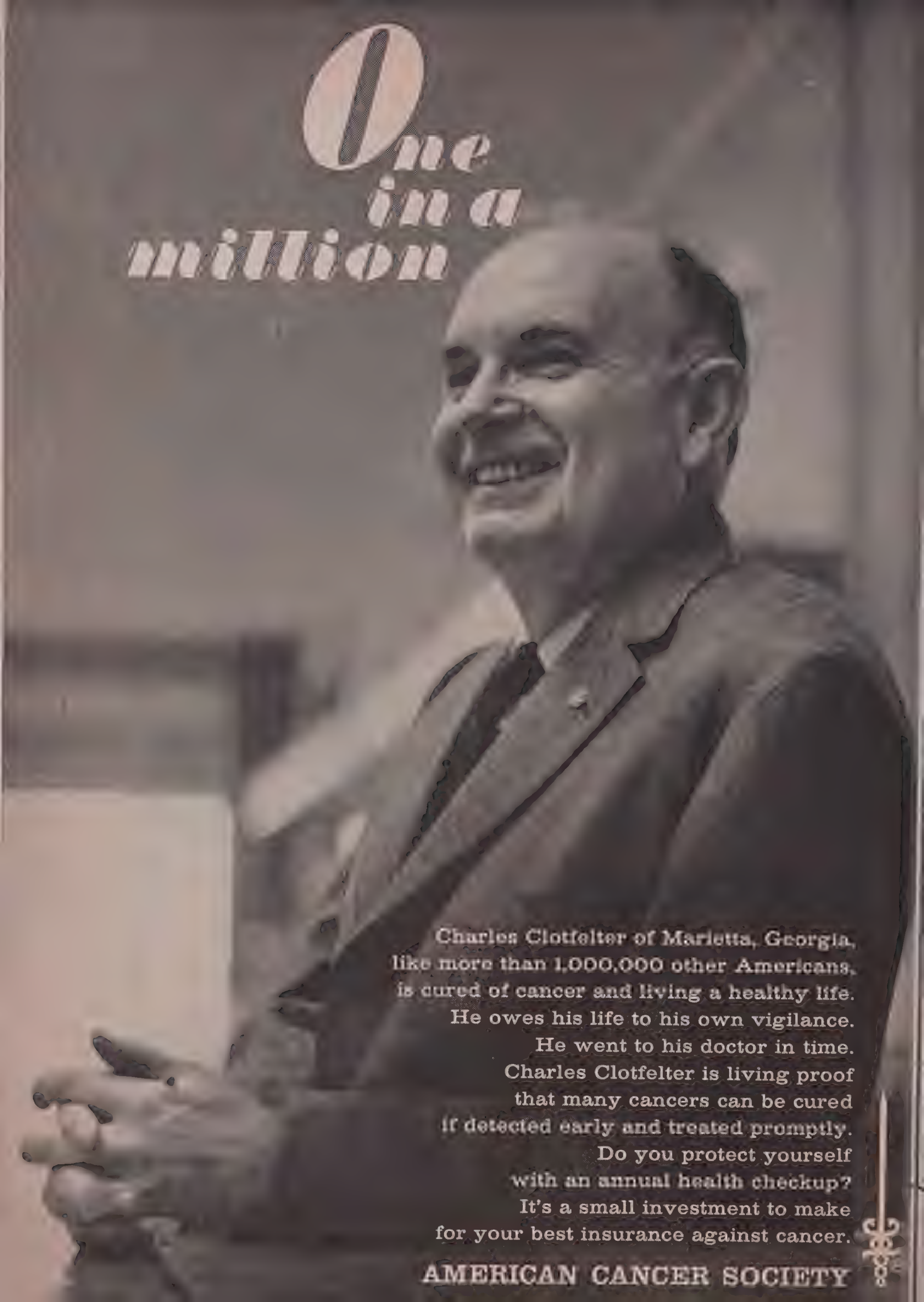

Charles Clotfelter of Marietta, Georgia,
like more than 1,000,000 other Americans,
is cured of cancer and living a healthy life.
He owes his life to his own vigilance.
He went to his doctor in time.
Charles Clotfelter is living proof
that many cancers can be cured
if detected early and treated promptly.
Do you protect yourself
with an annual health checkup?
It's a small investment to make
for your best insurance against cancer.

AMERICAN CANCER SOCIETY

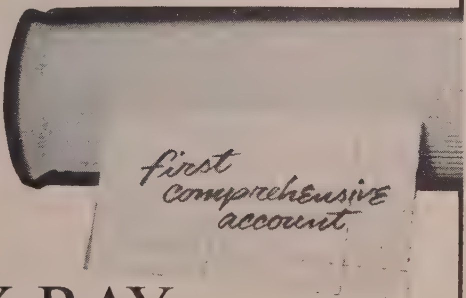

X-RAY MICROSCOPY

V. E. Coslett and W. C. Nixon
Cavendish Laboratory, Cambridge University

X-ray microscopy is now widely used for the examination of plant and animal tissues, of living organisms, of minerals, metals, paper, fibres and fabrics. It is of especial value since it allows microanalysis of specific chemical elements to be carried out in a non-destructive manner.

The authors, leaders in the development of this technique, here present the first comprehensive account of its use. They discuss the three systems of X-ray microscopy, the fundamental systems involved, and the pertinent details of application in biology, medicine, metallurgy, and technology. Numerous line drawings, including detailed diagrams of microscopic apparatus, illustrate the text. An appendix of absorption and emission data, a valuable bibliography, and thirty-two plates, among them a number of impressive micrographs, help to make this a most useful and important reference book. *$15.00*

Cambridge University Press,
32 East 57th Street, New York, N.Y.

ADVANCED SOLID STATE RESEARCH & DEVELOPMENT

Senior scientists and engineers are needed to fill new positions in our rapidly expanding research and development laboratories near San Francisco. Our broadening interests have created challenging positions for individuals with significant backgrounds in the following fields:

SURFACE PHYSICS AND CHEMISTRY
ELECTROCHEMISTRY
ELECTRON MICROSCOPY
MAGNETIC THIN FILMS
EVAPORATED CIRCUITRY
SEMICONDUCTOR MATERIALS
ELECTRO-OPTICS
ADVANCED CIRCUIT DEVELOPMENT
MICROWAVE PHYSICS

A Ph.D. Degree or commensurate experience is especially desirable.

Applicants are invited to send detailed resumes, including salary history and requirements, to Mr. Donald Palmer. Palo Alto interviews for qualified applicants will be arranged from anywhere in the United States. All inquiries strictly confidential and acknowledged promptly. All qualified applicants will be considered regardless of race, creed, color or national origin.

FAIRCHILD
SEMICONDUCTOR
844 CHARLESTON ROAD • PALO ALTO, CALIFORNIA

An equal opportunity employer.

laser physicists

Hughes' broad experimental program in the development of new LASER techniques, components and systems is being enlarged. With the unusually varied and significant applications of LASERS, the opportunities created through this expansion will be professionally rewarding and exciting and of long range promise. Three of the several openings are indicated below. We invite your inquiry.

1. **PHYSICISTS** A background in experimental techniques (optical spectroscopy, flash photometry, etc.) involving phenomenon at optical frequencies, an advanced degree or compensating experience and demonstrated ability will be preferred. We will also consider Physical Chemists with strong backgrounds in optical physical techniques.
2. **ELECTRONIC ENGINEERS or PHYSICISTS** Pulse circuit techniques experience is required.
3. **SYSTEMS ENGINEER** About five years of experience, preferably in radar systems, and a physical, as opposed to a mathematical, orientation are required.

Airmail your resume to:
Mr. Robert A. Martin, Supervisor of Employment, Hughes Aircraft Company, Culver City 23, California.

CREATING A NEW WORLD WITH ELECTRONICS

HUGHES

HUGHES AIRCRAFT COMPANY
AEROSPACE DIVISIONS

WE PROMISE YOU A REPLY WITHIN ONE WEEK

PERIODICAL PUBLICATIONS
OF THE
INSTITUTE OF PHYSICS AND
THE PHYSICAL SOCIETY

●

Journal of Scientific Instruments

A monthly publication dealing with the principles, construction and use of scientific instruments.
U.S.A. $17.00 £6 per annum

British Journal of Applied Physics

A monthly publication dealing with applications of physics, especially in industry.
U.S.A. $17.00 £6 per annum

Proceedings of the Physical Society

A monthly publication containing papers describing original work in physics.
U.S.A. $36.00 £12 12*s*. per annum

Reports on Progress in Physics

An annual publication containing comprehensive reviews—issued in April.
U.S.A. $12.30 £4 6*s*. per annum

all above prices include
postage and packing.

Available from:

The Institute of Physics
and The Physical Society

47 Belgrave Square, London S.W.1

Gaertner Precision Optical Bench Assembly

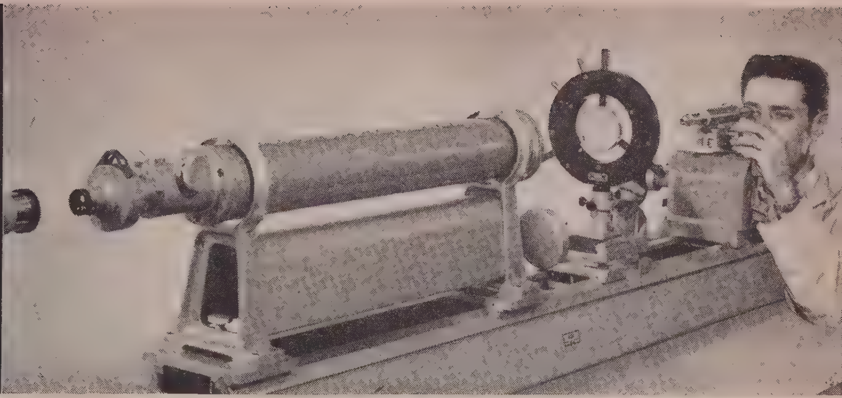

Useful in checking optics and for experimental instrumentation setups

The Precision Optical Bench is a versatile measuring instrument consisting of a lathe-bed-type base, light source, collimator with interchangeable filters and targets, nodal slide and microscope with three-dimensional adjustment. Focal lengths, resolving power and the various aberrations of optical parts and systems can be measured.

The several components can be used independently for special test setups, mock-ups and experimental instrumentation—providing linear and angular motions and measurements, alignment and stable support.

Double and single rod benches and a large selection of carriages, holders and supports provide a complete selection from which to choose.

Gaertner offers a wide range of optical and measuring instruments, including special modifications, design and manufacture of special instruments and optical systems, and manufacture of subassemblies and instruments from customer sketches and drawings.

Send for bulletin 156-59

Designed and manufactured in the U.S.A. by

Gaertner
SCIENTIFIC CORPORATION
1246 Wrightwood Ave., Chicago 14, Illinois • BU 1-5335

- **STUDENT SECTION NEWSLETTER**
- **SPEAKERS For STUDENT SECTIONS**
- **MOVIES and FILM STRIPS For STUDENT SECTIONS**
- **GRADUATE SCHOOL INFORMATION**
- **PLACEMENT INFORMATION**
- **PHYSICS TODAY**

The above is some of the information sent systematically to all American Institute of Physics Student Sections. There are now 5,000 student members in over 170 sections.

A booklet describing in detail the procedure for establishing Student Sections and the benefits which student organizations derive from membership will be sent upon request. Address all inquiries to:

Mrs. Ethel E. Snider, National Secretary
Student Sections
American Institute of Physics
335 East 45th Street
New York 17, N. Y.

PHYSICIST

Research in Field of

GASEOUS ELECTRONICS

or

PLASMA PHYSICS

to conduct basic experimental investigations of electronic and ionic collision phenomena. PhD. or equivalent. Experience desirable but not essential.

For further information contact Dr. L. M. Chanin, Physical Electronics Section, Minneapolis-Honeywell Research Center, 500 Washington Avenue South, Hopkins, Minnesota.

We are an equal opportunity employer.

Honeywell
H HONEYWELL *First in Control*

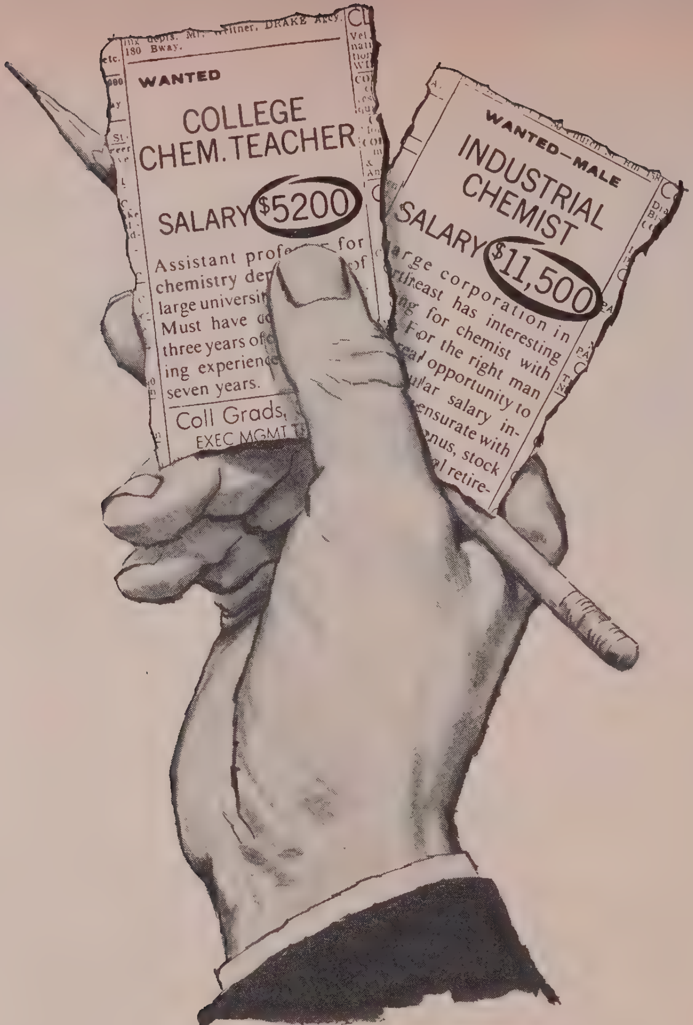
WANTED
COLLEGE CHEM. TEACHER
SALARY $5200
Assistant profe... for chemistry dep... of large universi... Must have ... three years of... ing experience seven years.
Coll Grads,
EXEC MGMT
WANTED—MALE
INDUSTRIAL CHEMIST
SALARY $11,500
...arge corporation in ...rtheast has interesting ...ng for chemist with ... For the right man ...eal opportunity to ...ular salary in... ...ensurate with ...onus, stock ...al retire-

WHICH JOB WOULD YOU TAKE?

If you're like most of us, you'd take the job with the more tempting salary and the brighter future.

Many college teachers are faced with this kind of decision year after year. In fact, many of them are virtually bombarded with tempting offers from business and industry. And each year many of them, dedicated but discouraged, leave the campus for jobs that pay fair, competitive salaries.

Can you blame them?

These men are not opportunists. Most of them would do anything in their power to continue to teach. But with families to feed and clothe and educate, they just can't make a go of it. They are virtually *forced* into better paying fields.

In the face of this growing teacher shortage, college applications are expected to *double* within ten years.

At the rate we are going, we will soon have a very real crisis on our hands.

We *must* reverse this disastrous trend. You can help. Support the college of your choice today. Help it to expand its facilities and to pay teachers the salaries they deserve. Our whole future as a nation may depend on it.

It's important for you to know more about what the impending college crisis means to you. Write for a free booklet to: HIGHER EDUCATION, Box 36, Times Square Station, New York 36, N.Y.

ADVERTISING COUNCIL PUBLIC SERVICE

Sponsored as a public service,
in co-operation with the Council for Financial Aid to Education

HIGHER EDUCATION
KEEP IT BRIGHT

Hamilton-Zeiss Electron Beam Group offers an unusual opportunity for

PHYSICISTS
ELECTRON BEAM
APPLICATIONS

Responsible for the analytic and experimental studies related to development of unique Electron Beam processes for fabrication of electronic devices. Investigations will include materials such as semiconductors, intermetallics and ferrites; studies materials effects such as junction phenomena, photo conductivity, and ferromagnetism.

Key responsibility: imaginative application of Electron Beam technology to construction of electronic devices. Advanced degree in Physics or EE preferred, 7-10 years R & D experience. Salary commensurate with experience.

Please reply to Mr. A. J. Fehlber,
Supervisor, Professional and Scientific Recruiting

HAMILTON STANDARD DIVISION
UNITED AIRCRAFT CORP.
Bradley Field Rd., Windsor Locks, Conn.
An equal opportunity employer

RADIATION AND WAVES IN PLASMAS

The Fifth Lockheed Symposium on Magnetohydrodynamics

Edited by Morton Mitchner

Seven papers were presented during the fifth Lockheed-sponsored symposium on recent experimental and theoretical work in magnetohydrodynamics. Contributors are Albert Simon, Ira Bernstein, Gordon Kino, John Wilcox, David Beard, James Drummond, Oscar Buneman, William Drummond. $4.25

Order from your bookstore, please

STANFORD UNIVERSITY PRESS

PHYSICIST

Metrologist

Challenging assignment in the research and development of nuclear weapons for a physicist with an interest in metrology and optics, who desires to make significant contribution to the science of gauging.

Requires degree plus one year applicable experience and U.S. citizenship. Will consider recent M.S. degree in lieu of experience.

This position is in our Livermore Laboratory, located in the sunny, smog-free Livermore Valley . . . country living just minutes from San Francisco.

Sandia Corporation offers liberal employee benefits including vacation, retirement and insurance plans, an educational assistance program, and paid relocation allowance. An equal opportunity employer.

Write to:

Mr. V. G. Pappas
Professional Employment Section 510.
SANDIA CORPORATION
P. O. Box 969
Livermore, California

SANDIA
CORPORATION
LIVERMORE. CALIF.

INDEX TO ADVERTISERS

Name — *Page*

AEROSPACE CORPORATION xix

AKADEMIE–VERLAG xxii

ALLOYD ELECTRONICS CORP. .. v

ARNOLD ENGINEERING CO. vii

BELL TELEPHONE LABORATORIES iii

CAMBRIDGE UNIVERSITY PRESS xxv

CENTRAL SCIENTIFIC CO. xxiii

Manufacturers of Cenco physical apparatus and instruments to meet all requirements of University, College and High School Physics Laboratories. Specializing in high vacuum pumps and development of instruments and apparatus for various sciences.

THE EPPLEY LABORATORY, INC. xxxii

FAIRCHILD SEMICONDUCTOR CORP. xxv

GAERTNER SCIENTIFIC CORP. .. xxvii

Spectroscopes, spectrometers, spectrographs, spectrophotometers, heliostats, measuring microscopes, comparators, cathetometers, reading telescopes, interferometers, chronographs, dividing machines, etc.

GENERAL RADIO CO. .... Cover 3

Manufacturers of electronic measuring instruments: vacuum-tube voltmeters, amplifiers, and oscillators; wave analyzers, noise meters and analyzers, stroboscopes, laboratory standards of capacitance; inductance and frequency; impedance bridges, decade resistors and condensers, air condenser and variable inductors; rheostats, variacs, transformers; other laboratory accessories.

Name — *Page*

GRANVILLE-PHILLIPS COMPANY xxxii

HAMILTON STANDARD, & DIV. OF UNITED AIRCRAFT CORP. . xxix

HUGHES AIRCRAFT CO., AEROSPACE DIVISIONS xxvi

IBM DEVELOPMENT LAB. xxiii

KEITHLEY INSTRUMENTS, INC. xiii

Vacuum tube electrometers, microammeters, kilovoltmeters, static detectors, meg-meg-ohm-meters, high gain dc amplifiers, dc vacuum tube voltmeters, high input impedance ac isolation amplifiers.

LOCKHEED MISSILES & SPACE CO. vi

LOS ALAMOS SCIENTIFIC LAB. . ix

McGRAW–HILL BOOK CO., INC. . xxii

MINN–HONEYWELL xxvii

NRC EQUIPMENT CORP. xv

Manufacturers of standard and special high vacuum components, equipment, and systems / including mechanical booster, and diffusion pumps; gauges; valves; seals; connectors; melting and heat-treating furnaces; coaters; impregnators; gas in metal analyzers; driers and freeze driers; altitude chambers and leak detectors.

NORTHEAST SCIENTIFIC CORP. . xiv

INDEX—*Continued*

Name	*Page*
PERMANENT EMPLOYMENT AGENCY	xxii
PHILIPS ELECTRONIC INSTRUMENTS	x, xi, xxi
RAMO-WOOLDRIDGE LABS.	Cover 4

Research, development, and manufacture in the field of electronic systems for commercial and military applications, and in the field of guided missiles.

Name	*Page*
S. A. M. E. S.	viii
SANDIA CORPORATION	xxix
SPERRY RAND RESEARCH CENTER	iv
STANFORD UNIVERSITY PRESS	xxix
SYLVANIA ELECTRONICS SYSTEMS	xvii
AMHERST LABORATORIES	
TEKTRONIX, INC.	Cover 2.

Manufacturers of Cathode-Ray Oscilloscopes, Auxiliary amplifiers, square-wave generators, vacuum-tube characteristic-curve tracers, L.C. Meters, constant-amplitude generators, operational accessories.

Name	*Page*
WELCH SCIENTIFIC CO., W. M.	xx

Manufacturers of high-vacuum pumps, both mechanical and diffusion; vacuum gauges; electrical measuring instruments; physics equipment; and other items for the physical and chemical laboratories.

POSITION OPEN

PHYSICS DEPARTMENT
OKLAHOMA STATE UNIVERSITY

Has openings for persons interested in combining teaching and academic research. Especially urgent is the need for staff to guide and supervise the research of both M.S. and Ph.D. candidates. Appointments effective immediately or as convenient. Rank Associate Professor or Professor. Salary dependent upon experience but competitive.

If interested, write to:
H. E. Harrington, Head
Stillwater, Oklahoma

TUBULAR SLIDE CONTACT RHEOSTATS
RESISTORS
Toroidal Winding Machines
REX RHEOSTAT CO.
149-a Babylon Tpke. Roosevelt, L. I., N. Y.

For ULTRA-HIGH VACUUM or ULTRA-CLEAN SYSTEMS

All-metal bakeable valves • Elbows, tees, crosses, nipples • Variable leaks
Flanged metal to glass seals • Bakeable capacitance manometers • Flanged bellows assemblies

AVAILABLE FROM STOCK

At right are some of the standard Granville-Phillips components available from stock. None contain organic materials. All are bakeable to 450°C and useful at 10^{-10} mm Hg or lower. Right-angle valves presently available in ½", 1", 2", 4", and 6" sizes, straight-through valves in ½", 1", 2½", and 4" sizes. Complete line of demountable plumbing. Custom designs on request.

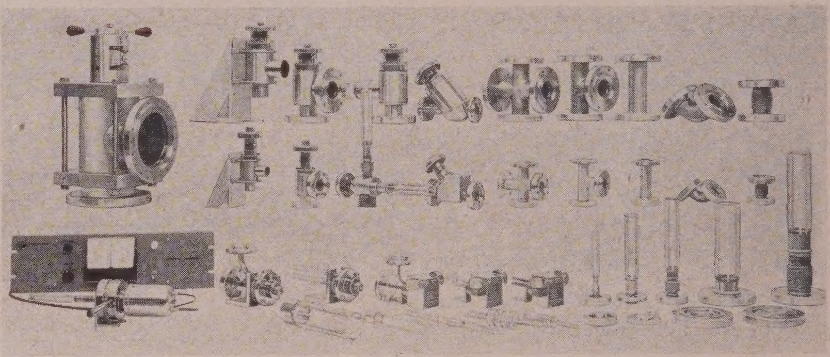

WRITE OR TELEPHONE FOR COMPLETE CATALOG

Granville-Phillips Company

P. O. Box J-198 Pullman, Washington • telephone LOgan 4-1130

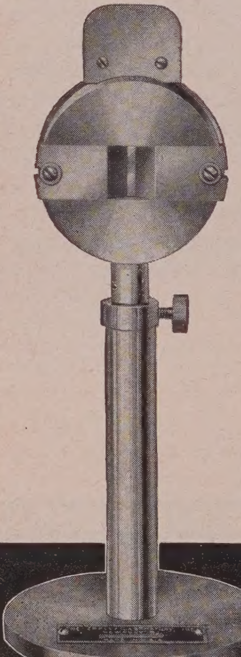

EPLAB Thermopiles

For many years the thermopile has been the accepted instrument for measuring Radiant Heat from Radiant Heaters at the American Gas Association Testing Laboratory in Cleveland, Ohio. Since 1930, when Vandaveer first described his work in this field,* an Eppley thermopile has been used for this purpose in hundreds of tests and the results have been consistent and accurate to within 1 per cent.

This is but one of the many applications in the field of radiant energy measurements for which Eppley Thermopiles are ideally suited. They may be obtained with windows of different materials, and various types of black are available for receiver coatings.

All Eppley Thermopiles are supplied with a certificate of calibration, this calibration being made against a Standard Lamp from the National Bureau of Standards.

If you have a problem involving the measurement of radiant energy we invite you to write us, describing your problem in as much detail as possible. We will be glad to make recommendations and there will be no obligation.

**Vandaveer, Industrial & Engineering Chemistry, Vol. 22, page 596, June 1930.*

BULLETIN NO. 3 ON REQUEST
ADDRESS: 6 SHEFFIELD AVE., NEWPORT, R. I.

THE EPPLEY LABORATORY, INC.

SCIENTIFIC INSTRUMENTS
NEWPORT, RHODE ISLAND, U. S. A.

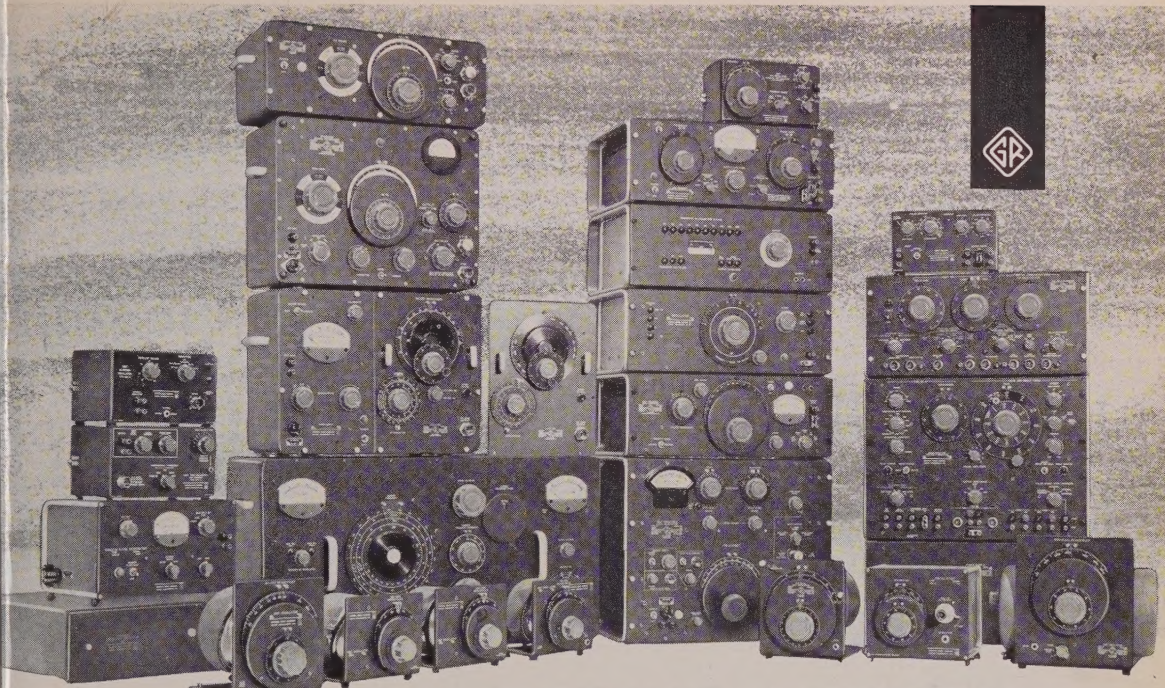

GENERATORS

LOW FREQUENCY, AUDIO, RF, SWEEP

0.01-1000c 3-phase, 4-phase, and variable-phase outputs for servo and feed-back circuit measurements. 1305-A, $940.

20c-500 kc three generators in one; high- and low-impedance sine-wave outputs, and square-wave output. 1210-C, $180*.

20-15000c in 27 fixed-frequency steps; additional coverage from 2-15c with optional extension unit. Very low harmonic distortion, less than 0.1%. 1301-A, $595.

10c-100 kc extremely stable RC oscillator, output voltage constant ±1 db. 1302-A, $500.

20c-40 kc essentially constant output voltage (±0.25 db for 20c-20 kc), very low distortion. Ideal for frequency-response testing of audio equipment. 1304-A, $680.

20c-12 Mc, and 30 Mc to 42 Mc, sine waves; 20c to 2 Mc, square waves. Can be set to any center frequency from 20 kc to 12 Mc or 36 to 42 Mc and driven at any sweep width up to ±6 Mc. Sweep rate is 60 cps. 1300-A, $1950.

5kc-50 Mc 1 watt output at rf; internal 400- and 1000-cps modulation. Excellent shielding for bridge use. 1330-A, $635.

STANDARD-SIGNAL GENERATORS

5 kc-50 Mc up to 2 volts open-circuit output. 20c to 15 kc external, or 400c internal modulation adjustable from 0 to 80%. 1001-A, $975.

16 kc-50 Mc 4 volts open-circuit output. Incremental frequency changes possible to 0.01%. 50c to 15 kc external, or 400c and 1000c internal modulation adjustable from 0 to 100%. 805-C, $1975.

40-250 Mc, 1021-AV, $740;
250-920 Mc, 1021-AU, $725;
1 volt out at 50 ohms. 30c to 15 kc external or 1 kc internal modulation adjustable from 0 to 50%. Both instruments use same cabinet, power supply, and modulation unit, $290. VHF Oscillator Unit $450, UHF Unit $435.

RF, VHF, UHF

0.5-50 Mc, 1211-B, $295*
50-250 Mc, 1215-B, $210*
65-500 Mc, 1208-B, $230*
180-600 Mc, 1209-BL, $260*
250-960 Mc, 1209-B, $260*
450-1050 Mc, 1361-A, $285*
900-2000 Mc, 1218-A, $465*

The best general-purpose oscillator buy available anywhere . . . compact . . . low-cost . . . covers wide frequency range with single-dial control . . . high output . . . good shielding . . . excellent stability . . . useful for all types of laboratory measurements or can be built into special assemblies . . . readily adapts to sweep operation . . . can be modulated by other signal sources.

PULSE GENERATORS

Popular general-purpose Pulser; repetition rates, 30c, 60c, and 100c to 100 kc in X1, X2, and X5 steps or 15c to 100 kc continuous with external drive. Duration, 0.2 μsec to 60,000 μsec. Output: 20v max. open circuit. 1217-A, $250*.

Pulse, Sweep, and Time-Delay Generator . . . a complete pulse system; repetition rates 0 to 250 kc, duration 25 mμsec to 1.1 sec, time delay 1 μsec to 1.1 sec, delay repetition rates 0 to 400 kc, sweep durations from 3 μsec to 120,000 μsec. 1391-B, $2025.

Time-Delay Generator; two independent delay circuits: 0 to 1.1 sec, and 0.5 μsec to 0.5 sec; can be combined for a total delay of 1.6 sec, or used independently as a coincidence circuit for producing pulse bursts. 1392-B, $1095.

SPECIAL-PURPOSE GENERATORS

Random-Noise Generator; 5c to 5Mc broadband noise source with up to 3v output. 1390-B, $295.

Time/Frequency Calibrator; compact secondary frequency standard with fixed outputs at 10 Mc, 1 Mc, 100 kc, and 10 kc; harmonics usable to 1000 Mc. Short-term accuracy after standardization is 2 parts in 10^7. 1213-D, $310*.

Standard-Frequency Oscillator; the "heart" of the G-R Frequency Standard. A 5-Mc crystal oscillator with a short-term stability of better than 1 part in 10^{10} per minute, as measured with 1-second samples. 1113-A, $1550.

Klystron Oscillator; compact microwave source covers range from 2.7 to 7.46 Gc (depending on klystron used). Internal 1-kc square wave modulation; may be pulse or frequency modulated from external source. 1220-A, $235* (less klystron).

*Unit Power Supply required; $50 extra.

Write for Complete Information

GENERAL RADIO COMPANY
WEST CONCORD, MASSACHUSETTS

NEW YORK, WOrth 4-2722
District Office in Ridgefield, N. J.
WHitney 3-3140

CHICAGO
Oak Park
Village 8-9400

PHILADELPHIA
Abington
HAncock 4-7419

WASHINGTON, D.C.
Silver Spring
JUniper 5-1088

SAN FRANCISCO
Los Altos
WHitecliff 8-8233

LOS ANGELES
Los Angeles
HOllywood 9-6201

IN CANADA
Toronto
CHerry 6-2171

Progress in mechanizing some of the intellectual functions has been partial and uneven.

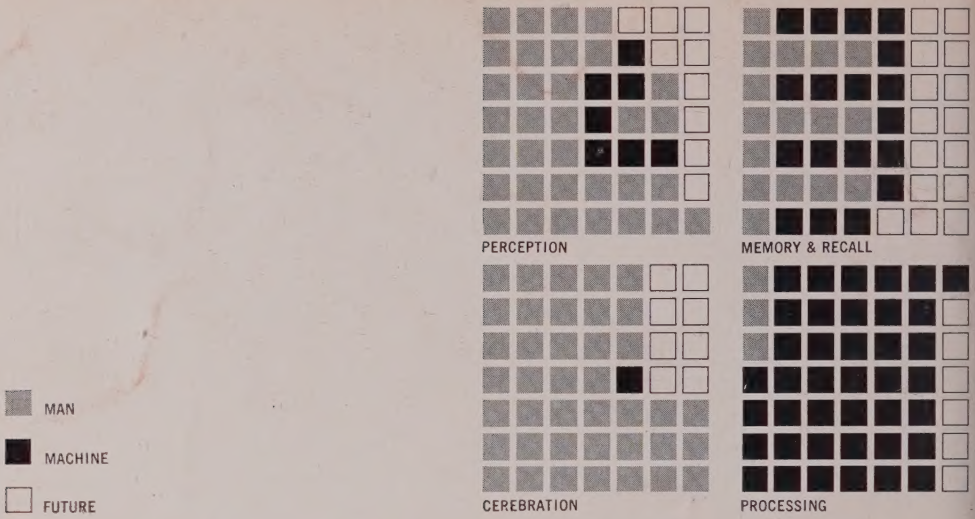

INTELLECTRONICS... Extending Man's Intellect By Electronics

Through the ages, from the invention of the wheel to the development of nuclear power plants, scientists and engineers have used matter and energy in various ways to extend man's physical powers. The needs of modern civilization now call for a greater emphasis on helping man do tasks that lie in the intellectual, rather than the physical, domain. Progress in mechanizing some of the intellectual functions has been partial and uneven, as the diagram above suggests. Our goal is to achieve a synthetic intelligence—part human and part mechanical—which combines the strongest features of both to produce a new order of intellectual power exceeding that of either men or machines operating separately.

At Ramo-Wooldridge's new Intellectronic Research Laboratory, fundamental research is being carried on in such fields as applied quantum mechanics, theoretical intellectronics and the physical phenomena associated with computer components and devices. The program includes exploration of the "room at the bottom," as exemplified by the non-equilibrium population of energy levels, the behavior of systems at temperatures near absolute zero, and other atomic and molecular properties as yet not fully exploited. Theoretical intellectronics involves the study of adaptive and self-teaching machines, and the investigation of methods for achieving a more efficient use of computers in the solution of physical problems. Still other lines of research are concerned with novel concepts of the function and organization of computers, such as the use of optical elements and the investigation of new methods of memory arrangements.

Physicists holding a Ph.D. degree or equivalent are invited to discuss their research interests in these areas with Dr. Burton D. Fried, Director, Intellectronic Research Laboratory. Inquiries may be directed to R. L. Eddy at

RAMO-WOOLDRIDGE

A DIVISION OF

THOMPSON RAMO WOOLDRIDGE INC.

8433 FALLBROOK AVENUE • CANOGA PARK, CALIFORNIA